Preparation of bismuth modified electrodes for the CO_2 reduction reaction

Sara Usai, M.Sc.

School of Chemical Science
Dublin City University

Research supervisors:

Prof. Robert J. Forster

Dr. Mary Pryce

Dr. J. James Walsh (Optum Health Services)

A thesis submitted for consideration for the award of:

Doctor of Philosophy

September 2021

Declaration

I hereby certify that this material, which I now submit for assessment on the programme of study leading to the award of Doctor of Philosophy is entirely my own work, and that I have exercised reasonable care to ensure that the work is original, and does not to the best of my knowledge breach any law of copyright, and has not been taken from the work of others save and to the extent that such work has been cited and acknowledged within the text of my work.

Signed: 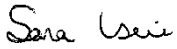 ID No.: 16213960

Date: September 07, 2021

Acknowledgments

First, I would like to thank Prof Robert Forster from the bottom of my heart for welcoming me to his research group in such a critical time of a PhD that is the last year. I am incredibly grateful for all his guidance, support, enthusiasm and kindness. His approach to science and research was incredibly inspiring to me. Second, I would like to thank Dr Loanda Cumba, not only for her contribution to the work but for all the help, the suggestions, the explanations, the scientific discussions and to show me, without knowing it, that for women in science it is possible to succeed. However, it would be unfair to thank only the scientist and not Loanda the person, for her support, for all the time spent together in the lab and outside. Those are precious moments and I will always keep them with me. I would also like to thank Dr James Walsh for his guidance and support in the first years of my PhD and for giving me the opportunity of starting my journey.

I would like to extend my gratitude to the technical staff at the School of Chemical Science. Veronica, Ambrose, Aisling, Damien, Mary, John, Vinny, Catherine, Conor and Mary have been fantastic helping me anytime I had a problem. They always had a kind word, and they always found the time to listen to me or simply for a chat. The time spent in the department would have been incredibly harder without their support.

A big thanks go to Dr Emma Coyle for all the help on the synthetical part of the work and to Dr Ross Laundy for the help with SEM and XPS analyses.

I would like to thank the guys from lab X154, from the first day over the years, Helena, Asmita, Jess, Steve, Kae and Mathavan made me feel at home and they adopted me as part of their group. Another special thanks go to Karmel, Shane and Nyanta, for being always there for me. I cannot not mention all the colleagues in DCU for the great time spent together. I had lovely moments with them.

I would like to extend my appreciation to the members of the Forester's group. Fionn, Ellie, Amanda, Eadaoin, Angelo and Miren welcomed me without reserve and made me feel one of them from the first moment. I really appreciated it!

I would like to thank my friends back in Sardinia and around the world for being there and understand my absences during these last four years. In no particular order, Lera, Franci, Lau, Michele, Nicoletta, Sara Atzori, Sara Argiolas, Roberto, Michela, Oi, Elisa, Elena, Vale, Nenna and Nicolas. I knew I could always count on you. Thanks to Stefano, for understanding me, for his help and patience. I extremely value your presence in my life. I need to reserve a special thanks to Serena, the other component of the azeotrope I belong to. I cannot describe how grateful I am for

the help and the support you gave me during the last 12 years, and, of course, you were there without failing in these difficult last four! I also need to thank Nicola, for his presence, help and understanding. His persona has been inspirational for me. If I become the person and the scientist that I am, it is also because of you.

I reserve a special thanks to two incredible people I was lucky enough to meet during my time here in Ireland. To my soul's sister Roberta for all the support and patience, for the unconditional understanding and the scientific and personal advice. You really have been a piece of my Sardinia in Ireland. To Dr Declan, for the huge help with the thesis, for the scientific discussions, for being constantly there for me in every step of this experience, for understanding and truly believing in me. I do not think I will be ever able to express my gratitude for all the support you constantly gave me.

Finally, I would like to thank all my family, but especially my mum, my brother, my sister-in-law, and my sister, for simply being there, constantly, no questions asked. You were always there, when it was easy but especially when it was hard.

Gràtzia de coru a totus!

Table of Contents

List of Abbreviations

[1-CM-3-MIM]	1-carboxymethyl-3-methylimidazole
[1-CP-3-MIM]	1-carboxypropyl-3-methylimidazole
AcO^-	Acetate
ATR	attenuated total reflection mode
BE	Bulk Electrolysis
BF_4	tetrafluoroborate
Bi-CMEC	Bismuth−Carbon Monoxide Evolving Catalyst
Bi-GC	Bismuth-Glassy Carbon
BMIM	1-Butyl-3-methylimidazolium
CCS	Carbon Capture and Storage
CCU	CO_2 Capture and Utilisation
CDR	Carbon Dioxide Removal
CE	Counter Electrode
CEs	current efficiency
CNT	Carbon Nanotubes
CO_2RR	CO_2 Reduction Reaction
CPE	Control Potential Electrolysis
CPMI	1-(3-cyanopropyl)-3-methyl imidazolium
CV	Cyclic Voltammetry
CVs	Cyclic Voltammograms
DBU	1,8-diazabicyclo[5.4.0]undec-7-ene
DES	Deep Eutectic Solvent
DFT	Density Functional Theory
DI	dionisated
DMSO	Dimethyl sulfoxide
EDX	Energy Dispersive X-ray Spectroscopy
EMIM	1-ethyl-3-methylimidazolium
ECSA	Electrochemical Surface Area
ESI-MS	ElectroSpray ionization-Mass Spectroscopy
FAP	tris(pentafluoroethyl)trifluorophosphate
Fc/Fc+	Ferrocene/Ferrocenium
FE	Faradaic Efficiency
FEPA	Federation of European Producer of Abrasives
FE-SEM	Field Emission Scanning Electron Microscopy
FTIR	Fourier-transform infrared spectroscopy
GB	Grain Boundaries
GCE	Glassy Carbon Electrode
HEMIM	1-(2-Hydroxyethyl)-3-methylimidazolium
HER	Hydrogen Evolution Reaction
HMIM	1-Hexyl-3-methylimidazolium
HSA	High Surface Area
IL	Ionic Liquid
IPCC	Intergovernmental Panel on Climate Change

ISO	International Organization for Standardization
M	metal
Magn	Magnification
MEA	monoethanolamine
MeCN	Acetonitrile
MW	Molecular Weight
NHE	Normal Hydrogen Electrode
NMR	Nuclear Magnetic Resonance
NN	Nanoneedle
NP	Nanoparticle
NW	Nanowire
OD	Oxide-Derived
ORR	dioxygen reduction reaction
OTf	trifluoromethane sulfonate
PEG	polyethene glycol
PF6	Hexafluorophosphate
POHIL	1-(3-hydroxypropyl)-3-methylimidazolium
QRE	Quasi-Reference Electrode
RE	Reference Electrode
RHE	Reversible Hydrogen Electrode
SCE	Saturated Calomel Electrode
SEIRAS	Surface-Enhanced Infrared Absorption Spectroscopy
SEM	Scanning Electron Microscopy
SHE	Standard Hydrogen Electrode
SPE	Screen Printed Electrodes
SS-Ag-NPs	Similar Sized Ag Nanoparticles
TBA	Tetrabutylammonium
TCB	Tetracyanoborate
TEM	Transmission Electron Microscopy
THF	Tetrahydrofuran
WE	Working Electrode
XANES	X-ray Absorption Near Edge Structure
XPS	X-ray Photoelectron Spectroscopy
XRD	X-ray powder diffraction

List of Symbols

Roman symbols

symbol	meaning
E_{ad}	applied potential for deposition
E_{pa}	anodic peak potential
E_{pc}	cathodic peak potential
E_h	highest potential applied
E_l	lowest potential applied
r_f	roughness factor
A_{real}	real surface area
A_{geo}	geometrical area
Q_{exp}	experimental charge
j	current density
j_a	anodic current density
j_c	cathodic current density
$A_{capacitance}$	area obtained from capacitance value
i_{max}	maximum current for the current transient
i_p	current at the peak maximum
i_{pa}	current at the anodic peak maximum
i_{pc}	current at the cathodic peak maximum
t_{max}	time at which the maximum current was observed in the current transient
Q_A	anodic charge
Q_C	cathodic charge

Greek symbols

symbol	meaning
Φ	diameter
ν	scan rate
σ	charge density
ΔE_p	peak to peak separation

List of Figures

List of Tables

Abstract

Preparation of bismuth modified electrodes for the CO_2 reduction reaction

Sara Usai

In this work, several Bismuth electrodes were produced for the electrochemical reduction of CO_2. Systematic studies were performed to investigate how modification of the surface of the electrodes would influence the catalytic activity of the system. The modifications were performed, by first, performing several electrodepositions, in order to obtain electrodeposits with different characteristics (Bi modified electrodes); and second, using co-catalysts (ionic liquids, ILs). During the electrodepositions, the morphology and distribution of the particles were investigated as a function of the deposition parameters with a view to optimising the bismuth surface coverage, the electrocatalytic properties and the meso to nano porosity so as to enhance mass transport. By controlling the waveform and additives within the deposition solution, several types of bismuth micro- to nano-structures could be produced ranging from fractals to approximately spherical particles. Bulk Bi electrodes were also produced so that a standard Bi electrode was set for comparison purposes. Finally, the Bi electrodes were then tested for the reduction of CO_2 in aqueous solution in the absence and presence of commercial (1-Butyl-3-methylimidazolium tetrafluoroborate) and modified (1-carboxypropyl-3-methylimidazole tetrafluoroborate) ILs. The systems investigated within this work did not show high selectivity toward CO_2 reduction and the main process at the electrode surface was the production of H_2. The different parameters influenced the selectivity and the catalytic currents marginally. In addition, the modified Bi electrodes did not show a good stability during catalysis. For this reason, to try and increase the stability of the Bi catalysts, screen printed Bi electrodes were produced. The electrodes were produced first by preparing inks using Bi metal particles and then printing them on inert substrates. The obtained electrodes were characterised and finally tested via preliminary cyclic voltammetry experiments. This approach allowed more robust electrodes and higher reproducibility.

Chapter 1 : Introduction and literature survey

1.1 Generalities and importance of CO_2 reduction

In the last 50 years, the amount of carbon dioxide (CO_2) in the atmosphere has increased exponentially as a result of human activities, leading to global warming[1]. Normally, CO_2 is present in the atmosphere at around 25% of the greenhouse gas total[2]. The greenhouse gases are compounds able to absorb a significant portion of the infrared (IR) radiation arriving from the sun and trap it between the atmosphere and the surface of the Earth. This process is called the greenhouse effect and it is one of the main factors determining the surface temperature of the Earth[3,4]. The presence of greenhouse gases is therefore necessary to maintain sustainable conditions for life[5]. Among the greenhouse gases, CO_2 is essential for the survival of plants as it is one of the primary reagents for the production of glucose during photosynthesis. The quantity of CO_2 is balanced by a variety of phenomena happening in the atmosphere and on the surface, the totality of which is called the carbon cycle. Briefly, the carbon cycle consists of two main processes of CO_2 exchange of: one, between the atmosphere and the oceans and two, between the atmosphere and terrestrial ecosystems. Since 1900, the oceans had absorbed 330 gigatons of CO_2 from the atmosphere, while the terrestrial ecosystems 450 gigatons. On the other hand, they had emitted around 330 and 440 gigatons of CO_2, respectively[6]. Anthropogenic emissions constitute a significant portion of the emitted CO_2 but they are not balanced by any other processes. For this reason, human activity is the main cause of the increase of the CO_2 levels in the atmosphere in the last century[7,8]. This quantity increased by around 8% between 2002 and 2019: from 373 to 411 ppm (Figure 1.1)[9], at a rate of 2.11 ppm per year, while it was half this magnitude (1.06 ppm per year) from 1965 to 1974[10].

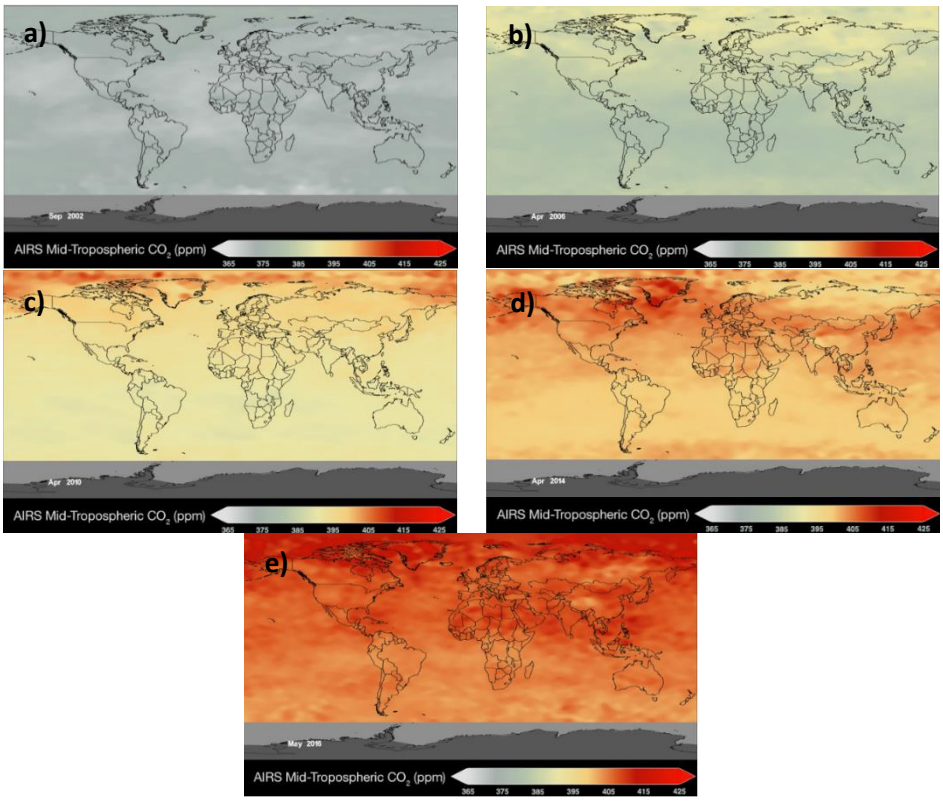

Figure 1.1: Mapping of the quantity of CO_2 in the atmosphere obtained with the Atmospheric Infrared Sounder (AIRS) during a period of 14 years. Imagines acquired in a) 2002, b) 2006, c) 2010, d) 2014 and e) 2016. The quantity of CO_2 is represented by a range of colours, starting from light grey (365 ppm) to intense red (425 ppm)[9]

Rising levels of CO_2 in the atmosphere have resulted in several consequences. For example, an increase of the positive radiative forcing phenomenon is observed as a consequence of higher concentrations of greenhouse gases, meaning that more solar radiation is absorbed by the atmosphere and emitted to the surface, with a consequent rise in the global temperature. Higher temperature values lead to larger quantities of moisture in the atmosphere resulting in an intensification of precipitation[2]. Interestingly, even if an increase in the mean precipitation is observed, some areas became drier, such as the subtropical regions and the tropical countries of Africa and Indonesia[11]. Another phenomenon stemming from the increase of the global temperature is the decrease of the area and the thickness of the Arctic sea ice that causes, among other effects, the rise of the sea levels[12]. If CO_2 emission are solely considered, the effects of an increase of this compound in the atmosphere can be varied, such as modifications in the physiology of organisms[11] and the acidification of the oceans, resulting from the formation of carbonic acid and consequently of bicarbonate and carbonate species[13]. On the basis of these findings, it is therefore necessary to both reduce CO_2 production, caused by the intensification of industrial activities and by the increase of energy exploitation, and to decrease the actual quantity in the atmosphere[14]. According to the first of the series of the special reports in the current Sixth Assessment Report (AR6) of the Intergovernmental Panel on Climate Change (IPCC), "the Special Report on Global Warming of 1.5 °C (SR15)"[15], it is necessary to reach net zero emissions by 2050,

meaning that the emissions of CO_2 need to be balanced by CO_2 capture, to maintain global temperature rise below 1.5°C, acknowledged as the temperature above which catastrophic effects will likely be observed. For this reason, the synergy between Carbon Dioxide Removal (CDR) and Carbon Capture and Storage (CCS) techniques is necessary[16,17] to ensure the removal of the quantity of CO_2 already present in the atmosphere without any additional release. Several processes can be used for the capture of CO_2 and both chemical and physical methods can be equally convenient[18]. The removal of CO_2 from streams of gas (such as methane) has been performed using aqueous amine solutions since the 1930s[19]. In this process, the CO_2 is chemically adsorbed by the amines (via carbene formation) and reversibly stripped in a subsequent thermal regeneration step[20]. This technique is nowadays commercially available and 30 % aqueous monoethanolamine (MEA) solution is most commonly used for this application[21] (see Figure 2.1 for MEA structure).

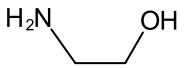

Figure 1.2: monoethanolamine (MEA) structure

Unfortunately, for regenerating the amine solution a large amount of energy is necessary (the 30% of the total energy of the power plant would be estimated to be necessary for the recovery of the amine solution), making the process not particularly economically favourable for large scale CO_2 capture[21]. For this reason, several techniques and adsorbents have been tested and employed for different applications[22]. Ionic liquids (ILs), are of particular interest seemed to be particularly interesting as, among other properties, they present low vapour pressure and very high solubility of CO_2[23]. In addition, as they are currently under investigation as co-catalysts for the electrochemical reduction of CO_2[1,24–26], they can be considered particularly suitable for CO_2 Capture and Utilisation (CCU) processes. CCU processes can be physical or chemical: in the first case, captured CO_2 remains unreacted and can be directly used in industry or in several products such as dry ice, fire extinguishers, carbonate beverages and aerosols[27]; the chemical utilisation processes involved the capture and successive transformation of CO_2 into useful compounds or fuels[28]. Several compounds such as urea[29], dimethyl carbonate[30], dimethyl ether[31] and different polymers[32] can be synthesised by using CO_2 as a starting material.

A very interesting and useful application is the utilisation of CO_2 for the production of fuels, as allows the use of an unwanted product to obtain energy. The research performed in this area has increased significantly as several fuels can be obtained from CO_2: the production of C1 products such as CO[33], methane[34], methanol[31] or multi-carbon products (through Fisher-Tropsch reaction)[35]. The major challenge is triggering the reduction of CO_2, as it is a particularly stable molecule and a significant amount of energy is necessary[28,36–38]. Several approaches have been used for converting

CO_2 into fuels, from thermochemical[39] to biological[40] and from electrochemical[41] to photochemical[42] processes. Currently, the adoption of electrochemical and photochemical systems appears to be the most promising methods for the utilization of CO_2[37]. In particular, electrochemical CO_2 reduction seems to be the most convenient as the photocatalysts currently in use are usually rare and expensive and they can support current densities of only around 10-20 mA/cm^2, while common electrocatalysts can reach current densities 10 times higher[42]. In order to develop a functioning system for the CO_2 reduction reaction (CO_2RR), thermodynamic and kinetics consideration must be assessed. In order to be reduced, the shape of CO_2 needs to change from linear to bent, as the known intermediate radical anion, $CO_2^{-\bullet}$ [43], exhibits a bent configuration[44]. In aqueous solution at a concentration of 1 M, at neutral pH and at room temperature and pressure, the necessary energy for the formation of the intermediate is around 2 eV (Figure 1.3a), that, in terms of standard potentials vs the Normal Hydrogen Electrode (NHE), is equal to -1.90 V[44] (Reaction r1.5). Since all CO_2RR steps, except the one electron reduction to the $CO_2^{\cdot-}$ radical anion, are proton-coupled, the reactions exhibit Nernstian electrochemistry, meaning that the potential for the half reaction as a function of the pH is given by the Nernst equation (see Equation 1.1)[45].

$$E = E^0 + \frac{RT}{nF} ln \frac{C_O}{C_R} \quad (1.1)$$

where E is the potential for the half reaction; E^0 is the formal potential for the reaction; R is the universal gas constant, F is the Faraday constant, T is the temperature (in K), C_O is the concentration of the specie in the oxidised form; and C_R is the concentration of the specie in the reduced form. This has implications for the state CO_2 occupies in solution (Figure 1.3b). In theory this is advantageous as a specific pH value one product can be favoured over another by applying a specific potential. However, this is not actually straightforward, as the kinetics of the reactions needs to be also considered (for example in the case of HER vs CO_2RR).

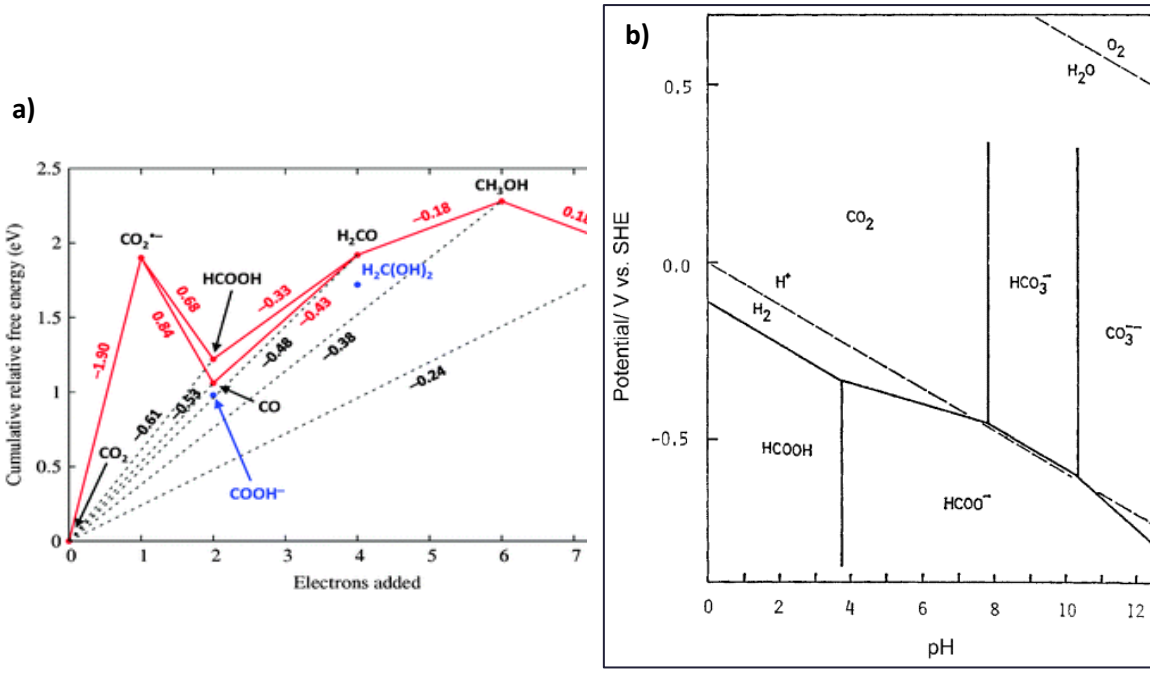

Figure 1.3: a) Latimer-Frost diagram for the multi-electron and multi-proton reduction of CO_2[44]; b) Pourbaix diagram for a CO_2-saturated aqueous solution[43]

The possible one-carbon atom products that can be formed in a CO_2-saturated aqueous system with the correspondent necessary potential are shown in the reactions (r1.1) to (r1.6). Reaction (r1.1) represents the one-electron reduction of CO_2 to the bent intermediate $CO_2^{-\bullet}$. All the standard potentials in Reaction from (r1.1) to (r1.6) are against NHE, at pH 7.

$$CO_2 + e^- \rightarrow CO_2^{-\bullet} \quad E^\circ = -1.90\,V \tag{r1.1}$$

$$CO_2 + 2H^+ + 2e^- \rightarrow CO + H_2O \quad E^\circ = -0.53\,V \tag{r1.2}$$

$$CO_2 + 2H^+ + 2e^- \rightarrow HCOOH \quad E^\circ = -0.61\,V \tag{r1.3}$$

$$CO_2 + 4H^+ + 4e^- \rightarrow HCHO + H_2O \quad E^\circ = -0.48\,V \tag{r1.4}$$

$$CO_2 + 6H^+ + 6e^- \rightarrow CH_3OH + H_2O \quad E^\circ = -0.38\,V \tag{r1.5}$$

$$CO_2 + 8H^+ + 8e^- \rightarrow CH_4 + H_2O \quad E^\circ = -0.24\,V \tag{r1.6}$$

The formation of methane (r1.6), methanol (r1.5) and formaldehyde (r1.4) are multi-electron and multi-proton reductions that need an adequate reservoir of electrons, such as organometallic catalysts or metal electrodes, and a ready source of protons. For this reason, aqueous systems can be considered particularly suitable for CO_2 reduction. However, the competing reaction for the reduction of CO_2, the Hydrogen Evolution Reaction (HER), occurs at more positive potentials (r1.7)

than the formation of $CO_2^{-\bullet}$, making CO_2RR particularly challenging in aqueous solutions. Therefore, it is necessary to carefully evaluate the concentration of protons in the system, and the design of catalysts and working electrodes which exhibit favourable kinetics for CO_2RR over HER. The approach used in this work to try an decrease the importance of

$$2H^+ + 2e^- \rightarrow H_2 \quad E^\circ = -0.41\,V \tag{r1.7}$$

In conclusion, in the last 55 years, CO_2 concentration in the atmosphere increased of almost 100 ppm because of anthropogenic activities contributing to global warming and consequently to several negative consequences for our planet. The capture and utilisation of CO_2 presents several challenges, such as the capture of CO_2 from the atmosphere in order to store and then utilise it; the intrinsic stability of the CO_2 molecule; and the coexistent, competitive HER, that occurs at more positive potentials than the CO_2RR. For this reason, several approaches and techniques have been under investigation to solve these challenges. As far as the utilisation of CO_2 is concerned, the electrochemical reduction of CO_2 seems to be particularly promising, especially when using metal electrodes.

1.2 Metal electrodes for electrocatalysis

Metal electrodes have been extensively used as electrocatalysts for a wide range of applications[46]. For example, metal electrodes have been investigated for the catalysis of several types of reaction, including the hydrogen evolution reaction (HER), the oxygen evolution reaction (OER)[47], the synthesis of organic molecules[48,49] and inorganic transformations[50]. Noble metals exhibit high conductivity, chemical and thermal stability, low toxicities and resistance to oxidation. These properties with their ability of accelerate and control the rate of many types of reactions make them excellent candidates as catalytists[51]. However, because of their low abundance and high costs, less expensive but equally active alternative materials have been sought[52,53]. Other approaches have been used, e.g., the formation of thin metal films, the use of metal nanoparticles (NPs), modification of surfaces with other metals or the formation of alloys[54], using more abundant, more sustainable and low costs metals, like Co, Fe, Ni, Cu, Bi[47,55–59], or their oxides[60]. Some of these metals are actually by-products of other metals extraction (like Bi) or easier to recover and recycle (like Cu). Here, the use of Bi as a metal electrode for electrocatalytic applications will be discussed.

1.3 Bi electrodes

Bismuth is an element in Group 15 that presents metal characteristics but shares many properties with semiconductors and insulators. For this reason, it is considered a semi-metal[61]. It has an electronic configuration of $[Xe]4f^{14}5d^{10}6s^26p^3$ and it uses the 3p electrons to form bonds.

For this reason, the majority of its compounds present an oxidation state of +3.[62] Bismuth is a soft metal that forms large and brittle crystals[63]. It presents a silver-pinkish colour with shades of different colours (from yellow to green and from blue to pink) depending on the thickness of the native oxide. Bi has the highest resistivity and diamagnetic properties among the metals[63]. In addition, because Bi (bismuth) presents particular transport properties, it has been investigated for electronic applications[64,65]. Bismuth and its compounds are used for other several applications, such as cosmetics, paints, medicine, formation of alloys and for thermoelectric devices. In the last 20 years, Bi electrodes have attracted increasing attention in electrochemistry in a variety of applications because of its environmentally friendly character[66]. In comparison with other heavy metals like lead, arsenic and mercury, Bi presents low toxicity[67]. In addition to being a relatively abundant element, bismuth is a by-product of other metal refining, like Pb, Cu and Sn, making its price relatively low and stable[68].

Since the beginning of the 21st century, the use of Bi electrodes for substituting mercury electrodes in the detection of heavy metals has been established because of their similar electrochemical behaviour and comparable results[69–71]. They have shown a very similar potential window (the negative potential limit is around -1.6 V vs Ag/AgCl in acetate buffer solutions) and a similar response for heavy metal detection. Bi and Hg present similar responses even when deposited as a thin film on different substrates (like carbon)[69]. The characteristic that makes Bi electrodes good candidates for the detection of heavy metals is the ability of Bi to form alloys with several metals. Once the alloy is formed, the quantity of the other metal can then be quantified via stripping voltammetry[72]. A variety of metals have been detected using Bi electrodes, like lead[73], cadmium[74], thallium[75], molybdenum (VI)[76], nickel[77], cobalt[78] and zinc[79]. These heavy metals were detected via stripping voltammetry, in several samples such as water[80], soil[81], biological samples[82], herbs[83], ceramics[84] and food[85]. In addition, Bi electrodes have been used to detect a variety of organic molecules like riboflavin[86], neonicotinoid pesticides[87], phenol[88], nitrophenols[89], quinine[72] and the mycotoxin deoxynivalenol[90]. Recently, Bi electrodes have been investigated for energy applications. For example, in the field of energy storage they have been used as anodes for magnesium-ions batteries[91–93]. In addition, its oxide, Bi_2O_3, has been extensively investigated as a promising supercapacitor[94–98]. Another application in which Bi has been attracting increasing attention is the electrochemical reduction of CO_2 because of its ability to suppress the HER[99–106]. The generalities of the CO_2 reduction are discussed in Section 1.1, while the use of Bismuth for this application is considered in depth in the final section of this literature review (see Section 1.6.1.1).

In this project two types of Bi electrodes were produced and investigated: a bulk Bi electrode and several Bi film electrodes. Bulk electrodes are usually formed from a solid piece of the polycrystalline metal covered by an insulator material. Film metal electrodes consist of a conductive substrate on which a film (with thicknesses ranging from the micro to nanometre scale), of the active metal, is deposited[107]. The main advantages of using metal film electrodes are the lower cost in comparison with bulk electrodes, as only a small amount of metal is required, and the fact that a cheap substrate can be used. In addition, because the film needs to be deposited on the substrate in a separate step, the characteristics of the film can be tailored for specific applications. Film metal electrodes can be prepared in a variety of ways. As far as the Bi electrodes are concerned, physical and electrochemical methods can be used based on the desired thickness and final application[108]. Some examples are: sputtering[109,110], evaporation[111,112], and electrodeposition[113–115].

1.4 Preparation of Bi electrodes

In this project several Bi electrodes were produced via electrodeposition using glassy carbon as a substrate. Several electrodes were prepared by changing several deposition parameters. For this reason, in this literature review, the preparation of Bi film electrodes via electrodeposition will be discussed in detail.

1.4.1 Electrodeposition

Electrodeposition allows the coating of a conductive substrate immersed in a solution containing the salt of the material to be deposited, which is done via electrochemical reduction[116,117]. When the deposit is metallic, in most cases it is crystalline, therefore, electrodeposition is also called electrocrystallisation[117]. The process can be performed using an external power supply (electrodeposition) or without it (electroless deposition) using a chemical reducing agent[118]. Electrodeposition has been extensively used because of its high reproducibility, low costs, easy scalability, velocity, and ease in tuning the features for fabricating materials with micro and nanostructures [116,119–121]. As far as electrodeposition is concerned, there are two main ways to start the formation of the deposit: by applying a fixed potential (potentiostatic method) or by applying a specific current density (galvanostatic method). Both techniques have their advantages and disadvantages, but in general, potentiostatic depositions are used when control over the particle morphology is desirable and the underlying mechanism are to be studied[122], while galvanostatic electrodeposition was demonstrated to be more effective in controlling the quantity of material electrodeposited and therefore the thickness of the film[123,124]. For the production of Bi electrodes, both techniques have been widely used. One of the main advantages of using electrodeposition is

the high versatility in producing electrodeposits with different characteristics. However, this could also be a disadvantage as several factors need to be controlled to obtain the desired film.

1.4.1.1 Factors that influence electrodeposition

Several factors influence the characteristics of an electrodeposited film, like pH, temperature, time, composition of the electrodeposition bath, type of substrate, mass transport conditions, applied potential (for potentiostatic electrodeposition) or current density (for galvanostatic electrodeposition) and the presence of additives[125,126]. In this section some of these factors are presented and discussed and their influence on the final deposit is given. In particular, the factors discussed here are:

1. the magnitude of the applied potential (for potentiostatic electrodeposition) or current density (for galvanostatic electrodeposition)
2. the modes of application of the potential
3. the influence of the substrate on the overpotential
4. the use of additives

Current density and applied potentials are two decisive parameters as they control the nucleation and the deposition rate[117,127,128]. When they are changed, the morphology of the particles is usually affected. This has been observed for different metallic electrodeposits like nickel[127], iron[129], tin[130] and copper[131]. For example, in tin electrodeposits[130], lower current densities (<0.3 A/cm^2) resulted in pyramidal crystallites, while when a range of current densities between 0.5 and 1.0 A/cm^2 were used, dendritic structures were observed. As far as Bi electrodeposits are concerned, similar trends have been observed[115,132–141]. Despite the fact that these parameters were not varied withing this project, as will be seen, many other parameters were varied, which highlights the many conditions that influence the final characteristics of the prepared deposit. In a work of Das and Sangaranarayanan[132], different morphologies were obtained for Bi crystallites when three different potential values were applied. In a deposition solution containing 10 mM of $Bi(NO_3)_3$, at -0.15 V triangle particles were obtained, at -0.3 V microspheres were formed and at -0.5 V tripods were produced (see Figure 1.4).

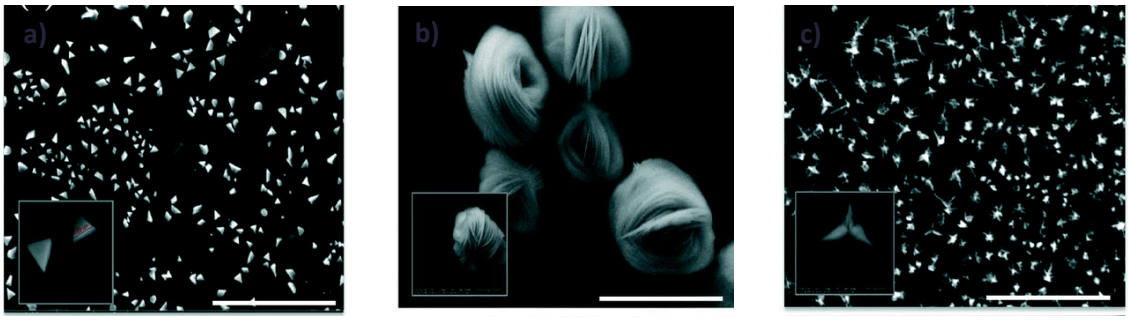

Figure 1.4: SEM images of of various microstructures: a) triangles; b) spheres; and c) tripods. The different morphologies were obtained by changing the applied potential for the electrodeposition

The applied potential is important for the features of the electrodeposit as it determines the rate of the deposition process and the adsorption of the active components from the solution[117]. For this reason, the value of the applied potential is important to finely tune the electrodeposit. To investigate the effect of the applied potential, potentiodynamic studies of the electrode-deposition bath system are usually performed. It is common practice to acquire cyclic voltammograms (CVs) or linear sweep (LS) curves before the electrodeposition steps, to obtain information about the equilibrium, the nucleation potential and the type of processes that control the electrodeposition. In Figure 1.5a, the CVs obtained with an n-GaAs(111)B electrode in a deposition bath containing 2 mM of Bi^{3+} is shown[142]. The grey curve corresponds to the first scan, while the blue to the second scan. The difference in the position of the cathodic peak potential (E_{pc}) in the two curves is due to the presence of adsorbed H_2 on the substrate in the first scan. In the blue curve, two crossovers are observed: the more positive crossover (≈ 0.0 V vs Ag/AgCl) is the potential of equilibrium for the reaction Bi^{3+}/Bi^0, while the more negative one (≈ -0.1 V vs Ag/AgCl) is the onset potential of the Bi nucleation on a different substrate than Bi. This means that the difference between the two crossovers is the overpotential, η, for the nucleation of Bi on the n-GaAs(111)B electrode. By varying the value of the overpotential, the rate of nucleation can be modified, as it can be seen from the current transient curves in Figure 1.5b.

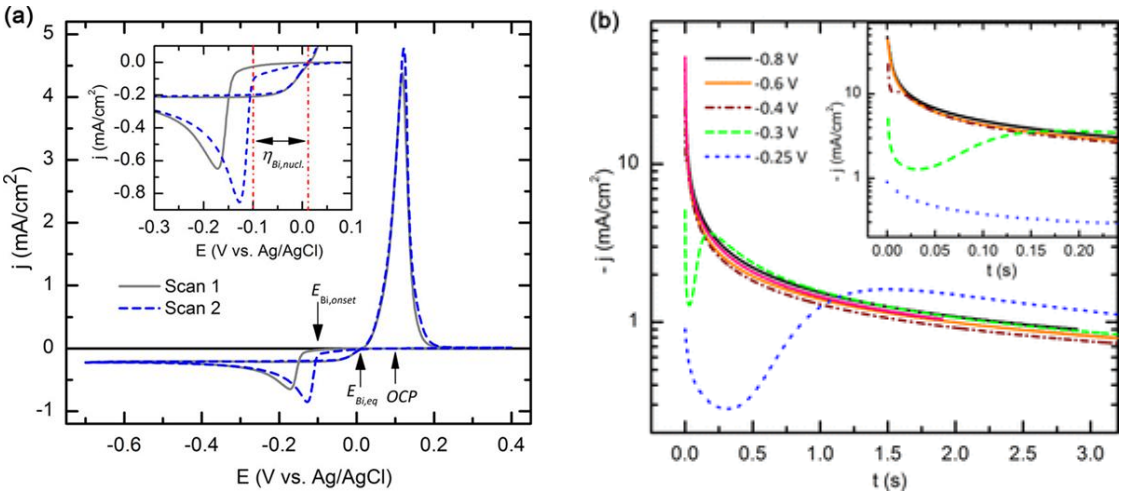

Figure 1.5: a) Cyclic voltammetry scans performed at 10 mV/s on the GaAs(111)B substrate in the 2 mM Bi(III) solution and b) Current density transients for Bi nucleation on n-GaAs(111)B substrates at different overpotentials [142]

The type of nucleation and growth can be evaluated by fitting the current-time transients. If the growth is under diffusion control, the end of the transient will be in agreement with the Cottrell Equation[115], which means that a linear response is observed between the current and $t^{-1/2}$ (see Equation (1.2)[45]).

$$i = \frac{nAFc_j^0\sqrt{D_j}}{\sqrt{\pi t}} \qquad (1.2)$$

where i is the current, n the number of electrons, F the Faraday constant, A the area of the (planar) electrode, c_j^0 the initial concentration of the reducible analyte j, D_j the diffusion coefficient for the species j and t the time. If the electrodeposition is under diffusion control, the type of nucleation can be evaluated using several models[143]. For example, for a two-dimensional (2-D) nucleation, the Bewick, Fleischmann and Thirsk model can be used[144]. On the other hand, for a three-dimensional (3-D) nucleation, the Scharifker and Hills model for 3-D multiple nucleation sites with diffusion-controlled growth can be used[145]. The Scharifker and Hill model describe the 3-D nucleation between two limiting cases: the progressive and instantaneous nucleation. The progressive case is characterised by slow rates of nucleation, while the instantaneous by fast rates of nucleation, leading to the coexistence of nucleation during the growth of the crystallites in the first case, while a well-separated distribution over time of the nucleation and growth on the second case. The effect of the applied overpotential on the deposition mechanism and the morphology of the Bi particles was investigated by Yang and Hu on glassy carbon electrodes (GCE)[115]. By using the Scharifker and Hills model, they observed that, at the same concentration of Bi precursor (20 mM in 1 M HNO_3), a variation of the applied potential lead to a change in the mechanism of nucleation and growth. By increasing the applied potential (-0.3 V), smaller and more densely packed crystallites are observed (Figure 1.6a), a factor that well corresponds with the instantaneous mechanism. On the other hand,

for a less negative applied potential (-0.1 V), the crystallites are larger and less densely distributed on the surface, a characteristic of progressive nucleation (Figure 1.6b).

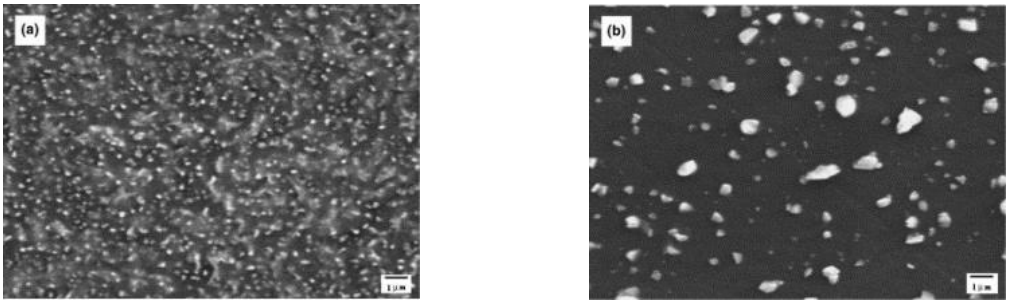

Figure 1.6: SEM micrographs of bismuth electrodeposits on glassy carbon electrodes obtain in solution 20 mM Bi^{3+} in 1 M HNO_3, for 10 seconds (a) −300 mV (b) −100 mV [115]

Similar results were obtained in another study[133], in which Bi was electrodeposited on fluorine-doped tin oxide (FTO) coated glass substrates from solutions containing $Bi(NO_3)_3$ and the complexing agent triethanolamine (TEA). Nucleation was progressive for low applied potentials (-0.25 and -0.3 V vs SCE), while for more negative potentials (up to -0.5 V vs SCE), nucleation was instantaneous. In contrast, for the deposition of Bi on indium tin oxide (ITO) coated glass substrates from a solution 21 mM of $Bi(NO_3)_3$ in HNO_3 1M[135], the nucleation was always purely or close to purely instantaneous regardless of the potential. Similarly, in the work of O'Brien and co-workers[146], the dependence of the overpotential on the morphology of the particles was investigated. The Bi films were deposited on an Au film previously deposited onto p-Si(0 0 1) substrates with a 10 nm Cr adhesion layer from a deposition solution containing 10 vol % glycerol solution, 20−100 mM $Bi(NO_3)_3$, 1.15 M potassium nitrate, 0.33 M L-tartaric acid and nitric acid (see Figure 1.7). By varying the overpotential the compactness of the film and the morphologies of the particles changed. Specifically, at -0.05 V equiaxed grains (that are particles having equal dimension in all directions) densely packed to obtain a relatively smooth surface. Similarly, at -0.1 V the equiaxed grains were observed, however the film was rougher, because of large crystallites emerging from the surface. The films deposited at -0.2 and -0.3 V exhibited needle-like crystals over a layer of nanometre sized grains. The significant difference in the morphology of the particles at the highest and lowest applied potentials was attributed to the fact that the lowest potential is very close to the onset deposition, whereas -0.3 V is in the diffusion limited regime and close to the hydrogen evolution potential.

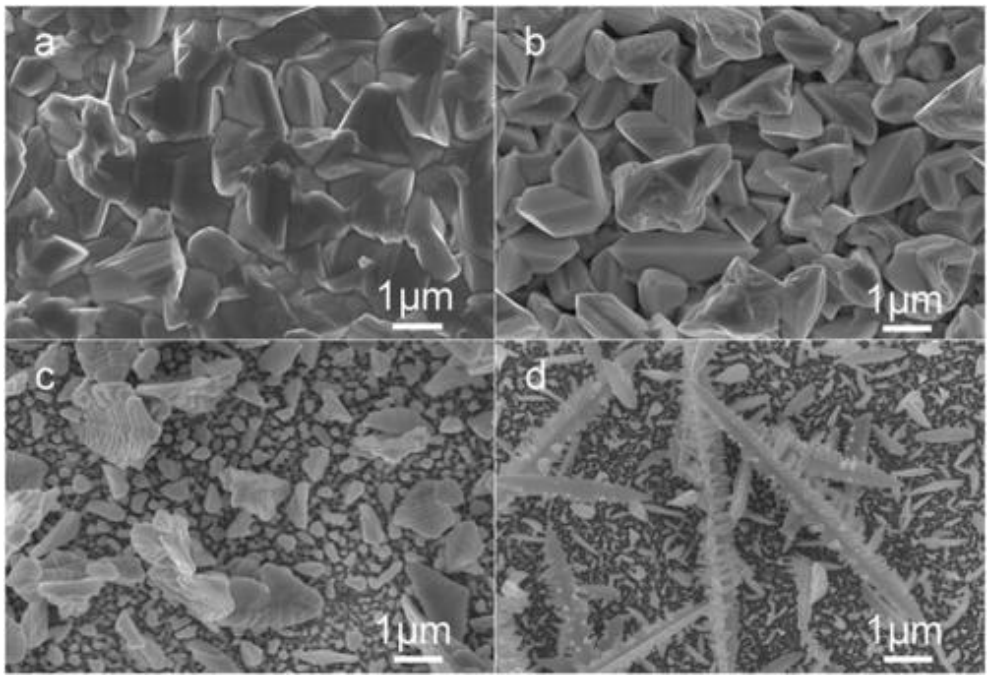

Figure 1.7: SEM images of bismuth films deposited from a 20 mM Bi(III) deposition solution at (a) −0.05, (b) −0.1, (c) −0.2, and (d) −0.3 V [146]

Not only does the value of the potential or the magnitude of the current density impact on both the morphology and the distribution of the particles, but also the way in which it is applied i.e. continuously or in pulses[121]. The latter method consists of the application of a fixed potential for a certain time, called time on (t_{on}), followed by a time off (t_{off}). The sequence t_{on} - t_{off} is repeated for a certain number of times, called cycles. Usually, during the time off, the open circuit potential (OPC) is applied, so that the current flowing into the system is equal to zero. Pulsed electrodepositions have been extensively used for their ability to improve deposition rates and the quality of the coating[128]. The pulse duration can vary largely, from a few milliseconds to several seconds. The pulsed electrodeposition is advantageous because it allows the control of the diffusion layer, the grain size and nucleation[147]. In particular, the t_{off} allows the ions from the bulk to move toward the cathode, replenishing the diffusion layer of new metal ions that were previously consumed during the t_{on}.[147] In addition, it permits the rearrangement of the deposited atoms on the surface of the electrode, creating space for the formation of new nuclei[147]. Pulsed electrodeposition has been used for the deposition of several metals, including Bi. Park et al.[141] investigated the effect of pulsed electrodeposition on the morphology of Bi films electrodeposited on a Cu plate. By increasing the number of the cycles from one to six, the particles became thinner and presented a nanoflake shape with thin and sharp edges. However, by increasing the number of the cycles up to fifteen, the crystallites merged, forming bigger crystallites. Increasing the number of the cycles in this manner can be undesirable if a large area-to-volume ratio is pursued such as for catalytic applications. Therefore, it is important to tune the parameters to achieve an

optimal morphology for a specific system. By changing the overpotential, the characteristic of the film and the sizes of the nanoflakes varied. For the lowest overpotential (25 mV), the surface of the substrate was not completely covered by the crystallites, while for the highest overpotential (-100 and -120 mV) a more efficiently covered surface was observed. The size of the particles increased as well, but the size distribution was broader with a median value equal to 83 ± 37 nm, 173 ± 37 nm and 349 ± 82 nm for 25, 50 and 80 mV respectively. Above 100 mV, polyhedrons instead of nanoflakes were obtained: the deposit was porous and the particles did not present sharp edges anymore. Similarly, in another study[148], a comparison between the deposits obtained via direct and pulsed electrodeposition was performed. The deposition was performed in a solution of 33 mM $Bi(NO_3)_3$ and 32 M HCl at -0.2 V vs Ag/AgCl on Cu hollow fibre electrodes. The direct electrodeposition was carried out for different times (30, 60, 120, 240 and 300 s), while for the pulsed electrodeposition the number of cycles was varied (number of cycles: for 30, 60, 90, 120 and 150; t_{on} = 1 s t_{off} = 5 s). By direct electrodeposition, the substrate was completely covered after 300 s and large amorphous microparticles were obtained. When the pulsed electrodeposition was used, nanosheets were formed. This difference in morphology is due to the gradient of concentration formed at the surface of the electrode during continued electrodeposition. In the first few seconds of the deposition, the nucleation of the seed occurs but the uniform growth stops because the Bi concentration at the surface of the electrode is insufficient. The nucleation rate is higher for pulsed electrodeposition as the time off allows the Bi ions to move into the diffusion layer. In general, pulsed electrodeposition leads to a more controlled and parametrically defined deposit, however, continuous electrodeposition is still broadly applied because of its simplicity and the wealth of well-recorded parameters available in the literature. Similarly, the nucleation overpotential is also discussed extensively within studies examining the electrodeposition of metals. It is important to highlight that conditions chosen in designing the system will directly influence the subsequent overpotential and therefore the growth of the film.

For example, the nucleation overpotential is influenced by the nature of the substrate, as it is dependent on the interaction between the substrate material and the metal that needs to be deposited[117]. Several works have investigated the electrodeposition of Bi on carbonaceous substrates[115,149–153]. However, extensive research has been done on the electrodeposition of Bi on metal surfaces like Cu[64,102,137,154,155], Ag[156], Au[114,157], Al[114], Pt[113,114], Ti[158], Bi[101], and on some metal oxide substrates like alumina[159], ITO[132,138,160] and FTO[133,138]. Vladislavić et al.[149] performed a comparison of the nucleation of bismuth on different carbon substrates: carbon fibre microelectrodes (CFME), glassy carbon (GCE) and graphite electrode (GPE). The electrodeposition was performed in 0.5 M HNO_3 solutions with different concentration of Bi^{3+} salt. At a fixed

concentration of Bi^{3+}, CGE and GPE did not show significant difference in the mechanism of nucleation and growth: at 10 mM, the nucleation was instantaneous, at 1 and 0.5 mM it was progressive, regardless of the potential applied, suggesting a concentration dependence on the formation of the electrodeposits. On the other hand, on CFME a concentration dependence was not observed, likely due to the types of active sites (segmented surface) presented on the carbon fibre surface. This suggests a strong influence of the structure of the substrate on the electrodeposition of Bi. An improvement of the electrodeposition process on carbon substrate, was performed in another study[150], in which the electrodeposition of Bi was performed on carbon cloth (CC) and thermically treated carbon cloth (TCC). The thermal treatment was performed at high temperatures in the presence of O_2 to increase the oxygen functionality on the surface of the electrode. After thermic treatment, the concentration of O increased from 1.2 to 6.5%, with oxygen-carbon functionalities being C=O, C-OH and COOH, with a quantity of 2.37, 2.32 and 1.81%, respectively. The surface of the thermally treated electrode was less smooth with several defects that increase the surface area (see Figure 1.8 1c and 1d). The electrodeposition was performed in a solution containing Bi_2O_3 and 3 M HCl. Bi_2O_3 was added to obtain solutions of $BiCl_3$ with concentrations of 1, 5 and 10 mM. When Bi was electrodeposited from a 1 mM solution and a current density of 320 mA/cm^2 was applied on CC, the Bi particles presented a size between 0.8 to 2 µm, three times larger than on TCC (Bi size range: 200-400 nm). In addition, the particles on TCC were better distributed and higher in number (Figure 1.8 1e and 1f). Via DFT calculations, it was predicted that the oxygen-functional groups are the anchoring sites for Bi during electrodeposition on TCC instead of the pristine carbon surfaces. This means that the presence of the O functionalities allows, not only a more uniform distribution of electrodeposited bismuth nanoparticles, but a stronger interaction between the Bi film and the substrate, leading to a more stable deposit. When the concentration of Bi^{3+} was increased, more Bi was electrodeposited on the surface of the TCC, and an increase of the particles size was observed (Figure 1.8 2a, b and c).

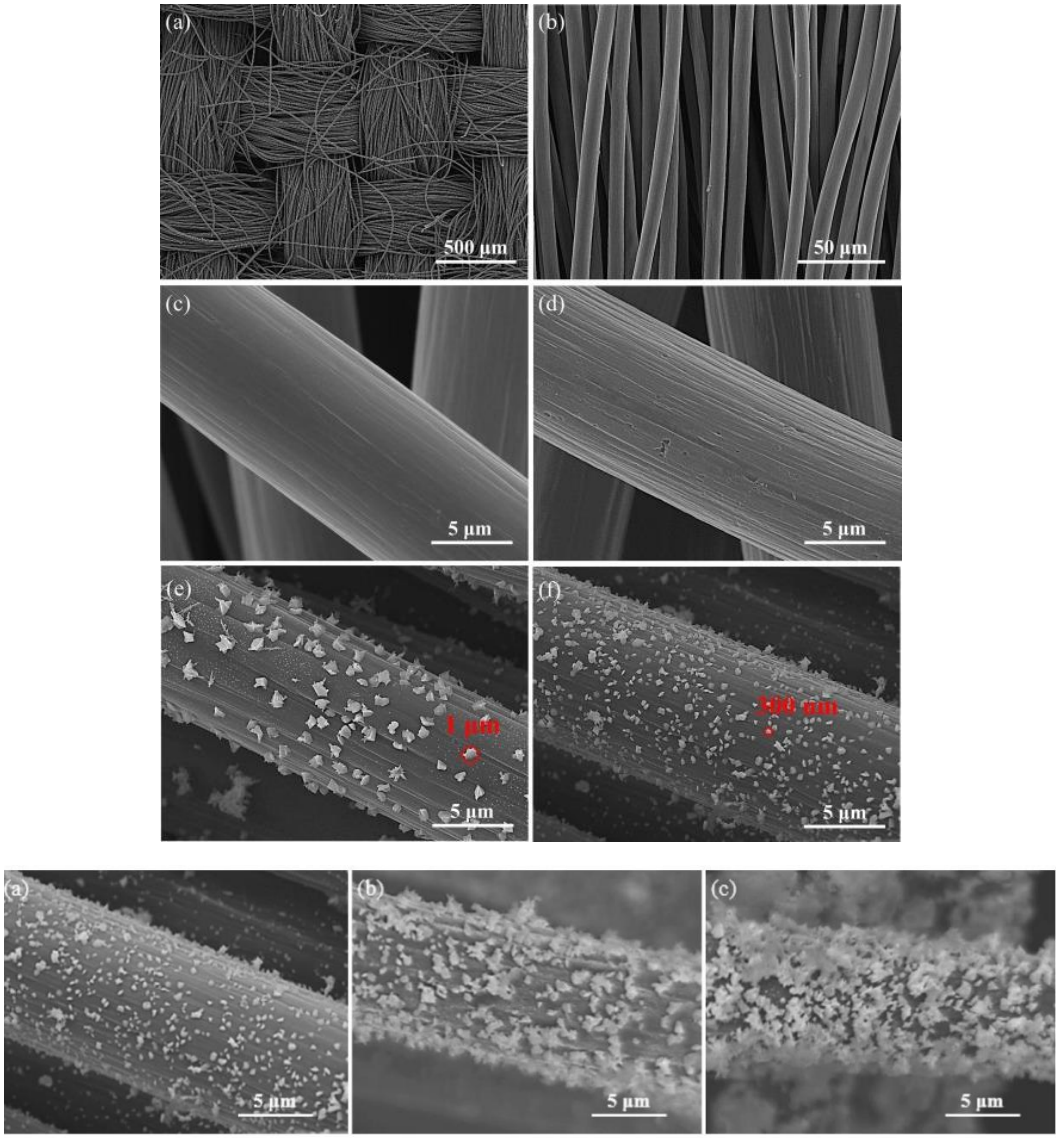

Figure 1.8: 1) SEM images of (a–c) carbon cloth (CC) electrode at different magnifications, (d) thermally treated carbon cloth (TCC) electrode, (e) CC electrode after Bi electrodeposition (BiNP-CC) and (f) the thermally treated electrode with Bi nanoparticles (BiNP-TCC); 2) SEM image of TCC with electrodeposited Bi nanoparticles at the Bi^{3+} concentration of (a) 0.001, (b) 0.005 and (c) 0.01M [150]

It has been shown GCEs present fewer interactions with bismuth in comparison with metal substrates. However, GCEs as substrates are quite advantageous because firstly, they are cheaper than most metals, and secondly, they can be inert for catalytic processes, like the CO_2 reduction reaction. The difference in interactions between glassy carbon and metals was demonstrated by Hsieh et al.[140], who studied the electrodeposition of Bi on four different substrates: GC, Ni, Pt and Au in a solution containing 10 mM $Bi(NO_3)_3$ and ethaline (1 mol equivalent of choline chloride and 2 mol equivalent of ethylene glycol) with a water content of 1.87wt% at 30°C. Cyclic voltammetry (CV) and chronoamperometry were performed to study the influence of the substrate on the Bi deposit. The morphology of the films was then analysed via scanning electron microscopy (SEM). On Ni and GC, the equilibrium and nucleation crossovers are observed during CV measurements,

suggesting an overpotential-driven nucleation/growth mechanism. The nucleation potential is less negative on Ni than on GC, indicating a stronger interaction between Ni and Bi than GC and Bi. On the other hand, on Pt and Au, underpotential deposition (UPD) is observed, leading to a smaller overpotential for the nucleation of Bi to occur. UPD consist of the deposition of a metal ion on a different metal surface at a potential less negative than the equilibrium potential for the reduction of the metal[161] and it usually occurs when the work function of the substrate is higher than the one for the metal being deposited. The work functions for Pt and Au (5.65 and 5.1 eV respectively) are higher than the one for Bi (4.22 eV)[162]. To verify the dependence of the nucleation potential on the material of the electrode, scan rate studies were performed and the E_{pc} for the different substrates were plotted as a function of scan rates (Figure 1.9). Au showed the least negative E_{pc} at any scan rate, while GC was the most negative. The fact that the steepness of the curve for GC is higher than for the metals, suggests a higher nucleation rate on metal substrates than on GC. The chronoamperometric studies were performed for Pt, Ni and GC electrodes at different potentials. In general, linear diffusion growth was observed, as the current showed a linear response versus $t^{-1/2}$, following the Cottrell equation. The nucleation mechanism was observed to depend on the nature of the substrate: on Pt and Ni, the nucleation was progressive for all the applied potentials, while on GC the nucleation tended to an instantaneous mechanism. The influence of applied potential was pronounced on GC, as at more negative potentials, the experimental curve deviated more from the theoretical curve. The morphological characterisation was performed on Bi films deposited on Ni substrate at the three applied potentials (-0.04, -0.07 and -0.10 V vs Ag/AgCl). The morphology was observed to be potential dependent. Specifically, smaller grains and a higher number of crystallites were produced at more negative potentials, suggesting faster nucleation growth than at lower potentials (Figure 1.9B, C, D). However, the deposit was coarser at higher overpotentials, while at -0.04 and -0.07 V the deposits were more compact and denser. This is due to the higher current densities produced at more negative applied potentials.

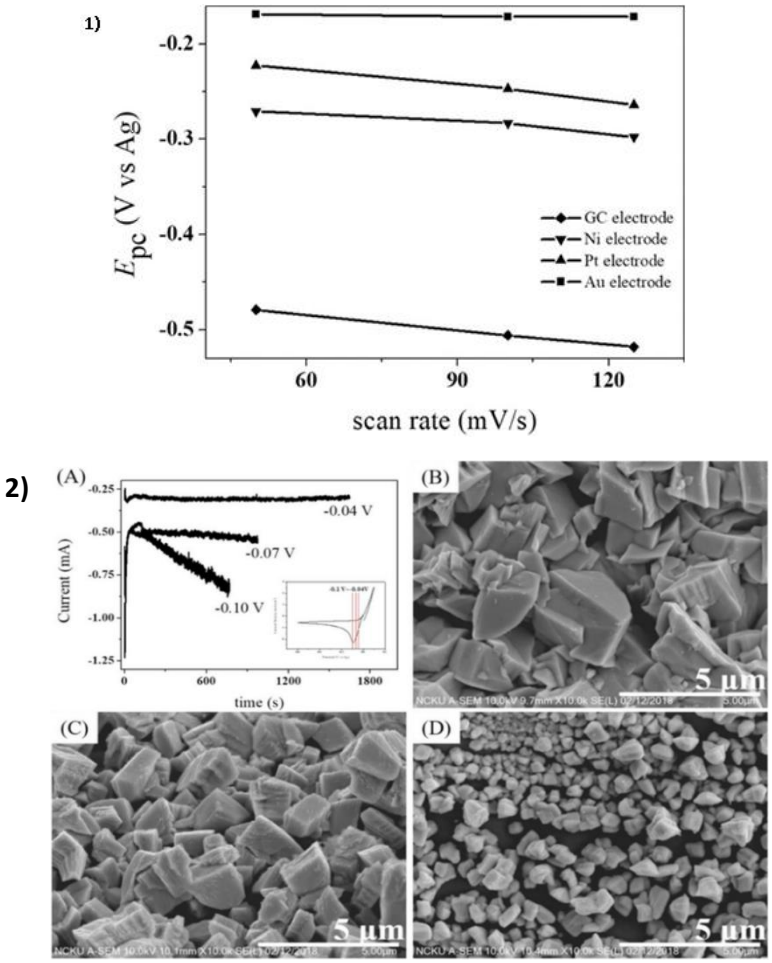

Figure 1.9: 1) Plots of the cathodic peak potential, E_{pc}, vs. scan rate of the cyclic voltammograms; 2) (A) The i-t curves recorded during the constant potential deposition of Bi on Ni foils from an ethaline DES containing 50 mM Bi(III) at the indicated potential at 30°C. Inset in (A) is the CV recorded for this solution. The SEM images of the deposits obtained at (B) −0.04, (C) −0.07, and (D) −0.10 V vs Ag/AgCl[140]

In contrast, the deposition of Bi from a deposition bath containing 10 mM $Bi(NO_3)_3$ did not show differences in the shape of the particles when Au and Cu were used as substates[157]. A rough deposit with grain sizes varying between 1 and 5 microns was observed on both substrates. However, the texture (where in this case the 'texture' refers to the distribution of the crystallographic orientations) of the deposit was stronger for Bi on Au than for Bi on Cu. This was likely due to the matching of the lattice of the Bi (0 1 2) plane with the Au (1 1 1) plane. Similarly, Giurliani et al.[156] electrodeposited Bi on two different substrates: bare Ag and a Bi layer previously formed on an Ag surface after UPD and no differences in the physical characteristic of the deposit were observed at low overpotentials (-0.74, -0.49 and -0.51 V). On the other hand, at -0.53 and -0.55 V, on Ag substrate, the ordered structure observed at low overpotentials disappeared and the roughness of the Bi film increased. In a different work[139], for the same current density value, the morphology, thickness and mechanical stability of the deposit did not change for two different substrates: stainless steel and titanium. When metal oxide electrodes were used, a significant difference in the

morphology of the particles was observed. Bilican et al.[138] studied the electrodeposition of Bi on three different substrates: a Si/Ti/Au glass, an FTO glass and an ITO glass (see Figure 1.10). Under the same deposition conditions (5 mM Bi^{3+} in 1.5 M HNO_3, applied potential = -0.28V), sharper dendrites were observed on FTO than on ITO. In general, at a fixed potential, the size of the particles was the most influenced feature by the nature of the substrate: smaller particles were formed on Si/Ti/Au, while particles up to 2x bigger were found on ITO. On FTO glasses wider polyhedrons accompanied with small dendrites were observed. Interestingly, at -0.28 V the film compactness increased with the trend Si/Ti/Au<FTO<ITO, suggesting stronger interaction forces between the Bi deposit and ITO. Two separate studies investigated the electrodeposition of Bi on FTO and ITO in similar conditions. In the first[135], Bi was electrodeposited from a solution 20 mM of Bi^{3+} on ITO at -0.22 V, and an instantaneous mechanism was suggested. In the second[133], Bi was electrodeposited from a solution 20 mM of Bi^{3+} and a potential on FTO at -0.25 V, and a progressive nucleation mechanism was observed. This might suggest that the active sites on ITO and FTO have a different interaction with Bi atoms.

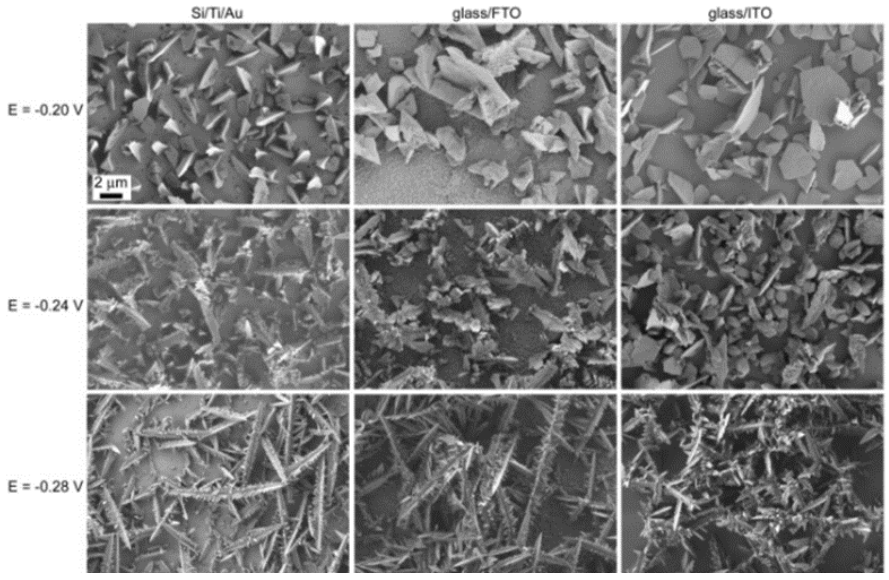

Figure 1.10: SEM images of bismuth electrodeposited at −0.20 , −0.24 , and −0.28 V for 250 seconds from a deposition bath containing 5 mM $Bi(NO_3)_3{\cdot}5H_2O$, 1.5 M HNO_3 and 0.05 M $NaC_6H_{11}O_7$ bath on Si/Ti/Au, glass/FTO, and glass/ITO substrates. The scale bar in the first image is valid for all images [138]

Another factor that strongly influences the characteristics of the electrodeposits is the composition of the deposition bath. The deposition bath can be modified by changing several factors like the concentration of the precursor salt; the acid used to dissolve the Bi salt, and therefore the pH of the solution; and the addition of an additive. A variety of electrolytes can be used for the electrodeposition of metals, and their concentrations can vary significantly from 100 to 600 g/L[128]. For Bi salts, the concentrations can vary from 350 to 380 g/l[163]. Several works studied the effect of the concentration of Bi precursor and the type of acid used for its dissolution, on the

final deposits[64,108,115,150,155]. For example, Yang and Hu[115] observed that by varying the concentrations of $Bi(NO_3)_3$, the nucleation mechanism of Bi on GCE varies: at higher concentrations, a 3-D instantaneous mechanism was observed, while by decreasing the concentration, the mechanism changed to a 3-D progressive (Figure 1.11). This suggests that high concentrations are useful for obtaining a denser and more uniform deposit. This is because, during the electrodeposition, metal ions in solution can form new nuclei on the substrate or participate in the growth of the pre-existing nuclei. High concentrations of metal precursor can promote both growth and nucleation, however, the preference of one process over the other will depend on interaction energies. If the interactions between substrate and metal are higher than the metal-metal interactions, the formation of new nuclei will be favoured. On the other hand, if the substrate-metal interactions are lower than the metal-metal ones, then growth will be preferred. Interestingly, for 20 mM Bi^{3+} solution, the beginning of the transient follows the instantaneous mechanism, while for longer times the curves move toward the progressive nucleation. This might be due to the relatively high concentration of Bi cations. For the first seconds, the concentration is high enough to favour high nucleation rates and suppress the growth. However, after six seconds, the rate of nucleation decreases and the Bi cations are probably forming new nuclei but at the same time increasing the size of the pre-existing ones.

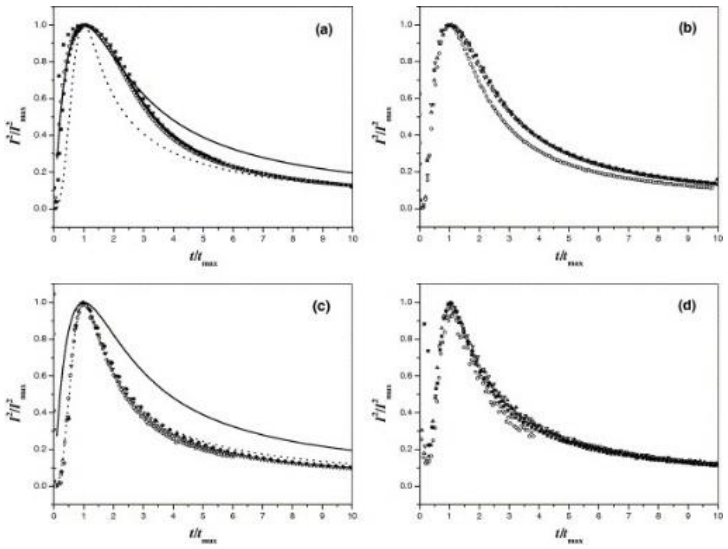

Figure 1.11: I^2/I_{max}^2 vs. t/t_{max} plots for bismuth electrodeposition onto glassy carbon electrodes from 1 M HNO_3 solutions containing (a) 20, (b) 10, (c) 5, and (d) 1 mM Bi^{3+}. The electrode potential was stepped from 0 to (■) −100, (○) −150, (▵) −200, (▿) −250, () −300, and (☒) −350 mV. The theoretical transients for instantaneous (solid line) and progressive (dotted line) nucleation were calculated according to the Scharifker–Hills model [115]

Rajamani et al.[64], studied the effect of the concentration of Bi^{3+} and HNO_3 on the morphology of Bi film on Cu substrates. For a concentration of 0.2 M HNO_3, different morphologies were observed when the Bi^{3+} concentration was changed to 1, 10 and 20 mM. Specifically, in 1 mM solution, thin,

nano-sized hexagons were obtained; in 10 mM, branched, nano-sized hexagons were observed; and in 20 mM, large crystallites were formed (Figure 1.12).

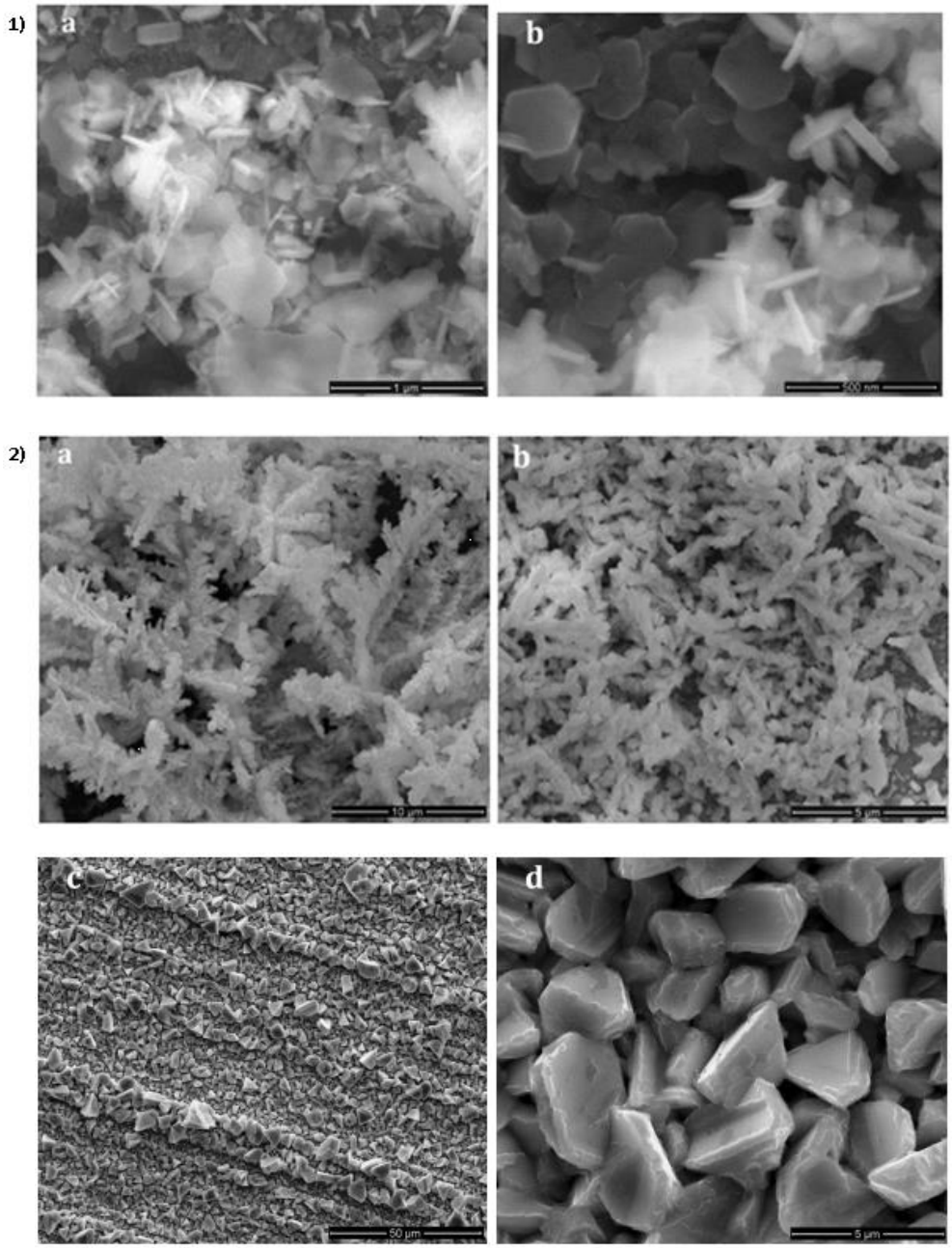

Figure 1.12: SEM images of bismuth electrodeposition onto copper substrate are obtained at different Bi^{3+} concentration bath conditions for 360 s and 10 mA/cm2 ; 1) (a), (b): 10mM Bi^{3+} in 0.2M HNO_3, 2) a), b): 1 mM Bi^{3+} in 0.2M HNO_3 c, & d) 20 mM Bi^{3+} in 0.2 M HNO_3 [64]

Different morphologies were also observed when, for a fixed Bi^{3+} concentration, the concentration of the acid was varied from 0.2 to 1.0 M (with increments of 0.2 M for each different deposition). In general, the lower the acid concentration, the smaller the hexagonal particles. For slower rates, the hexagons tend to fuse into sheets and further interconnect in a sheet-like morphology. The formation of hexagons was explained in kinetics and thermodynamic terms. From a thermodynamic

point of view, the hexagon corresponds to a minimum of the total energy of the system because of ionic forces, van der Waals forces between hexagons and surface adsorption interactions with the substrate. From a kinetic point of view, hexagonal geometry is observed because of the relative reduction rates of Bi and nitrate ions. When the rate of Bi deposition decreases (due to other competing reactions, like the reduction of nitrate at Cu electrodes or hydrogen evolution), the hexagons become bigger. The dependence of the characteristics of the deposit on the composition of the deposition bath was also investigated by Moral-Vico et al. [108]. They studied how the morphology and the resistivity of two films changed when electrodeposited from two different deposition solutions. The first solution, contained 10 mM $Bi(NO_3)_3$ and 1 M HNO_3, while the second consisted of 15 mM $Bi(NO_3)_3$, 1.35 M glycerol, 1.15 KOH and 0.33 M DL-tartaric acid. The pH of the solutions was adjusted to zero by adding 16 M HNO_3. The potential was applied constantly (direct electrodeposition) or using a dynamic potential sweep. For the direct electrodeposition, a potential equal to -0.25 V vs Ag/AgCl was applied, while for the dynamic electrodeposition, the open circuit potential was first applied, then sweep to -0.25 V and finally back to 0.00 V. The speed of the sweep was 10 mV/s. The final shape of the crystals was similar for all the samples, but different grain sizes were observed. For similar current densities, the dynamic deposition produced smaller grains (2.2 ± 0.2 μm) than the direct electrodeposition (3.0 ± 0.2 μm). Consequently, the roughness was higher for the dynamic deposit than for the continuous one. That means that by changing the potential during the electrodeposition, the nucleation rate was favoured. On the other hand, higher thicknesses are favoured for the constant deposition, as the charge per thickness is 1.2 times higher for the sample obtained with dynamic electrodeposition. In general, lower current densities were observed for the first solution, suggesting that the rate of growth is higher for the solution containing glycerol and DL-tartaric acid.

Variations of pH influence several factors, like the overpotentials values and the current densities. In addition, for very low pH values, the hydrogen evolution reaction is favoured, therefore a modification of the growth and the relative rate of growth and nucleation is observed. For example, Yang[119] demonstrated that simultaneous hydrogen evolution can be used to tune the morphology of the Bi crystallites. The same was observed for Zn electrodeposits[164], in which the influence of the formation of H_2 bubbles on the shape of the crystallites was studied using microradiography with coherent X-rays in real-time on the formation of fern-like dendrites (Figure 1.13).

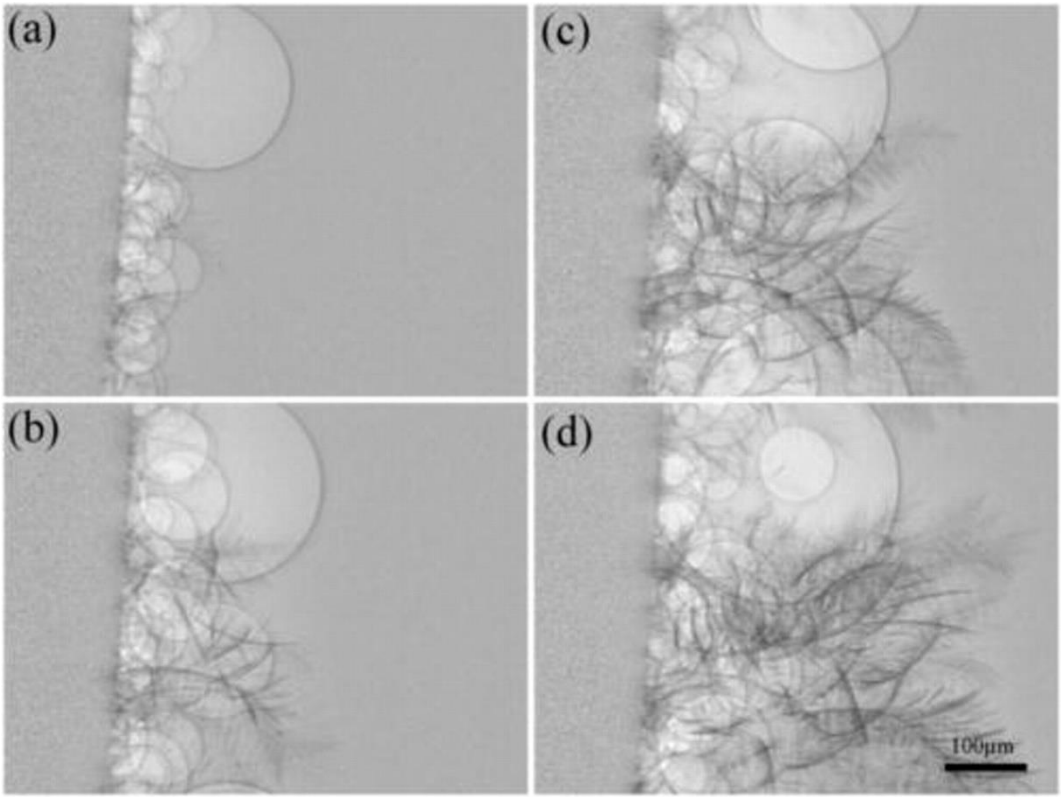

Figure 1.13: Sequential microradiographs of fern-shaped dendrites growth at -1.8 V on Cu rod from a solution containing 2.2 M $ZnCl_2$ and 4.8 M KCl, taken at different times: (a) 5.4, (b) 10.6, (c) 15.8, and (d) 21 seconds [164]

According to Narasimman et al.[165] additives are used to modify several processes during the electrodeposition, like the agglomeration of the particles, to increase the volume fraction of the particles in the deposit, and to improve the dispersion of the crystallites. Additives can have several functions in the electrodeposition bath. For example, they can block the surface of the electrodes via complexation, or they can decrease the diffusion of the species adsorbed on the cathode, favouring the nucleation process rather than the growth. In addition, they can affect the relative rate of the hydrogen evolution reaction and influence the nucleation overpotential[128]. A large number of additives have been used during the electrodeposition of bismuth, from organic molecules like ethylenediaminetetraacetic acid (EDTA)[114]; triethanolamine (TEA)[133]; sodium citrate[155]; thiocyanate[166] to inorganic salts like KBr[153,167–169]. Additives have been used in the electrodeposition of Bi to tune the morphology of the particles. However, there have been a few cases in which additives were used to allow electrodeposition of Bi in basic media[151,166]. Bi electrodeposition is mainly performed in acidic media as its precursors are not soluble in neutral and basic solutions. To obtain a high concentration of Bi in solution, very acidic concentrations are needed. Unfortunately, strongly acidic medias are inconvenient as they can dissolve many materials precluding the use of some as substrates. It has been demonstrated in another study[151] that it is possible to perform pulsed electrodeposition of Bi on carbon felt from Bi_2O_3 at basic pH by adding 2,2-Bis(hydroxymethyl)-2,2',2'-nitrilotriethanol (Bis-Tris). By modifying the applied current density

and the concentration of the Bi precursor, several morphologies and different coatings were obtained. In general, at the higher concentrations and long times off, incomplete coating of the substrate was observed, while for lower concentrations and short times off homogenous coating was observed both in the external and internal fibres of the carbon felt (see Figure 1.14). The morphology was tuned by modifying the current densities values. For low current densities, powdery deposits were observed, while with high current densities, dendritic structures were observed. Dendrites are undesirable for certain applications, as they make the coating fragile and less mechanically stable. As mentioned earlier the tuning of specific parameters to achieve an optimum morphology is desirable. For example, in catalytic applications, dendrites present good surface to volume ratio and as such potential for catalysis. However, their fragility, presents a disadvantage when applied practically, as will be seen in this work, and so the formation of the film must be tuned so as to achieve both of these parameters in suitable balance for the intended application.

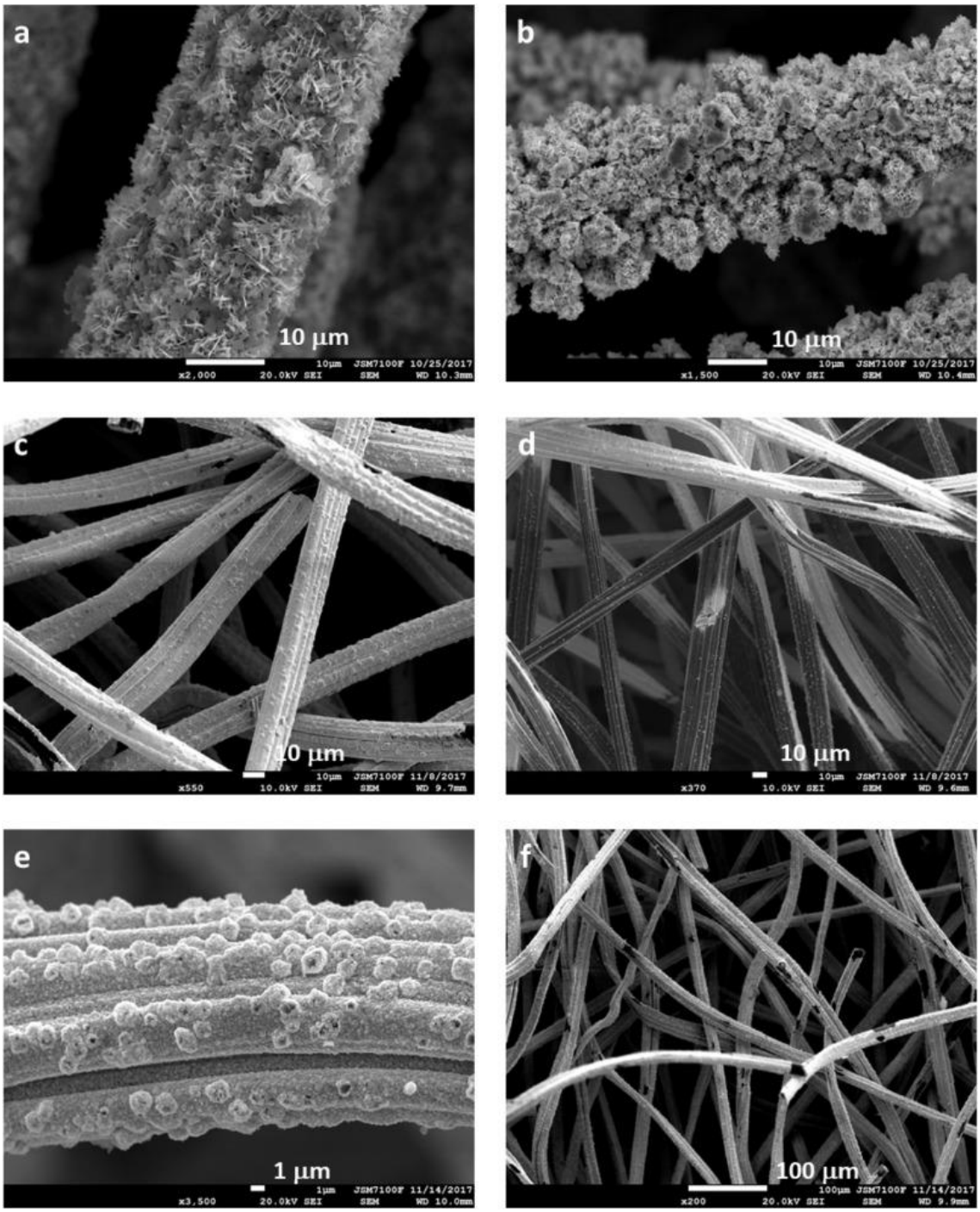

Figure 1.14: SEM images for different samples obtained via pulsed electrodeposition in a 5 mM Bi^{3+} solution with 2,2-Bis(hydroxymethyl)-2,2',2'-nitrilotriethanol applying a current of 4.3 mA/cm^2 for 1 second and followed by a time off equal to a) and b) 5 seconds; c) and d) 10 seconds; and e) and f) 15 seconds [151]

In another study, Bi deposition was performed galvanostatically on Cu substrates from a deposition bath containing $Bi(OH)_3$, perchlorate acid and different organic additives[170]. The additives were a surfactant, synthanol; two dyes, acridine yellow and safranin violet; and two aromatic compounds, cresol, resorcinol (see Figure 1.15 for the structures of the molecules). Each additive was used for one electrodeposition process with a concentration of 1g/L. An additional deposition was performed with a mixture of synthanol and resorcinol, with a concentration of 0.5 g/L for each

additive. The presence of the organic additives changed the electrochemical response by varying the potential range at which the deposition occurs under diffusion control. In the absence of additives, a plateau was observed in the polarisation curve between -0.2 and -0.5 V. This means that the presence of these compounds will allow a greater degree of control, and, by modifying the potential range, facilitates the avoidance of overlap with other undesirable processes. For example, the hydrogen evolution reaction can be detrimental to production when a non-porous deposit is sought, though, it may be desirable in other situations.

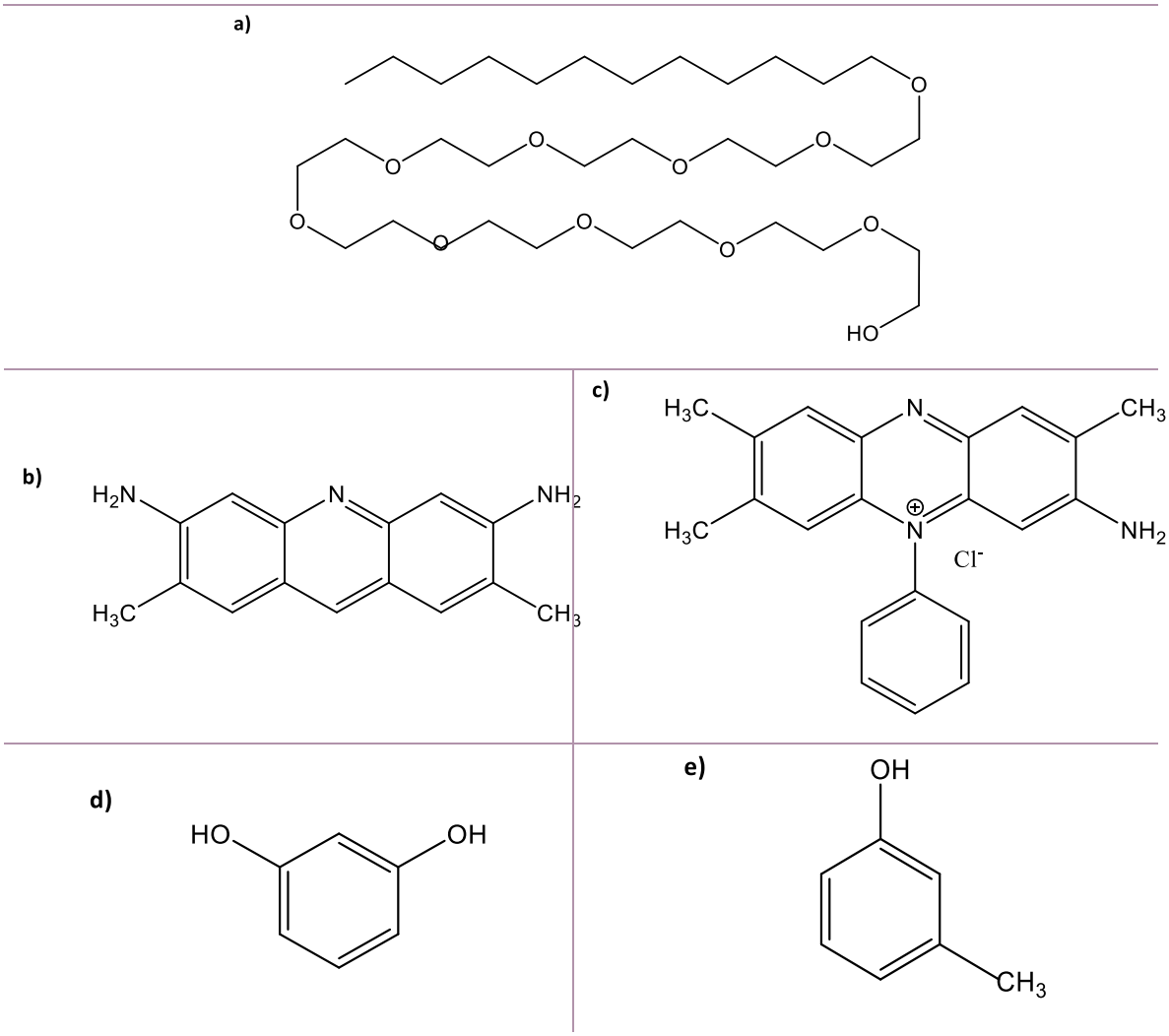

Figure 1.15: structures of the additives used in the work of Tishkevich et al. [170] for the deposition of Bi on Cu substrate. a) synthanol; b) acridine yellow; c) safranin violet; d resorcinol; and f) cresol

The addition of synthanol did not change the diffusion potential range significantly, however, when resorcinol was added to the solution the plateau disappeared, suggesting the deposition happened under kinetics control. On the other hand, when the safranin violet was added, the potential range for the diffusion control increased significantly, being between -0.5 V to -0.65 V. The effect of acridine yellow was similar, but to lesser extent (potential range: -0.1 V to -0.45 V). The pronounced increase in the diffusion potential range in the presence of the two dyes was attributed to the

passivation of the electrodes by these molecules. Due to the partially negatively charged nitrogen in the ring, acridine yellow was adsorbed on the anode, making the diffusion of Bi to the cathode slower. On the other hand, when safranin violet was used, the cathode was passivated by the dye because of the partial positive charge on one of the N atoms, making the reduction of Bi^{3+} difficult. As far as the physical characteristics of the electrodeposit are concerned, the presence of additives influenced the texture of the film. The grains decreased in size and a more dense, flat deposit was formed when resorcinol, cresol and synthanol were used. The smallest particles were obtained for the mixture of synthanol and resorcinol suggesting the two additives facilitated nucleation and promoted a more compact and less rough deposit. In addition, the film formed in the presence of the additives showed a stronger adhesion on the Cu substrate than for the deposits formed in the absence of additives. It has been demonstrated before that the presence of an additive can also improve the homogeneity of the deposit[155]. For example, sodium citrate was used in a solution of $Bi(NO_3)_3$ and HCl. The deposition was performed on a Cu substrate at -0.15 V for 300 s (total Q = 1.03 mC). The presence of the citrate resulted in better uniformity of the film: a homogeneous structure made of aggregated spherical particles with sizes on the order of the few nanometers was observed. The deposit produced in the absence of citrate showed a mixture of structures homogeneously distributed on the surface (see Figure 1.16A1, A2 and A3). On the other hand, when citrate was used, a uniform and homogeneous film was observed. Similarly, Karar et al.[152] studied the effect of ammonium chloride on the electrodeposition of Bi films. Bi was electrodeposited on a glassy carbon disk (A = 0.03 cm^2) from a solution containing 2.2 mM of $BiCl_3$ in choline chloride/urea deep eutectic solvent. Deep eutectic solvents (DESs) have similar properties to ionic liquids (ILs). Ionic liquids have been extensively used as solvents for their ability to dissolve a wide variety of organic compounds and, in electrochemistry because of their large electro-inactive windows. DESs have the additional advantage of being more environmentally friendly, relatively inexpensive. By increasing the concentration of ammonium chloride, the current of the cathodic peak for the reduction of Bi increased 1.36x times due to the increase of conductivity of the solution. The yield of deposition increased by ≈ 8% for a threefold increase of additive concentration. This was likely due to an increase in the nucleation rate in the presence of the additive. The mechanism for the nucleation and growth was observed to be progressive for different overpotentials and additive concentrations. However, the morphology of the electrodeposits changed significantly at different concentrations of ammonium chloride. At the lowest ammonium chloride concentration, the film was porous, while by increasing the concentration, the film which resulted was more compact. The grain sizes decreased with an increase in concentration of additive, suggesting a faster nucleation rate. The presence of an additive may favour nucleation over growth then, as was suggested by

Narasimman et al.[165]. This means that, for example, if a deposit for catalytic applications is being sought, lower concentrations of ammonium chloride should be used, while, for a coating process, higher concentrations would be preferred. And so, both the concentration and chemical nature must be tested for each individual system on a case-by-case basis when considering the use of additives.

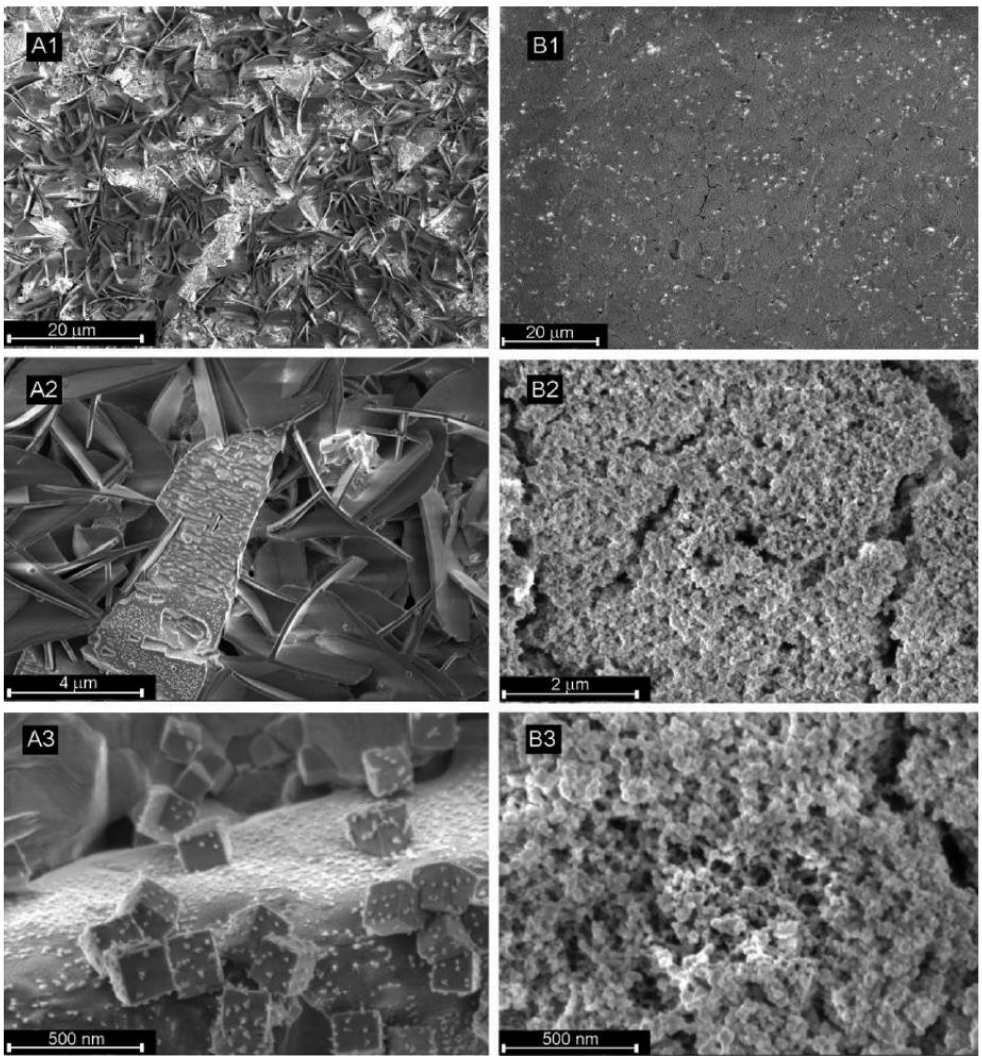

Figure 1.16: Field emission SEM micrographs of the Bi film electrodes electrodeposited onto a copper electrode in deposition bath containing A) without and B) with citrate at different magnifications [155]

Zhong et al.[153] studied the change in morphology when KBr was used as an additive. The Bi particles were deposited on thermally treated carbon papers at -0.35 V vs SCE in a deposition bath containing 20 mM $Bi(NO_3)_3$ and 1 M HCl for different amounts of time. In the absence of KBr, flowerlike structures were observed, while when KBr was added (0.25 M) nanodendritic structures were formed. The structure of the nanodendrites was investigated by separating the crystallites in their components via intense ultrasonication. The dendrites were formed by nanowires with diameters ranging from 20 to 70 nm in diameter, suggesting a diffusion-controlled aggregation (that occurs

only a low metal concentrations) into the final dendritic shape. The formation of dendrites generally occurs for slow nucleation and fast growth rates[171]. The change in morphology in the presence of KBr was attributed to the ability of Br^- ions to act as capping agent by complexing Bi^{3+}. In this way, the adsorption rate of the Bi cations and their reduction rate was increased.

In conclusion, electrodeposition is a facile and versatile method to produce metal film electrodes. Different techniques have been used to produce Bi film electrodes and their characteristics have been tuned changing a variety of parameters. The parameters can be divided into two categories: physical (the current density, the potential and the substrate) and chemical (the composition of the deposition bath, which includes the concentration of the precursor, the pH and the presence of additives). By changing these parameters, films with different morphologies, thicknesses and homogeneities can be obtained. Considering the fact that the deposits produced within this work are used for catalytic applications, surfaces with high surface-to-volume ratio would be preferred. Based on the literature discussed, the parameters that influence the nucleation and growth rate should be controlled, such as the concentration of the Bi precursor and the presence of additives. In addition, continuous or non-continuous application of the potential/current can be a good way of tuning the deposition rate of the particles.

1.5 Characterisation of Bi electrodes

In this section, the electrochemical characterisation of Bi electrodes will be presented. In particular, the behaviour of Bi electrodes in aqueous electrolytes in a large potential window will be discussed, as the experiments performed within this work were all performed in aqueous solutions. For this reason, a deep understanding of the behaviour of the Bi electrodes in this environment is necessary. Then, a brief outline of the methods used for evaluating the microscopic area of electrodes will be presented followed by a discussion of the differences between low and high area metal electrodes and their importance in catalysis.

1.5.1 Electrochemical behaviour of Bi electrodes

When investigating an electrochemical system, the potential window is one of the first characteristics studied. The size of a potential window depends on three major factors: the electrolyte, the solvent and the working electrode[172]. In general, a wide potential window with a low background current is preferable as it allows a large range of potentials for the electrochemical measurements. The oxidation and the reduction potentials of the electrolyte and solvent determine the limit of the potential window of a specific solution[173]. So, for an aqueous system, the limits of the potential window are given by the electrolysis of water, i.e. the oxidation of water for the

production of O_2 at anodic potentials, and its reduction for the hydrogen evolution at cathodic potentials[174]. For a metal electrode, the extent of the potential window is limited by its oxidation at positive potentials and by the HER at negative potentials[175]. Depending on the measurements that need to be performed, a specific potential window is preferred. For example, if the process under investigation occurs at positive potentials, an electrode with a large anodic potential window is preferred. As far as Bi electrodes are concerned, their wide cathodic potential window allows their use for reduction processes. For this reason, Bi electrodes have been used as substitutes for Hg electrodes. The similarities of Hg and Bi electrode potential windows are shown in Figure 1.17 (curve c and d). The increase in current at around -0.3 V is due to the oxidation of Bi metal.

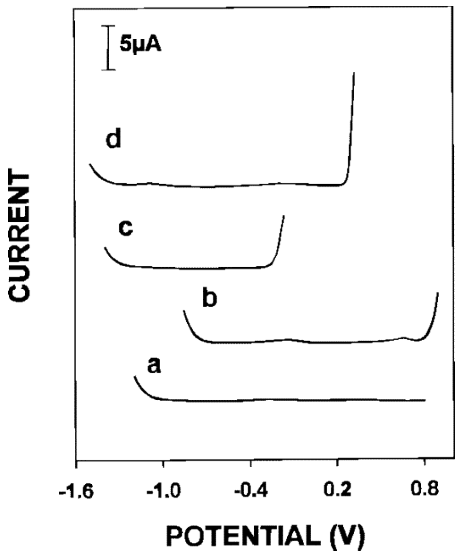

Figure 1.17: Potential window for carbon-fibre electrodes for a) the bare carbon-fibre electrode; coated with b) Au, c) Bi and d) Hg in an acetate buffer solution [69]

When the potential is swept to more positive potentials, a large and broad peak is observed (see Figure 1.18). This peak is attributed to the oxidation of the Bi metal to Bi_2O_3[176–178]. When the potential is then swept back to negative potentials, a second peak, around -1.2 V, corresponds to the reduction of the Bi oxide formed in the anodic scan[176–178]. The reaction for the formation of the oxide is shown in Reaction r1.8 below:

$$2Bi\ (s) + 3H_2O\ (aq) \longrightarrow Bi_2O_3\ (s) + 6H^+\ (aq) + 6e^- \qquad (r1.8)$$

No experimental proof for the exact number of electrons exchanged was found in the literature. However, the majority of the Bi compounds in nature present a stoichiometry that confirm a charge of 3+ or, for some organometallic compounds, Bi cations with charge 5+ have been found[63]. The value for the electrochemical reversible potential is pH dependent and it can be calculated using Equation (1.3):

$$E_{rev} = 0.371 - 0.0591 \times pH \;\; in\, V \; vs \; NHE \tag{1.3}$$

The sudden increase of current after -2.0 V is due to HER[177]. The CVs present some differences in shape when the pH of the solution is varied. For example, different current efficiencies (CE) for the reduction/oxidation reactions, current values and cathodic and anodic peak potentials are observed (see Figure 1.18). The CE is the ratio between the charge associated with the cathodic process (Q_C) and the charge associated with the anodic process (Q_A) (see Equation (1.4) below).

$$CE = \frac{Q_C}{Q_A} \tag{1.4}$$

The change in shape and position of the curve as a function of the pH was observed in several other works[81,89,178–180]. In general, the higher the pH, the more the curve is shifted toward negative potentials. The decrease of the cathodic and anodic current maximum (i_{pc} and i_{pa}) at low pH values is due to the dissolution of Bi_2O_3 in acidic solutions[63,181]. This means that less oxide is present when the cathodic sweep is performed, therefore less charge is passed during reduction, leading to lower currents[177]. For this reason, the majority of the studies of the Bi oxide formation and reduction are performed in highly basic solutions and especially in the presence of borate salts[176–179,182,183], in which no dissolution of the Bi oxide film is observed is observed[176].

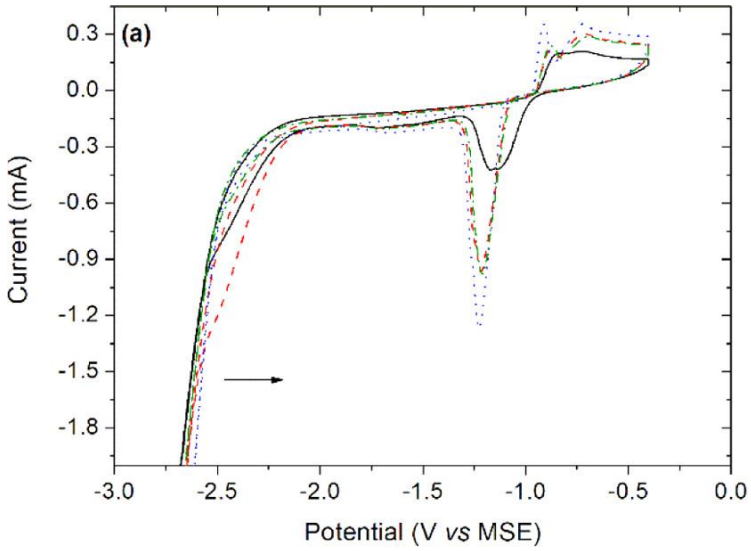

Figure 1.18: Cyclic voltammetry analysis on a bismuth disk electrode (1.5 mm diameter) of a solution of 0.1 mol L–1 Na2SO4 at pH 3 (black solid line), pH 7 (red dashed line), pH 10 (green dash dotted line), pH 13 (blue dotted line) (pH adjusted with H2SO4 or NaOH); Scan rate: 100 mV/s; RE: mercury-mercurous sulphate (MSE) [184]

The mechanisms for the oxidation of Bi and the reduction of Bi oxide have been proposed to be different[185]. Several works were performed to understand the nucleation and growth of the Bi oxide on the metallic Bi surface. Here, several studies and the proposed mechanisms will be presented and discussed, first for the oxidation of metallic Bi and then for the reduction of its oxide.

1.5.1.1 Oxidation of metallic Bi

Williams and Wright[177] studied the formation of Bi oxide in different solutions via CV measurements. The CVs of Bi electrodes in basic solution is shown in Figure 1.19. The cyclic voltammogram was divided into five potential regions, two in the anodic and three in the cathodic part of the CVs. These potential regions were set for clarity by the authors, and they are:

- **AB**: oxidation of the Bi surface;
- **BC**: thickening of the anodic film previously formed;
- **AE:** reduction of the anodic film;
- **EF:** potential range between the reduction peak and the potential window limit;
- **FG:** hydrogen evolution reaction;

In the AB region, two peaks are present, and they represent the peak for the oxidation of metallic Bi to Bi oxide (r1.). The number of peaks varied depending on the pH of the solution, the method used for the preparation of the electrode and the anodic overpotential. Specifically, if the overpotential for the nucleation of the oxide exceeded a critical value, then two or more peaks were observed. If one peak was observed, the associated process was found to be the formation of the oxide monolayer. In the BC region, a current plateau that stays constant for ≈ 0.5 V, with a current value equal to i_G is present. This current plateau is associated with the thickening of the anodic film as, both the current and the electric field are not varying, meaning that, from a kinetics point of view, the system is in a steady state. ϵ_R (that here represents the potential) is the reversible potential for reaction (r1.) and it lies between ϵ_{AN} (the anodic onset potential) and ϵ_{CN} (the cathodic onset potential), that are all strongly influenced by the pH of the solution. In the AE region, the peak for the reduction and formation of the metallic Bi is present. The FG region is the potential region in which the hydrogen evolution reaction occurs, as can be seen by the sudden increase of the current.

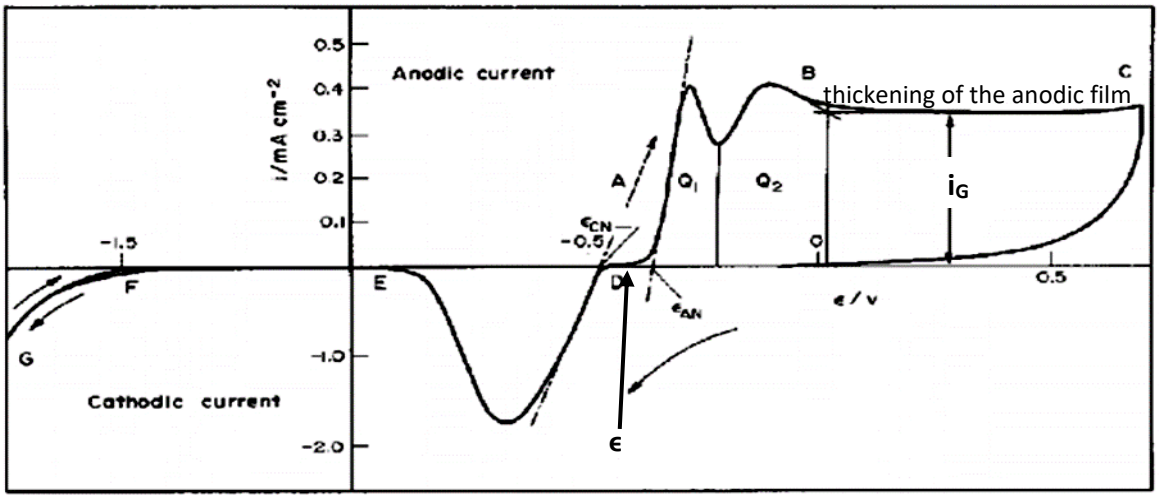

Figure 1.19: Cyclic voltammogram of Bi in basic electrolyte (pH=12.6) acquired at v= 0.11 V/s; The arrows show direction of the scan. ϵ_{AN} is the anodic onset potential; ϵ_{CN} is the cathodic onset potential; ϵ_R is reversible potential for the Bi oxidation/reduction reaction; Q_1 and Q_2 are the charges associated with the first and second anodic peak; i_G is the magnitude of the current passed during the thickness of the oxide film. The potential window was from 0.7 to -1.7 V[177]

The shape of the CV is influenced by the cations and anions in solution. This was observed when the electrolyte in solution was changed, for example when sulphate or phosphate salts were used instead of borates[179,182,186]. The nucleation mechanism for the oxide formation was proposed to be a *progressive nucleation* with formation of areas of Bi oxide that spread through the surface. The formation of the nuclei occurs via three steps: 1) OH^- species are adsorbed on the surface of the electrode; 2) areas or "patches" of Bi oxide are formed; and 3) growth of the pre-existent nuclei and formation of new ones. In weakly acidic media, before the nucleation step, a dissolution-precipitation mechanism was proposed, this means that the Bi metal is dissolved at the solution/electrode interface and then it is deposited on the surface of the electrode in crystalline form. The mechanism of growth was evaluated at different neutral and basic pH values. It was found that at pH<8.5, the oxidation occurs at the film/solution interface and the Bi ions are injected into the film for the growth of the oxide layer, while at pH>8.5, the ions migrate through the metal film and therefore the oxidation occurs at the metal/oxide interface (for a representation of the interfaces see Figure 1.20).

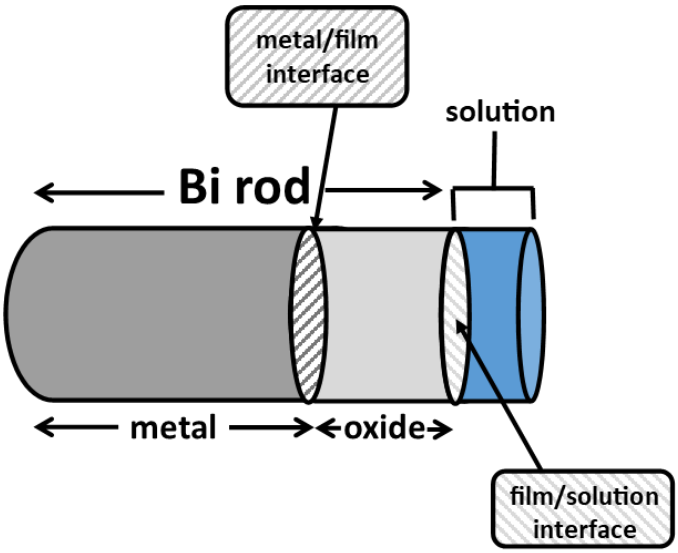

Figure 1.20: Scheme of a Bi rod in contact with the solution. The electrode contains metal and oxide layers. The Bi rod was coated with a glass tube, so the part in contact with the solution was the frontal part and not the lateral section.

Similar conclusions were reached by Grubač and Metikoš-Huković[176], when they investigated the mechanism of nucleation and growth of Bi oxide with cyclic voltammetry and potential step techniques. Scan rate studies showed a linear trend between the $v^{1/2}$ and the anodic peak potential (E_{pa}), as well as between $v^{1/2}$ and the maximum anodic current density (j_{pa}), suggesting a diffusion-controlled solid-state process. The current at the plateau was linearly dependent on $v^{1/2}$, meaning that the growth of the Bi oxide is also controlled by diffusion. A three-step mechanism for the nucleation of the oxide particles was suggested: 1) adsorption of the O species, like OH^- and H_2O; 2) diffusion of the adsorbed species to the limits of the oxide patches; and 3) incorporation of the adsorbed species into the oxide patches, in accordance with the one described by Williams and Wright[177]. Using the potential step techniques, the rate determining step for the oxide formation was concluded to be the diffusion of the adsorbed species toward the oxide patches (step 2). The Scharifker-Hills method was used to identify the nucleation mechanism. The experimental current transients were in accordance with the 3-D progressive nucleation mechanism with diffusion-limited growth. In addition, by using the Scharifker-Hills method, it was possible to calculate the density of the active sites, which results in values in the order of 10^9 cm^{-2}, a number six orders of magnitude smaller than the theoretical number obtained using the density of the geometric sites. This means that only one of one million of sites on the Bi surface is active for oxide nucleation.

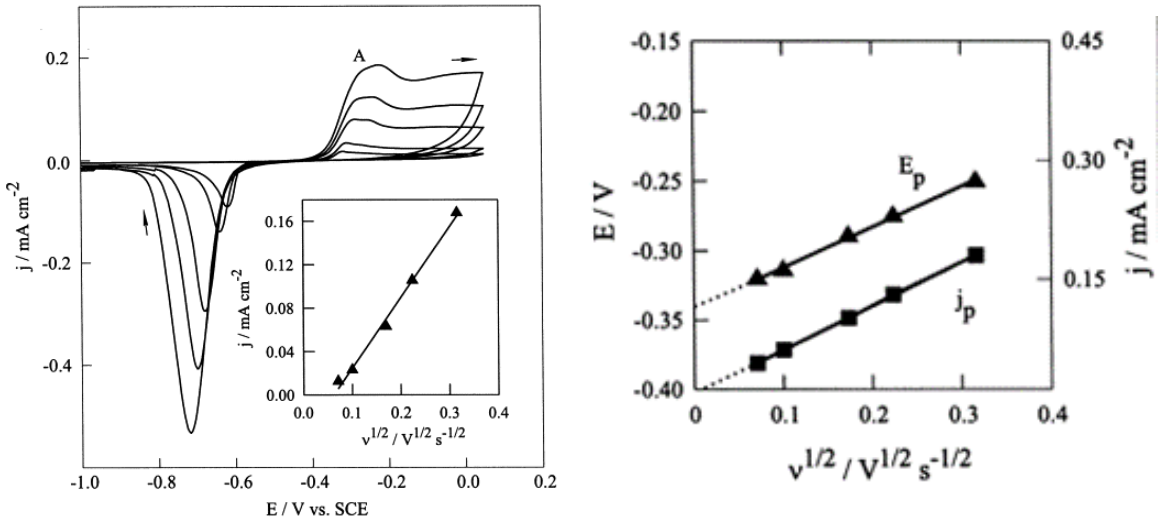

Figure 1.21: a) scan rate study of a bismuth electrode in a Na–borate buffer solution, pH=9.2. v=5, 10, 30, 50 and 100 mV s–1. In the inset: dependence of the plateau current at E=0.0 V on the square root of the scan rate; b) dependence of the anodic peak potential (E_{pa}) and the anodic peak current (j_{pa}) on the square root of the scan rate [176]

By way of contrast, Pérez et al.[185] studied the formation of the Bi oxide at the early stages of the process using CV and optical measurements. Two different Bi electrodes were used: one mechanically polished and the other mechanically polished and then electrochemically reduced. The first method did not allow the complete elimination of the native oxide from the surface of the electrode, while the second lead to the complete removal of the oxide. This was proposed using CV measurements results: the electrode with the native oxide did not present a well-defined anodic peak and the current plateau started after the onset potential current, while for the electroreduced electrode, an additional peak was observed before the plateau (see Figure 1.22). This was confirmed by *in-situ* optical measurements. However, the measurements required the use of models, that might not describe the experimental results appropriately. In addition, fresh prepared electrodes might present different thickness of the native oxide in comparison with old ones and a discussion on the complete removal of the native oxide layer for old electrodes was not presented. Measuring the dielectric properties of the film, the formation of the first 20 nm of oxide on the electroreduced Bi film was monitored and a multilayer growth was suggested for the formation and growth of the anodic layer. Specifically, a three-stage multi-layer growth model was proposed. In the first stage, a porous oxide layer grows, consuming the electroreduced Bi layer (which has a different structure than the metal substrate), until a certain thickness is reached. Then, the oxide starts growing at the expense of both the electroreduced layer and the bulk Bi metal underneath. At the last stage, the oxide grows at the metal/oxide interface, as the electroreduced Bi layer is completely oxidised.

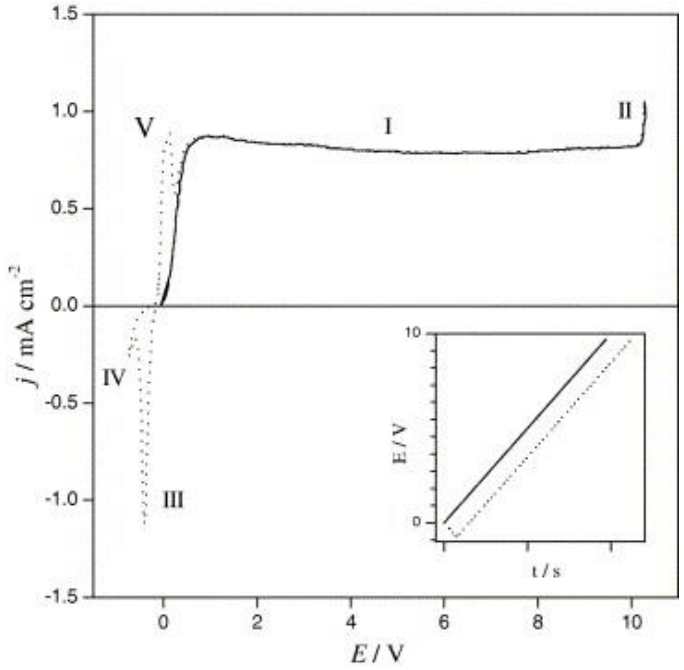

Figure 1.22: CVs of bismuth electrodes at 0.1 V/s in a 0.1 M Na_2HPO_4 (pH 10) solution obtained during the anodic growth of Bi oxide on: a fresh mechanically polished surface (solid line); and a surface obtained by the electroreduction of the native oxide layer (dashed line). Inset: applied potential in time [185]

Based on the literature findings, the growth of Bi oxide seems to present a diffusion-limited mechanism, having as a limiting step the diffusion of the Bi^{3+} ions through the oxide layer and finally to the metal substrate. This means that the growth occurs at the metal/film interface. The same mechanism was proposed for other valve metals like Al[187], Nb[188], Ti[189] and Ta[190].

1.5.1.2 Reduction of Bi oxide

While the oxidation of Bi was investigated by several authors in the 1970s, the reduction of the anodic layer was studied in depth around two decades after. One of the first works was performed by Williams[178] who theorised the mechanism of cathodic reduction of Bi oxide on a qualitative basis. Observing the colour change at the surface of the electrode and with some CV measurements, he suggested that Bi oxide reduction occurs at the metal/electrolyte interface and not at the metal/film interface, as for the formation of the oxide. When the anodic layer is formed, a range of colours is observed at the surface of the electrode because of the change in the thickness of the oxide layer. Different colours of the electrode surface were observed within this thesis and they will be discussed in Chapter 3. When the Bi oxide is reduced in acidic solutions, the same variation in colour is observed but reversed in time (see Figure 1.23). However, for cathodic reductions, the last colour of the variation is observed immediately at the surface of the electrode, suggesting that the oxide layer is not being reduced at the metal/film interface, but directly on the film/electrolyte interface. In addition, CV measurements show that by changing the amount of oxide that is reduced

at the cathodic scan, the successive anodic curve presents a peak for the nucleation of the oxide and the anodic current increases as a function of the amount of oxide cathodically reduced. If the reduction happens at the metal/film interface, no peak for the nucleation of the oxide should be observed, but only a low current due to the thickening of the oxide. In addition, the anodic nucleation potential changed when different quantities of oxide were reduced in the cathodic scan, suggesting that the nucleation of the Bi oxide occurs on a different surface than the Bi substrate.

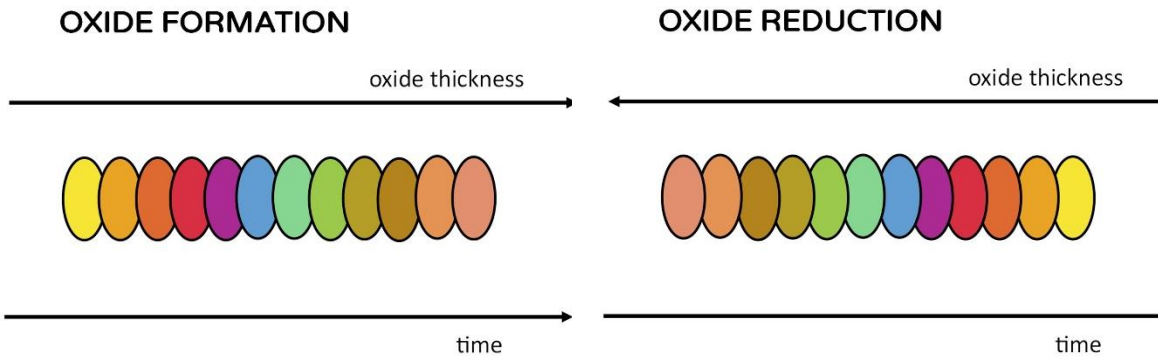

Figure 1.23: Example of the colour variation as a function of thickness and time for the a) anodic formation and b) chemical reduction of the Bi oxide. The colour variation is representative of Bi oxide thickness on the order of the nanometres[191]. It is therefore not necessarily representative of the macroscopic change, but it is used as a reference. The time represents the duration of the applied potential

The same mechanism was confirmed later by different authors[183,185,192]. For example, Grubač and Metikoš-Huković[183] studied the mechanism of the nucleation and growth of the Bi^0 after anodic oxidation of the surface. To understand the mechanism of the reduction, scan rate studies were performed in a range of values between 5 and 100 mV/s. The kinetics of the reduction of the anodically formed film, was evaluated using: 1) The dependence of E_{pc} and j_{pc} as a function of square root of the scan rate; and 2) The influence of the cathodic scan potential limit ($E_{l,c}$) on the shape of the anodic current profile. E_{pc} and j_{pc} showed a linear response as a function of the square root of the scan rate, suggesting a diffusion-controlled mechanism for the reduction of the Bi oxide. In addition, the height and position of the reduction peak were not dependent on the electrolyte stirring, suggesting that the cathodic process occurs in solid phase. Based on the CVs obtained at different $E_{l,c}$, it was noticed that the re-oxidation of the Bi film occurs at a more positive potential than the reversible potential of the Bi/Bi_2O_3 couple, meaning that the anodisation of the Bi metal occurs on a different surface: the electroreduced Bi metal. The author suggested that the electrons migrated from the bulk of the metal to the surface passing through the oxide film (see Figure 1.24 and Reaction (r1.9)).

$$e^-\ (\text{metal}) \longrightarrow e^-\ (\text{surface}) \qquad \text{(r1.9)}$$

The electrons will be in the film/solution interface where there is higher probability for them to be trapped in anion vacancies (see (r1.10) to form neutral centres (F_1):

$$O_o + H_2O\ (aq) + 2e^-\ (surface) \longrightarrow 2OH^-\ (aq) + F_1 \qquad (r1.10)$$

where O_o is the lattice oxide ions that are reduced by the electrons (e^-(surface)) trapped at the solution/interface and the F_1 is the neutral centre formed by the oxidation of the lattice oxide ions. Once the F_1 centre is formed, Bi metal appears at the surface of the oxide and the electrons trapped on the surface diffuse, producing Bi metal from the Bi cations and the neutral centre F_1. The new Bi metal formed is smaller in volume (as Bi_2O_3 occupies between 18 and 25% more space than Bi metal, depending on the oxide phase[177]; density Bi=9.78 g/cm^3; density α-Bi_2O_3 = 8.9 g/cm^3;[185]) and porous, allowing the solution to enter into contact with the oxide film underneath and continue the reduction. For this reason, it was suggested that the reduction continues inside the oxide film forming small channels that present a dendritic shape, where the Bi metal is accumulated. In the last stages of the reduction, the electroreduced Bi^0 spreads over the metal substrate and the reduction is limited by the resistance inside the pores between the Bi deposits. This mechanism was found to occur for the reduction of other metal oxides, like Sb_2O_3 and SnO_2.

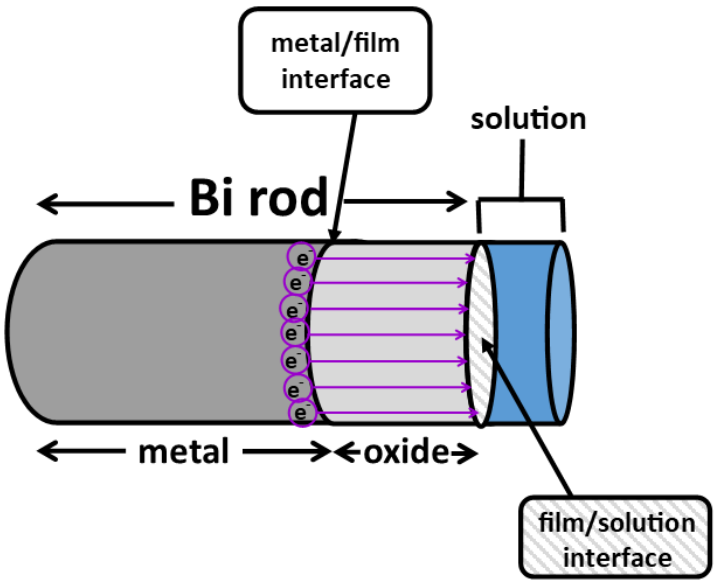

Figure 1.24: Scheme of the reduction of the Bi oxide for a Bi electrode in contact with the solution. The Bi rod was coated with a glass tube, so the part in contact with the solution was the frontal part and not the lateral section. Only few electrons at the boundary of the metal/ film interface are show for clarity. The purple arrows represent the migration of the electrons from the metal through the oxide layer before the reduction step

The mechanism of reduction at the very initial stages was then studied using the potential step technique at different applied potentials. Initially, the spike due to the double layer charging was observed in the current transient, then a decrease and a following increase of current was noticed, until a maximum value of current density (j_{max}) was reached at a certain time (t_{max}). A decay of the current is then observed in the last section of the current transient. As the applied potentials

becomes more negative, the j_{max} increases, while t_{max} decreases. The rising part of the transient (before the maximum) showed a linear dependence with t^3. This relationship is observed when a 3-D progressive nucleation and growth under charge transfer control is the mechanism for the formation and growth of the nuclei. To further investigate the mechanism, the Scharifker-Hills method was used and the experimental transients did not fit either the progressive or the instantaneous mechanism theoretical curve, suggesting that the growth is not under diffusion control. The equation for the nucleation and growth under charge transfer control is given by the Equation (1.5)[144,193].

$$j(t) = nFk_2 \times \left[1 - e^{\left(-P_2 t_i^3\right)}\right] \times e^{\left(-P_2 t_i^3\right)} \qquad (1.5)$$

where $P_2 = \frac{\pi M^2 k_1^2 A}{3\rho^2}$; $t_i = t - P_3$; and $P_3 = \frac{zFD^{\frac{1}{2}}\Delta c}{\pi^{\frac{1}{2}}}$. k_1 and k_2 are the rate constants for the crystal growth in parallel and perpendicular direction to the surface of the electrode, respectively; M is the molecular weight; ρ is the specific weight; D is the diffusion coefficient; Δc the concentration gradient for the diffusion of the species; and A is the nucleation rate constant. P_3 is extrapolated experimentally from the j vs t^3 plot. Equation (1.5) is valid for the transients acquired at -0.6 and -0.68 V. For more negative potentials, a more complex model was needed. The transient has two contributions: *one* from the progressive nucleation and 3-D growth under charge transfer control and *the second* is related to the instantaneous nucleation and 2-D growth under diffusion control. See Figure 1.25 for the fittings of the current transients.

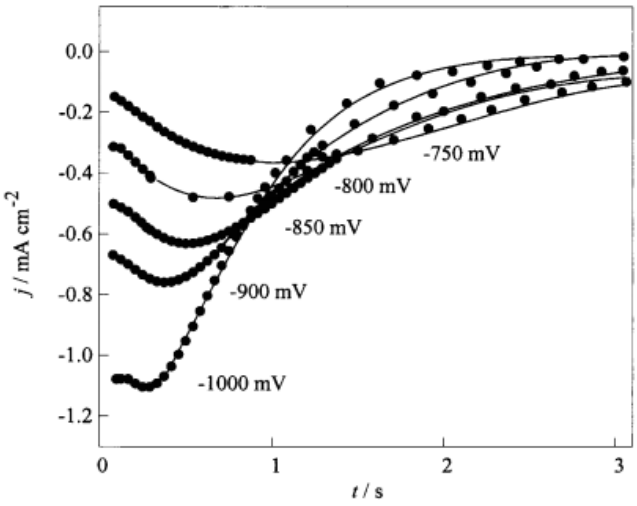

Figure 1.25: Fitting of the current transient data (full traces) according to more complex model. Points are taken from the current transient run between -0.75 and -1.0 V [183]

The first contribution describes the rising part of the transient, while the second describes the initial decay of the current after the double layer charging. This means that, in general, the mechanism of

the reduction of Bi_2O_3 is progressive nucleation and a 3-D growth under charge transfer control, while for high overpotentials a mixed mechanism is observed. The mixed mechanism is instantaneous nucleation and 2-D growth under diffusion control followed by a progressive nucleation and 3-D growth under charge transfer control.

Similarly, Pérez et al.[185] studied the reduction of anodic layers for two different electrodes: one mechanically polished and one electroreduced. As mentioned in the previous paragraph, the mechanically polished electrode presented a native oxide layer, so, to obtain an oxide-free surface, a negative sweep was performed at 1 mV/s. The surface was successively anodised sweeping the potential in positive direction at 10 mV/s. Using ellipsometry (a technique that measures the change of polarisation upon reflection or transmission), the dielectric properties of the Bi electrode surface during the reduction were investigated to understand the changes of the Bi surface during the process. When the native oxide is reduced in the cathodic scan, a decrease in its thickness was observed. In addition, the presence of another process, happening simultaneously to the oxide reduction, was also identified. When the oxide is formed anodically, different dielectric properties in comparison with the native oxide were observed, suggesting a different mechanism for the formation of the anodic oxide and the reduction of the native layer. A change in dielectric properties was observed at the beginning of the oxidation process for the electrochemically reduced film, suggesting the presence of an additional process. This was observed for the electroreduced film but not for the mechanically polished electrode. For this reason, it was reasonable to conclude that the additional process was the formation of the first monolayer of Bi oxide before growth. When comparing the dielectric response for the electroreduced and the mechanically treated surfaces, different responses were obtained. The authors suggested that the difference was due to the morphology of the Bi surface. Specifically, the electroreduced Bi surface was porous with voids having a prolate shape, while the mechanically polished surface was non-porous. The porosity of electroreduced Bi surfaces was also examined via SEM imaging by Romann and Lust[194]. They used two different methods to produce an electroreduced Bi surface. The first method consisted of three steps: 1) a potential of 1 V was applied for one second to form the anodic film; 2) the potential was stepped to -2 V for 0.5 seconds; and 3) the potential was fixed at -1.2 V for 10 s. For the second method the potential was held at -2.2 V for five minutes without a preceding oxidation step. The surface of the Bi after each treatments are shown in Figure 1.26. For the first method (Figure 1.26, left), the morphology of the deposit was not homogeneous: a combination of dendrites, made of nanowires with diameters of about 60 nm, and pyramidal compact Bi crystals, with size of 800 nm, was present. When the second method was used, the formation of overlapping scale-like structures on a portion of the surface was observed. In addition, a porous deposit was observed. The scale-

like texture can be due to a chemical or electrochemical etching of the surface. The roughness factor was calculated after the reduction steps using the capacitance values: for the first method a surface roughness of 220 was obtained, while for the second method, a value 20x smaller was obtained (r_f=10.4). This was expected as the surface obtained with the first method presented a more porous morphology than for the second. It was suggested that the porosity of the surface could be due to the decomposition of volatile bismuth hydrides (see r1.11a), formed simultaneously with the hydrogen evolution. The reaction led to dissolution of Bi, especially at Bi surface defects and corners of the crystals faces, followed by decomposition to Bi nanoparticles (see r1.11b).

$$Bi\ (s) + 3H_{ads} \longrightarrow BiH_3\ (g) \qquad \text{(r1.11a)}$$

$$2\ BiH_3\ (g) \longrightarrow 2Bi\ (s) + 3H_2\ (g) \qquad \text{(r1.11b)}$$

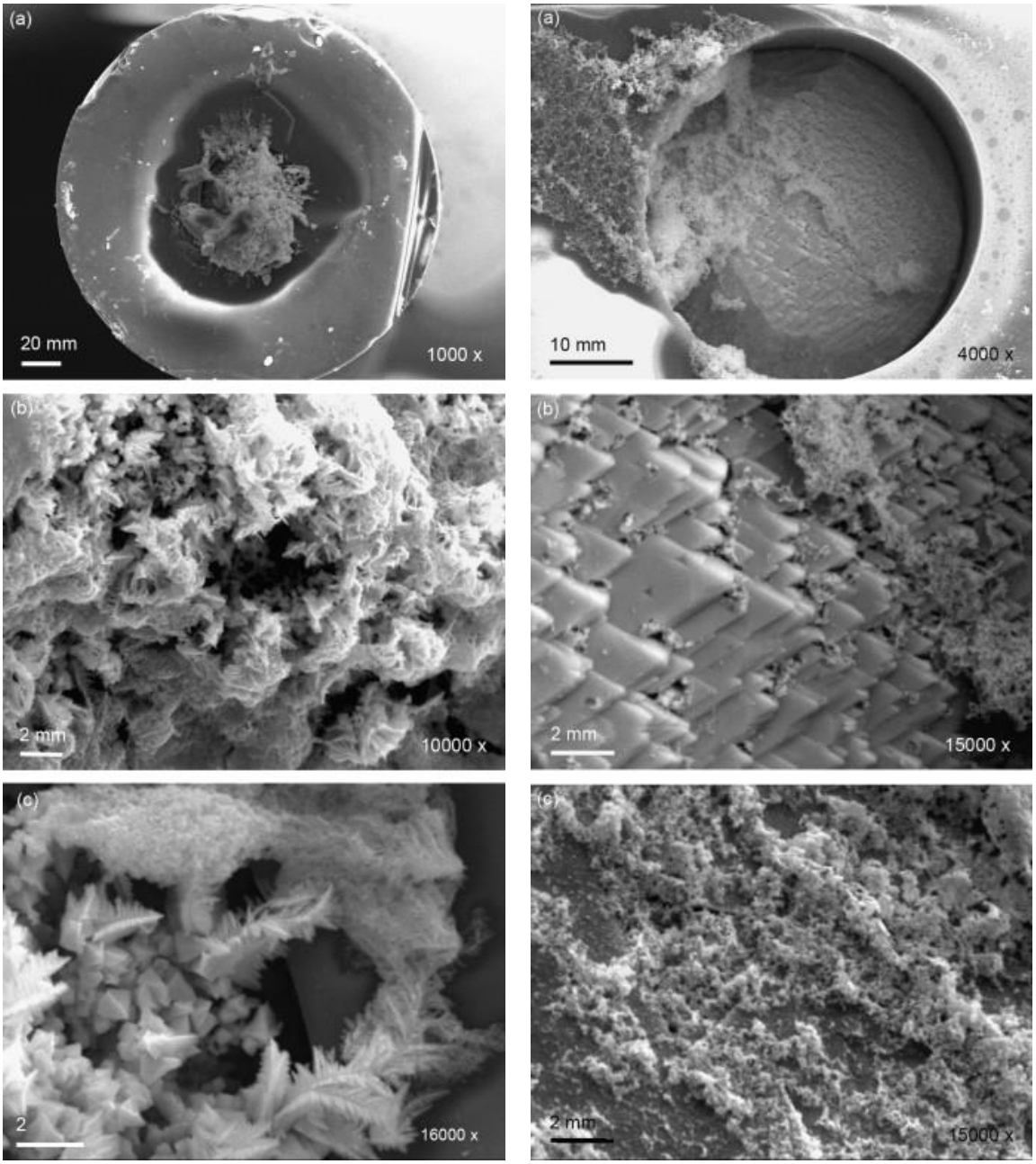

Figure 1.26: SEM images for Bi microelectrode at different magnification after left) dissolution and electrodeposition steps; and right) after 5 min holding at −2.2 V. The experiments were performed in 0.1 M LiClO4 aqueous solution [194]

Based on the findings of these two studies, if a pure metallic Bi surface is desired, then the native oxide must be removed via electrochemical treatments. It would also seem that the reduction of the oxide layer will result in a porous morphology. Therefore, it is reasonable to expect that a pure metallic Bi surface will always present a porous morphology.

The formation of Bi hydrides was also suggested by a successive work of Pérez et al.[192] in which an additional peak at cathodic potentials during CV experiments was observed. The reduction was performed after anodisation of the Bi metal surface, during which different amounts of charge was passed to study the reduction of oxide layers with different thicknesses. When very thin layers of Bi_2O_3 were present, the CE for the reduction/oxidation process was close to 1 at several scan rates,

suggesting that the oxide layer was completely reduced. When the thickness of the anodic oxide increased, the peak attributed to the reduction of the oxide overlapped to the current response for HER, making the evaluation of the Q for the reduction process difficult. However, if the negative scans were performed at very low scan rates (1 mV/s) the reduction peak was well defined and an additional peak was observed. This peak appears only when the thickness of the oxide layer increased, while for thin oxide layers, the second peak was not present (see Figure 1.27).

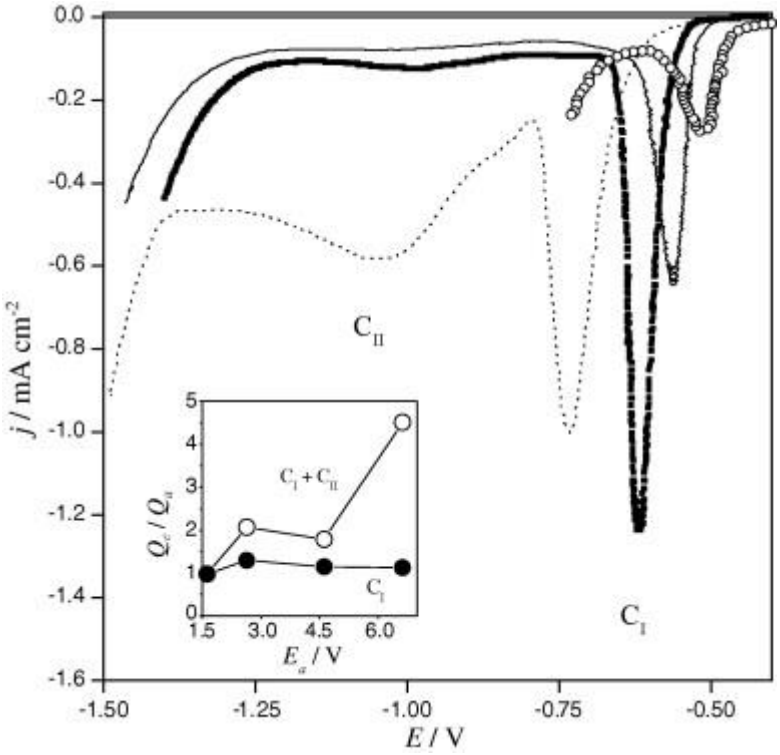

Figure 1.27: CVs for the reduction of Bi2O3 films grown up to different formation potentials (Ea): (○) 1.6 V, (—) 2.6 V, (■) 4.6 V and (···) 6.6 V. 0.1 M Na2HPO4 (pH = 10) of at 1 mV/s. Different potentials lead to different thickness of the Bi oxide. Inset: Q_c/Q_a ratio as a function of E_a for the cathodic charge of C_I (●) and the total cathodic charge ($C_I + C_{II}$) (○)

If the CE was calculated using the charge under the first peak (C_I) without considering the second peak (C_{II}), the response was always very close to one. However, when the C_{II} was considered, higher CEs were obtained. Considering that this range of potentials are too negative to allow the formation of any oxide layer, the second peak must be due to the occurrence of another process. The presence of an additional process was also observed via electrical impedance spectroscopy (EIS). A charge transfer resistance that decreases as the potential became more negative was measured, suggesting that the charge transfer is associated with a cathodic process. In addition, the capacitance changed as a function of the applied potential, suggesting the presence of some species on the surface of the electrode that increase the more the potential becomes negative. Considering the range of potentials, the presence of hydrogen on the surface was suggested to be the cause of the increase in capacitance: during the reduction of the native oxide film, adsorbed hydrogen reacts with Bi metal to form BiH_x species. These species eventually decompose to produce H_2 that is

incorporated into the Bi network and stored in the film during the anodisation. The presence of the BiH_x species was also suggested in other works[195]. The presence of a hydrogen zone in the metallic network of the electrode is confirmed by the difference in dielectric characteristics during the reduction of the anodic film. This was further confirmed using CV measurements. First, the mechanically polished electrode was electroreduced to remove the native oxide layer. Then two potential sweeps were applied: 1) from OCP to a positive potential; and 2) from the positive potential back to the OCP. Finally, the OCP was applied for a certain period of time. Two different final positive potentials were chosen: 0.01 and 0.49 V. In the first case, a thin layer of anodic oxide was formed, while for the second potential a thicker layer was obtained. When the potential was swept to the least positive potential, the oxide was almost completely reduced during the scan back to OCP value and the reduction of the rest of the oxide film was observed during the following 50 seconds at OCP. On the other hand, when the potential was swept to 0.49 V, the oxide layer was not reduced during the negative scan. A decrease of the thickness was then observed when the OCP value was held for 350 s. In addition, the oxide was not completely reduced even after an additional 100 seconds. The decrease of the Bi oxide at the OCP value meant that the Bi oxide was reduced, however, this cannot have occurred via electrochemical reduction, as the OCP is too positive to trigger the reaction. In addition, no chemical dissolution was observed, meaning that the reduction of the anodic layer is occurring through another mechanism. The authors suggested that the reduction of the oxide was indeed electrochemically triggered, but chemically reduced by the hydrogen present on the network of the film. When the anodic layer was thin (sweep until 0.01 V) the hydrogen in the metal network reduced the oxide layer completely, while for a thicker anodic film, the hydrogen cannot reduce everything, as the transport of the hydrogen in the metal framework cannot reach the oxide/electrolyte interface. In addition, the mechanism of electroreduction was different to the one observed for the chemical reduction process described above. Specifically, the chemical reduction occurs at the oxide/electrolyte interface and continues toward the oxide/metal interface, thanks to the migration of electrons from the metal toward the porous metal/oxide interface. Based on these studies, it seems that the Bi hydrides are being formed during the reduction of the oxide layer, however, no analytical detection of these species has been performed. Therefore, there is no conclusive evidence to support this assertion.

In conclusion, the anodisation of Bi metal occurs with a different mechanism than the electroreduction of the anodic oxide. This was observed in different works that used combinations of different techniques, like CV, potentiostatic, optical and EIS measurements. In particular, the nucleation of the anodic oxide was suggested to be a 3-D progressive nucleation mechanism with diffusion-limited growth. The limiting step for the growth was the diffusion of the Bi^{3+} ions through

the oxide layer. This means that the growth of the oxide occurs at the metal/film interface. On the other hand, the nucleation of the Bi^0 after anodisation at high overpotential was a mixed mechanism consisting of instantaneous nucleation and 2-D growth followed by a progressive nucleation and 3-D growth under charge transfer control. This process led to the formation of a porous electroreduced film. The growth of the reduced film occurs at the film/solution interface, with a mechanism that involves transport of electrons from the metal/film interface to the surface of the electrode, where the reduction and nucleation takes place. The porosity of the electroreduced layer is probably due to the reaction of Bi metal with the surface adsorbed hydrogen to give BiH_x species, that decompose forming H_2 that is trapped in the metal network.

1.5.2 Area of electrodes and surface roughness

When describing the surface of an electrode one of the characteristics that needs to be taken into consideration is the area of the electrode as it is strictly connected with the activity and the electrochemical performance of the electrode as it is a measure of the number of active sites[196]. In general, two areas are often considered in electrochemistry: the geometrical area and the real area. The geometrical area is defined as "*the projection of the real surface on a plane parallel to the macroscopic, visible phase boundary*[197]". On the other hand, the real area considers all the concavities, convexities and crannies present on the surface that are not visible macroscopically[198]. Usually, the real area (A_{real}) is larger than the geometrical area (A_{geo}) and, considering that defects are usually larger than the atomic scale, molecules and ions can diffuse and adsorb on these imperfections. It is, therefore, necessary to use the real area or the electrochemical surface area (ECSA) when electrochemical reactions are considered. The geometrical and the real area are related to each other by the nondimensional roughness factor (r_f). The relation between these quantities is shown in Equation (1.6).

$$r_f = \frac{A_{real}}{A_{geo}} \tag{1.6}$$

There are several ways to calculate the ECSA of an electrode and each method has its advantages and disadvantages. The methods to calculate real area were discussed in detail by Trasatti and Petrii[198], and this section will discuss the methods that are most relevant for this work.

The A_{real} can be calculated using in-situ or ex-situ methods. The method for calculating the area is chosen depending on the physical nature of the electrode (liquid or solid) or its chemical nature (pure metal, metal oxide or non-metal). For example, the real area of liquid metal electrodes like

pure mercury electrodes is calculated using the drop weight method, which is based on the calculation of the mass of the liquid dropped in a capillary for a fixed period of time[199]. For solid electrodes, several methods can be used. For example, Pt, Ni and a few other transition metals are able to adsorb hydrogen in solution at specific potentials. For this reason, it is possible to calculate the area of the electrode by performing CV in the potential range in which adsorption of hydrogen occurs. When hydrogen is adsorbed on a surface, a peak in the CVs is observed. By integrating the area below this peak, the charge associated with the adsorption process (Q_{exp}) is obtained, and the area can be calculated from the ratio between Q_{exp} and the standard surface charge for the specific material. The standard surface charge represents the charge associated with the bonding of one hydrogen atom with each metal atom on the surface. This value is usually expressed in $\mu C/cm^2$ and it is related to the volume density of the specific metal. An exhaustive explanation of this method was provided by Doña Rodríguez et al.[196] that showed how the ECSA of Pt electrodes can be calculated using the hydrogen adsorption method. The CVs acquired with Pt electrode in H_2SO_4 is shown in Figure 1.28, in which the peaks associated with the adsorption of a monolayer of hydrogen (first peak) and the successive layers (second peak) are clearly shown (see inset in Figure 1.28).

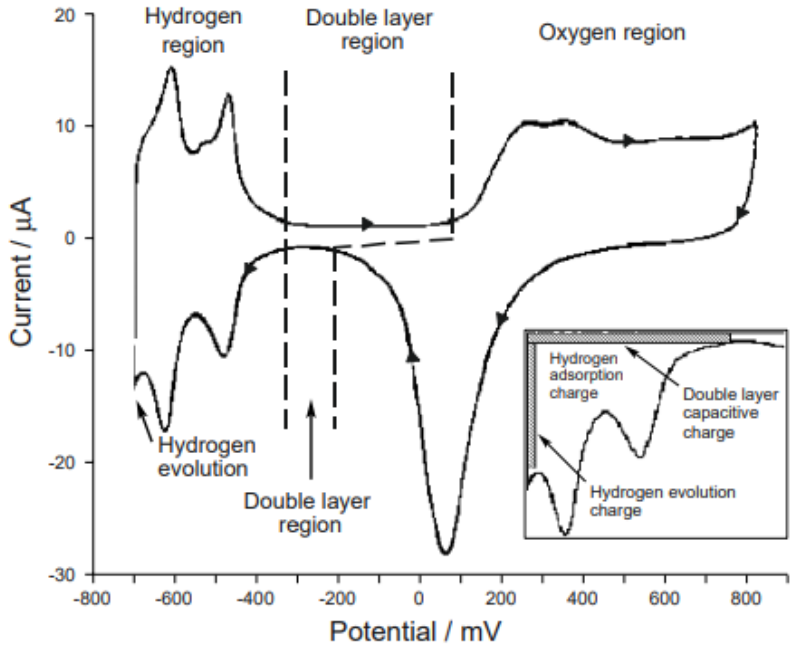

Figure 1.28: CVs for a platinum electrode in contact with a 0.5 M H_2SO_4 solution. The inset shows the different charge distribution in the hydrogen region [196]

This method is very convenient, as it allows an in-situ measurement of the real area with accuracies around 90%. However, it presents several limitations. First, this method does not take into consideration the double layer charging, needing a post-correction; second, the formation of the monolayer of hydrogen needs to be complete and the process needs to be finished before HER

starts. It is important to remember that the completeness of the monolayer formation might not ever be reached as the molecules of the solvent can be adsorbed. Similarly, oxygen adsorption can be used to calculate the ECSA of transition metals like Au[200,201], Ag[202] and Bi[101]. For example, Bonroy et al. estimated the ECSA and roughness factor of several Au electrodes produced via electrodeposition via oxygen adsorption method (see Figure 1.29).

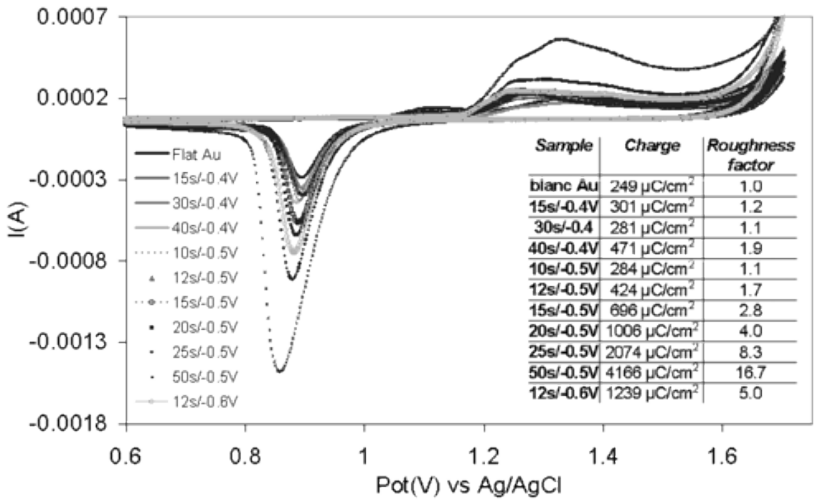

Figure 1.29: Determination of the surface roughness of the gold samples using oxygen adsorption method via CV in 0.5 M H_2SO_4. The charge per surface area under the cathodic peak and the roughness factor for the different gold surfaces are presented in the table [201].

Knowledge of the roughness factor allowed the researchers to understand which deposition conditions would lead to the most porous electrode. The oxygen adsorption method exploits the formation of an oxide monolayer on the surface of the metal. Once the oxide monolayer is electrochemically formed, it is reduced and the charge related to the reduction process (Q_{exp}) is divided by the standard charge to obtain the ECSA. The oxide monolayer can be formed via anodic potential sweep or anodic current pulse. In the first case, oxidation of the impurities present in the system can occur simultaneously with the oxidation of the metal; in the second case, the time of the application of the current pulse needs to be chosen carefully to avoid deposition of oxygen multilayers. The oxygen adsorption method shares many of the limitations with the hydrogen adsorption method which were listed above. Its accuracy is lower than that of the hydrogen adsorption method as the affinity between oxygen and metal can be stronger than between hydrogen and metal.

If a non-metallic electrode is used, cyclic voltammetry measurements can be used to obtain the double layer capacitance of the electrode and therefore the ECSA. The measurements need to be performed in a small range of potentials where only non-faradaic processes happen. Several scans are performed at different scan rate values (scan rate study) and the value of current in the middle of the potential range is plotted as a function of the scan rate value. To obtain the ECSA, the

measured double layer capacitance is divided by a standard capacitance. This method is often used when large or porous surface areas are measured. For a more detailed discussion of the capacitance method, see Section 1.5.2.1.

Another method often used when a non-metallic electrode is characterised is the mass transport method. During a potential sweep, a reactant, that after an electron transfer process, is replenished at the surface of the electrode via diffusion will produce a current that is proportional to the real area of the electrode (see Equation (1.7))

$$i_p = A\left(kn^{\frac{3}{2}}D^{\frac{1}{2}}C\right)v^{\frac{1}{2}} \tag{1.7}$$

where A is the area of the electrode, k is a numerical constant that is determined empirically, n is the number of electrons exchanged during the electron transfer process, D is the diffusion coefficient, C is the concentration of the reactant and v is the scan rate. This method has been used for the calculation of ECSA for a variety of electrodes, from carbon-based electrodes[203,204] to metal electrodes like Au[205], Ni[206] and Cu[206]. The main limitation of this method is the fact that is not suitable for surfaces in which high porosity and roughness are present as the diffusion layer has a macroscopic order of magnitude and therefore the roughness will be detected at the same order of magnitude. In addition, the method assumes that a homogenous distribution of the current is present on the surface of the electrode. This is not always true for surface containing asperities (like electrodes containing micro or nanostructures).

Several ex-situ techniques are commonly used, like microscopy, X-ray and porosimetry. One of the most used methods among the ex-situ techniques is the Brunauer, Emmett and Teller (BET) method. It consists of the physical adsorption of probe molecules in gas phase (adsorbate) on the surface of the electrode. In this way, the saturated surface concentration can be obtained, and the area calculated. The adsorbate is inserted in a tube with the surface to analyse, and to allow the complete coverage of the surface with a monolayer of gas, its pressure is increased, while the temperature is kept constant. Once the surface is completely covered, the molecules are desorbed and the number of molecules adsorbed on the surface is obtained. Usually, N_2 is used for BET measurements as it is inert and tends to adsorb on the majority of solids. However, several adsorbates can be used, like Ar, CO_2, O_2, CO and H_2O and the choice of a specific adsorbate depends on the nature and porosity of the material[207]. Even though BET measurements are extensively used it is often not straightforward to make a direct comparison with the electrochemical surface area as the adsorption of the molecules can occurs on sites that might not be electrochemically active,

for this reason, BET measurements results should be used as qualitative information and the value of the real area should be confirmed with other techniques.

1.5.2.1 Capacitance

When an electrode is immersed in a solution, a double layer is formed. The double layer has specific electrochemical properties depending on the nature of the electrolyte, of the electrode and their interactions (like the adsorption of the ions on the electrode surface)[208]. The double layer behaves as a capacitor, meaning that, when a potential is applied, a certain amount of charge is stored and a current, called charging current, flows. The stored charge is the result of the adsorption of the cations and anions in solution on the surface of the electrode[209]. For this reason, measurements of the double layer capacitance of a specific system provide information on parameters like the area, the structure and the chemical nature of the electrode, and the interactions between the species in solution and the surface of the electrode[208,210,211]. The double layer capacitance is often measured using three different techniques: galvanostatic charge/discharge measurements, CV or impedance[211,212]. In particular, impedance is usually used to calculate the differential capacitance, that is defined as the change in charge density as a result of small perturbation in potential. By way of contrast, potentiostatic methods are used to obtain the integral capacitance, that is an average of the differential capacitance over a certain potential range[45,213]. Galvanostatic methods can be used for both differential and integral capacitance. The double layer capacitance has often been used to estimate the electrochemical surface area (ECSA) of the electrode. To calculate ECSA using the double layer capacitance, a standard capacitance is needed (see Section 1.5.2). Usually, the standard capacitance is obtained from the atomically smooth planar surface of the metal under investigation[214]. In the absence of the standard capacitance, the ECSA can simply be estimated. However, it is important to highlight that capacitance is strongly influenced by the nature of the metal, therefore a complex composition, like in the case of metals that tend to naturally form oxides, might lead to an incorrect calculation of the ECSA of the electrode. In addition, the electrolyte can have undesirable effects, as some ions adsorb on the surface of certain metals but not on others. For this reason, the double layer capacitance should be only used to compare areas of different samples of the same material[198]. The double layer capacitance of Bi electrodes has been calculated in different works and different values were obtained, depending on the surface of the electrode and the electrolyte used[153,194,215–217]. For example, Hung et al.[215] used the double layer capacitance to compare the surface area of different Bi electrodes. Different substrates were used for each Bi electrode to test the influence of the substrate on the reduction of CO_2: the first was a mesoporous hollow kapok-tubes (MHKTs) electrode, the second was carboxylic multi-walled carbon nanotubes (cMWCNTs) electrode; and

the third was a reduced graphene oxide (rGO) electrode. The double layer capacitance was calculated via scan rate study in a potential window of 0.6 - 0.7 V. The double layer capacitance value was obtained plotting Δj (= j_a - j_c) at 0.65 V vs the scan rate (see Figure 1.30) The values obtained for the three electrodes were quite similar, with Bi@MHKTs having the highest value (1.27 and 1.35 times higher than for Bi@MWCNTs ad Bi@rGO, respectively), suggesting that the MHKTs electrode has the highest ECSA.

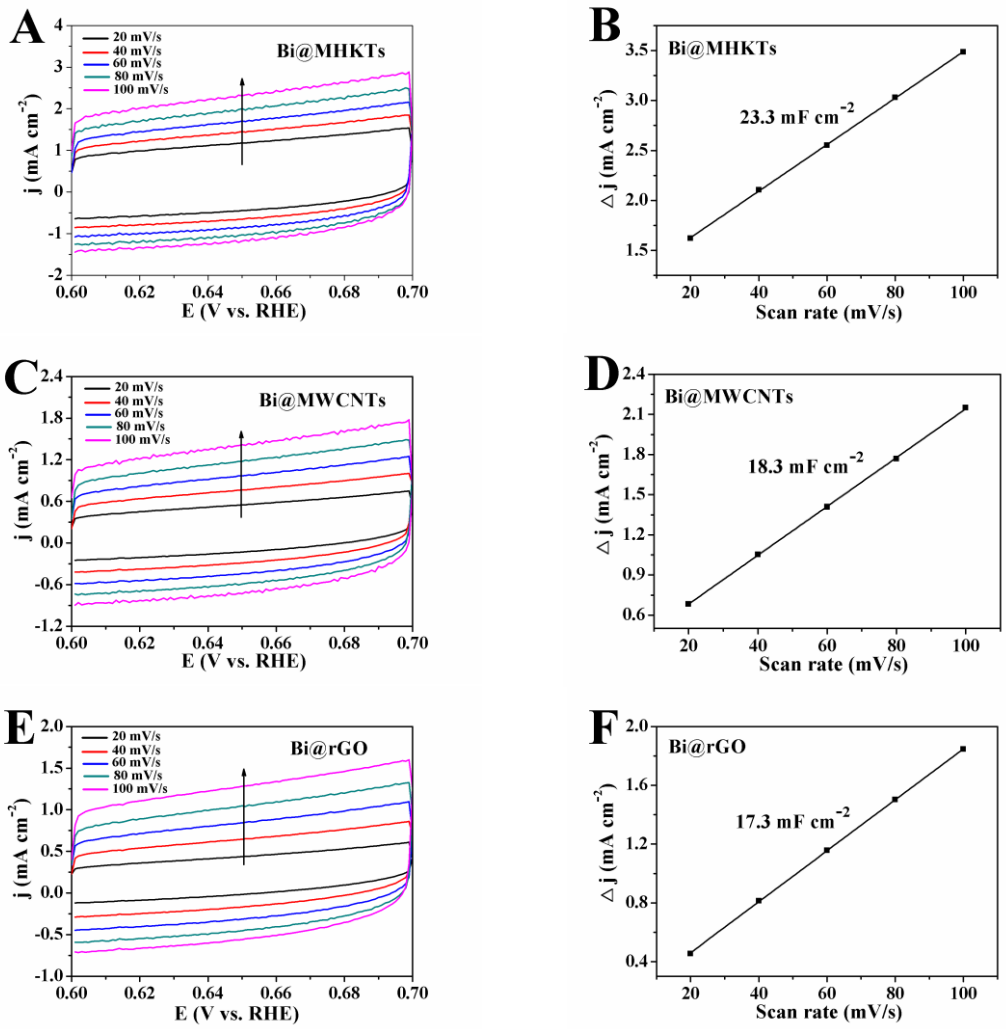

Figure 1.30: CVs of (A) Bi@MHKTs, (C) Bi@MWCNTs and (E) Bi@rGO measured in N_2-saturated 0.5 M $KHCO_3$ aqueous solution at scan rates from 20 to 100 mV s-1, respectively. Charging current density differences plotted against scan rates for (B) Bi@MHKTs, (D) Bi@MWCNTs and (F) Bi@rGO.

By way of contrast, Zhong et al.[153] compared the double layer capacitance of two Bi electrodes obtained via electrodeposition. The first electrode, Bi-A, was electrodeposited in a deposition solution that did not contain KBr, while the second electrode, Bi-B, was electrodeposited in the presence of KBr. Bi-A presented a flower-like morphology, while Bi-B showed nanodendritic structures. The double layer capacitance was calculated via scan rate study and it was found to be equal to 0.184 mF/cm^2 for Bi-A, and to 1.973 mF/cm^2 for Bi-B, a value 10 times higher. This was

attributed to a larger surface area of Bi-B due to the presence of the nanodendritic tructures that presented smaller particles. However, the composition of the two electrodes is slightly different and a higher content of Bi metallic is present in Bi-B than in Bi-A. This can be a contributing factor in the difference in the capacitance values. Similarly, in another study[102], the double layer capacitance of several Bi electrodes obtained using two different electrodeposition techniques was measured. Two electrodes were produced via direct electrodeposition with different deposition times: 60 seconds (DC-60s) and 120 seconds (DC-120), while four other electrodes were produced via pulsed electrodeposition. One cycle of t_{on} and t_{off} was performed for the first electrode (PC-1c), three cycles were performed for the second electrode (PC-3c), six for the third electrode (PC-6c) and nine for the fourth electrode (PC-9). The lowest capacitance was observed for DC-60s (0.398 $\mu F/cm^2$) and the highest for PC-6c (82.2 $\mu F/cm^2$). Interestingly, DC-120 showed the second highest capacitance (40.4 $\mu F/cm^2$), suggesting that the capacitance is not simply influenced by the type of electrodeposition. Amongst the PC electrodes, the trend observed was: PC-6c > PC-9c > PC-3c > PC-1c. In particular, PC-6c showed a capacitance 6.3 times higher than PC-9c and 203 times higher than PC-1c. This variation in the capacitance values was attributed to a difference in ECSA, specifically to the number of nanoflakes, and to the width of their edges. In another study[194], Bi microelectrodes were electrochemically modified to obtain a porous surface and the double layer capacitance was calculated. The porous electrodes were obtained using two methods: for the first electrode (BiCCE 1), a potential of 1 V was applied for 1 second, followed by a potential of -2.2 V for 0.5 seconds to allow the formation of Bi^0 on the surface; for the second electrode (BiCCE 2), a potential of -2.0 V was applied for 5 minutes. The capacitance of BiCCE 2 was equal to 36.0 $\mu F/cm^2$, 1.64x times higher than for BiCCE 1, indicating a higher porosity for BiCCE 2. The porosity of the electrodes was then examined via SEM imaging.

The variation of the double layer capacitance due to the nature of the electrode material was investigate by Teng and Teng[216]. The capacitance of BiOCl nanosheet electrodes was measured for two different samples, obtained using two different synthetical procedure. Nanosheets with (V_{Bi}-BiOCl) and without bismuth vacancies were produced, mixed into a carbon ink and deposited on the substrate. The CVs for the scan rate study were acquired between 0 and 0.8 vs SCE. The capacitance was calculated to be 6.3 mF/cm^2 for BiOCl and 17.3 mF/cm^2 for V_{Bi}-BiOCl. The difference in the capacitance values was attributed to the adsorption of the Na cations on the surface of the electrodes. In the case of V_{Bi}-BiOCl, the cations are more strongly adsorbed than on BiOCl because of the Bi vacancies. Considering that the native oxide layer is formed quickly at the surface of bismuth, it is important to consider the effect of the metal oxide on the capacitance of the double layer. Bi_2O_3 has attracted increasing attention as a possible supercapacitor material for

its low cost, environmental friendliness and high theoretical specific capacitance[218]. Its specific capacitance (that is the capacitance per mass of material) can vary significantly from 94 to 1350 F/g depending on factors like the morphology of the Bi_2O_3 particles or the substrate used for the electrode[219,220]. These numbers are from three to four orders of magnitude higher than the ones obtained for Bi metal, suggesting that a surface with a mixture of metal and metal oxide could greatly influence the capacitance of the double layer and therefore the values obtained for ECSA.

In summary, several methods for the calculation of the ECSA were discussed. Each method presents advantages and disadvantages and the choice of one over another needs careful considerations of the electrode used, its composition (for example the presence of native oxide) and its roughness factor. For this reason, in this work, several techniques were used for the calculation of the ECSA and their values compared. However, as Bi electrodes present a native oxide layer, the oxygen adsorption method seems to be the most suitable option for the calculation of the ECSA of Bi electrodes.

1.5.3 Type of surfaces: polycrystalline vs micro- and nanostructured electrodes

The real area of an electrode is a very important feature for an electrode. This is particularly true when the surface under investigation is an electrocatalyst, as the ECSA is directly proportional to the number of the active sites for catalysis[196,206]. For this reason, using the geometrical area to normalise the currents obtained during a catalytic process can lead to a significant deviation in the calculation of the current density value. The difference between geometrical area and real area becomes even more pronounced if micro- or nanostructures are present on the surface of the electrode. The presence of micro- or nanostructures can significantly increase the density of active sites and, therefore, the surface area[221]. In several studies, the ECSA of planar and micro- or nanostructured metal electrocatalysts has been calculated via a variety of methods. In this section, some of these studies are presented and discussed using CO_2 reduction electrocatalysts as an example. In the context of CO_2 reduction, it has been demonstrated before that micro- and nanostructured electrodes present several advantages over polycrystalline electrodes, like lower onset potential for CO_2 reduction, higher selectivity and stability[222]. Several methods have been used for the calculation of the ECSA, such as capacitance[202,223–225] and oxygen adsorption method[101,202,226]. The calculation of ECSA between polycrystalline and nanostructured electrodes has also being investigated using the oxygen adsorption method for Ag and Bi electrodes[101,202]. Koh et al.[101] calculated the ECSA for a Bi foil and a Bi dendrites electrode. To obtain the Bi dendrite electrode, the Bi dendrites were electrodeposited on a Bi foil, which was previously prepared via e-

beam evaporation on a Cu substrate (Figure 1.31a, b and c). The ECSA of the Bi dendrite electrode was clearly higher than of the pristine Bi foil: the charge under the reduction peak (see Figure 1.31d) for the Bi dendrites electrode was three times higher than for the pristine Bi foil (for Bi dendrites electrode, Q_{exp}= 7.07 mC/cm^2; for Bi foil, Q_{exp}= 2.28 mC/cm^2). As far as the CO_2 reduction is concerned, the Bi dendrite electrodes were able to reduce CO_2 with high selectivity (89% formate at an overpotential of 710 mV vs RHE) and stability (12 h). On the other hand, the pristine Bi foil presented lower selectivity (55%) and it reached its max (80%) at higher overpotentials (-0.9 V vs RHE). The FEs at the same potentials for Bi dendrites is 1.6x times higher than for Bi foil, suggesting that the magnitude of ECSA is related to the catalytic activity of the electrodes.

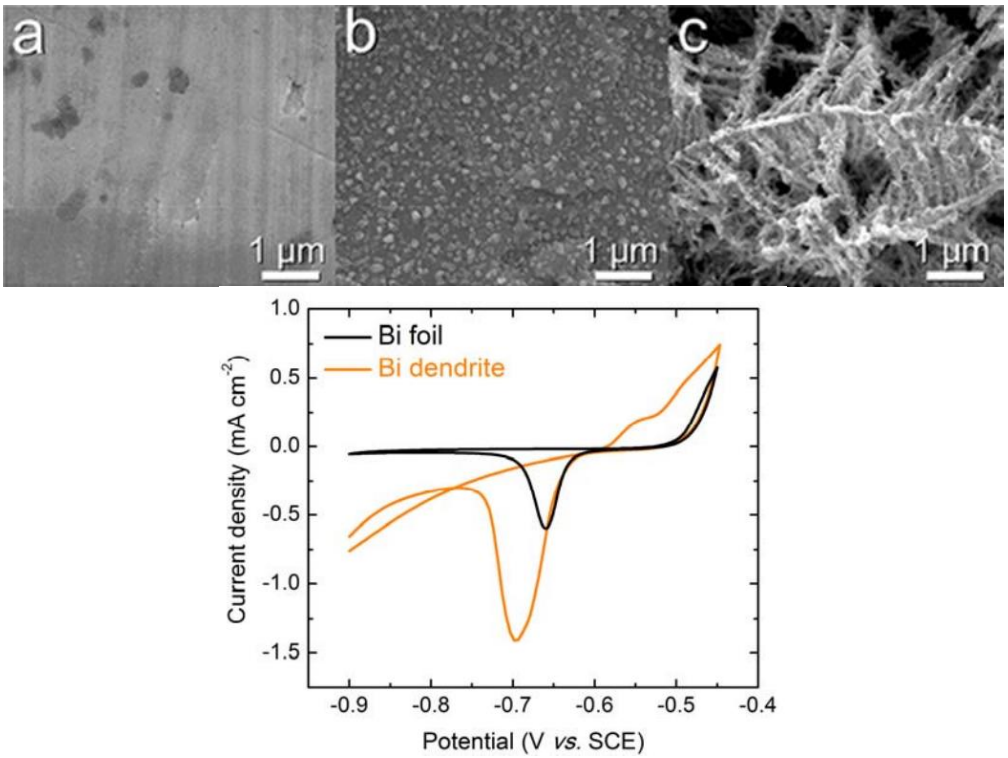

Figure 1.31: Morphological characterization of Bi dendrite electrode. SEM images of (a) pristine Bi foil, (b) e-beam deposited Bi, and (c) Bi dendrites; d) Electrochemical surface area (ECSA) measurements of the Bi foil and the Bi dendrite electrode using the oxide monolayer method [101]

Similarly, Daiyan et al.[202] measured the ECSA of Ag foam and Ag foil electrodes using the oxygen adsorption method and qualitatively evaluated them using the voltammetry method. The Ag foam electrode ($AgFoam_{60}$) was produced via galvanostatic electrodeposition on Ag foil using hydrogen bubbles as a template where the Ag particles can nucleate and grow. The sizes of the pores were between 10 and 50 microns. $AgFoam_{60}$ presented a higher charge under the reduction curve than Ag foil (Figure 1.32c), suggesting a higher ECSA. In addition, the adsorption of OH^- is around 100 mV lower in $AgFoam_{60}$ than on Ag foil, suggesting stronger binding of OH^- on the $AgFoam_{60}$ substrate and therefore the presence of more active sites. The higher number of active sites was confirmed during catalysis measurements as the CO current density (j_{CO}) was 46 times higher for $AgFoam_{60}$

than for Ag foil. The higher ECSA of $AgFoam_{60}$ was confirmed by the capacitance values obtained for the two electrodes (see Figure 1.32a and b). The capacitance value for $AgFoam_{60}$ was 34 times higher than for Ag foil. The discrepancy between the increase in capacitance values (34x) and the increase in the magnitude of the current density (46x) for $AgFoam_{60}$ might be due to possible interference with the surface and the solution during voltammetric measurements[198].

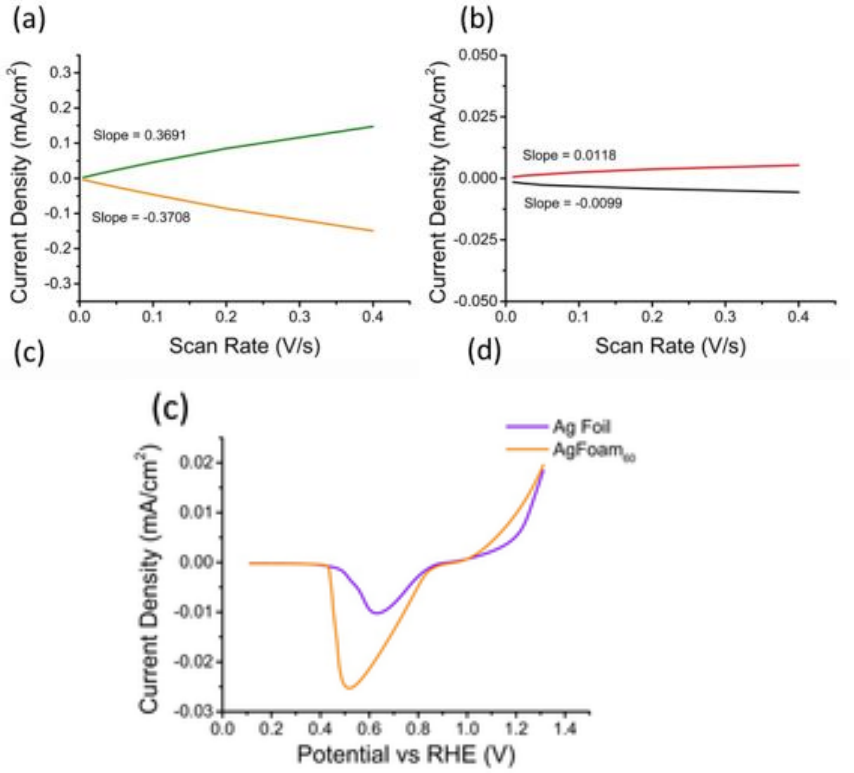

Figure 1.32: Current density plots at various CV scan rates for (a) $AgFoam_{60}$ and (b) Ag foil. The double layer capacitance was calculated by averaging the absolute values of cathodic and anodic slopes of the linear fits. c) Adsorption affinities of OH− ion on AgFoam60 and Ag foil performed in Ar saturated 0.1 M NaOH electrolyte [202]

The majority of the studies for CO_2 reduction, normalise the current to the geometrical area[222]. As shown before, a significant difference between the ECSA of polycrystalline electrodes and electrodes produced with NPs is observed. Therefore, it seems reasonable to assume that this kind of normalisation can lead to erroneous conclusions, as a current density normalised to the geometrical area can be significantly larger than the one normalised to ECSA. For example, voltammetry was used to measure the ECSA of some oxide derived (OD) Cu NPs electrodes[223]. Two electrodes were prepared by, first, electrochemically cleaning a copper foil and then oxidised it in an oven for 1 h at 500 °C. The first electrode, OD Cu 1, was reduced during CO_2 reduction electrolysis at 7.5 mA/cm^2 until a charge between 10 - 12 C/cm^2 was passed. For OD Cu 2, the foils were reduced by placing them in a tube furnace under H_2 atmosphere at 130 °C for 2 hours. The capacitance was calculated after bulk electrolysis at 1 and 12 hours. The capacitance, and therefore the ECSA, decreased by 1.6 mF for OD-Cu 1 and 0.7 mF for OD-Cu 2 during the 11 h of electrolysis. The

capacitance of OD-Cu 1 was equal to 4.6 mF and for OD-Cu 2, it was calculated to be 1.8 mF. This means that a higher ECSA was obtained when the electrochemical reduction was performed in comparison with the thermal reduction. As far as the catalytic activity of the electrocatalyst is concerned, differences in CO current density (j_{COredn}) were observed when the current was normalised to the geometrical area (geometric j_{COredn}) or the ECSA (normalised j_{COredn}). A difference of one order of magnitude was observed for the current densities: 10^{-1} mA/cm^2 for geometric j_{COredn} and 10^{-2} mA/cm^2 for normalised j_{COredn}. In addition, for geometric j_{COredn}, OD-Cu 1 presented slightly higher current densities, while for the normalised j_{COredn}, the current density was higher for OD-Cu 2 (see Figure 1.33b and c).

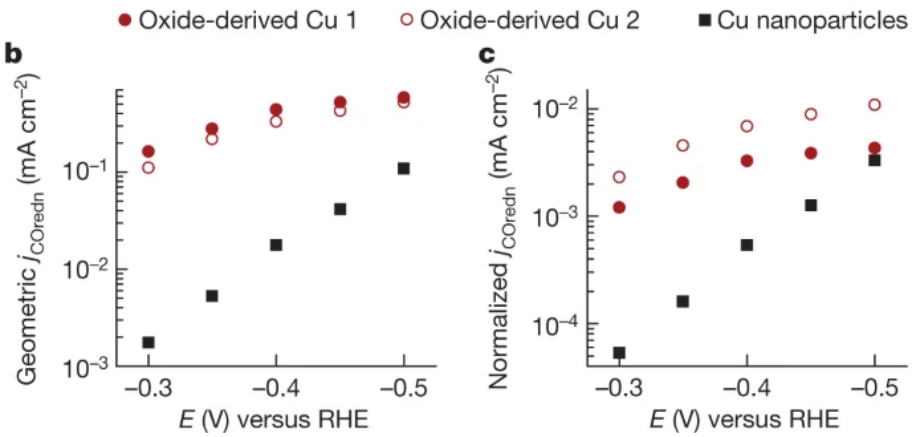

Figure 1.33: b) Geometric current densities for CO reduction; c) Surface-area-normalized current densities for CO reduction[223]

In this case, the difference in catalytic activity for the two OD electrodes is not dramatically different. However, it shows that the use of the geometrical area might lead to an assumed conclusion which may not be reflective of the true value. In contrast, Li and Kanan[224] showed that the increase of surface area for an oxide derived Cu electrode in comparison with a Cu polycrystalline electrode is not directly proportional to the increase of the current densities and the faradaic efficiencies. The ECSA was calculated via voltammetric method and the capacitance was equal to 13.9 mF/cm^2 for the oxide derived Cu electrode, while it was 29 µF/cm^2 for the polycrystalline electrode. This means that the area was 480x larger for the nanostructured electrode, while the current densities and the faradaic efficiencies were only around 30x higher, suggesting that the ECSA is not representative of the number of active sites for CO_2 reduction. However, it is important to highlight that calculation of ECSA via voltammetry method is actually advised against for metal oxide electrodes, as the mechanism of charging an oxide is more complex than for metals, because of the strong dependence of the metal oxide surface on the solution pH and the potential sweep show[198]. In general, it seems that high surface area electrodes showed an increased catalytic activity towards CO_2 reduction. However, care needs to be taken when

comparing the catalytic activity of different electrodes based on the current density values, as performing the normalisation of the current using the geometrical area might lead to erroneous conclusions. Furthermore, normalisation of the current using the geometrical area instead of the ECSA can also result in an apparent shift on the onset potential for the catalytic process. This is simply due to the mathematical correction, however, it is clear that this can be problematic if the potential chosen is lower in comparison with the one at which a significant quantity of the final products can be detected. It is important to highlight that micro- and nanostructures can present different composition and crystal structures than their flat counterparts, two factors that are well known to influence the catalytic activity of CO_2 reduction[100,101]. In addition, mass transport on micro- and nanostructures is different than on flat electrodes[222]. This suggests that, even if the ECSA plays an important role in the electrochemical characteristics of an electrode, a broader approach needs to be taken into consideration.

In conclusion, a significant difference was observed between the ECSA of flat polycrystalline and micro- or nanostructured electrodes, regardless of the method used for its calculation. In general, micro- and nanostructured electrodes present higher area and this will result in a difference in current densities when one area or the other is used for the normalisation. This could lead to erroneous evaluation of the catalytic activity of an electrode. For this reason, the area used for the normalisation of the current should careful evaluated.

1.6 Application: electrochemical CO_2 reduction

In this section, the application for Bi electrodes investigated within this project will be discussed. For a discussion on the high-level challenges posed by the increase of CO_2 concentration in the atmosphere see Section 1.1.

1.6.1 Electrocatalysts for CO_2 reduction

Over the last three decades, homogeneous and heterogeneous catalyses have been used extensively for CO_2 reduction, providing encouraging but different results in both cases. In heterogeneous catalysis, the system under investigation is composed of two or more different phases. A common example is the synthesis of ammonia from N_2 and H_2, (the Haber process), where the catalyst is solid while the other reactants (N_2 and H_2) are in the gaseous phase[227]. On the other hand, the entire system has only one phase when homogeneous catalysis is employed (for example, the acid catalysis of esters to acids). Both approaches have advantages and disadvantages and, as far as CO_2 reduction is concerned, the two types of catalysis are used widely. For the heterogeneous electrocatalysis of the CO_2 reduction reaction, four main groups of materials are used: 1) metals, 2)

metal oxides/sulphides/nitrides, 3) metal complexes, and 4) organic molecules. For all these classes, either aqueous or organic solvents are used as a reaction medium, leading to different reduction products and efficiencies. pH variations and the nature of electrolytes used during experiments are two other key factors.

In the last 20 years, several metals have been tested for CO_2 reduction. Several research groups investigated the ability of different metals to produce different products. The main carbon products that can be obtained from the reduction of CO_2 on metal electrodes are formate[228,229], CO[230,231], methanol[232,233], oxalate[234] and hydrocarbons with more than two carbon atoms[235–238]. Additionally, H_2 is formed from protons in solution as a by-product. In general, copper electrodes yield the production of several compounds such as linear hydrocarbons, CO, alcohols and aldehydes[236], while the use of Ag, Au and Zn electrodes leads predominantly to CO formation. By way of contrast, Sn, In, Pb and Bi tend to favour formate while Pt, Fe and Ni tend to favour H_2 only (ie: CO_2RR is disfavoured)[239]. Obtaining one product in preference over others is attributable to several factors intrinsic to the metals used, including the overpotential for H_2 production, the relative rates of competing reactions and the adsorption strength of both CO_2 and its reduction products. The degree of adsorption is a crucial aspect in the selectivity of final products as it can affect the course of the reaction. In fact, the choice of a metal with a high adsorption for both CO_2 and its products (of which CO should be considered as it is the first intermediate between CO_2 and more reduced compounds) can in time lead to a lack of active sites for CO_2 molecules (i.e.: surface poisoning), as products formed during the reaction do not readily desorb. On the other hand, a metal with low CO_2 adsorption ability leaves free active sites for protons, leading to an increase in H_2 formation. For this reason, a metal that presents a high overpotential value for hydrogen production and medium adsorption for CO_2 and the products obtained during the reduction reaction should be preferred. The first factor is particularly advantageous, as the main competing reaction (hydrogen production) is less likely to take place in these conditions. The main focus of the following section will be the discussion of the production, characterisation and use of different Bi electrodes for CO_2 reduction.

1.6.1.1 CO_2 reduction with Bismuth electrodes

The first application of bismuth electrodes for CO_2 reduction reported in the literature was performed in a work of Hara *et al*.[104]. In their work, different metals were used in a bicarbonate electrolyte at high pressure of CO_2 (30 atm). On Bi working electrode and at a potential equal to -1.42 V vs Ag/AgCl, mostly formate was produced (FE_{HCOOH}≈83%) and small amounts of H_2, CO and CH_4 were detected (FEs were equal to 6.3, 3.3 and 0.17% respectively). In addition, they claimed that the selectivity of the products was due to the type of metal and not to the pressure of CO_2.

After this pioneering work, the enhancement of the faradaic efficiency, the improvement of selectivity and the lowering of the overpotentials was sought using different Bi electrodes and adjustment of the system conditions. The additional advantage of using bismuth in electrodes for the reduction of CO_2 is the likelihood of suppressing H_2 evolution at potentials close to the CO_2 reduction overpotentials.

1.6.1.1.1 Preparation of Bi electrodes for CO_2RR: substrates and electrodeposition

Frequently, bismuth particles are placed on carbon-based electrodes (mostly glassy carbon and carbon paper) using different techniques such as drop casting[240,241] or electrodeposition[153,240]. Carbon substrates are particularly appropriate because of their low cost and the fact that they are inert towards the CO_2RR. For example, in a work of Zhang *et al.*[240], BiOCl nanosheets were first mixed with Nafion and then deposited on a Glassy Carbon electrode (GCE). The modified GCE was then converted into a high-surface-area Bismuth (HSA-Bi) electrode in-situ by immersing it in 0.5 M $KHCO_3$ and applying a potential equal to -1.3 V vs SCE for 60 min. The as-obtained electrodes exhibit nanosheets with sizes around 10 nm that formed aggregates with sizes between 60 and 100 nm. Their composition consisted of mainly Bi(0), as via EDX, Bi atomic ratio was equal to 83%, while it is around 34% in BiOCl. In addition, X-ray powder diffraction (XRD) analysis showed the presence of the 012 plane in HAS-Bi electrode, typical of the Bi metallic. The last two results confirmed the reduction of BiOCl to metallic Bi. In comparison with commercial Bi, the HSA-Bi electrode presented a surface area 6x higher but FEs for formate 7x larger at -1.40 vs SCE (Figure 1.34). Therefore, the higher catalytic activity of the modified electrode cannot be solely resulted from an increase in the surface area, but it might be caused by microscopic structure and the crystal size.

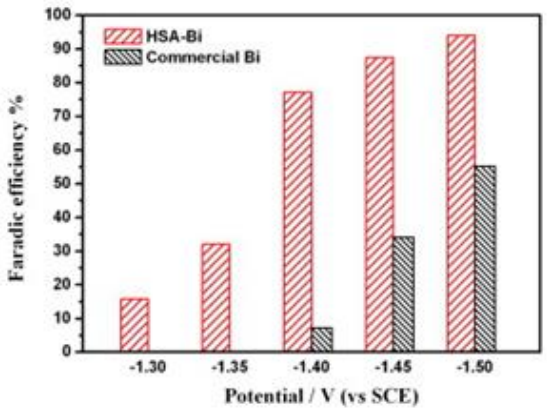

Figure 1.34: Formate faraday efficiencies using HAS-Bi and commercial Bismuth electrodes at different potentials[240]

The faradaic efficiencies increased as a function of the potential, reaching their maximum (92%) at -1.50 V. For more negative potentials, a decrease in faradaic efficiencies was observed, probably due to the competitive HER. In a different work[153], bismuth was electrodeposited on a carbon paper

electrode and the catalytic performances of the system were tuned by changing the parameters of the deposition. First, the substrate was immersed in a solution 1.2 M of HCl with 20 mM of $Bi(NO_3)_3$ and a potential of -0.35 V vs SCE was applied. By adding in the electrodeposition solution 0.25 mol/L of KBr or by changing the time of the deposition, different morphologies and therefore catalytic activities were observed. The electrode obtained in the presence of KBr (electrode Bi-B) consisted of nanodendritic structures, while in the absence of KBr (electrode Bi-A) a flower-like structure was observed (Figure 1.35a-d). Bi-B showed higher catalytic activity than Bi-A at all the applied potentials (Figure 1.35e), likely due to the higher number of catalytic sites of Bi-B, resulting from the presence of the high surface area dendrites. At Bi-B, the faradaic efficiencies for formate were from 1.1 to 2 times larger than at Bi-A: at -1.8 V, FE_{HCOO^-}= 96.4% for Bi-B, 10% higher than for Bi-A (FE_{HCOO^-}= 84.7%).

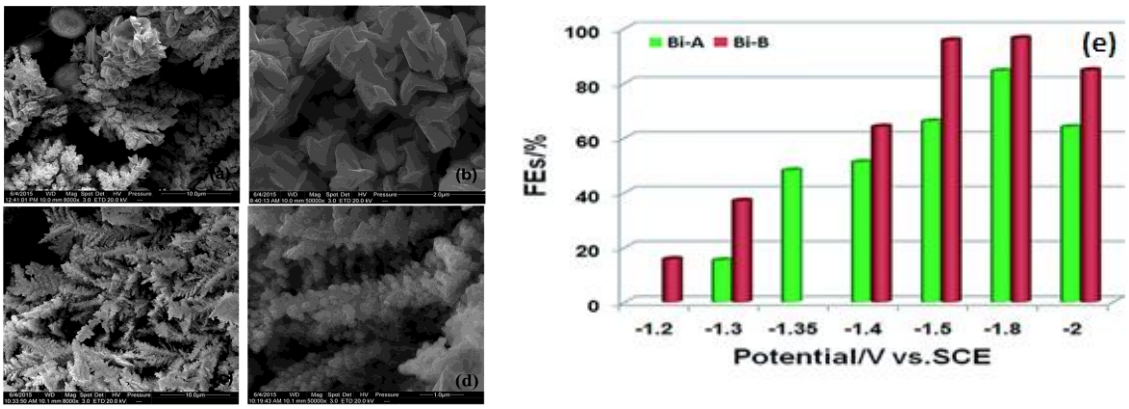

Figure 1.35: Morphology of Bi-A (a, b) and Bi-B (c, d) electrodes; e) FE for formate production at different potentials for both electrodes[153]

Another material often used as substrate for the production of Bi electrodes is copper. In this work of Lv *et al*.[154], a film of Bi was electrodeposited onto a cleaned Cu foil from a solution of choline chloride, oxalic acid and 10 mM $Bi(NO_3)_3$. Before applying a potential of -1.0 V vs Ag/AgCl, the solution was stirred at 50°C for 10 hours. The Bi/Cu electrode showed rod-like features and composition of mixed Bi^{3+} and Bi^0 with a ratio of 92:8. It is important to note that CO_2RR has been extensively reported on materials that consist of Bi(0), Bi(III) and mixed oxidation states. CPE measurements were performed in a CO_2-saturated solution of 100 mM $KHCO_3$ and potentials between -1.4 to -1.7 V were applied. As can be seen in Figure 1.36, the Bi/Cu electrode showed a FE for formate equal to 91.3% at -1.5 V vs Ag/AgCl, 6 times as higher than the one obtained with Bi foil. However, considering the intrinsic catalytic activity of Cu for the CO_2RR, a careful evaluation of the source of the reduction products needs to be done. Therefore, because of their inert nature, carbon substrate will be the superior choice even if it has been demonstrated that the interaction

between Bi and metals is higher than with glassy carbon (see Section 1.4.1.1), meaning that a better electrodeposit will be more easily achieved.

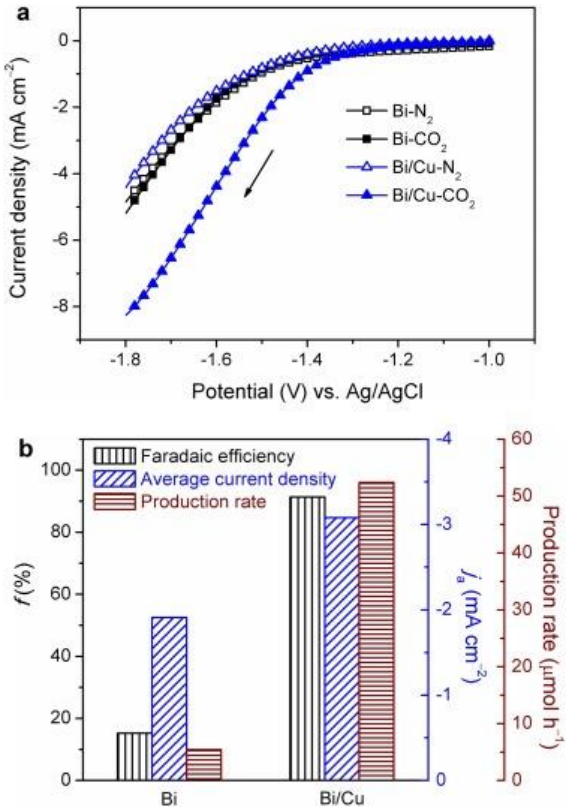

Figure 1.36: Comparison between Bi/Cu electrodes and Bi foil: a) current density under N_2 and CO_2 and b) faradaic efficiency for formate[154]

The type of technique used for the formation of the Bi particles significantly affects the characteristics of the electrode. For example, using a pulsed electrodeposition technique instead of a continuous electrodepositon led to the production of completely different electrodes. In an interesting study[102], electrodeposition was performed immersing a Cu foil in a solution 33 mM of $Bi(NO_3)_3$ in HCl and applying a potential equal to -0.1 V vs Ag/AgCl. Three different electrodes, DC-60s, DC-120s and PC-6c, were obtained by applying the chosen potential for different periods of time. In particular, for the formation of DC-60s, the potential was held for 60 seconds and nanodot-shaped Bi particles were observed; for the development of DC-120s, the potential was kept constant for 120 seconds and irregular pellets, assembled to form dendrites, were found; finally, for the production of PC-6c, the potential was applied 6 times for 10 seconds, followed each time by a quiet time of 40 seconds, and nanoflake particles were obtained. A scheme of the deposition procedures and the correspondent morphologies is shown in Figure 1.37A.

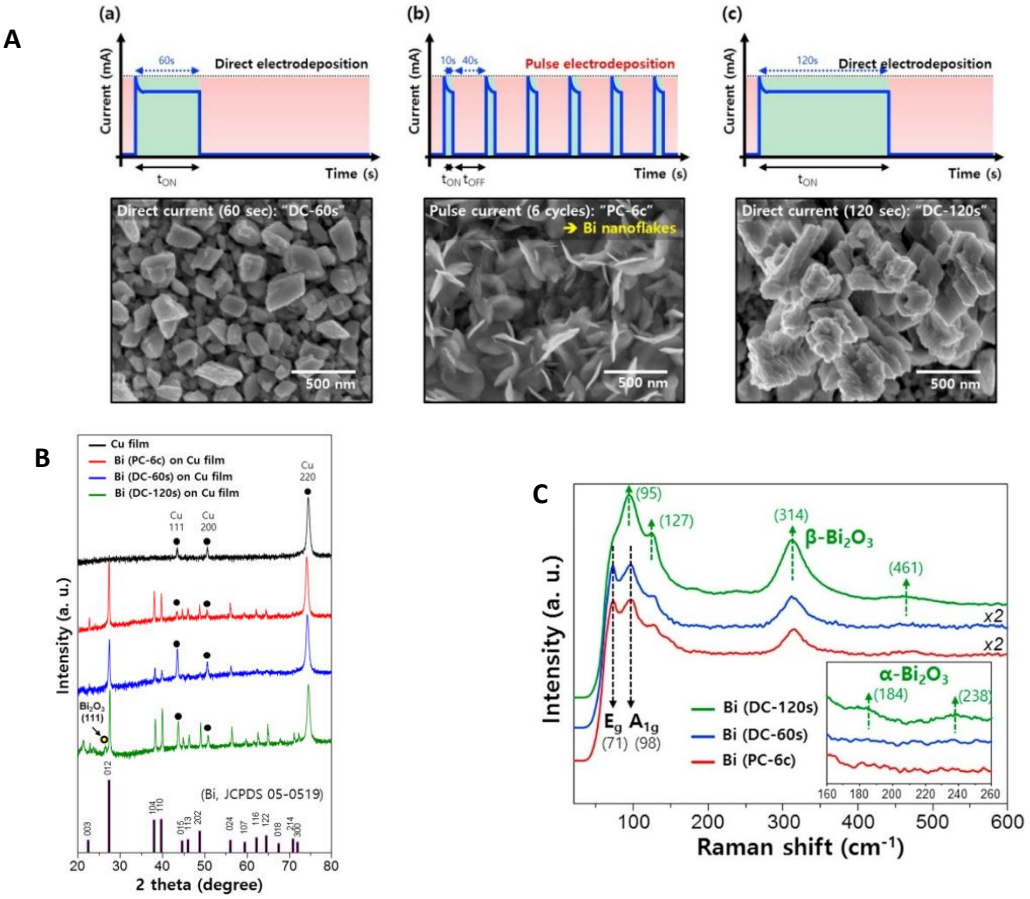

Figure 1.37: A) Amperometric current-time curves and morphologies of a) DC-60s, b) PC-6c and c) DC-120s; B) XRD spectra for the Cu substrate and the three Bi electrodes; C) Raman spectroscopy for the three samples[102]

XRD analyses were performed and polycrystalline structures were observed for all the three samples (Figure 1.37B). Interestingly, only the DC-120s electrode presented the (111) facet of Bi_2O_3, while this plane is completely absent in the other two electrodes. This dissimilarity can be explained considering the time needed for a crystal phase to grow: PC-6c and DC-60s have the same total deposition time (60 seconds) that could be insufficient for this facet to be formed. The composition of the surface of the electrodes was studied via XPS analysis. For all three samples, the $4f_{7/2}$ peak at 159.5 eV was detected, confirming the presence of Bi^{3+} and therefore of bismuth oxides. From the O 1s peak, it was not possible to obtain more information about the differences in the oxidation of the films as the intensity of the peak was very similar for all three electrodes. More information about the oxides present in the films were obtained via Raman Spectroscopy (Figure 1.37C). Peaks at 127, 314 and 461 cm^{-1}, typical peaks of β-Bi_2O_3, were detected on all three electrodes, while the bands for α-Bi_2O_3 (184, 238 and 461 cm^{-1}) are present only in sample DC-120. Metallic bismuth was found in both DC-60s and PC-6c films (peaks at 71 and 98 cm^{-1}), while it was absent in DC-120 electrodes. After CPE analyses at different potentials (Figure 1.38), all three electrodes showed the production of formate. For example, PC-6c was able to produce formate with faradaic efficiencies higher than 60% within a broad range of potentials (from 0.4 to -1.1 V vs RHE). At high

overpotential, a higher FE for formate was obtained using DC-60 than PC-6c. Both Bi PC-6c and DC-60s reached their best catalytic activity at -0.6 V vs RHE with FEs around 100%. Even if also DC-120 reached its best catalytic performances at -0.6 V, its FE was equal only to 93%.

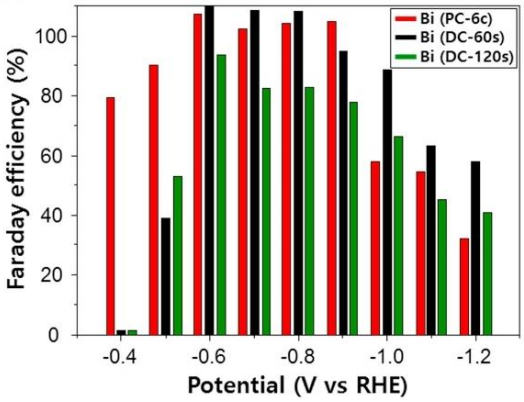

Figure 1.38: Faradaic efficiencies for $HCOO^-$ obtained using Pc-6c, DC-60s and 120s in a CO_2 saturated solution of $KHCO_3$ 0.1 M

The authors suggested that the best catalytic performances of Bi PC-6c, in comparison with the other two electrodes, could have resulted from the presence of a high number of thin edges and sharp corners in the nanoflakes. Starting from the assumption that electric fields in high-curvature structures can affect ionic concentrations and, specifically, the concentration of K^+ around the catalyst, COMSOL Multiphysics simulation was used to investigate the influence of the edge thickness and of the angle amplitude at the corner of the catalyst particles on the electric field. In general, it was observed that corners and edges increased the electric field respectively by 1.5x and 2.5x more than facets. In addition, by changing the angle at the corner from 5 to 70°, a decrease of the electric field of almost 2.5x was obtained. Since the nanoflakes presented thinner and sharper edges than nanodots and nanodendrites, a high electric field can be formed, resulting in greater activation of the reduction reaction. Similarly, Jiang et al.[242] compared three Bi electrodes obtained using three different electrodeposition methods: a constant potential (CP), a direct current (DC), and a pulsed-current (PC) electrodeposition. The three electrodes presented different morphologies: hexagonal sheets were observed for CP electrodes, cuboid structures for DC and dendritic crystallites for PC. XRD analysis showed mainly planes correspondent to the metallic species, while XPS showed the presence of Bi oxide, suggesting the presence of the native oxide on the surface of the Bi crystallites. The ECSA was determined using the double layer capacitance values. The CP electrodes exhibited the highest capacitance, suggesting a larger ECSA, probably due to the higher number of corners and edges in the hexagonal plates. The electrodes were tested in 0.1 $KHCO_3$ under N_2 and CO_2. All the electrodes showed a peak around -0.5 V, that is attributed to the reduction of Bi^{3+} to Bi^0, while an additional peak was observed at around -1.6 V only under CO_2

atmosphere. This peak is attributed to the electroreduction of CO_2, as it was always absent for the experiments in N_2-saturated solutions. CP electrodes showed higher faradaic efficiencies for formate than the other two electrodes at all the potentials. The lowest selectivity was observed for DC, with values of FEs for formate that did not exceed 60%. The higher catalytic activity of PC was attributed to the higher content of sharp edges and corners that increase its ECSA and can improve the local electric field. The effects of the electrodeposition parameters on the catalytic activity towards CO_2 reduction was investigated also by Koh et al.[101]. In their work, a 100 nm layer of Bismuth was deposited via e-beam evaporation onto a Cu foil and successively immersed in a solution of 20 mM $Bi(NO_3)_3$ with ethylene glycol. After, a potential of -1.8 V vs Ag/AgCl was applied for 60 seconds, followed by a resting time of 2 seconds. This reduction step was repeated for 10, 20 or 30 times, resulting in the formation of several Bi dendrite electrodes. After some preliminary catalytic experiments, the electrode obtained after 30 steps of reduction showed the best catalytic activity and it was used for the characterization and the following catalytic tests. The CPE measurements were performed at different potentials in 0.5 M $KHCO_3$ using the Bi dendrite electrode and the Cu foil covered with the e-beam deposited film of Bismuth as control. The obtained faradaic efficiencies for both electrodes are shown in Figure 1.39a and b: at low overpotential, Bi dendrite electrodes showed higher faradaic efficiencies for formate than for H_2 at low overpotentials, likely due to a different mechanistic pathway observed in the presence of the nanodendrite structures. Specifically, at -0.8 V vs RHE, a faradaic efficiency for formate 8x higher than for H_2 was obtained, while with a bismuth foil, the ratio of $HCOO^-$ to H_2 was equal to 4.4. On the other hand, at high overpotentials, Bi dendrite electrodes cannot suppress the HER efficiently and the FE for formate drops below 30% at -1.2 V vs RHE. Differently, faradaic efficiencies at Bi foil remain almost unchanged for potentials between -1.1 and -1.4 V vs RHE. In addition, Bi foil reaches the maximum of catalytic activity at higher overpotential than Bi dendrites electrodes (E= -1.0 V vs Ag/AgCl) and with smaller FEs (less than 80%). At the potential corresponding to the maximum activity for Bi dendrite electrode (E_{max}= -0.8 V), Bi foil exhibited a FE for formate almost 2x smaller. Both Bi foil and Bi dendrite electrode showed negligible CO production, meaning that Bi showed an intrinsic selectivity toward only two products.

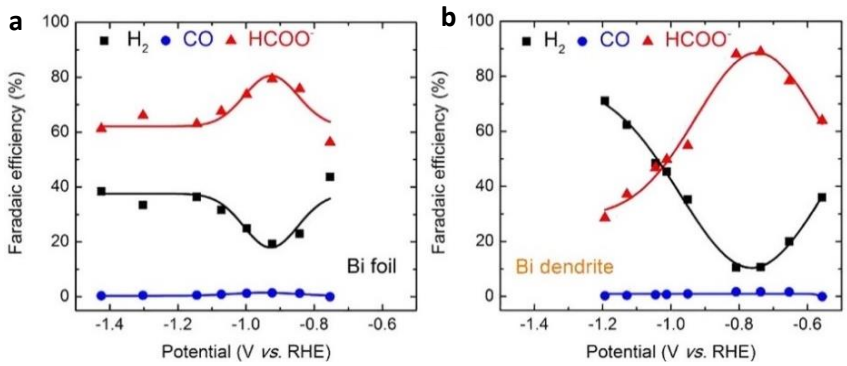

Figure 1.39: Faradaic efficiencies for CO, H_2 and $HCOO^-$ obtained after CPE measurement with a) Bi foil and b) Bi dendrites electrodes[101]

The authors suggested that the difference in the catalytic activity between the Bi dendrite electrode and the Bi foil must be mechanistic as the difference in surface area between the two electrodes is not large enough to justify the variation in the catalytic performances: the surface area of a Bi dendrite electrode is only 3x higher than the Bi foil. Based on DFT calculations, it was concluded that *OCOH intermediate was formed as more stable than*COOH and *H+CO. The *OCOH intermediate is stabilised on the planes (012), (110) and (104) rather than the plane (003) and, as shown in XRD analysis, the first three planes are present in Bi dendrite electrode, while the (003) one is preferentially developed in the Bi foil. This explains the lower FEs for formate at Bi foil than at Bi dendrite electrodes. It is clear that several characteristics can be modified by changing the techniques used for the production of an electrode and that its catalytic properties are strongly dependent on those characteristics. However, the choice of one characteristic over another is strongly dependent on the desired results. Despite the plethora of parameters varied above, there exists a lack of procedural guidance on how to obtain specific characteristics.

1.6.1.1.2 Preparation of Bi electrodes for CO_2RR: composition of the electrode

When a catalyst is investigated, an important parameter that needs to be considered is the composition of the electrode and in the case of Bi, the intrinsic presence of the oxide needs to be taken into account. The effect of Bi oxide on the reduction of CO_2 was investigated by Pander III *et al*.[103] by comparing pure bismuth foils and foils electrochemically oxidised. For the oxidation to occur, the Bi foil was immersed in a solution 25 mM of H_2SO_4 followed by the application of a potential of 3 V vs Ag/AgCl for 3 minutes. In addition, a reduced Bi electrode, referred as HBr etched electrode, was produced by immersing the Bi foil in boiling HBr for several minutes. After being rinsed with DI water, the electrode was immediately inserted into the electrochemical cell in order to minimise the formation of the natural oxidation of the metal in contact with air. The three different electrodes showed similar morphology (Figure 1.40A) while a variation on the composition (Figure 1.40B) based on the different treatments was observed: non-treated electrodes showed a

mixture of Bi^{3+} and Bi^0 but with a higher concentration of Bi^{3+}; HBr etched foils presented almost exclusively the signal attributed to the Bi^0 form; anodized electrodes exhibited only the peaks for Bi^{3+} species; and the anodized electrode displayed the presence of both Bi^{3+} and Bi^0 after the electrolysis measurements displayed the presence of both Bi^{3+} and Bi^0 after the electrolysis measurements (curve d).

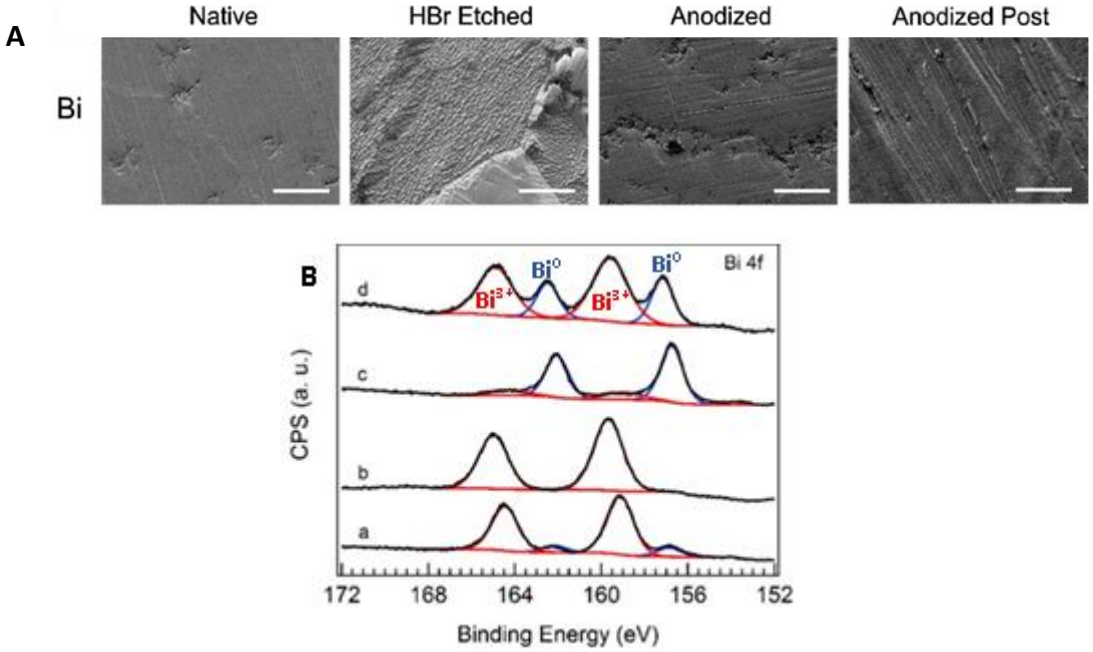

Figure 1.40: A) SEM images of the three electrodes and the electrode after electrolysis; B) Curves obtained after XPS analysis for the Bi foils: (a) native oxidation; (b) anodized; (c) etched in HBr; and (d) post-electrolysis sample of an anodized electrode; the curves in red represent Bi^{3+}, while the ones in blue Bi^0 [103]

ATR-IR in-situ measurements were performed to ascertain if CO_2 is reduced at a Bi oxide site or a metallic one. Detecting the presence and the possible changes on the Bi oxide layer during electrolysis experiments would clarify the role of this species on the catalysis. As Bi_2O_3 does not exhibit clearly identifiable vibrational modes in the IR region and an inversely proportional relationship exists between the intensity of the water peak and the thickness of oxide layers, the water signal in the IR spectra were monitored as a proxy for oxide layer thickness. Specifically, by observing the changes in the water signal during the application of different potentials under Ar and CO_2 atmospheres, the variation in the natural oxide layer was studied. When the experiments were performed under Ar atmosphere, no significant changes were detected as a function of the applied potential. This might suggest the absence of the native Bi oxide layer at negative potentials. When the solution was saturated with CO_2, no peaks typical of carbonate species (1500 and 1385 cm^{-1}) were observed prior the application of the potential, meaning that CO_2 does not bind on Bi oxide sites directly, but probably on metal sites. Considering that at the anodized electrode, values of FE_{HCOO^-} are very similar to the ones obtained at the native electrode (Figure 1.40a), the absence

of the oxide layer might be confirmed also under CO_2 atmosphere. The similarity in the faradaic efficiencies at the anodized and native electrodes would suggest that the increase in the quantity of oxide on the surface does not significantly enhance the catalytic activity. While the presence of oxide seems not to influence the catalytic activity, the pH of the electrolysis solution does. To investigate a possible correlation, CPE measurements were performed in solutions with different pH and current densities for each product were plotted as a function of the pH of the solution. In Figure 1.40b, it can be observed that for both formate production (depicted with diamonds) and for H_2 formation (squares) a maximum at pH 5 was found. However, the production of H_2 does not increase significantly by increasing the pH, while a 3x increase is observed at pH 6.5 for formate current densities. In addition, H_2 evolution drops when CO_2 is added to the system triggering the production of formate. Therefore, it possible to conclude that the sites for CO_2 are competing with the ones for HER.

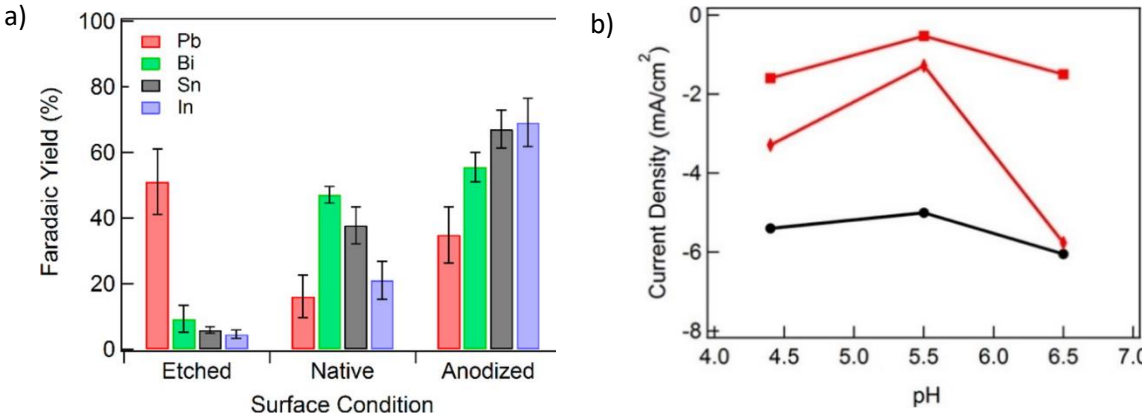

Figure 1.41: a) Formate FE for the three different types of electrodes. Bismuth electrode is shown in green; b) current densities as a function of pH. Black curve: measurement performed in a solution 0.1 M of K_2SO_4 under Ar atmosphere; red curves: CO_2 saturated solution where the squares represent current densities for H_2 production and the diamonds the ones for formate[103]

In more recent studies, Bi electrodes were produced via deposition on carbon substrates (like glassy carbon, carbon plates or carbon papers) of ink formulations containing Bi particles. These studies focused on the preparation of formulations with bismuth oxide particles, because inks need to be dried in ovens at medium-high temperatures, a step that induces the oxidation of the bismuth particles. The majority of the ink based Bi electrodes have shown similar selectivity: large quantities of formate are produced, a variable amount of hydrogen is evolved, and small volumes of CO are formed. Different preparation methods led to different selectivity and catalytic performances. For example, Bi particles prepared with two distinct synthetic procedures showed different morphologies[243]. Because of this, different faradaic efficiencies were observed, likely as a consequence of dissimilar mechanisms for the reduction of CO_2. One of the electrodes, Bi_2O_3-A, was prepared via hydrothermal synthesis followed by successive calcination at 600°C for 8h while the

second electrode, Bi_2O_3-B, was obtained via a precipitation method. The morphology of the two electrodes is shown in Figure 1.42A and their composition in Figure 1.42B. In Figure 1.42B(b), only one set of peaks can be observed, typical of Bi^{3+}species, meaning that both Bi_2O_3-A and Bi_2O_3-B consist of solely Bi oxide.

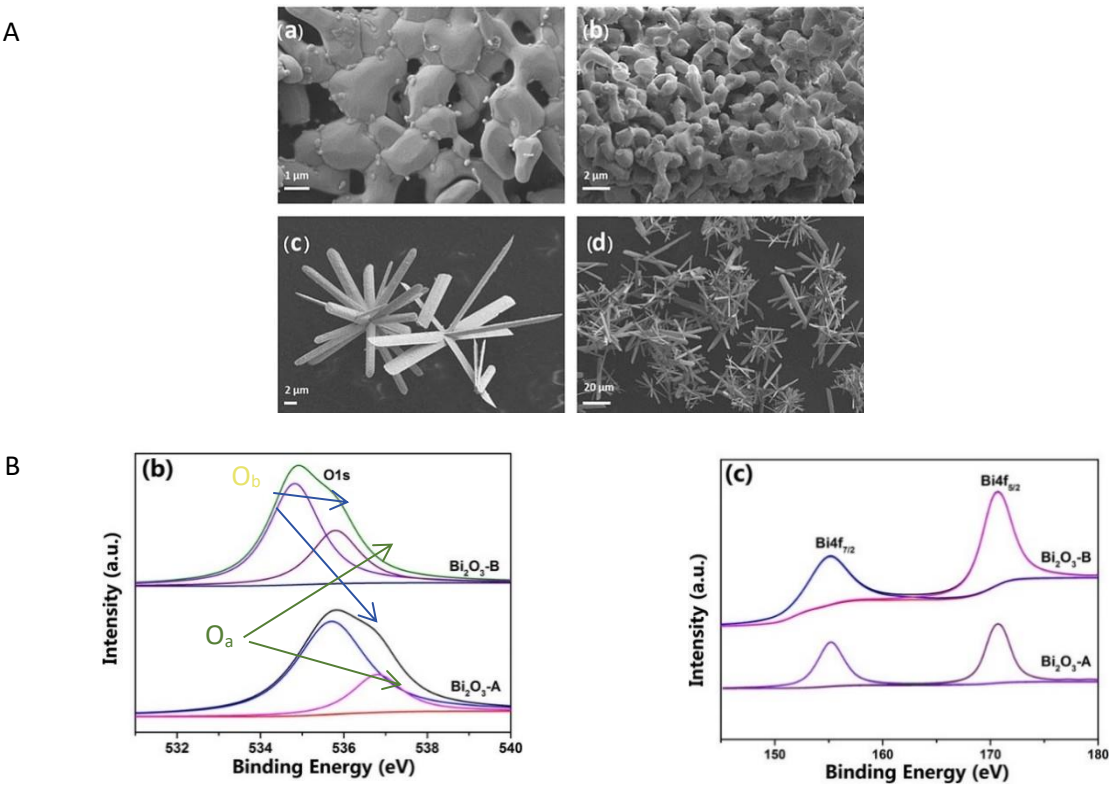

Figure 1.42: A) SEM images of (a) and (b) Bi_2O_3-A and (c) and (d) Bi_2O_3-B; B) XPS spectrum for the two electrodes: zoom on b) the O1s peak and c) the Bi $4f_{7/2}$ and $4f_{5/2}$ signals.[243]

The difference between the two electrodes originated from the mode of bismuth bonding to oxygen: the XPS data describes how O directly bonded to Bi (O_b, curves indicated with blue arrows) is less intense in the Bi_2O_3-A electrode than in the Bi_2O_3-B electrode. In contrast, the peak due to absorbed oxygen (O_a, curves indicated with red arrows) has higher intensity for electrode A than the electrode B. By determining the double layer capacitance, it was demonstrated that the irregular nanoparticles of Bi_2O_3-A (see Figure 1.42A (a) and (b) for morphology of the particles) have higher electrochemical area than the nanorods of Bi_2O_3-B, probably due to the presence of more cavities and edges on the surface of the first electrode. All these features might be the reason behind the higher selectivity for formate, within the entire range of applied potentials (Figure 1.43A). In addition, the superior catalytic activity of Bi_2O_3-A was confirmed by electrokinetic studies (Figure 1.35B (a) and (b)) that showed a lower Tafel slope (166 mV dec^{-1}) for Bi_2O_3-A electrodes,

suggesting a high reaction rate, or in general a better catalytic activity, and probably a single-one electron transfer as a rate-determining step.

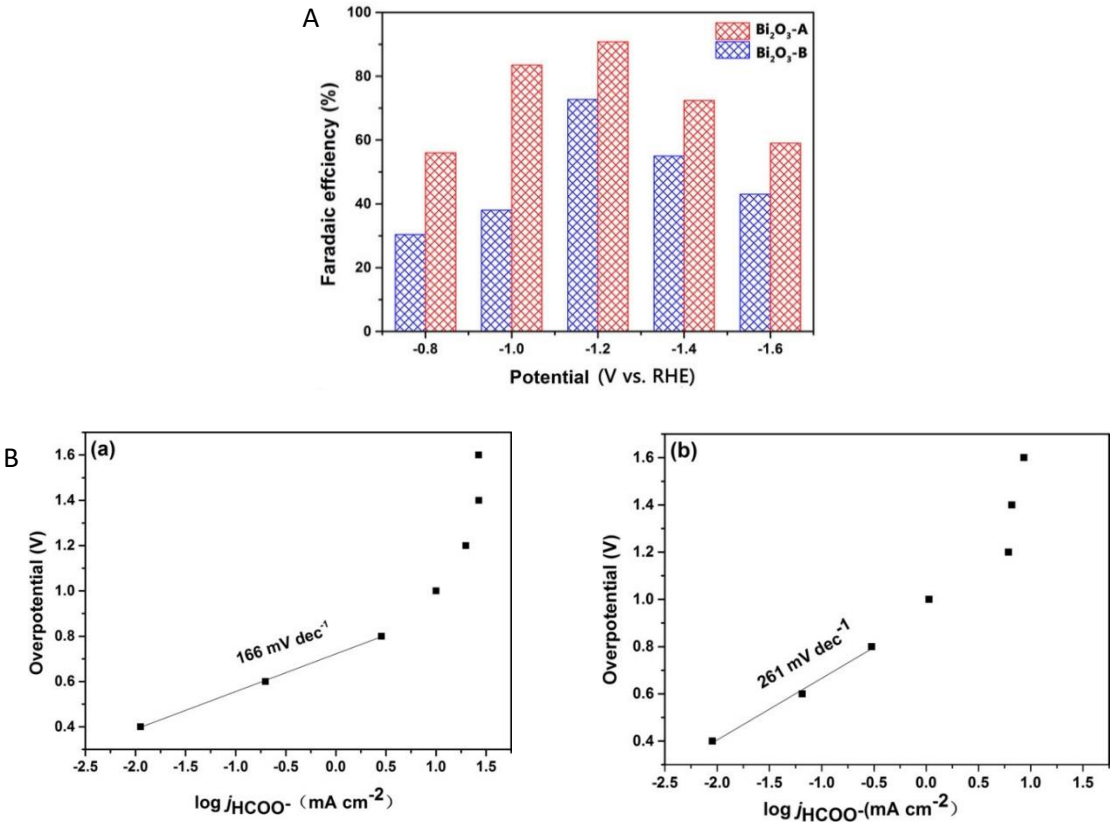

Figure 1.43: A) Formate faradaic efficiencies for the two electrodes; B) Tafel plots for (a) Bi_2O_3-A and (b) Bi_2O_3-B[243]

In a study of Lee and co-workers[244], the composition of a Bi_2O_3 ink electrode was studies using in situ X-ray absorption near edge structure (XANES) analysis. The Bi_2O_3 particles were synthesised via a completely different approach: the solvothermal method. This was done by mixing the bismuth precursor in ethylene glycol and ethanol instead of water. In a consecutive step, the compound BiO_x/C was obtained by mixing with carbon black and the so-obtained mixture was inserted in an autoclave. The ink was then prepared mixing BiO_x/C with Nafion and ethanol to homogeneously disperse the solid parts of the ink and finally drop casted on glassy carbon plate. The electrocatalytic activity of the electrode was evaluated in 1.0 M $NaHCO_3$/$NaClO_4$ solution and the results were compared with commercial Bi_2O_3 and Bi powders. BiO_x/C electrodes showed high selectivity (above 80%) for formate in a range of potentials from -1.3 to -1.9 V vs Ag/AgCl (Figure 1.44a), while hydrogen production is significant only within two potential ranges: from -1.2 to -1.3 V and between -1.8 V and -2.0 V. As expected, CO production is negligible, with the highest FE being equal to 1.4% at -1.3 V vs Ag/AgCl and with an average of 0.3% over the entire potential range. Commercial Bi_2O_3 presented an FE higher than 80% a potential between -1.4 V and -1.9 V vs Ag/AgCl, potentials 0.1 V more negative than BiO_x/C (Figure 1.44b). In addition, the drop in FE for commercial Bi_2O_3 is around

50x greater than for BiO_x/C after -1.9 V vs Ag/AgCl. By using NaCl as the electrolyte, instead of the mixture carbonate/perchlorate, high faradaic efficiencies for formate were obtained (Figure 1.44c) even if higher overpotential needed to be applied.

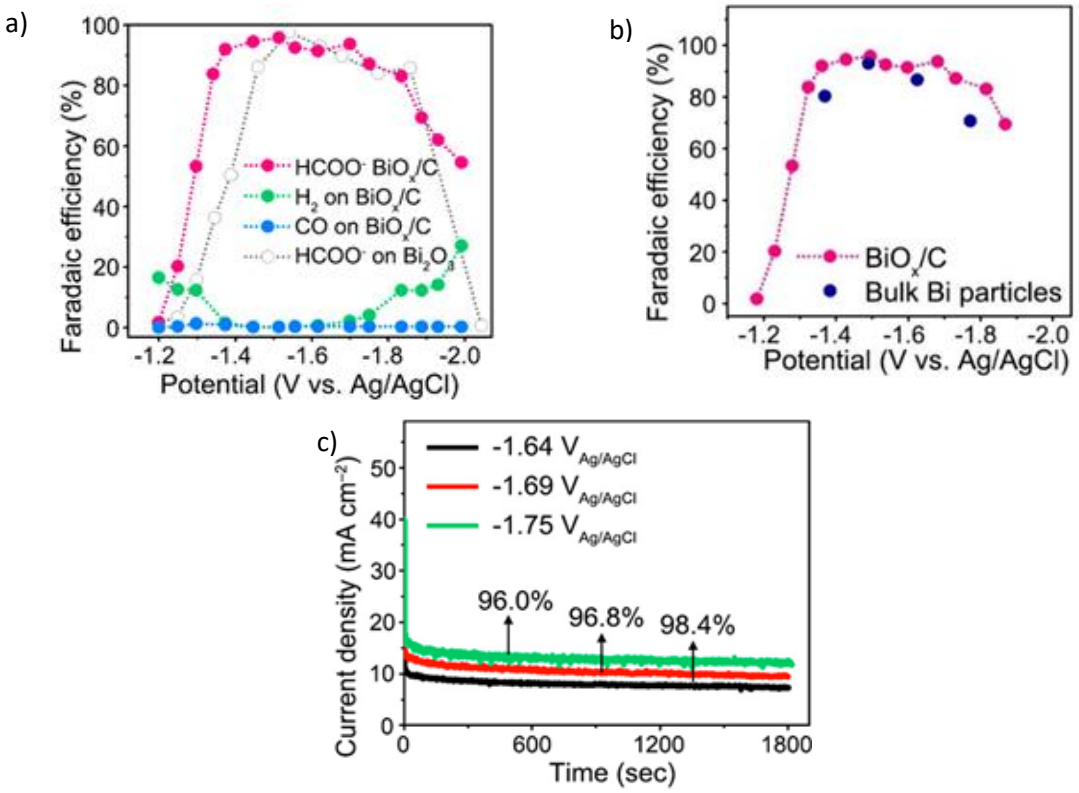

Figure 1.44: a) Faradaic efficiencies for BiO_x/C electrode and commercial Bi powders electrode in 0.5 M $NaHCO_3$ and 0.5 M $NaClO_4$ under CO_2; b) comparison of faradaic efficiency for formate between bulk Bi particles and BiO_x/C electrode; c) current densities and faradaic efficiencies for HCOO– at BiO_x/C electrode at several potentials in 0.5 M NaCl.[244]

During catalysis experiments, the valence of the bismuth in BiO_x/C was monitored via XANES analysis: before the electrocatalytic experiment, the valency of Bi was equal to +3, while when a potential equal to -1.51 V vs Ag/AgCl was kept constant, a +0.5 average valency was calculated. Starting from this value, it was possible to determine that the majority of the Bi particles were in 0 state during the catalysis, while only 16.6% have valency equal to 3+. The pH dependence of the system was studied for low and high potentials: at fixed pH, a sharp increase in current density for formate is observed a more negative potential than -1.4 V vs Ag/AgCl (Figure 1.45a). In addition, by plotting the logarithm of the current density obtained at -1.39 V as a function of the pH (Figure 1.45b), it possible to observe a linear dependence until pH units reach a value equal to 6.49, showing a first-order dependence of j_{HCOO^-} on $[HCO_3^-]$. The authors suggested that a first-order dependence of j_{HCOO^-} on $[HCO_3^-]$ resulted from the inverse proportionality between $[H^+]$ and $[HCO_3^-]$ at fixed $[CO_2]$, that indicates that HCO_3^- is involved in the rate determining step of the reaction, confirmed also by the higher acidity of HCO_3^- in comparison with H_2O.

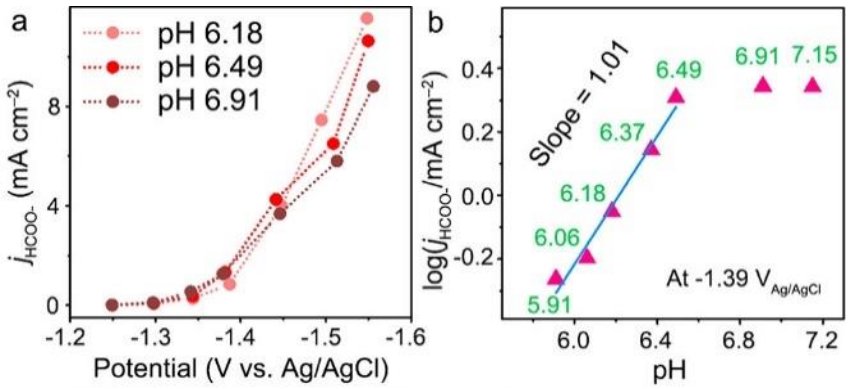

Figure 1.45: a) current densities for formate at several potentials for three different pH values; b) logarithm of current densities as a function of pH at fixed potential[244]

In a recent study[106], the presence of Bi oxide during the electrocatalytic reduction of CO_2 was monitored using operando Raman spectroscopy. The electrodes were produced using dynamic hydrogen bubble template electrodeposition, in order to obtain a porous film. The Bi crystallites, which presented a dendritic structure, were packed together to form a film with a homogeneous distribution of pores at the microscopic level. The diameter of the pores varied from 15 to 90 µm depending on the deposition time. The electrode was then thermally annealed to form a fully oxidised Bi_2O_3 foam film. The presence of the oxide in the films was determined first ex-situ before and after electrolysis via XRD and XPS analyses. Both techniques showed the presence of Bi oxide and Bi metal before and after electrolysis. In addition, XPS showed the presence of two types of bismuth-oxygen bonding: Bi-O and Bi-OH before and after electrolysis. However, the composition was attributed to the storage conditions and the particular formation history of the sample more than the electrolysis experiments. The changes in the surface of the electrodes were investigated at different applied potentials and in solution under N_2 or CO_2 atmospheres. The operando Raman experiments showed the formation of Bi-subcarbonate species under potential application in both N_2 and CO_2-saturated solutions. The presence of these species is higher at low overpotential, while they are absent at higher overpotentials. This suggests the complete reduction of the Bi^{3+} to metallic Bi during the first phases of electrolysis at high potentials but not at lower overpotentials. Catalysis experiments were performed using three different electrodes: the Bi foam electrode, the fully oxidised Bi foam electrode and a Bi foil (the final one used as a control). Both Bi foam electrodes presented high FE for formate, with the Bi oxide foam electrode having the largest range of potentials (around 1 V) at which a formate FE of ≈100% was obtained (Figure 1.46a). Comparable current densities were observed for the two Bi foam electrodes, with a maximum at ≈ -1.75 V vs RHE (Figure 1.46). In addition, a change in morphology of the Bi crystallites at the nanometer scale and an increase in ECSA were observed during catalysis at low overpotentials, suggesting the continued formation of subcarbonate ($(BiO)_2CO_3$) species at the expenses of the Bi-O species during

the electrolysis, not only on the surface of the electrode, but probably in deeper layers. This could be due to the presence of the large pores that allow the electrolyte to enter in contact with the layers underneath the surface.

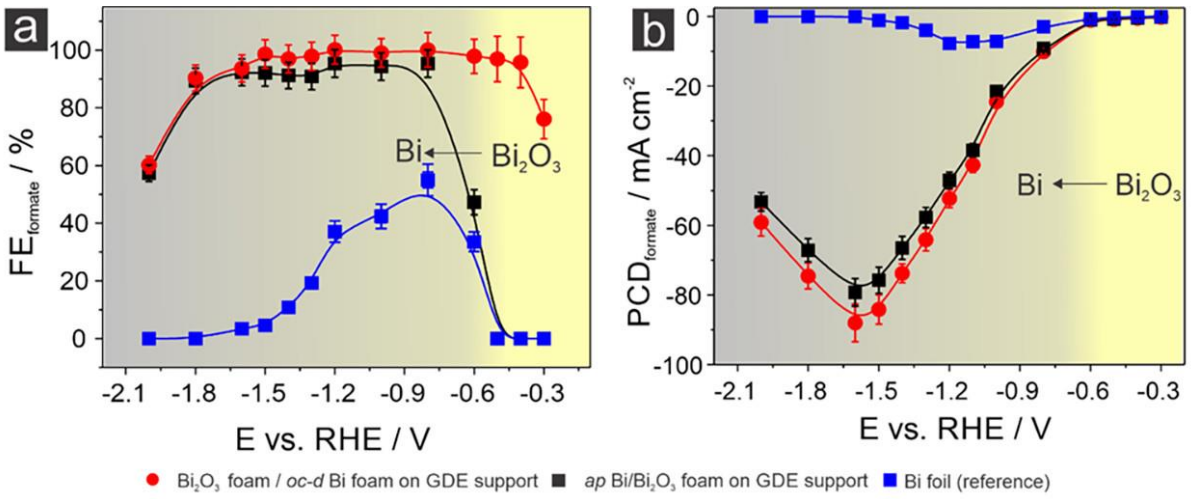

Figure 1.46: (a) formate FE vs E plot; results of the Bi oxide foam electrode (Bi_2O_3/oc-d) are compared with the Bi foam electrode (ap Bi/Bi_xO_y) and a Bi foil catalyst (reference); (b) formate product distribution vs E plot [106]

All the Bi inks discussed up to now have been produced using Bi oxide rather than metallic Bi. In contrast, in a recent study of Zhang *et al*[100]., metallic bulk Bi was prepared by mixing Bi shards with Ar-saturated isopropyl alcohol, to obtain Bi particles that are composed of sheets packed together with Na^+ ions between each layer. For obtaining the Bi nanosheet paste four steps were performed. First, the mixture was exfoliated by ultrasonication for 30 h for separating the Bi sheets. Second, the mixture was soaked in hydrazine overnight for removing any trace of oxides; after, the mixture was washed with ethanol and dried under vacuum to obtain clean and separated nanosheets. Finally, the Bi nanosheets were mixed with acetylene black, polyvinylidene fluoride and N-methyl pyrrolidone for producing the final paste. The Bi nanosheet paste then brushed on carbon papers. The average size of the Bi nanosheets was 450 nm via Transmission Electron Microscopy (TEM) analysis, while the presence of solely Bi^0 was detected via XPS analysis and confirmed with Raman spectroscopy (Figure 1.47a and b).

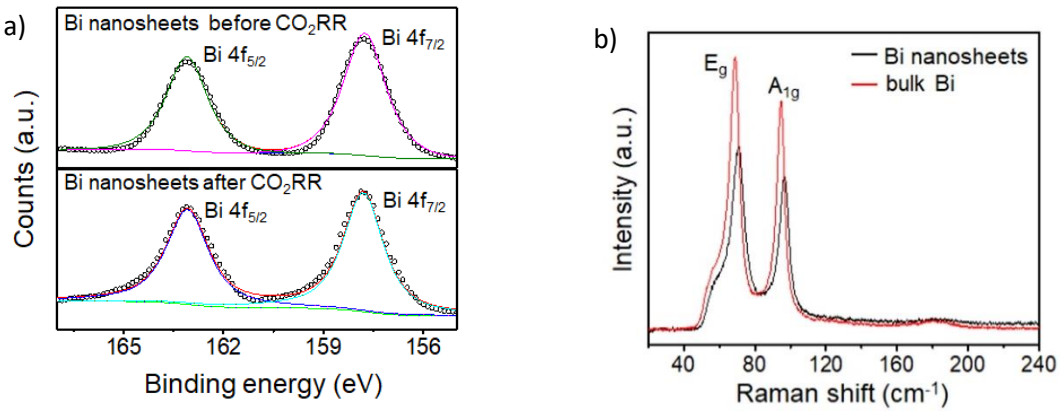

Figure 1.47: a) Zoom on the Bi 4f peaks of the XPS spectrum of Bi nanosheet; b) Raman spectrum for Bi nanosheets and bulk Bi powders[100]

The electrocatalytic experiments were performed using the Bi-nanosheet paste-electrode and two different control electrodes: Bi bulk paste and the blank paste electrode, which consist of simply acetylene black and polyvinylidene fluoride brushed on carbon paper. From the current density and the faradaic efficiencies as a function of the potential for the three electrodes (Figure 1.48) greater catalytic activity and selectivity towards formate of the Bi nanosheets paste electrodes in comparison with the two control electrodes was observed. At Bi nanosheets, the maximum production of formate was obtained at -1.1 V vs RHE: at the same potential, FE_{HCOO^-} was 1.3xhigher than at Bi bulk paste electrodes and 17x higher than at the blank paste electrode. By using Bi nanosheets electrode, the faradaic efficiency for formate was always higher than 40% in a range of potential from -0.5 to -1.2 V vs RHE, while for Bi bulk paste electrodes, only a small quantity (FE> 5%) is produced at the lowest potential. Both the Bi bulk and Bi nanosheets electrodes produced formate, hydrogen and CO. Interestingly, at lowest and highest potentials (-0.5, -0.6 V and -1.2 V) the greatest quantity of CO was observed, though it was more than 4x smaller than the quantity of formate.

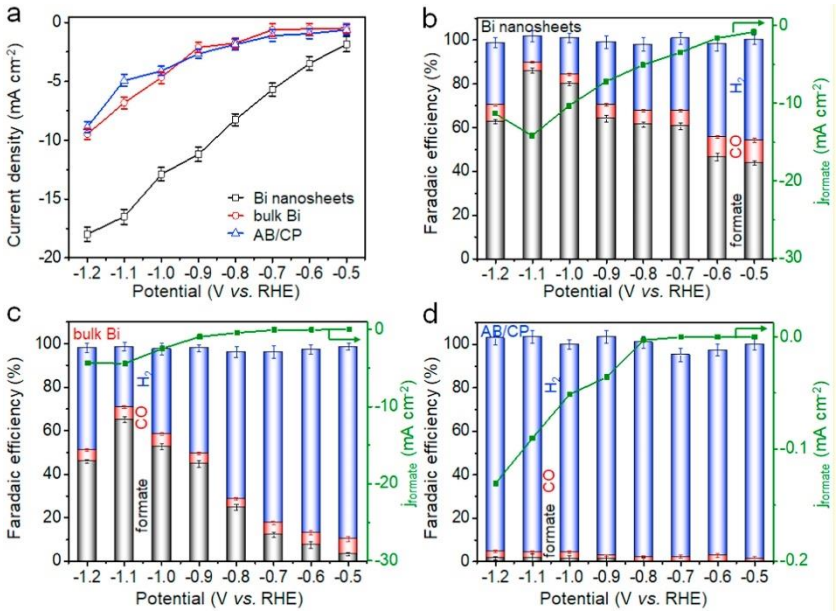

Figure 1.48: a) current densities for the three electrodes in CO_2-saturated 0.1 M $KHCO_3$ aqueous solution; FE_{HCOO^-} for b) Bi nanosheets c) Bi bulk and d) blank ink electrodes[100]

The higher catalytic activity of the Bi nanosheets in comparison with the one obtained at the bulk Bi might result from the presence of corner and edges in the first catalyst. The authors demonstrated that the catalytic activity is inversely proportional to the thickness of the sheets: as bulk Bi has thicker particles than Bi nanosheets (Bi bulk is formed by a series of Bi nanosheets piled together), it might explain lower performances of the control electrode. In addition, the roles of the edges in the catalytic activity were investigated via DFT calculations and the free Gibbs energy for facets and edges were calculated. At the plane 012 (the plane that showed the highest intensity in the XRD spectrum), the energy for the formation of the intermediate *HCOOH was calculated to be the lowest (slightly smaller than 0 eV) at the edges, while it was 4 times higher at the facets. The plane 003 exhibited the lowest energy (-0.41 eV) for the formation of the intermediate *OCOH at the edges, suggesting that the formate production happens preferentially according to the mechanism showed in reaction from r1.12 to r1.15, rather than one involving the formation of *HCOOH.

$$CO_2\ (sol) \rightarrow {}^*CO_2\ (ads) \qquad \text{(r1.12)}$$

$${}^*CO_2\ (ads) + e^- + H^+ \rightarrow {}^*OCOH\ (ads) \qquad \text{(r1.13)}$$

$${}^*OCOH\ (ads) + e^- + H^+ \rightarrow {}^*OCOOH\ (ads) \qquad \text{(r1.14)}$$

$${}^*OCOOH\ (ads) \rightarrow HCOOH\ (sol) \qquad \text{(r1.15)}$$

In contrast, a mechanism that involved *COOH as intermediate instead of *OCOH was proposed in a work of Zhang *et al*.[99]. Bi-NPs were synthesised by using polyethene glycol (PEG) 10000 as a capping agent and the particles of Bi^{3+} were reduced to Bi^0 by using hydrazine for different times. The mechanism was proposed on the basis of electrokinetic measurements: as a Tafel slope equal to 94 mV dec^{-1} was obtained, a first one-electron transfer was suggested to be the rate-determining step followed by a protonation step and a second one-electron transfer. For the preparation of the electrodes, an ink was produced by mixing the Bi-NPs with a Nafion solution and isopropyl alcohol and, finally, it was coated on a carbon paper. The change in the reduction times, the variation of the quantity of hydrazine and PEG resulted in different Bi-particle morphologies (Figure 1.49A and B).

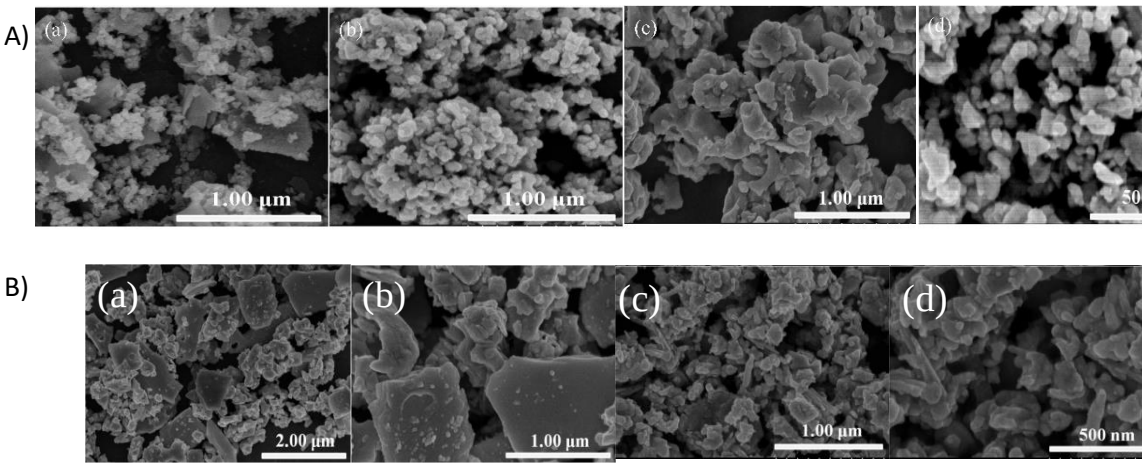

Figure 1.49: A) SEM images of Bi-NPs obtained at different reduction time (a) $Bi_{30\text{-}50}$ _ t_r = 50 min, (b) $Bi_{30\text{-}80}$ _ t_r = 80 min and (c) $Bi_{30\text{-}110}$ _ t_r =110 min; B) SEM images of Bi-NPs obtained for different PEG quantities: (a) and (b) $Bi_{15\text{-}80}$ _PEG=15 mg, (c) and (d) $Bi_{45\text{-}80}$_ PEG= 45 mg [99]

Recently, Yang et al.[105] studied the use of Bismuthene as a catalyst for CO_2 reduction instead of Bi-NPs. Bismuthene is a monolayer of Bi atoms with a hexagonal-arranged array. Bismuthene nanosheets with thicknesses varying from 0.65 to 11.3 nm were synthetised by reducing the Bi precursor. The Bismuthene was then mixed with a Nafion solution to form a paste and dropped onto a GCE or a carbon paper. Three different electrodes were prepared: 0.65nm-BiNSs, 4.2nm-BiNSs and 11.3nm-BiNSs using the different Bismuthene nanosheets. The thinnest Bismuthene layer showed mostly (1 1 1) crystal facet exposed, while for thicker layers (0 1 1) facet was predominant. XRD, XPS and Raman spectroscopy analysis was used to characterise the NS and only Bi^0 was detected on the Bismuthene layers. The catalytic activity was found to be thickness dependent: higher current densities and less negative onset potential were observed for 0.65nm-BiNSs than for the other two electrodes. 100% FE for formate was obtained at -0.58 V, a potential of ≈ 0.2 V less negative than for 4.2nm-BiNSs and almost 0.3 V than for 11.3nm-BiNSs. The difference in the catalytic activity was further investigated by evaluating the ECSA and the physical

adsorption of CO_2 on the different Bismuthene electrodes. Higher ECSAs and a CO_2 volume ten times higher was physically absorbed on the thinnest Bismuthene layer, suggesting a higher number of active sites for this electrode than for the other two. This is clear by looking at the lateral section of the layer: the Bi atoms are placed in a zig-zag fashion, exposing a large number of Bi atoms (see Figure 1.50). However, this means that by increasing the amount of Bismuthene on the surface of the substrate, less active sites are available for CO_2 and therefore the large-scale of Bismuthene electrodes will lead to less active electrodes. To overcome this problem, Bismuthene was mixed with a carbon black ink that allowed the distribution of Bismuthene, avoiding the stacking of the different layers. When the carbon black Bismuthene ink was tested for CO_2 reduction, higher current densities were obtained and 4x higher formate FEs were obtained. The ECSA for the Bi ink was calculated using the double layer capacitance obtained via scan rate study and it resulted to be eight times higher than for the 0.65nm-BiNSs electrode. However, it is not clear if the values were corrected for the double layer capacitance contribution from the carbon black component of the electrode, making it unclear if the increase in ECSA is actually due to higher Bismuthene active sites or if some contribution of the carbon substrate is increasing the capacitance value.

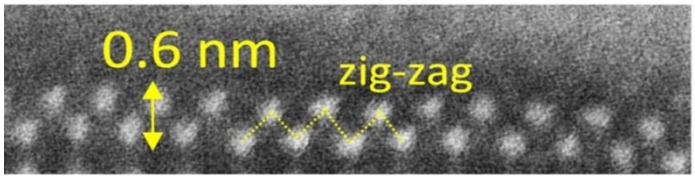

Figure 1.50: lateral HAADF-STEM image of a Bismuthene nanosheet: the single-atom thickness of the layer with the zig-zag structure [105]

1.6.1.1.3 Bi electrodes and ILs

In general, bismuth electrodes show selectivity mostly for formate and hydrogen, making their use difficult for wider applications. To overcome this limitation DiMeglio and Rosenthal prepared a Bismuth electrode for CO production in an organic environment.[169] A film of Bismuth particles was electrodeposited on a glassy carbon electrode from a 20mM $Bi(NO_3)_3$ solution with 0.5 M KBr and 1.0 M of HCl by applying constant potential until 3 C/cm^2 of charge was passed. The so-obtained electrode (Bi-CMEC electrode) was then tested in acetonitrile with 20 mM ionic liquid. The authors proposed that the selectivity of the electrode from formate to CO resulted from the presence of ionic liquids, as in the absence of these compounds a negligible activity was observed (Figure 1.51). In the study, different ionic liquids were tested: the solutions contained [EMIM], [BMIM] and [BBMIM] (1-butyl-2,3-dimethylimidazolium) cations. Both $[EMIM]BF_4$ and $[BMIM]BF_4$ showed very similar catalytic activity with faradaic efficiencies for CO of 93 and 95%.

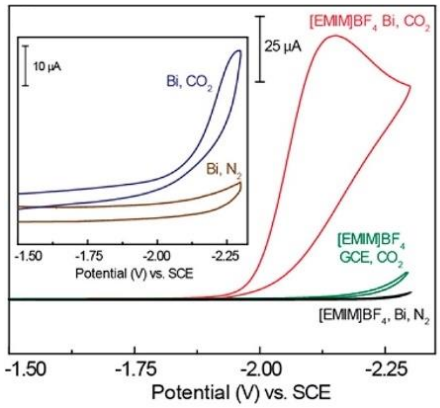

Figure 1.51: CV traces recorded for Bi-modified and bare GCEs in MeCN containing 20 mM [EMIM]BF_4. Inset: Bi-modified GCE in MeCN without IL.[169]

In a successive work, electrodeposition was performed in-situ, by using a Bi precursor that has an organic soluble anion: bismuth trifluoromethane sulfonate ($Bi(OTf)_3$)[245]. In this way, prior to the catalytic experiments, a potential of -2.0 V vs SCE was applied in a CO_2-saturated solution of acetonitrile containing both the Bi salt and 300 mM [BMIM]OTf. Faradaic efficiencies for CO ranging from 79 to 87% were obtained by using different counter ions and modifying the concentration of the ionic liquid. The same electrode, but prepared ex-situ, was then compared with electrodes of three other different post-transition metals (Pb, Sb and Sn), obtained following the same electrodeposition procedure[230]. Catalytic experiments at all four metal electrodes were performed in a solution of [TBA]PF_6 in acetonitrile containing 300 mM [BMIM]OTf_3. At -1.95 V vs SCE, only Sb electrodes did not show significant catalytic activity, while both Bi and Sn exhibited very similar FE_{CO} (78 and 77% respectively). At the same potential, Pb electrodes showed a 40% FE for CO, that increased to 80% when a potential of -2.05 V vs SCE was applied. Interestingly, Sn, Pb and Sn electrodes produced a certain amount of formate, making Bi the most selective among the four electrodes. In addition, as showed in Figure 1.52a and b, Bismuth electrode exhibited also the most positive onset potential and the highest current density.

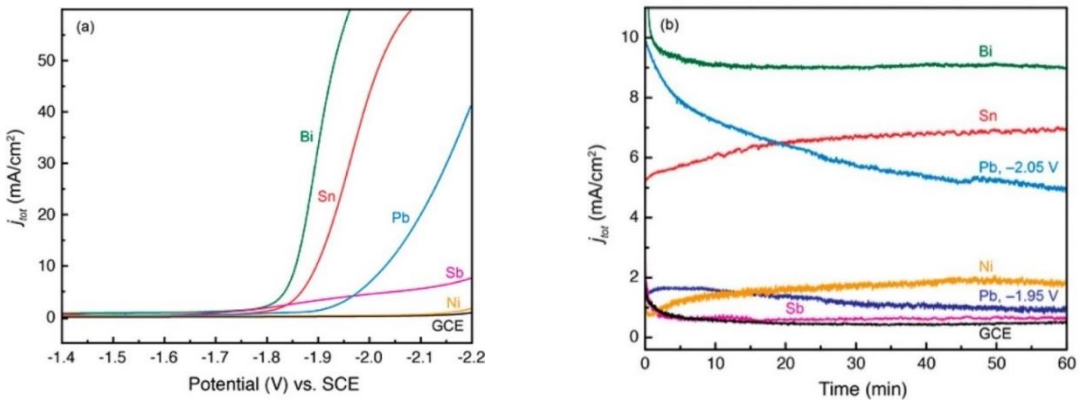

Figure 1.52: a) LS for CO_2 reduction in 300 mM [BMIM]OTf_3 and acetonitrile for the four post-transition metal electrodes; b) CPE for the same system and electrodes[230]

In a work of Atifi and co-workers, the Bi-CMEC electrode was then tested with another family of ILs and the catalytic activity of the system was compared with imidazole-based one[167]. The conjugate acid of 1,8-diazabicyclo[5.4.0]undec-7-ene (DBU) was chosen among several ILs as the proton attached to the N is a better acid than the one present in position 2 in the methylimidazole ring (see Figure 1.53), meaning that it would donate its proton more easily than $[BMIM]^+$ in non-aqueous solvents.

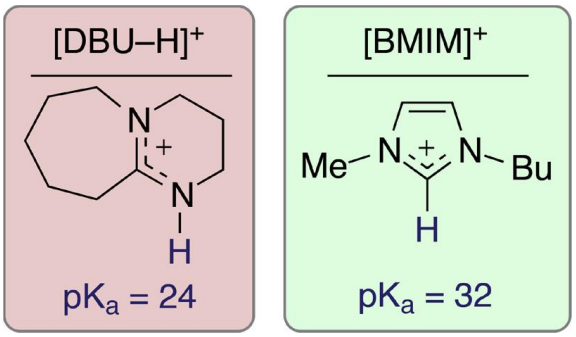

Figure 1.53: Conjugate acid of DBU (DBU-H) and BMIM cations. The pK_a for the two proposed hydrogens involved in the CO_2 reduction are showed[167]

The selectivity of the system containing [DBU-H] cations shifted from CO formation towards formate production: at -1.8 V vs SCE, FE_{HCOO^-} around 74% was calculated, 7x bigger than the one obtained with [BMIM] cations. However, the system Bi modified electrode/$[DBU\text{-}H]^+$ produced small an amount of CO and H_2 (22 and 2% respectively), making the system Bi modified electrode/$[BMIM]^+$ more selective, as FE_{CO}= 84%, $FE_{HCOO^-} = 10\%$ and FE_{H_2}<0.5%. A remarkable increase in faradaic efficiencies was observed using Bi NPs ink electrodes[168]. The Bi NPs were synthesised using trioctylphosphine (TOP) as a capping agent and, by changing its quantity, particles of different sizes were obtained. The Bi NPs were then mixed with Acetylene black and prior the addition of Nafion, the ligand was removed. Finally, the ink was drop cast onto a GC electrode. The Bi NPs with a size of 36 nm showed the best catalytic performance when used in a solution of 100

mM [BMIM]OTf in acetonitrile, with faradaic efficiencies of around 96%, at overpotential of less than 100 mV and a current density for CO production almost three time bigger than the one obtained classical electrodeposited electrodes (Figure 1.54c, a and d).

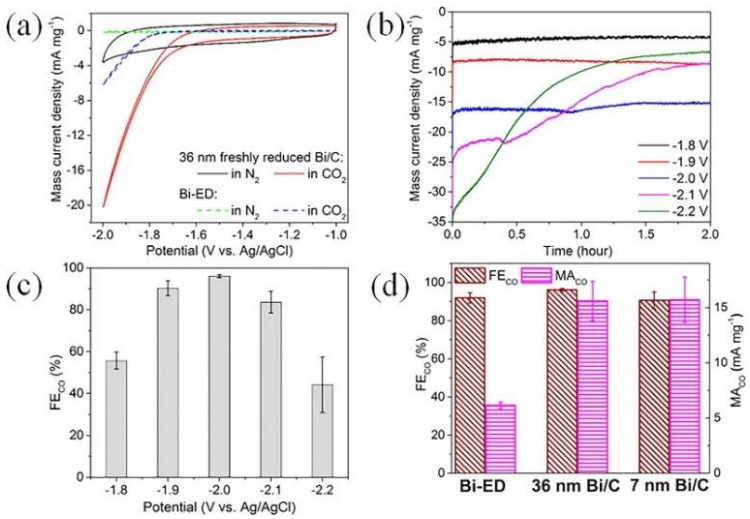

Figure 1.54: a) Cyclic voltammograms of 36-nm Bi NPs ink and classical electrodeposited Bi electrodes (Bi-ED) in a solution of 100 mM [BMIM]OTf and MeCN; (b) Current densities curves at different potentials and (c) corresponding FE_{CO}; (d) FE_{CO} and mass activity for CO formation (MA_{CO}) on Bi-ED, 356 nm and 7 nm Bi NPs inks[168]

In conclusion, Bi electrodes have attracted increasing attention in the field of electrochemical reduction of CO_2 because of the low toxicity and costs of this metal. Most of the works have directed their attention into the production of Bi micro- or nanostructures, using several methods, mostly electrodeposition and production of Bi particles-based inks. In addition, the selectivity of the system has been modified by using ionic liquids as co-catalysts in organic solvents. In general, the works present in the literature follow a similar modus operandi: first, several electrodes are produced changing some synthetic parameters to obtain different physical characteristics (for example, size and morphology); second, the electrodes are characterised investigating the crystal and chemical composition; and, finally, catalytic experiments are performed and the responses obtained with the different electrodes are compared. However, the literature lacks a systematic study of the modification of a certain (or a group of) characteristic with the intent of investigating the effect of one specific parameter on the catalytic activity (for some examples see Chapter 4, Figure 4.1) in both electrodeposited and ink-based electrodes. It is important to highlight that these inks are applied by drop-casting or brushing pastes or inks onto carbon substrates, a method that does not ensure high reproducibility. In addition, considering the tendency of using the geometrical area to normalise the current, the effects of the real area on the catalytic activity of the system are not investigated. Finally, the works involving the use of ILs have been performed only in organic media and experimental studies in aqueous systems are not present.

1.7 Aims of the work

The aim of this project was the production and characterisation of Bi modified electrodes for the electrochemical reduction of CO_2 and to compare their properties and characteristics in order to improve their catalytic activity.

Based on the results found in the literature (see end of the previous section) the main objectives were:

1. Systematic study of the effects on the catalytic activity of:
    a. Surface modification
    b. Use of co-catalysts
2. Increase the stability of the electrodes

To meet these objectives, several secondary objectives were set. For **objective 1.a**:

- Setting a standard for the Bi electrodes by producing a flat bulk Bi electrode (Chapter 3)
- Producing Bi micro- or nanostructures via electrodeposition and systematically changing the deposition parameters to change the number and the type of the catalytic active sites (Chapter 4)
- Calculation of the ECSA of the electrodes

For **objective 1.b** (Chapter 5):

- Preliminary study of commercial imidazolium-based ILs using several metal electrodes, including the Bi microstructured electrodes produced within this work
- Synthesis of ILs containing carboxylic acid functionality to test the ability of ILs to behave as intramolecular proton donors and further increase the catalytic activity of the system
- Investigation on the ability of the ILs to tune the selectivity of the system toward the CO_2RR

For **objective 2** (Chapter 7):

- Production of screen printed electrodes (SPEs), a reproducible, stable and low-cost type of electrode

All the electrodes produced within this work were then tested to probe their catalytic activity towards the CO_2RR (Chapter 6).

Chapter 2 : Materials and methods

2.1 Introduction

In this chapter, the materials and the instrument used for the experimental work are listed, and the methods used for the experimental work described. The preparation procedures for the different types of electrodes are presented in detail. In addition, the main principles for the most used technique within this work (cyclic voltammetry) are discussed.

The materials for the experimental work were chosen so as to be as environmentally friendly as possible, in the limits of procedure feasibility. For example, bismuth was favoured over other metals because of its low toxicity and cost. In terms of the size of the particles, sizes close to the nanometre where preferred were possible, as smaller particles have been suggested to have higher catalytic activities. In general, the highest purity for the compounds was preferred and anhydrous compounds were chosen for the synthesis of the ionic liquids.

Screen printed electrodes were produced to shorten and ease the production times. For the production of the inks, biodegradable and biocompatible solvents and binders were used.

Techniques like cyclic voltammetry (CV) and bulk electrolysis (BE) were chosen based on the different needs for the specific experiments. For example, BE allowed a better control on the charge passed during the deposition experiments and to apply a fixed potential in comparison with CV.

2.2 Materials

Bismuth nitrate pentahydrate (reagent grade, 98%, Aldrich), sodium sulfate (anhydrous, ≥99.0%, Fluka), potassium chloride (ACS reagent, 99.0-100.5%, Sigma Aldrich), tetrabutylammonium hexafluorophosphate (≥99.0%, Sigma-Aldrich), tetrabutylammonium tetrafluoroborate (≥99.0%, Fluka), deuterium oxide (99.9 atom% D, Aldrich), deuterium chloride 20 wt % solution in D_2O (100.0 atom % D, Acros Organic), sodium deuteroxide solution, 40 wt % in D_2O (99 atom % D, Aldrich) and DMSO (Fisher) were used as received. Nitric acid (>69%, Sigma-Aldrich) and sulphuric acid (for analysis ACS, Fisher) were diluted appropriately before use. Milli-Q water (18.2 MΩ) was used for all aqueous solutions. CO_2 (N4 grade) and Ar (N5 grade) were purchase from Air Products. The calibrant gas for the GC was a custom ordered mixture of 200 ppm carbon monoxide, 500 ppm hydrogen and 200 ppm methane (Calgaz).

All commercial ionic liquids (ILs) were used as received: 1-butyl-3-methylimidazolium tetrafluoroborate (≥98.0%, Aldrich), 1-ethyl-3-methylimidazolium tetrafluoroborate (for electrochemistry, ≥99.0% (HPLC), Sigma-Aldrich), 1-(2-hydroxyethyl)-3-methyl-imidazolium tetrafluoroborate (≥98.0%, TCI) and 1-(3-cyanopropyl)-3-methylimidazolium chloride (≥98.5%, Sigma-Aldrich).

For the electrochemical experiments, the Ag, Au, Pt (d=0.2 mm) and Glassy (d=0.3 mm) disk electrodes (IJ Cambria Scientific Ltd.) were polished with an aqueous suspension of 0.3 µm alumina on a polishing cloth (Buehler) prior use. Bi rod (10.0 mm, 99.999%, cast sticks, Goodfellow Cambridge Limited) was cut and the cylinders were used to produce bulk electrodes. The surface of the bismuth bulk electrodes was treated using sandpaper and/or alumina slurry. Carbon felt (3.18 mm, 99.0%, Alfa Aesar) was used as received.

Bi microparticles (45 µm, 99.5+%, Goodfellow Cambridge Limited) for the ink formulation were used as received. Polymethyl methacrylate (Sigma-Aldrich), polyglycol monoethyl ether acetate (99%, Fisher), (poly)vinyl chloride (low molecular weight, Sigma-Aldrich), (poly)vinyl acetate (Sigma-Aldrich), graphite and carbon black (Imerys Graphite & Carbon) were used as received.

The reagents for the synthesis of the carboxylic acid ILs were used as received: 1-methylimidazole (for synthesis, ≥99.0%, Merck), ethyl bromoacetate (≥98.0%, Sigma-Aldrich), methyl 4-chlorobutyrate (≥98.0%, Aldrich), hydrochloric acid (~37%,Fischer), sodium tetrafluoroborate (≥97.0%, Merk), diethyl ether (analytical grade, Sigma-Aldrich), tetrahydrofuran (anhydrous, ≥99.9%, Sigma-Aldrich), acetone (Laboratory Reagent, ≥99.5%, Merk) and acetonitrile (MeCN, anhydrous, 99.8%, Sigma-Aldrich).

All the organic compounds were disposed of in the liquid organic waste containers in accordance with the rules of the School of Chemical Sciences. The inorganic solutions and the solid waste (bismuth metal) were disposed of in separate containers for disposal by the contracted waste management company. Acids and bases were neutralised prior to disposal.

2.3 Instrumentation

For the synthesis of the ILs, the solvents were removed using a Buchi R-210 rotary evaporator connected to a PC 3001 Vario Pro pumping unit and dried under vacuum using an Edwards Direct-drive rotary vane vacuum pump, dual mode, 2.3 cfm, 115/220 VAC. The purity of the samples was monitored using ^{1}H (600 and 400 MHz, Bruker) and ^{19}F NMR (400 MHz, Bruker) spectroscopy. High resolution mass spectra (HRMS) were recorded at the Mass Spectrometry Unit in the School of Chemistry, Trinity College Dublin, on a Bruker Compact mass spectrometer. The system has a mass resolution of 30 000 (FSW @ 1222 m/z) and mass accuracy better than 1−2 ppm RMS error (depending on calibration mode). Agilent Tune Mix-L was used for calibration; control software were otofControl 4.1 and Data Analysis 4.4. Samples were infused via syringe pump at a rate of 150 µL/h. ESI± experiments were recorded over the range of 50−2000 m/z. Other conditions were as follows: end-plate offset 500 V capillary 4500 V, nebulizer 2.0 bar, dry gas 8.0 L/min, and dry temperature 180 °C. Elemental analyses were performed at the Microanalytical Laboratory section

of the School of Chemistry and Chemical Biology, University College Dublin (UCD), with a Varian 55B Spectra AA Atomic Absorption Spectrometer equipped with an Exeter Analytical CE 440 elemental analyser.

Cyclic voltammetry was performed using a CHI electrochemical work station (model 660A or 760e), with various working electrodes and 1 M Ag/AgCl (J Cambria Scientific Ltd.) or 3 M Ag/AgCl as aqueous reference electrodes (built in-house) and Pt wire/coil as counter electrode. A screen printed electrode adaptor (Kanichi) was used for the experiments performed with screen printed electrodes. A screen printed Ag/AgCl electrode was used as reference (pseudo Ag/AgCl) and a carbon screen printed electrode was used as a counter. The solutions were purged with argon, nitrogen, or CO_2 for 10 or 15 minutes prior experiements. The scan rate was 100 mV/s for all the experiments if not differently stated. Alternatively, MeCN was used as an organic solvent with [TBA]PF_6 or [TBA]BF_4 (0.1 M) as supporting electrolyte, while, in aqueous solutions, 0.1 M Na_2SO_4 was employed. The pH of the solution was varied using H_2SO_4 or NaOH at various concentrations while keeping the purged solution under a blanket of the relevant gas to ensure a common value between Ar/N_2 and CO_2 experiments. pH values were measured using a HANNA 2211-02 pH/MV/C bench meter equipped with a Hanna general purpose combination pH electrode (Single junction) which was calibrated with standard buffers prior to each use.

Controlled potential electrolysis (CPE) was performed using amperometric i-t curve as electrochemical technique and the experiments were carried out in a H-cell separated by a glass frit using a CHI electrochemical work station 660A with the catholyte stirred during the entire experiment (see Figure 2.1). The volatile reduction products were identified by withdrawing 500 µL samples from the head space of the cathode compartment using a gastight syringe and injecting these samples onto a gas chromatograph (Varian CP-3800; VICI, pulsed discharged detector, D-4-I-VA38-R). Helium was used as the carrier gas for CO detection. The liquid phase reduction products (i.e.: formate) were quantified using ^{1}H NMR (600 MHz, Bruker) spectroscopy.

Figure 2.1: Set-up for the CPE experiments. The working and the reference electrodes are inserted in one of the two compartments of the H-cell, while the counter was placed in the other. The cell was sealed with parafilm to decrease the loss of gaseous products and reagent

ATR-FTIR spectroscopy was carried out using a PerkinElmer Spectrum 100 FT-ATR spectrometer equipped with a diamond/ZnSe crystal operating in transmittance mode. Raman spectra were obtained using a Horibo 'Jobin Yvon' HR800 UV spectrophotometer equipped with a torus 532 and a mpc^{3000} from Laser Quantum as laser source. A x20 microscope objective was used to focus the laser onto the samples. The x-axis was calibrated versus laser line (0 nm) and silica (520 cm^{-1}). SEM images were acquired using a Hitachi S-3400N Variable Pressure SEM with an acceleration voltage of 20 kV and a current probe of 30 or 50 mA. EDX and high-resolution SEM images were obtained using a Hitachi S5500 Field Emission SEM (GAB04A). X-ray photoelectron spectroscopy (XPS) analyses were performed at the Centre for Research on Adaptive Nanostructures and Nanodevices (CRANN), Trinity College Dublin, with a VG Scientific ESCAlab Mk II, under ultra-high vacuum conditions (1 x 10-9 mbar) using a hemispherical analyser and Al Kα X-rays (1486.6 eV). The emitted photoelectrons were collected at a take-off angle of 90 ° from the samples surface. The analyser pass energy was set to 100 eV for survey scans and 20 eV for high-resolution core scans, yielding an overall resolution of 1.5 eV. Photoemission peak positions were corrected to C 1s at a binding energy of 248.8 eV. Peak fitting analysis was performed using CasaXPS (Ver. 2.3.19). The Bi 4f spectra were normalized and fitted using an asymmetrical line shape on the metal and a Voigt function on the oxide features with each core level assigned a single Gaussian and Lorentzian value for all the oxide components.

For the preparation of the inks a high-shear PRO250 homogeniser equipped with a PROscientific Saw-Tooth generator probe was used to mix the ink. The screen printed electrodes were printed

with a DEK Horizon APiX Screen Printer, using a customised mesh screen, that define the shape and the size of the electrodes.

2.4 Methods

2.4.1 Synthesis of [1-CM-3-MIM]BF_4

1-carboxymethyl-3-methylimidazole tetrafluoroborate was synthesised performing some modification to a literature method[246]. First, 1-(2-ethoxy-2-oxoethyl)-3-methyl-1-imidazolium bromide ([1-(2-EO-2-OE)-3-MIM]Br) was synthesised by adding dropwise ethyl bromoacetate (5.5 mL, 60 mmol) into a solution of THF (50 mL) and 1-methylimidazole (4.0 mL, 50 mmol) under nitrogen atmosphere. The reaction mixture was stirred at 0 °C for 1 h, and then warmed at room temperature for another 3 h. The THF was removed and the product washed with 3 aliquots (10 mL) of diethyl ether. The product was dried under vacuum at 60°C overnight. Successively, the intermediate product was refluxed at 100°C with one equivalent of 37% HCl for 4 hours, the solvent was removed under reduced pressure and the 1-carboxymethyl-3-methylimidazole bromide ([1-CM-3-MIM]Br) was washed with 15 mL of acetone and successively with 3 aliquots (15 mL) of diethyl ether. The solvent was removed and the white powder was dried under vacuum at 60°C overnight. Then [1-CM-3-MIM]Cl was treated through standard anion metathesis[247] by mixing it with equimolar quantity of $NaBF_4$ in 100 mL of anhydrous acetonitrile. The suspension was stirred and refluxed for 12 hours. The final product was filtered and dried under vacuum at 60°C overnight.

Step 1: synthesis of [1-(2-EO-2-OE)-3-MIM]Br

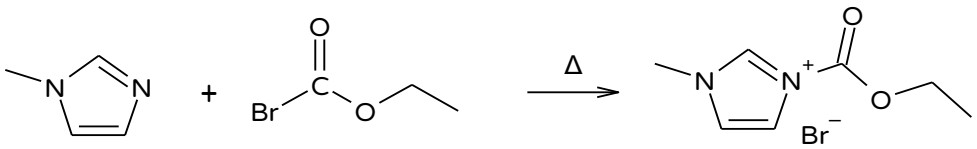

Figure 2.2: Scheme of reaction for the formation of [1-(2-EO-2-OE)-3-MIM]Br

Step 2: Hydrolysis of [1-(2-EO-2-OE)-3-MIM]Br to [1-CM-3-MIM]Br

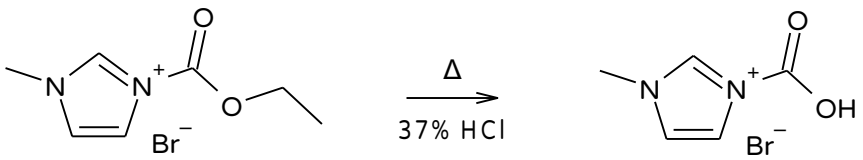

Figure 2.3: Scheme of reaction for the formation of [1-CM-3-MIM]Br

Step 3: counter-ion exchange

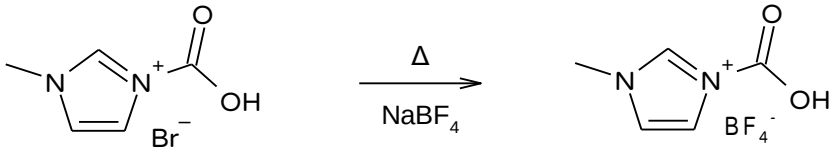

Figure 2.4: Scheme of reaction for the formation of [1-CM-3-MIM]BF_4

2.4.1.1 Data

The final product was analysed via ^{1}H NMR spectroscopy, ^{19}F NMR, ATR-FTIR, ESI-MS and elemental analysis. The purity of the intermediate compound was monitored via ^{1}H NMR analysis.

- *[1-CM-3-MIM]Br*

^{1}H NMR: δ = 3.90 (s, 3H), 5.07 (s, 2H), 7.45 (s, 1H), 7.47 (s, 1H), 8.72 (s, 1H) ppm.

- *[1-CM-3-MIM]BF_4*

^{1}H NMR: δ = 3.81 (s, 3H), 4.93 (s, 2H), 7.36 (t, ^{3}J(H-H)= 1.6 Hz, 2H), 8.68 (s, 1H) ppm; ^{19}F NMR: δ = 150.52 (s), 150.47 (s) ppm; ESI-MS: 141 [cation]$^+$; elemental analysis calcd (%) for $C_6H_9N_2O_2BF_4$: C 31.61, H 3.98, N 12.29; found: C 29.99, H 3.92, N 11.39; elemental analysis calcd with water: C 30.18, H 4.31, N 11.73.

2.4.2 Synthesis of [1-CP-3-MIM]BF_4

1-carboxypropyl-3-methylimidazole tetrafluoroborate was synthesised according to literature methods[248]. First, 1-(4-buthoxy-4-oxomethyl)-3-methyl-1-imidazolium chloride ([1-(4-BO-4-OB)-3-MIM]Cl) was formed by mixing methyl 4-chlorobutyrate with an equimolar quantity of 1-methylimidazole. The reaction mixture was stirred and refluxed at 60°C for 24h and then washed with diethyl ether. The ester was refluxed for 1 hour with 37% HCl and the solvent removed under reduced pressure. The intermediate product was washed with 1 aliquot of acetone (15 mL) and 3 aliquots of diethyl ether (15 mL). The cleaning procedure was repeated until the product become a white powder and the desired purity was reached. Finally, the 1-carboxypropyl-3-methylimidazole chloride ([1-CP-3-MIM]Cl) was dried under vacuum at 60°C overnight. The counter-ion exchange was performed according to the procedure used for the formation of [1-CP-3-MIM]BF_4.

Step 1: synthesis of [1-(4-BO-4-OB)-3-MIM]Cl

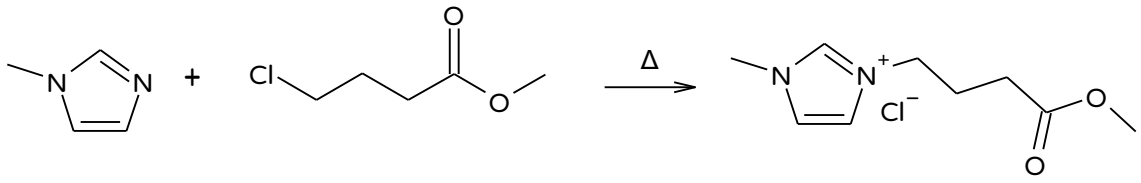

Figure 2.5: Scheme of reaction for the formation of [1-(4-BO-4-OB)-3-MIM]Cl

Step 2: Hydrolysis of [1-(4-bO-4-Ob)-3-MIM]Cl to [1-Cp-3-MIM]Cl

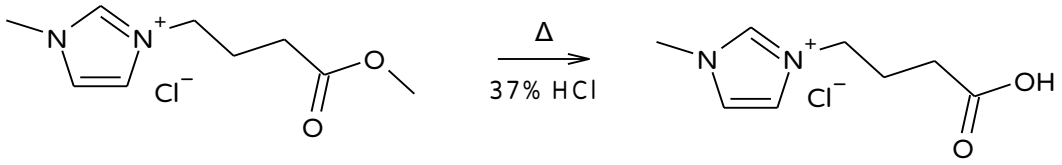

Figure 2.6 Scheme of reaction for the formation of [1-CP-3-MIM]Cl

Step 3: counter-ion exchange

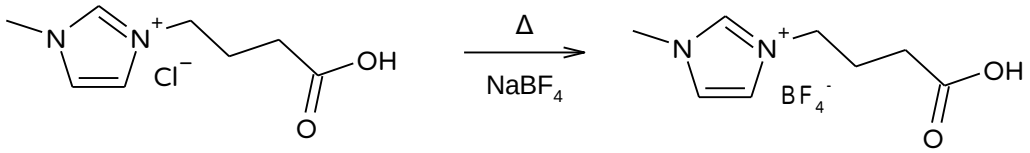

Figure 2.7: Scheme of reaction for the formation of [1-CM-3-MIM]BF_4

2.4.2.1 Data

The final product was analysed via ^{1}H NMR spectroscopy, ^{19}F NMR, ATR-FTIR, ESI-MS and elemental analysis. The purity of the intermediate compounds was monitored via ^{1}H NMR analyses. The [1-CP-3-MIM]Cl was further analysed via elemental analysis.

- *[1-(4-BO-4-OB)-3-MIM]Cl*

^{1}H NMR: δ = 2.21 (m, 2H), 2.49 (t, ^{3}J= 7.32 Hz, 2H), 3.69 (s, 3H); 3.92 (s, 3H), 4.29 (t, ^{3}J= 7.20 Hz, 2H), 7.48 (t, ^{3}J= 1.74 Hz, 1H), 7.54 (t, ^{3}J= 1.74 Hz, 1H), 8.79 (s, 1H) ppm.

- *[1-CP-3-MIM]Cl*

^{1}H NMR: δ = 2.15 (m, 2H), 2.41 (t, ^{3}J= 7.08 Hz, 2H), 3.86 (s, 3H), 4.23 (t, ^{3}J= 7.38 Hz, 2H), 7.41 (s, 1H), 7.47 (s, 1H), 8.72 (s, 1H) ppm; elemental analysis calcd (%) for $C_8H_{13}N_2O_2Cl$: C 46.95, H 6.40, N 13.69, Cl 17.32; found: C 46.50, H 6.29, N 13.51, Cl 17.05.

- *[1-CP-3-MIM]BF_4*

^{1}H NMR: δ = 2.04 (m, 2H), 2.43 (t, ^{3}J= 7.02 Hz, 2H); 3.88 (s, 3H), 4.24 (t, ^{3}J= 7.14 Hz, 2H), 7.42 (s, 1H), 7.47 (s, 1H), 8.70 (s, 1H); ppm ^{19}F NMR: δ = -150.39 (s), -150.43 (s) ppm; ESI-MS: 169 [cation]$^+$; elemental analysis calcd (%) for $C_8H_{13}N_2O_2BF_4$: C 31.61, H 3.98, N 12.29, F 33.34, Na 0.00, Cl 0.00; found: C 35.90, H 4.85, N 10.55, F 28.23, Na ≤0.36, Cl 0.00; elemental analysis calcd with water: C 36.20, H 5.25, N 10.55, F 28.23, Na 0.78.

2.4.3 Preparation of the Bi disks

Bi disk electrodes were prepared by first turning a 10 mm a Bi rod to diameters of 4.2, 6.2 and 8.3 mm using a metal lathe. A disk, approximately 5mm high, was then cut off (Figure 2.8a and b) and then soldered to a copper wire (Figure 2.8c), the edges coated with epoxy resin and inserted into a close fitting glass cylinder (Figure 2.8d). (Figure 2.8e). The purchased rod contained numerous voids from the casting process and a section was chosen to minimise these defects in the surface of the cut disk.

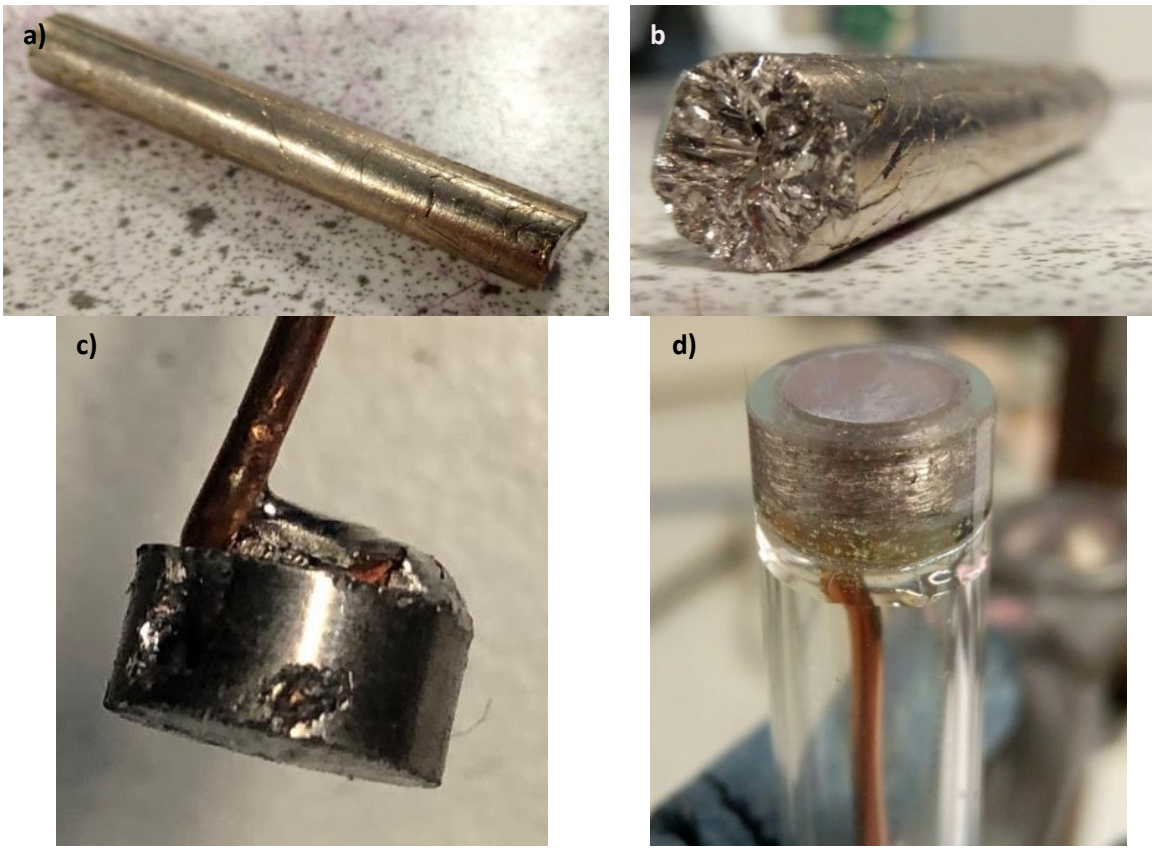

Figure 2.8: Steps for the preparation of Bi disks: a and b) Bi rod; c) connection between the Bi cylinder and the copper wire; d) Bi cylinder after being inserted into a glass cylinder and sealed with epoxy resin to avoid leakages; and e) four Bi disk electrodes

2.4.4 Preparation of Bi-GC electrodes

The glassy carbon electrodes (GCE) were polished first with an aqueous suspension of 0.3 µm alumina on a polishing cloth (Buehler), sonicated in deionized water, rinsed sequentially with deionized water and acetone, and dried under a flow of nitrogen. Successively the polishing procedure was repeated by using an aqueous suspension of 0.05 µm alumina. The GCEs were immersed in a de-oxygenated solution of HNO_3 1 M containing 20 moles/L of $Bi(NO_3)_3 \cdot 5H_2O$ and a cyclic voltammogram (2 cycles) was acquired with a 3 M Ag/AgCl RE and a Pt wire/coil as a CE. On the basis of the E_{pc} value, the applied potential for the deposition was selected. The electrode was electrochemically cleaned by applying a potential of +0.5 V vs Ag/AgCl for two minutes and briskly agitated in the solution to remove all the possible impurities from the surface. Bulk electrolysis (BE) measurements were performed by applying a potential of -0.132 V vs Ag/AgCl until a charge of around 6.0×10^{-1} C/cm^2 was applied. The electrode was then rinsed with milli-Q-water, acetone and dried under a gentle stream of N_2. For the multi steps Bi-GCs, different amount of charge, in different steps, was passed during BE experiments (Figure 2.7). The applied potential for BE experiments was selected by adding an overpotential of 15 mV to the E_{pc} value.

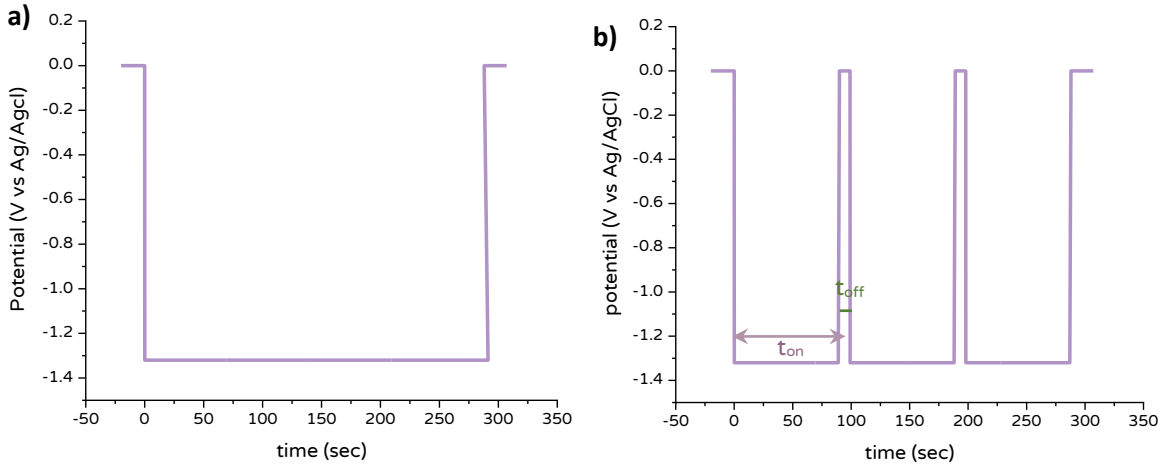

Figure 2.9: Examples of wave forms used during the electrodepositions: a) Bi-GC and b) Bi-GC(3:3)S electrodes

2.4.5 Ink formulation and electrode screen printing

The inks and screen printed electrodes (SPEs) were kindly formulated and printed by Dr Loanda Cumba. Briefly, the ink components for the working electrodes were mixed together using a homogeniser and the texture of the ink was optimised by modifying the amount of the solvent and binders. Two different ink formulations were prepared. The components of the inks are shown in Table 2.1. For each formulation three different inks were produced: one carbonaceous ink and two Bismuth inks. The two Bi inks were a pure bismuth ink and a carbon/bismuth ink mixture. The content of bismuth in the carbon/bismuth ink was 10 or 40% w/w and, according to the manufacturers, the Bi particles presented a maximum particle size of 45 µm. In general, all the ink formulations contained conductive materials (graphite and carbon), the polymeric binder and two different organic solvents. The only exception was the pure Bi-based ink that did not contain any carbonaceous components as conductive fillers. The silver/silver chloride reference electrode was included by screen-printing Ag/AgCl paste.

Table 2.1: components for the two ink formulations used for the preparation of the screen printed electrodes

Formulation number	Carbonaceous components	Bi particles	solvents	binders
1	Graphite	Bi microspheres (max diameter: 45 µm)	polyglycol monoethyl ether acetate	polymethyl methacrylate
	Carbon Black			(poly)vinyl chloride
2	Graphite		polyglycol monoethyl ether acetate	(poly)vinyl acetate
	Carbon Black			(poly)vinyl chloride

Plastic sheets were used as substrates. For the printing procedure of working SPEs, the substrates were inserted into the mesh screen and the screen inserted into the screen printer. The

ink was placed on top of the screen and printed at a pressure equal to 10 or 12 kPa, depending on the type of ink. Once the ink was printed on the substrate, the sheets with the printed electrodes were dried in an oven at 60°C for 15 minutes. The screen-printed electrodes were then cut with a length of 3.5 cm and a width of 0.35 cm (see Figure 2.10a) to be inserted into the screen-printed adaptor electrodes (see Figure 2.10b). A layer of insulator of 2.0 cm was applied on the top of the conductive path to obtain a well-defined and constant working area of 0.071 cm^2 (see Figure 2.10a).

Figure 2.10: a) scheme of a SPE; b) screen printed adaptor used for the electrochemical experiments

Four different types of electrodes were printed: a pure carbonaceous SPE (C/G-SPE) containing carbon and graphite; a carbon/Bi electrode (C/G/Bi-SPE), a pure Bi metal SPE (Bi M-SPE) and a two-layer SPE, that consisted of a layer of pure carbonaceous ink and a top layer of pure Bi metal ink (Bi M_C/G-SPE). Each of these electrodes can be seen in Figure 2.11. The carbonaceous SPEs present a black colour (see Figure 2.11a), while after the addition of the Bi microparticles, a lighter colour was achieved. The Bi M-SPE presented a light grey colour (see Figure 2.11c and d). For the two-layer electrode, the printing resulted in the two layers being offset and a small part of the carbonaceous electrode was exposed (Figure 2.11c).

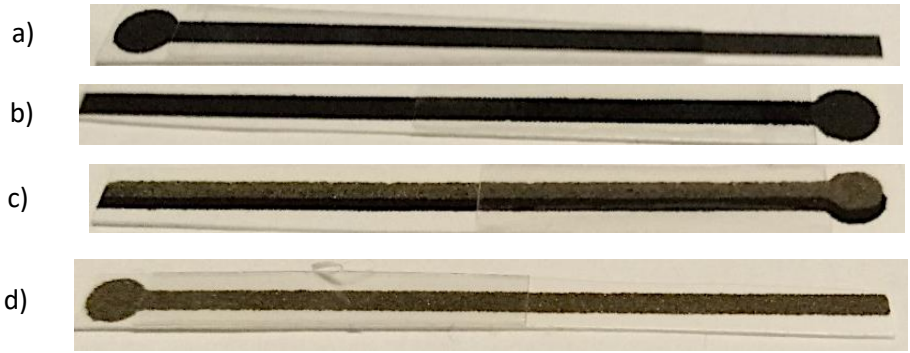

Figure 2.11: a) a pure carbonaceous SPE (C/G-SPE) containing carbon and graphite; b) a carbon/Bi electrode (C/G/Bi-SPE), c) a layer of pure Bi metal ink (Bi M_C/G-SPE; and a pure Bi metal SPE (Bi M-SPE) and d) a two-layer SPE, that consisted of a layer of pure carbonaceous ink

2.5 Techniques and procedures for data analysis

2.5.1 Cyclic voltammetry

Cyclic voltammetry (CV) is an electrochemical technique used to investigate the reduction and oxidation processes[172]. It is one of the potential sweep techniques and it describes how the current (i) changes as a function of the potential (E) and the time (t):

$$i = f(E, t) \tag{2.1}$$

CV can be described in terms of triangular waveform, as the potential is initially swept to an initial potential (E_i) to a second potential (E_s) and then to a final potential (E_f). Sometimes, E_s and E_f correspond, but not necessarily. An example of an input waveform and the scape of a classic current response are shown in Figure 2.12a and b, respectively. The graphs of the current response as a function of the potential are called cyclic voltammograms (CVs).

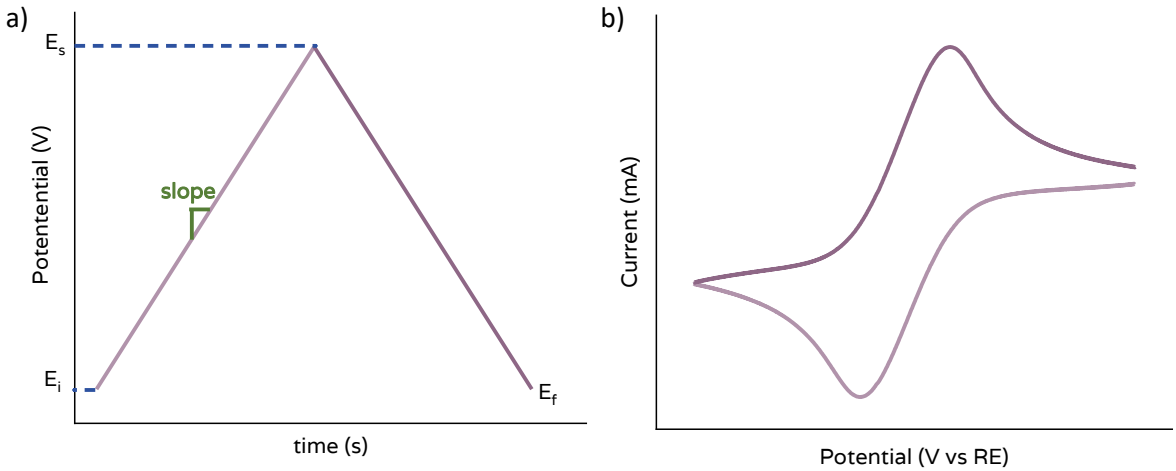

Figure 2.12: examples of a) an input waveform and b) the correspondent current response. The curve in light purple represents the forward scan while the dark purple one the backward scan. RE is a general reference electrode

The velocity at which the potential is swept is called scan rate (v). The scan rate is the slope of the line that represents the potential swept (see Figure 2.12a) and it is usually expressed in mV/s. Scan rate significantly influence the CVs, as it didacts the thickness of the diffusion layer (δ). The diffusion layer is that portion of the solution in contact with the electrode (electrode-electrolyte interface), in which the electrochemical reactions occur (the electroactive species can be in solution or adsorbed on the surface of the electrode)[172]. It is important to highlight that the dependence of the diffusion layer on the scan rate is valid for macroscopic electrodes and not for micro-, o smaller, electrodes (unless very high scan rates are applied)[175]. The shape of the CVs depends mainly on two factors: the kinetics of the process and the diffusion of the species in the diffusion layer.

In terms of experimental conditions, the CV measurements are performed in a vessel called electrochemical cell and a three-electrodes configuration is used. During the experiments, the potential is measured between the working electrode (WE) and the reference electrode (RE), while the current is measured between the working and the counter electrode (CE). High concentrations of a salt, called electrolyte, are dissolved in water (or other suitable solvent) to ensure good conductivity. The electrolyte chosen should not interact with, or present electroactivity at potentials similar to, the electroactive species (the analyte). Usually, the concentration of the electroactive species is around 10^{-3} M while for electrolyte concentration around 10^{-1} M are often selected[175]. However, other analyte concentrations can be employed depending on the system under investigation and its applications. During the CV, when the potential is swept, the analyte is oxidised and the reduced (or vice versa). In the CO_2RR context, cyclic voltammetry gives insights on the reduction process. Usually, CVs in solutions saturated with an inert gas (in which CO_2 is absent) and in CO_2-saturated solutions are carried out and the difference in shape, current and potential values are used to preliminary evaluate the ability of a system to reduce CO_2. In addition, CV gives information on the suitability of a specific set-up (electrode-electrolyte system) to be employed for the CO_2RR (for example, potential window limits, background currents). In contrast, when the electrodeposition of Bi was performed, the cyclic voltammograms were used to extrapolate the main parameters needed for the deposition: the applied potential and its correspondent current. CV was also used for the calculation of the double layer capacitance and to understand if the analyte is freely diffusing in solution or adsorbed on the electrode by performing scan rate studies.

In conclusion, CV is a powerful electrochemical technique that can be used for several application. In particular, a large quantity of information can be obtained, especially when preliminary experiments are performed. However, the response obtained by sweeping the

potential is quite complex as it is dependent on the kinetic of the process under investigation and the mass transport of the species in solution. Therefore, care needs to be taken when interpretating

2.5.2 Bulk electrolysis methods

Bulk electrolysis methods are used when large area electrodes and long experimental times are needed[45]. Bulk electroanalysis can be operated in two main modes: (1) controlled potential (potentiostatic techniques) and (2) controlled current (galvanostatic techniques). In the first case, a constant potential is applied and the current versus time is measured, while in the second case, the current is held constant and the curve of potential versus time is obtained. In this work, only potentiostatic techniques were used: the amperometric i-t curve technique and bulk electrolysis with coloumetry. The first technique was employed for the catalytic experiments, while the second was carried out for the electrodeposition of the Bi crystallites on the GCE. For both techniques, a specific sample interval can be chosen while the main difference between them is the quantity recorded by the potentiostat. During the amperometric i-t curve technique the chosen potential is applied constantly for a fixed amount of time (that is set prior the starting of the experiment) and the *current* is recorded as function of the time. On the other hand, when bulk electrolysis with coloumetry is used, the integrated *charge* is recorded as function of time. This allows a better control of the charge passed during the experiment, an essential aspect for the electrodepositon of the Bi deposit, considering that all the Bi modified electrodes were produced passing the same amount of total charge or a specific portion of it. Figure 2.13 shows an example of a typical waveform for bulk electrolysis techniques and the correspondently current response. The peak of current observed in the first seconds of the experiment is due to the charging of the double layer caused by the application of the potential in the cell (see Chapter 4 for a detailed discussion of the current transient).

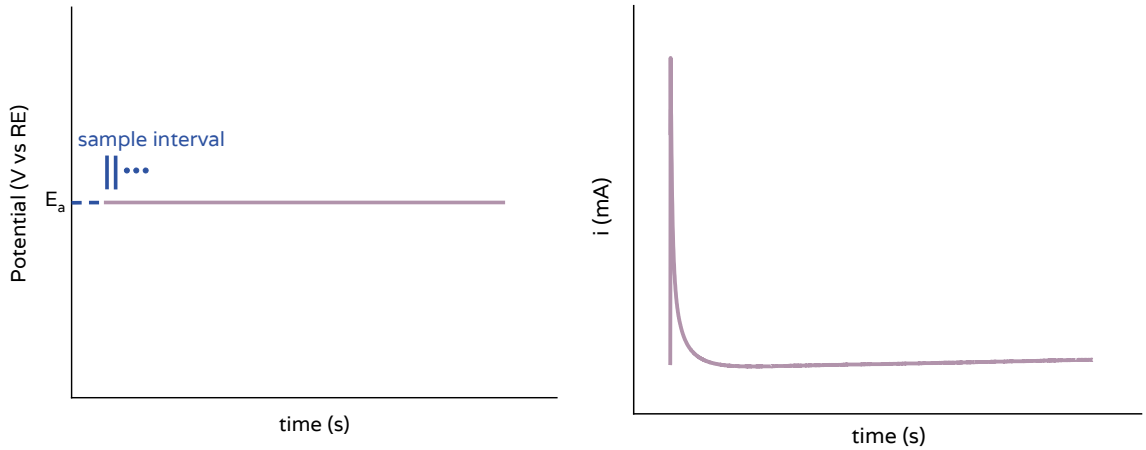

Figure 2.13: example of a typical a) waveform and c) current response observed during bulk electrolysis techniques. E_a is the applied potential and RE is a general reference electrode

In both catalysis and electrodeposition experiments, the main principle considerated is the Faraday's Law of Electrolysis (see Equation 2.2), that states that the mass of a compound produced, or a metal electrodeposited, is proportional to the charge (Q) in Coulomb passed during the experiment[175]:

$$mass = \frac{QM}{nF} \tag{2.2}$$

where M is the molecular weight of the compound, n is the number of electrons transferred and F is the Faraday constant. It is important to highlight that the quantity of products produced during catalysis were calculated in terms of faradic efficiency of the process and not mass.

2.5.3 Laviron method

The heterogeneous electron transfer rate constant (k^0) can be calculated using several methods (see Chapter 3, Section 3.3.5). If diffusionless electrochemical processes are dominant, k^0 is calculated using the Laviron method[249]. This procedure uses the peak to peak separation as the main experimental parameter for the calculation of k^0, allowing the calculation of the electron transfer rate constant by simply performing scan rate studies. Equation (2.3a) and (2.3b) are employed for the calculation of the k^0 for oxidation and reduction processes respectively[249]:

$$k_a^0 = \frac{(1-\alpha)nF\nu_a}{RT}\ (a) \qquad\qquad k_c^0 = \frac{\alpha nF\nu_c}{RT}\ (b) \tag{2.3}$$

where α is the electron transfer coefficient, n is the number of electrons exchanged during the process, F the Faraday constant, R the ideal gas constant and T the temperature in K. ν_a and ν_c are the scan rate for the anodic and cathodic process. In order to use these two equations, the ratio $\frac{\Delta E_p}{\mathrm{n}}$ needs to be larger than 200 mV/s[249]. For this reason, the calculation was performed using the lowest scan rate that presented a ratio larger than 200 mV/s (in this case 50 mV/s). To calculate the electron transfer rate coefficient, the graph of the E_{pa} and E_{pc} as a function of the logarithm of the scan rate was plotted and the slope of the anodic and cathodic branches were extrapolated and inserted into Equation (2.4a) for the anodic process and Equation (2.4b) for the cathodic process:

$$slope = \frac{2.3RT}{(1-\alpha)nF}\ (a) \qquad\qquad slope = -\frac{2.3RT}{\alpha nF}\ (b) \tag{2.4}$$

Chapter 3 : Bismuth disks electrodes

3.1 Introduction

Since the advent of catalysis, one of the main focuses has been to engineer materials to create as favourable conditions as possible to accelerate reactions[250]. Recently, there has been an increased focus on improving the catalytic activity of different metals, including platinum, gold, silver, copper[43,202,251–253] and, most relevant to this work, bismuth[103,254]. Bulk electrodes can be used as controls when the properties of micro- or nanostructured electrodes are investigated. In this chapter, the production, the physical and electrochemical characterisation of bulk Bi electrodes is presented. In particular, scanning electron microscopy (SEM) images acquired during the preparation of the surface are presented as well as capacitance values, electrochemical surface areas, and investigations into the formation and reduction of the Bi oxide. The production and characterisation of a flat bulk Bi electrode allowed the setting of a standard for the other Bi electrodes produced within this work (see Chapter 4).

3.2 Polishing procedure

The unpolished Bi disk were prepared (see Chapter 2 Material and Method Section 2.4.3 for their production) and preliminary tested using CV to check the quality of the connections (Figure 3.1). The parameters for the measurements were chosen based on the future catalysis experiments: 0.1 M Na_2SO_4 was used as electrolyte and a negative potential window was selected (highest potential applied was equal to -0.8 V and lowest potential was -2.0 V).

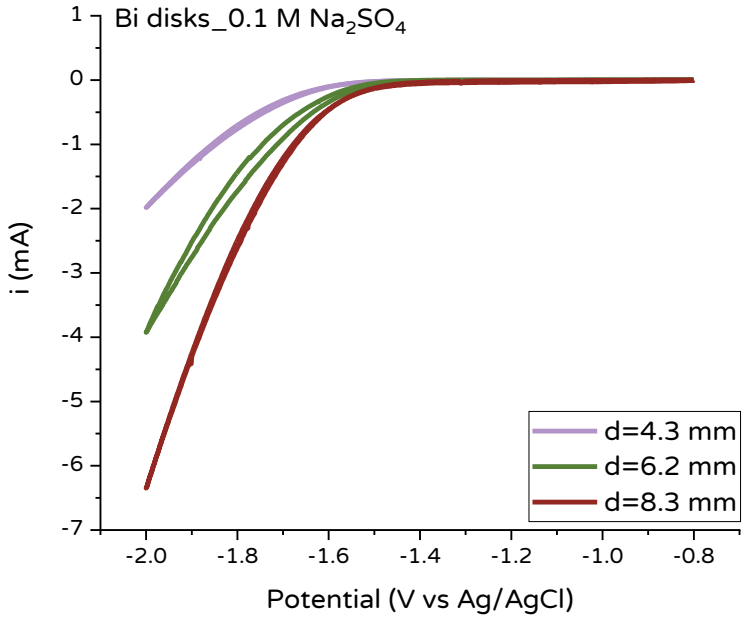

Figure 3.1: CVs for the three unpolished Bi disks in 0.1 M Na_2SO_4; scan rate=100 mV/s

Figure 2.8c shows that the cast bismuth rod has many casting defects and some gaps/holes/pits. Mechanical polishing procedures are used to activate the electrodes (i.e. the removal of any impurity accumulated from the atmosphere or previous experiments) and to obtain flat, clean, homogenous surfaces[172,255]. For this reason, the Bi disk electrodes were polished using, first, sandpaper and, finally, alumina slurry. Specifically, twelve steps were performed: the first six steps with micro grit type sandpaper (Table 3.1, from the lowest to the highest grit number) and the final five steps with alumina slurry (from the biggest to the smallest particle size).

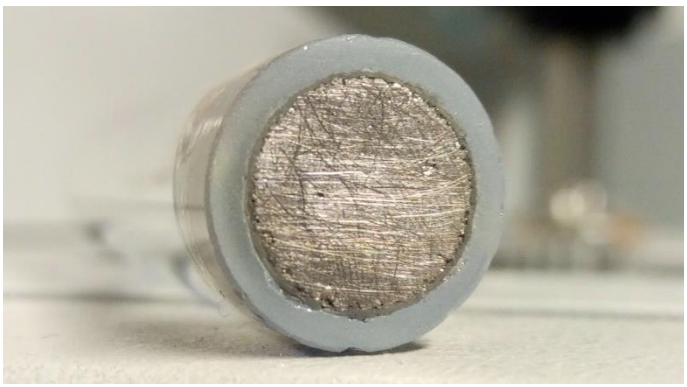

Figure 3.2: Bi disk before polishing procedure. Diameter equal to 8.3 mm

The grit and the size of the particles used for this process are showed in Table 3.1.

Table 3.1: Grit and particle size of the polishing abrasives used during the polishing procedure

Polishing material	step	ISO/FEPA grit designation [a]	average particle diameter [µm][256,257]
sandpaper	1	P320	46.2
	2	P400	35.0
	3	P600	25.8
	4	P800	21.8
	5	P1000	18.3
	6	P1200	15.3
alumina slurry	1	-	12.5
	2	-	5.0
	3	-	1.0
	4	-	0.3
	5	-	0.05

a. sandpapers are classified by ISO 6344-3:2013 and FEPA-Standards 43-1:2006

Photographs and SEM images were acquired before the polishing procedure, after polishing with sandpaper and after polishing with alumina slurry. This allowed the changes in the surface of the metal, during the polishing steps, to be monitored. Pictures were also taken after each polishing step (images for Bi disk with diameter equal to 8.3 mm only are shown here).

By decreasing the particle size, the surface of the metal appeared smoother (see Figure 3.3): the deep and sharp scratches are significantly reduced and those still present are less deep. While a considerable difference could be noticed when the electrode was polished with the P320 and P600 sandpaper, no appreciable differences could be observed visually after polishing with P800, P1000 and P1200 one.

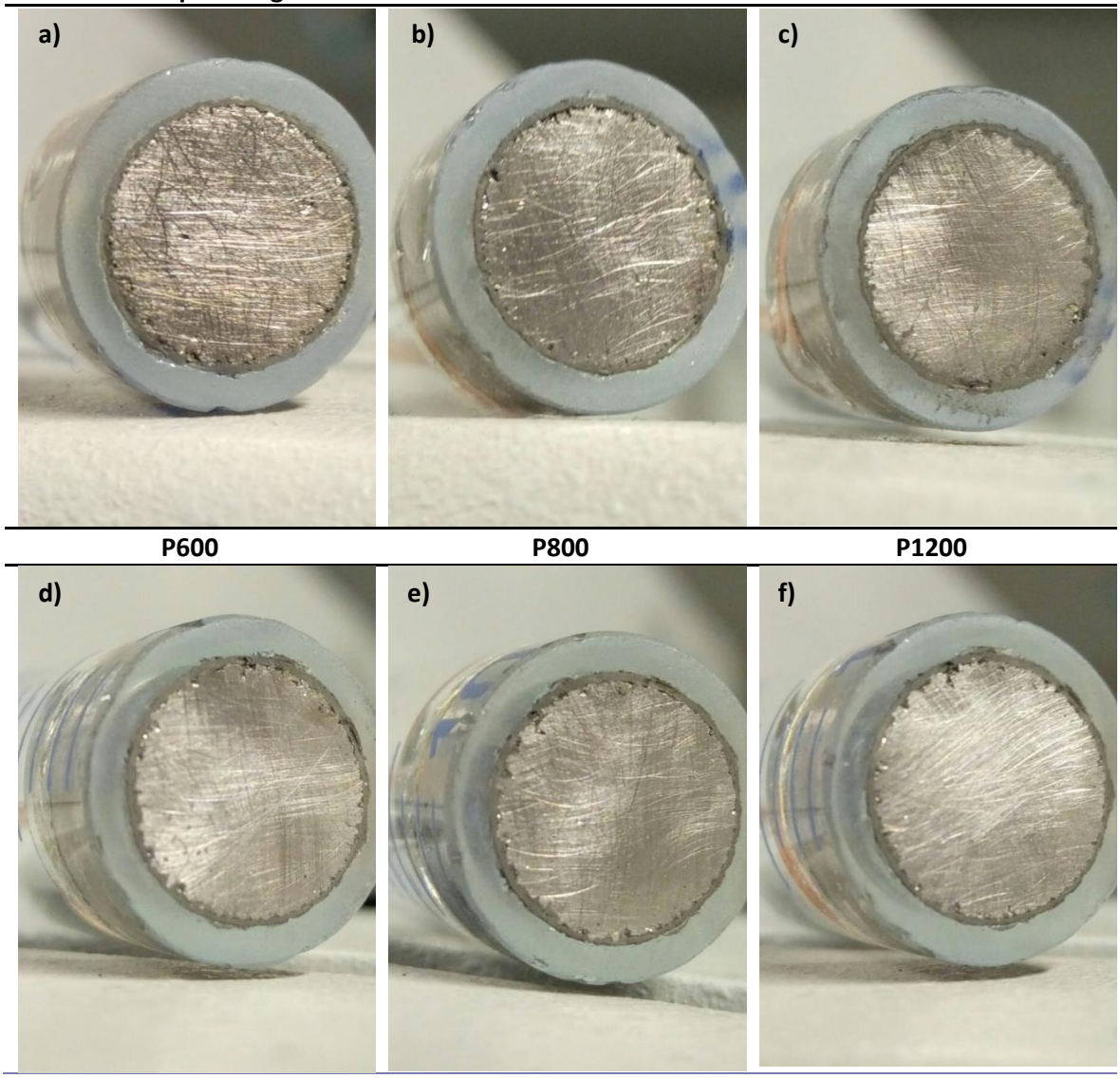

Figure 3.3: Photos of Bi disk (Φ=8.3 mm) after each sandpaper polishing step: a) P320; b) P400; c) P600; d) P800; e) P1000; and f) P1200

In Figure 3.4, the photos of the electrode during the polishing procedure with alumina slurry are shown. The particles of alumina used are smaller than the one used for the sandpaper procedure, ensuring additional smoothness and more flat surfaces. After the first polishing step with alumina slurry (Figure 3.4a), no significant changes were observed form the last polishing step performed with sandpaper). Several scratches were present, but they are considerably less deep. During the polishing step with alumina slurry, the Bi surface looked shinier in comparison with the electrodes

in Figure 3.2 suggesting that the surface is smoother and the defect on the surface are smaller than for the electrodes polished with sandpaper. In general, after the final polishing steps, it was not possible to notice any significant difference in the smoothness of the surface by simply observing the electrode.

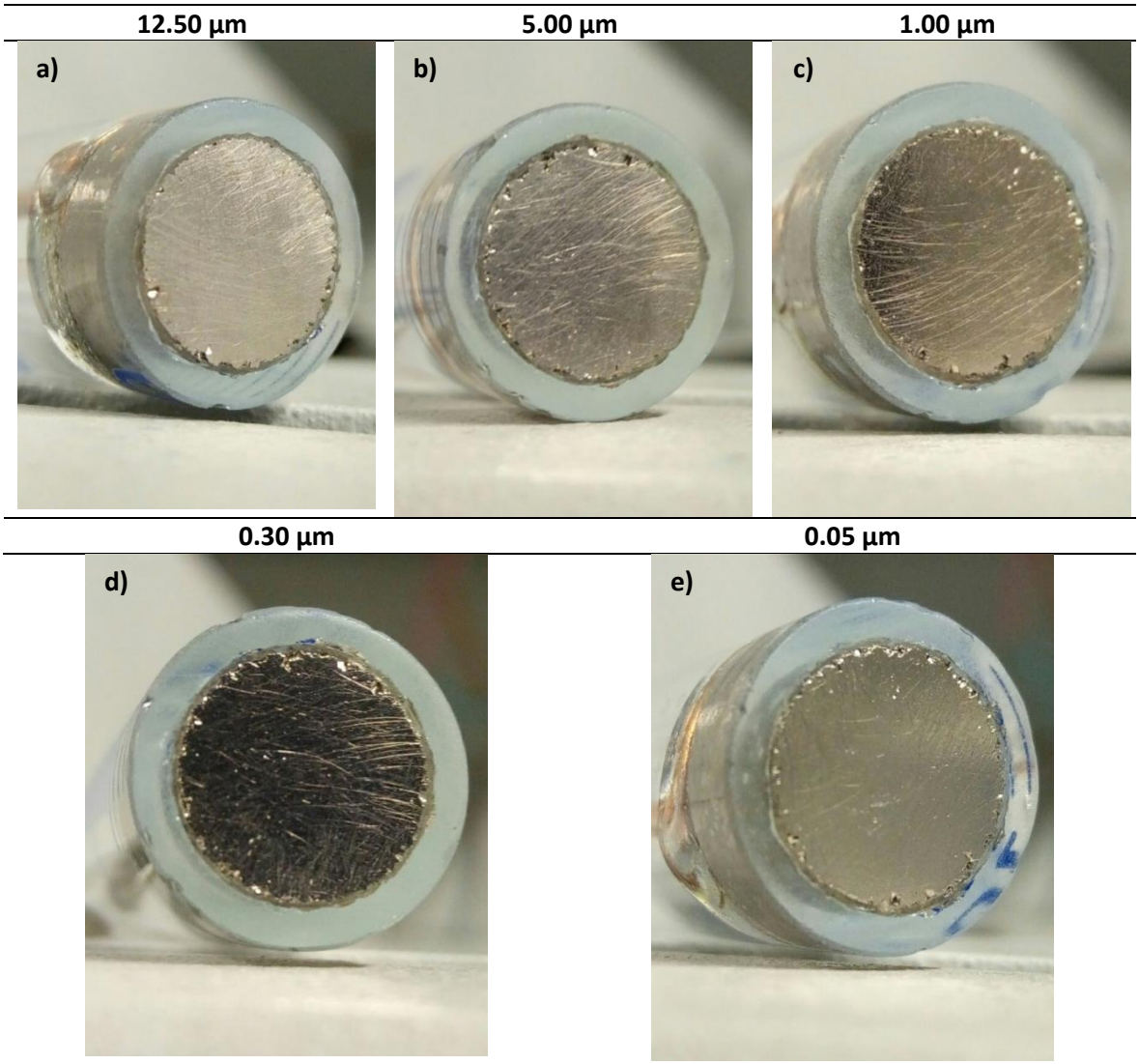

Figure 3.4: Photos of Bi disk (Φ = 8.3 mm) after each sandpaper polishing step: a) 12.5 µm; b) 5.0 µm; c) 1.0 µm; d) 0.3 µm; and e) 0.05 µm. The roughness of the electrode surface decreases with the size of the abrasive particles

3.3 Characterisation of the Bi disks

3.3.1 SEM imaging

The SEM images at low magnification for Φ = 4.2 mm Bi disk are shown in Figure 3.5 (for Φ = 6.2 and 8.3 mm electrodes see supporting information). It is evident how the surface of the metal became smoother after the polishing procedure with sandpaper (Figure 3.5b) and alumina slurry

(Figure 3.5c). SEM imaging only provides qualitative information about the changes of the surface for a quantitative measure see Section 3.3.2.

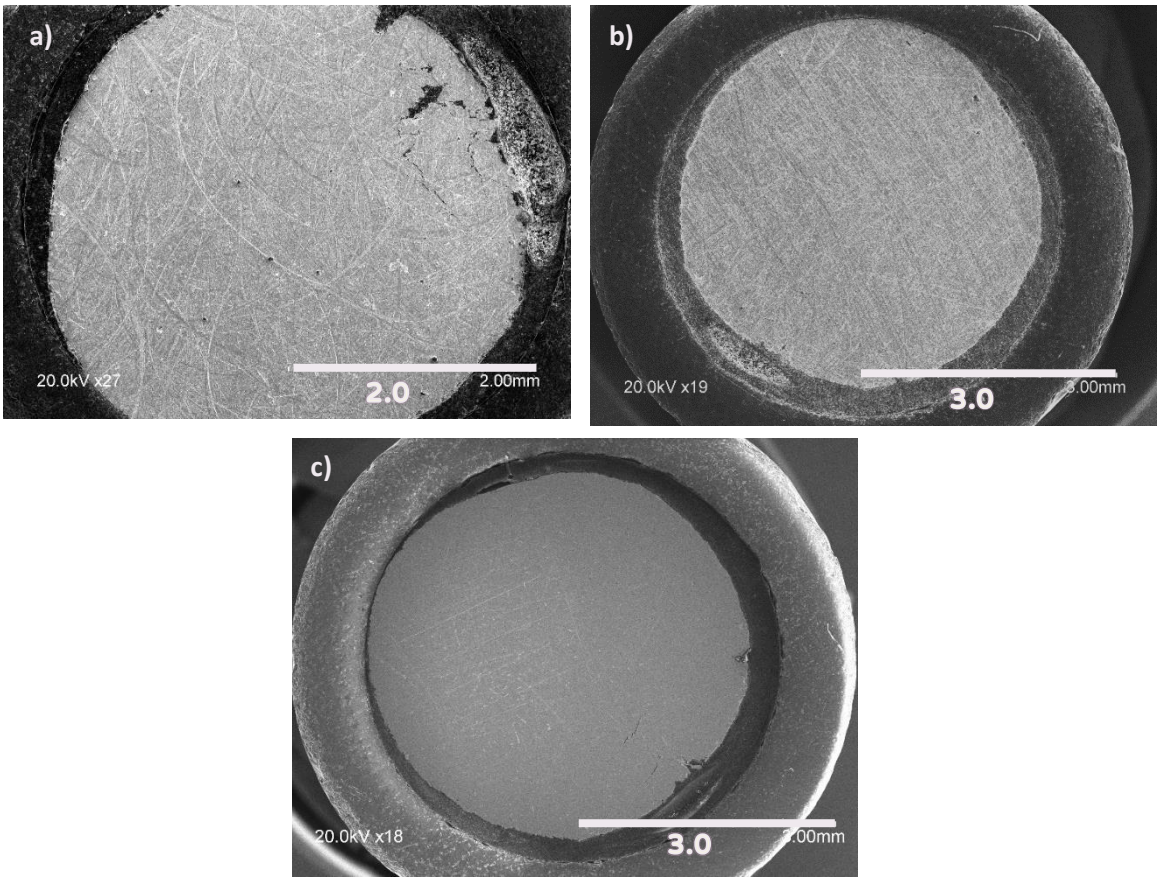

Figure 3.5: SEM images for Bi disk (Φ= 4.2 mm) a) before any polishing step (Magn= x27); after polishing procedure with b) sandpaper (Magn= x19); and c) alumina slurry (Magn= x18). The accelerating voltage was equal to 20 kV

In Figure 3.6, the SEM images at higher magnification (Magn= x500) are shown. Here, it is possible to observe how the polishing process changed the surface of the electrode: in Figure 3.6a, very deep and wide scratches in several directions are present. After the polishing procedure with sandpaper (Figure 3.6b), the scratches were still present, but they looked less wide and deep. On the other hand, after polishing with alumina slurry (Figure 3.6c), the surface was smooth and clearly more homogeneous: only thin lines and small gaps are noticeable.

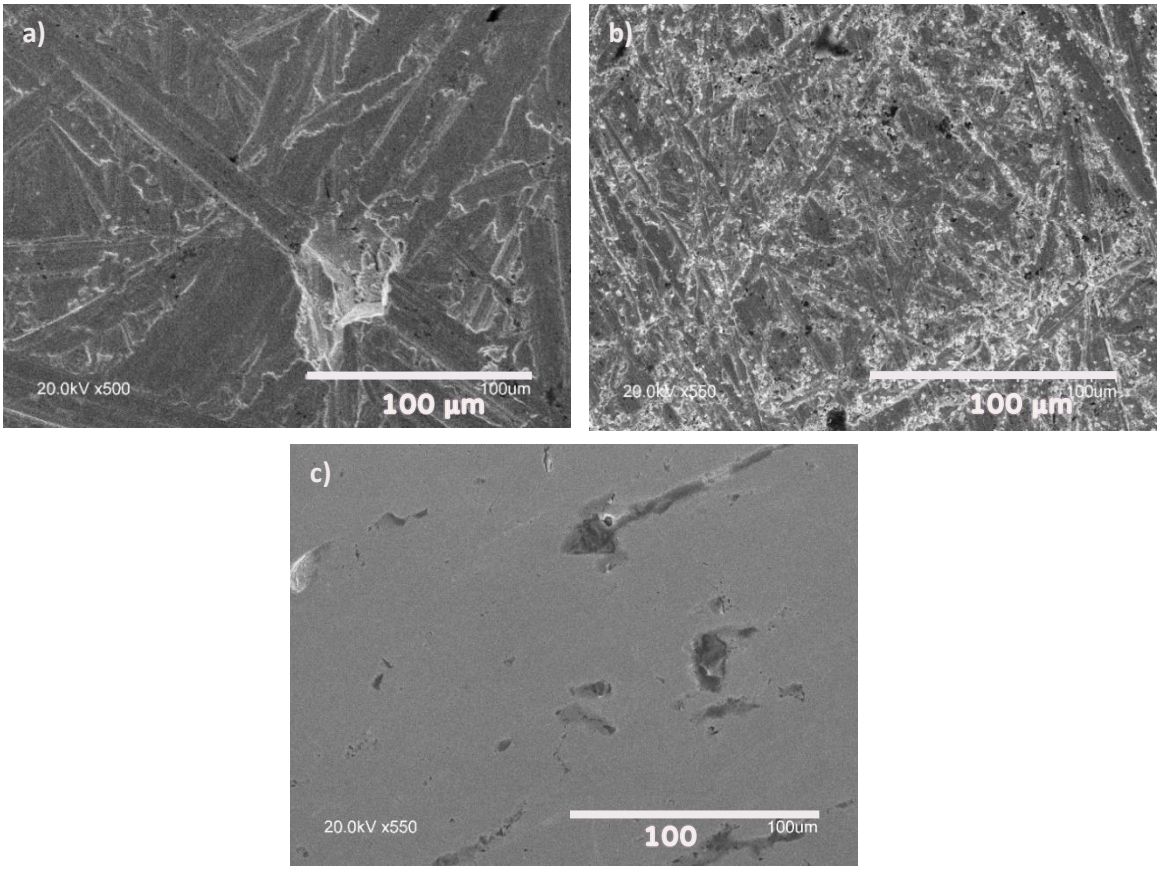

Figure 3.6: SEM images for Bi disk (Φ= 4.2 mm) a) before any polishing step (Magn= x500); after polishing procedure with b) sandpaper (Magn= x550); and c) alumina slurry (Magn= x550). Accelerating voltage 20 kV

3.3.2 Real surface area: the oxygen adsorption method

Knowledge about the electrochemical surface area (ECSA) or real surface area (A_{real}) of the working electrode is essential to quantifying the catalytic activity [196]. Several experimental methods can be used to determine the real surface area and they are divided in two categories*: in-situ* and *ex-situ* methods[198]. In this work, the calculation was performed via the oxygen adsorption method (see Chapter 1, Section 1.5.2 for description of the method), in which a monolayer of oxide is formed on the surface of the electrode by applying a positive potential and then completely reduced. This method was chosen because it allowed calculation of the electrochemical active sites, while considering the roughness of the surfaces (this is not always ensured when the mass transport method is used). The measurements were performed in a solution of aqueous 50 mM KOH, at a scan rate equal to 10 mV/s and the CVs for the three Bi disks are showed in Figure 3.7a, b and c. The peak present between -0.7 and -0.6 V correspond to the reduction of the oxide monolayer formed during a previous anodic scan. By integrating the area below the curve (Figure 3.7d), it was possible to obtain the amount of charge passed (Q_{exp})during the process [200,201,258]. The measurement was repeated three times for each electrode.

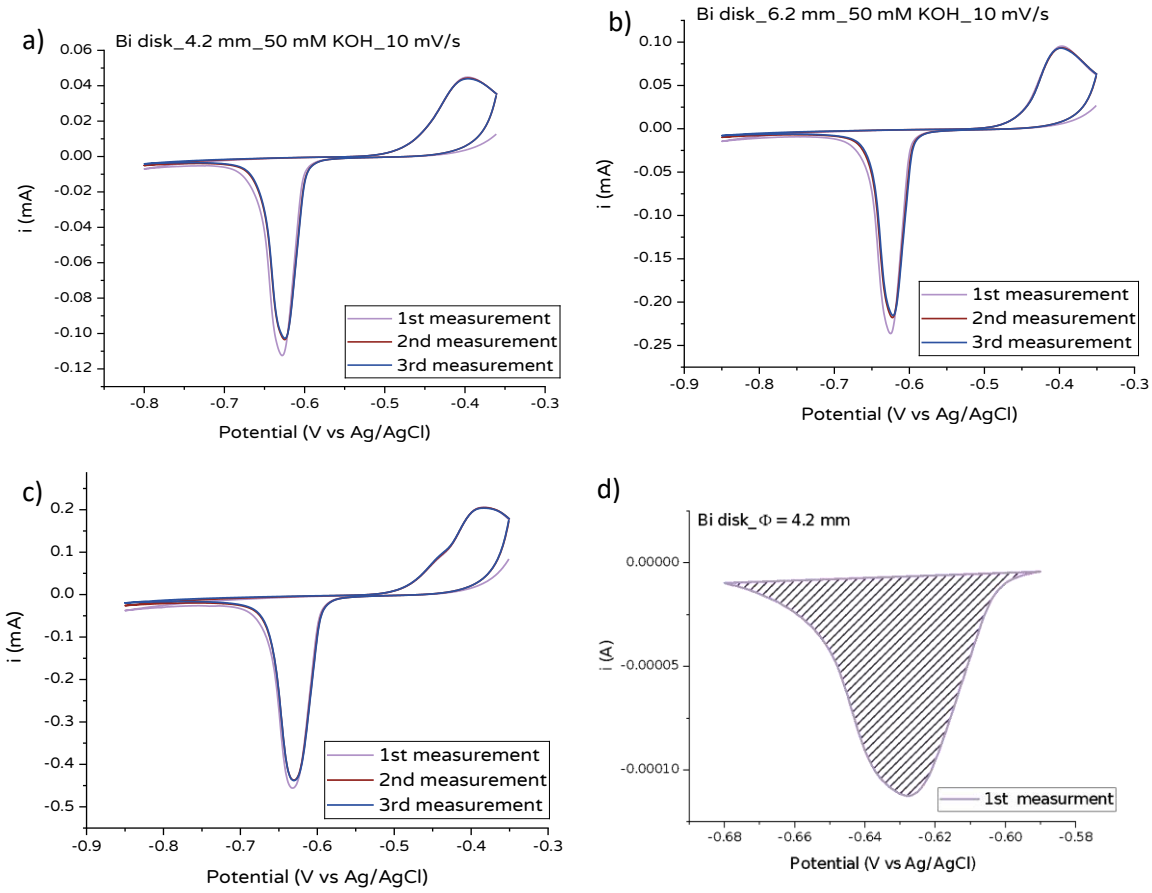

Figure 3.7: CVs for the oxygen adsorption method obtained in 50 mM KOH for different Bi disks with diameter equal to a) 4.2; b) 6.2; c) 8.3 mm; and d) integration of the area below the reduction curve for obtaining the charge passed during the reduction of the monolayer. Scan rare: 10 mV/s. Scan rate: 10 mV/s. The reduction peak represents the oxidation of the oxide layer formed during a previous anodic cycle

The Bi disk real surface area was then obtained by using the charge denisty (σ) and the atom packing density of a reference material. In this case, Au was chosen as reference as its charge denisty has been previously calucalted and suggested to be equal to 390 µC/cm^2.[198] Knowing that Au and Bi packing density are 10.21 and 21.31 cm^3/mol respectively[259], it was possible to calculate the theoretical σ_{Bi} (= 187 µC/cm^2). Once the value of the charge was obtained for the three measurements, the real area of the Bi disks was obtained by dividing the average Q_{exp} by the theoretical σ_{Bi}. Finally, by using Equation (3.1)[198], it was then possible to calculate the roughness factor (r_f), for the Bi disks (see Table 3.2).

$$r_f = \frac{A_{real}}{A_{geo}} \qquad (3.1)$$

Table 3.2: Experimental charge, roughness factor, geometrical and ESA for the three Bi disks obtained via the oxygen adsorption method

Diameter Bi disk [mm]	Q_{exp} [µC]	A_{geo} [cm^2]	A_{real} [cm^2]	r_f	average r_f
4.2	360±9	0.14	1.92 ± 0.08	13.89	14.0 ± 0.7
6.2	749±23	0.31	4.0 ± 0.2	13.28	
8.3	1728±15	0.54	8.0 ± 0.1	14.75	

The average roughness factor value calculated here was similar to values obtained by other authors. For example, a roughness factor of microelectrodes[194], for which a potential of -2.1 V was applied for five minutes, was equal to 10.4. By way of contrast, a value of 15.8 was obtained for Bi rods that were first mechanically polished with 0.05 µm alumina, and then electrochemically reduced to remove the native oxide layer[183]. It was suggested that the high r_f, and therefore the large area, was due to the formation of a porous Bi metal film layer when a cathodic sweep was performed. An increase in the roughness factor of the electroreduced Bi surface was also also observed in another study[177]: after the reduction step, the roughness factor was estimated from the differential capacitance and it was calculated to be equal to 10.

Knowing the area of the electrode and the Q_{exp}, it was possible to calculate the charge per unit area: the charge density for the Bi bulk electrodes was equal to 2719 µC/cm^2. A similar result was reported by Koh et al[101], that measured the Q_{exp} for a Bi foil, obtaining a value of 2280 µC/cm^2.

The real area was also calculated after each polishing step for the Φ =8.3 mm Bi disk and the results are shown in Table 3.3.

Table 3.3: Real area and roughness factor calculated using the oxygen adsorption method for Bi disk Φ= 8.3 mm calculated after each polishing step

sandpaper		
grit	A_{real} [cm^2]	r_f
P320	18.4 ± 0.2	34.1
P400P	17.6 ± 0.5	32.5
P600P	16.1 ± 0.3	29.7
P800P	20.8 ± 0.2	38.4
P1000	22.8 ± 0.6	42.1
P1200	23.2 ± 0.7	42.9
alumina		
size [µm]	A_{real} [cm^2]	r_f
12.50	15.5 ± 0.6	28.7
5.00	13.3 ± 0.6	24.5
1.00	11.3 ± 0.4	20.8
0.30	10.9 ± 0.3	20.1
0.05	8.0 ± 0.1	14.7

The real area values obtained during the sandpaper polishing procedure initially decreased from 18.4 to 16.1 cm^2 to then increased again to 23.2 cm^2. The variation on the area depends on the size of the particles on the sandpaper[255]. After the first polishing step with alumina slurry, the area decreased again to 15.5 cm^2. By decreasing the particles size of the alumina, the real area further reduced to 8.0 cm^2, a value approximately half that obtained for the first polishing step. This trend was expected as the polishing procedure flattened the surface of the electrode by removing scratches and imperfections present on the metal rod[260] (see SEM images). The large change in real area (and therefore in r_f), is likely due to the softness of the bismuth metal. It has been observed previously that, during mechanical polishing, softer metals tend to have a large variation in their area than hard ones[261]. The last two steps of the polishing procedure were also performed on a gold polycrystalline electrode (Φ = 0.2 mm) in order to obtain the roughness factor for a somewhat harder metal - Mohs's hardness are 2.5 and 2 for Au and Bi respectively[262]. As expected, the roughness factor for the Au electrode was lower than the one for the Bi disks (r_f = 1.37 ± 0.06).

Successively, the charge passed during the reduction of the oxide monolayer was obtained at different scan rates in order to understand the type of correlation that exists between the charge passed and the scan rate. For example, if oxide formation was slow, sub-monolayer coverages might be observed at high scan rates while if place exchange was relatively rapid, multiple oxide layers could form at slow scan rates. As expected, by increasing the scan rate an increase in the peak current was observed (see Figure 3.8)[172].

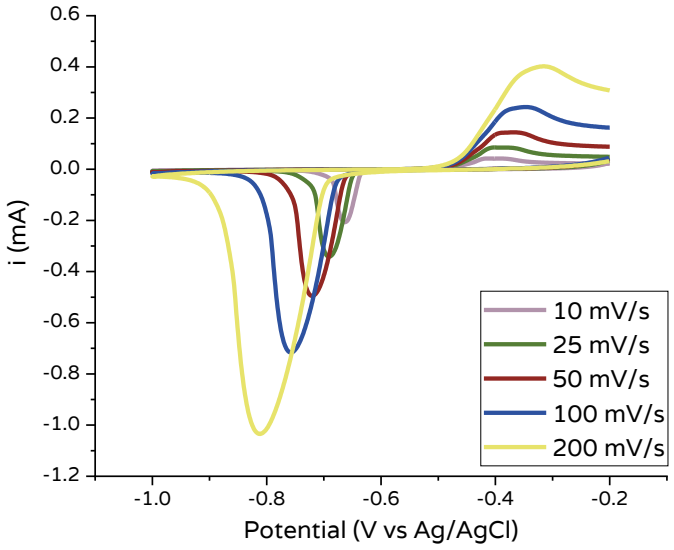

Figure 3.8: Scan rate study for the reduction of the oxide monolayer performed in 50 mM KOH. WE = Bi disk, Θ= 4.2 mm

As illustrated in Table 3.4, the charge passed during the reduction of the monolayer decreased as the scan rate increased. In particular, a decrease of 20% is observed when applying the highest scan rates in comparison with the lowest. This means that when the potential is applied for longer period

of time (low scan rates) more oxide is formed and therefore more oxide is reduced during the cathodic scan. On the other hand, for high scan rates, the potential is applied for less time and less oxide is formed. It is important to highlight that it might be difficult to obtain a homogeneous Bi oxide monolayer. The surface of the electrodes presents several defects and a long time might be required for the OH^- molecules to diffuse through, therefore the current should flow for long enough to allow the diffusion and the oxidation of the Bi surface. In addition, formation of the an additional layer (different from the first) can occur simultaneously with the first layer[263]. For this reason, a careful selection of the scan rate values used for the experiments needs to be done, as, if the scan rate is too fast, OH^- ions will not be able to diffuse through the diffusion layer and reduce the Bi metal, while if the scan rate is too slow, there is a high possibility to form multilayers. The same general principle is valid for the reduction step.

Table 3.4: Charge passed during the cathodic process for the reduction of the oxide monolayer at different scan rate

scan rate [mV/s]	area [W]	Q [C]
10	7.5×10^{-6}	7.5×10^{-4}
25	1.7×10^{-5}	6.7×10^{-4}
50	3.1×10^{-5}	6.3×10^{-4}
100	6.0×10^{-5}	6.0×10^{-4}
200	1.2×10^{-4}	6.0×10^{-4}

3.3.3 Capacitance measurements

Scan rate dependent cyclic voltammetry in potential regions where faradaic processes are absent can be used to obtain the double layer capacitance [264]. Knowing the double layer capacitance is very useful as it can give important information about the area, the structure and the chemical nature of the electrode surface and the interactions between the electrodes and the species in solution[208,210,211]. To obtain more information about the Bi disk electrodes surface, the capacitance for the three Bi disks was measured. The capacitance values were obtained by plotting the cathodic charging currents densities, at one specific potential (the potential in the middle of the CV curve) as a function of the scan rate. The double layer capacitance corresponded to the slope of the linear fit. The scan rate study was initially performed after each polishing step for the Bi disk with a diameter of 8.3 mm (see Figure 3.9 and Table 3.5.) In Figure 3.9a, an example of the scan rate dependence study for the calculation of the capacitance is shown. Figure 3.9b and c show the linear fit curves for the entire polishing process.

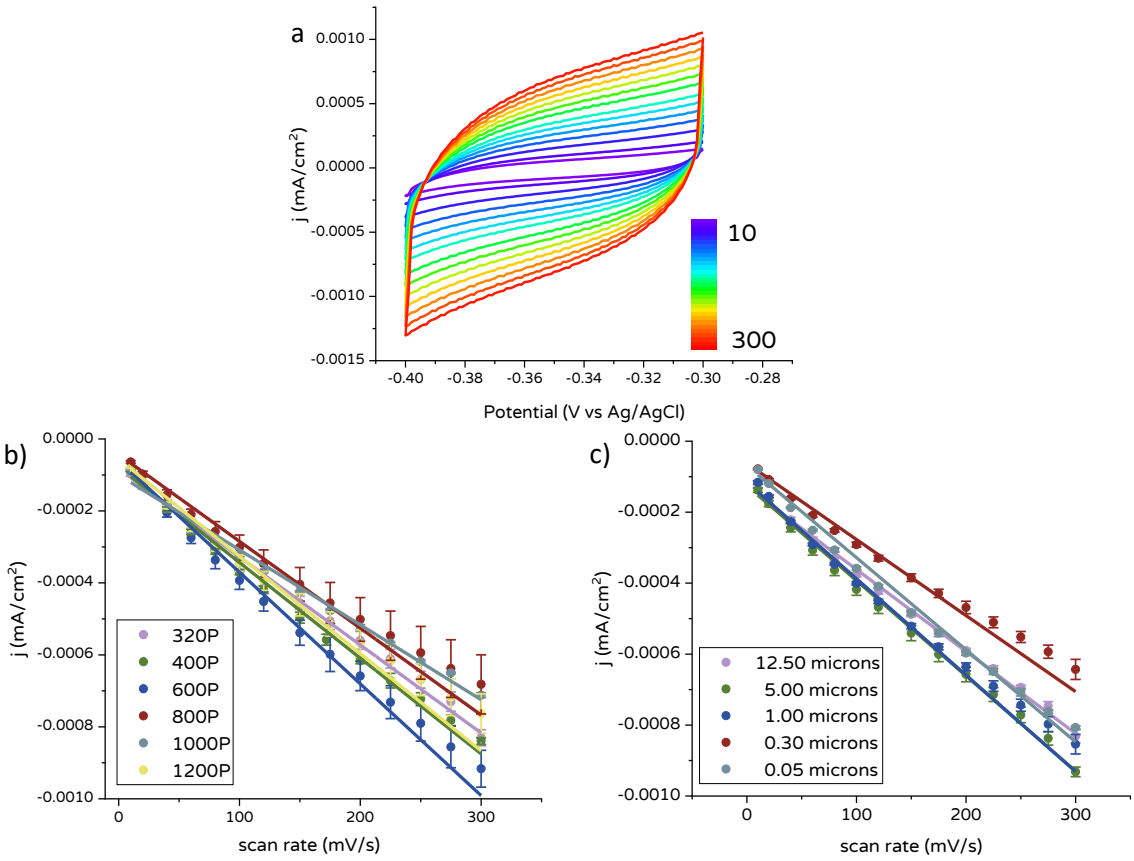

Figure 3.9: a) Scan rate studies in 0.1 M Na_2SO_4 for Φ =8.3 mm Bi disk (polishing step=0.05 µm alumina); cathodic charging currents as a function of the scan obtained after each polishing steps with b) sandpaper; and c) alumina slurry

As can be seen in Table 3.5 and Figure 3.9b and c, the capacitance measured for each polishing step does not change considerably: a maximum of 22% error was calculated. This means that the double layer structure did not change considerably during the polishing procedure. This was expected as, during this process, only the area of the surface changed not the chemical nature (composition, oxidation state) of the metal[265].

Table 3.5: Capacitance values for the Bi disk (Θ = 8.3 mm) calculated during the polishing procedure. The capacitance was obtained performing the scan rate study in a potential range in which only non-faradaic processes are present. The area used for the normalisation was the A_{real} calculated using the oxygen adsorption method

sandpaper	
grit	**capacitance** $\left[\frac{\mu F}{cm^2}\right]$
P320	2.45 ± 0.05
P400	2.66 ± 0.06
P600	3.10 ± 0.09
P800	2.41 ± 0.09
P1000	2.08 ± 0.05
P1200	2.7 ± 0.1
alumina	
size [µm]	**capacitance** $\left[\frac{\mu F}{cm^2}\right]$
12.50	2.31 ± 0.05
5.00	2.68 ± 0.05
1.00	2.72 ± 0.09
0.30	2.14 ± 0.07
0.05	2.60 ± 0.07

The capacitance values for the Bi disks Φ =4.2 and 6.2 mm are shown in Table 3.6. The measurements were performed after the last polishing step (alumina 0.05 microns). The linear fitting curves for the three electrodes are shown in Figure 3.10.

Table 3.6: Capacitance values for the three Bi disks obtained via scan rate study after polishing with alumina 0.05 µm slurry (last step of the polishing procedure). The capacitance was obtained performing the scan rate study in a potential range in which only non-faradaic processes are present. The area used for the normalisation was the A_{real} calculated using the oxygen adsorption method

Φ Bi disk [mm]	**capacitance** $\left[\frac{\mu F}{cm^2}\right]$	**average capacitance** $\left[\frac{\mu F}{cm^2}\right]$
4.2	3.1 ± 0.1	2.7 ± 0.4
6.2	2.31 ± 0.04	
8.3	2.60 ± 0.07	

As expected, the capacitance values for the three Bi disks are comparable (for average capacitance, error = ± 0.4 $\frac{\mu F}{cm^2}$), because the chemical nature of the metal is the same and the only difference is the diameter of the electrodes. Considering that the charging currents are proportional to the real area of the electrode[266], the calculations were performed using the current densities (i.e. the current was normalised to the real area of the electrode) allowing comparison of the capacitance values for the three electrodes.

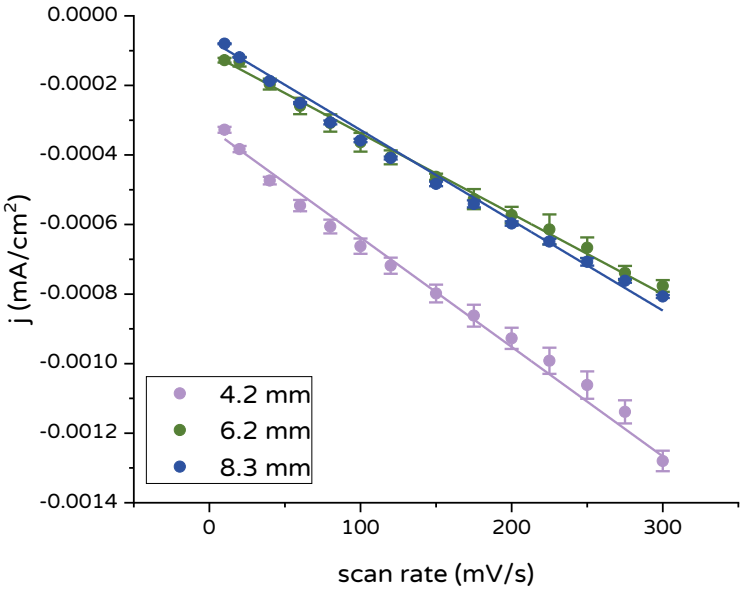

Figure 3.10: Cathodic charging currents as a function of the scan rate for the three Bi disks: Φ Bi disk= 4.2 mm in purple; Φ Bi disk= 6.2 mm in green; and Φ Bi disk= 8.3 mm in blue. The measurements were performed after mechanical polishing with 0.05 µm alumina slurry (last step of the polishing procedure). The area used for the normalisation was the A_{real} calculated using the oxygen adsorption method

The capacitance values obtained here are smaller than those found in the literature[177,192,194], which vary from 18 to 36 µF/cm^2. The relatively small capacitance obtained within this work may be due to the fact that the measurements were performed in a potential range at which the oxide layer is not reduced. This can influence the capacitance values in two ways: first, the surface is not pure Bi metal but a mixture of Bi metal and Bi oxide due to the presence of the native oxide layer (it has been demonstrated before that mechanically polishing Bi electrode does not give an oxide free surface[185]); and second, the formation of the porous metal film that has been observed in previous works was likely not formed. On the other hand, the Bi electrodes investigated in the literature were *all* electrochemically reduced before capacitance measurements, with the intention of complete removal of the native oxide. This means that the roughness factor calculated in this work may not actually be representative of the electrode surface used for the capacitance measurements. In addition, it is important to consider that the area used for normalising the current presented in literature might not be the ECSA. This might be the cause behind the higher capacitance values than the ones obtained within this work.

3.3.4 Scan rate studies

To further characterise the surface of the electrodes, scan rate studies were performed. The experiments were carried out using two different electrolytes: Na_2SO_4 and $KHCO_3$. These solutions are used for the catalytic experiments. As the solutions used for the catalytic experiments were

CO_2-saturated, the scan rate studies were performed in both the N_2- saturated solution (the blank) and CO_2-saturated solutions. A diagrammatic scheme of the four systems is shown in Figure 3.11.

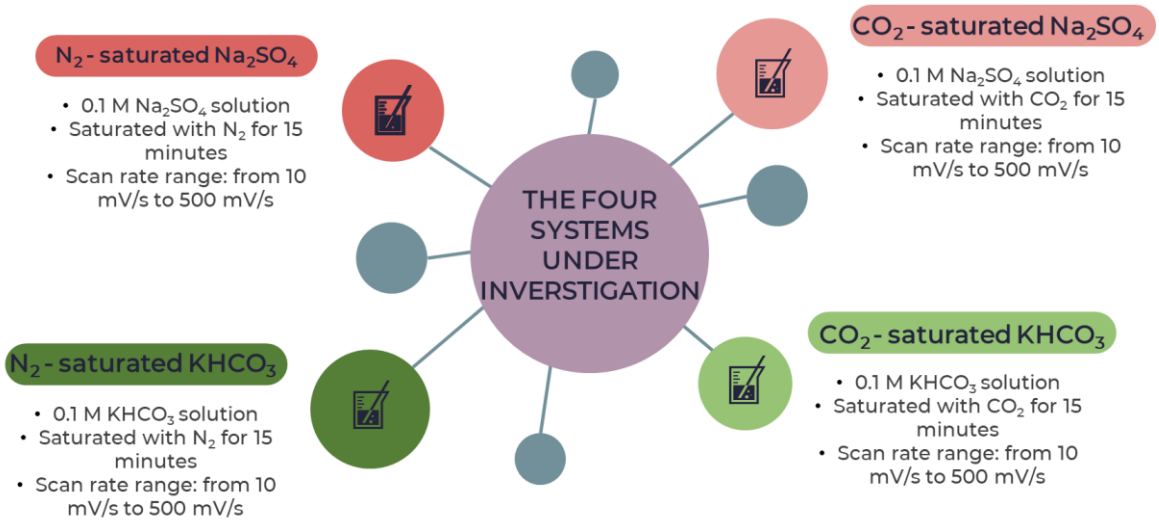

Figure 3.11: Diagrammatic representation of the four systems used for the scan rate studies

3.3.4.1 Na_2SO_4

The scan rate studies were performed in a N_2-satured solution of Na_2SO_4 over a large potential window, from +1.0 to -2.0 V (see Figure 3.13a). For these experiments Bi cylinder electrodes with diameter of approximately 9 mm and a thickness of around 2 mm were prepared (see Figure 3.12). These electrodes were produced for catalysis experiments (see Chapter 6) to obtain an increase in the surface area, making a direct comparison with microstructured Bi electrodes possible (see Chapter 4).

Figure 3.12: Bi cylinder electrode used for the scan rate study. The electrodes were polished with 1200P sandpaper for 1 minute prior each experiment

The CVs presented two well defined peaks, one around -0.20 V vs Ag/AgCl for the oxidation of Bi and the second at -1.10 V for its the reduction (for v = 100 mV/s), while the current after 0.1 V is attributed to the thickening of the Bi oxide layer[176,177,185,241,267]. In basic solutions, the growth of the oxide is described by a current plateau, while here an increase is observed before the plateau (see CV at 10 mV/s, Figure 3.14b). The increase has been observed in solutions with pH < 8.5 and it is due to the formation of a crystalline deposit[177]. This deposit is formed after the dissolution of the electrochemically formed Bi oxide followed by precipitation of $Bi(OH)_3$ or Bi_2O_3. By integrating the area under the cathodic and anodic peaks, the charge for the anodic (Q_A) and cathodic (Q_C) processes are obtained. By dividing the Q_C by the Q_A, current efficiency (CEf) was calculated (see Equation 1.3 in Chapter 1) for the highest and the lowest scan rate, and they are shown in Table 3.7. Obtaining current efficiencies with values close to one means that the charges passed during the cathodic and the anodic scan are the same, therefore the oxide formed in the anodic sweep is then reduced completely during the cathodic scan. In this case, at the lowest scan rate, the charge under the cathodic peak is higher than the charge under than the anodic peak, suggesting the presence of another process during the cathodic scan. This process can simply be the hydrogen evolution reaction (HER), that occurs in similar potential ranges, as proposed elsewhere[177]. In addition, it is important to remember that the reduced Bi^0 presents a higher surface area, so the difference in current, and therefore in charge, can be due to the higher ECSA. The formation of BiH_x species during the reduction of the anodic film has been proposed[192,194,195]. The peak attributed to the formation of Bi hydrides has been only observed at very low scan rates (1 mV/s). Considering that the lower scan rate used here was 10 mV/s (Figure 3.14b), it is probable that the peak is not differentiated/resolved from the cathodic reduction peak. Another possible reason for the higher magnitude of Q_C is that some oxide is still present from the previous scans (the scan rate study was performed starting from the highest to the lowest scan rate) and because of the longer time required for the scan, the oxide that was not reduced previously is finally reduced. On the other hand, at 500 mV/s, the CEf value was around one. It is likely that at high scan rates, the potential is swept too fast for the other process to occur or to significantly influence the value of the charge. Another possibility is that a part of the charge in the cathodic peak is actually due to the additional cathodic process and that not all the oxide is reduced. This would mean that the reduction is a slower process than oxidation. A difference in the rates processes of the oxide formation and reduction is possible, as the mechanisms for the oxide formation and its reduction are different[183,185].

Table 3.7: current efficiencies, cathodic and anodic charges calculated integrating the area under the cathodic and anodic peaks for CVs performed with Bi cylinders electrodes at 10 and 500 mV/s. Electrolyte: N_2-saturated Na_2SO_4

Scan rate [mV/s]	Q_A [mC]	Q_C [mC]	CEf
10	61.8	89.6	1.4
500	15.9	15.7	1.0

Figure 3.13b shows a linear dependence between the i_p and the scan rate for both the cathodic and anodic processes, in accordance with what is found in the literature[176,183]. This linearity has been explained in terms of diffusion controlled nucleation for both Bi oxide and the electro-reduced Bi^0.

At low scan rates, 10 mV/s (see Figure 3.14b) and 25 mV/s (not shown), in the anodic section, two peaks were observed, while at high scan rates only the first peak, attributed to the formation of the monolayer of Bi oxide[185], is observed. The number of the anodic peaks depends on the experimental conditions and it is strongly dependent on the nucleation potential (the potential at which the oxide starts to form on the surface of the electrode) that is also influenced by the pH of the solution[177]. The absence of the second peak at high scan rates might be simply due to the scan rate and the high iR drop (for 500 mV/s, -0.78 < iR < 0.52 V). In addition, the surface at which the potential is swept at 10 mV/s is probably different than for the highest scan rates as several cycles were already performed. This means that the surface may be more porous and some unreduced oxide may be present.

Figure 3.13a shows that the peak to peak separation (ΔE_p) between the oxidation (-0.32 V < E_{pa} < + 0.01 V) and the reduction (-0.80V < E_{pc} < -1.54 V) peaks is quite large. An increase in the peak to peak separation as a function of the scan rate was observed by other authors for Bi bulk electrodes in borate solutions[176,177,183], with a variation between 0.65 and 0.6 V at low scan rates (around 10 mV/s). These values are 2x times higher than the ones obtained here (see Table 3.9). Experiments in concentrated sulfuric acid solutions have been performed and showed that the peak to peak separation was smaller (ΔE_p = 0.3 V) than in basic solutions[186]. In a solution 0.05 M of Na_2SO_4, the peak to peak separation was calculated to be around 0.4 V at 10 mV/s[179], a value very similar to the one obtained in this work. From Figure 3.13c it can be seen that the iR drop increases significantly with increasing scan rate.

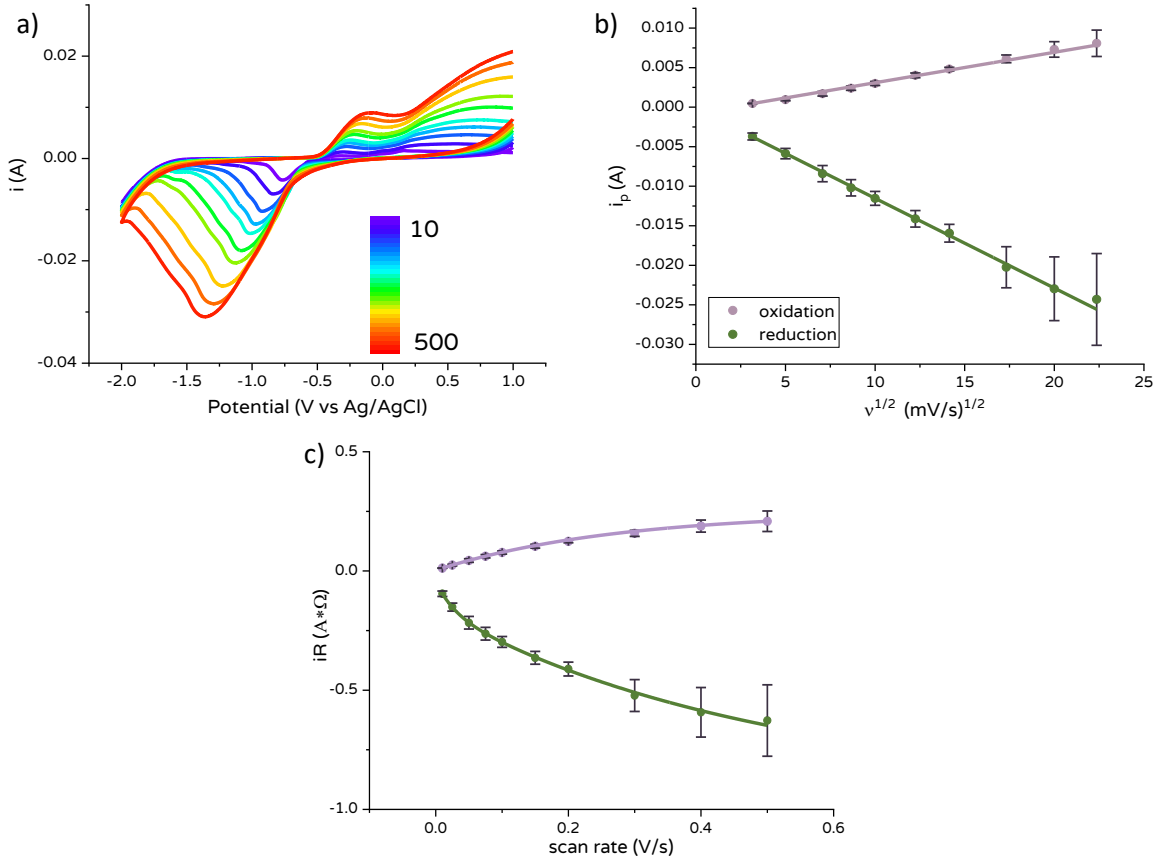

Figure 3.13: a) scan rate study for the formation and reduction of Bi oxide in Na_2SO_4 under N_2; b) i_p for both cathodic and anodic processes vs square root of scan rate obtained from the scan rate study showed in a; c) iR drop vs scan rate for both reduction (green) and oxidation (purple) calculated at i_p; The fitting was described by the equation presented in the Appendix; c) i_p vs square root of the scan rate

To understand if the large peak to peak separation is simply due to the uncompensated resistance or if the kinetics of the reaction is influencing the shape of the CVs, the uncompensated resistance was plotted as a function of the scan rate (Figure 3.13b). An exponential dependence was observed (equation shown in the caption of Figure 3.13), suggesting that the uncompensated resistance plays a significant role in the peak to peak separation even at the lowest scan rate (for 10 mV/s, a 100 mV of iR drop was calculated). For this reason, the CVs were mathematically corrected for the uncompensated resistance and the results are shown for the highest scan rate used (500 mV/s) in Figure 3.14a and for the lowest (10 mV/s) in Figure 3.14b. The mathematical correction was performed using Equation (3.2)[45]:

$$E_{corrected} = E_{applied} - iR \qquad (3.2)$$

where i is the measured current in A and R is the resistance in Ω (the values of resistance for the solution under N_2 and CO_2 are shown in Table 3.8).

Table 3.8: resistance of the interface electrode solution for Bi cylinders in 0.1 M Na_2SO_4

gas	Resistance [Ω][a]
N_2	24.8
CO_2	20.8

[a] calculated at open circuit potential (OPC)

From the CVs, it is clear that the iR drop significantly influences the E_p values. As expected, the higher the scan rate, the higher the peak to peak separation[268]. At 10 mV/s, the magnitude of the peak to peak separation is lower than at 500 mV/s, before and after the iR drop correction, demonstrating that the iR drop influence is lower for low scan rate values. In addition, in the curve obtained at 500 mV/s after the mathematical correction (purple curve, Figure 3.13a), the reduction peak seems distorted and excessively toward more positive potentials. This could it be due to over-compensation in the CV. The same is not observed for the CV obtained at 10 mV/s, suggesting that the cause of the possible over-compensation is relevant only at high scan rates. The excessive shift of the reduction peak could be due to the high currents passed at the highest scan rate values that inflate the $E_{corrected}$ (see Equation 3.2). Considering that this effect is observed only for high scan rate values, it is possible that the E_{pc} and ΔE_p might not be representative of the real response of the electrodes for this scan rate, but that the correction is acceptable for values of scan rate lower than 300 mV/s.

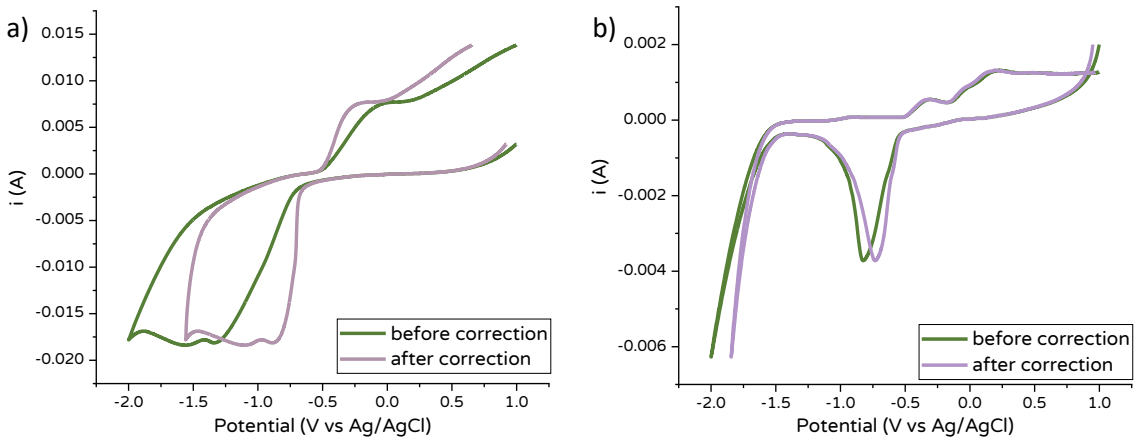

Figure 3.14: CVs for the reduction an oxidation of Bi in Na_2SO_4 0.1 M under N_2 atmosphere as recorded (green line) and after mathematical correction for iR drop acquired at a) 500 mV/s and b) 10 mV/s

ΔE_p was calculated for the CVs before and after mathematical correction at each scan rate (see Table 3.9). Before the correction, ΔE_p values varied from 490 mV to 1500 mV. After the mathematical correction, the ΔE_p values decreased significantly (from x1.3 to x2 times lower), but the peak to peak separation were still quite large (from 380 to 700 mV), suggesting slow kinetics for the oxidation-reduction of Bi. It is important to highlight that after the correction, the experimental error for some of the experiments is higher than the ΔE_p value (scan rate between

200 and 500 mV/s, for CO_2). For this reason, these values are not going to be considered in the later discussion as they would not give meaningful insight.

Table 3.9: ΔE_p for the oxidation and reduction of bismuth calculated at different scan rate values before and after mathematical correction of the CVs. The experiments were performed in 0.1 M Na_2SO_4 first under N_2 and then under CO_2

scan rate [mV/s]	ΔE_p before correction [V]		ΔE_p after correction [V]	
	N_2	CO_2	N_2	CO_2
10	0.49 ± 0.04	0.63 ± 0.02	0.38 ± 0.04	0.49 ± 0.05
25	0.60 ± 0.06	0.73 ± 0.02	0.42 ± 0.08	0.47 ± 0.07
50	0.74 ± 0.09	0.86 ± 0.03	0.5 ± 0.1	0.4 ± 0.1
75	0.8 ± 0.1	0.94 ± 0.04	0.5 ± 0.1	0.4 ± 0.1
100	0.9 ± 0.1	1.02 ± 0.05	0.6 ± 0.3	0.4 ± 0.2
150	1.0 ± 0.1	1.11 ± 0.05	0.7 ± 0.4	0.3 ± 0.2
200	1.1 ± 0.2	1.17 ± 0.05	0.5 ± 0.2	0.3 ± 0.3
300	1.4 ± 0.1	1.31 ± 0.06	0.6 ± 0.3	0.2 ± 0.3
400	1.5 ± 0.1	1.4 ± 0.1	0.6 ± 0.3	0.2 ± 0.3
500	1.5 ± 0.2	1.5 ± 0.1	0.7 ± 0.4	0.3 ± 0.4

Considering that the Bi electrodes investigated within this work were produced to investigate the CO_2 reduction process, the scan rate study was performed in CO_2-saturated solutions, in order to understand if and how the presence of CO_2 would influence the formation of Bi oxide and its reduction. The CVs, at different scan rates, are shown in Figure 3.15a. The variation of the iR drop as a function of the scan rate is shown in Figure 3.15c and the ΔE_p values are shown in Table 3.9. The CVs after and before mathematical corrections for the CVs performed at 500 mV/s and 10 mV/s are shown in Figure 3.15d and e, respectively.

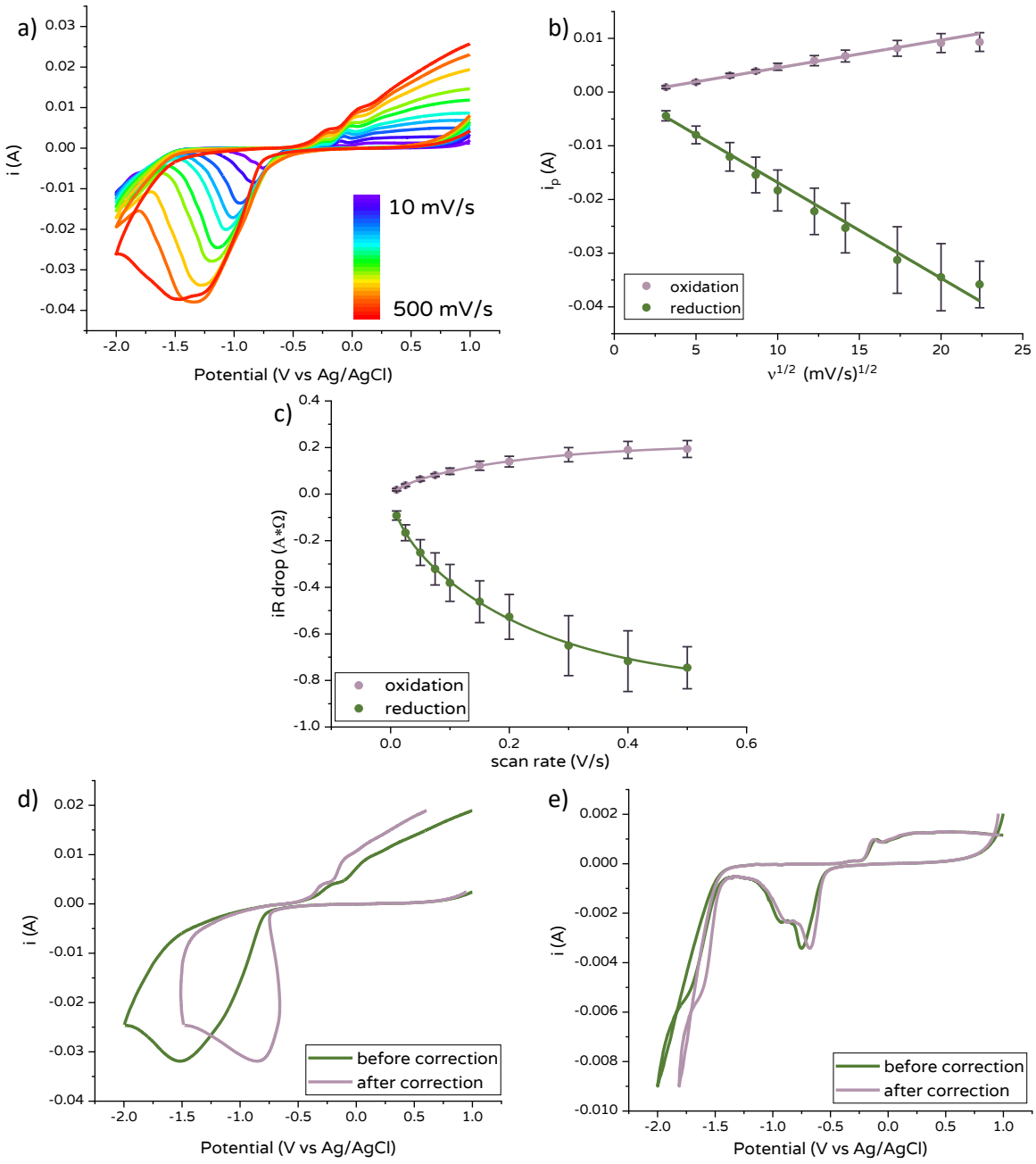

Figure 3.15: a) scan rate study for the formation and reduction of Bi oxide in Na_2SO_4 under CO_2; b) i_p for both cathodic and anodic processes vs square root of scan rate obtained from the scan rate study showed in a; c) iR drop vs scan rate for both reduction (green) and oxidation (purple) calculated at Ip. For fitting equation see Appendix; CVs for the reduction an oxidation of Bi in Na_2SO_4 0.1 M under CO_2 atmosphere as recorded (green line) and after mathematical correction for iR drop acquired at c) 500 mV/s and d) 10 mV/s

The shape of the CVs under CO_2 is similar but present some observably different features than under N_2. In the anodic region, two peaks at high scan rates are observed before the current plateau, while only one is observed at 10 mV/s (see Figure 3.15d and e). In addition, a small feature around -1.7 V was observed for scan rates lower than 150 mV/s. This can be linked with the adsorption and/or reduction of CO_2, considering its absence in the curves obtained in N_2-saturated solution. A similar feature has been observed before for Bi electrodes in the presence of CO_2 in several studies[103,241,269,270]. As discussed earlier, the presence of single or multiple peaks in the

anodic region of the CVs depends on the experimental conditions and surface of the electrode. Considering the fact that the presence of CO_2 decreased the pH by two units, it is possible that the discrepancy observed between the cyclic voltammogram shape under CO_2 and N_2 is due to the difference in the values of the pH. The presence of an additional peak may also be due to the formation of different species in CO_2-saturated solutions. It should be noted that it *has been* demonstrated that the formation of $(BiO)_2SO_4$ species can occur during the anodic scan in concentrated H_2SO_4 solutions[186]. However, in H_2SO_4 solutions, the presence of two well separated peaks in the reduction scan was observed, while here it was not. It is possible that at high sulphate concentrations and acidic pH values, the formation of $(BiO)_2SO_4$ is more favoured than in 0.1 M solutions of Na_2SO_4 or that, considering that at 10 mV/s a shoulder is observed in the reduction peak, the peak for the reduction of the $(BiO)_2SO_4$ species is not separated from the main reduction peak. Interestingly, at 10 mV/s, the anodic peak does not present the two peaks anymore (see Figure 3.15e), suggesting a possible change on the electrode surface during the cathodic sweep. The difference in the surface composition after the scan rate study was clear with visual observation of the electrode (see Figure 3.16). Additional experiments to investigate the composition of the electrodes (like XPS or XRD) would provide useful insight following the scan rate studies.

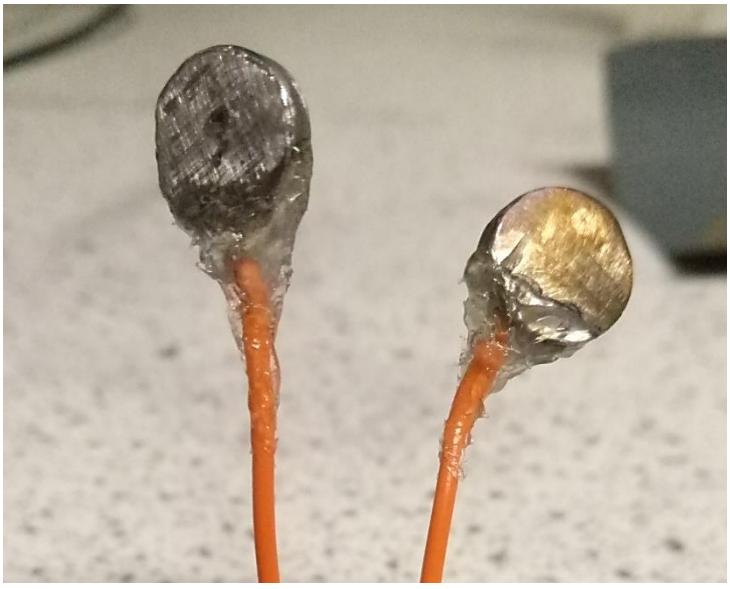

Figure 3.16: Bi cylinder electrodes before (left) and after (right) scan rate study experiments in N_2-satured Na_2SO_4 solution. The change in colour of the right electrode suggests a change in the composition of the surface after the experiments

CEf were calculated for the lowest and the highest scan rate values and the results are shown in Table 3.10. The CEf values are similar to the ones obtained in N_2-saturated solutions, however, slightly higher CEf were observed in CO_2-saturated solutions. The additional charge measured is likely linked to the reduction of CO_2, considering the fact that the increase is observed at both scan rates.

Table 3.10: current efficiencies, cathodic and anodic charges calculated integrating the area under the cathodic and anodic peaks for CVs performed with Bi cylinder electrodes at 10 and 500 mV/s. Electrolyte: CO_2-saturated Na_2SO_4

Scan rate [mV/s]	Q_A [mC]	Q_C [mC]	CEf
10	81.0	118.2	1.5
500	33.4	36.0	1.1

The peak to peak separations in CO_2-saturated solutions before the iR drop correction (see Table 3.9) were around 1.2x times higher than for N_2-saturated solutions at lower scan rates (10, 25 and 50 mV/s), while they became comparable at higher scan rates. On the other hand, after iR drop correction, ΔE_p was higher in CO_2-saturated solutions for the lowest scan rates, while when the scan rate was increased, comparable values were obtained. However, the experimental error for the corrected CVs at high scan rates is quite large, as such they are not considered in this discussion and only the values at low scan rates are considered. The higher ΔE_p values might suggest that the presence of CO_2 influences the oxidation and reduction reaction, which may be due to its adsorption on the metallic Bi and the Bi oxide surface[271].

As the catalytic experiments would be performed in a second electrolyte ($KHCO_3$), the scan rate studies were also performed in this electrolyte.

3.3.4.2 $KHCO_3$

The same set of results presented for the experiments performed in Na_2SO_4 (Figure 3.15) were obtained in $KHCO_3$. For a detailed discussion see the Appendix. In general, a linear response for the graph of the i_p versus the square root of the scan rate was observed under N_2, suggesting that the mechanism for the formation of Bi oxide and its reduction was not influenced by the electrolytes used. In contrast, in CO_2-saturated solutions, only the cathodic branch presented a linear response on the entire range of scan rate values and a linear trend for the anodic branch was observed for scan rate values between 10 and 150 mV/s. As by plotting the i_p versus the scan rate a non-linear trend was observed, a change in the mechanism of the oxidation of Bi is unlikely. After the scan rate study modification on the colour of the surface was observed as observed in Na_2SO_4 solutions. As for the other systems investigated here (see scheme in Figure 3.11), the peak to peak separation increases when the scan rate increases (see Figure A.3.2c and d and Table A.3 in the Appendix). The ΔE_p for the measurements performed in CO_2-saturated solutions were ≈1.3x times higher than in N_2-saturated solutions before mathematical correction for the iR drop and between 1.3 and 2x times higher after mathematical correction. A similar change in ΔE_p values was observed in Na_2SO_4, confirming that the presence of CO_2 influences the reduction and oxidation of the electrode surface. Interestingly, for the ΔE_p obtained in different electrolytes, higher values were observed for the experiments performed in CO_2-saturated $KHCO_3$ solutions before and after mathematical

correction than in CO_2-saturated Na_2SO_4 solutions. Specifically, before the mathematical correction the ΔE_p in $KHCO_3$ was between 1.2x and 1.4x times higher, while after mathematical correction, it was from 1.2x to 1.75x higher in $KHCO_3$ than in Na_2SO_4. A schematic qualitative description of the difference in ΔE_p values for N_2- and CO_2-saturated solutions of Na_2SO_4 and $KHCO_3$ before and after iR drop correction is shown in Table 3.11. The higher ΔE_p values in CO_2-saturated $KHCO_3$ solutions suggests that the kinetics for the reduction and oxidation of Bi is slower in $KHCO_3$ than in Na_2SO_4. It is reasonable to suggest that the process slowing the oxidation/reduction reaction is the adsorption of CO_2 (see discussion in Section 3.3.4.1 for the experiments performed in Na_2SO_4), as the concentration of CO_2 in $KHCO_3$ should be higher than in Na_2SO_4, because the presence of HCO_3^- ions shifts the equilibrium of dissolution of CO_2 in water toward the left (see Reaction r3.1)[272].

$$CO_2 + H_2O \rightleftharpoons H_2CO_3 \rightleftharpoons H^+ + HCO_3^- \rightleftharpoons H^+ + CO_3^{2-} \quad \text{(r3.1)}$$

Table 3.11: Variation of the ΔE_p for the reduction and oxidation of Bi in the different systems investigated in this work: in N_2- and CO_2-saturated 0.1 M $KHCO_3$ and Na_2SO_4 solutions

	ΔE_p in different solutions: $KHCO_3$ vs Na_2SO_4			
gas	**N_2**		**CO_2**	
Mathematical correction	**before**	**after**	**before**	**after**
Difference of ΔE_p in the two different solutions	Comparable in the experimental error range at any scan rate	Comparable in the error range at any scan rate (high scan rates not considered because of the high experimental errors obtained in Na_2SO_4)	Higher in $KHCO_3$ at any scan rate	Higher in $KHCO_3$ at low scan rates (high scan rates are not considered because of the high experimental errors obtained in Na_2SO_4)

3.3.5 Heterogeneous electron transfer rate constant

To gain insight into the kinetics of the oxidation and reduction processes, the heterogeneous electron transfer rate constants (k^0) were calculated for the four different systems. In general, depending on the experimental conditions, several methods can be used. For processes that involve species diffusing in solution, methods like the one proposed by Nicholson (for reversible systems)[273] or Kochi (for irreversible systems)[274] can be used[275]. On the other hand, if diffusionless electrochemical processes are dominant, the Laviron method can be used[249]. All these methods use the peak to peak separation as the main experimental parameter for the calculation of k^0, allowing the calculation of the electron transfer rate constant by simply performing scan rate studies. Based

on the linear response obtained plotting i_p versus $v^{1/2}$, a method for diffusion-control process should be used for the calculation of k^0 for the systems under investigation here. However, in this case, the diffusing species are not in solution, but inside the electrode itself (solid state diffusion). In particular, the Bi^{3+} ions and the electrons are the diffusing species for the oxidation and the reduction, respectively[177]. For using Nicholson or Kochi methods the species needs to be diffusing in the diffusion layer, while for Bi electrodes the diffusion occurs into the electrode. For this reason, even if the species cannot be considered properly adsorbed on the surface, the apparent heterogeneous electron transfer rate constant was calculated using the Laviron method. Considering the fact that the processes are under diffusion control, it is important to highlight that the results might not give an exact evaluation of the rate constant. In addition, poor linearity of the graphs obtained using this method are expected. The Laviron method was applied for all four systems mentioned above: in Na_2SO_4 and $KHCO_3$ solutions, first, under N_2 and then under CO_2. For details on the Laviron method see Chapter 2, Materials and Methods, Section 2.5.3.

The Laviron method was then used to for the calculation of k^0_c and k^0_a in Na_2SO_4 and $KHCO_3$ solutions. The plots of the E_p versus the log(v) for N_2- and CO_2-saturated solutions are shown and discussed in detail in the Appendix, (see Figure A1.a,b and Figure A.2a, b), while the α and k^0 values are gathered in Table A.1 and TableA.2. Briefly, in both Na_2SO_4 and $KHCO_3$, the values of k^0 for the reduction are comparable under N_2 and CO_2, suggesting that the presence or absence of CO_2 did not influence the rate of reaction, in contrast with the conclusions based on the ΔE_p values. On the other hand, the k^0 values are smaller in CO_2-saturated $KHCO_3$ than in CO_2-saturated Na_2SO_4 solutions (from 1.2x to 3x times lower), suggesting slower kinetics in $KHCO_3$ than in Na_2SO_4 in the presence of CO_2, in accordance with the ΔE_p values (see Table 3.11). In addition, it is important to highlight that the plots of the E_p versus the log(v) for N_2- and CO_2-saturated solutions did not. These discrepancies are probably due to the incapacity of the Laviron method to efficiently describe the processes during the formation of Bi oxide and its reduction (solid state diffusion).

3.4 Conclusions

In conclusion, Bi disk electrodes were prepared and characterised with a combination of physical and electrochemical techniques. The surface of the electrodes was treated via mechanical polishing and a decrease of the roughness was observed during the polishing procedure via visual inspection of the surface and SEM images. This was further confirmed via the calculation of the ECSA performed using the oxygen adsorption method. It is important to highlight that care needs to be taken when this method is used in order to avoid under- and, especially, overestimation of the

ECSA. For this reason, the experimental conditions needs to be carefully chosen and the intrinsic issues to the technique need to be taken into account. The measurements of the capacitance allowed to set a standard capacitance that can be then used for the calculation of the capacitance of microstructured Bi electrodes (see secondary objectives of objective 1.a, Section 1.7). Scan rate studies in aqueous solutions enable the study of the formation of the Bi oxide and its reduction. Slow kinetic for the processes was suggested based on the values of the peak to peak separation in both inert atmosphere (N_2) and in CO_2-saturated solutions. This was confirmed when the heterogeneous electron transfer rate constants (k^0) were calculated using the Laviron method and the k^0 for the reduction was significantly smaller than for the oxidation, suggesting that the reduction of the Bi oxide might require long time to be complete. In the context of the CO_2RR, this can be problematic as the reduction of the Bi oxide layer on the surface of the electrode occurs a negative potentials and part of the energy designated for the reduction of CO_2 can be used for the reduction of the oxide. However, Laviron method did not satisfactorily describe the two processes and the employment of a more suitable technique is needed.

Chapter 4 : Bi modified electrodes formation

4.1 Introduction

In the previous chapters, it was highlighted how the geometrical area is not reflective of the real area of the electrode and how this can lead to inaccurate conclusions. The importance of the microscopic features on the surface of the electrode for catalytic applications is well known. Therefore, it would be beneficial to introduce artificial microstructures that would have the role of increasing the area-to-volume ratio. With that in mind the production of electrodes containing structures that can increase the real area of the electrode was pursued. It is important to highlight that the magnitude of the surface area is not the only parameter influencing catalysis. The characteristics of these structures can play an essential role in the activity of a catalyst[276]. Herein the effects that different characteristics of micro-structured electrodes can have on catalytic reactions using CO_2 reduction as an example will be evaluated. The electrochemical reduction of CO_2 has been investigated using different modified Bi electrodes[101,168,277]. Recently, there has been an increased focus on improving the catalytic activity[215,278,279] and understanding the CO_2 reduction mechanism[102,280,281]. The systems investigated include: electrodeposited Bi crystallites[102,141,154,282]; drop-cast pastes containing Bi micro or nanoparticles (NPs)[278,283,284]; and Bi single atoms[105,285]. Several factors impact the catalytic activity of the system, from the composition of the solution (electrolyte, concentration of CO_2)[286–288] to the mode of transport of reagents and products between the electrode surface and the bulk of the solution[289–292] as mass transport can influence the kinetics of the overall reaction[293] and, sometimes, its selectivity due to the influence of the mass transport to reaction pathways[294]. In Figure 4.1, some of the most important challenges during the electrocatalytic reduction of CO_2 on Bi modified electrodes are highlighted: the binding of CO_2 on the surface of the metal (green section), which is related to the quantity and the composition of Bi on the substrate; the desorption of the reduced products (red section); the selectivity of the catalyst toward CO_2 reduction reaction (CO_2RR) and not toward hydrogen evolution reaction -HER- (blue section). Finally, the stability of the catalyst plays a central role (yellow section). In the experimental work presented in this chapter, these four problems were considered, and particular attention was paid to increasing the number of sites per geometric square centimetre of the electrode for the binding of CO_2 (see section in green).

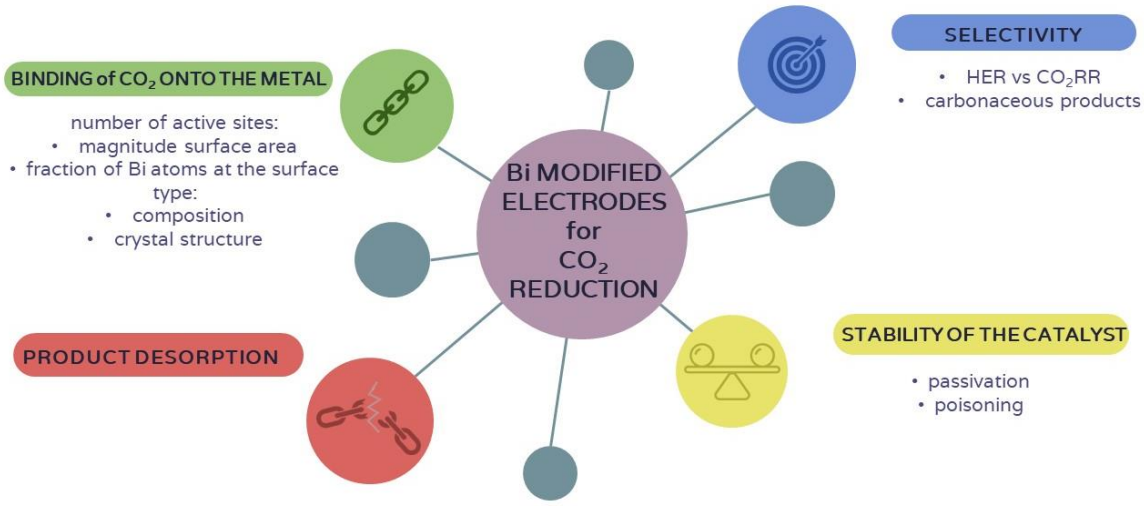

Figure 4.1: Key factors that influence the catalytic activity of the CO_2 reduction reaction. The factors highlighted here are specifically related with the catalyst (Bi modified electrode) while the ones related with other parts of the system (like electrolyte composition and mass transport) are not listed

Specifically, in the first part of the chapter, the production and characterisation of a novel Bi modified electrode for CO_2 reduction in aqueous solution is described. Several approaches were used to try and improve the catalytic performances of the electrode by increasing the fraction of the bismuth atoms on the surface and the surface area of the electrode. This was done by performing several electrodepositions modifying several deposition parameters. The parameters changed are schematised in Figure 4.2. While the discussion above focuses on CO_2 reduction, the principles highlighted are applicable to catalytic reactions in general.

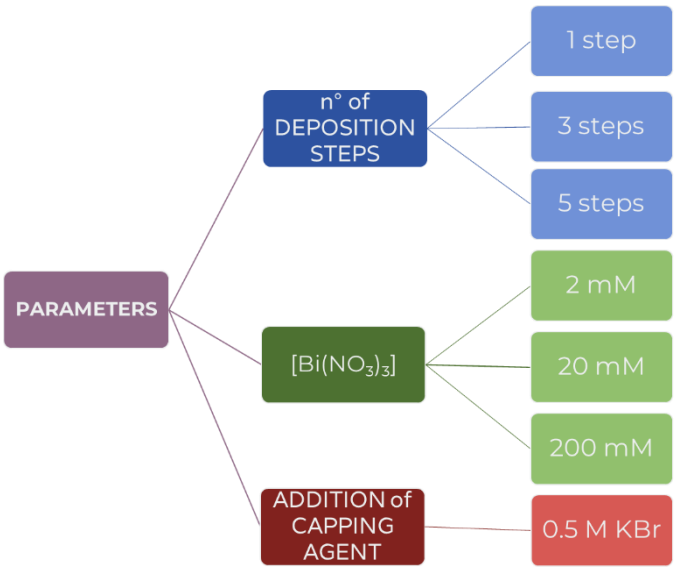

Figure 4.2: Parameters changed to obtain different Bi modified electrodes in order to modify the number and the type of active sites of the deposit

4.2 Electrodeposition of Bi films on GC electrodes

The deposition of bismuth was performed on a glassy carbon electrode (GCE) in a deposition bath containing $Bi(NO_3)_35H_2O$. As $Bi(NO_3)_3$ forms a white insoluble precipitate ($BiONO_3$) when added into water[295,296], the bismuth salt was always dissolved in acidic media. Prior to deposition, CV measurements were performed in nitric acid to ensure the absence of competitive reactions in the range used for the deposition (Figure 4.3). Specifically, the CVs were carried out at different scan rates. When the scan rate was varied, no peaks were present in the potential range in which the Bi peaks were expected ($E_{pc} \cong$ -0.15V and $E_{pa} \cong$ 0.20 V vs Ag/AgCl)[102,115,119,132]. The increase in current observed around -0.35 V was reported previously and it was attributed to H_2 evolution[297]. For this reason, the potential window used for the cyclic voltammetry measurement at GCE was between -0.3 V and 0.3 V.

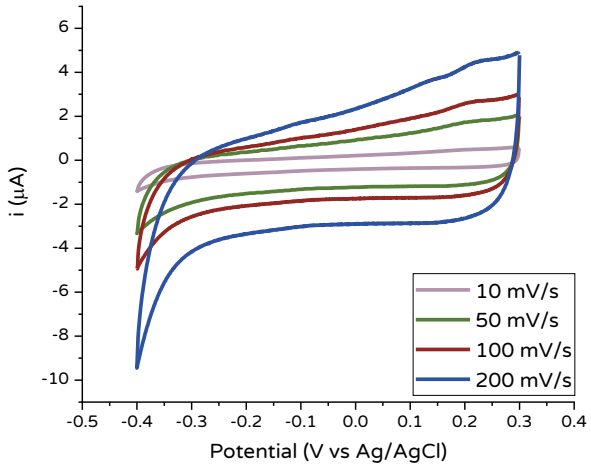

Figure 4.3: Scan rate study performed in 1 M HNO_3 at GC electrode. The scan rate values were chosen between 10 and 200 mV/s

The electrodeposition of bismuth on a glassy carbon was performed in a bath containing 1 M HNO_3 and 20 mM of $Bi(NO_3)_3$. Each time Bi was deposited on a GCE, three main steps were performed. First, cyclic voltammetry was run to obtain the value of the cathodic peak potential, E_{pc} (Figure 4.4a). The cyclic voltammogram was first acquired in the potential range used for the bare GCE in HNO_3 and then the negative vertex was extended to -0.5 V to obtain a complete cathodic peak. A broad peak for the reduction of Bi^{3+} to Bi^0 is observed around -0.1 V vs Ag/AgCl (Figure 4.4a), while the intense peak around 0.1 V is attributed to the stripping of the metallic Bi [115,166]. Between the cathodic and anodic waves, two crossovers were observed. The difference in potential between the two crossover corresponds to the overpotentials needed for the nucleation of the Bi particles on foreign substrates[115,134,298]. In this case the overpotential was equal to 47 ± 0.9 mV. This value is quite similar to the one found in the literature[115].

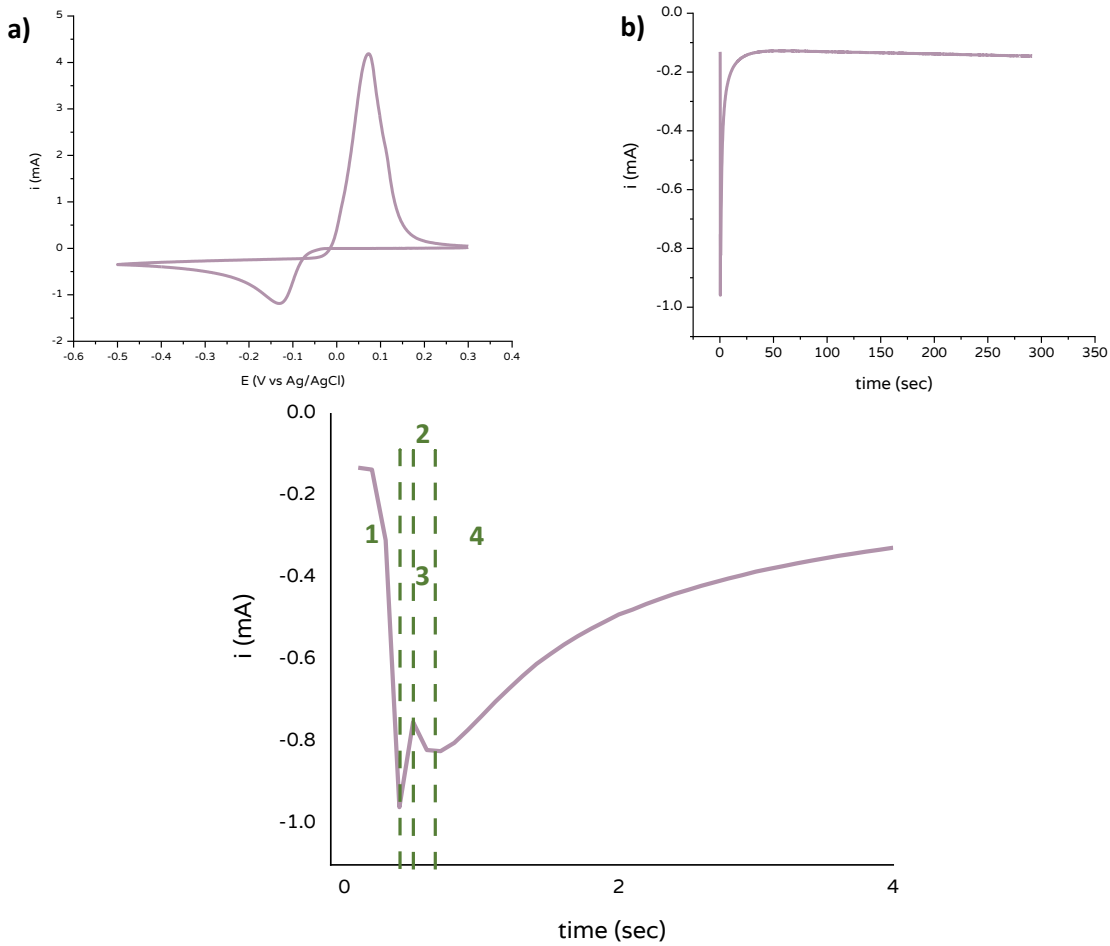

Figure 4.4: a) cyclic voltammogram obtained with a GC electrode in a deposition bath containing 20 mM $Bi(NO_3)_3$ in 1 M HNO_3; b) typical bulk electrolysis measurement for the deposition of bismuth at -0.132 V vs Ag/AgCl (last step of the electrodeposition); and c) first 15 seconds of the current transient for the bulk electrolysis measurement (sampling frequency: 0.1 s). The numbers represent the different phases of the deposition

Second, a potential equal to 0.5 V vs Ag/AgCl was applied for 2 minutes and the electrode vigorously agitated in the solution bath to remove possible residues of deposited bismuth present on the surface of the electrode after the CV. Third, a potential of -0.132 V vs Ag/AgCl was applied in one step until a certain amount of charge was passed (Figure 4.4b). Several experiments were performed passing different amounts of charge to ensure a macroscopically uniform film without loss of crystallites in solution after removing the electrode from the cell. The final amount of charge passed was equal to 4.2 $x10^{-2}$ C. The thickness of the deposited film was calculated considering the final deposit as a cylinder, with the height being the thickness of the film (see Equations (4.1a) and (4.1b(4.1b)):

$$thickness = \frac{Volume}{Area} \qquad (4.1a) \qquad\qquad Volume = \frac{\frac{QM}{nF}}{\rho} \qquad (4.1b)$$

where Q is the charge passed during the deposition in C; M is the molar mass of the metal deposited (208.98 g/mol); n is the number of electrons transferred during the process (in this case 3); F is Faraday's constant (96,485.34 C/mol) and ρ is the density of the metal (9.78 g/cm^3). The numerator

of Equation (4.1b) correspond to the mass of the Bi deposited. For the calculation of the thickness, the geometrical area was used, that is equal to 0.071 cm^2. If one assumes a 100% faraday efficiency and that a uniform layer is formed, 3.03 $x10^{-5}$ g of Bi was deposited and a thickness of 0.4 μm should be obtained. The thickness of the film was not confirmed via SEM analysis because of the impossibility of tilting the bulky GC electrode inside the SEM chamber.In Figure 4.4b, a negative current is observed when the electrodeposition potential ($E_{electrodepositon}$= -0.132 V vs Ag/AgCl) was applied, indicating a reduction process occurring at the electrode surface. A sharp increase of current is observed at short times and followed by a decay of the current. A constant current is observed after 45 seconds, with a value around -0.13 ± 0.01 mA. At short times (Figure 4.4c), it is possible to observe four main features in the current transient: first, a sudden and sharp increase of the current immediately after the potential pulse (see region 1 in the transient); second, a fast decay of the current (region 2); third, a second increase of the current (region 3); and fourth, when a maximum is reached, a long decay (region 4). The first increase of current is due to the charging of the double layer as a consequence of the application of the chosen potential. After that, the nucleation and growth of the metal started, and a decrease of current was observed. As a consequence of the formation of new species on the substrate (Bi nuclei), an increase of electroactive area occurred, leading to an increase of the current. At this point, the substrate is covered by the metal particles in such a way that the growth (and the possible formation of new nuclei, depending on the mechanism) of the particles switch from a hemispherical to a linear diffusion control on the entire area of the electrode (slow decay of the current)[145,263] (see Section 4.3 for detailed discussion of the current transient). The potential was applied until the chosen experimental charge was passed (4.2$x10^{-2}$ C), leading to the formation of a grey film on the surface of the electrode. After rinsing the electrode with Milli Q water and acetone, the electrode was dried by leaving it uncovered for several minutes to air dry. A typical bismuth on glassy carbon electrode (Bi-GC) is shown in Figure 4.5a: it exhibited a rough surface and metallic grey colour. A first investigation of the surface of the electrode was performed using an optical microscope. The edge of the Bi-GC disk is shown in Figure 4.5b. The deposited material (part 1) appears crystalline, and the surface is macroscopically uniform. The grey area (part 2) is the Teflon from the body of the GC electrode.

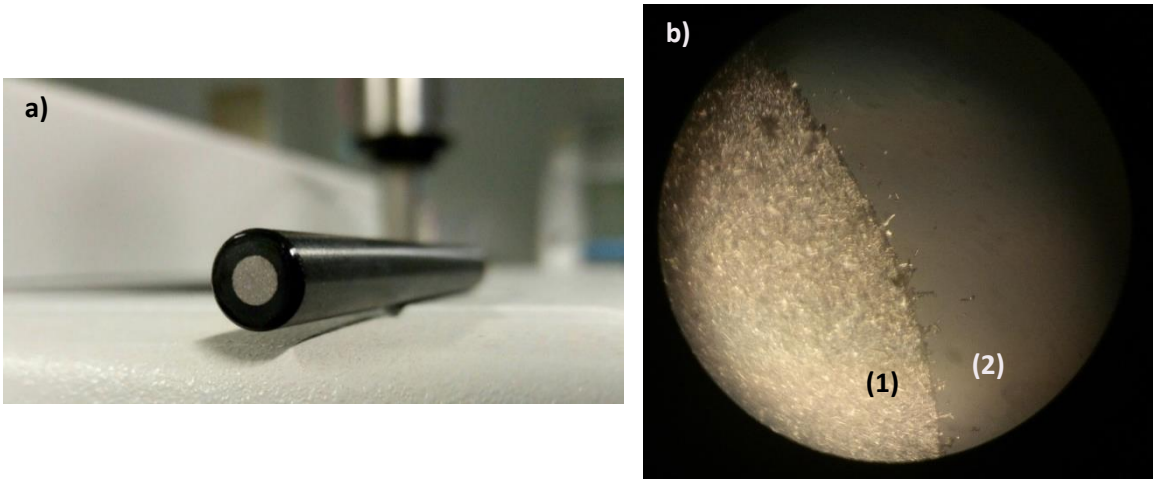

Figure 4.5: a) photo of a Bi-GC electrode (d = 3 mm) obtained in a 20 mM $Bi(NO_3)_3$ bath applying a potential of -0.132 V vs Ag/AgCl until a charge equal to 42 mC was passed; and b) image of a section of the Bi- GC electrode at Magn.= 20x. The photo shows the Bi film (1) and the Teflon from the body of a freshly prepared GC electrode (2). The image was acquired with an optical microscope

4.2.1 Characterisation of the modified Bi electrodes

The characteristics of an electrocatalyst can strongly influence their general performances[299]. In particular, several studies demonstrated that morphology and composition of metal electrocatalysts for CO_2 reduction affect the amount of products produced[281,300], the selectivity[301,302] and the total reaction rates[303]. For this reason, the morphology and then the surface composition of the Bi-GC electrode were examined. To investigate the morphology of the electrode at microscale, SEM was performed. In Figure 4.6a and b, crystallites with different dimensions and several larger agglomerates on the surface of the glassy carbon are observed. At higher magnification (Figure 4.6c and d), it is possible to see that the roughness of the surface is due to particles of different sizes with a dendritic structure, exhibiting a bipyramidal form at magnification of 2.0, 5.0 and 10.0k (Figure 4.6e, f, and g). Several incisions and sharp-cornered protuberances (sawtooth shaped) are present on the entire surface of the dendrites (Figure 4.6g). The sawtooth shaped areas are probably due to corners of thin sheets packed to develop the pyramidal form. Some of these sheets are visible in Figure 4.6e, f (highlighted with red circles). Similar morphologies were observed in a work of Kim et al.[102] in which a bismuth film was electrodeposited on a GC electrode using $Bi(NO_3)_3$ and HCl: different electrodes were produced by applying a potential of -0.1 V continuously for different periods of time or by applying the potential in pulses (potential is applied for a fixed time followed by an "off-time" before the following application). Pulse electrodeposition has been performed as it leads to structures with sharp corners and edges, functionalities that increase the catalytic activity of the system toward CO_2 reduction. When the potential was applied for 60 s, nanodots were formed, while by increasing the deposition time to 120 s, dendritic structures were observed. For a deposition longer than 150 seconds, particles very similar to the bipyramidal structures with size larger than 2 µm were

observed. Considering that the average length of the deposition performed in this work was 300 seconds, twice as long as in the above-mentioned study, very similar results were obtained.

From the images at high magnification, incomplete coverage of the substrate was observed, with the underlying glassy carbon surface (appearing as black regions in the image) being visible. It is probable that this is related with low number of nucleation sites formed during the electrodeposition. It has been observed before for Sn[130], and Bi[119] that high absorption of hydrogen on the substrate would lead to low coverage of the substrate because of a decrease in the rate of nucleation. Large dendrites are not present across the entire surface of the electrode and the electrode is mostly covered by small crystallites. These small crystallites are probably particles that did not complete the growth after the nucleation because of the presence of hydrogen bubbles. Generally, at high current densities smaller grains are obtained as more energy is provided and nucleation is promoted rather than growth[304]. Considering the presence of both small and large crystallites, it is possible that the magnitude of the current density at the surface of the electrode might not be favouring one process over the other. The length of the bipyramids varied between 10 and 30 µm (see Figure 4.6c). A similar morphology has been obtained before with a similar deposition bath (1M HNO_3 and 50 mM Bi^{3+})[132], and overpotentials (-0.15 V vs Ag/AgCl), suggesting that the concentration of the precursor salt (and the acid) has a significant influence in the rates of formation and growth of the Bi crystallites.

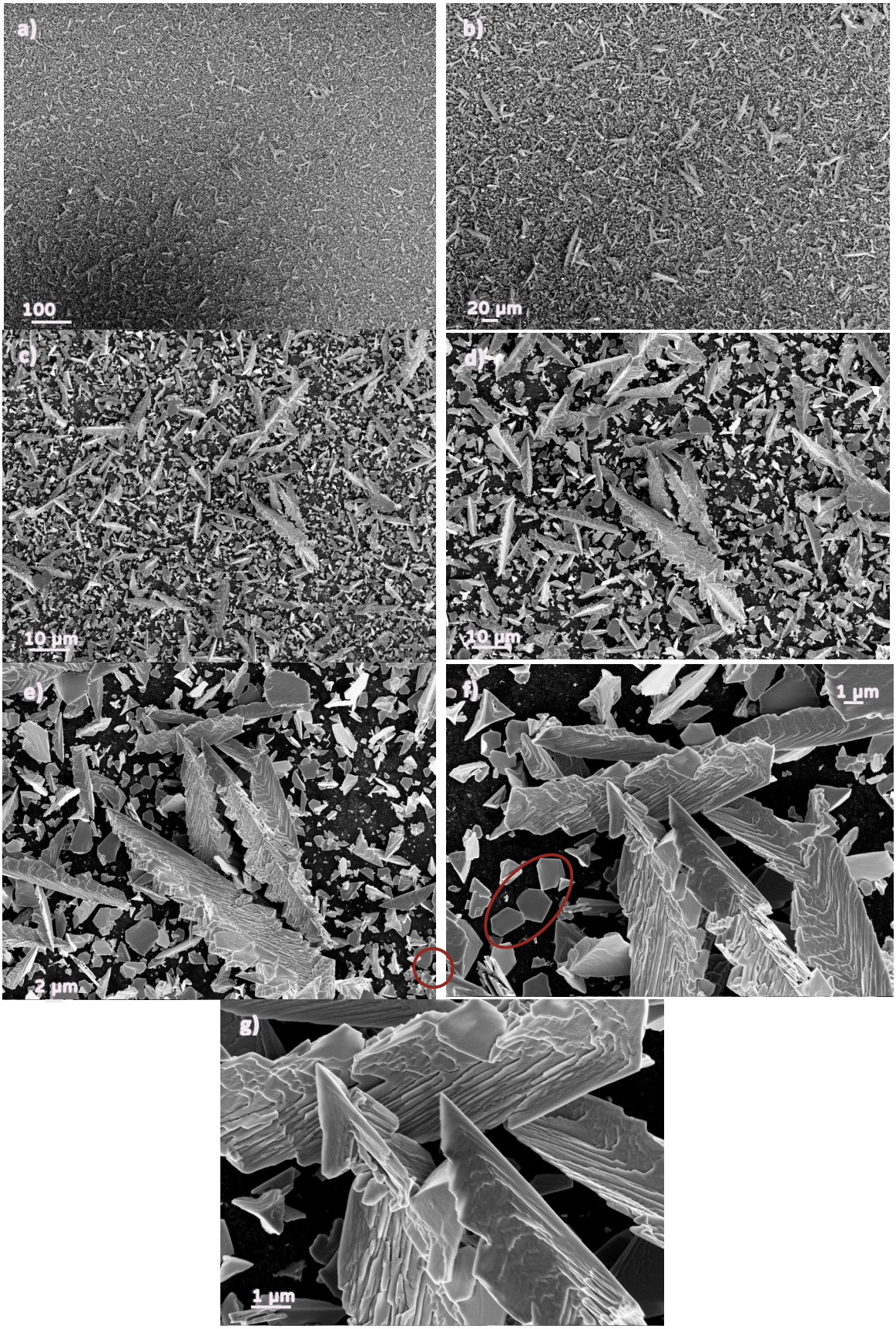

Figure 4.6: SEM images of Bi-GC electrode obtained by applying -0.132 V vs Ag/AgCl until a charge equal to 42 mC was passed a bath containing 20 mM $Bi(NO_3)_3$ in 1 M HNO_3. The geometrical area was equal to 0.07 cm^2. Magnifications equal to a) 0.1k; b) 0.2k; c) 0.5k; d) 1.0k; e) 2.0k f) 5.0k and g) 10.0k. SEM images were acquired with an acceleration voltage of 20 kV

To study the composition of the electrode both EDX and XPS analyses were performed. Because it was not possible to insert a bulky glassy carbon electrode in the SEM chamber, the electrodeposition was performed on another carbon-based electrode. To verify that a different substrate would not influence the deposition and consequently the morphology of the particles, after the deposition, SEM images were acquired for the Bi carbon felt (Bi-CF) electrode. As shown in Figure 4.7a, the particles on the CF substrate exhibited the similar morphology observed for on GC. On CF, the bipyramids grew forming more complex and larger dendritic structures. Probably, the presence of the Bi dendritic complex structures resulted from the presence of the carbon fibres, which act as a more efficient nucleation sites in comparison with the GC surface. The bipyramidal structures deposited on the CF exhibited the same size of the one on the GC (10 to 30 µm), while the dendritic structures can have a dimension that ranges from 40 to 60 µm (Figure 4.7b). An additional confirmation of the presence of thin layers forming the trigonal bipyramidal structures is shown in Figure 4.7e, in which the incisions in a fragment of a dendritic structure is present.

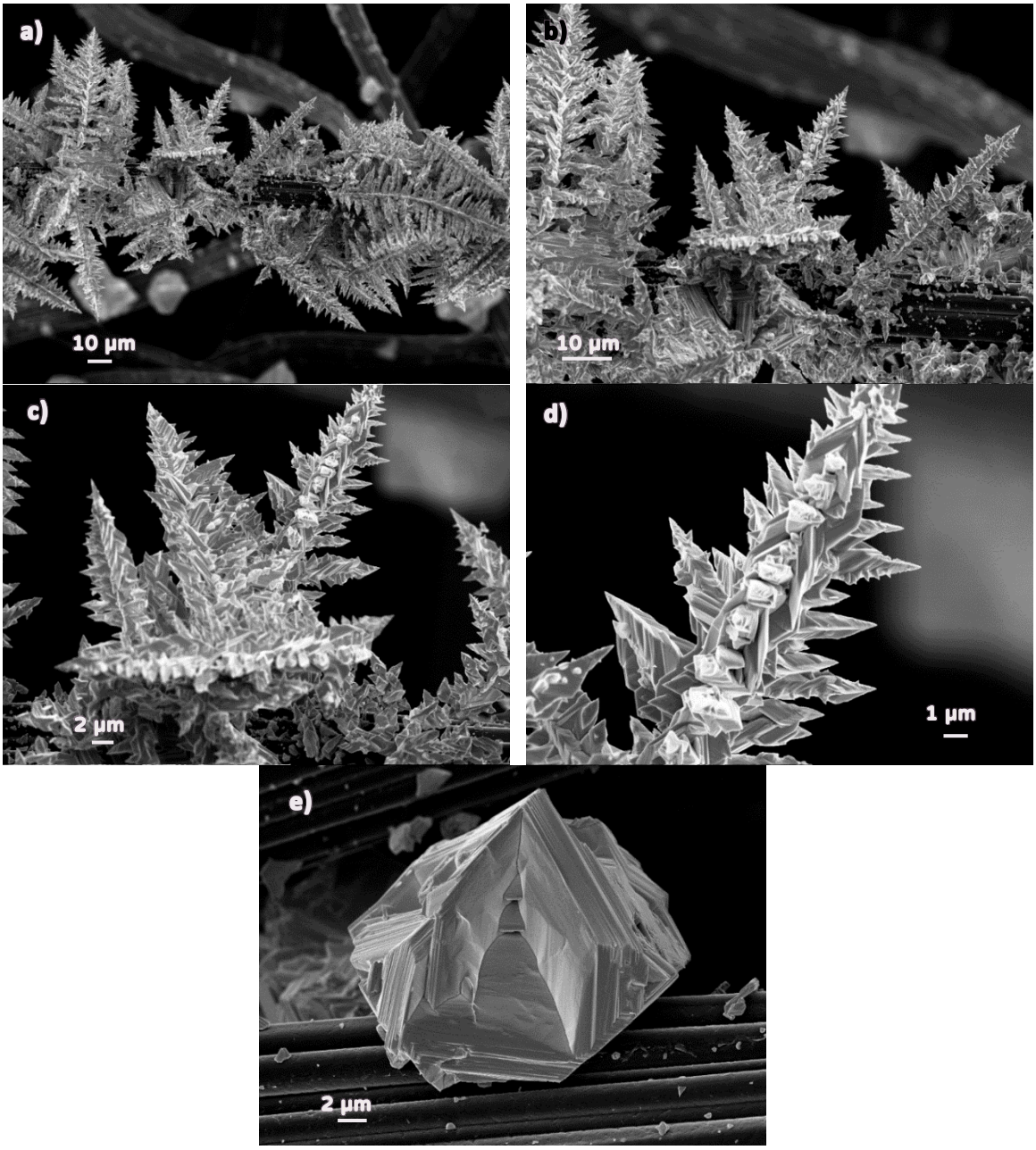

Figure 4.7: SEM images of Bi particles on a carbon felt (CF) electrode after deposition in a 20 mM $Bi(NO_3)_3$ solution after application of a potential equal to -0.132 V until a charge equal to 42 mC was passed. The geometrical area was equal to 0.07 cm^2. Magnification a) 0.5k, b) 1.0k, c) 2.0k, d) 5.0k and e) 3.0k. SEM images were acquired with an acceleration voltage of 20 kV

In Figure 4.8, the EDX maps of a fragment of a dendrite structure are shown. The element with the highest percentage in weight was carbon (77.6%), followed by bismuth and oxygen (14.4 and 6.3% respectively). The carbon signal was considerably higher than the bismuth, likely due to the lack of complete coverage of Bi crystals (as can be seen in SEM images) and the minor thickness of the bismuth film in comparison with the penetration depth of the X-rays (using the Casting's formula[305], it was estimated to be approximately 2.5 µm). Small quantities of nitrogen were detected, but very close the limit of the detection of the instrument. For this reason, it is not possible to confirm the

presence of nitrogen and, consequently, of nitrogen-based species in the structures, due to residue unrinsed electrolyte.

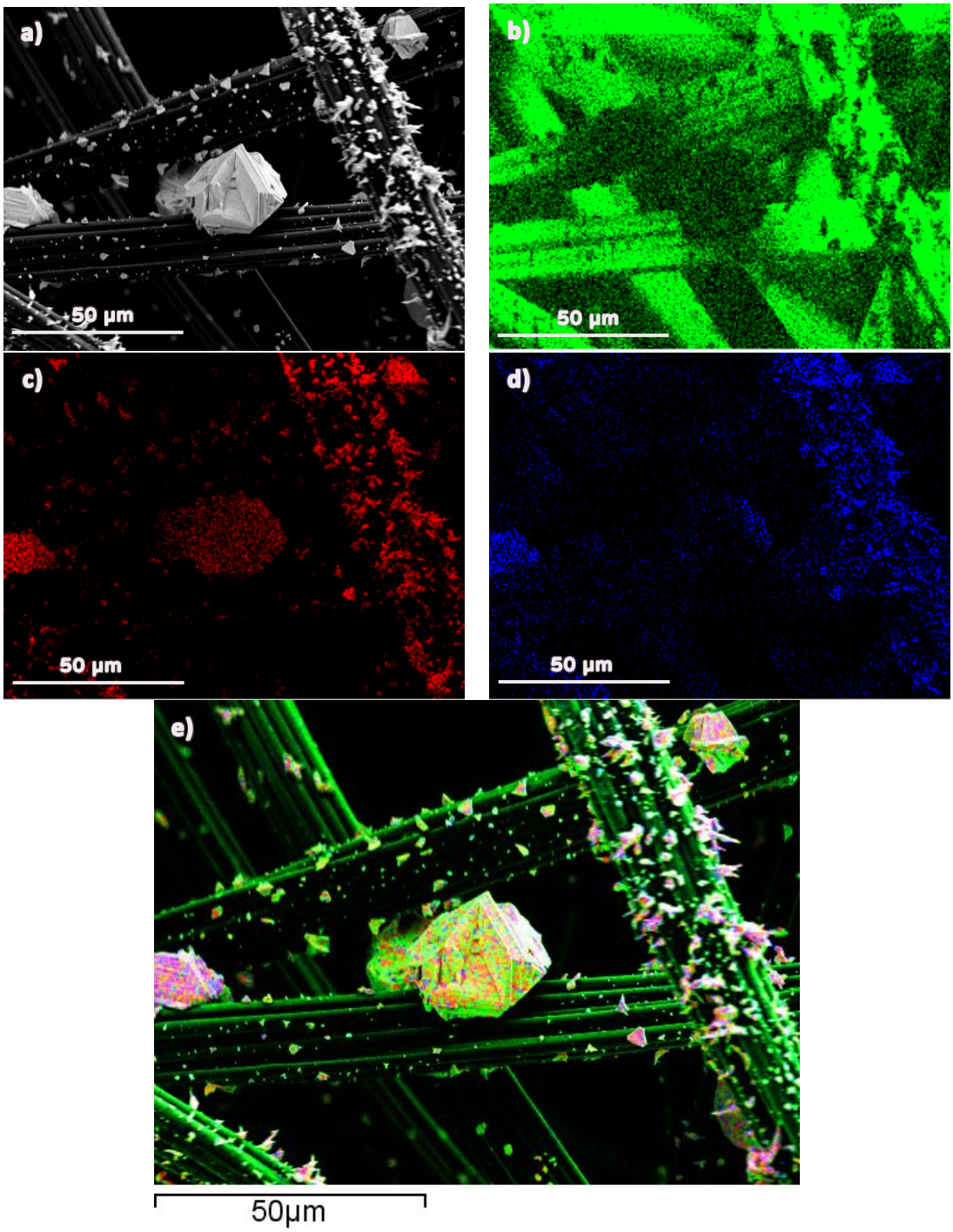

Figure 4.8: a) SEM image of a fragment of a dendrite structure from deposition on carbon felt electrode used for EDX mapping; EDX mapping for b) carbon; c) bismuth; d) oxygen and e) overlapping of the maps of the three elements. The electrode was obtained by applying a potential equal to -0.132 V vs Ag/AgCl until a charge equal to 42 mC was passed. The geometrical area of the electrode was 0.07 cm²

As it can be seen in Figure 4.8c and d, the highest intensities are detected for bismuth and oxygen. This suggests that the microdendrites contain both Bi and oxygen, rather more than solely bismuth, suggesting the presence of Bi_2O_3 particles. The EDX map also revealed that both Bi and O are co-

located, further suggesting Bi_2O_3. A certain degree of Bi oxide was expected as samples were not analysed immediately following production, but rather stored prior to analysis, allowing for the oxidation of particles on the surface of the film. The EDX results were confirmed by XPS analysis in which four peaks between 155 and 168 eV were detected (Figure 4.9a), with values very similar to the binding energy of Bi^{3+} ($4f_{7/2}$=159.0 eV and $4f_{5/2}$=164.3 eV; peaks separation is equal to 5.3 eV)[306] and Bi^0 (binding energy equal to 157.0 and 162.3 eV)[307]. The first and the third peak are more intense than the other two, suggesting that more Bi^{3+} than Bi^0 is present in the sample. Specifically, the ratio Bi^{3+} to Bi^0 is equal to 2:1, meaning that, on the surface, the quantity of Bi^{3+} species is ca. 2x higher than Bi^0. However, it is important to highlight that the sampling depth of the X-rays in XPS experiments is between 1 to 10 nm[308], a length that cannot be representative of the entire thickness of the Bi deposit but only of the surface of the electrode that readily undergoes oxidation in air[65]. The presence of a metal oxide is confirmed also by the O 1s peak (Figure 4.9b) that exhibited binding energies below 530 eV, typical values for metal-oxygen bonds[309]. As it can be seen from the survey spectrum (Figure 4.9c), no nitrogen peak was detected (peaks for nitrogen are located around 400 eV) confirming that no significant residual nitrate ions from the deposition bath were present on the surface of the electrode. Therefore, it is reasonable to conclude that in the surface of the bismuth film, the Bi^{3+} species are balanced only by O^{2-} species and, given the non-stoichiometric Bi:O ratio, the surface consists of both Bi^0 and Bi_2O_3. This is commonly observed for XPS of electrodeposited Bi films[103,153,154,168,169,240,245,310].

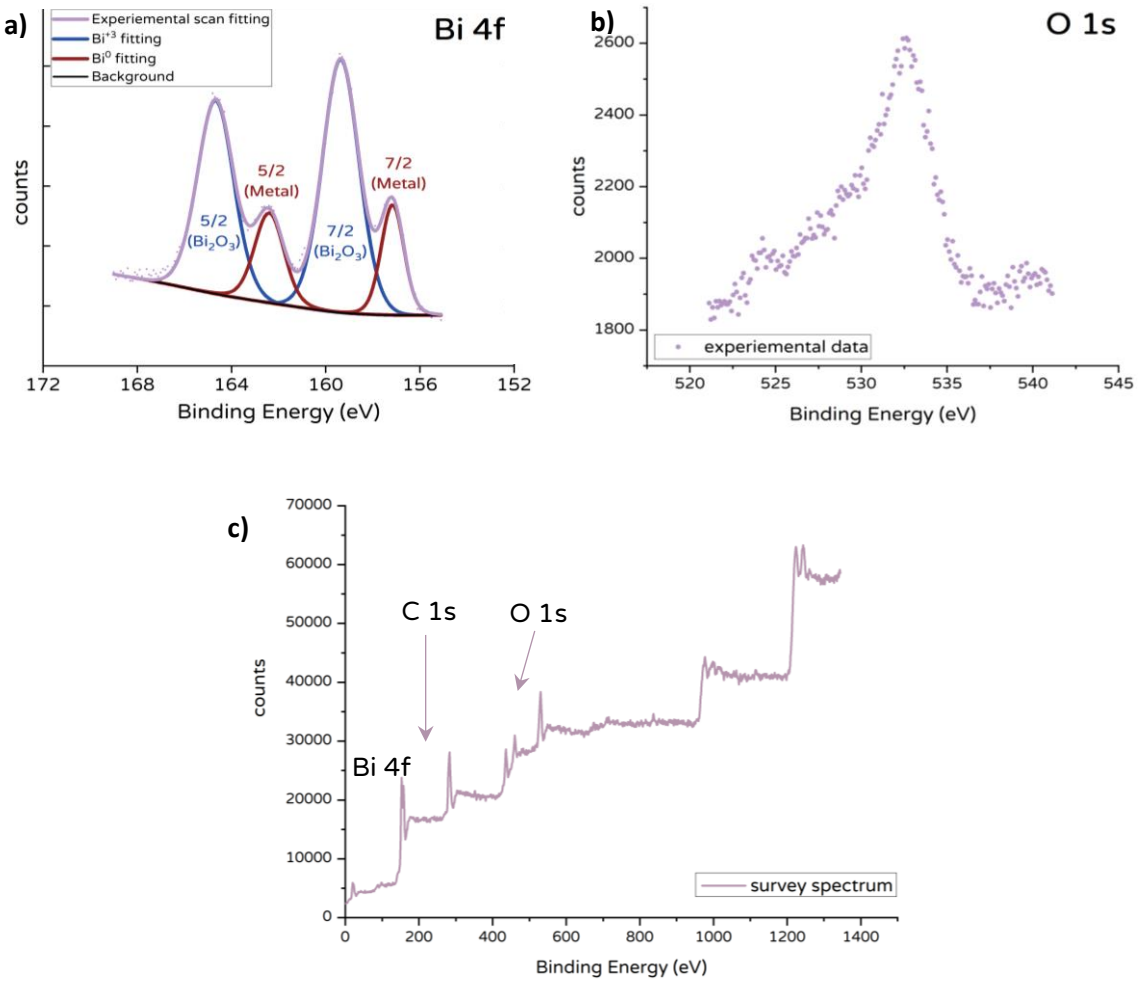

Figure 4.9: XPS spectrum of the Bi-GC electrode. Spectrum of the a) Bi 4f peak; b) O 1s peak; and c) survey spectrum. The fitting was performed only for a. The analyser pass energy was set to 100 eV for survey scans and 20 eV. The electrode was obtained by applying a potential equal to -0.132 V vs Ag/AgCl until a charge equal to 42 mC was passed in a solution of 20 mM $Bi(NO_3)_3$. In 1 M H NO_3. The geometrical area of the electrode was 0.07 cm^2

The presence of Bi_2O_3 was confirmed via Raman Spectroscopy (Figure 4.10a). The spectrum presented the three typical bands of the β-Bi_2O_3 phase[311] at 128, 315, and 461 cm^{-1}, while it is not possible to observe the bands of the α phase. The two intense bands at 1353 and 1598 cm^{-1} are assigned to the glassy carbon[312,313]. Unfortunately, because of the detection limits of the instrument, it was not possible to observe peaks for metallic Bi. The typical peaks for Bi metallic are at 71 and 98 cm^{-1} with the presence of a small band at 188 cm^{-1}, due to the second-order harmonic[311]. As it is possible to observe from Figure 4.10, the lower limit of the spectrum is at 70 cm^{-1} and the first distinguishable peak is after 100 cm^{-1}, making impossible to observe the two peaks for the metallic species. In addition, the signal to noise ratio is too high for observing clearly the second harmonic. Through a combination of SEM/EDS, XPS and Raman spectroscopies it was therefore possible to identify the electrodeposited dendrite films as consisting of both Bi^0 and the β-phase of Bi_2O_3. A similar composition have been obtained previously[132] for electrodes having Bi

particles with similar morphology: when dendrites were obtained, the presence of β-phase was observed.

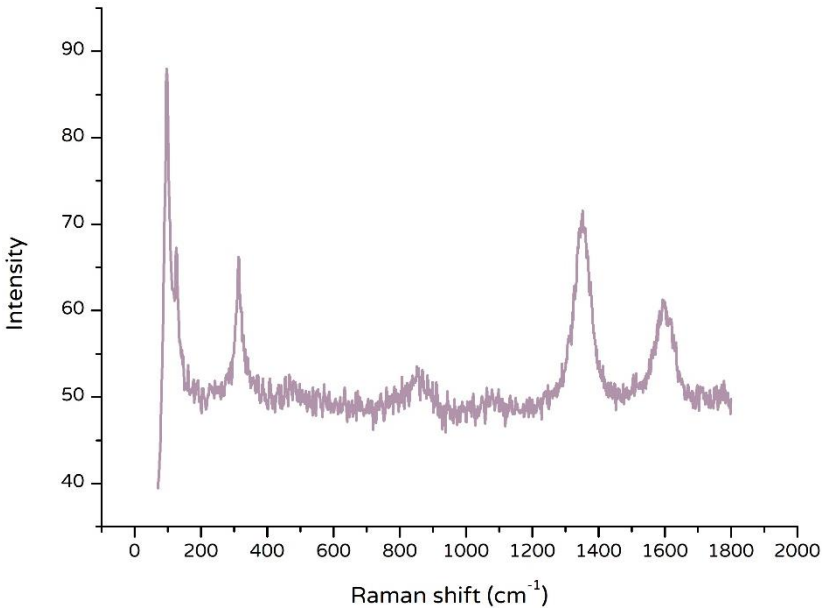

Figure 4.10: Raman spectrum of the Bi-GC electrode. The excitation wavelength for the measurement equal to 532 nm. The electrode was obtained by applying a potential equal to -0.132 V vs Ag/AgCl until a charge equal to 42 mC was passed in a solution of 20 mM $Bi(NO_3)_3$. In 1 M H NO_3. The geometrical area of the electrode was 0.07 cm^2

As it is possible to observe in the SEM images, the electrode exhibited a rough surface and, because of the presence of microdendrites, it is possible to assume that the electrode has a significantly large surface area.

On the basis of the SEM images, more depositions were performed to increase the uniformity of the film and to investigate the influence of the electrodeposition parameters on the morphology of the particles. Three different parameters were changed: 1) the wave form; 2) the concentration of the precursor; and 3) the composition of the deposition bath (addition of a capping agent). A list of the parameters changed during deposition and how these changes should modify the deposited crystallites are shown in Figure 4.11. It is important to highlight that these factors are strictly interconnected, and therefore can be quite challenging to tune them in such a way that they will influence only one aspect of the final deposit. A quantitative measurement of the real area of the electrodes was performed after all the different electrodes were produced and initially characterised with SEM imaging.

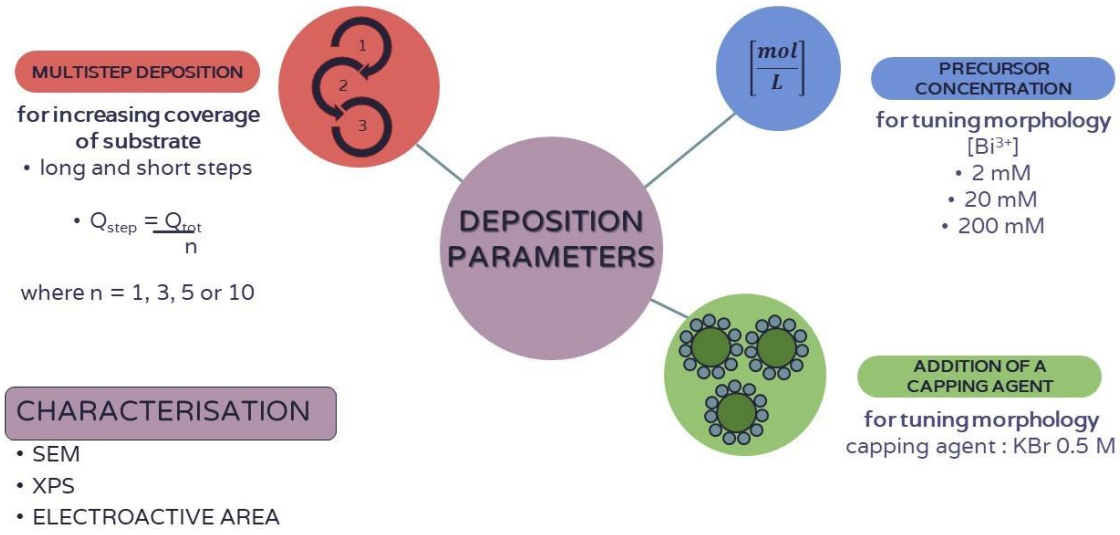

Figure 4.11: Deposition parameters changed for the preparation of different Bi modified electrodes and the following characterisation performed. The desired effects by the modification of the parameters are also included

4.2.2 Deposition parameters: continued and stepwise deposition

Based on SEM images and composition analyses, it is clear that the Bi crystallites do not completely cover the surface of the substrate, as several areas of the GCE were exposed. This is unwanted as it is desirable to limit to the minimum any contribution from the substrate. For this reason, additional deposition procedures were performed to cover the substrate more efficiently, increase the quantity of bismuth deposited and therefore minimise impact of the substrate on the catalysis measurements. Considering that small crystallites would pack closer to each other than the bigger ones, covering the surface of the glassy carbon more efficiently, a deposition method that should produce an electrode composed by small particles was performed. For this reason, a multistep electrodeposition was performed. In multistep electrodepositions the potential is applied in several steps, followed by a time off, in contrast with a single step deposition in which the charge is passed in a single step. This is advantageous as repeated short steps favour nucleation by increasing nucleation rate (higher current density) and the time off limits the growth of the nuclei, increase the diffusion of the ions in solution to the surface of the electrode and allowing other particles (like H_2) to diffuse from the deposit[121,147,314]. In addition, the highly acidic media (pH = 0.02) and the potentials used for the deposition favour the H_2 evolution especially on GC substrates, while Bi film would significantly supress it[119]. For these reasons, a multi-step deposition would give less H_2 evolution. In Table 4.1, the values of the applied charge and the number of steps performed during each electrodeposition are shown. The electrode in the first row of the table is the Bi modified electrode obtained with a single-step deposition (see Section 4.2) for more info about the

single-step deposition) and it is shown for comparison. The applied potential for the multistep deposition was -0.132 V vs Ag/AgCl for all the electrodes. For a guide to the naming system of the multi-step electrodes see Figure 4.12 below.

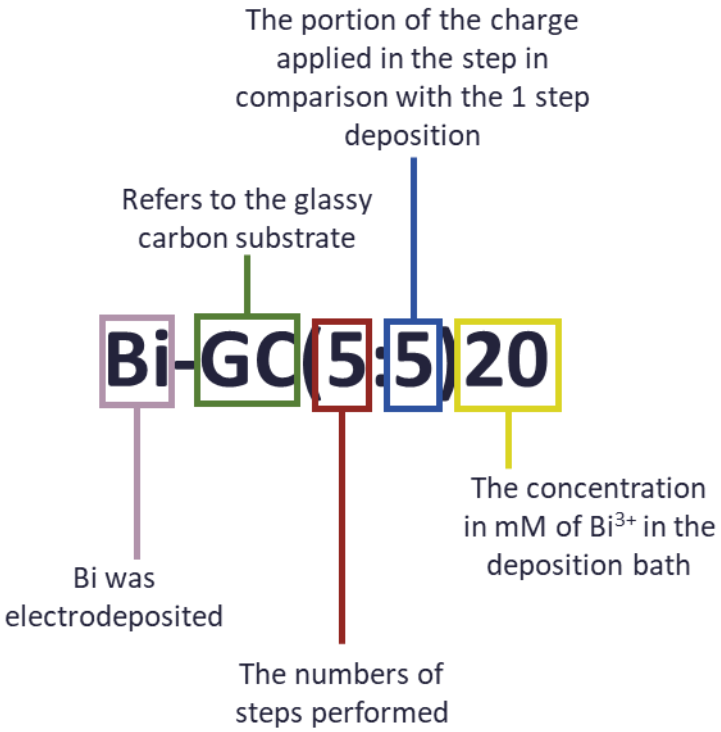

Figure 4.12: Guide to the naming system of the Bi multi-step electrodes

Table 4.1: Parameters for the electrodeposition of multi and single-step Bi-GC electrodes

electrode	n° of steps	Q_{step} [C]	Q_{tot} [C]
Bi-GC	1	$4.2x10^{-2}$	$4.2x10^{-2}$
Bi-GC(3:3)20	3	$1.4x10^{-2}$	$4.2x10^{-2}$
Bi-GC(3:3)20L	3	$4.2x10^{-2}$	$1.3x10^{-1}$

Initially, some preliminary depositions were performed to understand how the length of the deposition step can change the Bi film. Specifically, two different electrodes were produced using a multistep deposition: one with short steps and another with long steps. For the first multi-step deposition electrode (Bi-GC(3:3)20), the total charge passed during the single-step deposition was kept constant but divided into *three smaller different steps*. A resting time of 10 seconds between each step was applied, this resting time allowed the diffusion of the Bi cations onto the substrate ensuring the replenishing of the diffusion layer after the application of the negative potential[102,147,315]. However, for Bi-GC(3:3)20L (where L stand for long), three steps were performed but, in this case, the charge per step was equal to $4.2x10^{-2}$ C, leading to a total charge three times higher. The SEM images of the three different electrodes are shown in Figure 4.13.

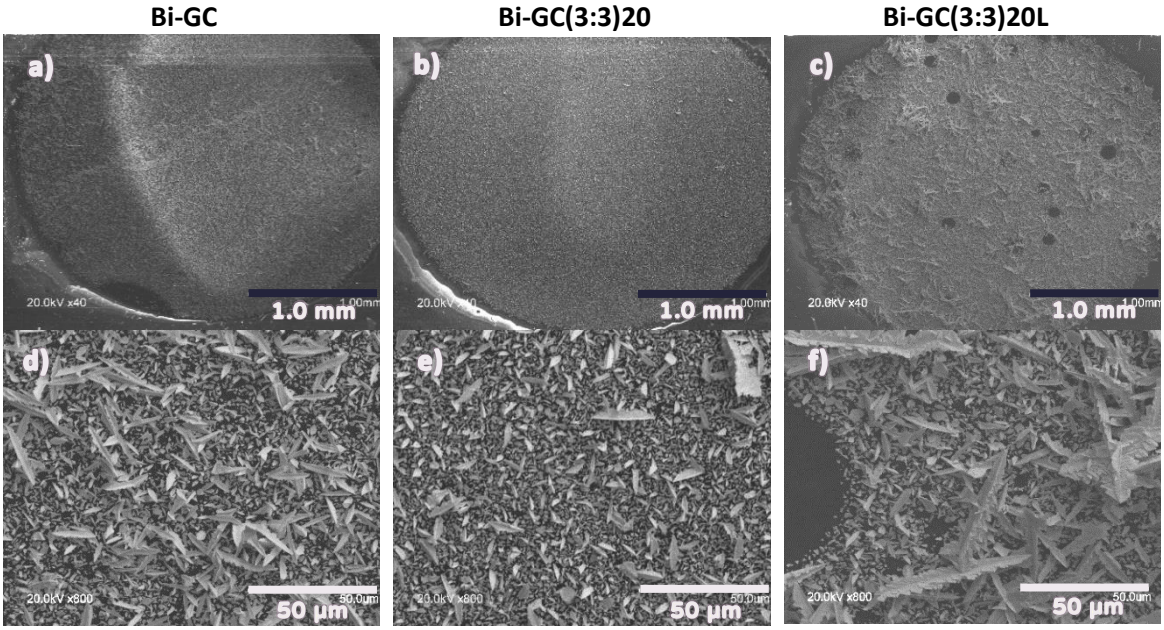

Figure 4.13: SEM images for Bi-GC (a and d), Bi-GC(3:3) (b and e) and Bi-GC(3:3)L (c and f). Magn = x40 for a, b and c; Magn = x800 for d, e and f. The three electrodes were prepared in a solution bath containing 20 mM Bi(NO3)3 and 1 M HNO3. Bi-GC was prepared applying 42 mC of charge in one step, while for Bi-GC(3:3)20 the same amount of charge was applied in 3 different steps. For Bi-GC(3:3)L, three deposition steps were performed, and in each step 42 mC of charge were applied

The two deposition methods did not lead to any significant differences in the morphology of the particles as in all the three electrodes dendritic structure were present, suggesting that the length of the step did not influence the shape of the particles and to obtain different morphologies other parameters need to be changed. Several parameters can be changed to tune the morphology of the particles (see Diagram 1). For example, Das and Sangaranarayanan showed how different morphologies can be obtained for Bi crystallites by varying the applied potential[132]: for a deposition bath containing 10 mM of $Bi(NO_3)_3$, triangle particles were obtained at -0.15 V, microsphere at -0.3 V and tripods at -0.5 V. This occurred because the applied potential modified the rate for nucleation and growth of the particles enabling the tuning of size and shape of the particles[127]. This means that a parameter that modifies the distribution of the current on the surface of the electrode can change the rates of formation and therefore the aspect of the particles. By examining the images at lowest magnification (Figure 4.13a, b, and c) a significant difference in the coverage of the substrate was observed. Bi-GC(3:3)20 seemed to have the most uniform film, while the Bi-GC(3:3)20L had the least uniform, with the presence of some large gaps. These gaps likely resulted from the formation of bubbles during the deposition, presumably as a consequence of H_2 evolution. This phenomenon is frequently observed (and even exploit it to obtain porous films[119]) in electrodeposition procedures. The formation of H_2 is due to the presence of H^+ in solution and absorbed on the surface of the substrate[316]. Considering the experimental conditions described above, it is clear that a high quantity of protons is present and because of the long deposition time, small bubbles can increase

in size, covering areas of the electrode and therefore preventing the formation of the film or even ruining the film already present. The trend of the dimension of the particles is Bi-GC(3:3)20L >Bi-GC >Bi-GC(3:3)20, suggesting that the longer the potential is applied the more the particles grow. In addition, for Bi-GC(3:3)20, the less aggregated dendritic structures observed on the surface might also indicate that shorter steps allow the formation of a large number of nucleation sites that do not fully grow.

At the two highest magnifications (Figure 4.14), several images were acquired focusing on three different areas of the electrodes in order to probe the homogeneity of the film among the entire surface of the electrode. In Figure 4.14 only the images acquired in one area are shown.

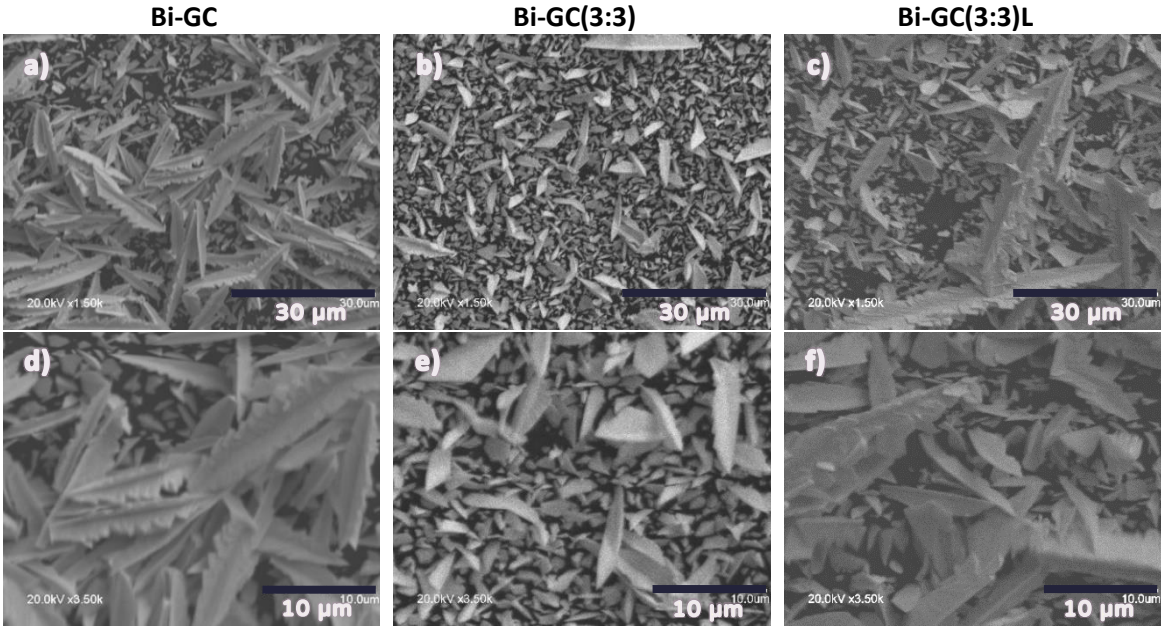

Figure 4.14: SEM images for Bi-GC (a and d), Bi-GC(3:3) (b and e) and Bi-GC(3:3)L (c and f). Magn = x1.5k for a, b and c; = x3.5k for d, e and f. The three electrodes were prepared in a solution bath containing 20 mM Bi(NO3)3 and 1 M HNO3. Bi-GC was prepared applying 42 mC of charge in one step, while for Bi-GC(3:3)20 the same amount of charge was applied in 3 different steps. For Bi-GC(3:3)L, three deposition steps were performed, and in each step 42 mC of charge were applied

The consistency of the deposition across the surface of the substrate increases from Bi-GC(3:3)20 > Bi-GC > Bi-GC(3:3)20L. The surface of the Bi-GC(3:3)20 electrode is covered more efficiently because of the smaller dimensions of these particles in comparison with the ones present on the other two electrodes. This suggests that shorter steps will produce smaller particles that are placed closer to each other, producing a more compact film. This was expected, as shorter steps followed by a resting time allows for the rearrangement of the deposited atoms making space for other nuclei to form in the following step and therefore producing more uniform, less porous and rough films[147]. This has been observed before for tin and nickel deposits[130,317]: by applying the current density in different steps (a study of the effect on the variation of the length of time on and off was also performed) a finer deposit was observed, while when the potential was applied for

long time, larger crystallites and more porous film was obtained. Similar behaviour was observed also for Bi-Te deposits[318]: when very short steps were performed (on the order of milliseconds) a more compact film was obtained, while increasing the time on bigger crystals were observed. For catalysis purposes, better coverage, and a higher bismuth surface area, is preferable for several reasons. First, the magnitude of the surface area is directly related with the number of atoms on the surface, second, the smaller the particles the higher the area-to-volume ratio[276]. Therefore, nanostructures will present higher number of active sites for catalysis. In addition, a better coverage of the substrate will be diminishing the influence of the substrate on the system. For example, it is well known that glassy carbon does not exhibit activity for CO_2 reduction and will promote competitive HER, meaning high surface coverage is very important for a better selectivity[319]. It is important to highlight that SEM images give only qualitative information about the coverage of the substrate. For a quantitively measure of the surface area see Section 4.4.

For this reason, other bismuth deposits were produced with short step deposition in order to monitor the appearance of the electrodeposited film. In Table 4.2, the electrodes formed with different short stepwise deposition sequences are listed. For these electrodes, the Q_{step} was equal to the one applied for the production of Bi-GC(3:3)20 (Q_{step} = 1.4x10^{-2} C, a third of the Q passed in the one-step deposition); and the parameters for the formation of Bi-GC(3:3)20 are inserted in Table 4.2. For this set of electrodepositions, the influence of the *number of steps* on the film formation was investigated to understand how it would affect the uniformity of the film on the electrode surface. For the Bi-GC(5:3)20 electrode, five steps were performed, leading in a total charge 1.7x larger than the one passed for Bi-GC(3:3)20, while, for Bi-GC(10:3)20, the number of the steps was equal to ten, with a total charge 10x higher than Q_{step} and more than three times bigger than for Bi-GC electrode.

Table 4.2: Parameters for the short step electrodepositions of Bi-GC electrodes. The number of the steps were three, five or ten. The same amount of charge was applied for each step

electrode	n° of steps	Q_{step} [C]	Q_{tot} [C]
Bi-GC(3:3)20	3	1.4x10^{-2}	4.2x10^{-2}
Bi-GC(5:3)20	5	1.4x10^{-2}	7.1x10^{-2}
Bi-GC(10:3)20	10	1.4x10^{-2}	1.4x10^{-1}

In Figure 4.15, the SEM images for the two new electrodes are shown. The Bi-GC(10:3)20 electrode presented more aggregated dendrites in comparison with Bi-GC(3:3)20 and Bi-GC(5:3)20 electrode (Figure 4.16). The more significant presence of larger dendrites in the electrode produced with the higher number of steps might suggest that after a certain amount of charge is passed (or a certain number of nucleation sites is reached), new nucleation sites are not formed and existing crystallites

simply tend to grow larger. This is confirmed in in Figure 4.15d and f, where the size of the dendritic structures is around 50 µm while for Bi-GC(3:3)20 it is around 10 µm.

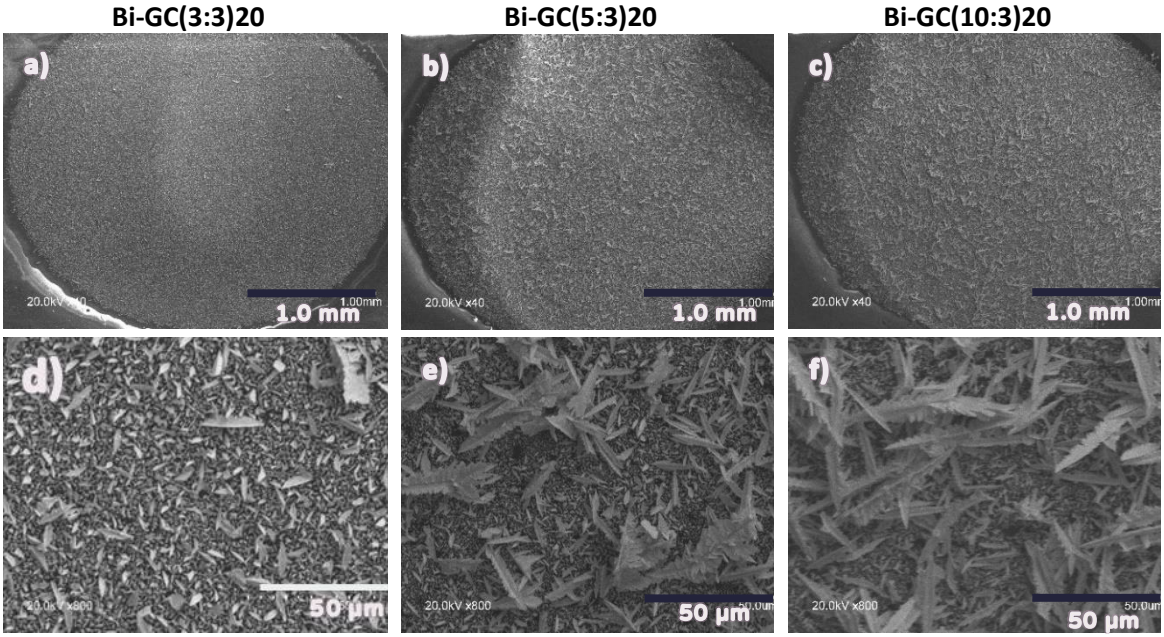

Figure 4.15: SEM images at low magnification and for Bi-GC electrodes produced with short step deposition. Magn = x40 for a, b and c; = x800 for d, e and f. The three electrodes were prepared in a solution bath containing 20 mM $Bi(NO_3)_3$ and 1 M HNO_3. Different amounts of steps were applied depending on the type of electrode, but the charge for each step was the same for all the electrodes

In Figure 4.16, representative images of the three electrodes acquired at high magnification are shown. At magnifications of x1.5k and 3.5k, images of three different areas of the electrodes were captured to investigate the homogeneity of the films across the electrode. The images of Bi-GC(3:3)20 are shown on the left for reference. At magnification equal to 3.5k, it was evident that Bi-GC(10:3)20 (right column) exhibited the lowest coverage. A possible explanation might be that once the crystals reach a certain dimension, they do not grow uniformly in all the directions, resulting in the formation of particles that are not well packed. In addition, because of the longer deposition times, the charge was higher than for the other electrodes and therefore a higher quantity of Bi is deposited on the GCE surface. For this reason, it is possible that some crystallites became too heavy and they fell from the electrode surface ending up in solution. In addition, the longer the film stayed in contact with the solution the higher the probability that some of the crystallites will re-dissolve in solution, as Bi metal forms $Bi(NO_3)_3$ in concentrated nitric acid solutions[320]. Usually, dissolution of Bi metal is performed in significantly higher concentrated solution of HNO_3 than the one used in this work[321], however it was observed dissolution of a Bi film detached form the electrode surface. When the Bi film was left in the deposition bath for a few hours, bubbles were developed and a green colour was observed on the surface of the Bi film, suggesting the formation of NO_x gases from the dissolution of metallic Bi[321]. The green colour points

to the presence of the equilibrium between of NO_2 (yellow in solution) and N_2O_3 (blue) formed during the dissolution.

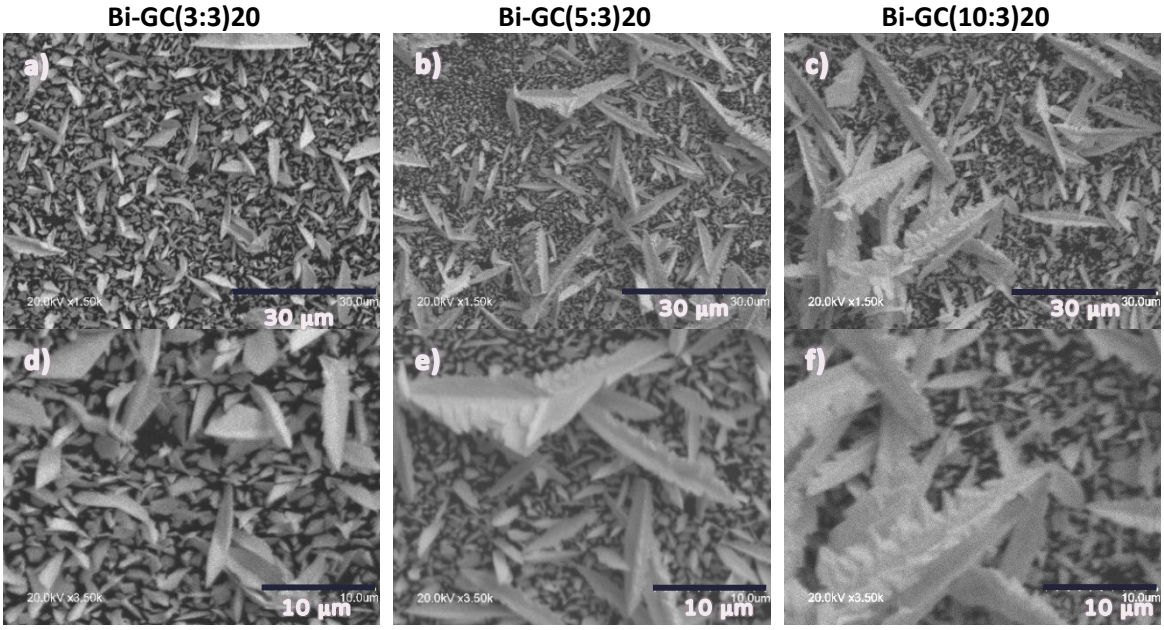

Figure 4.16: SEM images at high magnification for Bi-GC electrodes produced with short steps deposition. Magn = x1.5k for a, b and c; = x3.5k for d, e and f. The three electrodes were prepared in a solution bath containing 20 mM $Bi(NO_3)_3$ and 1 M HNO_3. Different amounts of steps were applied depending on the type of electrode, but the charge for each step was the same for all the electrodes

Successively, a deposition with even shorter steps was performed to understand if a reduced *quantity of charge per step* would lead to a more uniform coverage than the one obtained for Bi-GC(3:3)S. The idea behind this is that if the deposition is stopped during the growth process (see last part of the transient curves in Figure 4.27 Section 4.3), new possible nucleation sites on both the substrate and the Bi film can be formed, favouring the nucleation processes instead of the growth of pre-existing crystals. In Figure 3.13, a comparison between Bi-GC(3:3)20 and an electrode produced with five steps was done (Bi-GC(5:5)20). The charge per step for Bi-GC(5:5)20 was equal to $8.4x10^{-3}$C, almost half that of the other Bi-GC electrodes produced via short step deposition (for three steps deposition $Q_{step} = 1.4x10^{-2}$ C) . In Table 4.3, the amount of charge per step and the value of the total charge passed are shown. Like in the other tables and figures, Bi-GC(3:3)20 is used as a reference.

Table 4.3: Parameters for two different short step electrodepositions of Bi-GC electrodes

electrode	n° of steps	Q_{step} [C]	Q_{tot} [C]
Bi-GC(3:3)20	3	$1.4x10^{-2}$	$4.2x10^{-2}$
Bi-GC(5:5)20	5	$8.4x10^{-3}$	$4.2x10^{-2}$

From Figure 4.17d, bigger crystals are observed when five steps are used. This would confirm what was observed when Bi-GC(3:3)S, (5:3) and (10:3) electrodes were compared: once a certain amount

of charge is passed, further electrodeposition results in crystallite growth rather than increasing the number of nucleation sites.

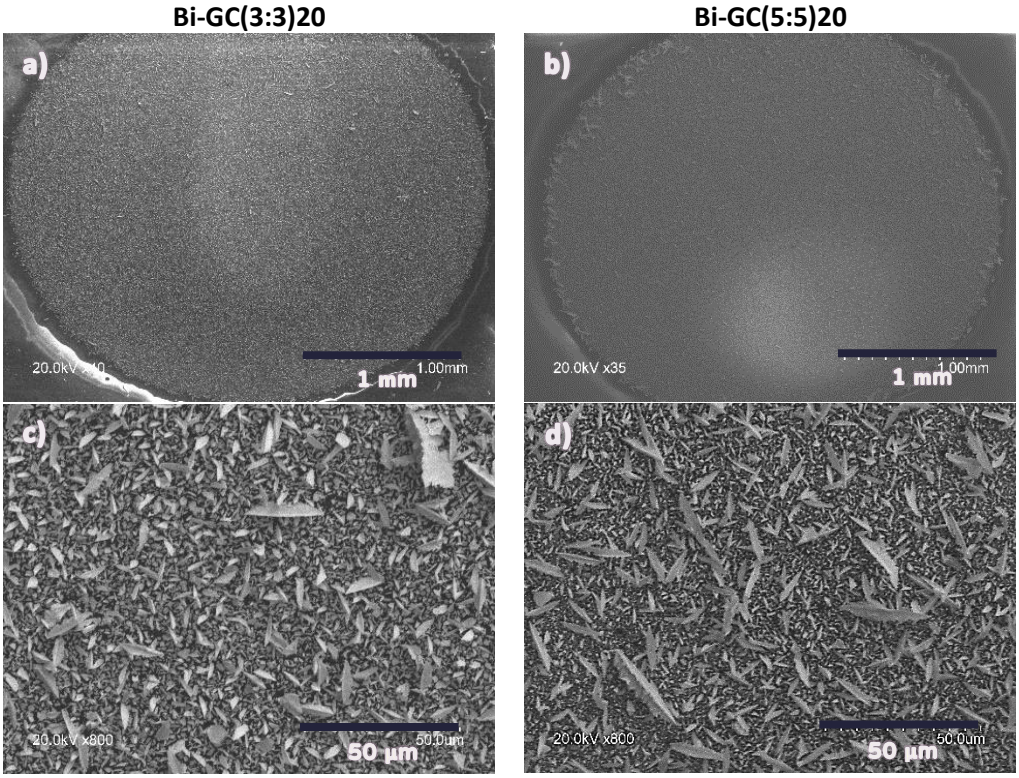

Figure 4.17: SEM images at low magnification of the two Bi-GC electrodes produced with 3 (on the left) or 5 (on the right) short steps but the same amount of total charge passed. Magn = x40 for a and b; = x800 for d and c. The two electrodes were prepared in a solution bath containing 20 mM $Bi(NO_3)_3$ and 1 M HNO_3. The charge per step was higher for Bi-GC(3:3)20 than for Bi-GC(5:5)20

In Figure 4.18, it can be seen that the crystallites in Bi-GC(5:5)20 are smaller than in (3:3)20, confirming that the less the charge per step, the smaller the fragments on the surface of the electrode. In addition, the high magnification images displayed the presence of larger crystals in Bi-GC(5:5)20 than in (3:3)20.

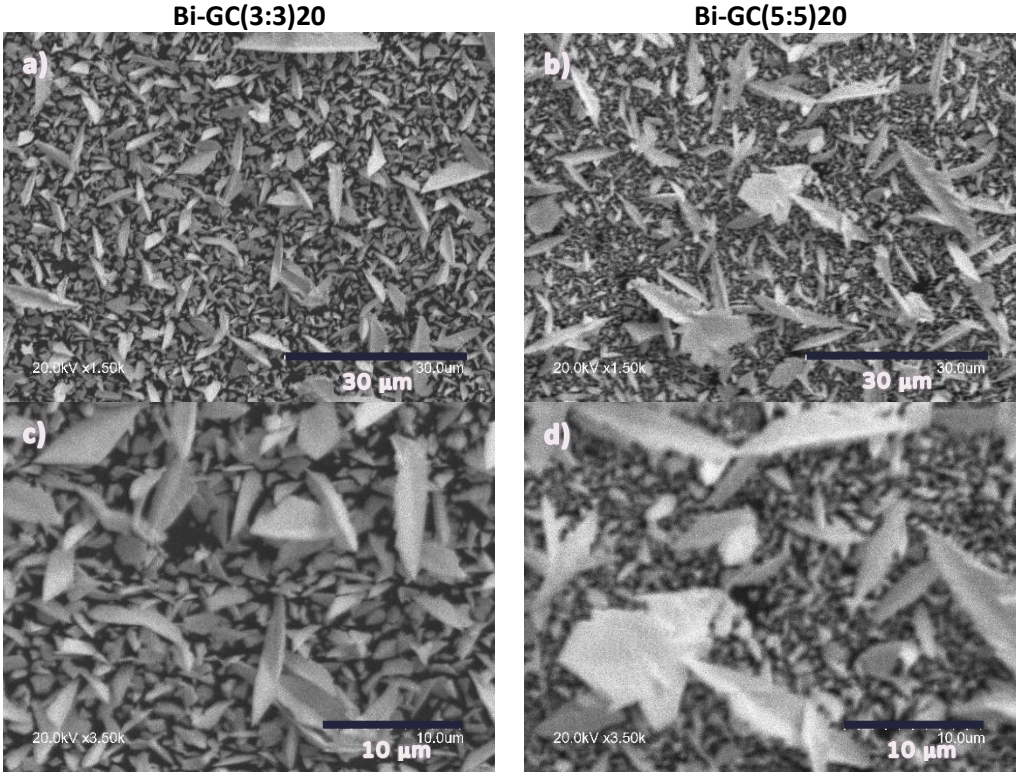

Figure 4.18: SEM images at high magnification of the two Bi-GC electrodes produced with 3 (on the left) or 5 (on the right) short steps but the same amount of total charge passed. Magn = x1.5k for a and b; = x3.5k for c and d. The two electrodes were prepared in a solution bath containing 20 mM $Bi(NO_3)_3$ and 1 M HNO_3. The charge per step was higher for Bi-GC(3:3)20 than for Bi-GC(5:5)20

Based on the SEM images, the most uniform electrodeposits was observed for three electrodes: Bi-GC(3:3)20, Bi-GC(5:3)20 and Bi-GC(5:5)20. For this reason, XPS analyses were performed on these three most promising electrodes to monitor any possible change in elemental composition due to the introduction of stepwise deposition sequences. Figure 4.19 compares the Bi 4f peaks of the three electrodes obtained with a stepwise deposition and the Bi-GC. All four spectra exhibit very similar features: specifically, a mixed composition (Bi^{3+} and Bi^0), with a larger contribution from Bi^{3+} (Bi^{3+}/Bi^0 ratios around 2:1). The binding energies at the maxima differ by a maximum of 0.7 eV among the four electrodes (Table 4.4) and the peak separation for each species was equal to 5.3 eV for all the sample. Based on these findings, it is reasonable to assume that a stepwise deposition does not change significantly the composition or the morphology of the electrodeposits.

Table 4.4: Parameters extracted from the XPS spectra (Bi 4f region) for the electrode produced in a in a solution bath containing 20 mM $Bi(NO_3)_3$ and 1 M HNO_3. The charge was passed in one step for Bi-GC, while in multi steps for the other three electrodes

electrode	$Bi^{3+}{}_{5/2}$	$Bi^{0}{}_{5/2}$	$Bi^{3+}{}_{7/2}$	$Bi^{0}{}_{7/2}$	$\frac{Bi^{3+}}{Bi^{0}}$
Bi-GC	164.67	162.46	159.36	157.20	2.04
Bi-GC(3:3)20	165.04	162.49	159.71	157.31	2.16
Bi-GC(5:3)20	164.73	162.53	159.42	157.23	2.39
Bi-GC(5:5)20	164.74	162.54	159.43	157.23	2.04

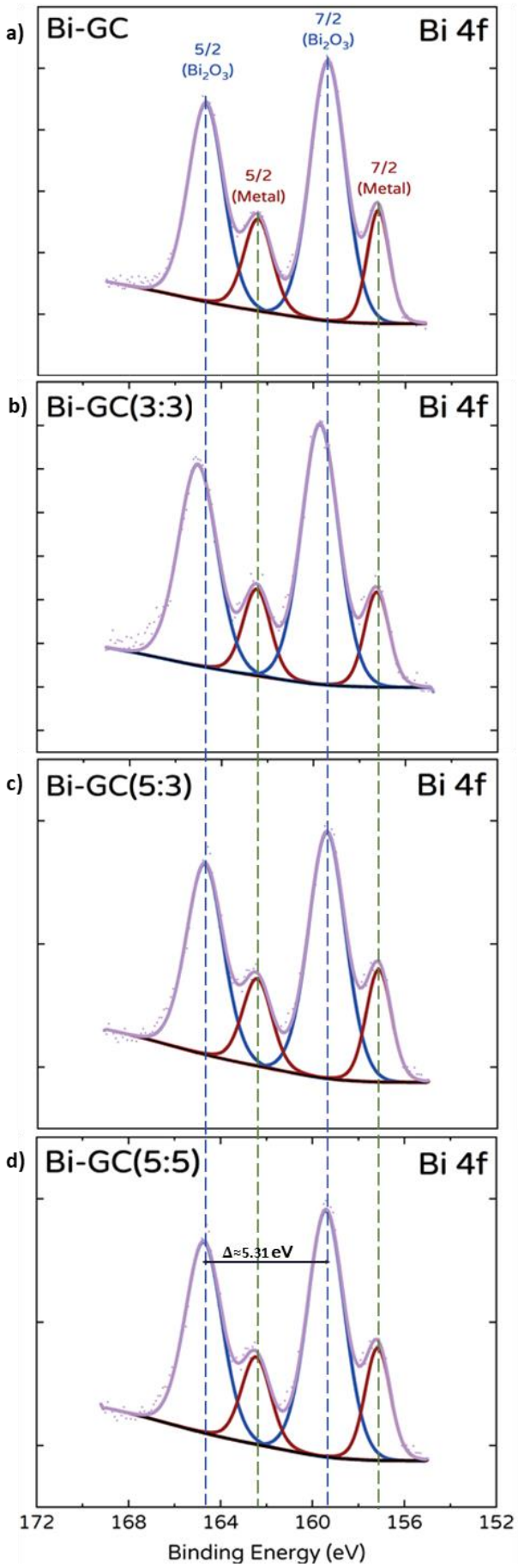

Figure 4.19: XPS spectrum of the Bi 4f peak for: a) Bi-GC, b) Bi-GC(3:3)S; c) Bi-GC(5:3) and d) Bi-GC(5:5) electrodes

4.2.3 Deposition parameters: concentration of the Bi precursor

Catalytic activities are strongly influenced by the shape and size of the catalysts[322]. For this reason, it is important to be able to control the morphology and the size of the catalytic particles. There are several ways of modifying the structure of an electrodeposited film, among others, the concentration of the precursor salt has been investigated before for Bi electrodeposits [126,128]. In general, increasing the concentration of the precursor will increase the deposition rate, leading to a change in the size and shape of the deposited particles[117]. This has been observed before for Bi electrodeposited films[132]: at the same overpotential, increasing the concentration of Bi^{3+} five times, dendrites structures were obtained instead of tripods. For this reason, different electrodepositions were performed varying the concertation of $Bi(NO_3)_3$. For all the Bi deposits previously obtained, a 20 mM solution of $Bi(NO_3)_3$ was used. To understand to which extent the concentration of the precursor modifies the Bi film, two deposition baths were prepared using different concentration of the Bi precursor: 2 and 200 mM. The electrodeposition procedure was the same used for the 20 mM bath except for the applied potential (E_{ad}) during the BE experiments. In this case, E_{ad} was calculated by adding an overpotential of 15 mV to the E_{pc} extracted from the CVs acquired for each GC electrode. The concentration of the Bi precursor, the charge passed during the BE experiments and the number of the steps for each electrode is showed in Table 4.5.

Table 4.5: Parameters for two different short step electrodepositions of Bi-GC electrodes performed in a deposition bath containing 2 or 200 mM of Bi precursor

Conc. [mM]	Electrode	n° of steps	$Q_{step\_theoretical}$ [C]	$Q_{step\_experimental}$ [C]	Q_{tot_exp}[C]
2	Bi-GC(3:3)2	3	$1.4x10^{-2}$	1.400 (±0.003) $x10^{-2}$	4.201(±0.009) $x10^{-2}$
	Bi-GC(5:3)2	5	$1.4x10^{-2}$	1.404 (±0.003) $x10^{-2}$	7.0201(±0.001) $x10^{-2}$
	Bi-GC(5:5)2	5	$8.4x10^{-3}$	8.417 (±0.004) $x10^{-3}$	4.208 (±0.001) $x10^{-2}$
200	Bi-GC(3:3)200	3	$1.4x10^{-2}$	1.6 (±0.9) $x10^{-2}$	4.7 (±0.2) $x10^{-2}$
	Bi-GC(5:3)200	5	$1.4x10^{-2}$	1.4 (±0.2) $x10^{-2}$	6.9 (±0.9) $x10^{-2}$
	Bi-GC(5:5)200	5	$8.4x10^{-3}$	1.1(±0.2) $x10^{-2}$	5.3 (±0.6) $x10^{-2}$

In the case of the 200 mM bath, the current passed during the electrodeposition was two orders of magnitude higher for the electrodes produced in 200 mM bath (≈ 10 mA) than in the 20 mM one (≈ 0.1 mA). Therefore, it was not possible to pass exactly the same amount of charge per step each time. For this reason, the average value for all the experiments is shown. In contrast, for the other two deposition baths, the charge passed for each step was consistently equal to the theoretical charge. Figure 4.20 shows the cyclic voltammogram obtained in the deposition bath with the two different precursor concentrations.

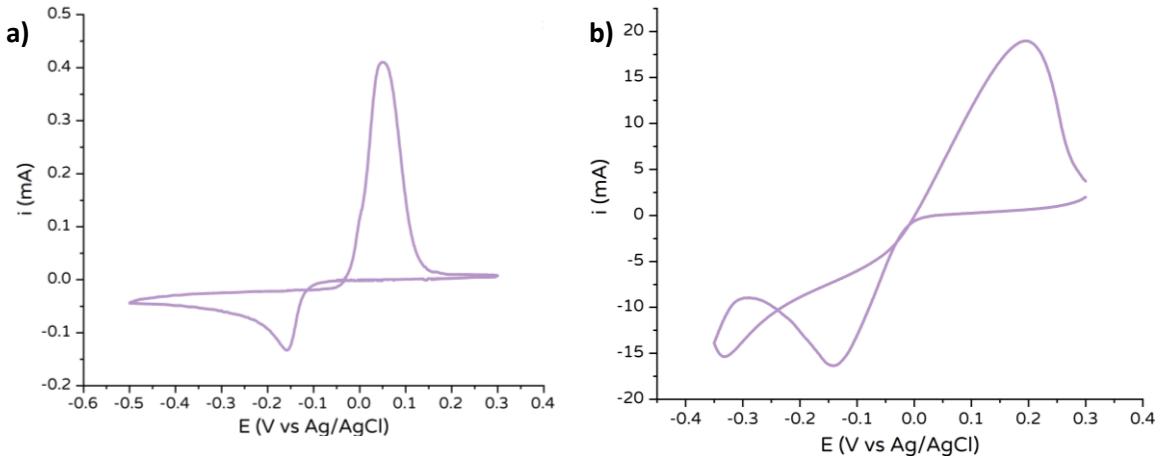

Figure 4.20: CV of the deposition bath containing a) 2 mM and b) 200 mM of $Bi(NO_3)_3$ in solution of 1 M HNO_3 .WE = GCE. The geometrical area of the WE was 0.07 cm^2. Scan rate = 100 mV/s

The CVs for 2 mM $Bi(NO_3)_3$ were very similar to those obtained in the 20 mM solution, while for the 200 mM solution a higher peak to peak separation was observed (see Table 4.6), likely due to a high iR drop. To understand if the concentration of $Bi(NO_3)_3$ influenced the morphology of the crystallites, SEM images were acquired for all the electrodes. In general, all the electrodes obtained in the different baths presented a grey film.

Table 4.6: Concentration of Bi precursor salt and correspondent peak to peak separation for the cathodic and anodic feature obtained for the CVs acquired at scan rate equal to 100 mV/s

[Bi^{3+}]	ΔEp [V]
2 mM	0.21
20 mM	0.21
200 mM	0.34

4.2.3.1 2 mM $Bi(NO_3)_3$

In Figure 4.21, the SEM images acquired at four different magnifications for the Bi-GC(3:3)2 electrode are shown. The particles presented a dendritic morphology: the shape of the trunk of the dendrite had the same shape observed in the films electrodeposited in a 20 mM deposition bath but, in this case, the crystallites exhibited longer secondary dendrites arms (Figure 4.21e). Similar morphology has been observed in previous study by Yang[119] in a 1 mM Bi^{3+} deposition bath. The shape of the secondary arms was attributed to a suppression of the lateral growth due to formation of H_2 bubbles around the trunk. On the surface of Bi-GC(3:3)2 only ungrown triangular particles were observed, in contrast with the previous electrodes (20 mM Bi^{3+} bath, Figure 4.6), in which hexagonal plates were observed. The same has been observed elsewhere[132]: at higher Bi^{3+} concentration (50 mM), hexagonal particles were deposited, while at lower concentrations (10 mM), triangular crystallites were formed. This suggests that the concentration of the Bi precursor salt influences the crystalline structure, favouring the relative formation rates of specific facets both

at the formation of the crystal seeds and during the growth[323]. In this work, some areas of the electrode (Figure 4.21a), large clusters were observed, especially at the edges of the glassy carbon surface. At high magnification (Figure 4.21b-d), it is evident that the film is not homogenous and unform, as part of the glassy carbon surface is exposed, and clusters of more compact layers of crystallites are present. During the deposition, several bubbles were formed remaining on the surface for the entire deposition step. Once the electrode was rinsed and the bubbles consequently eliminated, that part of the GC electrode remained uncovered. Presence of large bubbles and consequent pits on the electrodeposit film were observed for Bi-GC(3:3)20L (see Figure 4.13). These two electrodes have longer deposition times in comparison with the other electrodes, factor that allows the increase in size of the small H_2 bubbles produced during the electrodeposition.

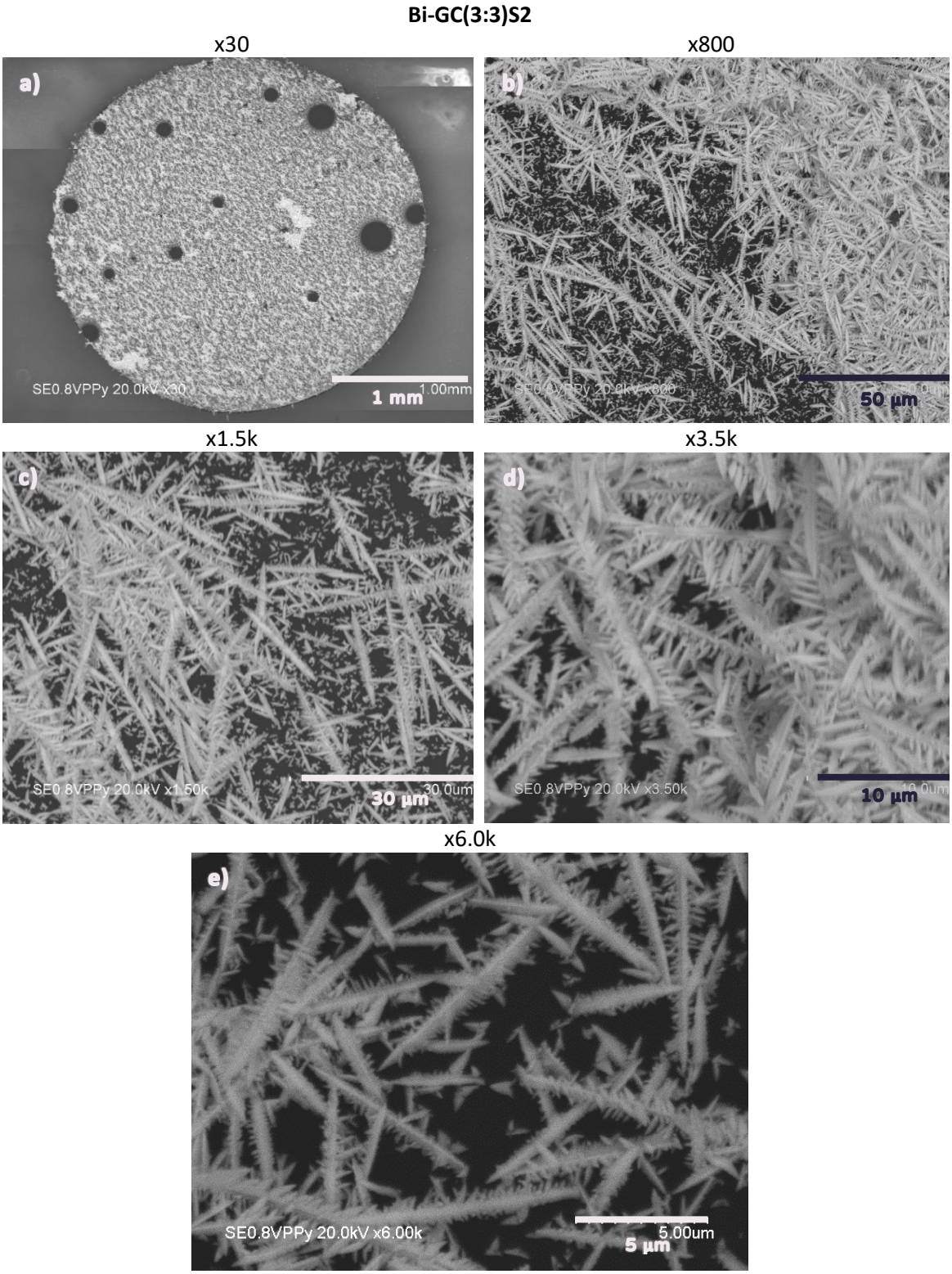

Figure 4.21: SEM images for Bi-GC electrodes produced with a three-steps deposition method in a bath containing 2 mM $Bi(NO_3)_3$ and 1 M HNO_3. The total charge, equal to 42 mC, was applied in three different steps. Magnifications equal to a) x30; b) x800; c) x1.5k; d) x3.5k; e) 6.0k. The images were acquired with an acceleration voltage of 20 kV

In the areas where multilayers of crystallites are present (see area in which the charging is higher in Figure 4.21a), the surface of the glassy carbon is almost completely covered. On the other hand,

the areas with less large structures, that represented the majority of the electrode surface, resulted in a very low coverage as crystallites are placed far away from each other (Figure 4.21c and e).

When shorter five steps were applied, the crystallites presented short primary and secondary arms are (Figure 4.22). In comparison with Bi-GC(3:3)2, the small crystallites are more compacted on the surface of the electrode, giving a more uniform film in the absence of the large structures. As for the three steps deposition, bubbles were formed during the entire deposition, making challenging the formation of a continuous film and the reproducibility of the electrodes (Figure 4.22a).

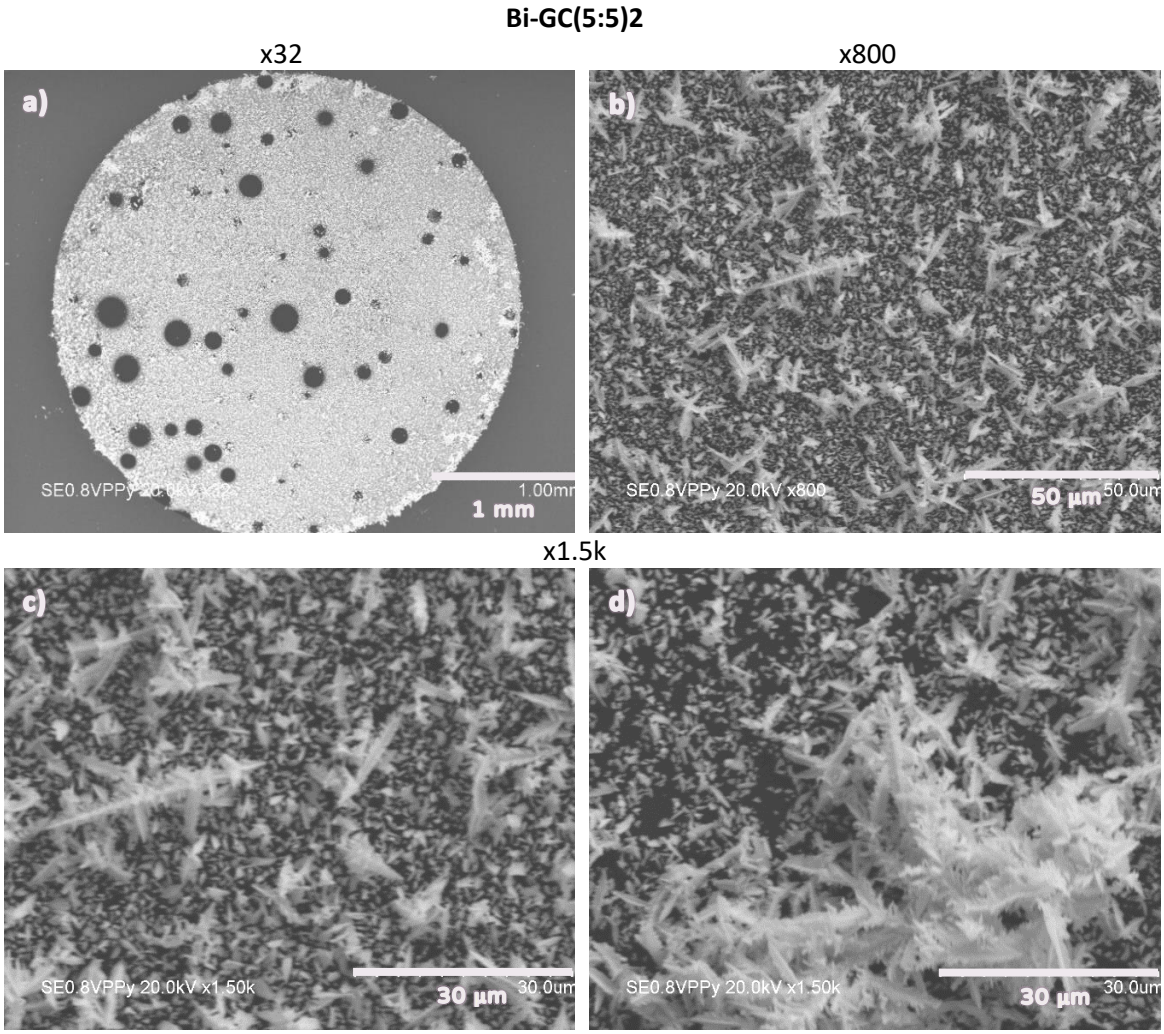

Figure 4.22: SEM images for Bi-GC electrodes produced with a five-steps deposition method in a bath containing 2 mM $Bi(NO_3)_3$ and 1 M HNO_3. The total charge, equal to 42 mC, was applied in five different steps. Magnifications equal to a) x32; b) x800; c) x1.5k; and d) x3.5k. The images were acquired with an acceleration voltage of 20 kV

In general, a deposition performed using a low concentration of Bi precursor led to the formation of films with larger crystallites and clusters. The formation of larger structures is probably due to the larger times necessary for the theoretical charge to pass for each step. This is evident by making a comparison between the films obtained with a three and five steps deposition: the longer the

step the larger and more complex the structures. Unfortunately, the long deposition time seems to promote the growth of H_2 bubbles at the electrode interface and the consequent presence of circular areas where the surface of the glassy carbon is completely exposed. A very similar morphology was obtained for Bi-GC(5:3)2, with the surface homogenously covered with dendrites agglomerates as the one observed in Figure 4.22d.

4.2.3.2 200 mM $Bi(NO_3)_3$

By increasing the concentration of the Bi precursor salt in the deposition bath, a different morphology was observed. When three deposition steps were performed, small polygonal plates were observed (Figure 4.23). The size and the shape of the plates are not consistent and both large and small crystallites with hexagonal, pentagonal, quadrilateral or triangular shape were present. The variety of sizes and shapes can be attributed to different nucleation rates at different active sites[119]. This suggests a not uniform current density on the surface of the electrode. At high magnification (Figure 4.23c and d), it was possible to observe that some of the plates aggregated forming irregular agglomerates. As for the films obtained in a 20 mM $Bi(NO_3)_3$ bath, the coverage of the GC electrode is poor, as a lot of the glassy carbon surface is exposed. In addition, several bubbles were formed during the deposition process, leaving several areas of the electrode uncovered from Bi crystallites. As shown in Table 4.5, it was not possible to pass precisely the same amount of charge for each step because of the large current produced during the experiments. This is probably due to the high concentration of the Bi precursor salt, as each step was less than 2 seconds long, a time around x45 and x800 lower than for a deposition in a 20 mM and 2 mM $Bi(NO_3)_3$ bath, respectively.

Bi-GC(3:3)200

x40 x800

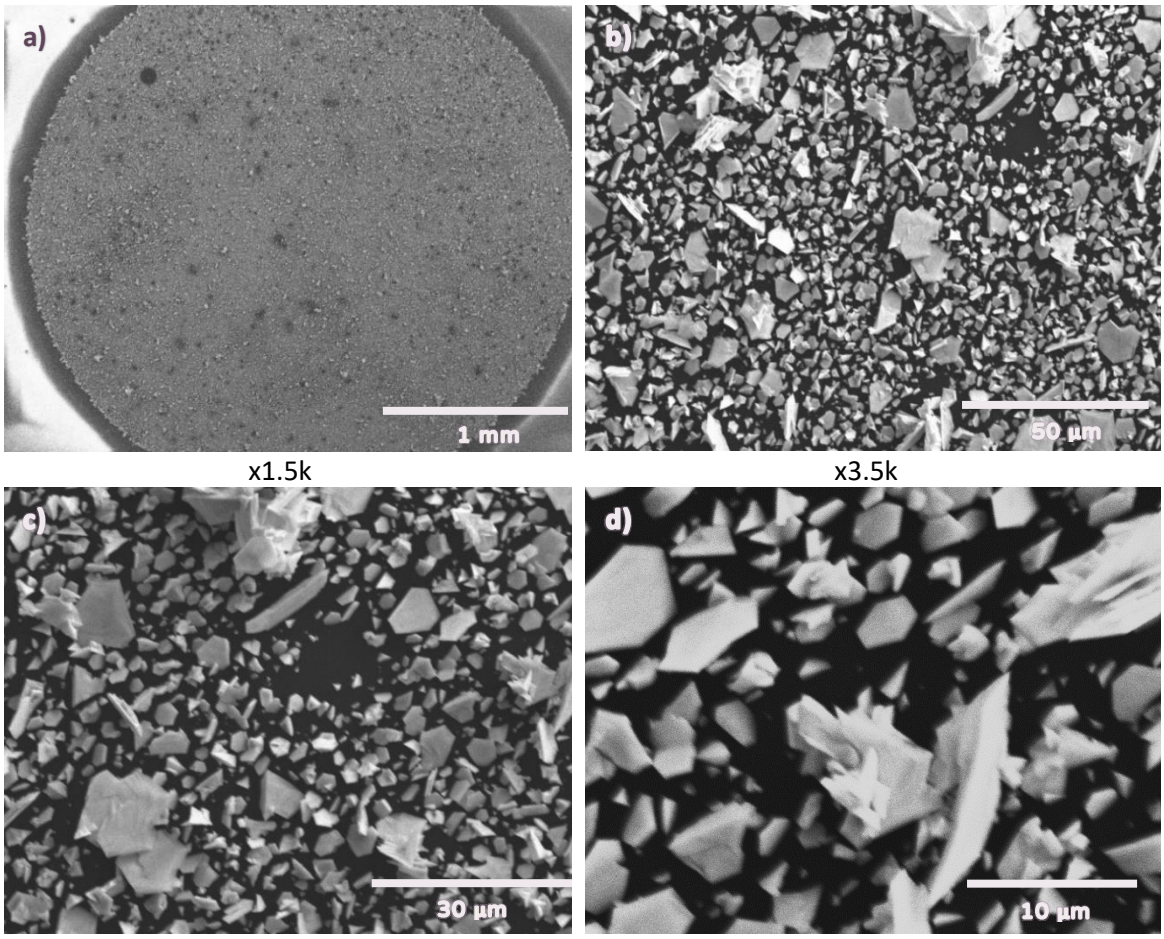

Figure 4.23: SEM images for Bi-GC electrodes produced with a three-steps deposition method in a bath containing 200 mM $Bi(NO_3)_3$ and 1 M HNO_3. The total charge, equal to 42 mC, was applied in three different steps. Magnifications equal to a) x40; b) x800; c) x1.5k; and d) x3.5k. The images were acquired with an acceleration voltage of 20 kV

A more uniform deposit was obtained when two additional steps were added (Bi-GC(5:3)200 – see Figure 4.24) as more bismuth was deposited.

Bi-GC(5:3)200

x40 x800

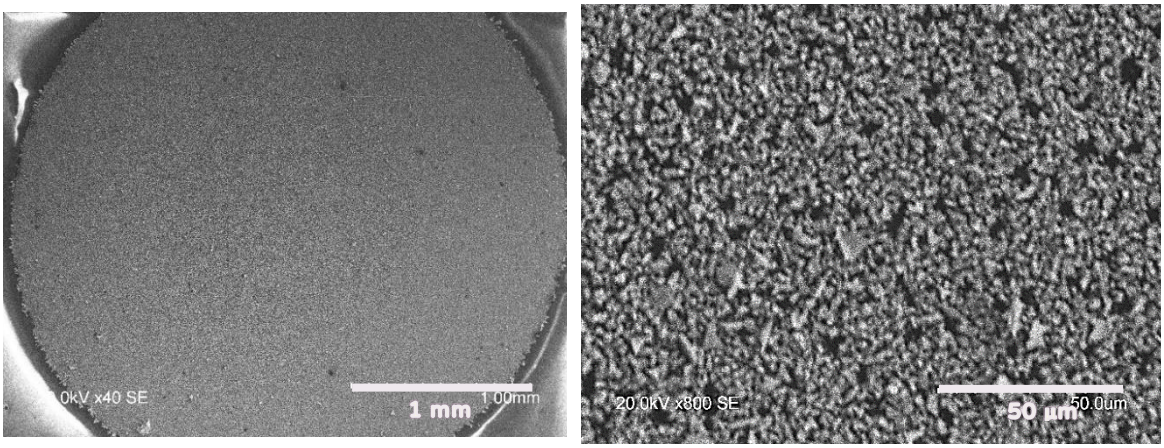

Figure 4.24: SEM images for Bi-GC electrodes produced with a five-steps deposition method in a bath containing 200 mM $Bi(NO_3)_3$ and 1 M HNO_3. The total charge was applied in five different steps. Magnifications equal to a) x40; and b) x800. The images were acquired with an acceleration voltage of 20 kV

When a five-step deposition was performed (Bi-GC(5:5)200), the shape of the particles formed was not consistent: some plates were observed but several amorphous crystallites were observed (Figure 4.25b-d). As it can be seen in both high and low magnification images, the deposit was not uniform and several pits were present. This is probably due to the high currents passed during the electrodeposition as it has been demonstrated before[130] that high current densities favour the hydrogen evolution reaction and the formation of less compact and adherent deposit. As for the three steps deposition, it was not possible to obtain a consistent amount of charge passed for each step, as the time necessary to pass the theoretical charge was around 0.5 s, a very short time that made challenging to interrupt the measurement once the desired amount of charge was reached.

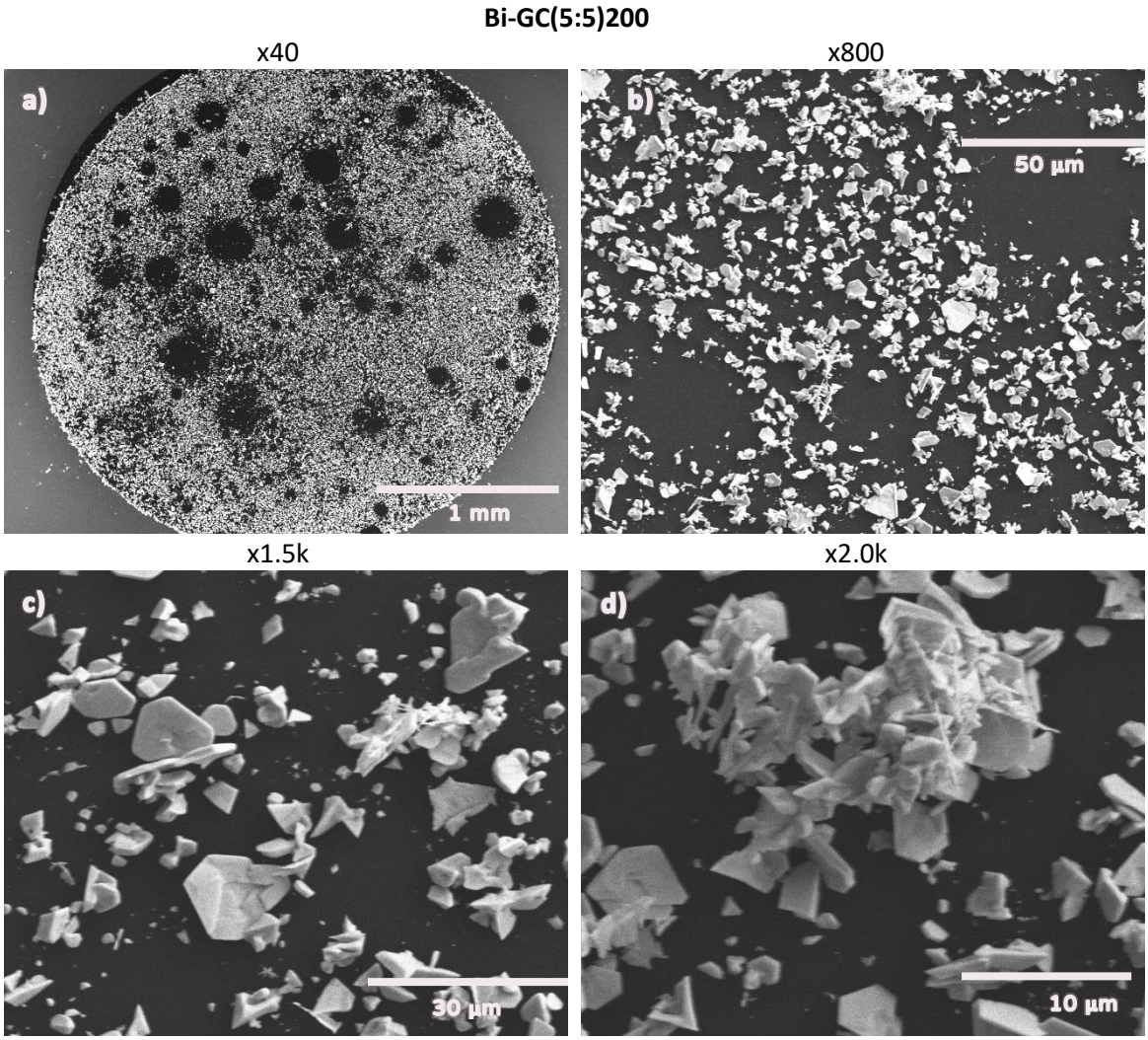

Figure 4.25: SEM images for Bi-GC electrodes produced with a five-steps deposition method in a bath containing 200 mM $Bi(NO_3)_3$ and 1 M HNO_3. The total charge, equal to 42 mC, was applied in five different steps. Magnifications equal to a) x40; b) x400; c) x1.5k; and d) x2.0k. The images were acquired with an acceleration voltage of 20 kV

4.2.4 Deposition parameters: presence of an additional salt

An additional compound in the deposition bath can act as capping agent controlling the size and morphology of metal particles[324]. Usually, to tune the size and avoid aggregation of the metal nanoparticles, organic molecules such citrate, polyvinyl pyrrolidone (PVP) and Poly(amidoamine) (PAMAM) have been used[325–327]. Unfortunately, the removal of these compounds is not always straightforward but is often necessary to avoid unwanted interferences of the capping agent in the processes like catalysis[325,328]. The presence of a second salt in the electrodeposition bath can result in a different morphology of the particles because of the interactions with additional ions and the species in solution and consequently on the surface of the film[153,324]. Based on some literature examples[153,169], a new deposition bath was prepared comprising 0.5 M KBr and 20 mM $Bi(NO_3)_3$ solution and three different electrodes were produced: a single-step deposition electrode Bi-GC_0.5 (where 0.5 corresponds to the concentration of KBr), and two multi-step deposition electrodes Bi-GC(3:3)20_0.5 (three steps) and Bi-GC(5:3)20_0.5 (five steps). The deposition parameters used for the production of the electrodes are shown in Table 4.7.

Table 4.7: Parameters for two different short step electrodepositions of Bi-GC electrodes performed in a deposition bath containing 20 mmol/L of Bi precursor and 0.5 moles/L of KBr

Electrode	Concentration of $Bi(NO_3)_3$ [mM]	Concentration of KBr [mM]	n° of steps	Q_{step} [C]	Q_{tot} [C]
Bi-GC_0.5	20	500	1	$4.2x10^{-2}$	$4.2x10^{-2}$
Bi-GC(3:3)20_0.5	20	500	5	$1.4x10^{-2}$	$4.2x10^{-2}$
Bi-GC(5:3)20_0.5	20	500	5	$1.4x10^{-2}$	$7.1x10^{-2}$

The morphology of the particles for the three deposits are indistinguishable. For this reason, only the images for Bi-GC(5:3)20_0.5 are shown. From Figure 4.26, it is clear that the presence of KBr considerably changed the morphology and the size of the sample: the particles are now aggregated rounded structures, with the single particles having spherical or oval structures with size ≤ 3 µm. Because of the way the particles tended to aggregate and the lack of constant shape, it was not possible to find an average value for their size. The film is not uniform as several areas are uncovered around the mamillated agglomerates (Figure 4.26b). In general, it was not possible to obtain an uniform film, as several areas of the electrode remain uncovered.

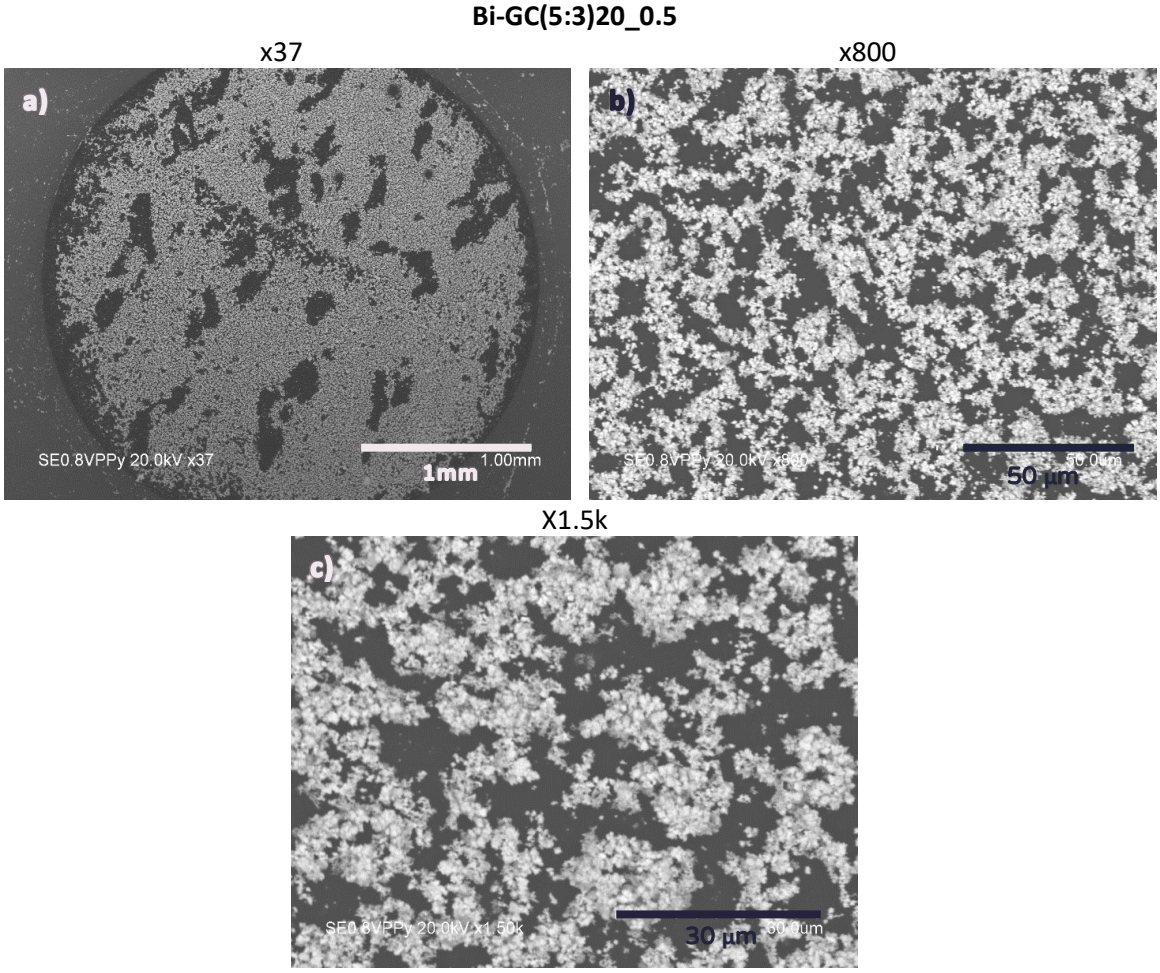

Figure 4.26: SEM images for Bi-GC electrodes produced with a five-steps deposition method in a bath containing 20 mmol/L of $Bi(NO_3)_3$ and 0.5 moles/L of KBr. and 1 M HNO_3. The total charge, equal to 42 mC, was applied in five different steps. Magnifications equal to a) x37; b) x800; and c) x1.5k. The images were acquired with an acceleration voltage of 20 kV

The different morphology and the shape of the particles is attributed to the presence of KBr. It has been demonstrated, via UV-vis measurements by Zhong et al.[153] that Br^- acts as a capping agent forming a complex ($BiBr_x$). This complex increased and accelerated the adsorption of the Bi^{3+} ions on the substrate, leading to an increase of the nucleation rate and therefore favouring the formation of small particles. In addition, the Br^- ions adsorbed on the Bi film during the deposition, influencing the growth of the particles. Spherical morphologies were obtained applying a potential of -0.56 V vs Ag/AgCl for concentrations of KBr equal to 0.01 M, a concentration fifty times lower than the one used in this work. This difference could be due to the overpotential applied for the electrodeposition, as within this work a potential equal to -0.13 V vs Ag/AgCl was applied.

4.3 Nucleation mechanism study

To understand the possible nucleation mechanism for the different Bi crystallites, the current transients obtained during the deposition processes were analysed and the Scharifker and Hills models for 3-D-growth used[145]. The models describe the two extreme cases of nucleation kinetics:

instantaneous and progressive. To understand the mechanism of growth and nucleation on the GC substrates, the experimental I_{max} (the maximum current observed in the current transient) and t_{max} (the time at which the maximum current was observed) were extrapolated from the current transients and the ratio $\frac{I^2}{I_{max}^2}$ was plotted as a function of $\frac{t}{t_{max}}$. The theoretical curves for the two mechanisms were obtained using Equation (4.2) and (4.3) for instantaneous and progressive nucleation respectively[145].

$$\frac{I^2}{I_{max}^2} = \frac{1.9542}{\frac{t}{t_{max}}}\left(1 - e^{-1.2564\frac{t}{t_{max}}}\right)^2 \quad (4.2)$$

$$\frac{I^2}{I_{max}^2} = \frac{1.2254}{\frac{t}{t_{max}}}\left(1 - e^{-2.3367\left(\frac{t}{t_{max}}\right)^2}\right)^2 \quad (4.3)$$

The models were applied for the current transients obtained in the deposition bath containing 2, 20 and 200 mM of $Bi(NO_3)_3$. The current transient obtained for the deposition performed in the presence of 500 mM KBr was also investigated. The experimental, the progressive and instantaneous curves are shown in Figure 4.27. The experimental curves are in good agreement with the 3-D nucleation model. In addition, a concentration dependence was observed: the nucleation mechanism changes from progressive (Figure 4.27a and b) to instantaneous (Figure 4.27c) by increasing the concentration of Bi^{3+} in the deposition bath. Specifically, for the 20 mM deposition bath, a mixed mechanism was observed: before the I_{max}, the mechanism is instantaneous, while immediately after a progressive trend is observed. This means that after the current pulse and during the increase of the electroactive area (i.e. when the current increase before I_{max} is reached), the nucleation rate is high, and a small number of sites are formed, while after I_{max}, the growth of pre-existing nuclei occurs while new nuclei are formed. For the lowest and highest concentration, the same mechanism was observed for the entire current transient. The dependence of the formation mechanism on the concentration was previously explained in terms of the reduction of the surface energy in the presence of a high or low number of ions at the liquid boundary film[298]. When the concentration is low, the ions in solution are more disperse. Once they are deposited on the substrate in metallic form, it is more probable that other ions, still in solution, will be deposited toward the nearest neighbour, forming small nuclei, than travel apart to increase the size of the pre-existing nuclei. On the other hand, if the concentration is high, many nuclei are formed at first and the new atoms will be deposited on the top of each other making the existing nuclei larger more than forming new ones. A similar trend was observed in two different works[115,149]: at the lower concentrations of Bi^{3+}, the experimental current transients were matching

the progressive theoretical curve, while at higher concentration instantaneous was the proposed mechanism. Interestingly, in both works, for 20 mM $Bi(NO_3)_3$ bath, an instantaneous mechanism was observed for the entire current transient. This can be the result of the different potential used during the deposition, as a potential dependence on the mechanism type was observed for 10^{-2} M concentrations of Bi^{3+}, but not for higher or lower ones. The potential dependence was also observed when Bi was deposited on FTO[329] and as well for other metals electrodeposited on foreign substrates[330], suggesting that the potential applied for the deposition is one of the main factors influencing the mechanism of nucleation and growth of the crystallites.

2 mm [$Bi(NO_3)_3$]

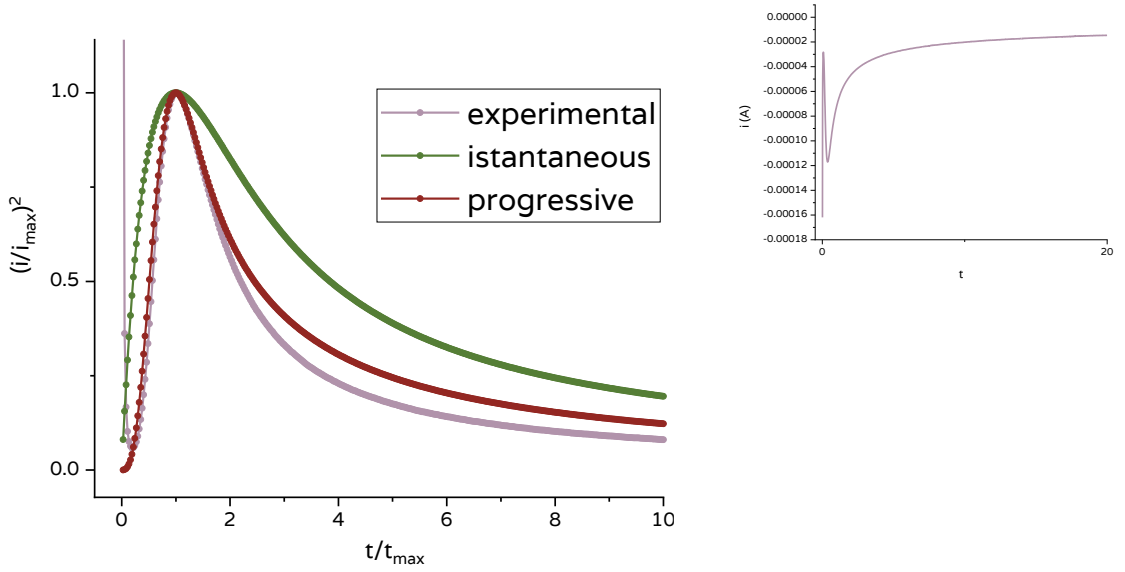

20 mM [$Bi(NO_3)_3$]

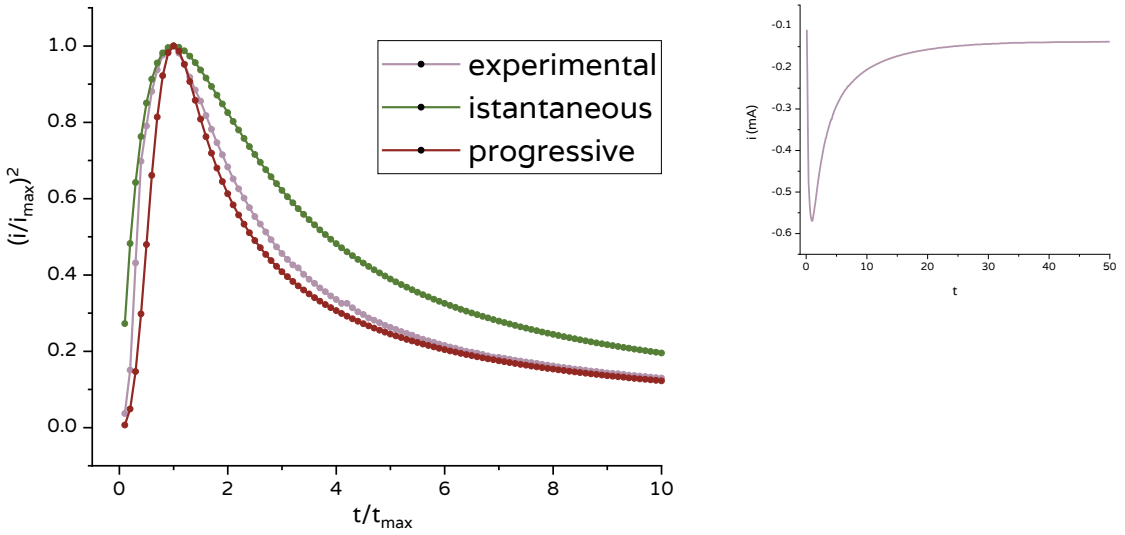

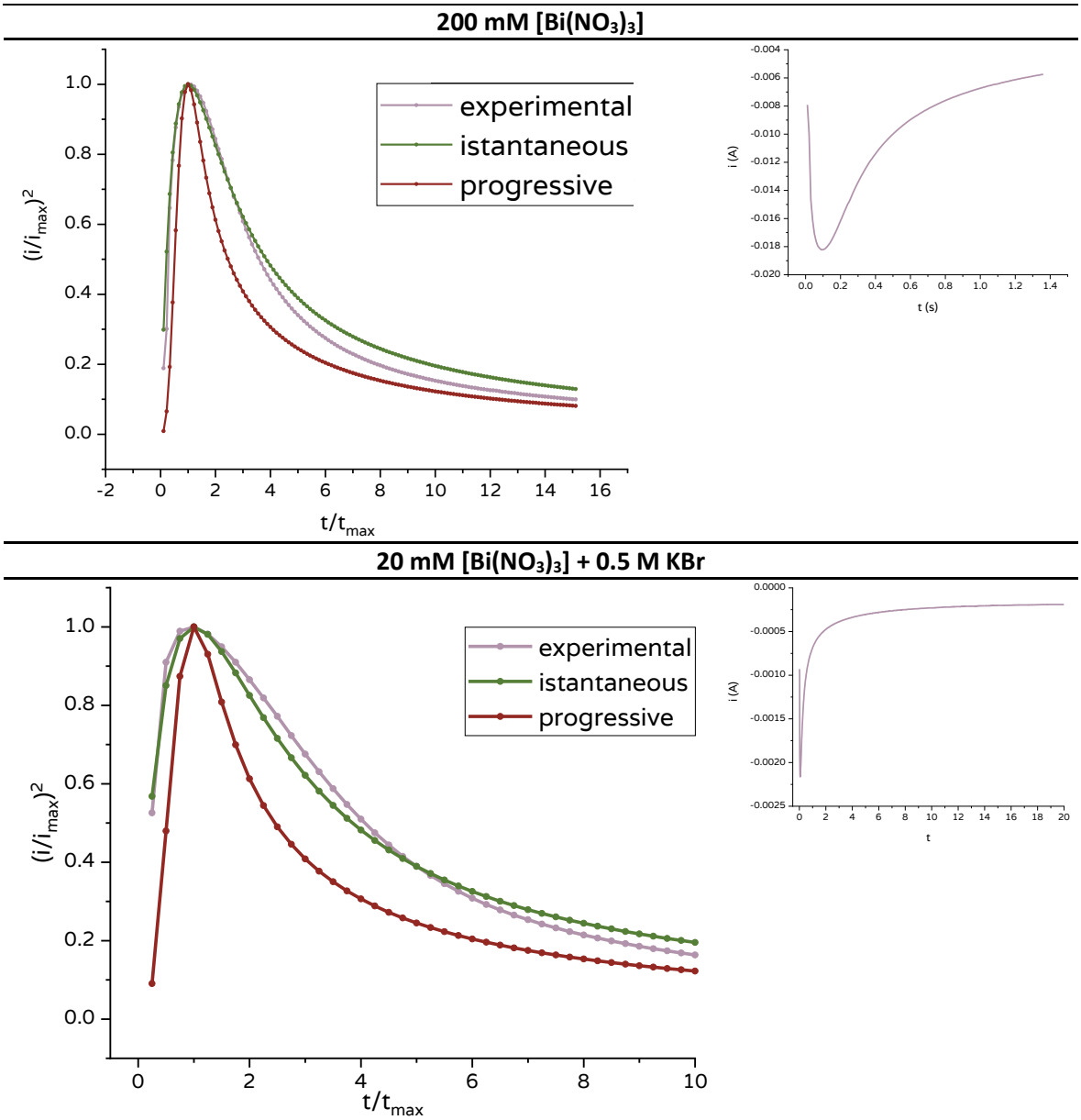

Figure 4.27: Experimental and theoretical curves for the Scharifker and Hills models of 3-D growth for deposition bath containing $Bi(NO_3)_3$ with concentration equal to a) 2 mM; b) 20 mM; c) 200 mM; and d) 20 mM + 500 mM KBr. The current transient for each deposition are shown in the insets

The mechanism for the formation of Bi crystallites in deposition bath containing 0.5 M KBr (Figure 4.27d) was found to be instantaneous Based on the theory proposed by Zhong et al.[153], the formation of $BiBr_x$ will favour the formation of small particles in two ways: first, it increases the adsorption of the Bi cations, second, it accelerates the reduction speed of the metal ions. In addition, at high concentrations of KBr, the excess Br^-, that did not form the complex with Bi^{3+}, adsorb on the Bi nanoparticles already formed on the substrate, blocking the growth of the Bi deposit and favouring the formation of new nuclei.

4.4 Real surface area: the oxygen adsorption monolayer

The real area of a nano- and micro-structured electrode can be significantly different from the geometrical area and results of the catalytic experiments can be misleading if the geometrical area is considered instead of the real one[331,332]. It was demonstrated before that several electrode parameters, such as the real surface area, the thickness and the structure of the porous film and can influence the catalytic activity of the electrode[222]. For this reason, it is very important to have quantitative information about the area of the different electrodes. To do so, the calculation of the real (or microscopic) area was performed via the oxygen adsorption method for all the modified Bi-GC electrodes. The CVs for only one electrode (Bi-GC(3:3)200) are shown in Figure 4.27 as an example. For each type of Bi modified electrode, three different electrodes were produced, and three measurements were performed for each electrode. The charge for the reduction process and the real area calculated for each modified electrode are shown in Table 4.8.

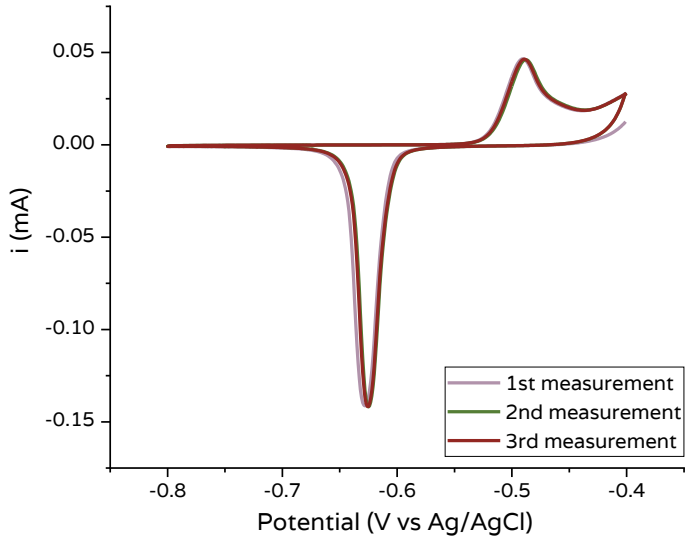

Figure 4.28: Cyclic voltammetry measurements for the calculation of the real area for the Bi-GC(3:3)200 electrode. The measurements were performed in 50 mM KOH at 10 mV/s

The microscopic areas of all the Bi modified electrodes are significantly larger than the geometrical ones. The real areas are from 12x to 84x times bigger than the geometrical ones and from 6x to 43x times bigger than those of the Bi disks (Θ = 4.2 mm was chosen for comparing the real areas of the micro-structured electrodes with planar ones) , as it has the most similar geometrical area among the three Bi disks produced), making the Bi modified electrodes possibly better candidates for catalysis, as higher area can mean the presence of more active sites that would be beneficial for the CO_2 reduction reaction[333]. In terms of magnitude of the area, it seems that the multi-step deposition did not significantly improve the area of the electrode. An exception was observed for the (5:3) electrodes that, for the higher Bi^{3+} concentrations, presented a very similar (20 mM) or even higher (200 mM) area than the one of the single-step deposition electrodes.

Interestingly, the electrodes produced using the low concentration baths presented the lowest area values or a very low reproducibility. However, a multi-step deposition seemed to have significantly improved the reproducibility of the electrode deposition when KBr was used as additive. Regardless, the electrode produced in the presence of 500 mM of KBr presented the highest area values for the Bi modified electrodes.

Table 4.8: Experimental charge, roughness factor, geometrical and real area for the Bi modified electrodes

Electrode	A_{geo} [cm^2]	average Q [µC]	A_{real} [cm^2]	r_f
Bi disk (4.2 mm)	0.13854	360 ± 16	1.92 ± 0.08	14
Bi-GC	0.071	485 ± 172	2.1 ± 0.9	29
Bi-GC(3:3)20		203 ± 17	1.08 ± 0.09	37
Bi-GC(5:3)20		311 ± 80	1.7 ± 0.4	23
Bi-GC(5:5)20		242 ± 106	1.3 ± 0.6	18
Bi-GC(3:3)2		226 ± 38	1.0 ± 0.2	14
Bi-GC(5:3)2		138 ± 30	0.83±0.03	12
Bi-GC(5:5)2		632 ± 251	3 ± 1	48
Bi-GC(3:3)200		342 ± 6	1.83 ± 0.04	26
Bi-GC(5:3)200		487 ± 92	2.6 ± 0.5	37
Bi-GC(5:5)200		192 ± 38	1.0 ± 0.2	14
Bi-GC0.5		485 ± 12	2.59 ± 0.06	36
Bi-GC(5:3)20_0.5		630 ± 67	3.4 ± 0.4	48

The real areas obtained for the Bi micro-structured electrodes vary between 0.8 and 3.4 cm^2. The largest difference in area is observed among electrodes with different morphologies, e.g. dendrites versus spheres. In general, electrodes with spherical particles (Bi-GC0.5 and Bi-GC(5:3)20_0.5) presented the highest areas (2.59 and 3.4 cm^2). Bi-GC(5:3)200, that presented small polygonal structures crystallites, showed a comparable real area with Bi-GC(5:3)20_0.5 (A_{real} = 2.6 cm^2). Its higher areas, in comparison with the electrodes presenting dendritic structures, could be due to the different layers of spheres formed (see Figure 4.26c). In addition, SEM images at high magnifications were not acquired, making impossible the study of the surface of the spherical particles, that might present imperfections that can increase the total area of the deposit. Bi-GC(5:5)2 presented a surface area equal to 3 cm^2. This high value was expected as the crystallites presented dendrites with complex secondary and tertiary arms, structures that are well known to have high surface areas[119,164,334]. However, the reproducibility of the electrode is quite low (standard deviation for the A_{real} values = ±1 cm^2), making the comparison difficult. On the other hand, Bi-GC(3:3)2 presented one of the lowest areas regardless of the complex structure of the dendrites (see Figure 4.21). This is due to low quantity of clusters of the complex dendrites, that were able to completely cover the substrate. In general, the electrodes produced in a 20 mM deposition bath (in the absence of capping agent) presented very similar areas (see from the 2nd to

5th row in Table 4.8), suggesting that, for the system investigated here, using a single or a multi-step depositions does not influence significantly the final real area of the film. As expected, a significant difference in real area is observed between bulk Bi electrodes (Bi disks) and micro-structured ones. In the first row of Table 4.8 the values of roughness factors and real area for Bi disk (4.2 mm diameter) are shown. Considering that the geometrical area of the Bi disk is two times higher, it is clear that the real area of the Bi micro-structured is notably larger. The roughness factors of Bi micro-structured electrodes vary between 18 and 48 (if the three electrodes with the lowest surface areas are not considered), a value 1.3 to 3.4 times higher than for Bi disk, making the Bi micro-structured electrodes better candidates for catalysis purposes in terms of magnitude of surface area.

4.5 Capacitance measurements

The capacitance of the Bi modified electrodes was calculated to compare the nature of the Bi crystallites (like composition and oxidation state) with the Bi bulk metal (from the Bi disks). To do so, the areas obtained from the capacitance values ($A_{capacitance}$) and from the reduction of the oxide monolayer method (A_{real}) are compared. The chemical nature of the bismuth surfaces is the same only if the two areas correspond[265]. To obtain $A_{capacitance}$, the capacitance values for the Bi modified electrodes were divided by a standard capacitance, obtained for the Bi disks in Chapter 3 (see Equation (4.4)).

$$A_{\text{capacitance}} = \frac{\text{Bi modified electrodes capacitance } [\mu\text{F}]}{\text{standard capacitance } \left[\frac{\mu\text{F}}{\text{cm}^2}\right]} \qquad (4.4)$$

The standard capacitance is the capacitance of an ideal flat surface of the electrode[265]. In this work, the standard capacitance was the average capacitance obtained for the Bi disks (see Chapter 3, paragraph 2.3). The capacitance was calculated by performing a scan rate study at a potential where there is no faradaic reaction. The capacitance of the modified Bi electrodes is the combination of the capacitance of the substrate and the capacitance of the crystallites. For comparison, the capacitance was also calculated for the bare GC. The capacitance (in µF), the $A_{capacitance}$ and the A_{real} for the Bi modified electrodes are gathered in Table 4.9

Table 4.9: capacitance values, area calculated via capacitance method ($A_{capacitance}$), A_{real} values calculated using the oxygen adsorption method and ratio between the area values calculated with the two different methods for all the Bi modified electrodes produced via electrodeposition in different deposition solutions containing $Bi(NO_3)_3$

Electrode	capacitance [µF/cm^2]	$A_{capacitance}$ [cm^2]	A_{real} [cm^2]	$\frac{A_{capacitance}}{A_{real}}$
Bi-GC	2.7 ± 0.1	2.1 ± 0.3	2.1 ± 0.9	1.0
Bi-GC(3:3)20	7.3 ± 0.2	2.9 ± 0.5	1.08 ± 0.09	2.7
Bi-GC(5:3)20	3.4 ± 0.3	3.7 ± 0.6	1.7 ± 0.4	2.2
Bi-GC(5:5)20	6.8 ± 0.2	3.3 ± 0.5	1.3 ± 0.6	2.5
Bi-GC(3:3)2	5.1 ± 2	1.9 ± 0.3	1.0 ± 0.2	1.9
Bi-GC(3:3)200	2.58 ± 0.08	1.8 ± 0.3	1.83 ± 0.04	1.0
Bi-GC(5:3)2	6.4 ± 0.3	2.0 ± 0.3	0.83 ± 0.03	2.4
Bi-GC(5:3)200	2.2 ± 0.2	0.7 ± 0.1	2.6 ± 0.5	0.3
Bi-GC(5:5)2	3.6 ± 0.4	4.0 ± 0.6	3 ± 1	1.3
Bi-GC(5:5)200	6.5 ± 0.2	2.4 ± 0.4	1.0 ± 0.2	2.4
Bi-GC0.5	2.5 ± 0.4	2.4 ± 0.4	2.59 ± 0.06	0.9
Bi-GC(5:3)20_0.5	1.5 ± 0.2	1.9 ± 0.3	3.4 ± 0.4	0.6

According to the results in Table 4.9, it could be assumed that the chemical nature of the Bi crystallites (i.e. the chemical and the crystallographic composition) is different from the Bi bulk of the Bi disks. All the areas are significantly different, except for Bi-GC and Bi-GC(3:3)S200. The two electrodes had in common the presence of hexagonal plates, that might have the same chemical nature of the Bi disk. However, even if the quantity of the hexagonal plates is high in Bi-GC(3:3)200, it is not in Bi-GC. One of the main factors that could have a significant influence in the nature of the Bi micro-structured electrodes and the Bi disks is the nature of the oxide layer (like the composition and the crystal structure) on the surface of the crystallites. Unfortunately, knowledge of crystal structure and composition of the crystallites are required to make a fair comparison. In contrast, for the same chemical and crystallographic composition, the difference in roughness factor should not significantly influence the capacitance values, as capacitance is area normalised (see Chapter 3, Section 3.3.3). In this case, a difference among electrodes produced with the same concentration of Bi precursor was obtained, but with a different number of steps (see Table 4.9). This might be due to differences in the quantity of the native oxide layer and the extent it was exposed to the solution because of the different size of the crystallites. This might also influence the quantity of the ions with the surface. In the literature, several values of capacitance for Bi micro and nanostructured electrodes are present[102,153,194]. The values obtained within this work are quite similar to the one obtained by Kim et al.[102]. They measured the capacitance for a series of Bi nanoflakes electrodes and the values varied from 0.4 µF/cm2 to a max of 13.1 µF/cm^2. The capacitance increased as a function of the quantity of edges and corners in the deposits. However, they did not discuss the possible contribution of the native oxide layer. Differently, larger capacitance for Bi electrodes were obtained in the work of Zhong et al[153]. For an electrode

presenting complex Bi dendritic structures capacitance equal to 1.93 mF/cm^2 was calculated, while for flower-like Bi deposit, a value of 0.184 mF/cm^2 was obtained. They suggested that the difference between the two capacitance values was a reflection of the different surface areas.

4.6 Conclusions

In conclusion, several Bi modified electrodes were produced via electrodeposition for the reduction of CO_2. Several bismuth electrodes were produced and then characterised. Among the parameters that influenced CO_2RR (see Figure 4.1), the ability of CO_2 to bind onto the metal was selected to try and modify the magnitude of the area and the fraction of Bi atoms on the surface (see green section in Figure 4.1) were performed. This was carried out by changing several deposition parameters, that also allowed changes on the type of active sites on the surface, as different chemical and crystal composition can be obtained (see **objective 1.a**, in Section 1.7). When the deposition parameters were modified a range of results were obtained:

• multistep deposition: no significant increase in the magnitude of the area and in the morphology of the particles was observed. However, the substrate seemed more covered because of the presence of smaller particles.

• different concentration of the Bi precursor: different morphologies were observed, suggesting a possible different fraction of Bi atoms on the surface or even different exposed crystal faces (objective 1.a). However, the long times required for the deposition at low concentration of Bi^{3+} (2 mM) and the rate at which the charge was passed for high Bi^{3+} concentrations (200 mM) made the deposition challenging and a poor quality of the deposit was obtained (i.e. low stability of the deposit. objective 2: not fulfilled).

• presence of an additive: different morphologies were observed, *suggesting a different fraction of Bi atoms on the surface* (objective 1.a). An increase of the area was observed for all the depositions performed. This was unexpected, as the morphology obtained in the presence of the additive was spherical, which should give a smaller area than dendritic structures. This might be due to the ability of the spheres to pack and cover the substrate more efficiently than the dendrites or to a faster mass transport of the OH^- ions in the presence of sphere than dendrites. The change in morphology was obtained because of the absorption of the anion of the capping agent on the surface of the substrate.

This suggests that only the last two parameters have an influence in the fraction of the Bi atom on the surface and therefore on the binding of CO_2 onto the metal (See Figure 4.1). However, a more

efficiently covered substrate is desirable as less contribution from the substrate will be observed during catalysis experiments, suggesting that performing a multistep deposition can be advantageous.

Chapter 5 : Imidazolium-based ionic liquids as co-catalyst for CO_2 reduction

5.1 Introduction

As discussed in Chapter 1 and shown in Figure 4.1, the overall electrocatalytic process is influenced by a number of transport and kinetic parameters. In particular, the rate of heterogeneous electron transfer, the adsorption of CO_2 at the interface and its interfacial concentration are important. These processes can be influenced by modifying the electrode surface, e.g., to enhance CO_2 binding or provide a more favourable local microenvironment for the reduction to occur. In the last fifteen years, ionic liquids (ILs) have attracted increasing attention due to their unique properties, making them suitable for use in a wide range of fields: from synthetic organic chemistry to catalysis[335] and from analytical chemistry to enzymatic reactions[336]. In particular, their application in electrochemistry, and specifically for CO_2 reduction, is growing as a result of promising results shown in the literature[24,25,167,169,231,337,338]. They are particularly interesting as, among other properties, they present low vapour pressure and high solubility for CO_2.[24] In addition to making them good candidates for CO_2 capture, it makes them suitable for CO_2 capture and utilisation (CCU), as it has been demonstrated that ILs behave as successful co-catalysts for the CO_2 reduction reaction[1,24–26]. Imidazolium ILs can increase the faradaic efficiencies and the selectivity of the reduction reaction[169,231] at several metal electrodes, including Ag[24,25,231], Au[337,339] and Bi[169,245], and directing the outcome of the reaction[167]. Here, the ability of imidazolium ILs to influence the CO_2 reduction reaction (CO_2RR) was investigated. First, some commercial ILs were tested via cyclic voltammetry (CV) using different metal electrodes in organic solutions. This established benchmark systems that could be directly compared with the literature, and then used to evaluate non-commercial ILs synthesised in-house. The non-commercial ILs were characterised and then preliminarily tested via CV for CO_2RR in both organic and aqueous systems. In addition, preliminary investigation via cyclic voltammetry under pH-control, supported by IR measurements, into the ability of these ILs to behave as proton-donor agents was pursued. Quantitative analyses were performed performing electrolysis experiments (see Chapter 6).

5.2 Preliminary tests for CO_2 reduction with several commercial imidazolium-based ionic liquids

Several commercial and newly synthesised imidazolium based ILs were initially tested via cyclic voltammetry (CV) under argon and CO_2 atmospheres to investigate their ability to reduce the overpotential for the reduction of CO_2 on different metal electrodes.

5.2.1 [EMIM]BF_4

In recent years, 1-ethyl-3-methylimidazolium cations ($[EMIM]^+$) have been used extensively as co-catalysts for the CO_2RR with Ag electrodes[25,231,340]. For this reason, [EMIM]BF_4 (see structure in

Figure 5.1) was chosen as a benchmark compound and a set of experiments was performed using an Ag disk working electrode (WE), a Pt wire counter electrode (CE) and an Ag wire with ferrocene dissolved in solution as a quasi-reference electrode (QRE). CV experiments were carried out in MeCN solution with 0.1 M $[TBA]PF_6$ as supporting electrolyte with and without 10 mM $[EMIM]BF_4$. In Figure 5.1, the cyclic voltammograms (CVs) for the system with and without IL, both under Ar and CO_2 atmospheres are shown. The current was considered as the electrochemical surface area (ECSA) for the Ag electrodes was not calculated and the normalisation of the current could not be performed.

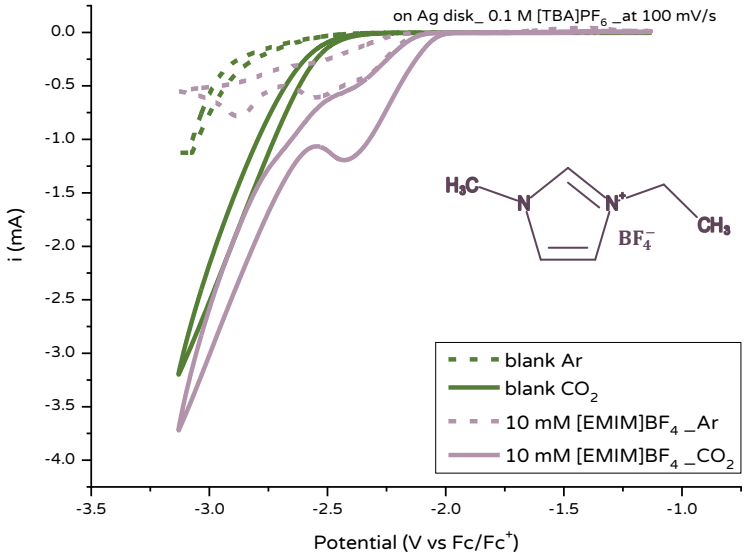

Figure 5.1: CVs at Ag electrode with (purple curves) and without (green curves) ILs (10 mM) under Ar (dashed curved) and CO_2 (solid curves) in a solution of $[TBA]PF_6$ 0.1 M. Scan rate = 100 mV/s . The structure of the IL is shown

The system without IL and under Ar (dashed green curve) showed an increase in current at around -2.7 V vs Fc/Fc^+. At the same potential, under CO_2 (solid green curve), the current was four times higher than under N_2. The higher current and the 0.15 V more positive onset potential for increase of current for the system under CO_2 is attributed to the intrinsic ability of the Ag electrode to reduce CO_2[238]. The increase of current observed at -2.7 V vs Fc/Fc^+ under Ar is likely due to H_2 evolution resulting from the natural presence of water in non-anhydrous MeCN and ILs, which is known to typically be <150 ppm[341]. In contrast, both under Ar and CO_2, when the IL is present in the system (purple curves), larger current densities and different features were observed in the reduction sweep. For the purple solid curve, the onset potential was around -2.1 V, around 0.1 V more positive than for the system under Ar with $[EMIM]^+$. For potentials more negative than -2.5 V vs Fc/Fc^+, the sharp increase in the current and the shape of the CVs is very similar to the one presented under CO_2 in the absence of IL (solid green curve). However, the higher current and the more positive onset potentials observed in the presence of the IL (solid purple curve) suggested an improvement

of the catalytic activity of the Ag electrode in the presence of ILs. The peak present around -2.4 V vs Fc/Fc^+ in the solid purple curve is ascribed to a process involving the IL, as it was observed at the same potential as well under Ar. In previous works[24,342,343], a peak at similar potentials has been observed under CO_2 and related to the formation of an imidazolium-CO_2 complex, while the peaks under Ar were attributed to reductions of the imidazolium ring to a carbene derivative and subsequent dimerization processes. The small peak present in the re-oxidation sweep at -1.4 V under CO_2 in the presence of IL has not been identified in the literature previously, but could potentially be due to the electrochemical release of CO_2 back into solution, which has been observed with CO_2/4,4'-bipyridine adducts previously[344].

Ag electrodes exhibited higher currents and more positive onset potential under CO_2 than under N_2 in the presence of $[EMIM]BF_4$, but to understand if this IL induces catalysis on other electrode materials, CV measurements were performed with different working electrodes. Gold, platinum and glassy carbon (GC) disks were tested in MeCN with 10 mM $[EMIM]BF_4$ and the reduction sweep curves are shown in Figure 5.2. Pt and GC electrodes showed similar activity with a small reduction peak around -2.8 V vs Fc/Fc^+. Comparable current and *distinctly* negative onset potentials were observed, with the onset potential for the current increase of Pt being more positive than GC. On the other hand, Ag and Au electrodes exhibited significantly more positive onset potentials (with a difference of almost 0.5 V) and a sharp increase in the current, with the Ag electrode having an onset potential 0.1 V more positive than Au. In general, it is evident that Au and Ag electrodes presented better activity for the reduction of CO_2 than Pt and GC electrodes. These results confirmed the literature findings, as it is well known that unmodified Pt and GC electrodes exhibit poor catalytic activity towards CO_2RR. On a Pt surface the CO produced from CO_2 reduction is strongly adsorbed on the surface of the electrode, poisoning the surface[43,345]. Similarly, the products produced during the reduction step are adsorbed irreversibly on the surface of the GC electrode, inhibiting the catalytic cycle[4, 9,10]. It is important to highlight that the currents were not normalised for these experiments as the real area for all the four electrodes was not calculated (see Figure 5.2). However, the differences in currents and onset potentials between Pt, GC and Au, Ag electrodes are sufficiently large for the general trends to be valid even if the roughness factors of Pt and GC electrodes were smaller than those for Ag and Au electrodes.

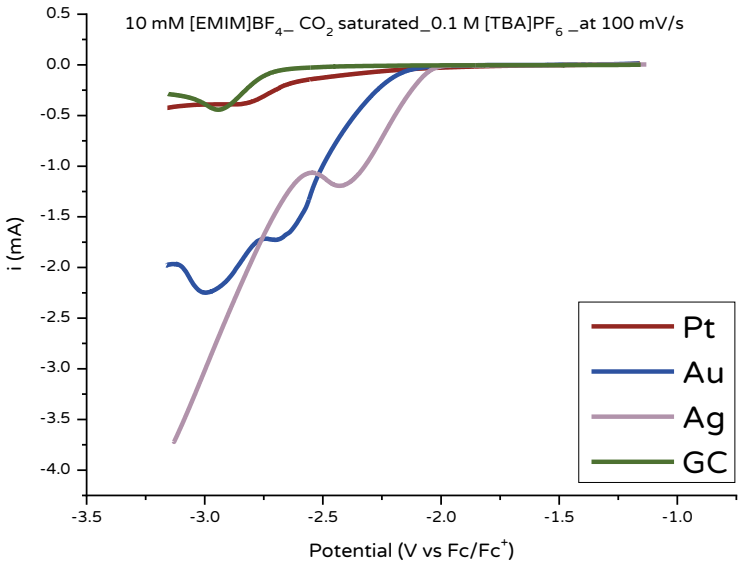

Figure 5.2: Reduction sweeps for a solution 10 mM of [EMIM]BF_4 under CO_2 atmosphere at different WE: platinum (red curve), gold (blue curve), silver (purple curve) and glassy carbon (green curve) disks. Electorlyte: 0.1 M [TBA]PF_6, scan rate = 100 mV/s

Experiments under Ar were performed to investigate the differences in catalytic activity of Ag and Au electrodes in the presence of IL (Figure 5.3). At Au electrode, only one reduction peak at -2.8 V vs Fc/Fc^+ was observed under Ar, while two peaks are present under CO_2. No peak was observed under Ar and CO_2 at the same potential in the absence of $[EMIM]^+$. As previously proposed for Ag electrodes, the reduction peak observed under Ar is probably due to reduction of the $[EMIM]^+$ to a carbene species as suggested in two different works[24,342]. The presence of the carbene specie was proposed after ^1H NMR analyses of the pure ILs and the catholyte after electrolysis experiments. After electrolysis, an additional set of peaks were observed for the hydrogens present in the imidazolium ring, suggesting the presence of an additional species formed during catalysis. The formation of a complex between the carbene species and CO_2 (the imidazolium-CO_2 complex) was reported in previous studies[346,347]. On the basis of this hypothesis, it is reasonable to consider the increase in current density at -2.7 V vs Fc/Fc^+ is due to reduction of CO_2. This would mean that the formation of the imidazolium-CO_2 complex at Ag electrode started at more positive potentials and considering the more positive onset potential, it is, therefore, reasonable to say that Ag electrode showed the best catalytic activity among the four electrodes tested in a solution 10 mM of [EMIM]BF_4.

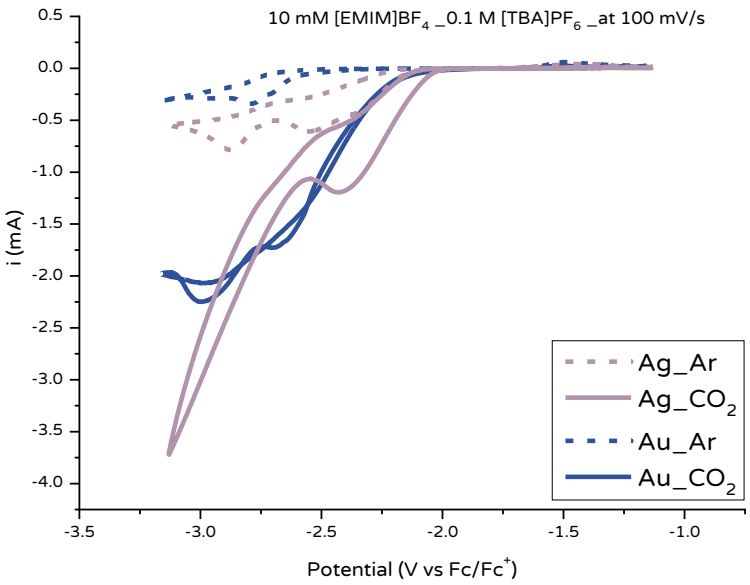

Figure 5.3: CVs of a solution of [EMIM]BF_4 10 mM at Ag and Au disk electrodes under Ar and CO_2. Electrolyte: 0.1 M [TBA]PF_6, scan rate = 100 mV/s

5.2.1.1 [EMIM]BF_4 in the presence of water

In the literature, CO_2RR at Ag has been proposed to occur via a proton-coupled electron transfer mechanism[43]. For this reason, a source of protons would increase the catalytic activity of the system and certain cases, like for imidazolium-based ILs[24], a lower pH was demonstrated to be necessary to observe any CO_2 reduction[348,349]. Considering some water is already present in non-anhydrous MeCN (<150 ppm[341]), the addition of protons in the system needs to be carefully controlled, as high proton concentrations would promote the hydrogen evolution reaction (HER), suppressing CO_2RR. For this reason, a new set of CV experiments (Figure 5.4) was performed adding an increased quantity of water in the system. It is important to highlight that the ILs are highly hygroscopic[350] and amount of water lower than 0.5% are presented (based on the data provided by the manufacturer), therefore care was taken to avoid the exposition of the IL to air. Sequential additions of water (the first addition was equal to 0.5% v/v) were followed by the acquisition of a cyclic voltammogram. The shape of the voltammograms remained unchanged after quantities of water smaller than 1.0 % v/v were added. For higher aliquots, the shape of the CVs changed significantly: the peak at -2.4 V vs Fc/Fc^+ (see purple, yellow and red curves) shifted to -2.9 V for the blue curve (2.0% v/v water) and to -2.75 V for the green curve (5.0% water) suggesting a decreasing in the catalytic activity towards CO_2RR or the presence of a different process dominating the overall CV response. For small amounts of added water (0.5 and 1.0 % v/v), the onset potential is slightly more positive (0.02 ≤ onset potential shift ≤ 0.03 V) than for the system with only trace adventitious water. In addition, a rise in the current ratio $\left(\frac{i_{CO_2}}{i_{Ar}}\right)$ at the same potential was observed, suggesting an increase in the catalytic activity of the system for small additions of water. Generally, an increase

in $\frac{i_{CO_2}}{i_{Ar}}$ was observed at higher water concentration, but a significant shift in onset potential was not observed. Similar results were obtained by Zhao *et al.*[24], but higher current densities were observed after additions of water and the shape of the CVs shape already changed with the addition of 1.0% of water. Considering that the concentrations of IL used for the experiments in the literature were 5x lower than in the present work, it is possible that because of the lower availability of protons from the imidazolium-based IL (pK_a of H in position 2 of the BMIM ring = 33.7)[167], the water became the major source of protons. At higher water concentrations (2.0 and especially 5.0% v/v) some noise was observed at negative potentials due to HER (Figure 5.4). This suggestion was confirmed by the addition of more water into the solution (Figure 5.5).

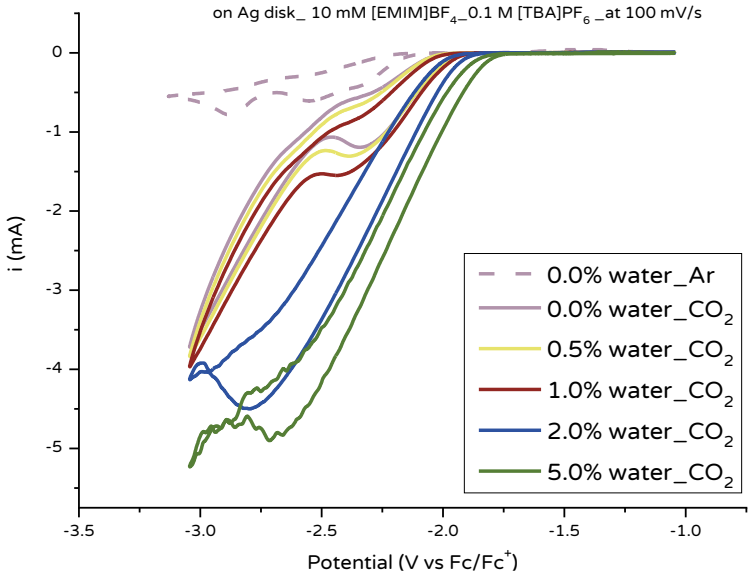

Figure 5.4: CV experiments in a solution of $[EMIM]BF_4$ 10 mM at Ag disk with concentrations of water between 0 and 5%. Electrolyte: 0.1 M $[TBA]PF_6$, scan rate = 100 mV/s

5.2.1.1.1 High content of water

An additional introduction of water led to a complete change in the shape of the voltammogram: for 25% and 50% water, the CVs presented a spike-like shape (Figure 5.5). Considering that the curves for the system under Ar (dashed) and under CO_2 overlapped almost perfectly and no significant differences in the onset potentials and current densities are observed, it is reasonable to conclude that the predominant process was likely the undesirable HER. Clearly at water concentrations of 25 and 50 %, no appreciable CO_2 reduction is occurring.

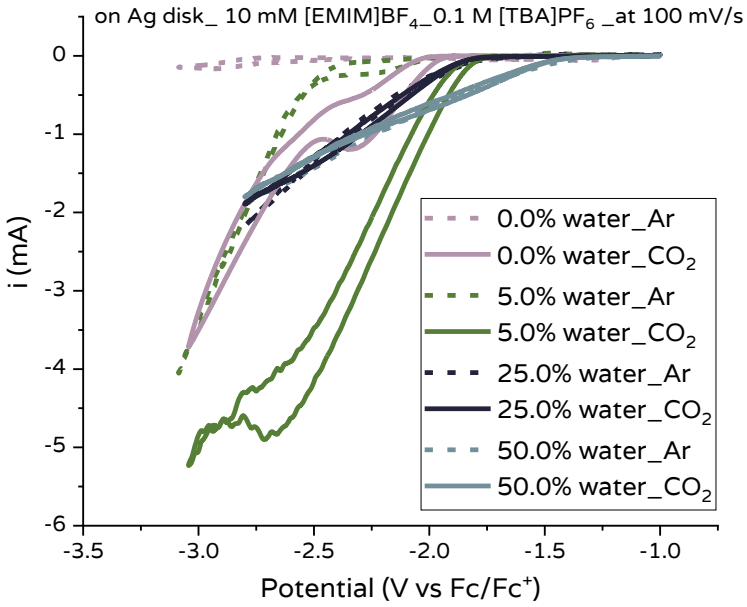

Figure 5.5: CV experiments at Ag disk in a solution of [EMIM]BF_4 10 mM at Ag disk with the presence of high concentrations of water. Electrolyte: 0.1 M [TBA]PF_6, scan rate = 100 mV/s

To better understand the role of the ILs and the water in improving the catalytic activity of Ag electrodes, CV measurements under Ar and CO_2, with and without IL, and at different concentrations of water were performed. Figure 5.6a and b, show that the addition of 0.5 and 1.0% v/v of water do not cause an appreciable improvement in the catalytic activity when compared with the system without addition of water: the current densities, onset potentials and shape of the CVs are very similar. In contrast, for the solution with 2.0% v/v of water, the current densities and the shape of the CV under Ar and CO_2 are significantly different (Figure 5.6c). Under CO_2, the first peak shifted to more negative potentials suggesting that more energy is necessary for the imidazolium-CO_2 complex to be formed.

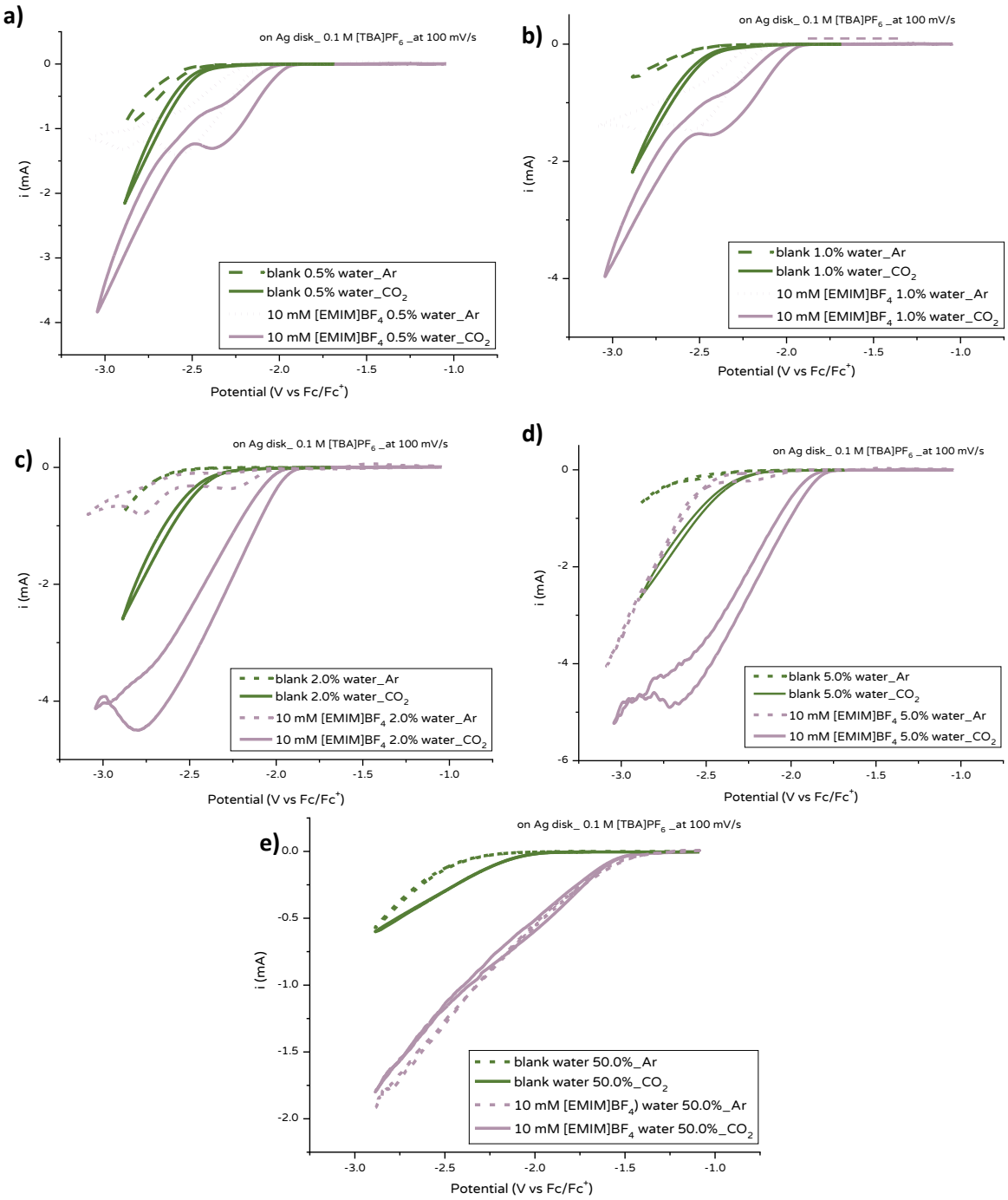

Figure 5.6: CVs with and without 10 mM IL, at Ag disk, under Ar and CO_2 for the system content of water equal to a) 0.5%, b) 1.0%, c) 2.0%, d) 5.0% and e) 50% v/v. Electrolyte: [TBA]PF_6 0.1 M. Scan rate = 100 mV/s

Interestingly, for 5.0 % v/v added water, the onset potential shifted negative by -0.4 V in comparison with the E_{onset} for the system with 2.0% of water. This reflects a shift from promoting CO_2RR to HER as a function of increasing proton concentration. By further increasing the content of water, the curves under Ar and CO_2 started slowly to approach one another, and eventually to overlap. In addition, for high concentrations of water, the shape of the CVs changed under Ar atmosphere, with the reduction peaks being less evident, suggesting the predominance of other processes at the electrode. In Figure 5.6e, the overlapping of the two curves in the presence of IL

was observed (water content: 50%). In summary, Figure 5.4-6 suggest that smalls addition of water (i.e. addition of a proton source) into the system increase the catalytic activity, while, for higher concentrations, HER is favoured. This was concluded by comparing the curves under Ar and CO_2 obtained when 25 and 50% v/v of water was added: the CVs presented very similar current densities and shapes, suggesting that the presence of CO_2 did not influence the processes happening at the electrode surface.

5.2.2 Other commercial ILs

Several other commercial imidazolium-based ILs were tested and compared with the benchmark compound ([EMIM]BF_4). It has been observed by Zhao et al.[24] that long alkyl chain in position 1 will present different current response during CV experiments. Here, CV experiments were performed using 1-butyl-3-methylimidazolium tetrafluoroborate ([BMIM]BF_4) to investigate the influence of the short alkyl chain in position 1. Based on the assumption that the CO_2 is linked to the carbon placed between the two nitrogen atoms[24] (see structure in Figure 5.3), different lateral alkyl chain might influence the stability of the CO_2 molecule in the imidazolium-CO_2 complex. In addition, the possible influence of a different functional group at the end of the lateral alkyl chain on the catalytic activity of system was studied by employing 1-(3-cyanopropyl)-3-methyl imidazolium chloride ([CPMI]Cl) and 1-(2-Hydroxyethyl)-3-methylimidazolium tetrafluoroborate ([HEMIM]BF_4). The structures of these three ILs are shown in Figure 5.7.

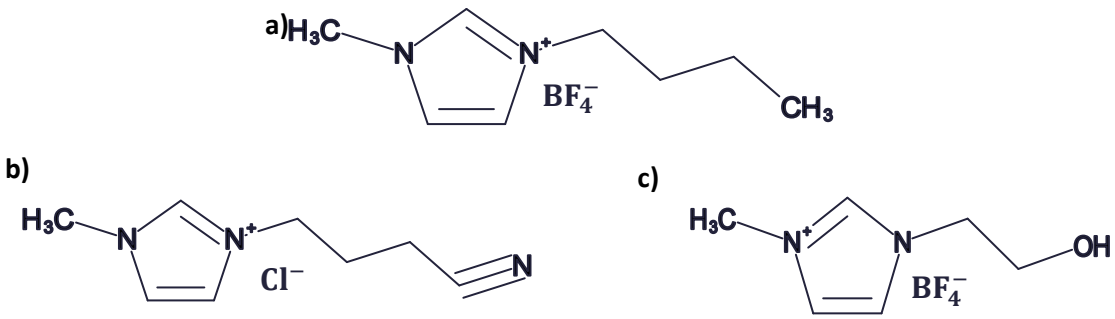

Figure 5.7: structure of three commercial ILs a) [BMIM]BF_4; b) [CPMI]Cl and c) [HEMIM]BF_4

In Figure 5.8 the reduction scans obtained for the system with 10 mM [BMIM]BF_4 under Ar and CO_2 are shown. Under Ar, [BMIM]BF_4 presented two reduction features, while [EMIM]BF_4 had presented three (see insert on the right), suggesting the occurrence of more reduction steps for the $[EMIM]^+$ ring than for $[BMIM]^+$ (see discussion in Section 5.2.1). This might be a consequence of the rotation of the longer alkyl chain of the BMIM cation, resulting in the hindrance of the carbon atoms in the ring and the consequent inhibition of possible successive processes of dimerization. The curve obtained with [BMIM]BF_4 under CO_2 (red curve) presented a very similar trend to the one observed

for [EMIM]BF_4 at the same conditions (purple curve), but with slightly different onset potentials and current densities, indicating a C2 alkyl chain results in slightly improved performance than C4.

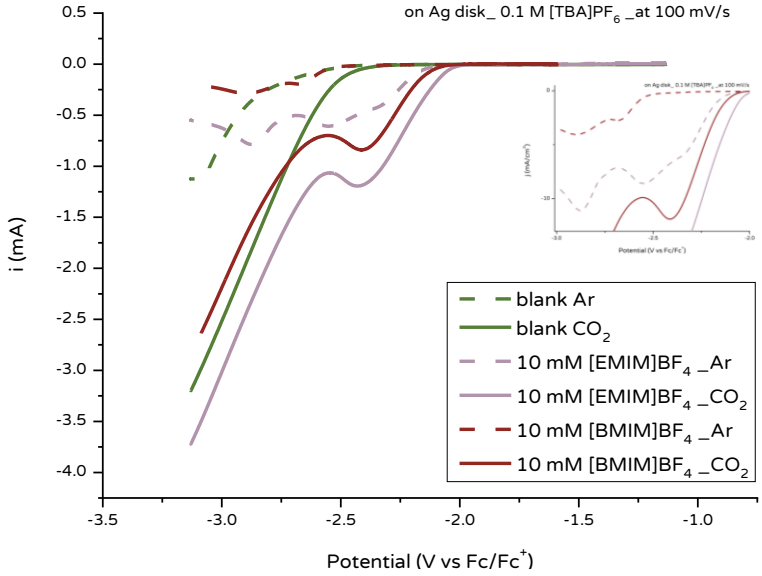

Figure 5.8: Comparison between 10 mM [BMIM]BF_4 and 10 mM [EMIM]BF_4 at Ag disk in 0.1 M [TBA]PF_6. The CVs were acquired at scan rate equal to 100 mV/s

In Figure 5.9a, the reduction sweeps for 10 mM [CPMI]Cl and [EMIM]BF_4 under both Ar and CO_2 are shown. Under Ar, [CPMI]Cl showed three reduction peaks as [EMIM]BF_4 with very similar onset potentials and current densities. Both the ILs presented the reduction peak at around -2.4 V attributed to the formation of the carbene derivate at similar values of potential, but [CPMI]Cl exhibited a less pronounced peak. In addition, the sudden increase of current around -2.4 V vs Fc/Fc^+ is slightly less sharp for [CPMI]Cl than for [EMIM]BF_4. It appears that the presence of cyanide group does not significantly affect the catalytic activity of the system. This is somewhat surprising as the cyano group should facilitate direct adsorption onto the Ag substrate via the nitrogen lone pair[351].

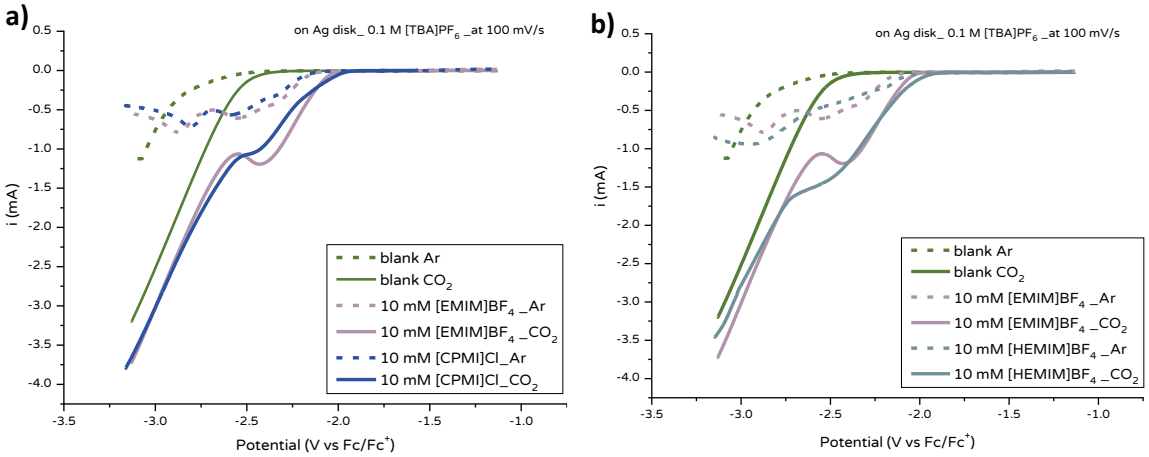

Figure 5.9: Comparison between [EMIM]BF_4 and a) [CPMI]Cl, b) [HEMIM]BF_4. CVs acquired in a at Ag disk in a solution of 0.1 M [TBA]PF_6. Scan rate = 100 mV/s

When a hydroxy group is present at the end of the alkyl chain (Figure 5.9b), a slightly different shape is observed in the reduction sweep. Under Ar (dashed light blue curve), the second reduction feature likely due to the reduction of the IL to the carbene derivate (see discussion in Section 5.2.1), that was present at around -2.5 V vs Fc/Fc^+ for the other ILs, disappeared. Under CO_2 (solid light blue curve), the peak around -2.4 V vs Fc/Fc^+ is less pronounced than for [EMIM]BF_4 and even than for [CPMI]Cl (see Figure 5.9a, solid dark blue curve). Similar current densities and onset potentials are observed for HEMIM and EMIM cations under both Ar and CO_2. Based on the similar onset potentials observed in the presence of both HEMIM and EMIM cations, it is therefore possible to conclude that the presence of a hydroxy group does not significantly improve the catalytic activity compared with EMIM cations. Considering that the length of the chain might be an influencing factor in the performance of the ILs, a comparison between [HEMIM]BF_4 and [BMIM]BF_4 was performed (Figure Figure 5.10). During this study, a paper by Jin et al.[352] was reported investigating the use of [HEMIM]BF_4 for CO_2RR. In this paper, the onset potential shifted positive by ca. 0.1 V in comparison with [BMIM]BF_4, suggesting that the presence of hydroxy group decreased the overpotential for CO_2 reduction. The enhanced catalytic performance of the system in the presence of [HEMIM]BF_4 was shown by DFT calculations to be due to the formation of a hydrogen bond between the -OH group and CO_2 that further stabilise the imidazolium-CO_2 complex. It has been suggested that in the absence of protons in solution, the proton needed for the protonation of the CO_2 reduction products (see Reactions r1.2-r1.6), is given by the C-H in position two in the imidazolium ring[352–355]. Considering that -OH group is a more efficient proton donor, i.e., has a lower pK_a, than a C-H group, the proton is likely provided by the -OH group instead of by the C-H in position

two in the imidazolium ring. This is interesting and suggests acidic pendant protons may be able to direct catalysis.

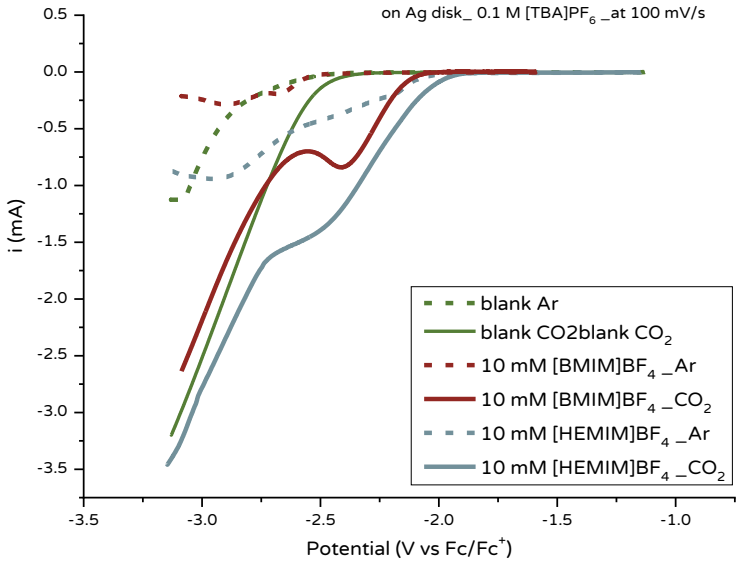

Figure 5.10: Comparison between the CVs obtained with Ag disk electrode in in a solution of 0.1 M [TBA]PF_6 in the presence of [BMIM]BF_4 (red curve) and [HEMIM]BF_4 (light blue curve). The CVs for the solution in the absence of ILs are presented in green. The systems under Ar are represented by the dashed curved, while under CO_2 by the solid curves

5.3 CO_2 reduction with non-commercially available ILs

Based on the results shown in Figure 5.10 and the work of Jin et al.[352] , it was postulated that an IL with a carboxylic acid functional group at the end of the alkyl chain may enhance CO_2RR capabilities because of the presence of acidic protons. Previously, increased catalytic activities have been observed in molecular catalysts for CO_2 containing carboxylic groups, e.g., metal complexes of Fe[353], Mn[354] and Ni[355] showed enhanced catalytic activity when carboxylic acid groups were added to the ligand framework which could freely rotate into the M-CO_2 co-ordination sphere and induce intramolecular proton-transfer (see Figure 5.11 for scheme). For this reason, imidazolium based ILs with carboxylic acid functionality were synthesised, characterised and then tested for CO_2 reduction.

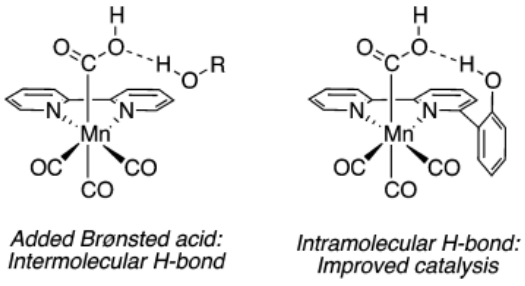

Figure 5.11: Scheme of intramolecular proton-transfer for inter and intramolecular H-bond for a Mn catalyst and CO_2 presenting a carboxylic acid group in the ligand structure and b) structure of [1-CM-3-MIM]BF_4

5.3.1 1st IL: 1-carboxymethyl-3-methylimidazole tetrafluoroborate ([1-CM-3-MIM]BF_4)

Considering that in the present work the IL with the shortest alkyl chain showed the best performances ([EMIM]BF_4), the carboxylic acid derivative of this imidazolium-based IL, 1-carboxymethyl-3-methylimidazole tetrafluoroborate ([1-CM-3-MIM]BF_4) was synthesised and characterised (see structure below in Figure 5.12). The synthetic procedure is detailed in in Chapter 2 (material and methods) together with the basic characterisation performed for the investigation of the purity of the final product. In particular, the purity of the compound was examined via ^{1}H and ^{19}F nuclear magnetic resonance (NMR) spectroscopy, elemental analysis and mass spectrometry. In the next section, the results of the characterisation are discussed in detail. It is important to highlight that the amount of water present in the final product was not detected. Prior each experiment, the ILs was dried overnight, and the collection of the product was performed under N_2 atmosphere to minimise the contact time with air and therefore the adsorption of water by the sample.

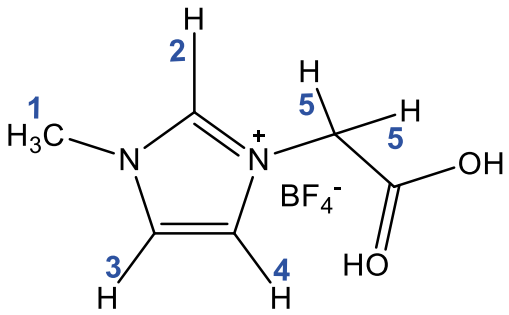

Figure 5.12: structure of 1-carboxymethyl-3-methylimidazole tetrafluoroborate ([1-CM-3-MIM]BF_4). The numbers in blue represent the position of the hydrogen atom in the molecule

5.3.1.1 Characterization of [1-CM-3-MIM]BF_4

The experimental chemical shifts for ^{1}H-NMR were in good agreement with the literature values[248]. ^{19}F NMR measurements were performed to understand if the counter-ion exchange process (see Method and Material section for more information) was successful and if some other anions were present. Two peaks were observed and they are due to the spin-spin interaction between ^{19}F and the two isotopes of the boron (^{10}B and ^{11}B)[356]. This was confirmed by the values of the two integrals, equal to 18.6 and 81.4, that correspond to the abundance of the two isotopes. Theoretically, the first signal should have been a quartet while the second one a septet, but experimentally two singlets were observed. This can result from two factors: the resolution of the instrument and the high viscosity of the IL[343]. Considering that the spectrum of the $NaBF_4$ showed two peaks[357], with the same ratio in intensity and integral values found for the IL, but with different multiplicity (a triplet was observed for the second peak), both factors contribute to the multiplicity observed experimentally. The compound was also analysed via mass spectrometry. The peak at the

highest intensity is the parent ion of the cation ($MW_{[1-CM-3-MIM]^+} = 141.14$ [248]). Two peaks observed at higher m/z values are due to aggregation of two or three imidazolium cations, as the imidazolium-based ILs tend to form clusters via hydrogen bonding[358,359]. The compound was analysed via elemental analysis for C, H, and N and the results are shown in Table 5.1. The deviation from the experimental values in comparison with the theoretical ones is due to the high hygroscopicity of the compound. If the calculations considered water as impurity, the values obtained with 0.6 molecules of water per molecule of IL are within the precision limit of ±0.4%.

Table 5.1: elemental analysis for [1-CM-3-MIM]BF_4

Element	content $\%_{theoretical}$	content $\%_{experimental}$	content $\%_{theor.\ with\ water}$
C	31.61	29.99	30.18
H	3.98	3.92	4.31
N	12.29	11.39	11.73

The presence of water in the compound and qualitative information about the hygroscopicity of the IL were tested via ATR-FTIR (attenuated total reflectance- Fourier-transform infrared) spectroscopy. A small quantity of sample was placed on the ATR crystal and several spectra were acquired at different times (Figure 5.13) to monitor the difference in the quantity of water incorporated by the IL on time after exposition to air. In general, the spectrum presented the typical modes of the imidazolium ring[360], such as the C-H stretching at 3188 and 2891 cm^{-1}; the ring stretching at 1424 and 1568 cm^{-1}; the in-plane ring bending at 824 cm^{-1}; and the H-C-N bending at 937 cm^{-1}. In addition, the presence of a carbonyl group was confirmed by the intense peak at 1743 cm^{-1}. The spectrum for t_0 was acquired immediately after the compound was placed on the crystal (the sample had previously been stored in a vial under vacuum) and it presented the band for -OH stretch (at 3572 cm^{-1}) and for -OH scissor mode (at 1628 cm^{-1}) with the lowest intensity. The two bands exhibited an increase of around 3% after 30 min, confirming the increase of water uptake in the sample[361,362].

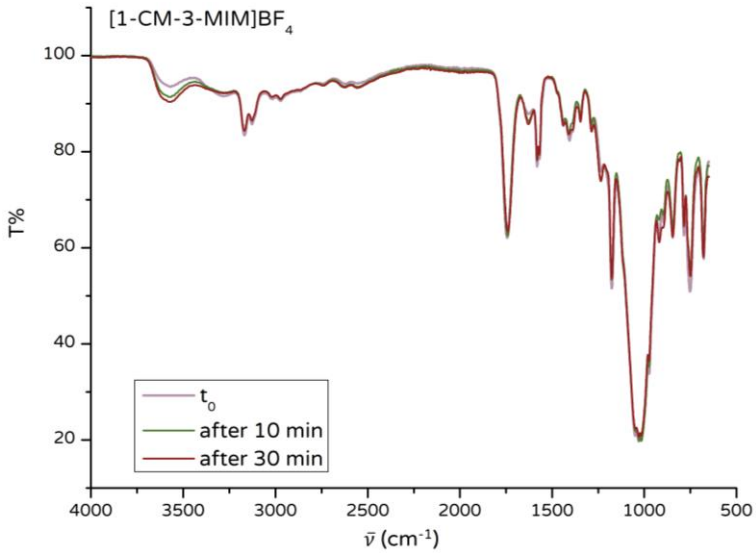

Figure 5.13: ATR-FTIR spectrum of [1-CM-3-MIM]BF_4 after different air exposure times

5.3.1.2 Electrochemistry

After the characterisation, the compound was preliminarily tested via cyclic voltammetry at Ag electrodes in MeCN under Ar and CO_2 atmospheres, respectively, to investigate its electrochemical behaviour. Ag electrodes were used as their electrochemical response in the presence of ILs is well known[24,25,43,231,349,363–365]. This allowed a proper understanding of the electrochemical behaviour of [1-CM-3-MIM]BF_4 and an easy and direct comparison with the commercial ILs. For the purpose of comparison, the concentration of the final solution was maintained at 10 mM. Under Ar atmosphere and in the present of IL (see Figure 5.14 dashed purple curve), a peak at -2.6 V vs Fc/Fc^+ is observed and it might be attributed to the formation of the carbene species, as proposed for the other imidazolium-based ILs. Interestingly, when the IL is added into the system, under Ar (solid green curve), the current significantly increased, while under CO_2 (solid purple curve), the current decreased. This suggests that the presence of the IL may retard CO_2RR or, considering the higher current observed under Ar, completely suppress both CO_2RR and the competitive HER.

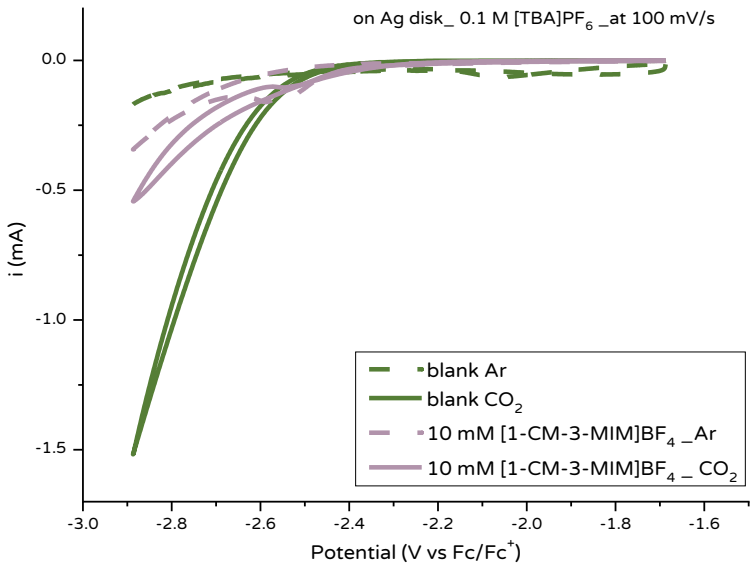

Figure 5.14: CVs at Ag disk electrode for [1-CM-3-MIM]BF_4 in a solution 0.1 M of [TBA]PF_6 under Ar and CO_2 atmosphere. Scan rate = 100 mV/s

To understand the role of the carboxylic acid group in the activity of the system and the causes of the loss of activity of the system toward the reduction of CO_2 in the presence of this IL in CO_2-saturated solution (see solid purple curve), experiments under pH control were required. Cyclic voltammetry at pH values above and below the pK_a of the IL are needed to monitor the CO_2RR response in the presence of the protonated and deprotonated forms of the carboxylic acid group. Consideration of pH values in a non-aqueous solution can be challenging both experimentally and theoretically, therefore the experiments were performed in aqueous solutions. In addition, performing the experiments in aqueous solutions would be particularly useful keeping in mind the scaling-up of the system, as water is an abundant and not aggressive solvent (as opposite to MeCN). Unfortunately, experiments performed using Ag electrode in water were unsuitable due to the limited potential window. In contrast, Bi electrodes have been demonstrated to largely suppress hydrogen evolution in aqueous solutions[101–104,153,158,169,240], thereby permitting access to a large potential window in aqueous electrolyte. Therefore, experiments were performed using a bismuth electrode obtained via electrodeposition on a glassy carbon electrode (Bi-GC). For information about the preparation and characterisation of Bi-GC, refer to the previous experimental chapter (Chapter 4).

5.3.1.2.1 Electrochemistry at Bi electrodes

Cyclic voltammetry experiments in pure aqueous solutions at Bi-GC produced very noisy voltammograms, probably due the production of H_2 gas bubbles, for this reason, a mixed solvent was used. A solution containing 25% of 0.1 M [TBA]PF_6 and 75% of water was employed for cyclic voltammetry experiments with [1-CP-3-MIM]BF_4 (10 mM) under Ar and CO_2. The pH of the solution

was set at values below and above the pK_a value (pK_a = 1.90[248]) using a 2 M $HClO_4$ solution. It is important to highlight that for these experiments, the pH of the bulk solution was monitored. However, it is clear that the bulk pH might not correspond with the interfacial pH during the electrochemical measurements[366], especially because the CO_2RR in aqueous systems produces OH^-, that can significantly increase the interfacial pH[43]. However, the bulk pH values were used as a starting point for a preliminary investigation of the system under pH control. The voltammograms obtained for the system at pH < pK_a are shown in Figure 5.15a, while the ones at pH > pK_a in Figure 5.15b. As illustrated in Figure 5.15b, the current densities for the system at pH above the pK_a are ten times lower than for the system at pH below the pK_a. At pH values above the pK_a, the CVs under CO_2 showed a reduction peak at -1.70 V vs RHE, probably due to the reduction of the imidazolium ring to the carbene derivative, while under Ar a small peak is observed at -1.82 V vs RHE. A difference of >14x in current density was observed under CO_2, suggesting the catalytic activity is greatly enhanced in the presence of the IL. In addition, under Ar and in the absence of [1-CM-3-MIM]BF_4, CVs exhibited a very similar shape to the one obtained under CO_2, in the presence of IL, suggesting that the system did not favour the HER. Interestingly, below the pK_a, the CVs in absence and in the presence of IL are quite similar, as small differences in both current densities and onset potentials were observed. In the absence of IL (red curve), a high level of noise was observed and the curve under Ar and CO_2 overlapped completely, suggesting the promotion of HER over CO_2RR at these low pH values. Most likely, the pH of the solution was sufficiently low to allow the HER to proceed at small overpotentials. This highly likely considering that the value of the standard potentials for HER is actually almost 1.5 V more positive than the one for the formation of the high energy intermediate $CO_2^{-\bullet}$, and 0.1 V more positive than the one for the formation of CO. In Figure 5.15c, it is evident that below the pK_a, the presence of IL did not increase significantly the catalytic activity of Bi-GC (see cathodic sweeps -the solid curves- below and above the pK_a under CO_2). In addition, probably because of the low pH of the solution, it was not possible to determine if the presence of a carboxyl acid group can act as a good proton donor for an intramolecular proton transfer, so other materials with higher pK_a values were considered.

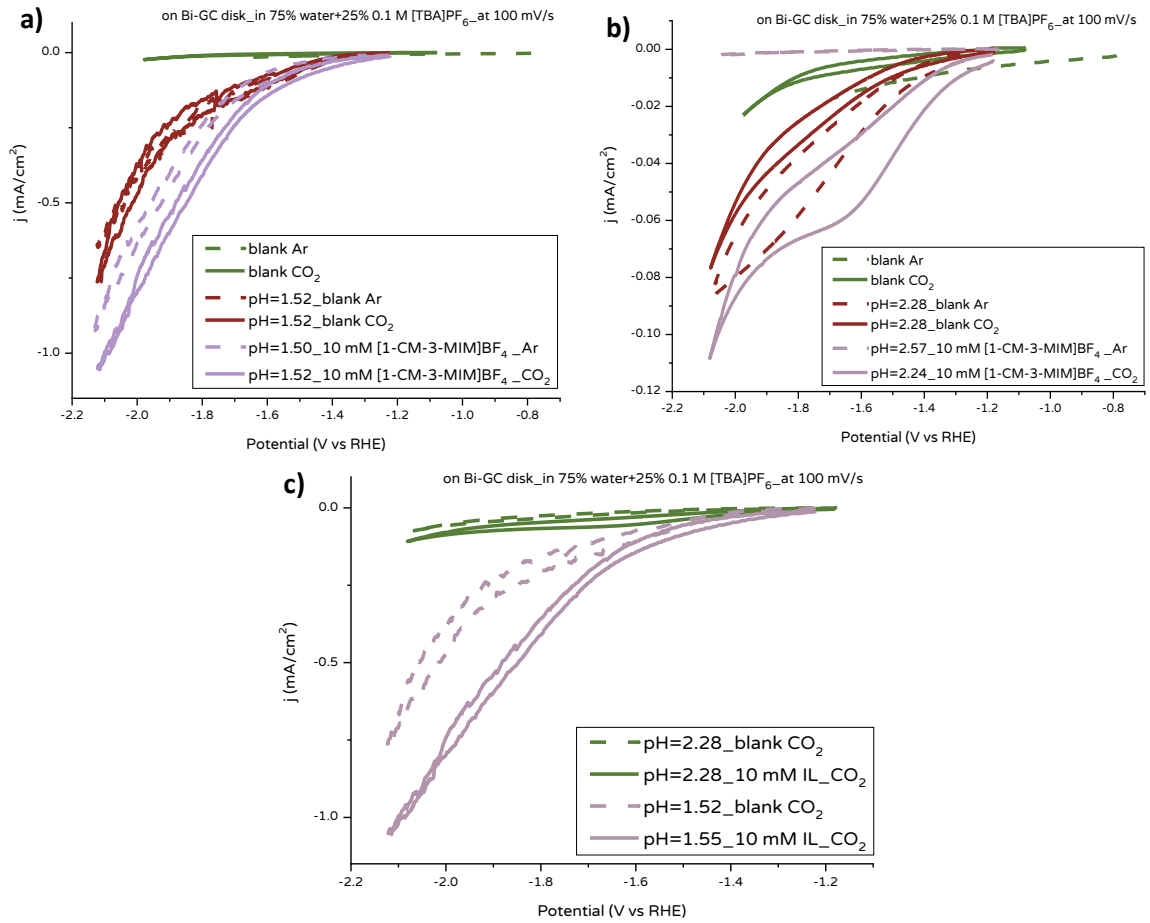

Figure 5.15: CVs for 10 mM [1-CP-3-MIM]BF_4 with Bi-GC electrode in a mixed H_2O/MeCN solution under Ar and CO_2 with pH a) below pK_a and b) above pK_a; c) comparison for the system under CO_2 at pH values below and above pK_a. Electrolyte: 75% water+25% 0.1 M [TBA]BF_4. Scan rate = 100 mV/s

5.3.2 2nd IL: 1-carboxypropyl-3-methylimidazole tetrafluoroborate ([1-CP-3-MIM]BF_4)

Based on the results obtained, it is reasonable to consider the pK_a of the compound to be too low for studying the role of a protonated and deprotonated carboxylic acid group for the reduction of CO_2, in aqueous electrolyte, even when using a Bi-GC working electrode. For this reason, a second imidazolium-based IL with a higher pK_a value was synthesised. This allowed the pH of solution to be kept higher than in the presence of [1-CM-3-MIM]BF_4. Considering that increasing the length of the alkyl chain of a carboxylic acid lead to an increase of the pK_a of the compound, a methylimidazolium-based IL with a longer chain was synthesised[367]. [BMIM]BF_4 has four carbon atoms in the lateral alkyl chain and it has been extensively used in literature with several metal electrodes (including Bi ones) and previously tested in this work, but no examples in the literature were found for a carboxylic acid derivative of this IL for the reduction of CO_2. Therefore, the carboxylic acid derivative of [BMIM]BF_4 was synthesised, characterised, and studied as co-catalyst for CO_2 reduction in aqueous solutions at Bi-GC electrode.

5.3.2.1 Synthesis and characterisation

The structure of the [BMIM]BF_4 carboxylic acid derivative, 1-carboxypropyl-3-methylimidazole tetrafluoroborate ([1-CP-3-MIM]BF_4) is shown in Figure 5.16. The compound was synthesised and characterised via ^1H and ^{19}F NMR spectroscopy, ATR-FTIR spectroscopy, mass spectrometry, and elemental analysis. Successively, cyclic voltammetry experiments were performed on Ag electrode and non-aqueous solutions to preliminary test the influence of this IL in the catalytic system and to compare the activity of this compound with [BMIM]BF_4 and [1-CM-3-MIM]BF_4. Finally, the role of the carboxylic acid group on CO_2RR was studied using a series of techniques.

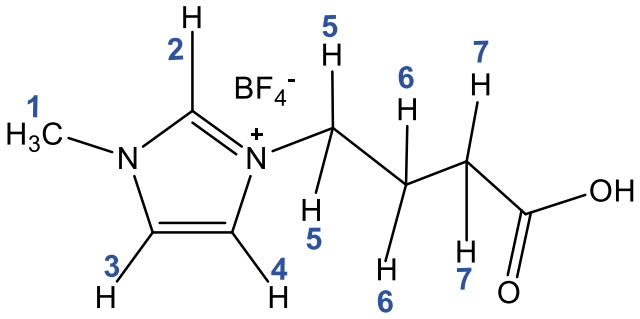

Figure 5.16: structure of [1-CP-3-MIM]BF_4. The numbers in blue represent the position of the hydrogen atom in the molecule

The ^1H-NMR spectrum of the purified compound was acquired and the experimental chemical shifts are in good agreement with literature values[248]. The ^{19}F-NMR spectrum presented two peaks, due to the coupling of the fluorine in the counter-ion with the two isotopes of the boron. The spectrum obtained after mass spectrometry measurement showed the most intense peak at 169.10 m/z, due to the parent ion of the cation ([1-CP-3MIM]$^+$), while the peak at 337 m/z is due to the formation of the cluster of two molecules of [1-CP-3-MIM]$^+$ formed via hydrogen bonding, as previously observed for [1-CM-3-MIM]BF_4. The compound was then analysed via elemental analysis for C, H, and N, F and for Na (Table 5.2). As for [1-CM-3-MIM]BF_4, the deviation from the theoretical values is due to the presence of water in the sample. In addition, a small amount of Na was detected, probably an impurity from the counter-ion exchange step (see Material and Method chapter). Considering a quantity of water equal to 0.41 moles of H_2O per mole of IL, the precision limit does not exceed the 0.40 %.

Table 5.2: elemental analysis for [1-CP-3-MIM]BF_4

Element	content $\%_{experimental}$	content $\%_{theor.\ with\ water}$
C	35.90	36.20
H	4.85	5.25
N	10.55	10.55
F	28.23	28.23
Na	≤0.36	0.78

ATR-FTIR analyses were performed on the purified compound and the spectrum is showed in Figure 5.17. The features exhibited by [1-CP-3-MIM]BF_4 are very similar to the one observed for [1-CM-3-MIM]BF_4 (Figure 5.13). The spectrum for t_0 was acquired immediately after the compound was placed on the ATR crystal (the sample had previously been stored in a vial under vacuum) and it presented the band for -OH stretch and scissor mode with the lowest intensity. The band at 3588.66 cm^{-1} exhibited an increase of around 0.7% after 10 min and a further increase to 5% after 20 min, confirming the increase of water uptake in the sample[361,362].

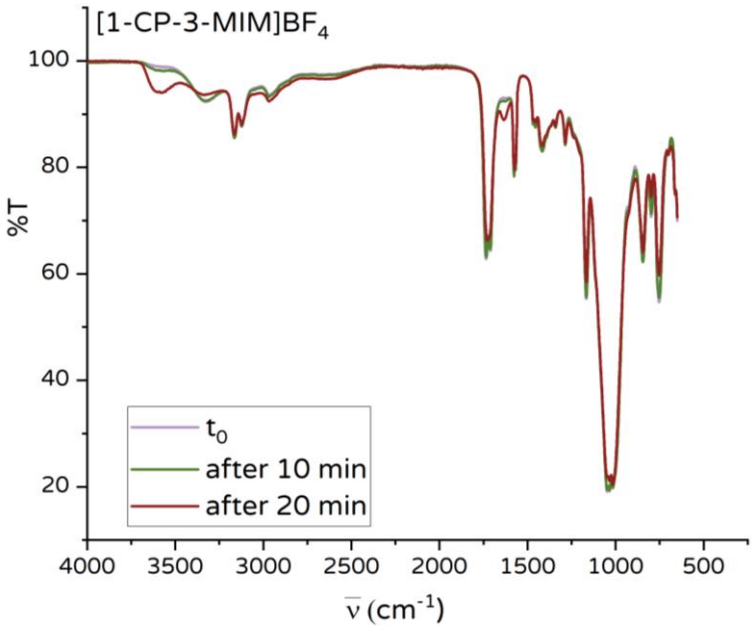

Figure 5.17: ATR-FTIR spectrum of [1-CP-3-MIM]BF_4 before and after air exposition

5.3.2.2 Electrochemistry

Cyclic voltammetry experiments were acquired in MeCN solutions at a silver electrode, allowing a direct comparison with [BMIM]BF_4. For clarity, only the reduction sweeps for both [1-CP-3-MIM]BF_4 and [BMIM]BF_4 are shown in Figure 5.18. Under Ar (dashed purple curve), two reduction peaks are observed at -2.1 and -2.4 V vs Fc/Fc^+, probably due to the formation of the carbene species and some dimerization process as observed for [BMIM]BF_4 [24]. Under CO_2 (solid curve), a shoulder is observed at around -2.0 V vs Fc/Fc^+, probably due to the formation of the carbene derivative specie at potentials 0.4 V more positive than in the presence of [BMIM]BF_4. In addition, the onset potential for [1-CP-3-MIM]BF_4 is 0.26 V more positive than for [BMIM]BF_4 (onset potential for [BMIM]BF_4 = -2.12 V, and for [1-CP-3-MIM]BF_4 = -1.86 V vs Fc/Fc^+).

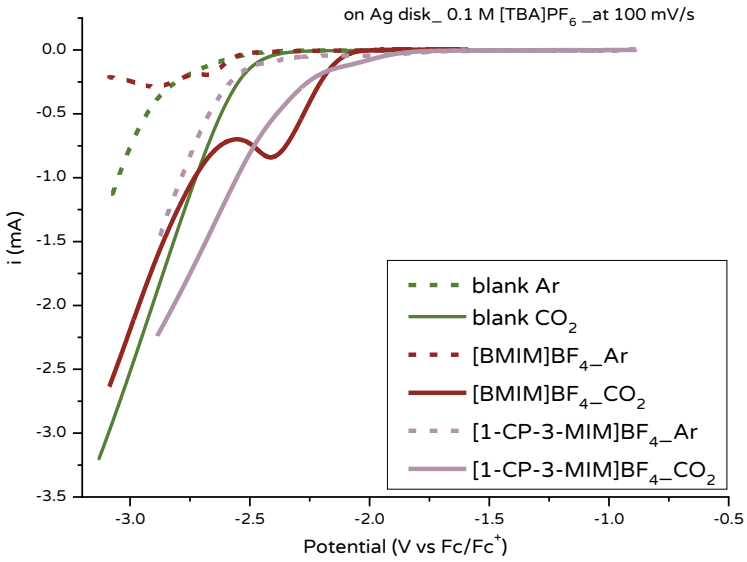

Figure 5.18: CVs for 10 mM [1-CP-3-MIM]BF_4 and [BMIM]BF_4 with Ag disk electrode in MeCN/0.1 M [TBA]PF_6 under Ar and CO_2 at Ag disk electrode. The CVs were acquired at scan rate equal to 100 mV/s

Cyclic voltammetry experiments were performed at Bi-GC electrode in aqueous media and controlling the pH of the solution. The pH of the solution containing 10 mM [1-CP-3-MIM]BF_4 had a higher pH than for [1-CM-3-MIM]BF_4 (pH = 3.41 ± 0.40) and no noise was observed in the cyclic voltammogram. Therefore, it was possible to perform the pH-controlled experiments in a pure aqueous solution. First, the pK_a of [1-CP-3-MIM]BF_4 in solution was measured performing an IR titration (Figure 5.19) and successively compared with cyclic voltammetry results (Figure 5.20).

The IR titration was performed in D_2O instead of pure water as H_2O presented an absorption peak around 1650 cm^{-1}, making challenging the observation of both the carboxylic acid and carboxylate bands, as they present the peaks at a very similar wavenumber (see Figure 5.19a). For this reason, during the experiments, the pH* (that is the direct reading in a D_2O solution of the H_2O-calibrated pH-meter) was measured and for the calculation of the pK_a, Equation (5.1) was used[368]

$$pK_a{}^{H} = 0.929 \times pK_a{}^{H*} + 0.42 \qquad (5.1)$$

where pK^{H^*} is the dissociation constant calculated from the direct reading of the pH-meter. The curves in Figure 5.19a were obtained by adding small aliquots of deuterium chloride (DCl) to a solution of the IL 10 mM in D_2O. Before the DCl was added, the pH* of the solution was first adjusted to neutral pH* values (around 6) with a solution of sodium deuteroxide (NaOD). The band at 1705 cm^{-1}, corresponding to the symmetric stretching of C=O (ν_s) in the carboxylic acid group[369,370], increased as the pH* decreased, indicating that the carboxylate group is protonated during the titration. Concomitantly, the peak at 1567 cm^{-1}, due to the asymmetric stretching of COO^- (ν_{as})[369,370], decreased in intensity as the pH decreases. The differences in intensity observed in the baseline resulted from the hygroscopicity of D_2O[371], as during the titration the solution was exposed

to air and the quantity of water incorporated by D_2O increased with time. For this reason, the additional water present in the sample was not subtracted from the blank, resulting in values of transmittance higher than 100%. The values of transmittance at 1705 and 1567 cm^{-1} were plotted as a function of the pH*, revealing two sigmoidal curves that intersect at the pK_a of the IL (Figure 5.19b).

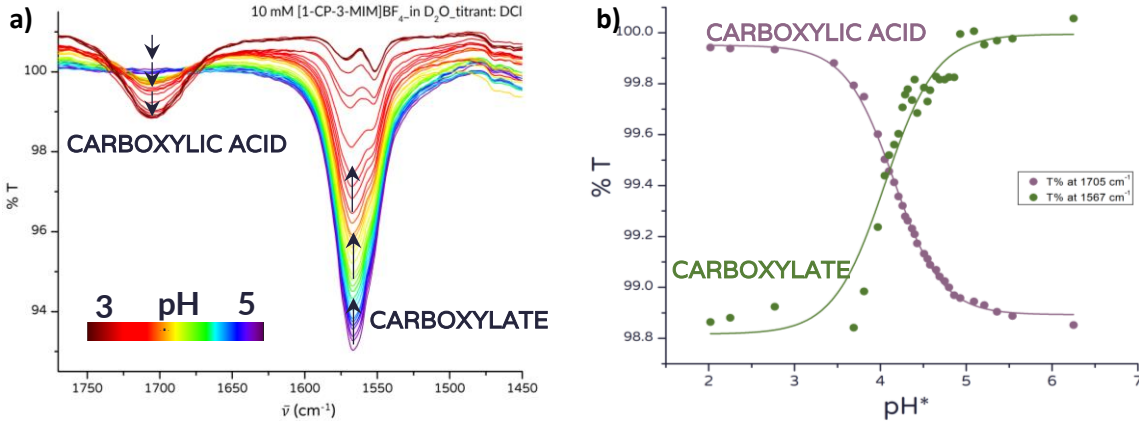

Figure 5.19: a) ATR-FTIR titration of a solution 10 mM of [1-CP-3-MIM]BF_4 in D_2O and b) transmittance as a function of pH for the carboxylate and the carboxylic acid bands. 0.05 µL aliquots of DCl were added to adjust the pH before acquiring each spectrum

The variation of current as a function of the pH in the presence of [1-CP-3-MIM]BF_4 was evaluated via cyclic voltammetry: CVs were acquired at different pH values in a solution 10 mM of [1-CP-3-MIM]BF_4 in 0.1 M Na_2SO_4 under CO_2 atmosphere. Then, the values of the current density at E_{pc} (cathodic peak potential) for each curve was plotted versus the pH of the solution (Figure 5.20b). For clarity, only the reduction sweep for each cycle is shown in Figure 5.20a. This allowed the evaluation of the pH values at which the IL was protonated or unprotonated and the response of the current density in the presence of the carboxylic acid or the carboxylate ion. As for the IR titration, the pH was first adjusted to a neutral value using a solution 6 M of NaOH and successively, small aliquots of H_2SO_4 were added to reach acidic pH values. Each point in Figure 5.20b is the mean of three different measurements. The current density values show a sigmoidal response, this allowed the extrapolation of the pK_a of the compound in solution. The values of the pK_a obtained using both ATR and CV measurements are shown in Table 5.3. According to the values in Table 5.3, the two experimental pK_a values are in good agreement with the literature value.

Table 5.3: pK_a values for [1-CP-3-MIM]BF_4 obtained via IR-titration and cyclic voltammetry. The literature value is insert for comparison

	pKa
literature	3.95[248]
j	4.1 ± 0.1
%T	4.23 ± 0.08

From Figure 5.20a, it is evident that higher current densities were measured for solutions with low pH values. As the pH was increased, the peak at -1.2 V vs Ag/AgCl tended to disappear, suggesting the total or partial suppression of the reduction process observed at low pH. In Figure 5.20c, only two curves (one above and one below the pK_a) are shown to clearly display the difference in shape and current density. The curve obtained at pH < pK_a (solid light purple curve) exhibited a clear peak at -1.18 V vs Ag/AgCl, while when pH > pK_a (solid dark purple curve) only a small shoulder is presented, with a current density two times lower than at pH= 3.43. In addition, under Ar atmosphere and at pH < pK_a, a current density around 20 times lower was measured at -1.18 V vs Ag/AgCl. This suggests that the increased current density under CO_2 may result from CO_2RR, despite the low pH. When the pH was increased (pH > pK_a), the two curves under Ar and CO_2 were closer to each other, implying that part of the current density observed during the experiments is due to HER. This is also suggested by the value of current density at -1.18 V vs Ag/AgCl under CO_2 that is only 1.7 times bigger than under Ar. Together, these two datasets (CVs above and below pK_a) reveal a non-linear dependence of current density on pH and, together with the IR titration data, suggest that protonated carboxylic acid groups on [1-CP-3-MIM]BF_4 plays a role in promoting CO_2RR.

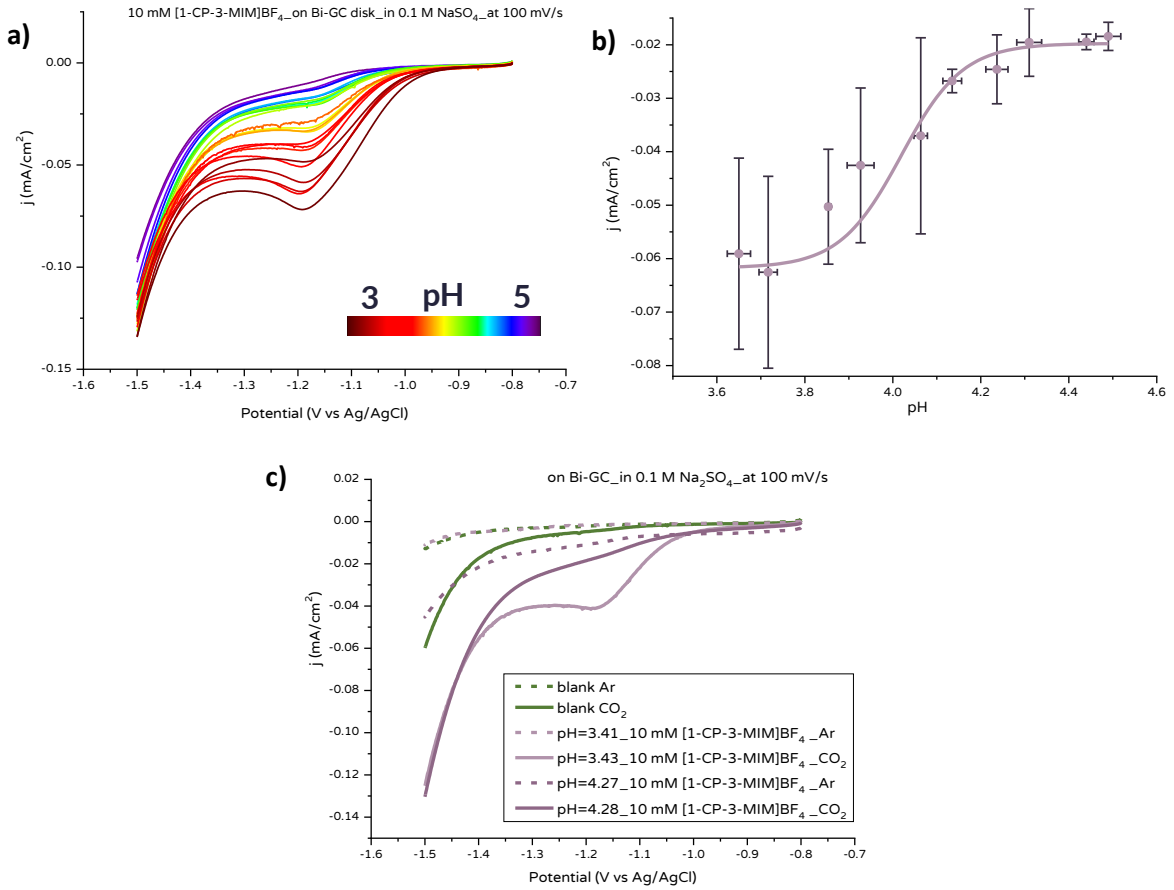

Figure 5.20: a) Reduction sweeps obtained at pH from 5.6 to 3.0 for a CO_2-saturated solution of [1-CP-3-MIM]BF_4 10 mM at Bi-GC electrode; b) current density values at E_{pc} as function of pH and correspondent fitting; and c) reduction sweeps for the solution at two different pH values: above and below pK_a. Electrolyte: 0.1 M Na_2SO_4, scan rate = 100 mV/s. The pH of the solution was adjusted using 10 µ aliquots of 1 M H_2SO_4

Successively, the influence of the concentration of [1-CP-3-MIM]BF_4 on the catalytic activity of the system was investigated by performing CV measurements in a CO_2-saturated solution of 0.1 M Na_2SO_4. In Figure 5.21, the current density at the E_{pc} was plotted as a function of the concentration of [1-CP-3-MIM]BF_4 for the solution at pH below (purple) and above (green) the pK_a value. As expected, in both cases, the current density increased with the concentration, in accordance with the literature findings[337]. This suggested that high concentrations of ILs improve the catalytic system. This can be due to two main reasons: first, the higher the number of IL molecules, the more the molecules of the CO_2 intermediate that are stabilised; second, the higher the concentration of ILs, the more CO_2 will be dissolved in solution[24]. The same trend was observed for the difference in current density between the two data sets. At the lowest concentrations (between 5 and 20 mM), a difference of 0.1 mA/cm^2 between the two data sets was detected, while at the highest concentrations (45 and 50 mM) the variation was almost twenty times bigger than for the lowest concentrations ($j_{pH=3.70} - j_{pH=4.20} \sim 1.9$ mA/cm^2). Based on literature findings[337], a plateau is expected at higher IL concentrations (>50 mM) because of saturation of the surface of the electrode by the IL.

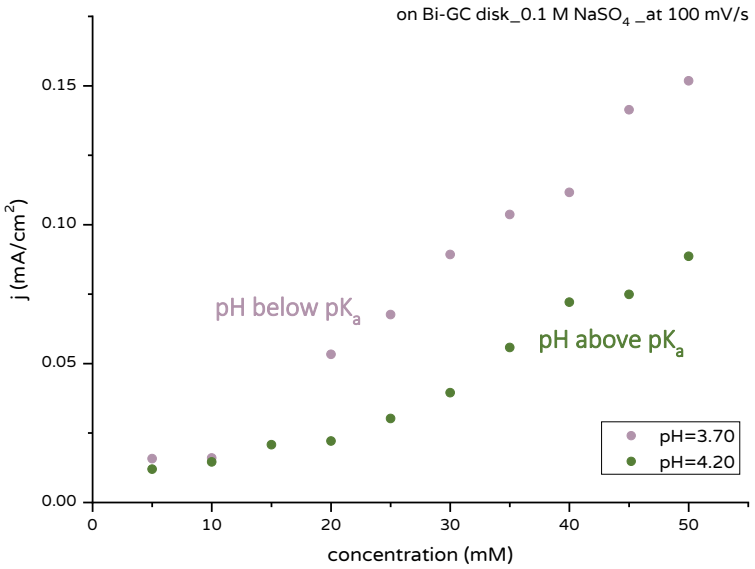

Figure 5.21: concentration dependence for [1-CP-3-MIM]BF_4 at Bi-GC electrode in CO_2 -saturated solution of Na_2SO_4 0.1 M for pH values of the solution above and below the pKa value. Scan rate = 100 mV/s

5.4 Conclusion

In conclusion, several commercial imidazolium-based ILs were preliminarily tested via cyclic voltammetry in organic electrolytes with different metal electrodes for CO_2RR. As far as the **objective 1.b** is concerned (see Section 1.7): the results were in good agreement with the literature, showing the Ag electrodes to be the best catalysts among the electrodes tested within this work. These established benchmark systems were used for investigating synthesised ILs and novel Bi

modified electrodes (objective 1.b). The commercial ILs showed a broadly similar response, with the IL containing a hydroxyl group at the end of the alkyl chain ([HEMIM]BF_4) presenting onset potentials between 50 and 110 mV more positive than the other ILs. In particular, it was observed that keeping the number of carbon atoms in the lateral chain the same, the presence of the hydroxyl group lead to an onset potential 0.11 V more positive, suggesting that, with an equal length of the lateral alkyl chain, a source of protons (the hydroxyl group) may increase the catalytic activity of the system. It was previously observed that the presence of a source of protons increased the catalytic activity of several systems towards CO_2RR[24,348,349]. Several compounds presenting a carboxylic acid group in their structure were able to increase the catalytic response of the system[353–355]. For this reason, in-house produced ILs with a carboxylic acid group at the end of the alkyl chain were synthesised: [1-CM-3-MIM]BF_4 and [1-CP-3-MIM]BF_4 (**objective 1.b**). To understand if the behaviour of the carboxylic acid ILs is influenced by the pH, cyclic voltammetry measurements were performed under pH control (below and above the pK_a of the ILs). The experiments were carried out using a modified bismuth electrode (Bi-GC). The Bi-GC was used to test the two carboxylic acid-ILs. However, only [1-CP-3-MIM]BF_4 was further investigated as [1-CM-3-MIM]BF_4 , at pH < pK_a, the system showed a high production of gaseous products (assumed to be HER). CVs of [1-CP-3-MIM]BF_4 exhibited higher current densities and lower onset potentials at pH values below the pK_a under CO_2 atmosphere in a solution of 0.1 M Na_2SO_4 (**objective 1.b**). Based on these preliminary results, catalysis experiments are necessary using, first, the commercial IL [BMIM]BF_4 and, second, the in house-build IL [1-CP-3-MIM]BF_4. In this way it would be possible to understand if [1-CP-3-MIM]BF_4 behaves as proton donor for the reduction of CO_2 and if the increase of the current observed at pH values below the pK_a is due to an increased selectivity of the system toward the reduction of CO_2 or if HER is the main process happening in the system (**objective 1.b**).

Chapter 6 : Catalytic experiments for CO_2 reduction

6.1 Introduction

Rising levels of anthropogenic CO_2 in the atmosphere have resulted in several alarming consequences for the environment and the planet[1,2]. For this reason, different approaches have been under investigation to reduce the emission and the quantity of CO_2 already present in the atmosphere. Among these approaches, the utilisation of CO_2 as a starting point for the production of fuels is considered particularly convenient. A large variety of products can be obtained using several methods such as thermochemical[39], biological[40], electrochemical[41] and photochemical[42] processes, with the last two being the most promising[37]. Several metal electrodes have been applied as electrocatalysts for the reduction of CO_2[43]. Au and Ag electrodes have been found to be the most promising electrocatalysts because of their high reactivity and selectivity. However, in the last decade, other metals, considered more sustainable and less expensive, have been investigated as electrocatalysts for the CO_2 reduction reaction (CO_2RR). Among those, Bi electrodes have been attracting increasing attention because of their ability to suppress the hydrogen evolution reaction (HER) while producing formate. The literature presents several examples of Bi electrodes able to reduce CO_2, with a particular focus on the production of electrodes able to increase the faradaic efficiency (FE) for formate[100,101,103] (i.e. tuning the selectivity of the system) or to shift the selectivity of the system to different products like CO[230,245]. The most common approach is the insertion of Bi micro- or nanoparticles on an inert substrate to study the effect of their morphology and crystalline structure on the catalysis. However, only a few examples of comparison between the bulk Bi electrodes and the Bi micro- or nanostructured particles are present. However, for bismuth a systematic investigation on the effect of the electrode area on the catalytic activity and comparison between the bulk and the micro- or nanostructured electrodes has not been reported. For this reason, catalytic experiments were performed using bulk Bi electrodes (preparation in Chapter 3) and then Bi film electrodes produced via electrodeposition (preparation in Chapter 4), to investigate their ability to reduce CO_2 in aqueous solutions. In addition, the effect of two different co-catalysts, two imidazolium based ionic liquids (ILs), on the catalytic performances of the system were investigated (see Chapter 5).

6.2 Electrocatalysis experiments with pure Bi metal electrode

For performing the electrocatalytic experiments, two electrodes were prepared by cutting cylinders of pure Bi metal with an area that would be comparable with those of the Bi modified electrodes (see Figure 6.1 and Chapter 3). This allowed a direct comparison of the catalytic activity of the pure Bi metal electrodes and the new Bi modified electrodes. From Figure 6.1, it can be seen that the surface of the electrode is not smooth, and it presented several holes, fractures and

depressions/defects due to the commercial casting of the rod. These features increase the area of the electrode and create areas where the removal of the oxidised surface is particularly difficult if not impossible. This is clear in Figure 6.1c, where the SEM image shows the presence of a solid in the area where the central hole is present.

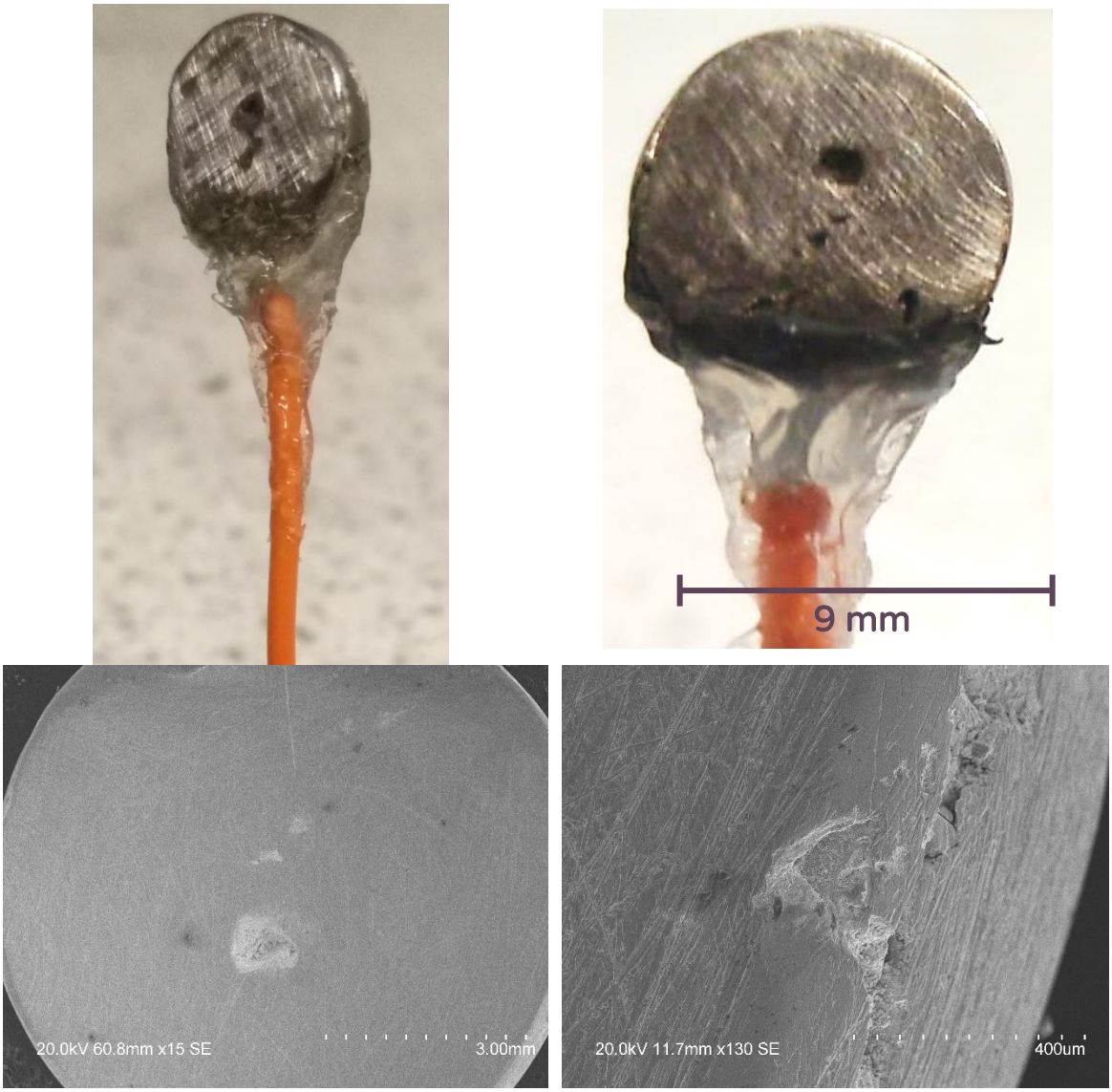

Figure 6.1: Bi cylinder used for catalysis experiments a) before polishing; b) close up image of the electrode; SEM image of the Bi cylinder after catalysis experiments c) at magnification equal to x15; and d) particular of the edge of the electrode, in which a fracture is present (magnification: x130); Epoxy resin was used to insulate the electrical connection

Usually, in the context of CO_2 reduction, the current density (j) is used to allow a comparison of the current response among different metal electrodes. For the normalisation of the current, the geometrical area is usually used[331,333,372]. However, this approach does not give a reliable estimate of the current density, since the surface roughness factor can be very large, even to several orders of magnitude for electrodes modified with nanostructured deposits[222,224,373,374]. When the geometric area is used, a nanostructured electrode would present a higher apparent current density than a flat, unstructured electrode, as the number of active sites is going to be larger.

However, it is important to highlight that if the current is normalised for the real area, the observed current at the nanostructured electrode would not necessarily be higher than the one observed for a planar electrode.This issue becomes even more significant If a comparison between different nanostructured electrodes is done: the current density obtained using the geometrical area could be misleading, as a higher observed current could simply be due to a higher area. Clearly, a high surface area is a desirable property for a catalyst to maximise the number of moles of substrate converted per unit time. However, a high surface area would not influence the selectivity. An example of how the normalisation to the geometrical or electroactive area could lead to erroneous evaluation is shown in Figure 6.2. Based on the CVs normalised to the geometrical area (see Figure 6.2a), the higher current response at the peak maximum and the more positive onset potential is presented by Bi-GC0.5 (purple curve). However, when the electrochemical surface area (ECSA) is used for the normalisation, the same electrode presented the lowest current density and the more negative onset potential among all the electrodes tested (Figure 6.2b). The normalisation to the geometrical area or ECSA might seem a factor that simply influences the value of j, however, it can lead to other parameters being evaluated incorrectly like the overpotential, selectivity and kinetics[222]. For example, Sun et al.[331] showed how using the geometrical area of a Co_3O_4 electrode for the oxygen evolution reaction (OER) influenced the Tafel plots. They observed that when j was normalised to the geometrical area, the activity for OER was higher than when the ECSA (based on the double layer capacitance method) and the BET area were used. In addition, they observed that when the current was normalised for the geometrical area, the activity of the Co_3O_4 electrode was higher than IrO_2 electrodes, while if j was obtained based on the oxide particle surface area IrO_2 electrodes presented higher activity.

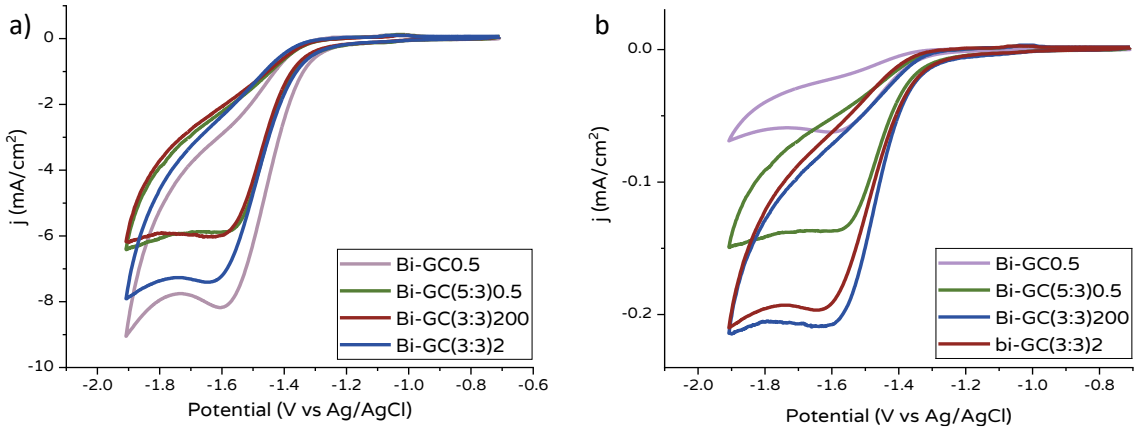

Figure 6.2: CVs for varies Bi-GC electrodes in CO_2-saturated Na_2SO_4 0.1 M solution. The current density was obtained by normalising the current for a) the geometrical area; and b) the electro active surface area based on the oxygen adsorption method

For this reason, in this work, the current was normalised to the electrochemical surface area (here called A_{real}) of the different Bi electrodes based on the oxygen adsorption method (see Chapter 1

and 3 for details). The diameter of the electrode, the charge under the reduction peak (see Figure 6.3), the roughness factor and the value of the geometrical (A_{geo}) and real (A_{real}) area of two Bi cylinders are shown in Table 6.1.

Table 6.1: Diameter, charge under the monolayer reduction peak, roughness factor, geometrical and real area of two Bi cylinders produced for catalysis experiments. The real area was calculated using the oxide monolayer reduction method

cylinder	d [cm]	Q_{exp} [µC]	A_{geo} [cm^2]	A_{real} [cm^2]	r_f
1	0.93	7461 ± 1677	2.28	40 ± 9	17
2	0.91	7909 ± 447	2.04	42 ± 2	21

Prior to each experiment, the cylinders were polished using sandpaper (grit = 1200P) for one minute to remove any possible impurities and the native oxide layer. The roughness factor obtained here is smaller than the values obtained for the Bi disks investigated in Chapter 3 (r_f = 43 ± 1). This can be due to the procedure used for the polishing the Bi cylinders: a polishing pad was not used in order to avoid breaking the delicate electrical connections of the electrodes, therefore, the sandpaper was directly applied on the electrode surface and small circular motions were performed. Considering that this technique did not allow a constant pressure and regular motions, it is likely that this was also the cause that led to the high standard deviation related to the real area obtained (see in Table 6.1 and in Figure 6.3). Based on the fact that the magnitude of the area was not perfectly reproducible, the real area was calculated after each catalysis experiment.

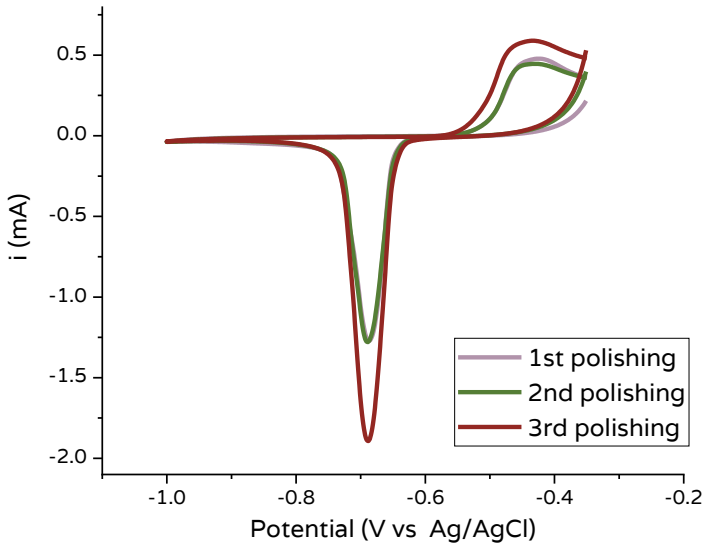

Figure 6.3: Cyclic voltammetry measurements for the calculation of the real area of Bi cylinder (1) electrode after three different polishing step using sandpaper (grit: 1200P). The measurement was performed in 50 mM KOH at 10 mV/s

6.2.1 Electrolysis experiments

To obtain quantitative information on the catalytic activity of the Bi cylinders toward CO_2RR, electrolysis experiments were performed. Electrolysis was performed using control potential electrolysis (CPE) technique in a H-type cell, using Ag/AgCl as RE and a Pt coil as CE. All the potentials

mentioned here are always expressed versus Ag/AgCl, unless otherwise states. The potential was applied for 30 minutes and after this time aliquots from the headspace and solution were analysed to obtain information about the compounds produced during the electrolysis. As mentioned in Chapter 1, CO_2RR is challenging because of the slow kinetics and the high number of competing reactions. In particular, HER presents a standard reduction potential more positive than the formation of the high energy intermediate $CO_2^{-\bullet}$, meaning that HER is thermodynamically favoured over the CO_2RR[375]. This is especially valid in aqueous solutions at low pH. Previous works on the reduction of CO_2 with Bi electrodes have shown that the selectivity of the reaction is strongly influenced by the potential applied during electrolysis[99,100,153,310], as the mechanism for the reaction has been demonstrated to be potential dependent[106,376]. For this reason, when a prospective electrocatalyst is under investigation for the CO_2RR, the optimal potential for the reaction is selected by testing a range of potentials. Here, electrolysis was carried out at four different potentials. The range was selected setting the most positive potential equal to the onset potential and each following experiment was performed by applying a potential 0.2 V more negative. To calculate the onset potential, two CVs were acquired: the first, under N_2 and the second under CO_2 atmospheres. If a significant difference in the current response was observed, the onset potential was calculated from the CV curve obtained under CO_2 atmosphere. An example of a set of CVs under N_2 and under CO_2 is shown in Figure 6.4a, in which a significant increase in current density in the curve under CO_2 (purple curve) was observed. Specifically, a current density ten times higher was observed under CO_2: j was equal to -0.2 mA/cm^2 at -1.71 V, while at the same potential but under N_2 atmosphere, j = 0.02 mA/cm^2. This is a typical feature of catalytic processes[377] and it has been observed before in several works. For example, Kumawat and Sarkar[241] observed a current density six time higher in CO_2-saturated solutions than in N_2-saturated solutions using a Bi modified electrode. Similarly, Lv et al.[154] investigated the CO_2RR using a Cu electrode modified with Bi nanoparticles and they observed, at -1.6 V vs Ag/AgCl, a current density equal to 4 mA/cm^2 under CO_2 and equal to 1.5 mA/cm^2 under N_2. The procedure for calculating the onset potential is shown in Figure 6.4b: the value was found from the intersection between two straight lines lying on the curve before and after the sudden increase in current density. The onset potential was equal to -1.46 V vs Ag/AgCl in Na_2SO_4 and to -1.48 V in $KHCO_3$. In Figure 6.4, the CVs obtained using one of the Bi modified electrodes (Bi-GC(3:3)200) is used as an example, and the same procedure was used for the Bi cylinders and for all the other Bi modified electrodes.

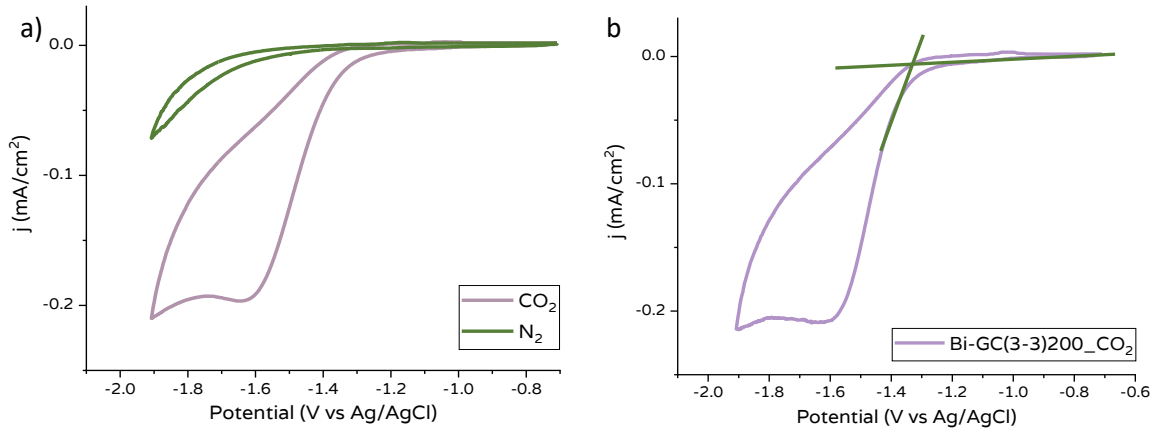

Figure 6.4: a) CVs under N_2 and CO_2 atmosphere on Bi-GC(3:3)200 electrode in 0.1 M Na_2SO_4; b) calculation of the onset potential for CO_2 reduction. Scan rate: 100 mV/s. The current was normalised to the real area based on the oxygen adsorption method. The second cycle is presented

It has been demonstrated that the medium used for the electrolysis experiments influences the catalytic performances of the system[287]. For example, the supporting electrolyte, the solvent, the pH and the concentration of CO_2 have been demonstrated to influence the outcome of the CO_2RR[43]. Bicarbonate salts are the most commonly used electrolytes for the reduction of CO_2, as they influence the reaction in several ways[378]. Specifically, it has been proposed that they are able to lower the pH at the electrode-solution interphase behaving as a buffer[43,287]; that they can act as proton donors after the reduction step occurred[379,380]; and that they shift the equilibrium toward CO_2(g) and therefore increase the substrate concentration in solution (see Reaction r3.1)[272]. For this reason, the catalytic experiments were performed in 0.1 M $KHCO_3$. The catalysis experiments were also performed in solutions containing a different electrolyte that did not contain bicarbonate anions for comparison: Na_2SO_4. SO_4^{2-} salts were chosen because, in the presence of ILs (see Chapter 5 and Section 6.3, here), H_2SO_4 was used to adjust the pH during the cyclic voltammetry and catalysis experiments. The different systems investigated with Bi cylinder electrodes for the CO_2RR are shown in Table 6.2. The pH of the solution is an important factor as CO_2 does not exist in this form in pH higher than 8 (see Pourbaix diagram in Figure 1.39). For this reason, the pH of the two solutions under N_2 and CO_2 were measured, and their values are shown in Table 6.2.

Table 6.2: Different systems used for the CO_2RR: electrolyte and their concentrations, gas used for the saturation of the solutions prior the catalytic experiments and pH of the solutions. The potentials values are exrepssed vs 1 M Ag/AgCl reference electrode.

electrolyte	concentration [M]	onset potential [V]	gas	pH
Na_2SO_4	0.1	-1.46	N_2	6.06
			CO_2	4.18
$KHCO_3$	0.1	-1.48	N_2	8.84
			CO_2	6.70

After controlled potential electrolysis experiments, the faraday efficiencies (FEs) were calculated using Equation (6.1):

$$FE = \frac{Q_{experimental}}{Q_{theoretical}} \times 100 \quad (6.1)$$

where $Q_{experimental}$ was calculated based on the amount of the specific product (H_2, CO or HCOOH) obtained during the experiment and $Q_{theoretical}$ represents the charge passed during the catalytic experiments. The FE obtained in Na_2SO_4 and $KHCO_3$ are showed in Table 6.3 and Table 6.4 respectively.

Table 6.3: FEs for the different products obtained after CPE experiements at pure Bi metal electrodes in 0.1 M Na_2SO_4. Time for electrolysis = 30 min. H_2 and CO were detected using gas chromatography while HCOOH using ^1H NMR measurements. The potentials values are vs 1 M Ag/AgCl reference electrode.

E_e [V]	electrolyte	gas	Q [C]	$\%FE_{H2}$	$\%FE_{CO}$	$\%FE_{HCOOH}$	$\%FE_{TOT}$
-1.46 (onset)	Na_2SO_4	N_2	0.4	49.0	0	1.0×10^{-2}	49.0
		CO_2	1.8	23.0	0	4.0×10^{-2}	23.0
-1.66		N_2	2.0	20.0	0	2.0×10^{-4}	20.0
		CO_2	8.2	0.2	4.6	7.0×10^{-2}	4.9
-1.86		N_2	10.4	6.0	0	0.0008	6.0
		CO_2	12.5	5.4	2.9	1.0×10^{-2}	8.4
-2.06		N_2	19.5	2.9	0	5.0×10^{-4}	2.9
		CO_2	19.1	3.2	3.1	0.1	6.4

Looking at the two tables, it is possible to conclude that both systems do not present significant catalytic activity toward CO_2 reduction. Several factors can be responsible for the lack of catalytic activity of the Bi cylinders, like the crystalline structure. This aspect is quite important as it influences the adsorption of the species (both the substrate and the intermediates) on the surface of the electrode. For example, Yang at el.[105] demonstrated via DFT calculations that the adsorption of CO_2 was strongly dependent on the facets exposed to the solutions. Specifically, the adsorption of the OCHO* intermediate on the crystal facet (111) in a Bi atomic monolayer (Bismuthene) was actually more energetically favoured than for the intermediate H*, as the free energy for the adsorption of OCHO* was equal to 0.8 eV, while for H*, it was equal to 1.3 eV. This was proposed to be the reason behind the higher selectivity for CO_2 reduction than for HER. On the other hand, the 011 facet underwent poisoning by the same carbon intermediate thus favouring HER. This reinforces the need for surface composition analysis before and after catalytic experiments (see discussion in Chapter 3, Section 2.4)

Another interesting observation is that the system seems to produce higher quantities of CO than formate, with FE_{HCOO^-} not exceeding 0.1%. This was unexpected as Bi electrodes are known for being CO_2-to-formate catalysts, like Sn, Pb, In and Cd electrodes[103,104,154,215,277]. Small quantities of CO have been observed in different works[100,101], but they never exceed the 10% of the total faradaic efficiency. It is important to highlight that, high FEs for formate on polycrystalline Bi metal electrodes are not generally observed and a mixture of H_2, CO and formate is produced during electrolysis. For example, in the literature on bulk Bi electrodes, four different ranges of ≈ 20, 35,

50 and 50% for FEs_{HCOO^-} were observed[103,101,154,267]. The highest FE_{HCOO^-} was obtained by Hara et al.[104] and it was equal to 82.7%. From the FE values in the literature, it is clear that the values obtained in this work are significantly lower, suggesting that the use of a polycrystalline electrode is not the cause for the low catalytic activity toward CO_2RR. FE for formate not equal to zero were calculated in N_2-saturated $KHCO_3$ solutions (see Table 6.4). Small amounts of formate under N_2 atmosphere have been observed before[99] (FE_{HCOO^-} = 2.1% in 0.5 M $KHCO_3$ at -1.45 V vs SCE) and it is due to the reduction of CO_2 formed from the equilibrium in water of HCO_3. In addition, considering the magnitude of the charge exchanged during the CPE experiments and the fact that the total FEs never reached a value close to 100% regardless of the potential applied, the electrolyte used and the gas used to saturate the solution (maximum FE_{TOT}= 49% in Na_2SO_4 and 24% in $KHCO_3$), it is likely that another process is occurring at the surface of the electrode during electrolysis. This process is probably not even linked with the presence of CO_2 as the total FEs are very low also under N_2. In both electrolytes the total FEs decreased as the potential become more negative, suggesting that the unwanted process is increasingly favoured at more negative potentials. It has been observed elsewhere that poisoning of different metal electrodes by the electrolyte ions can occur at certain potentials[272,379,381]. For example, at Au electrodes, poisoning by Na cations have been theorised: the Na ions block the surface of the electrode at negative potentials reducing the available sites for the adsorption of CO_2[272]. Specific adsorption of alkali on Bi electrodes and the consequent increase of the overvoltage for HER has been reported by Palm et al.[382]. In addition, it has been demonstrated in two different works, using DFT calculations, that the ions present in solution, strongly influence the performance of the system[383,384]. In particular, the presence of certain cations and anions can stabilise the formation of a specific intermediate and therefore favour a specific reaction pathway. However, no examples were found in the literature on the possible poisoning of the surface of the electrode by supporting electrolyte in the context of CO_2 reduction.

Table 6.4: FEs for the different products obtained after CPE experiements at pure Bi metal electrodes in 0.1 M $KHCO_3$. Time for electrolysis = 30 min. H_2 and CO were detected using gas chromatography while HCOOH using ^{1}H NMR measurements. The potentials values are vs 1 M Ag/AgCl reference electrode

E_e [V]	electrolyte	gas	Q [C]	$\%FE_{H2}$	$\%FE_{CO}$	$\%FE_{HCOO^-}$	$\%FE_{TOT}$
-1.48 (onset)	$KHCO_3$	N_2	1.3	21.8	0	2.0×10^{-3}	21.8
		CO_2	1.6	19.2	5.2	0.1	24.5
-1.68		N_2	7.9	8.1	0	3.0×10^{-3}	8.1
		CO_2	6.0	7.1	6.8	0.2	14.1
-1.88		N_2	8.2	8.4	3.0×10^{-2}	2.0×10^{-4}	8.4
		CO_2	12.8	4.6	5.5	0.1	10.2
-2.08		N_2	10.3	5.8	6.0×10^{-2}	2.0×10^{-2}	5.7
		CO_2	10.7	4.8	5.7	0.2	10.7

After the CPE experiments, a change in colour of the electrode from grey (see scratches in Figure 6.5) to yellowish in Na_2SO_4 was observed, suggesting a change in the surface composition. This colour was different from the colour observed on the metal left in atmospheric conditions, that was grey-pinkish, suggesting a different composition and/or thickness of the oxide layer. A similar colour was observed after scan rate studies (see Chapter 3) in Na_2SO_4, in which the formation of the Bi oxide and its reduction was induced.

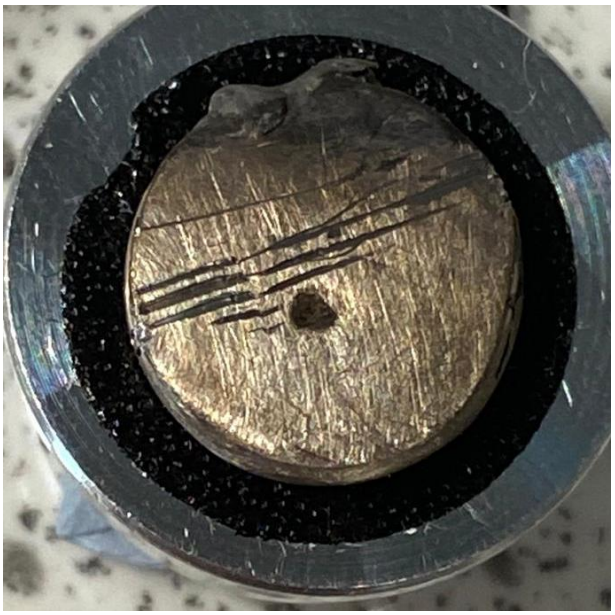

Figure 6.5: Bi cylinder after electrolysis experiments in Na_2SO_4. The grey lines in the middle were produced by scratching the electrode with a sharp tool to show the colour of the surface before catalysis, while the grey area on the top is where the epoxy resin covered the electrical connections. For a photo of the electrode surface see Figure 6.1

Even when the polishing step on the Bi cylinders was performed, it was not possible to completely remove the oxide layer, as in the first cycle of the CVs performed before the CPEs, a peak around -0.8 V vs Ag/AgCl (consistent with the reduction of Bi^{3+} to Bi^0 [177,385]) was observed. In addition, depending on the condition of formation of the oxide layer on the electrode surface (time, temperature, pressure), it might be possible that the Bi oxide is too thick to be completely removed by the negative potential applied during cyclic voltammetry. Similar behaviour has been observed for Cu electrodes[386]: depending on the environment in which they were exposed (air or aqueous solutions) and the time of exposition, the oxide was less or more thick and therefore more difficult to completely reduce. If this was the case, the more superficial oxide layer would be reduced during the first scan and the rest would be reduced during electrolysis. In addition, it has been observed before that the reduction of the native oxide layer in Bi[177,178,194] produces a porous surface. The formation of a porous surface during the application of a cathodic potential (like in the catalysis experiments) allows the deeper layers of oxide to be exposed and therefore to be reduced. This means that part of the charge passed during electrolysis would be due to the slow, continuous

reduction of the oxide. It has been demonstrated by Perez et al.[192] via optical techniques that the mechanical polishing may not completely remove the native oxide layer and that it is necessary to reduce the Bi oxide electrochemically or chemically[178]. The presence of a thick native oxide layer in conjunction with the impossibility of a thorough cleaning during the polishing step due to the defects present on the surface of the electrode suggest that some oxide is still present during electrolysis and that part of the charge passed during the experiments was actually used for its reduction. The presence of Bi oxide at negative potentials has been observed before by Lee et al.[244]: an electrode made with a carbon paste containing Bi oxide exclusively presented Bi^{3+} species before catalysis, while after a potential equal to -1.51 V vs Ag/AgCl was applied, only 16.6% of Bi^{3+} was detected (the composition was calculated using in situ X-ray absorption near-edge structure - XANES - analyses). Similarly, Dutta et al.[106] detected the presence of Bi oxide via operando Raman spectroscopy up to 120 minutes during the electrolysis experiments for the electrocatalytic reduction of CO_2 . It is important to highlight that the Bi electrodes studied by Dutta et al. were freshly prepared before experiments, meaning that they did not have aged oxide on the surface, while in this work the electrodes were simply regenerated via polishing with sandpaper, that may not ensure the complete removal of the native oxide layer[192]. To understand if any structural changes are present at the surface of the electrode after catalysis, SEM images were acquired (see Figure 6.6). After the CPE experiments and before the acquisition of the images, the electrodes were rinsed thoroughly with distillate water to remove any trace of the electrolytes. From the image at lower magnification, it is possible to observe some brighter areas (Figure 6.6a) that, by increasing the magnification, can be seen to be a porous solid (Figure 6.6b, c, d and e). At the highest magnification (Figure 6.6f), it is clear that the solid consisted of amorphous particles with various sizes. Similar morphology has been observed by Ammeloot et al.[386] on Cu electrodes after the exposure of the electrode to sodium chloride solutions and the formation of copper oxide was suggested. In contrast, Romann and Lust[194] observed the presence of some deposits after continued application of negative potential but they suggested that the deposit was in fact metallic Bi redeposited after the decomposition of Bi hydrides (see Equation 1.4a and b). The formation of Bi hydride during the application of negative potential has been also proposed by Pérez et al.[192]. However, no proof of the formation of Bi hydride was presented. As far as this work is concerned, an increase of the electrochemical area was observed after catalytic experiments. This could be an indication of the formation of the porous metallic Bi after decomposition of Bi hydrides, or it could be due to the exposition of deeper layers of Bi oxide due to the initial reduction of the most external layer. However, as no information on the composition of the electrodes was obtained, the chemical nature of the porous solid and a hypothesis over the other cannot be confirmed. Regardless of the

nature of the process involved, it can account for the additional charge passed during the electrolysis experiments and, therefore, explain the low values of the FE_{TOT}.

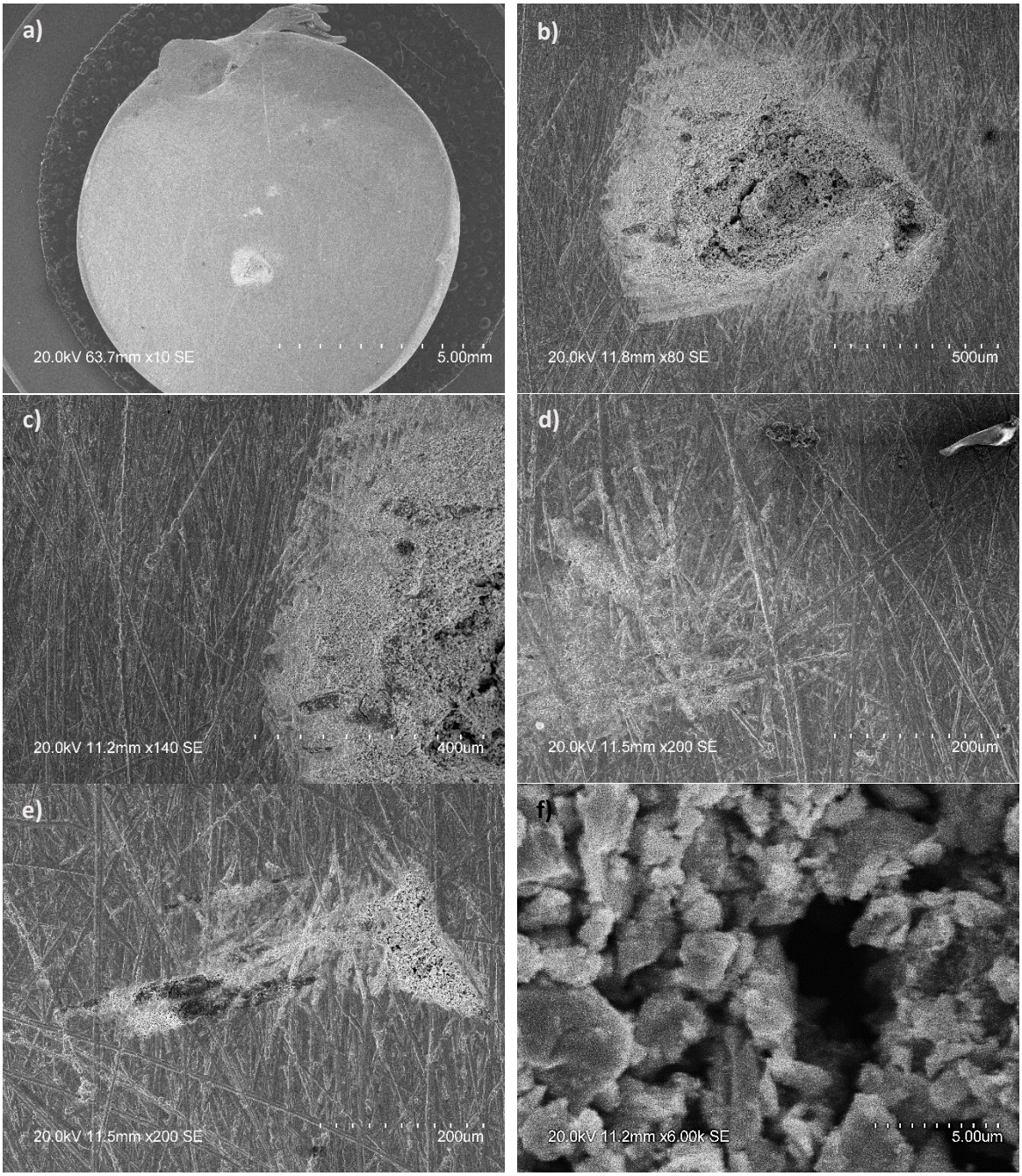

Figure 6.6: SEM images of the Bi cylinder after catalysis experiments at different magnifications: a) x10; b) x80; c) x140; d)x200; e) x200; and f)x6.00k. Image b) and c) are acquired in the same area, while d) and e) were acquired in two other different section of the electrode

Based on the results here, to gain insight on the nature of the processes occurring at the Bi electrodes, composition analyses of the electrode after, before and, preferably, during the catalytic experiments need to be performed. Information on the composition of the electrode would be useful in understanding the reaction pathways for the reduction of CO_2, as pure Bi metal surfaces would influence the CO_2RR differently than mixed Bi metal/ Bi oxide. For example, using a

combination of kinetic models and DFT calculations, Deng et al[387] suggested that the rate determining step (RDS) on Bi metal electrodes is the one-electron transfer step while, at Bi oxide electrodes, the RDS is the hydrogenation of the intermediate. In addition, the binding of CO_2 on the surface of the electrode (see green section in the diagram in Figure 4.1) has been demonstrated to be different depending on the composition of the electrode[271]. Therefore, the knowledge of the composition of the electrode would give deeper insight on the products obtained during catalysis.

6.3 CO_2 reduction modified Bi-GC electrodes

Electrolysis experiments for the CO_2RR were performed using the Bi modified electrodes produced via electrodeposition on glassy carbon electrodes (GCE) (see Chapter 4). This allowed a direct comparison of the catalytic activity between the bulk Bi electrodes and the microstructured Bi electrodes. In addition, the influence of the morphology of the Bi crystallites on the catalytic activity was evaluated. This would allow a deeper understanding of the possible impact that the presence of microparticles, the magnitude of the electroactive area and the morphology of the particles have on the key factors that influence the activity of the CO_2RR (see diagram in Figure 4.1).

The CPE was first performed in aqueous solutions containing 0.1 M Na_2SO_4. Considering the fact that it has been previously demonstrated that different morphologies of Bi crystallites influence the catalytic activity modifying the reaction pathway and therefore the selectivity[102,153,243,310], the experiments were performed with Bi modified electrodes with different morphologies (spheres and dendrites). Several electrodes with the same morphology were produced to improve the coverage of the substrate. Some of these electrodes presented a similar coverage of the substrate but different electroactive area (see Chapter 4 Section 4.3). For this reason, the electrodes that presented the best coverage and the higher real area were chosen for the catalytic experiments.

The onset potential, the range of applied potentials and the experimental systems were selected using the same principles discussed for the Bi cylinders (see previous section). In the case of the Bi modified electrodes, the extrapolation of the onset potential value was obtained for several electrodes. All the electrodes presented a similar onset potential that was around -1.35 V vs Ag/AgCl.

6.3.1 Influence of morphology on the catalytic activity of the Bi modified electrodes

First, a comparison on the catalytic activity between electrodes with different morphology is presented. In Table 6.5, the FE for hydrogen, CO and formate are shown for two different electrodes: Bi-GC0.5 and Bi-GC(5:3)200. The two electrodes presented spherical and dendritic crystallites respectively and the highest real areas among the other electrodes. For each applied

potential, an additional CPE experiment was performed using, as a working electrode, the bare glassy carbon electrode (GCE), which was the substrate used for the Bi deposition.

Table 6.5: FEs for the different products obtained after CPE experiements at several Bi modified electrodes and glassy carbon electrode under CO_2. Time for electrolysis = 30 min. H_2 and CO were detected using gas chromatography while HCOOH using ^1H NMR measurements. The potentials values are expressed vs Ag/AgCl 1 M reference electrode

electrode	morphology	E_c [V]	$\%FE_{H2}$	$\%FE_{CO}$	$\%FE_{HCOOH}$	$\%FE_{TOT}$
GCE	-		37.0	0	0.1	37.1
Bi-GC(5:3)200	dendritic	-1.35	45.1	0	4.8	49.9
Bi-GC0.5	spherical		42.5	0	1.9	44.4
GCE	-		39.0	5.1	0.7	44.8
Bi-GC(5:3)200	dendritic	-1.55	29.4	3.3	1.3	34.0
Bi-GC0.5	spherical		37.5	2.3	0.1	39.9
GCE	-		32.0	23.4	6.0×10^{-2}	55.5
Bi-GC(5:3)200	dendritic	-1.70	38 .0	3.1	0.1	41.2
Bi-GC0.5	spherical		26.4	1.6	0.2	28.2

Regardless of the morphology of the particles, a general trend can be observed (see Table 6.5): at -1.35 V, both the Bi electrodes produced formate (4.8 and 1.9% FEs) while no CO was detected. By increasing the applied potential, the quantity of formate produced decreased significantly, while the quantity of CO increased seven-fold. In particular, a decrease of formate of x3.2 and x19 times was observed at -1.55 V for Bi electrodes with spherical and dendritic morphologies, respectively. FEs for CO are around 2% for Bi-GC(5:3)200 and 3% for Bi-GC0.5, at both -1.55 and -1.70 V. Similarly, Zhang et al.[269], observed an increase in the production of CO at potentials higher than -1.50 V vs SCE using an electrode containing Bi microparticles, while in the range between -1.30 and -1.45 V vs SCE only H_2 and formate were detected. In contrast, Zhang et al.[100], detected the highest quantity of CO using a Bi nanosheet electrode at the most positive (-0.5 and -0.6 V vs RHE) and the most negative (-1.2 V vs RHE) potentials. However, even at the potential at which the production of CO was the highest, x4.5 times more formate and H_2 were detected. It has been previously suggested that Bi modified electrodes with different morphologies showed different catalytic activity[153,243,310]. For example, Qiu et al.[310] observed different selectivity between nanoflower Bi electrodes and nanorod Bi electrodes. In particular, at -1.5 V vs SCE a FE for formate almost x1.5 times higher was exhibited by the nanoflower Bi electrodes. However, this work is distinctive in that it has attempted to separate electrode area and morphology effects. Here, it appears that the morphology of the particles is not significantly influencing the catalytic activity of the system. However, it is important to note that, in general, it seems that the Bi modified electrodes do not show selectivity for CO_2 reduction, as the main product detected for all the experiments was H_2. Interestingly, at -1.70 V, when the bare GC electrode was used FE_{CO} = 23%, while using the Bi modified electrodes (Bi-GC(5:3)200 in this case), FE_{CO} = 3%. Based on these results, it seems that the presence of the Bi

crystallites inhibits the formation of CO. In addition, it seems that some other process is happening at the surface of the electrode, as the total faradaic efficiency is never equal or similar to 100%. Considering that no other products are detected after electrolysis, this means that the charge passed during the catalytic experiments is partially due to other processes other than catalysis. As proposed for Bi cylinders, this process is likely to be the reduction of the Bi oxide on the surface of the Bi crystallites. For a detailed discussion on the possible nature of the additional processes see section below and Section 6.2.1.

6.3.2 Influence of the area of the electrode

It has been proposed in the literature that the real area and the roughness factor of a working electrode influences the catalytic activity of a system, like the overpotential and the selectivity[222]. For this reason, different catalytic measurements were performed to monitor the difference in the selectivity as a function of the area of the electrode. First, two electrodes with ***similar*** real area were compared and, second, two electrodes with ***different*** areas were tested. To avoid any possible additional influence, the electrodes were chosen with the same morphology for each set of experiments. The two electrodes with *similar* area possessed *dendritic* structure, while those with different area presented spherical morphology. The real area values and the FE obtained are shown in Table 6.6.

Table 6.6: FEs for two Bi modified electrodes having same morphology and similar area. Time for electrolysis = 30 min. H_2 and CO were detected using gas chromatography while HCOOH using ^{1}H NMR measurements. The potentials values are vs 1 M Ag/AgCl reference electrode

electrode	A_{real} [cm^2]	E_c [V]	$\%FE_{H2}$	$\%FE_{CO}$	$\%FE_{HCOOH}$	$\%FE_{TOT}$
Bi-GC	2.1 ± 0.9	-1.35	64.5	0	2.6	67.1
		-1.55	17.1	5.0	0.1	22.2
		-1.70	36.0	6.4	6.0×10^{-2}	42.5
Bi-GC(5:3)20	1.7 ± 0.4	-1.35	45.1	0	4.8	49.9
		-1.55	29.4	3.3	1.3	34.0
		-1.70	38	3.1	0.127	42

In general, it seems that Bi-GC(5:3)20 showed a higher selectivity toward formate production than CO while, when Bi-GC was used more CO was produced (except at -1.35 V, potential at which both the electrodes did not produce any CO). This might be due to the fact that, even if the areas of the two electrodes are comparable, Bi-GC had more GC surface exposed than Bi-GC(5:3)20. From the experiments performed previously, at higher production of CO than formate, was observed when bare GCE was used (Table 6.5). However, also in this case, the FEs_{TOT} significantly deviated from 100%, suggesting that some other process is happening at the electrodes. It does not seem that the magnitude of the real area influenced the FE_{TOT}. For example, Bi-GC exhibited the highest FEs_{TOT}

with a maximum value x1.4 times higher than that obtained with Bi-GC(5:3)20, even if it presented an area x1.2 times lower. This suggests that the area did not influence the overall catalytic performances toward the CO_2RR.

Finally, the catalytic activities of two electrodes with same morphology but different area were compared (see Table 6.7). Two electrodes with spherical morphology, Bi-GC0.5 and Bi-GC(5:3)0.5, were tested applying one potential, -1.35 V.

Table 6.7: FEs for two modified Bi electrodes with same morphology but different area.Time for electrolysis = 30 min. H_2 and CO were detected using gas chromatography while HCOOH using ^{1}H NMR measurements. The potentials values are expressed vs 1 M Ag/AgCl reference electrode

electrode	E_c [V]	A_{real} [cm^2]	$\%FE_{H2}$	$\%FE_{CO}$	$\%FE_{HCOOH}$	$\%FE_{TOT}$
Bi-GC0.5	-1.35	2.59 ± 0.06	42.5	0	1.9	44.4
Bi-GC(5:3)20_0.5	-1.35	3.4 ± 0.4	46.9	0	4.2	51.1

The evolution of H_2 seems to be comparable for both of the electrodes and neither of them produced CO (probably because of the low potential applied). Interestingly, it seemed that the catalytic activity for formate is influenced by the real area of the electrode: twice the amount of formate was produced when the electrode with the largest area was used, suggesting that, for spherical Bi particles the real area of the electrode influenced the CO_2 reduction reaction.

Some additional experiments were performed in $KHCO_3$ with Bi-GC as a working electrode to understand if the presence of the bicarbonate salts increased the catalytic activity of the system. The FEs obtained for these experiments are shown in Table 6.8. The experiments performed in $KHCO_3$ did not exhibit higher FEs_{TOT}, suggesting that the low FEs_{TOT} are not due to the electrolyte as no improvement was observed.

Table 6.8: FEs for Bi-GC in 0.1 M $KHCO_3$.Time for electrolysis = 30 min. H_2 and CO were detected using gas chromatography while HCOOH using ^{1}H NMR measurements. The potentials values are expressed vs 1 M Ag/AgCl reference electrode

potential [V]	Q [C]	FE_{CO} [%]	FE_{H2}[%]	FE_{HCOO^-} [%]	FE_{TOT}[%]
-1.32	$1.4x10^{-2}$	0.0	30.5	3.1	33.6
-1.52	0.1	0.0	27.3	0.7	28.0
-1.72	1.1	9.0	12.1	1.2	22.3

In general, slightly higher FE_{TOT} values were observed for the Bi modified electrodes than for the Bi cylinders, as the maximum FE_{TOT} obtained using the Bi modified electrodes was equal to 68%, while with Bi cylinders it was equal to 24.49%. This suggests that the presence of microparticles increased the catalytic performance of the electrodes. It is important to highlight that, with both types of electrode, the major contribution to the FE_{TOT} was due to the evolution of H_2 and not to the formation a carbon products. However, the Bi modified electrodes presented higher FE for formate

than the Bi cylinders, which showed FEs_{HCOO^-} equal to or smaller than 0.2%. This may suggest that the presence of the microparticles influenced the selectivity of the system. However, it is important to highlight that because of the low FEs_{TOT}, an appropriate comparison between the effect of the morphology of the microparticles and the magnitude of the area of the electrode cannot be done.

Considering the low FE_{TOT} obtained with these systems, it is important to address the possible issue causing these low values. In general, regardless of the charge passed, low total faradaic efficiencies were observed. Usually, a part of the total charge is always dissipated as heat; however, this portion is normally low and it does not influence the efficiency of the reaction to a large extent (especially at laboratory scale). Production of oxalate has been observed for the reduction of CO_2, however, the production of this compound occurs in very specific conditions, that are significantly different from the one use within this work. Liquid chromatography experiments will confirm the absence of oxalate in the catholyte. This suggest that another process is happening during the CPE experiments that is not related with the CO_2RR or HER. As discussed for the Bi cylinders, two possible processes may be occurring during electrolysis: the reduction of Bi oxide and the formation of Bi hydride followed by redeposition of Bi particles on the surface of the electrode. First, to understand if the additional process involved a change in morphology of the Bi particles (i.e.: charge is going to electrocrystallization or related phenomena), or if some additional deposit is present, as in the case of the Bi cylinders, photographs and SEM images of a Bi-GC electrode were acquired before and after CPE measurements. The electrode showed significant damage after CPE measurements (see Figure 6.7b). This was confirmed by SEM images (Figure 6.7d), in which it is evident that the area on the bottom right corner of the electrode presented more glassy carbon surface exposed and the density of the particle decreased significantly. In addition, the quantity of the large crystallites decreased greatly, and mostly small particles or small fragments of the large particles were found (Figure 6.7f). Unlike in the work of Qui[310], no significant morphological changes were observed, suggesting that part of the charge measured was not due to some morphological change. In contrast with Bi cylinders, additional porous deposits were not observed (Section 6.1.1). Therefore, the additional process is likely to be the reduction of the Bi oxide.

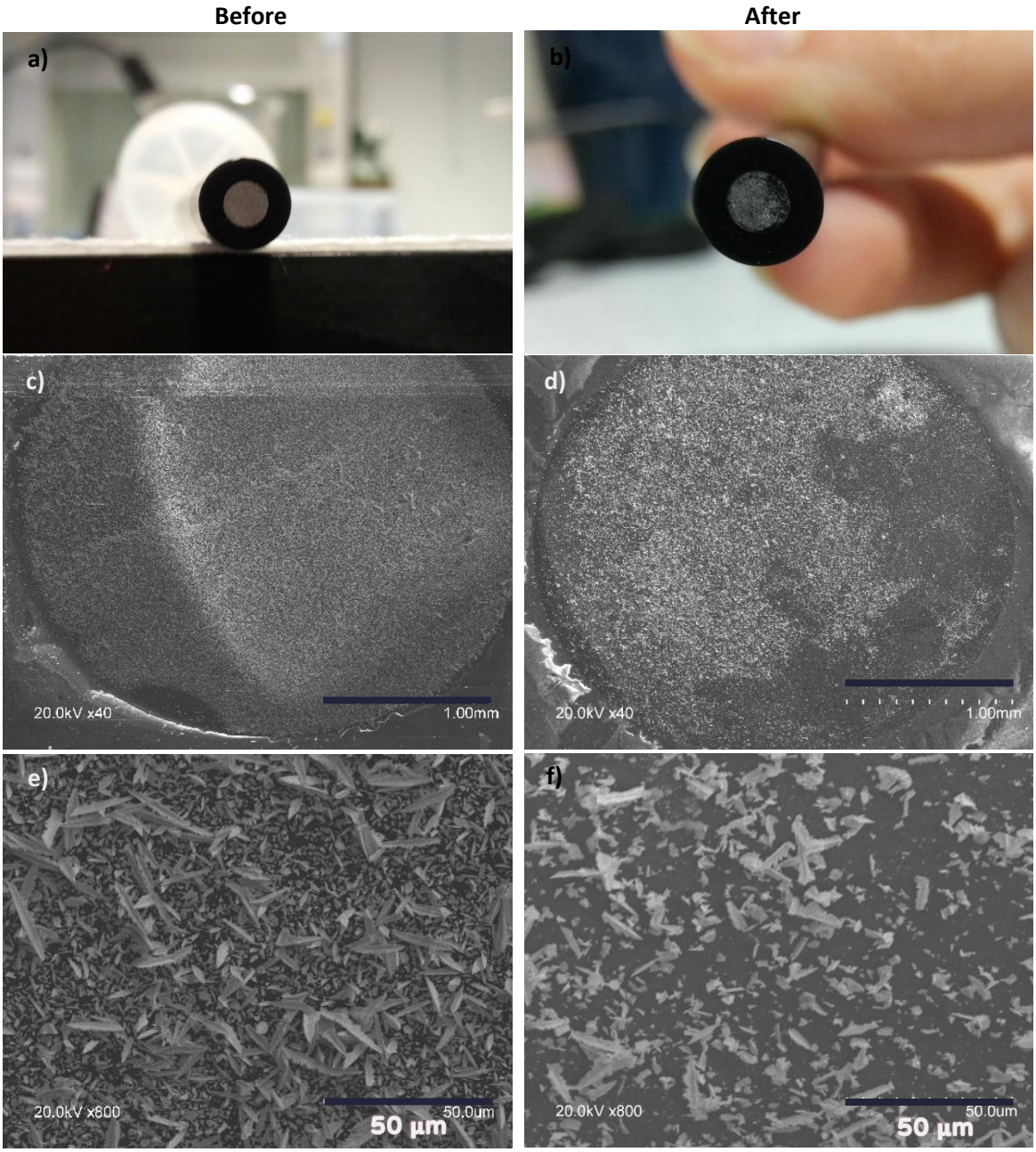

Figure 6.7: photograph of a Bi-GC electrode before a) and after b) CPE measurements. SEM images of a Bi-GC electrode before (left) and after (right) CPE measurements, at magnification equal to c) and d x40 and e) and f) x800. The accelerating voltage was equal to 20 kV

XPS analyses of the Bi modified electrodes performed before the catalytic experiments (see Chapter 4 Section 4.1) showed that the crystallites presented Bi^{3+} species. In particular, the ratio between the peak for the Bi^{3+} and the Bi^{0} species was 2:1. Based on the XPS analyses, it was suggested that Bi_2O_3 is present in/on the crystallites. This was confirmed by the CVs acquired before each CPE experiment. Figure 6.8 shows the CVs for three different Bi-GC(5:3)200 electrodes in CO_2-saturated solutions. A series of peaks between -0.6 and -1.4 V vs Ag/AgCl are present in the first cycle (solid curves), but they disappear in the second cycle (dashed curves). For all three electrodes, a large peak is observed around -0.7 V vs Ag/AgCl followed by a tail. This has been observed for Bi

polycrystalline electrodes by William and Wright[177], who suggested that the presence of the tail is due to the reduction of a thicker layer of Bi_2O_3. Considering that the electrodes were not produced the day the CPE measurements were performed, each electrodes has a different history. This is confirmed by the different peaks and tails observed in the 1st cycle of the CVs, suggesting different thicknesses of the Bi oxide on the electrodes. Similar results have been observed for Cu electrodes (see discussion for Bi cylinders)[386]. As discussed for Bi cylinders (Section 6.1.1), the absence of the peak on the second cycle, does not mean that the oxide is completely reduced before the CPE experiments and it is likely that during catalysis, part of the charge passed is used for the reduction of the Bi oxide.

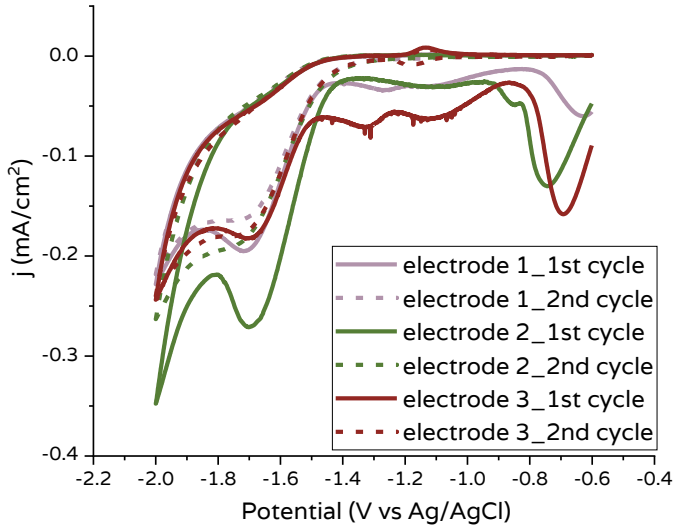

Figure 6.8: CVs with three different Bi-GC(5:3)200 electrodes in a CO_2-saturated 0.1 M Na_2SO_4 solution. The solid lines represent the 1st cycle, while the dashed lines the 2nd cycle. The current was normalised to the A_{real} (r_f = 37)

Based on these considerations and given the results obtained by Dutta et al.[106], who observed the presence of Bi_2O_3 on the surface of the electrode even up to 120 minutes during the CPE measurements (see discussion in Section 6.11), an additional experiment was performed by increasing the time for the CPE experiments from 30 to 90 minutes. Because the highest FEs_{TOT} were obtained at the most positive potential used (-1.35 V), the experiments were performed at this potential. Two different electrodes with spherical morphology were used for the experiments and the FEs are shown in Table 6.9. When Bi-GC0.5 was used, an increase of the FEs_{TOT} from 44.4 to 62.3% was observed, with the production of CO being the major contributor to the increase. This may mean that longer experiments are necessary to obtain significant amounts of carbon products, suggesting that the charge passed in the first period of the electrolysis experiments is used for the reduction of the Bi oxide. Interestingly, with Bi-GC(5:3)20-0.5 no appreciable difference in FEs_{TOT} is observed. These results contrast with Bi-GC0.5. However, it is important to highlight that the for the two Bi-GC0.5 electrodes and the Bi-GC(5:3)20-0.5 used for the shorter experiments, the time

passed between the preparation and the CPE experiments was shorter than for the Bi-GC(5:3)20_0.5 used for the long experiments, meaning that the story for the Bi on the surface of the last electrode is completely different than for the other three. This would confirm that depending on the conditions and the time of exposition to air, the oxide can be more difficult to reduce.

Table 6.9: FEs for two modified Bi electrodes with spherical morphology.The time for electrolysis was varieted. H_2 and CO were detected using gas chromatography while $HCOO^-$ using ^1H NMR measurements. The potentials values are expressed vs 1 M Ag/AgCl reference electrode

electrode	E_c [V]	t [s]	Q [C]	$\%FE_{H2}$	$\%FE_{CO}$	$\%FE_{HCOOH}$	$\%FE_{TOT}$
Bi-GC0.5	-1.35	1800	0.04	42.5	0	1.9	44.4
	-1.35	5400	0.2	48.9	14.0	0.2	62.9
Bi-GC(5:3)20_0.5	-1.35	1800	0.03	46.9	0	4.2	51.1
	-1.35	5400	0.1	50.4	0	0.8	51.2

Figure 6.9a shows the CVs of a Bi-GC electrode produced in advance, while in Figure 6.9b, the CVs of a freshly prepared electrode are showed. For the latter electrode, the Bi was electrodeposited, rinsed and let dry for a few minutes before being inserted into the CO_2-saturated solution. The first electrode presented the peak for the reduction of Bi_2O_3, while the second does not give a well-defined peak. However, by zooming on the potential range between -0.8 and -1.4 V (see Figure 6.9c), a small peak was observed. This means that the formation of the oxide on the surface of the electrode occurs and the Bi oxide is always present before electrolysis experiments.

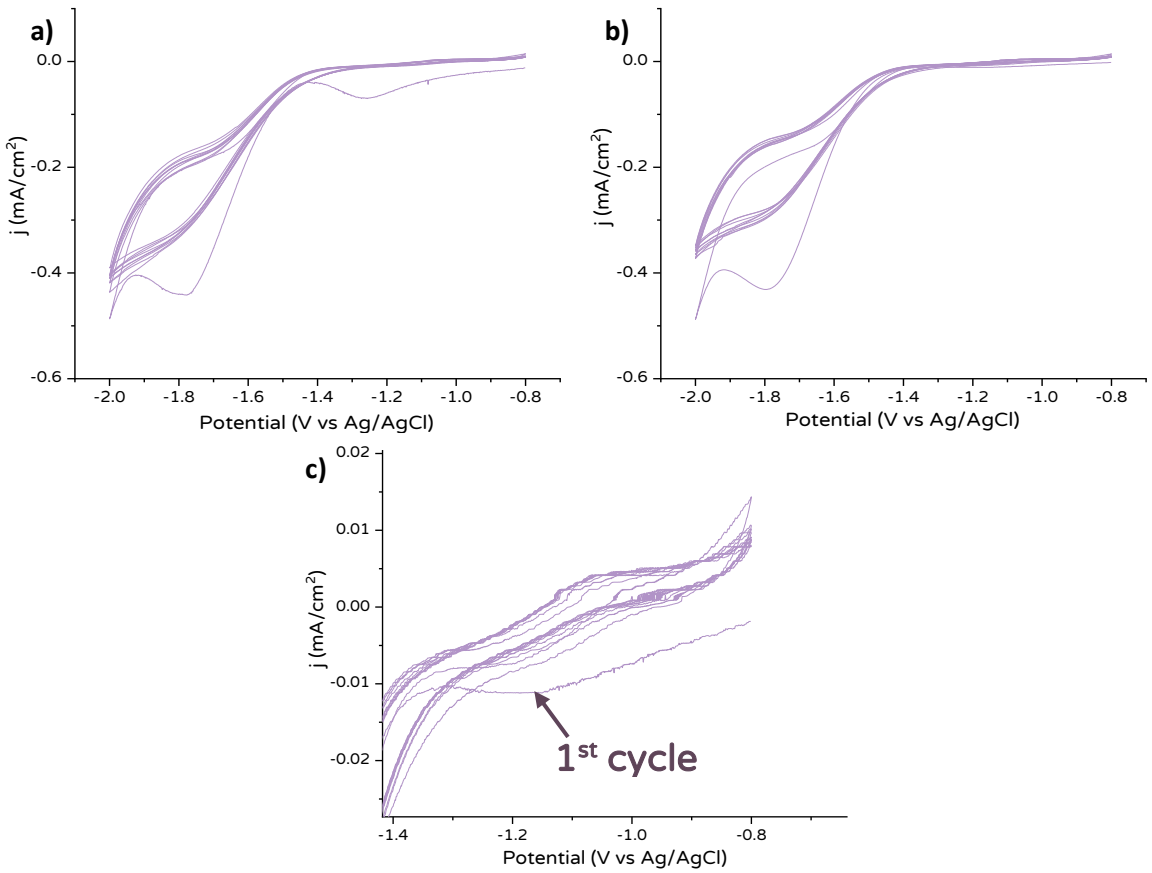

Figure 6.9: CVs acquired with Bi-GC in 0.1 M Na_2SO_4 containing 50 mM of ionic liquid for a) an old electrode and b) a freshly prepared electrode; c) zoom of the potential range in which the reduction of the Bi oxide is observed for the freshly prepared electrode. Ten cycles were performed at scan rate equal to 100 mV/s

In summary, it would seem that the use of Bi microparticles, regardless of the morphology or the magnitude of the area, increases the catalytic activity of the system, as higher FE_{TOT} are observed than for Bi cylinders. This is in agreement with the literature findings, in which an increased catalytic activity in terms of selectivity, current density and onset potential has been observed for electrodes containing micro- and nanoparticles[100,101,154]. However, the majority of these studies present the current normalised to the geometrical area and not to the ECSA, meaning that the current density is likely overestimated and the value of onset potentials may be shifted to more positive potentials, as can be seen in Figure 6.2. The Bi modified electrodes presented higher FEs for formate (between x1.5 and x30 times higher). Comparable FEs_{CO} were observed with Bi cylinders and Bi modified electrodes. This probably means that the number of the active sites and/or the composition of the Bi influences the binding of the CO_2 onto the metal (see green section in Figure 4.1). However, as the crystal composition of the two types of the Bi electrodes was not investigated, and the surface composition of the Bi cylinders before and after the catalytic experiments was not obtained, the possible influence of the composition of the surface on the catalytic activity cannot be confirmed. Based on the results obtained by performing long experiments (5400 s) with Bi modified electrode, the enhanced behaviour generated by the Bi

microparticles is probably due to the chemical composition of the surface. Large quantities of Bi oxide are expected on the Bi cylinders for two main reasons: first, the structure of the surface of the Bi cylinder that presents large quantity of defects; and second, the fact that the electrodes were used for several experiments and only polished before each experiment (not chemical etching was performed). In contrast, always fresh Bi modified electrodes were used for the experiments, ensuring a lower quantity of Bi oxide on the surface. In addition, to understand the binding of the CO_2 on the surface of the two types of Bi electrodes further investigation is required. This was planned to be done via BET analyses, but it could not be performed due to COVID restrictions. In general, for both the bulk Bi electrodes and the Bi modified electrodes, the major product was H_2. This means that the presence of the Bi microcrystallites did not direct the selectivity of the electrode toward CO_2RR, supressing the HER (see blue section in Figure 4.1). Both types of electrode presented Bi oxide prior to CPE experiments and the quantity of the oxide seems to be strongly dependent on the history of the electrode. For longer experiments, an improvement of the FE_{TOT} was observed, but, also in this case, the history of the electrode seems to play a significant role. For this reason, it is reasonable to conclude that a significant portion of the charge passed (around half) during electrolysis experiments is used for the reduction of the oxide. It is possible that, depending on the history of the electrode, significantly longer times are required to completely remove the oxide. This means that a fraction of the current passed is used for the reduction of Bi oxide and not for catalysis. In addition, the modified Bi electrodes were not robust enough, as after the experiments, the film was always partially damaged, leaving the surface of the GCEs uncovered. These two factors strongly influence the performance of the catalysts in terms of stability (see yellow section in Figure 4.1). Based on these findings, an attempt to increase the catalytic activity of the Bi electrocatalysts was performed.

6.4 CO_2 reduction at Bi-GC electrodes in the presence of ILs

A way to improve the activity of a catalyst is to use a co-catalyst. These species work synergistically with the catalyst to accelerate and control a chemical reaction, giving higher efficiencies in term of, for example, reactivity and selectivity than with the catalyst alone[388]. In the context of CO_2RR, ionic liquids (ILs), and in particular imidazolium based salts, have attracted increasing attention for their ability to capture high quantities of CO_2 in a wide range of experimental conditions[23,378,389–394]. More importantly they are able to stabilise the high energy intermediate $CO_2^{\cdot-}$.[231] In particular, the use of imidazolium based ILs for CO_2RR with Bi electrodes has shown an increased selectivity of the system (specifically toward CO production) and higher FEs[167,169,230,240]. For example, Medina-Ramos et al. showed in different studies[167,169,230] that with Bi electrodes in the presence of ILs only CO was detected and the production of formate was

completely suppressed. The selectivity of one product or another is strongly dependent of the intermediate adsorbed at the electrode surface and its formation depends on the crystalline structure, composition of the electrode, solvent (aqueous or organic) and additives[43]. This means that the ILs are capable of influencing two different keys factors of the CO_2RR: the selectivity and the binding of CO_2 onto the catalyst (see blue and green section in Figure 4.1)

For this reason, a commercial IL, 1-butyl-3-methylimidazolium tetrafluoroborate (for short [BMIM]BF_4) was tested to examine if an increased catalytic activity of the Bi-GCEs would be observed. Some novel ionic liquids were then synthesised (see Chapter 5) and tested to monitor their ability to influence the CO_2RR under controlled pH conditions.

6.4.1 Electrocatalysis in the presence of [BMIM]BF_4

Several types of imidazolium based ILs have been used with Bi nanostructured electrodes to increase their catalytic activity. Most studies have investigated the use of ILs in organic solvents like MeCN[167–169,230] as organic solvents decrease the influence of HER due to low proton concentration which is advantageous. However, organic solvents can be toxic and may cause degradation of the components of the system, making the CO_2RR in aqueous solutions attractive, inexpensive and more environmental friendly[395]. Therefore, it is of interest to investigate CO_2 reduction in aqueous solutions and in the presence of ILs. For this reason, 50 mM of the commercial IL [BMIM]BF_4 was used. The experiments were not performed in $KHCO_3$ as, when the IL was added, the solution become cloudy, suggesting a precipitation reaction. Several experiments were performed to understand if different surface areas of the electrodes and different morphology of the Bi crystallites affected the catalytic activity of the Bi modified electrodes in the presence of ILs. One potential was applied to preliminarily test the response of the different electrodes in the presence of [BMIM]BF_4. As for the other systems investigated in this work, the onset potential was chosen based on the CV acquired under CO_2 (see Figure 6.10). In the presence of CO_2, an increase of current followed by a peak was observed. Considering that these features are not present under N_2 atmosphere (not shown here), it is reasonable to assume that they are connected with the reduction of CO_2. Similar features have been observed with Bi film electrodes in MeCN the presence of ILs[169,245]. The value of the onset potential was -1.47 V. For this reason, a potential of -1.5 V was selected for the preliminary catalytic experiments.

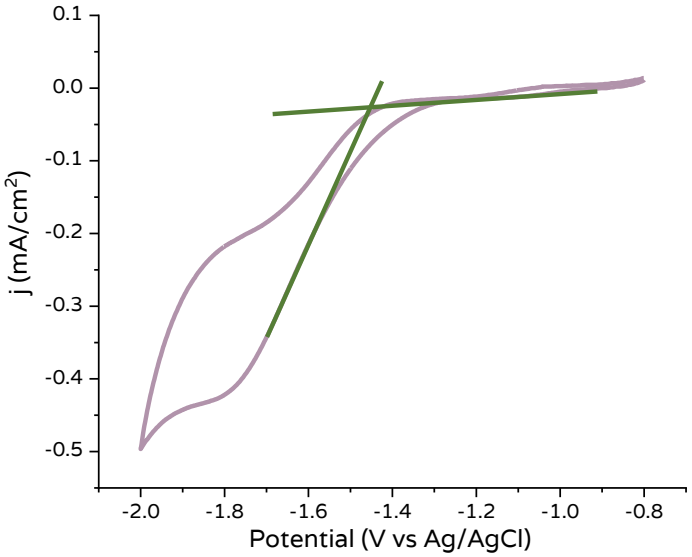

Figure 6.10: CVs obtained with Bi-GC electrode in 0.1 M Na_2SO_4 in the presence of 50 mM [BMIM]BF_4 under CO_2. Scan rate = 100 mV/s and procedure to calculate the onset potential. The current was normalised to the real area calculated via the oxygen adsorption method

The FEs obtained for six electrodes are shown in Table 6.10. In the presence of ILs, low total faradaic efficiencies were measured (max FE_{TOT} = 33.4%), suggesting that the presence of [BMIM]BF_4 did not improve the activity of the Bi modified electrode but actually suppressed it relative to the Bi modified electrodes in the absence of IL. This is in contrast with previous works that showed that the presence of ILs greatly increased the FEs. For example, DiMeglio and Rosethal[169] showed that Bi modified electrodes alone presented a FE for carbonous products equal to 48%, while in the presence of [BMIM]BF_4, it increased to 95%. Bi-GC(5:5)2, the electrode with the highest surface area (see Table 6.10), showed higher total faradaic efficiencies than the others (up to 11.6% more). The increase of the total FEs is mostly due to an increase of faradaic efficiencies for H_2 (up to 11.7 percent more) while no significant changes were noticed for formate and CO faradaic efficiencies. The charge passed during the experiments was three times larger for Bi-GC(3:3)2 and Bi-GC(5:5)2 (Q = 0.3 C) than for the other electrodes, an increase that cannot be attributed solely to the increase in the FE_{H2}. In addition, Bi-GC(5:5)2 presented an area three times smaller, suggesting that the magnitude of the area is not the main parameter influencing the values of the FE_{TOT}. These two electrodes were produced in a 2mM Bi^{3+} deposition bath and presented dendritic structures with long and complex secondary arms (see Chapter 4, Figure 4.19 and 4.20). It has been demonstrated previously using DFT calculations[102] that sharper and thinner corners are able to form higher electric fields than round or bulkier particles. It is possible that the increase in total FEs is due to a mixture of area and morphological effect. However, the total FEs are too low to find a trend in terms of surface area values and catalytic activity in the presence of ILs. In general, it seems that the presence of [BMIM]BF_4 did not increase the selectivity toward the production of CO, in contrast with the literature findings.

As for the Bi modified electrodes in the absence of ILs (see Section 6.3, Figure 6.6), after the CPE measurements, the Bi film was generally damaged, with more glassy carbon surface exposed.

Table 6.10: Products obtained after CPE experiments at several modified Bi electrode in a solution 0.1 M Na_2SO_4 and 50 mM [BMIM]BF_4 Time for electrolysis = 30 min. H_2 and CO were detected using gas chromatography while HCOOH using ^{1}H NMR measurements. The applied potential was equal to -1.5 V vs Ag/AgCl reference electrode

electrode	A_{real} [cm^2]	Q [C]	FE_{H2} [%]	FE_{CO} [%]	FE_{HCOO^-} [%]	FE_{TOT} [%]
Bi-GC(3:3)20	1.08 ± 0.09	0.1	17.1	4.2	0.5	21.8
Bi-GC(5:5)20	1.3 ± 0.6	0.1	18.6	3.4	1.2	23.2
Bi-GC(3:3)2	1.0 ± 0.2	0.3	24.1	1.8	0.4	26.3
Bi-GC(5:5)2	3±1	0.3	28.8	4.2	0.4	33.4
Bi-GC(3:3)200	1.83 ± 0.04	0.1	18.3	0.0	0.9	19.2
Bi-GC(5:5)200	1.0 ± 0.2	$9.0x10^{-2}$	22.0	0.0	1.6	23.6

An additional experiment was performed to compare the differences in catalytic activity as a function of morphology in the presence of [BMIM]BF_4. In Table 6.11, the faradaic efficiencies for each product obtained during CPE experiments with the electrodes produced with Bi-GC (spherical particles) and with Bi-GC(5:5)2 (dendritic particles) are shown.

Table 6.11: Products obtained after CPE experiments at the modified Bi electrodes in a solution 0.1 M Na_2SO_4 and 50 mM [BMIM]BF_4. Time for electrolysis = 30 min. H_2 and CO were detected using gas chromatography while HCOOH using ^{1}H NMR measurements. The potential values are expressed vs 1 M Ag/AgCl reference electrode

electrode	A_{real} [cm^2]	E_a [V]	Q [C]	FE_{H2} [%]	FE_{CO} [%]	FE_{HCOO^-} [%]	FE_{TOT} [%]
Bi-GC(5:5)2	3±1	-1.5	0.3	28.8	4.2	0.4	33.4
Bi-GC(5:3)20_0.5	3.4±0.4	-1.5	0.2	21.3	1.3	0.6	23.2

The Bi electrode presenting spherical particles showed a 10% lower total faradaic efficiency than the Bi modified electrode with dendritic morphology. This difference is due to a higher production of H_2 (+7.5%) and CO (+2.9%). FEs_{HCOO^-} Showed little variation. This is in agreement with the literature findings as it was previously shown that dendritic particles have higher catalytic activity than spherical because of the presence of edges and corners[396]. For example, spherical Au particles[397] presented lower reaction rates (precisely 2x lower) for reduction of organic compounds in comparison with Au dendritic particles. From the values of the total FEs, it is clear that the ILs did not improve the catalytic activity of the Bi modified electrodes. However, as far as the ILs are concerned, it is important to consider that part of the charge passed during the CPE experiments can be due to some decomposition or dimerization processes of the ILs[24,343]. For this reason, ^{1}H NMR measurements were performed before and after CPE measurements and no additional peaks were observed, meaning that [BMIM]BF_4 did not dimerise or decompose. Based on the findings reported here, it is clear that the charge passed during CPE experiments was not due to catalytic processes (CO_2RR and HER) or decomposition of the IL. This means that the main process occurring

during CPE experiments is likely the reduction of the oxide on the Bi crystallites, even in the presence of ILs.

6.4.2 Electrocatalysis in the presence of [1-CP-3-MIM]BF_4

Finally, some CPE experiments were performed in the presence of the IL 1-carboxypropyl-3-3-methylimidazolium tetrafluoroborate ([1-CP-3-MIM]BF_4 for short). In Chapter 5, Section 5.3.2.2, it was observed an increase in current densities during CV measurements under CO_2 in the presence of [1-CP-3-MIM]BF_4 when the pH of the solution was below the pK_a value. It is therefore important to understand if this increase resulted from CO_2RR and not from other side reactions (such as HER, decomposition or dimerization of the IL). For this reason, separate experiments were performed in solution at pH values above and below the pK_a, as this would allow any possible difference in the catalytic activity of the system to be monitored in the presence of the protonated or deprotonated carboxylic acid group. In addition, based on the concentration dependence results (see Figure 5.21 Chapter 5), the CPE experiments were performed at the highest concentration tested via CV measurements, i.e., 50 mM.

Four sets of experiments were performed with each set consisting of two experiments: one adjusting the pH of the solution below the pK_a value and the other above the pK_a value. The four different potentials were selected in the potential region between the first increase of the current (at around -1.0 V) and the second rise of current (at around -1.4 V). This allowed the CO_2RR to be investigated in the region around the peak at -1.2 V (see Figure 6.11). This type of feature have been observed before for imidazolium based ILs and has been attributed to the formation of IL- CO_2 complex[24,342].

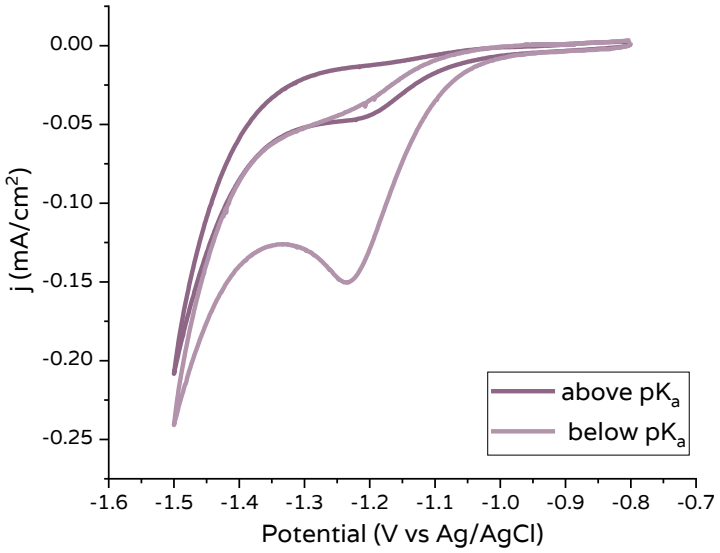

Figure 6.11: CVs with Bi-GC in the presence of 50 mM [1-CP-3-MIM]BF_4 in a solution 0.1 M Na_2SO_4 with pH below (light purple curve) and above (dark purple curve) the pKa

The peak at around -1.2 V decreased significantly when the pH of the solution was adjusted *above* the pK_a value, therefore it is reasonable to assume that the process is likely to be pH dependent. In Table 4.4, the faradaic efficiencies (FEs) obtained for each product after all the CPE experiments are summarised. From the obtained data it is evident that at all pH values and applied potentials mainly H_2 was obtained, with a maximum value of FE equal to 62.2%. As far as the two carbon products are concerned, their production is almost negligible. Small quantities of formate were detected at pH values above pK_a and at more positive potentials (-1.1 and -1.2 V vs Ag/AgCl), while CO production was observed at pH below the pK_a value and for more negative potentials (-1.3 and -1.4 V vs Ag/AgCl). A similar trend was observed in the literature before[269] when carbon paper containing a Bi-NPs ink was used as working electrode in a 0.5 M $KHCO_3$ solutions. In general, from Table 4.4, three main features are evident: first, the system produced mainly H_2, meaning the actual system is not suitable for the reduction of CO_2; second, the total FEs are moderate (maximum FE_{TOT} = 65.1%); and third, the quantity of the charge passed during each experiment is high in comparison with the FE_{TOT}. The high production of H_2 is likely due to the low pH of the solution. Bi electrodes are known for their ability of supress HER, however, it is possible that the pH of the solutions is too low and the selectivity is driven toward the evolution of H_2.

Table 6.12: Products obtained after CPE experiments at Bi-GC electrode in a solution 0.1 M Na_2SO_4 and 50 mM [1-CP-3-MIM]BF_4. Time for electrolysis = 30 min. H_2 and CO were detected using gas chromatography while HCOOH using ^{1}H NMR measurements. The potential values are expressed vs 1 M Ag/AgCl reference electrode

potential [V vs Ag/AgCl]	pH	Q [C]	FE_{H2} [%]	FE_{CO} [%]	FE_{HCOO-}[%]	FE_{TOT} [%]
-1.1	3.7	$7.3x10^{-2}$	54.2	0.0	0.0	52.2
	4.6	$1.8x10^{-2}$	62.2	0.0	2.9	65.1
-1.2	3.8	0.3	42.2	0.7	0.2	43.1
	4.6	$3.7x10^{-2}$	59.6	0.0	3.8	63.4
-1.3	3.7	0.4	48.6	2.3	$1.0x10^{-2}$	50.9
	4.6	0.1	39.0	0.0	0.2	39.2
-1.4	3.8	0.5	43.8	1.6	0.3	45.7
	4.7	0.2	39.2	0.0	0.4	39.6

As observed for the other electrolysis experiments performed within this work, the FE_{TOT} are not close to 100%, meaning that some other process is happening at the electrode surface. As far as the ILs are concerned, it is important to consider that the IL can undergo some decomposition or dimerization processes, resulting in a possible inhibition of the catalysis[343]. In addition, after catalysis with BMIM cations, the presence of carbene species have been observed by Zhao et al.[24] via ^{1}H NMR. These carbene species were identify as the active species for the formation of the imidazolium-CO_2 complex. For this reason, it is important to understand if carbene species were formed during catalysis or if some other compounds are formed from the decomposition and/or

dimerization of [1-CP-3-MIM]BF_4. After each CPE experiment, ^{1}H NMR measurements were performed, and in Figure 6.11 an example of the ^{1}H NMR spectrum after the CPE measurements is presented. The spectrum for the pure [1-CP-3-MIM]BF_4 is shown for comparison (red curve). In the curve after CPE (purple curve), no additional peaks were observed, meaning that it reasonable to assume that the concentration of a possible second species might be too low for being detected with the instrument or that only one species is present. This suggest that the IL did not appreciably decompose and that the carbene derivative of [1-CP-3-MIM]BF_4 was not present as the peaks are likely be due to [1-CP-3-MIM]BF_4 as the ppm values of the peaks are the same before and after CPE measurements.

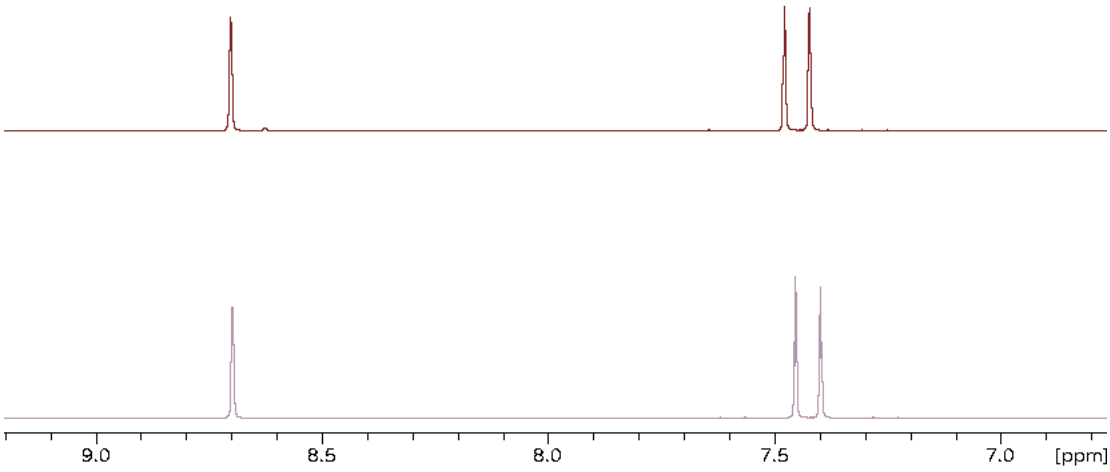

Figure 6.12: ^{1}H NMR spectra of red) pure [1-CP-3-MIM]BF_4 and purple) catholyte after electrolysis. Only part of the spectrum is presented to show the absence of peaks due to the carbene species after electrolysis

6.5 Conclusion

In conclusion, catalytic experiments were performed using two different types of Bi electrode: bulk Bi electrodes (Bi cylinders) and Bi film electrodes (Bi modified electrodes). The Bi modified electrodes were tested in the presence and in absence of two co-catalysts: the commercial [BMIM]BF_4 and the in-house produced [1-CP-3-MIM]BF_4. For the four different systems different results were obtained. In particular, for:

- **Bi cylinders**: low FEs_{TOT} were calculated (maximum FE_{TOT} = 49%) and higher production of CO than formate was detected
- **Bi modified electrodes (absence of ILs)**: an increase on the FEs_{TOT} was observed (maximum FE_{TOT} = 68%) in comparison with bulk Bi electrodes.

  The catalytic activity *was not* significantly influenced by the *morphology* but the formate production was influenced by the area of the electrode

- **<u>Bi modified electrodes (in the presence of ILs)</u>**: with:
    a) [BMIM]BF_4 : no increase in the FEs_{TOT} , FEs_{CO} and FEs_{COO-}.
    b) [1-CP-3-MIM]BF_4: no increase in the FEs_{TOT}, increase of FEs_{H2}

For **objective 1.a**, two parameters that could influence the surface of the electrodes were investigated: the type (1) and the quantity (2) of the active sites. Based on the results obtained it was clear that:

(1) Bi crystallites vs Bi modified electrodes: different chemical composition modify the catalytic activity
(2) Different ECSA: modify the catalytic activity; different morphology: did not modify the catalytic activity

In general, the composition of the surface has a significant influence on the catalytic activity.

For the **objective 1.b**, it was clear that the presence of co-catalysts (ILs) did not increase the selectivity of the system and the in house produced IL did not present intermolecular proton donor abilities.

For **objective 2**, it was clear that both bulk Bi and Bi modified electrodes did not present high stability as the Bi cylinders presented surface modification (identified with the colour change of the surface) and Bi modified electrodes after catalysis exhibited a larger portion of the substrate exposed due to loss of the Bi crystallites.

A common problem to all the catalytic systems was the low value of FEs_{TOT} that did not exceed the 68%, with the major contribution being the production of H_2 (low selectivity of the system). However, a minimum of 32% of the charge passed during the experiment could not be attributed to the main reaction products (H_2, CO, CH_4 and formate). The heat released during the process should not account for such large portion of the charge, and the formation of other products (such as oxalate) was excluded. Therefore, the presence of an additional process was suggested. Based on the results obtained, it is probable that the charge passed is used for the reduction of the Bi_2O_3 present on the surface of the Bi cylinders or the Bi crystallites.

Chapter 7 : Bismuth Screen Printed Electrodes

7.1 Introduction

Screen printed electrodes (SPEs) are low-cost, reproducible, disposable and portable platforms for electrochemical studies[73]. They consist of an inert substrate, e.g., polyester film, a conductive ink, and an insulation layer, which is printed manually or using an automatic screen printer. Generally, the ink formulations applied in screen printing process for the manufacture of sensos consist of conductive fillers (e.g., graphite, carbon and/or metals particles), and a mixture of binders and organic solvents used for dispersing and holding the conductive particles onto the substrate[398]. In the last three decades, a significant quantity of different inks, substrates and modification techniques have been studied to obtain cheaper and more active SPEs[399]. In general, SPEs are sensors used for analytical purposes, such as the detection of heavy metals[70,400,401], pesticides[87,402], bacteria[403,404], glucose[405,406] and a large variety of organic molecules[72,86,88]. Several types of SPEs can be produced depending on the application under investigation. Most SPEs are produced using carbonaceous materials, like graphite and/or carbon black, however, metals are frequently used to fabricate or modify SPEs[399]. Among metals, Bi SPEs has been widely applied for the detection of heavy metals and organic molecules in a variety of samples[407]. However, there has been no examples of bismuth SPEs for the reduction of CO_2. Usually, Bi (nano)particles are manually mixed with a polymer binder, solvent and carbon to form a paste that is brushed or sprayed on a substrate like carbon felt or cloth. These procedures do not provide perfectly reproducible electrodes even if the paste loading is kept constant. The printing of electrodes for the reduction of CO_2 may offer several advantages over the electrodes discussed in earlier chapters, such as the effective and reliable production of a large quantity of reproducible electrodes. For this reason, in this chapter, the production of bismuth SPEs, characterisation, and testing for CO_2RR is presented. In particular, two carbonaceous inks loaded with different quantities of Bi and a pure Bi metal ink were formulated and screen printed. Then, the morphology and the electrochemical properties of the SPEs were investigated and compared with the pure carbonaceous SPEs. In addition, the two-layer SPEs were produced using the pure carbonaceous and the pure bismuth metal ink (top layer). The results obtained with these electrodes gave an insight into a powerful strategy for the creation of large surface area electrodes with a high surface coverage of bismuth.

7.2 First ink formulation

For the composition, production and printing methods see the *Materials and methods* chapter (Chapter 2, Section 2.4.5). The type of ink, the active components present in the ink, and the name assigned to the electrodes after printing are shown in Table 7.1 (the compounds used to obtain the most suitable characteristics for printing the inks, like binders and solvents, are not listed here).

Table 7.1: type of inks, main components in the ink and name of the respectively screen printed electrodes.

ink	main components	electrode name
pure carbonaceous	carbon and graphite	C/G-SPE
carbonaceous + Bi particles	carbon, graphite and Bi microparticles	C/G/Bi-SPE
pure Bi metal	Bi microparticles	Bi M-SPEs
pure Bi metal ink on carbonaceous ink	Bi microparticles (outer layer), carbon and graphite (inner layer)	Bi M_C/G-SPE

7.2.1 Characterisation

A full characterisation was performed for the four types of SPEs. First, the surface morphology of the electrodes was examined using SEM to investigate the distribution of the Bi particles on the electrode surface after the printing process. The electrodes were tested in the two solutions selected for the catalysis experiments: the first containing, as an electrolyte, Na_2SO_4 and the second, $KHCO_3$ (electrolyte concentration: 0.1 M). In these two solutions, the resistance of the electrode was measured; the electrochemical behaviour in a large potential window investigated; the electrochemical active area (ECSA) and the capacitance calculated; finally then, the electron transfer properties were studied using ferrocenemethanol (FcMeOH) as a redox active probe. A schematic representation of the characterisation performed for all the SPEs investigated in this chapter is shown in Figure 7.1.

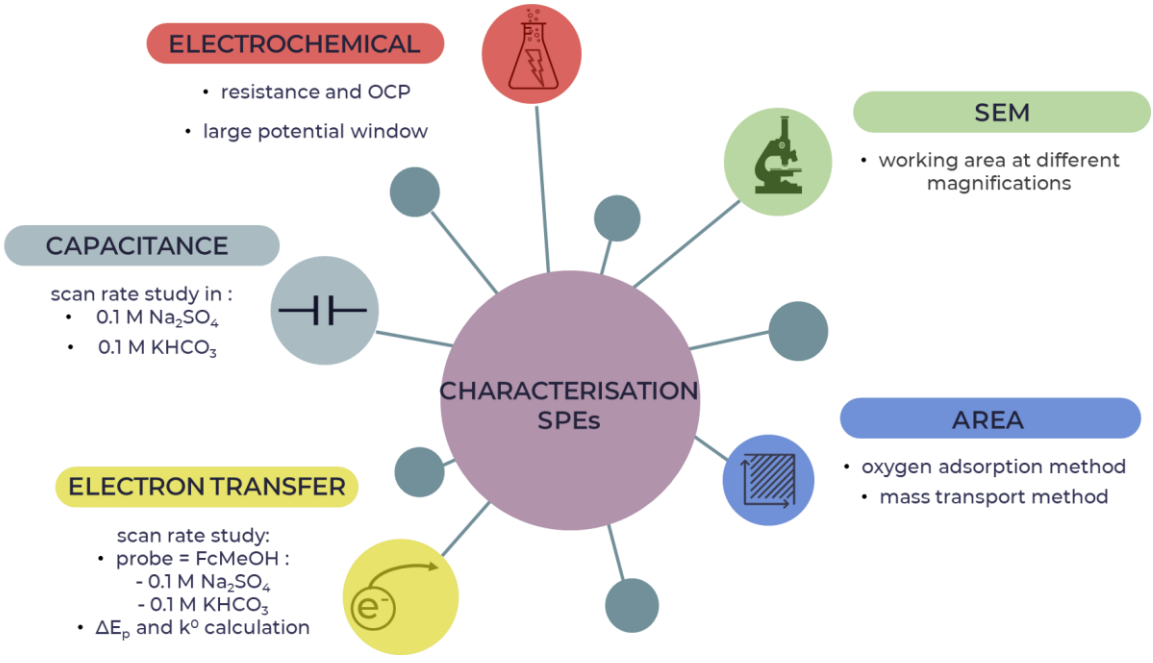

Figure 7.1: Diagrammatic scheme of the characterisation performed for the investigation of the SPEs

7.2.1.1 Physical characterisation: SEM

SEM imaging is commonly applied in the literature to examine the surface morphology of SPEs.

First, the carbonaceous SPEs were imaged and the SEM images are shown in Figure 7.2. The surface presents typical features of carbonaceous SPEs[408], i.e., flake-like graphite particles are present (see Figure 7.2b) and they are homogenously distributed on the entire surface of the electrode. The presence of the binder is also highlighted by the charging effect, which is apparent from the lighter and brighter features, especially at the edges of the flakes. The mesh pattern of the screen is evident and endows the surface with a certain degree of roughness. Pores and edges are abundant suggesting that the electrodes have a high surface area. For a comparatively flat surface see Chapter 6 Figure 6.7a.

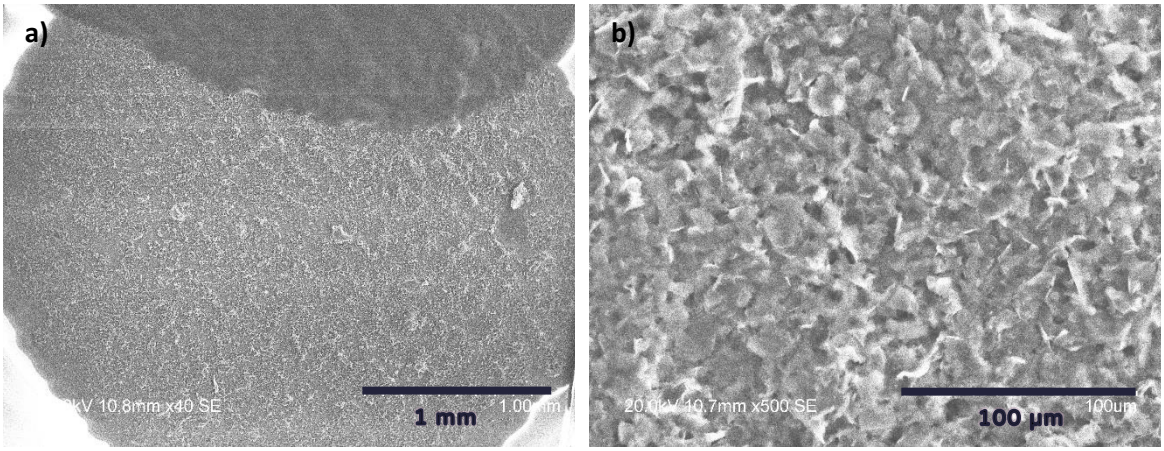

Figure 7.2: SEM images of G/C-SPE at different magnification: a) x40; and b) x500. The black semicircle at the top of the working area in image a) is the conductive paste used for creating a conductive connection between the substrate and the working area

In Figure 7.3, the SEM images for SPEs modified with 10% w/w of Bi (C/G/Bi-SPEs) are shown. The Bi microparticles are present on the entire surface of the electrode (see bright spheres in Figure 7.3). The microparticles were unaffected by the homogenisation process as the size and shape are the same as observed for the Bi microparticles before insertion into the ink (see Figure 7.3e). The size of the spheres is in good agreement with the value given by the manufacturer (max size: 45 µm), as particles between 31.9 and 45.9 µm were observed (see Figure 7.3d and e). The Bi microspheres are partially embedded in the carbonaceous ink with the ink completely or partially covering the surface of the particle (a clear example is given in Figure 7.3b and c). The presence of the Bi microspheres on the surface is an indication of the homogeneity of the ink, as, considering the low concentration and the high weight of the Bi particles, only a few microspheres are partially covered (for an example see red circles in Figure 7.3b). SPEs presenting well distributed Bi particles have been obtained by Niu et al. using the bulk method, but Bi_2O_3 was used as precursor and not Bi metallic[409]. This requires an additional electrochemical step to convert the Bi^{3+} to Bi^0, while, in

the case of C/G/Bi-SPEs, the electrodes could be used directly without any pre-treatment, making these SPEs an easier and faster option. However, it is important to highlight that the oxidation state of the Bi in the microspheres was not investigated, so it is not possible to confirm the formation of the native oxide.

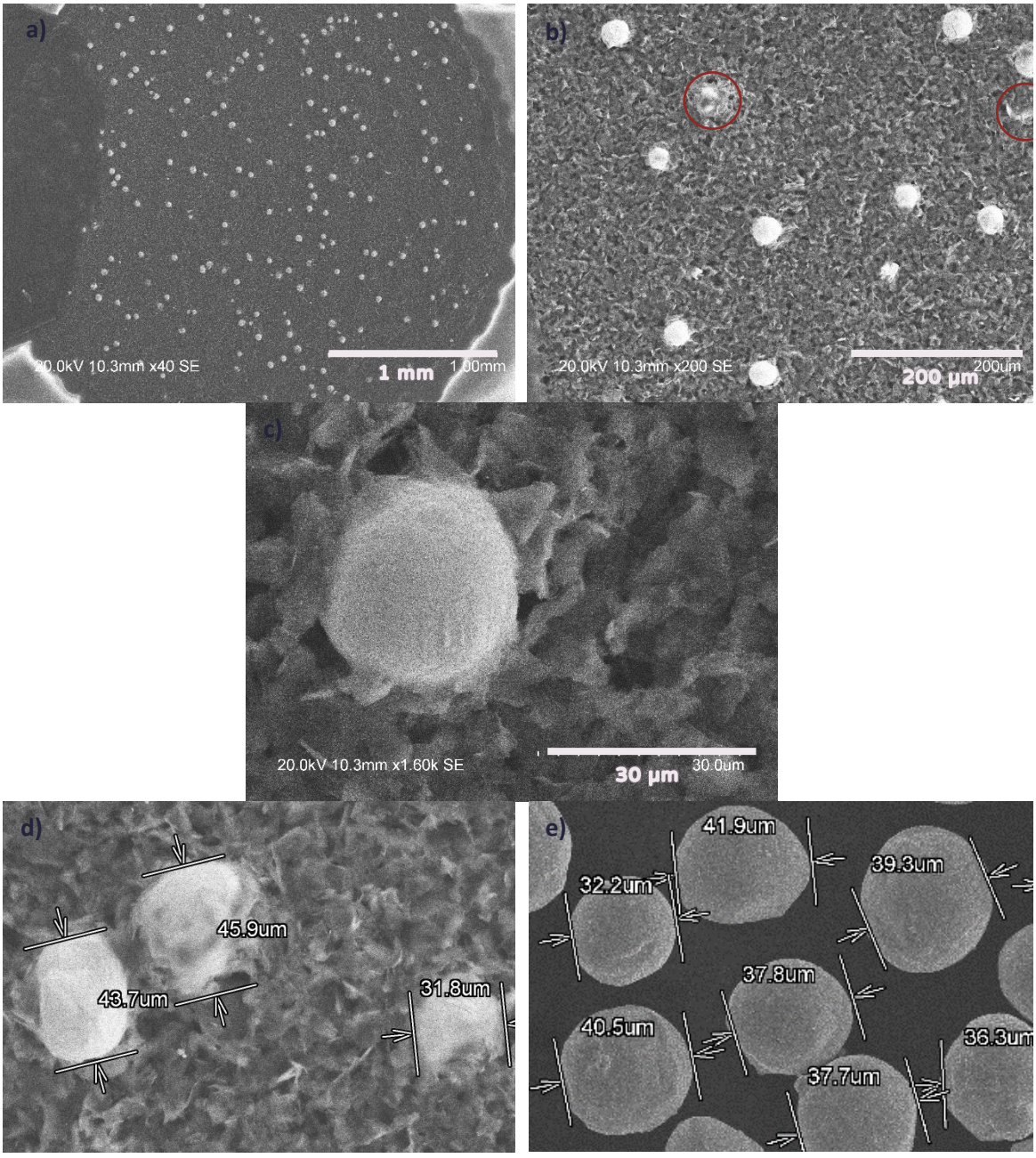

Figure 7.3: SEM images of C/G/Bi-SPEs at different magnification: a) x40; b) x200; c) x1.6k; d) x370; and e) image of the Bi microsphere as received from the manufacturer (magnification: x400). Accelerating voltage= 20 kV. The sizes in d) and e) were calculated using the SEM software. The black semicircle on the left of the working area in image a) is the conductive paste used for creating a conductive connection between the substrate and the working area

In Figure 7.4, the SEM images for Bi M-SPEs are presented. The Bi M-SPE in the figure does not present a homogenous layer of ink as the surface was altered during the brushing of the conductive paste for the SEM imaging (see left section in Figure 7.4a) for all the samples imaged. Unlike the

other electrodes, a rough circular shape was observed due to an overflow moving outside of the area defined by the screen. This is likely due to the high viscosity of the ink, given by the presence of Bi microparticles. Several layers of Bi microspheres are present one on top of each other (Figure 7.4b) and the presence of the binder between the single microspheres is clear by observing the webbed contour of the particles (see Figure 7.4b, c and d)[410]. The size of the microsphere was not modified during the preparation of the ink. The microspheres are not perfectly smooth, as they present *"stretch marks"*, pits and smaller fragments (not larger than few μm) on the surface (see Figure 7.4e). These characteristics are particularly useful as they may increase the real area of the electrode.

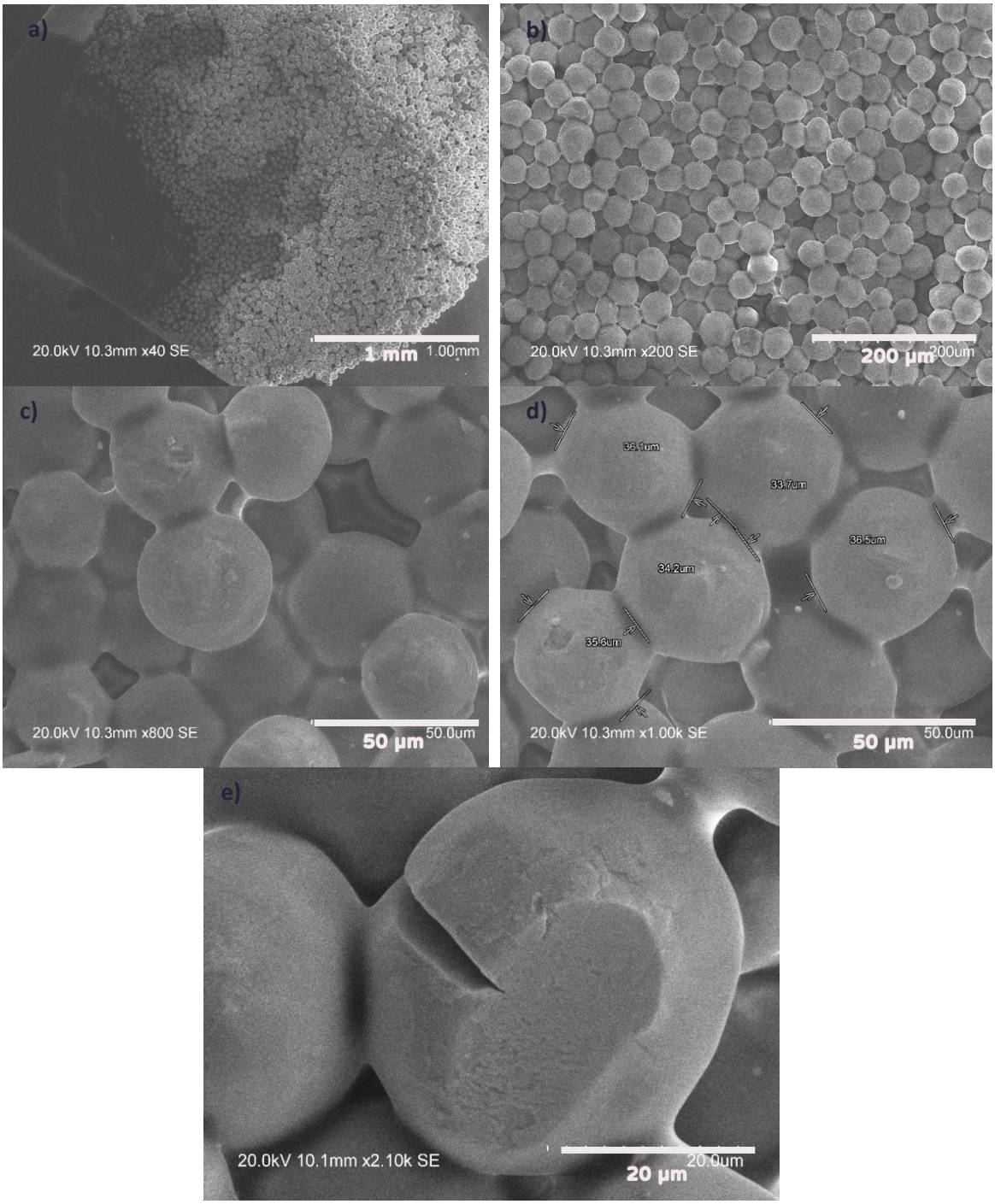

Figure 7.4: SEM images of Bi M-SPEs at different magnification: a) x40; b) x200; c) x800 and d) 1.0 k. The sizes in d and e were calculated using the SEM software. The black semicircle on the left of the working area in image a) is the conductive paste used for creating a conductive connection between the substrate and the working area

The same Bi M ink was printed on top of C/G-SPEs and the SEM images for the two layered SPE are presented in Figure 7.5. It is clear from Figure 7.5c that the two layers are not overlapping perfectly. At low magnification (Figure 7.5a), only the Bi M ink layer can be seen. However, at high magnification, the carbonaceous ink is clearly visible on one side of the electrode (see bottom part on Figure 7.5c) while it is not on the other side (see Figure 7.5b).

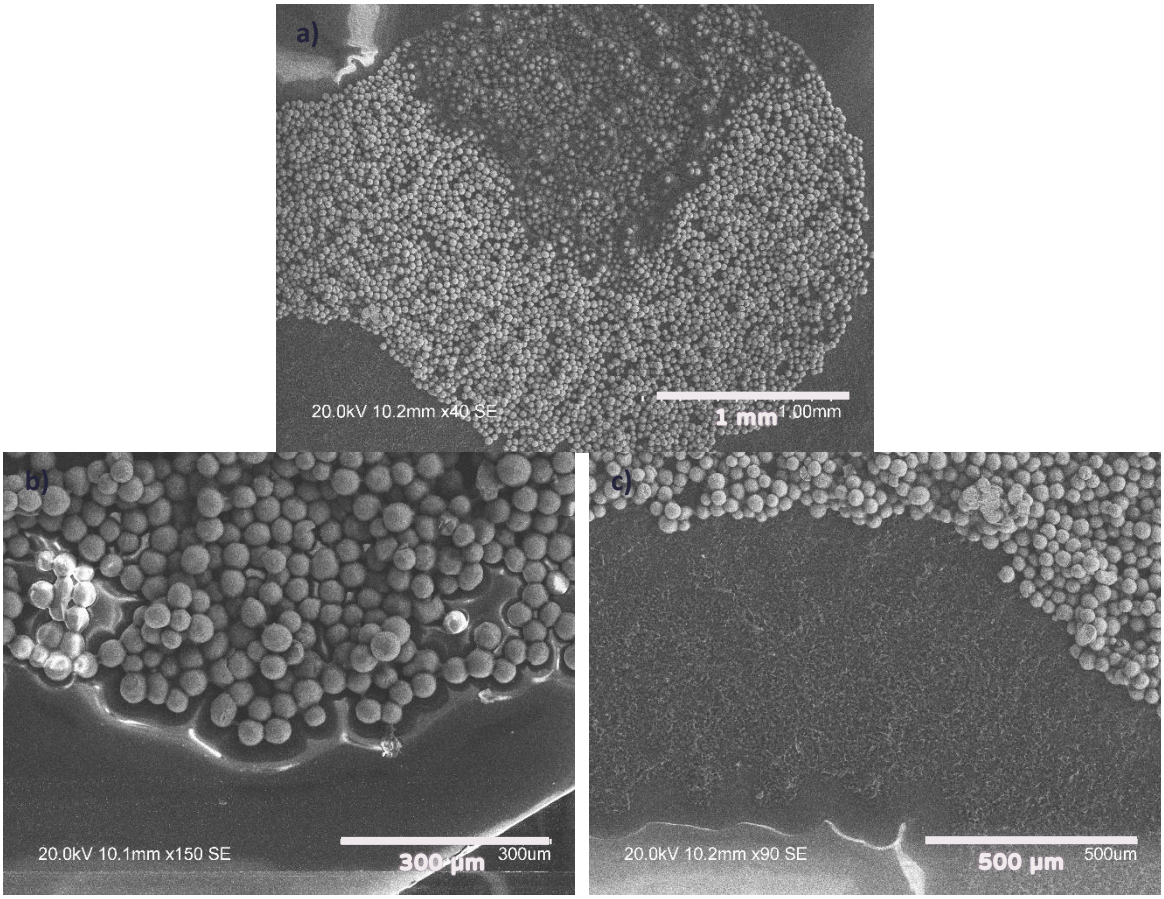

Figure 7.5: SEM images of Bi M_C/G-SPEs at different magnifications: a) x40: b) x150; and c) x90, where the C/G ink layer is exposed (bottom part of the image), as the two layers do not overlap perfectly. The black semicircle on the top of the working area in image a) is the conductive paste used for creating a conductive connection between the substrate and the working area

In general, the four types of SPEs present high homogeneity, with the substrate being completely covered by the ink. The Bi microspheres in C/G/Bi-SPEs are homogeneously dispersed on the entire surface of the electrode, although in low number. This was expected, considering the low concentration of Bi in the ink (10% w/w). Conversely, the surface of the SPEs is completely covered by the Bi microsphere for Bi M and Bi M_C/G-SPEs. However, the C/G ink is partially exposed in Bi M_C/G-SPEs, as during the printing the two layers were not overlapped perfectly. Surfaces similar to that observed for C/G/Bi-SPEs have been obtained by Martín-Yerga et al.[411] for SPEs containing Au particles. However, in that case, the metal particles were drop casted on the working area surface and not inserted directly into the ink formulation. This show that the inks here produced are comparable to SPEs modified via drop casting technique, allowing the removal of one production step.

7.2.1.2 Electrochemical characterisation

Electrochemical characterisation was performed by investigating the potential window, the electrochemical surface area (ECSA), the capacitance and the electron transfer abilities of the

electrode (see Figure 7.1). All the electrochemical characterisation was performed using a carbon SPE as counter electrode and an Ag/AgCl SPEs as reference electrode (RE). For this reason, all the potentials mentioned are always expressed versus pseudo Ag/AgCl, unless otherwise state.

Some preliminary experiments were performed, for all the four types of SPEs, to obtain the open circuit potential (OPC) values and the resistance of the electrodes (see Table 7.2). The values were measured in the two solutions used for electrocatalytic experiments: $KHCO_3$ and Na_2SO_4. The resistance of the SPEs is generally quite high (R >1000 Ω) in comparison with other type of electrodes (for example glassy carbon electrode present a resistance of a few Ω[412]) because of the high content of polymers[410]. However, Bi M electrodes presented resistance values in the order of the MΩ. This is due to the high resistivity of the Bi particles (electrical resistivity = 117 μΩcm. Value obtained from manufacturer). The Bi M-SPEs could not be tested further as the resistance was too high for the current to pass. Similar resistance values were obtained for Bi M_C/G-SPEs if the connector of the SPEs adaptor touched the pure Bi ink. On the other hand, if the connector of SPEs adaptor touched the C/G ink exposed on the conductive path, a resistance comparable with the other types of electrode (2231 ± 172) was measured. Because it was not possible to always insert the SPE into the adaptor ensuring that only the portion of the C/G ink was in contact with the connector of the adaptor, the Bi M_C/G-SPEs was not further characterised. (See Chapter 2, Section 2.3.4 for an image of the adaptor itself).

Table 7.2: OCP values and resistance for the four types of screen printed electrodes

electrode	electrolyte	OPC [V]	Resistance [Ω][a]
C/G-SPE	Na_2SO_4	0.02	1052 ± 48
	$KHCO_3$	0.03	1075 ± 22
C/G/Bi-SPE	Na_2SO_4	-0.02	1542 ± 128
	$KHCO_3$	-0.01	1782 ± 872
Bi M-C/G-SPE	Na_2SO_4	-0.38	2231 ± 172 **or** 4 (±2) x10^6
Bi M-SPE	Na_2SO_4	-1.1	5 (± 2) x10^6

[a] Calculated at OPC

The SPEs were tested via CV in N_2-saturated solutions of Na_2SO_4 and $KHCO_3$ using a large potential window (from 1.4 to -2.4 V vs pseudo Ag/AgCl). Figure 7.6a and b show results for the pure carbonaceous SPEs those containing Bi particles, respectively. For the CVs of C/G-SPEs, as, expected, no well-defined peaks were observed and the increase of current at -2.0 and +1.0 V are due to the reduction and oxidation of water, respectively. When C/G/Bi-SPEs were used, two clear features were observed: a large peak at negative potentials (from -0.7 to -1.7), related with the reduction of Bi oxide, and several peaks followed by a current plateau at positive potentials, due to the formation of Bi oxide[177,183,385]. The extent of the potential windows is similar for the two types

of SPEs. The potential window for the experiments performed in Na_2SO_4 is slightly larger than in $KHCO_3$, as the oxidation of water began at a potential 0.2 V more negative for C/G-SPEs. For C/G/Bi-SPEs, the beginning of the current increase is observed at around 1.2 V, a potential 0.3 V more positive than in $KHCO_3$. The anodic section of the CVs in $KHCO_3$ solutions (see Figure 7.6c, purple curve) present two peaks before the current plateau, while in Na_2SO_4 several peaks which are not well defined are present. As discussed in Chapter 3, Section 3.2, the number of peaks in the anodic section of the CVs for Bi electrodes is mainly influenced by the surface of the electrode and the pH of the solution. In this case, the composition of the surface is more complex than in the case of the Bi cylinder, due to the presence of the other components of the ink. Because more peaks were observed at lower pH than at higher pH, it is likely that the pH of the solution plays a significant role in the number of the peaks present in the CV for SPEs also. Similar results have been obtained by Lezi et al.[89], who tested Bi modified screen printed electrodes in aqueous solutions at different pH values. In their work, at the lowest pH values, a set of peaks was observed in the anodic region which were not well-resolved, while, when the pH was increased, the number of peaks decreased until only one peak was observed for the highest pH (pH=10). The number and nature of the peaks in the anodic sweep was not discussed by the authors, but the presence of more than one bismuth species formed during the anodic scan was mentioned. However, knowledge of the processes happening during the anodic sweep were not relevant to the work, as only negative potentials were applied for the application under investigation, therefore only the cathodic behaviour of the electrode was considered. Similarly, in this work, the SPEs were produced for the reduction of CO_2, meaning that only potentials more negative than -0.6 V are in fact applied during the experiments. Interestingly, in Na_2SO_4, a current plateau is present. This is in contrast with the results obtained using Bi cylinders as working electrodes (Chapter 3), in which an increase of current was observed. The increase in current has been attributed by Williams and Wright[177] to the dissolution of Bi oxide and re-precipitation of $Bi(OH)_3$ at pH <8.5. The absence of the increase in current when SPEs were used suggests that the dissolution of the Bi oxide might not occur, or at least it happens to lesser extent when the Bi particles are covered and surrounded by the components of the ink (see Figure 7.3b, c and d). In the cathodic section of the CVs in $KHCO_3$, the presence of a tail is observed at around -1.4 V vs pseudo Ag/AgCl. The presence and increase in current of a tail in the cathodic region has been observed by William and Wright when the anodic vertex was extended to more positive values[177]. They suggested that the tail represents the reduction of a different species of Bi oxide. It is important to highlight that when C/G-SPEs were tested in $KHCO_3$, a small increase in current was observed around the same potential range, meaning that the feature may be linked with the presence of an additional process in $KHCO_3$, related with the C/G ink. However, the current

observed in C/G-SPEs is approximately half, suggesting that the tail observed with C/G/Bi-SPEs contains a contributing process that occurs only in the presence of the Bi microspheres.

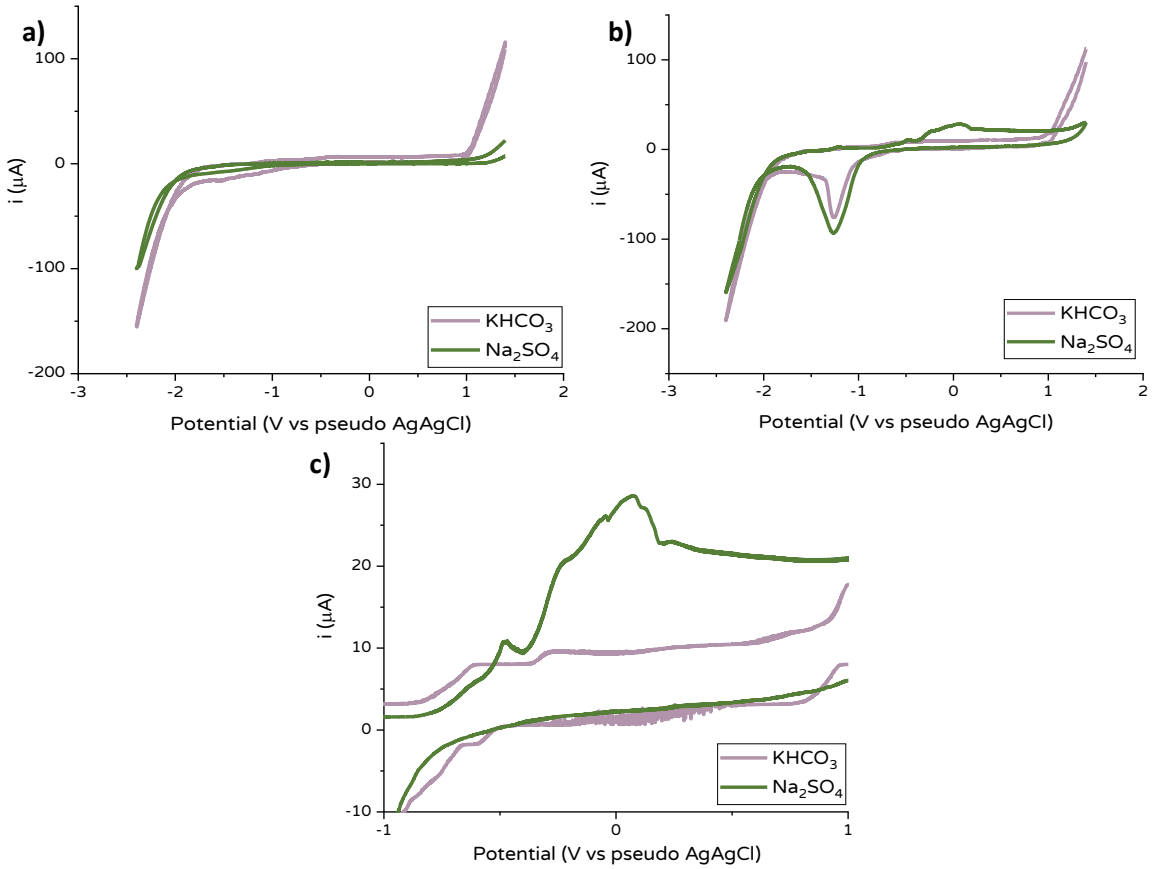

Figure 7.6: CVs for large potential window in two different electrolytes: 0.1 M KHCO3 (purple) and 0.1 M Na_2SO_4 (green) using a) C/G-SPEs and b) C/G/Bi-SPEs. c) zoom of the oxidation peaks at C/G/Bi-SPE. Scan rate: 100 mV/s. The second cycle is here shown

7.2.1.2.1 Electroactive area of the SPEs

The ECSA of an electrode is essential in understanding the extent to which electrode is electrochemically active[203]. For this reason, the ECSA of C/G/Bi-SPEs was calculated. As discussed in Chapter 1, there are several methods to calculate the ECSA of an electrode, and the choice of one over the other depends on the characteristics of the electrode under investigation[198]. As for all the other Bi electrodes used within this work, the electroactive area (here called A_{real}) of the SPEs was calculated via the reduction of an oxide monolayer formed previously (the oxygen adsorption method). The ECSA of the carbonaceous SPEs was calculated using the Randles–Ševćik equation (mass transfer method[198]), as this method is commonly used (using both voltammetric or potentiostatic techniques) for the calculation of the real area for SPEs[203]. In addition, the area of the C/G/Bi-SPEs was calculated using the mass transfer method and the values obtained with the two different methods were compared. The measurements for the oxygen adsorption method

were performed in a solution of 50 mM KOH, at a scan rate of 10 mV/s. An example of three measurements for a single SPEs electrode is shown in Figure 7.7, in which the peak between -0.83 and -1.1 V vs pseudo Ag/AgCl is attributed to the reduction of the oxide monolayer[100,101,267]. Three SPEs were tested, and for each electrode, three measurements were performed. From the real area values, it was possible to calculate the quantity of Bi present on the surface of the electrodes. This step is particularly important for SPEs as the percentage of metal in the ink might not be representative of the percentage in contact with the solution.

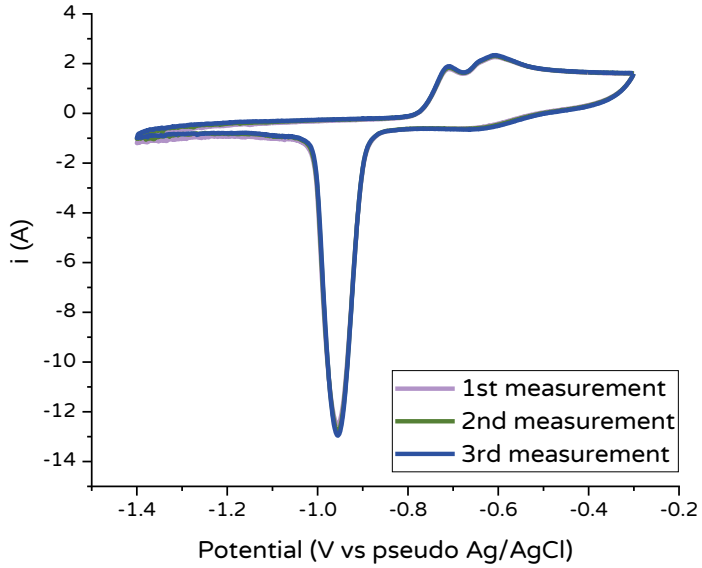

Figure 7.7: CVs for monolayer oxide reduction method obtained in 50 mM KOH for Bi scan rate: 10 mV/s

The values of charge, real area, roughness factor and quantity of Bi are shown in Table 7.3.

Table 7.3: Charge, geometrical and real areas, roughness factor and quantity of Bi for C/G/Bi-SPEs calculated via the oxygen adsorption method

electrode	Q_{exp} [µC]	A_{geo} [cm^2]	A_{real} [cm^2]	r_f	moles of Bi per area [nmoles/ cm^2]
C/G/Bi-SPEs	84 ± 17	0.07	0.45 ± 0.09	6 ± 1	1.0 ± 0.2

The A_{real} of the electrodes is quite low in comparison with the area of the modified Bi electrodes (Chapter 4), that present areas up to x7.6 times higher. This was expected, as the quantity of Bi in the ink is only 10% w/w, while the glassy carbon surface is almost completely covered with the electrodeposited Bi crystallites. The roughness factor of the C/G/Bi-SPEs is eight time smaller than the roughness factor of the Bi modified electrodes. This is not only due by the lower quantity of the Bi present on the surface of the SPEs, but also by the morphology of the particles. While the C/G/BI-SPEs presented microspheres, Bi modified electrodes presented dendritic crystallites, which present features that ensure a significant increase in the surface area[119,164,334].

Scan rate studies in the presence of a probe were performed in 0.1 M Na_2SO_4 for the calculation of the real area of C/G-SPEs and C/G/Bi-SPEs using the Randles–Ševćik equation (see Equation (1.7)) and the difference in area values obtained with the oxygen adsorption method are discussed here. The probe used for the scan rate study (see Figure 7.8a and c, for C/G-SPEs and C/G/Bi-SPEs respectively) was ferrocene methanol and the diffusion coefficient was set to 7.6 x 10^{-6} cm^2/s[413–415]. The i_p was then plotted as a function of $v^{1/2}$ (Figure 7.8b and d for C/G-SPEs and C/G/Bi-SPEs respectively) and the ΔE_p values for the lowest and highest scan rate values are shown in Table 7.4.

Table 7.4: Real areas for C/G-SPEs and C/G/Bi-SPEs calculated using Randles–Ševćik equation. Scan rate studies were performed in 0.1 M Na_2SO_4 and the scan rate was ranged between 10 and 500 mV/s

electrode	A_{geo} [cm^2]	A_{real} [cm^2]	r_f
C/G-SPEs	0.07	0.378 ± 0.003	5.2 ± 0.5
C/G/Bi-SPEs	0.07	G/ ± 0.002	4.8 ± 0.3

The A_{real} values for both the electrodes are comparable, suggesting that the presence of the Bi microspheres did not increase the area of the electrode. This is contrast with the values obtained using the oxygen adsorption method, as an area 0.45 cm^2 higher should be obtained for C/G/Bi-SPEs. It is important to highlight that the values of the area calculated with the oxygen adsorption method could be higher due to the formation a multilayer rather than a monolayer of Bi_2O_3 during the anodic scan (see Figure 7.7). However, a slightly higher surface area should be observed for C/G/Bi-SPEs as the Bi microspheres were not perfectly smooth (see SEM images), a factor that should increase the surface area. It is likely that the mass transfer method of the A_{real} may be underestimated, as the method is only able to detect surface roughness comparable to the diffusion layer thickness, that is in the order of micrometres (>10-100 µm)[198]. In addition, the mass transfer method requires a homogeneous distribution of the current that may be difficult to achieve on a surface with high surface roughness[198]. The real area is more than five times higher than the geometrical one, in accordance with the SEM images that showed high porous surfaces.

7.2.1.2.2 Electron transfer: Ferrocene methanol

One of the most important characteristics for a working electrode (WE) is the ability to support fast electron transfer[408]. For this reason, the rate of electron transfer was investigated using scan rate dependent CV. The scan rate studies for C/G-SPEs and C/G/Bi-SPEs in the presence of 1 mM ferrocene methanol (FcMeOH) are shown in Figure 7.8a and c, respectively. FcMeOH was chosen as a water soluble probe instead of the ferrocyanide redox couple, as it has been demonstrated that this probe showed a change in the peak-to peak separation with time when used for the characterisation of carbon-based SPEs[398]. The scan rate was varied from 10 to 500 mV/s and the

CVs shown here are not corrected for iR drop. Well defined peaks for the reduction and oxidation of Fc/Fc^+ were observed and the apparent potential (E^0) were equal to 0.085 ± 0.006 V and at 0.084 ± 0.002 V at 50 mV/s for C/G-SPEs and C/G/Bi-SPEs, respectively (see Table 7.5). The similarity of the values suggests that tpresence of Bi on the SPEs surface does not significantly influence the standard redox potential of the redox couple. The plot of the i_p as a function of the square root of the scan rate (Figure 7.8b and d for C/G-SPEs and C/G/Bi-SPEs, respectively) showed a linear trend, suggesting that the reaction at both of the electrodes is dominated by linear diffusion[45,172].

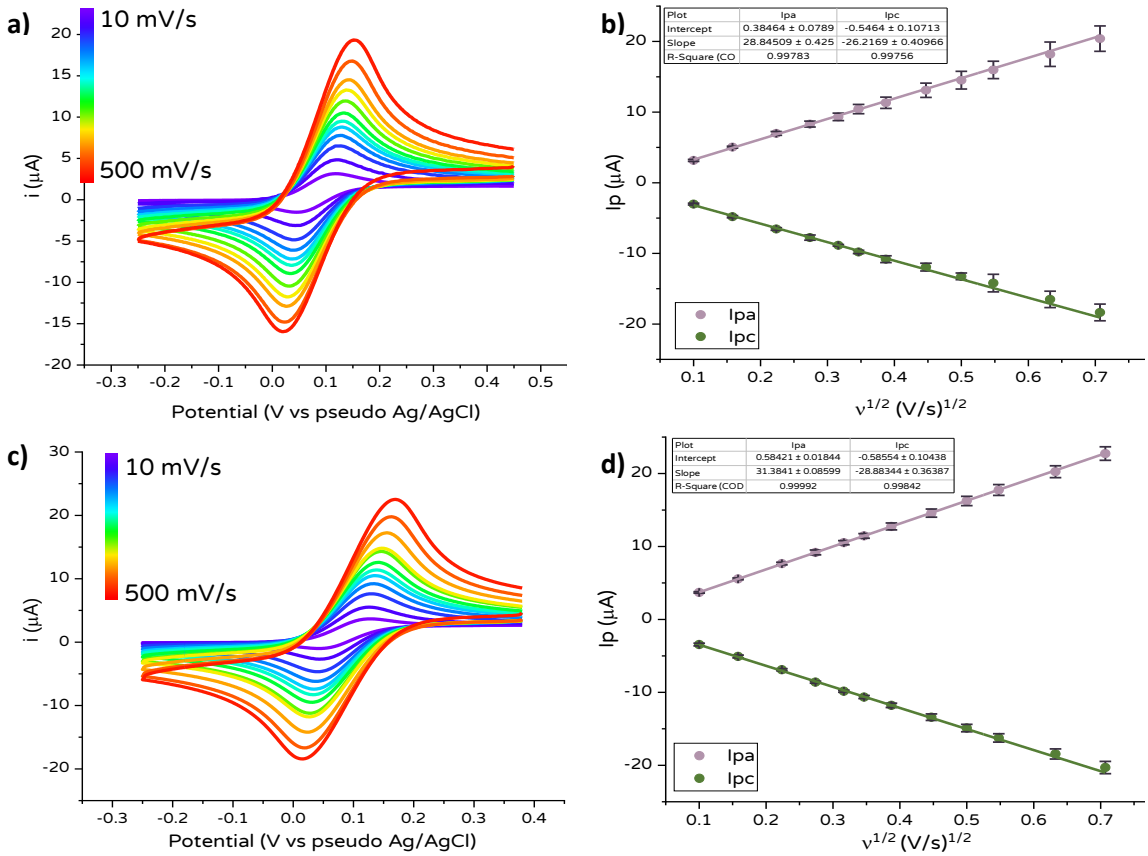

Figure 7.8: a) Scan rate study for C/G-SPE in 0.1 M Na_2SO_4 in the presence of 1 mM ferrocene methanol; b) plot of Ip anodic (purple) and cathodic (green) as a function of the square root of the scan rate at C/G-SPE; c) Scan rate study for C/G/Bi -SPE in 0.1 M Na_2SO_4 in the presence of 10 mM ferrocene methanol; and d)) plot of Ip anodic (purple) and cathodic (green) as a function of the square root of the scan rate at C/G/Bi-SPE

The ΔE_p for C/G-SPEs varied from 85 mV to 154 mV (see Table 7.5) depending on the scan rate applied, suggesting a quasi-reversible process[398]. Similar results for carbon SPEs were found in the literature. For example, Bishop and co-workers[398] calculated ΔE_p values equal to 90 ± 17 mV at 100 mV/s for in-house printed graphite SPEs. Similarly, Laschi et al.[416] obtained ΔE_p values of 0.110 ± 0.004 at 50 mV/s for carbon-based SPEs. In general, the ΔE_p values deviate from the standard value for a reversible one electron process (57 mV) because of solution resistance and slow electron transfers[172]. When SPEs are considered, additional factors can cause the increase in ΔE_p, like the presence of the binder that slows down the electron transfer, the type of graphite used and the

wettability of the surface[408]. The ΔE_p for C/G/Bi-SPEs is lower, as it varies from 73 to 131 mV, suggesting slightly faster kinetics on the C/G/Bi-SPEs than on the C/G-SPEs. Considering that the composition of the pure carbonaceous ink is the same for both types of electrodes, the lower ΔE_p values obtained for C/G/Bi-SPEs suggests that the presence of the Bi microspheres improved the electron transfer ability of the SPEs. This is in contrast with the results showed by Niu et al.[409] who observed an increase of the ΔE_p values when Bi/C SPEs were compared with commercial graphite screen printed electrodes. However, in their work, the resistance of the Bi/C SPEs was almost 17 times higher than the resistance for the commercial graphite SPEs, while in this work the resistance of the SPEs containing the Bi microsphere is only x1.5 times higher. The trends observed within this work are similar to those for Au modified SPEs[398]: the ΔE_p varied from around 10 mV when the Au NPs were deposited via layer-by-layer technique on the surface of the SPEs. This suggests that the other components of the ink actually have a higher impact on the kinetics than the presence of the Bi particles.

Table 7.5: Standard potential and ΔEp for Ferrocene methanol at C/G-SPEs and C/G/Bi-SPEs at two different scan rates in 0.1 M Na_2SO_4

electrode	E^0 at 50 mV/s	Scan rate [mV/s]	ΔE_p [V]
C/G-SPEs	0.085 ± 0.006	10	0.085 ± 0.009
		100	0.101 ± 0
		500	0.154 ± 0.002
C/G/Bi-SPEs	0.084 ± 0.002	10	0.073 ± 0.003
		100	0.091 ± 0.003
		500	0.131 ± 0.008

To obtain more information about the electron transfer ability of the SPEs, the heterogeneous electron transfer rate constant, k^0, of the process was calculated using the Nicholson method[273]. This method uses the relationship between the peak-to-peak separation and the scan rate. In Particular, k^0 is determined using equation (7.1)[273]

$$k^0 = \left[\frac{\sqrt{\pi D_R f \nu}}{\left(\frac{D_R}{D_O}\right)^{\alpha}}\right]\Psi \qquad (7.1)$$

where D_R and D_O are the diffusion coefficients for the probe in the reduced and oxidised form, respectively in cm^2/s, α is the charge transfer coefficient (that in this case is set equal to 0.5) and ν is the scan rate in V/s. Finally, $f = \frac{nF}{RT}$, where n is the number of electrons exchanged during the process, F is the Faraday constant in C/mol, R is the ideal gas constant in J mol/K and T is the

temperature in K. The variation of the parameter Ψ with ΔE_p is described by the graph presented in the work of Nicholson (see Figure 7.9).

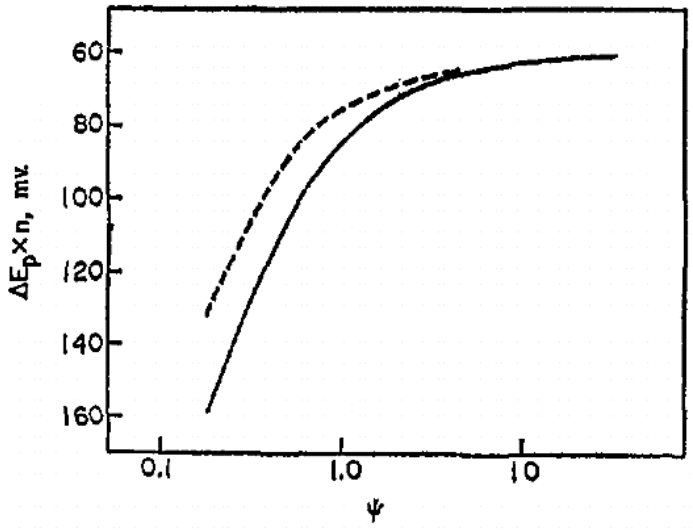

Figure 7.9: variation of the peak-to-peak separation as a function of Ψ. The dashed curve shows the variation observed on ΔE_p when iR drop is considered [273]

Considering that for ferrocene methanol $D_R = D_O$[398], Equation (7.1) can be re-rewritten:

$$k^0 = \Psi\sqrt{\pi D_R f \nu} \tag{7.2}$$

The method can be applied to a range of scan rate values for which the ΔE_p ranges between 57 and 250 mV, and fast scan rates that show a large iR drop cannot be used[273]. For this reason, the scan rate range usually used for the calculation of k^0 is between 10 and 200 mV/s[398].

The diffusion coefficient for ferrocene methanol in 0.1 M Na_2SO_4 was calculated using the Randles–Ševćik equation (see Equation (1.7)). Considering the peak-to-peak separation values obtained in this work (see Table 7.5), the equation for the quasi-reversible reaction was used for the calculation of the diffusion coefficient[203]:

$$i_p^{quasi} = \pm 0.0436\, nFAC\sqrt{\frac{nFD\nu}{RT}} \tag{7.3}$$

where n is the number of electrons exchanged during the electrochemical reaction, i_p is the peak current for the peak obtained during the forward scan (see Figure 7.8a and c), F is the Faraday constant (C/mol), ν is the applied scan rate (V/s), R is the universal gas constant, T is the temperature in Kelvin, A is the area of the electrode (cm^2) and D is the diffusion coefficient (cm^2/s). The diffusion coefficient values obtained were 7.3 (± 0.7) $x10^{-6}$ cm^2/s, when C/G-SPEs were used, and 6.8 (± 0.9) $x10^{-6}$ cm^2/s when C/G/Bi-SPEs were used (see Table 7.6), these values are

comparable with those found in the literature[413–415]. The two values are in good agreement as expected, and the diffusion coefficient it is not influenced by the type of working electrode used for the measurements[45].

The values of k^0 obtained on the two electrodes are shown in Table 7.6. Similar values have been obtained for commercial graphite electrodes, suggesting that the value of k^0 is influenced by the type and the quantity of the components[417,418]. The k^0 obtained for C/G-SPEs is comparable with those obtained for C/G/Bi-SPEs. This similarity may be due to the low concentration of Bi particles on the surface of the electrode or to the passivation of the Bi particles (see Chapter 3).

Table 7.6: Diffusion coefficient and the heterogenous rate constant for Ferrocene methanol at C/G-SPEs and C/G/Bi-SPEs in 0.1 M Na_2SO_4

electrode	D [cm^2/s]	k^0 [cm/s]
C/G-SPEs	7.3 (± 0.7) $x10^{-6}$	3.4 (± 0.2) $x10^{-3}$
C/G/Bi-SPEs	6.8 (± 0.9) $x10^{-6}$	6.4 (± 0.9) $x10^{-3}$

The experiments were then performed in $KHCO_3$ to study the behaviour of the SPEs in the other solution used for the catalytic experiments. The scan rate studies are shown in Figure 7.10a and c for C/G-SPEs and C/G/Bi-SPEs, respectively, while the plot of i_p versus the square root of scan rate is shown in Figure 7.10b and d. The characteristic peak for the reduction and oxidation of FcMeOH are present. However, the E^0 is significantly shifted in the positive direction (around 45 mV) in comparison with the Na_2SO_4 solutions (see Table 7.7). The peak current as a function of the square root of the scan rate presented a linear trend, and therefore the reaction occurs under diffusion control, as observed in Na_2SO_4 solutions.

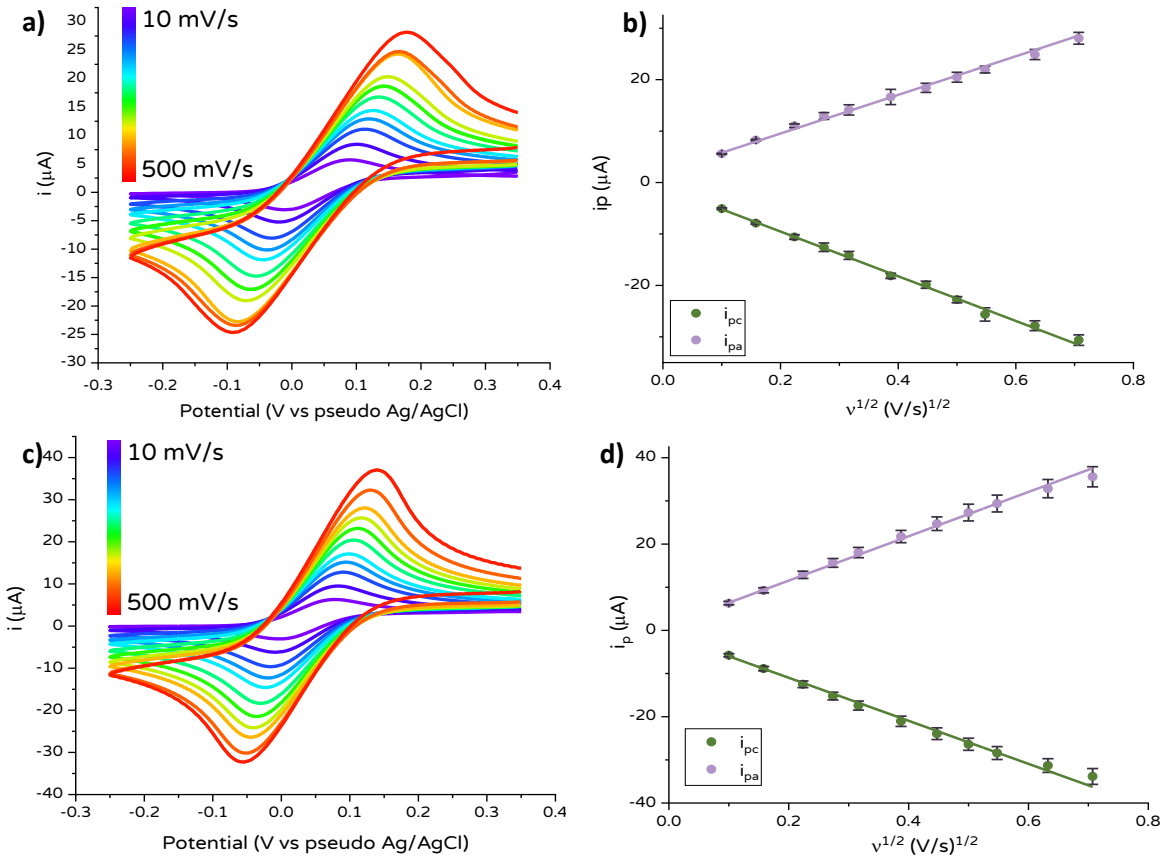

Figure 7.10: : a) Scan rate study for C/G-SPE in 0.1 M $KHCO_3$ in the presence of 1 mM ferrocene methanol; b) plot of Ip anodic (purple) and cathodic (green) as a function of the square root of the scan rate at C/G-SPE; c) Scan rate study for C/G/Bi -SPE in 0.1 M Na_2SO_4 in the presence of 10 mM ferrocene methanol; and d)) plot of Ip anodic (purple) and cathodic (green) as a function of the square root of the scan rate at C/G/Bi-SPE

The C/G-SPEs showed higher peak-to-peak separation than C/G/Bi-SPEs as observed in Na_2SO_4 solutions. In comparison with the CVs obtained in Na_2SO_4 solutions, the peak-to-peak separation in $KHCO_3$ solutions is clearly larger (see Figure 7.10a and c and Table 7.7). In particular, a ΔE_p of 70 and 136 mV larger is observed at 100 and 500 mV/s in $KHCO_3$ than in Na_2SO_4. This may be due to the slightly higher resistance of the electrode in $KHCO_3$ than in Na_2SO_4 (see Table 7.2).

Table 7.7: Standard potential and ΔEp for Ferrocene methanol for C/G-SPEs and C/G/Bi-SPEs at two different scan rates in $KHCO_3$

electrode	E^0 at 50 mV/s	Scan rate [mV/s]	ΔE_p [V]
C/G-SPEs	0.041 ± 0.004	10	0.10 ± 0.01
		100	0.17 ± 0.03
		500	0.29 ± 0.06
C/G/Bi-SPEs	0.0375 ± 0.005	10	0.081 ± 0.005
		100	0.121 ± 0.005
		500	0.194 ± 0.008

Then, the diffusion coefficient and the k^0 were calculated using Equation (1.7) and (7.2), respectively, and the results are shown in Table 7.8. The diffusion coefficient values increased

significantly, with values x2.5 times higher than those usually found in the literature[413–415]. However, similar values were obtained by Montiel et al.[419] though they did not offer any rationale for their observations, but suggested the formation of some aggregate in solution, without any additional specification on the nature of the possible aggregate, that could have played a role in the obtained value. On the other hand, the values of k^0 are very similar to those obtained in Na_2SO_4, suggesting that the solution used for the experiments does not significantly influence the k^0.

Table 7.8: Diffusion coefficients and heterogenous rate constant for Ferrocene methanol at C/G-SPEs and C/G/Bi-SPEs in 0.1 M $KHCO_3$

electrode	D [cm^2/s]	k^0 [cm/s]
C/G-SPEs	1.87 (± 0.7) $x10^{-5}$	3.4 (± 0.6) $x10^{-3}$
C/G/Bi-SPEs	2.04 ± (0.3) $x10^{-5}$	7.0 (± 0.8) $x10^{-3}$

7.2.1.2.3 Capacitance

In general, double layer capacitance values can provide important information about several characteristics of working electrodes, like their area, their structure and their chemical nature. In addition, the interactions between the electrodes and the species in solution can be monitored by measuring the capacitance[208,210,211]. For this reason, the capacitance of the SPEs was determined in Na_2SO_4 and $KHCO_3$ solutions to allow a comparison among the different electrodes and electrode-electrolyte interfaces. The current from the scan rate studies was normalised to the real area calculated using the mass transfer method, to allow a direct comparison between the two types of the SPEs. The scan rate studies in Na_2SO_4 for C/G-SPEs and C/G/Bi-SPEs are shown in Figure 7.11a and c, respectively, while the cathodic charging currents as a function of the scan rate are shown in Figure 7.11b and d. The scan rate values used for the cathodic charging current plot were between 10 and 300 mV/s. Looking at the scan rate study for both SPEs, it is clear that the capacitive current for C/G/Bi-SPEs is lower than for C/G-SPEs. Considering that the real area for the two types of SPEs is comparable, this suggests that the presence of Bi microspheres decreased the background current.

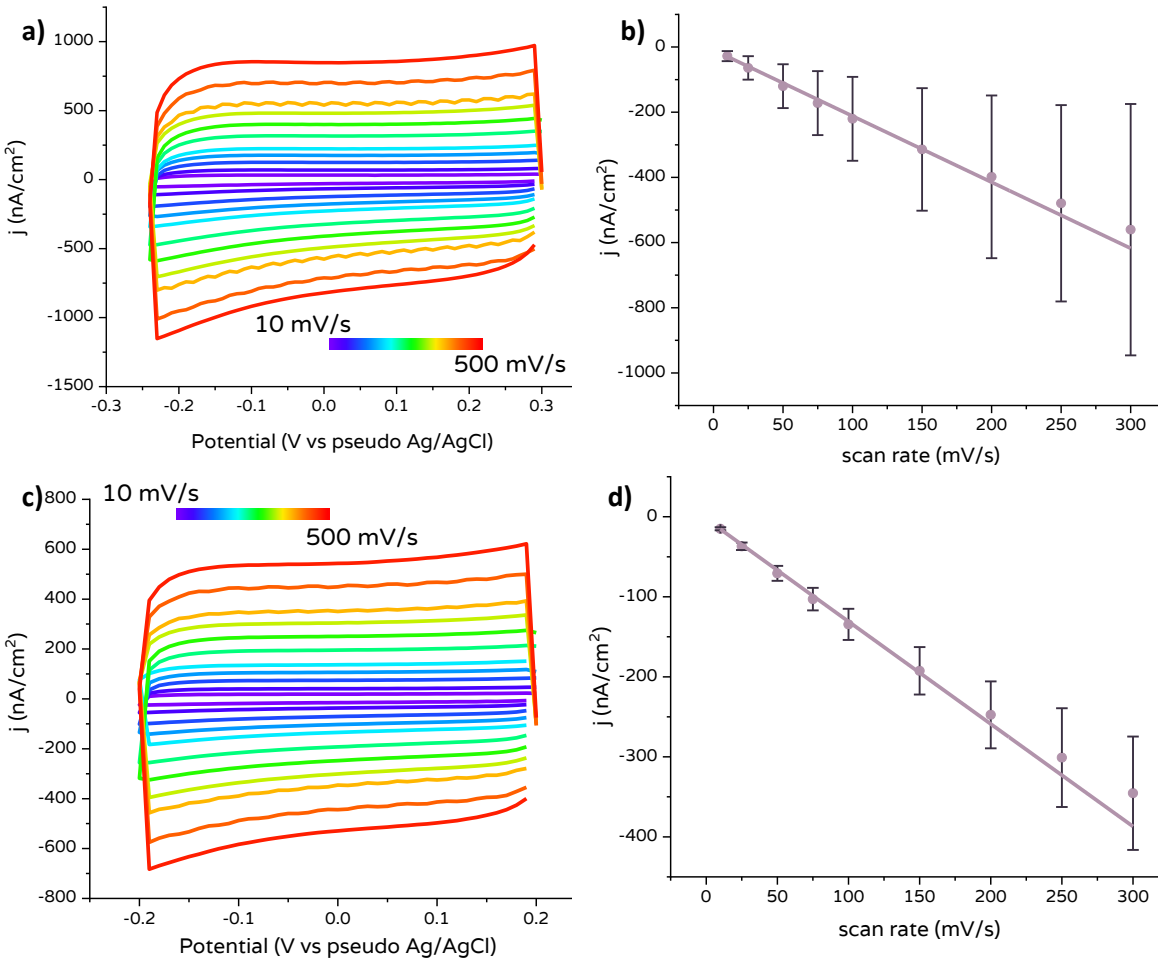

Figure 7.11: a) Scan rate studies in 0.1 M Na_2SO_4 for q) C/G-SPEs and c) C/G/Bi-SPEs; cathodic charging currents as a function of the scan rate for b) C/G-SPEs and d) C/G/Bi-SPEs

Then, the scan rate studies were performed in $KHCO_3$ (see Figure 7.12). The current densities in $KHCO_3$ for C/G-SPEs were approximately half those observed in Na_2SO_4, suggesting a lower capacitive background in $KHCO_3$ than in Na_2SO_4. On the other hand, slightly higher current densities were observed for C/G/Bi-SPEs in $KHCO_3$, suggesting that in $KHCO_3$ the presence of the Bi microspheres does not significantly modify the values of the background currents.

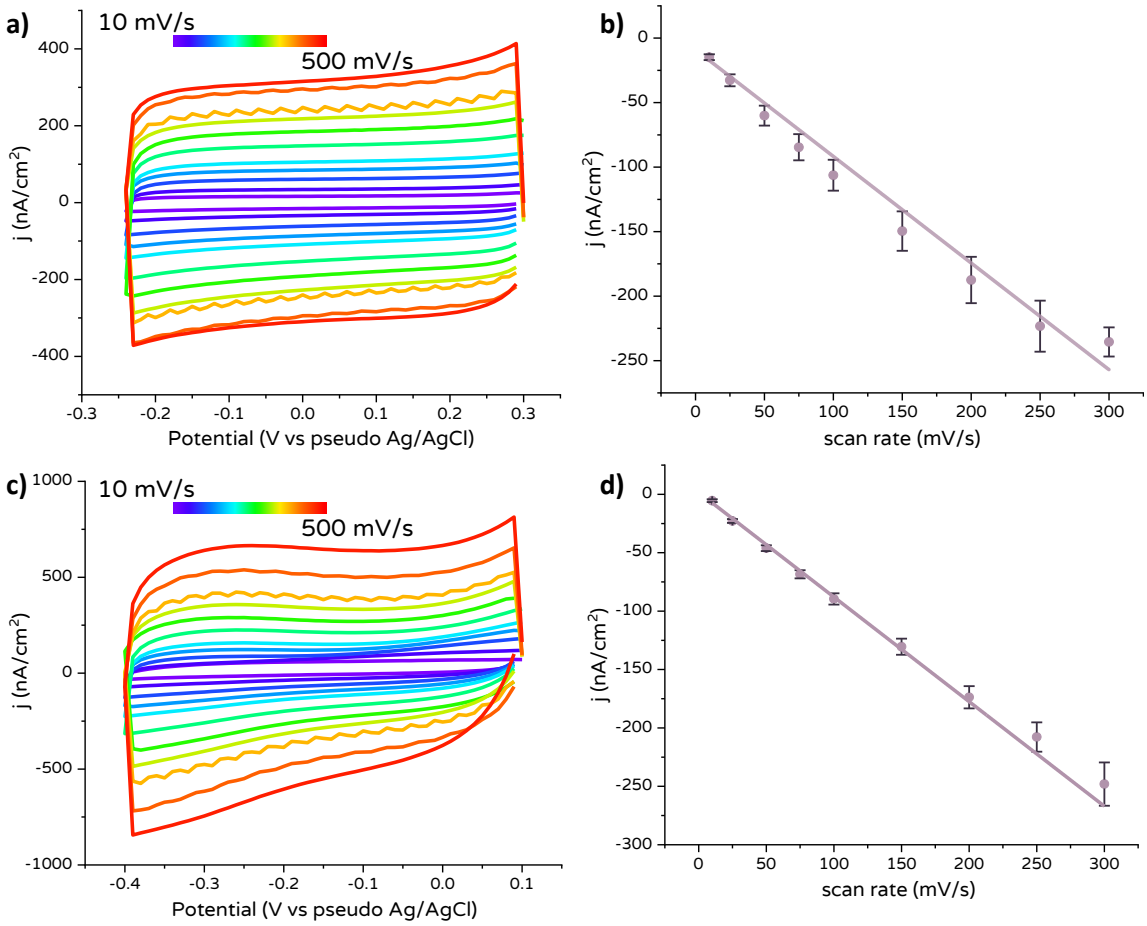

Figure 7.12: a) Scan rate studies in 0.1 M $KHCO_3$ for q) C/G-SPEs and c) C/G/Bi-SPEs. Scan rate interval: 10 - 500 mV/s; cathodic charging currents as a function of the scan rate for b) C/G-SPEs and d) C/G/Bi-SPEs $KHCO_3$. Scan rate interval 10 – 300 mV/s

The values of capacitance calculated for the two types of SPE are shown in Table 7.9. In general, values of capacitance smaller than 100 µF/cm^2 have been observed for carbonaceous SPEs in the literature[417,420,421], however, the values of capacitance obtained here are significantly lower, being, for all the SPEs, less than 2 µF/cm^2. Capacitance values in $KHCO_3$ were only about 50% of those in Na_2SO_4. In contrast, it seems that the presence of the Bi microspheres did not influence the values of capacitance, as comparable values were obtained in both solutions. A decrease in capacitance was expected in the presence of Bi, as low capacitance values were observed for Bi disk electrodes and Bi modified electrodes (see Chapters 3 and 4). However, it is important to highlight that the quantity of Bi microspheres is quite low, it is therefore likely that the contribution of the Bi on the capacitance is not enough to be detected. This will be discussed further later on within this chapter.

Table 7.9: Capacitance values for C/G-SPEs and C/G/Bi-SPEs

electrode	electrolyte	Capacitance $\left[\frac{\mu F}{cm^2}\right]$
C/G-SPEs	Na_2SO_4	1.92 ± 0.08
	$KHCO_3$	0.83 ± 0.04
C/G/Bi-SPEs	Na_2SO_4	1.25 ± 0.04
	$KHCO_3$	0.87 ± 0.02

7.2.2 Bi SPEs for CO_2 reduction

Preliminary experiments were performed using cyclic voltammetry to investigate the ability of SPEs to behave as electrocatalysts for the CO_2 reduction reaction. CVs for C/G-SPEs and C/G/Bi-SPEs were performed in both Na_2SO_4 and $KHCO_3$ solution under N_2 and successively under CO_2 atmospheres. The CVs obtained with C/G/Bi-SPEs in Na_2SO_4 and $KHCO_3$ solutions are shown in Figure 7.13a and b, respectively. In both solutions the CVs were recorded in N_2-saturated solutions (green curves) and CO_2-saturated solutions (purple curves). In the first cycle (light green and purple curves), a large and not well-defined peak under both N_2 and CO_2 is observed. The position of the peak shifted when different solutions and gas were used, and its size and shape were not constant when different electrodes were tested. Similar peaks have been observed when the native Bi is reduced in aqueous solutions (see Chapter 6)[240]. This suggests the presence of some of Bi oxide on the Bi microspheres, likely formed after contact with air. The peak was not present on the second cycle suggesting that the Bi oxide was completely reduced during the first cycle or any residual oxide is not electrochemically accessible.

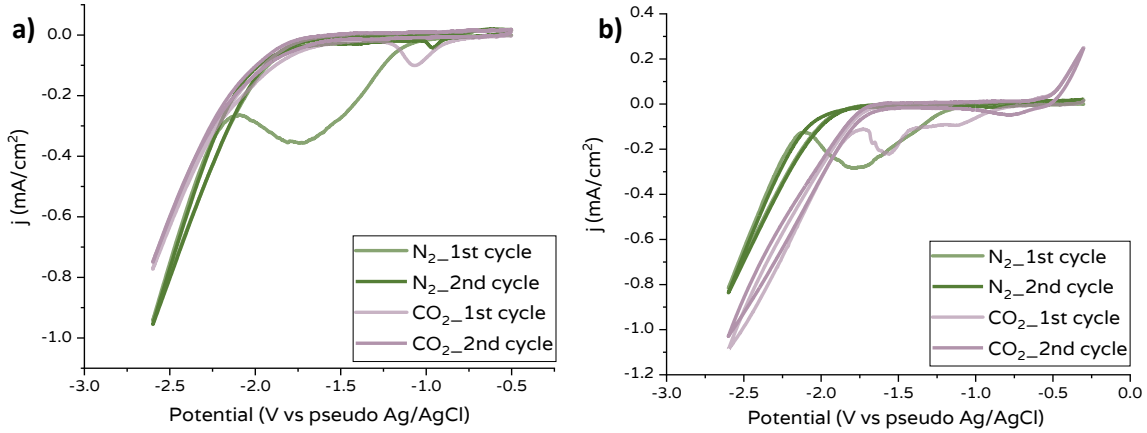

Figure 7.13: CVs on C/G/Bi-SPEs in a) 0.1 M Na_2SO_4 and b) 0.1 M $KHCO_3$ under N_2 (green) and CO_2 (purple). Scan rate = 100 mV/s The curves in light colour (both green and purple) represent the first cycle.

The second cycle for C/G-SPEs (green) and C/G/Bi-SPEs (purple) in Na_2SO_4 (Figure 7.14a) and $KHCO_3$ (Figure 7.14b) are shown above. In Na_2SO_4, C/G-SPEs presented a small feature around -2.0 V vs pseudo Ag/AgCl under CO_2 that is absent under N_2. The feature presented a current density around x1.3 times higher in the first cycle. Similar features have been observed before in carbonaceous

electrodes and they were attributed to CO_2 reduction[24,169,346]. The decrease of the current density is due to the irreversible adsorption of the reduction products on the surface of the carbon electrode, inhibiting the catalytic cycle[24,169,346]. C/G/Bi-SPEs presented a similar feature in the second cycle, but no significant difference in comparison with C/G-SPEs in the current density magnitude was observed. The same feature has been observed in another study for Bi electrodes and, as in the case of the carbon electrodes, it was attributed to the reduction of CO_2[241]. The onset potential observed when C/G/Bi-SPEs were used under CO_2 is 0.5 V more positive than with C/G-SPEs, suggesting that C/G/Bi-SPEs has potentially higher catalytic activity for CO_2RR than C/G-SPEs. However, a similar shift is observed under N_2, suggesting that the Bi present in the SPEs simply may present a better catalytic activity for both the hydrogen evolution reaction (HER) and CO_2RR. In $KHCO_3$, no small features were observed, however, the curve under CO_2 for C/G/Bi-SPEs (solid purple line) presented an onset potential 0.2 V more positive than under N_2. Based on this finding it seems that C/G/Bi-SPEs might present a slightly higher catalytic activity than C/G-SPEs for CO_2RR. As it is well known that Bi particles are catalytic toward CO_2RR[100–104,106], the similar performances of C/G-SPEs and C/G/Bi-SPEs and the general low performances observed for C/G/Bi-SPEs is likely due to the low concentration of Bi.

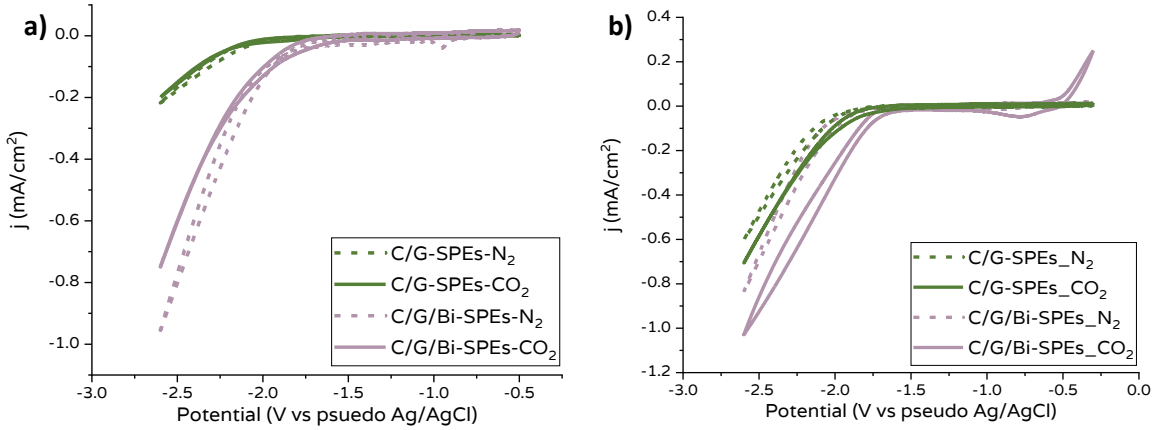

Figure 7.14: CVs on C/G/Bi-SPEs (green) and C/G/Bi-SPEs (purple) under N_2 (dashed line) and CO_2 (solid line) in a) 0.1 M Na_2SO_4 and b) in 0.1 M $KHCO_3$. Scan rate= 100 mV/s

To understand if a higher concentration of Bi resulted in a higher catalytic activity of the system, some CVs were acquired using Bi M_G/G-SPEs. To perform the experiments care was taken to ensure that the connector of the adaptor for the SPEs was in contact with the C/G ink. However, as mentioned previously, this is not always possible, and this experiment was performed to obtain qualitative information on the role of the concentration of Bi on the catalytic performances of the SPEs. From Figure 7.15, it would appear that the presence of higher concentration of Bi influenced the catalytic activity of the system toward CO_2RR. A peak around -1.5 V is observed in CO_2-saturated solutions, but not under N_2 atmosphere, suggesting that the peak is related to the reduction of CO_2.

The ratio between the current density at the maximum of the feature and the background current was equal to 61 in Na_2SO_4, more than one order of magnitude higher than for C/G-SPEs and C/G/Bi-SPEs. In addition, the feature is here at around -1.7 V, a potential almost 0.2 V more positive than for C/G and C/G/Bi-SPEs. In $KHCO_3$, the ratio was equal to almost 35, while when C/G-SPEs and C/G/Bi-SPEs were used, no peak attributable to CO_2 reduction was observed. Interestingly, no peak for the oxidation of the Bi oxide is observed for Bi M_C/G-SPEs, suggesting that the particles are shielded from air oxidation by some component within the ink, likely the binder. This may be due to the slightly different ratios of components used to produce the Bi M ink, as marginally different quantities were used to obtain the proper viscosity for the printing process. It is important to highlight that the feature is present only in the first cycle (here only the first two cycles are presented). This suggests that the surface of the electrode may be poisoned after the first cycle and the catalytic cycle is inhibited as has been observed for glassy carbon and Pt electrodes[24,43,169,345,346], in which the products are irreversible adsorbed on the active sites. It is therefore possible that the SPEs would not exhibit appreciable ability to reduce CO_2 during control potential electrolysis experiments. However, these are hypotheses, as electrolysis experiments need to be performed to quantitatively probe the activity of the Bi modified SPEs. Based on the current response observed for Bi M_C/G-SPEs, a second carbonaceous ink containing higher concentration of Bi was produced.

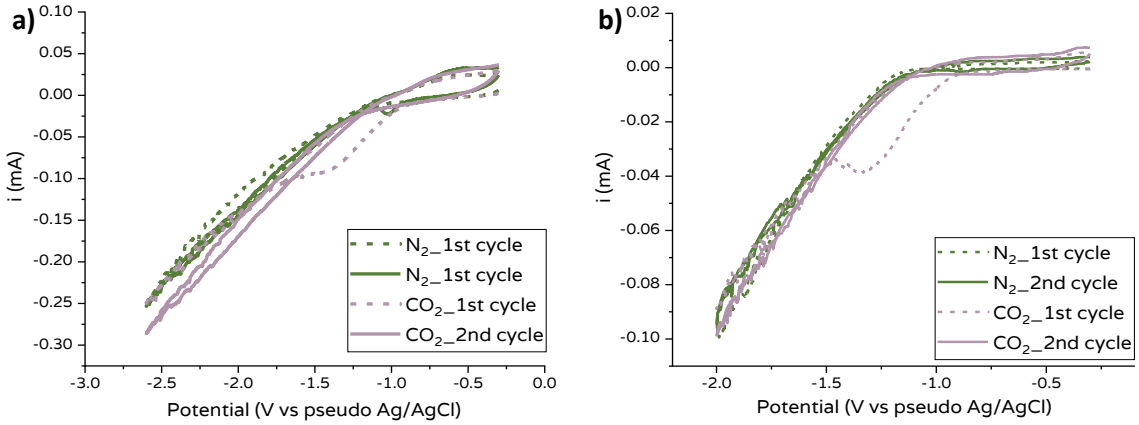

Figure 7.15: CVs on Bi M_C/G-SPEs under N_2 (green curves) and CO_2 (purple curves) in 0.1 M a) Na_2SO_4; and b) $KHCO_3$. The dashed lines represent the first cycle.

7.3 Second ink formulation

For the second ink formulation, a pure carbonaceous, a carbon/bismuth and a pure Bi ink were prepared. The general composition of the inks was similar to the first formulation (for details on the components of the second formulation see Chapter 2 Section 2.4.5) but the ratio between the components differed. Graphene and carbon black were used as carbonaceous components in which the Bi microspheres (max diameter 45 µm) were added. In the carbon/bismuth ink the concentration of Bi was equal to 40% w/w. The type of ink, the principal components present in the

ink, and the name assigned to the electrodes after printing are shown in Table 7.10 (the other components of the inks are not listed here). Based on the results obtained after the electrochemical preliminary tests, a pure Bi ink SPEs was not printed.

Table 7.10: inks and the name of the respectively screen printed electrodes

ink	main components	electrode name
pure carbonaceous	carbon and graphite	C/G_{40}-SPE
carbonaceous + Bi particles	carbon, graphite, Bi microspheres (40% w/w)	C/G/Bi_{40}-SPE
pure Bi metal	Bi microparticles	-
pure Bi metal ink on carbonaceous ink	Bi microparticles (outer layer), carbon and graphite (inner layer)	Bi M_C/G_{40}-SPE

The higher content of Bi in C/G/Bi_{40}-SPEs compared to C/G/Bi-SPEs was evident by comparing the colour of the SPEs colour of the SPEs by visual observation: the grey of C/G/Bi_{40}-SPEs was lighter than the one observed for C/G/Bi-SPEs. In contrast with the Bi M_C/G-SPEs, the two layers in the two-layers SPEs overlapped almost perfectly.

7.3.1 Characterisation

As for the SPEs printed using the first ink formulation, a full characterisation was performed: SEM images of the SPEs were acquired; preliminary electrochemical test were carried out; the ECSA was determined, the electron transfer ability investigated; and the capacitance measured. For a schematic representation of the characterisation performed for the SPEs see Figure 7.1.

7.3.1.1 Physical characterisation: SEM

SEM images were acquired for C/G_{40}-SPEs and C/G/Bi_{40}-SPEs (see Figure 7.16). The mesh pattern of the screen is more defined in C/G_{40}-SPEs than in C/G-SPEs (see Figure 7.16a). This is likely due to the different components used, their loading and therefore the way in which they passed through the mesh. Specifically, less aggregated particles (likely graphite) are present here than in C/G-SPEs. This is clear from Figure 7.16b, in which a smoother surface than for C/G-SPEs (see Figure 7.2) is observed. However, the pattern of the mesh and the presence of pores and edges ensure a certain degree of roughness of the surface, resulting in a high surface area. A qualitative comparison of the roughness area of the electrodes is presented in Section 7.3.1.2.1.

C/G/Bi_{40}-SPEs was seen to contain more Bi than C/G/Bi-SPEs as a higher number of spheres were present and a higher density distribution was observed (see Figure 7.16c and d). Because of this, some of the microspheres aggregated (see red circles in Figure 7.16c). This is in contrast with what was observed on C/G/Bi-SPEs, in which the particles were too dispersed to form aggregates. As

observed for the SPEs printed with the first inks, the preparation procedure did not affect the size of the Bi microspheres.

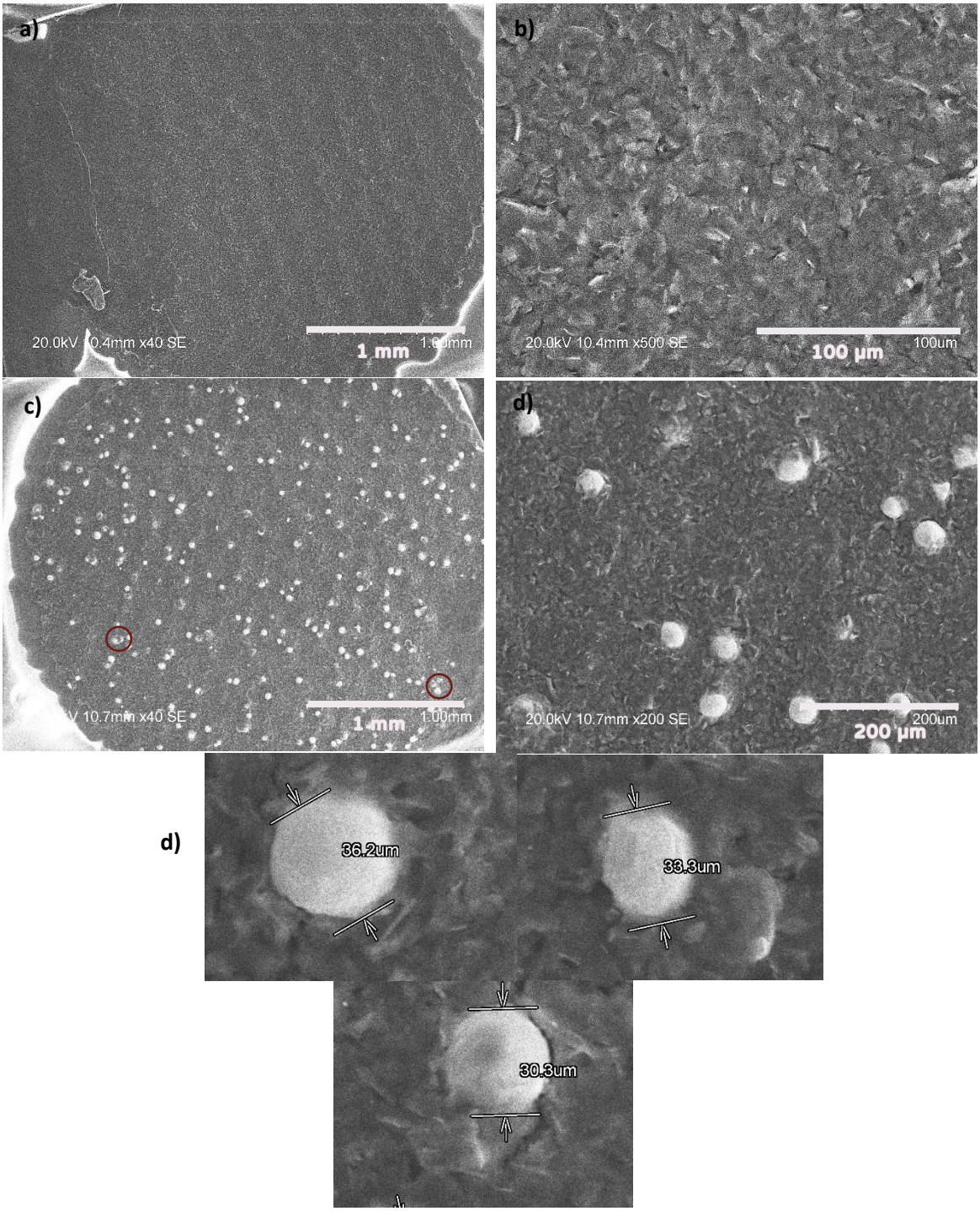

Figure 7.16: SEM images of C/G_{40}-SPEs at magnification equal to: a) x40; b) x500; and c) image of C/G/Bi_{40}-SPEs at magnification equal to x40; d) several Bi microspheres and their sizes present on the surface of the SPEs. The black semicircle at the left of the working area in image a) and on the bottom right corner in c) is the conductive paste used for creating a conductive connection between the substrate and the working area

7.3.1.2 Electrochemical characterisation

The SPEs were preliminarily tested to obtain information on the electrochemical behaviour in the two solutions under investigation: Na_2SO_4 and $KHCO_3$. Both OCP and the resistance were measured for the three types of SPEs printed and the results are shown in Table 7.11.

Table 7.11: Open circuit potential and resistance values for the three types of screen printed electrodes

electrode	electrolyte	OCP [V]	Resistance [Ω][a]
C/G_{40}-SPE	Na_2SO_4	0.06	1608 ± 162
	$KHCO_3$	0.03	1477 ± 277
C/G/Bi_{40}-SPE	Na_2SO_4	-0.06	1603 ± 88
	$KHCO_3$	-0.4	1802 ± 123
Bi M_ C/G_{40}-SPE	Na_2SO_4	0.59	3 (±4) x10^5

[a] calculated at OCP

The resistance of the C/G_{40}-SPE electrodes is comparable regardless of the solution used, the same as observed for the first ink formulation. However, the resistance of C/G_{40}-SPEs is around x1.5 times higher than for C/G-SPEs. This can be due to the nature of the polymers in the binder and the ratio between binder and conductive components. On the other hand, the resistance of C/G/Bi_{40}-SPE is comparable with the resistance of C/G/Bi-SPEs. This suggests that the amount Bi microspheres influences the resistance of the electrodes. A test on the two-layer SPEs (Bi M_ C/G_{40}-SPE) was performed and a resistance equal to 3 (±4) x10^5 Ω was obtained. Considering the fact that the two layers here overlapped almost perfectly, the connector of the SPEs adaptor was only in contact with the Bi M ink, that it is not conductive (see Section 7.2.1.2). To use a SPEs containing a layer of Bi M ink, printing the Bi M ink only on the working area and leaving the conductive path with the pure carbonaceous ink exposed would be necessary. For this reason, no characterisation was performed for the two-layer electrodes.

The two types of electrodes, the pure carbonaceous and the carbon/bismuth SPEs were then characterised in a large potential window: from 1.4 to -2.4 V. The CVs in Na_2SO_4 0.1 M (green) and $KHCO_3$ 0.1 M (purple) for C/G_{40}-SPEs and for C/G/Bi_{40}-SPEs are shown in Figure 7.17a and b, respectively. The C/G_{40}-SPEs do not show well defined peaks and the limits of the potential window are around -1.92 and 0.56 V in $KHCO_3$ and around -1.87 and 0.93 V in Na_2SO_4. A small increase in current followed by a steady state is observed at around -0.87 and -1.01 V in $KHCO_3$ and Na_2SO_4 respectively. The feature presented a higher current in $KHCO_3$ than in Na_2SO_4. The currents associated with the features would not be considered to be large (30 µA in $KHCO_3$ and 14 µA in Na_2SO_4), however, it is important to take into consideration this process when the CO_2 reduction reaction is investigated. As observed for the SPEs printed using the first formulated ink, the potential window in Na_2SO_4 is wider than in $KHCO_3$. Higher currents were observed with C/G_{40}-SPEs

than with C/G-SPEs in both solutions, suggesting a possible higher catalytic activity or a higher ECSA. When C/G/Bi_{40}-SPEs were tested, the typical peaks for the oxidation of Bi and the reduction of Bi oxide were observed[177,183,385]. Also in this case, higher currents were observed than for the SPEs printed using the first inks, however higher peak to peak separations were observed, especially in $KHCO_3$. Considering the higher resistance calculated for these SPEs, it is possible that the increase in current is due to a higher iR drop. A noisy current response was observed at cathodic potentials, suggesting a high quantity of gas bubbles, e.g., hydrogen, formed during the scan.

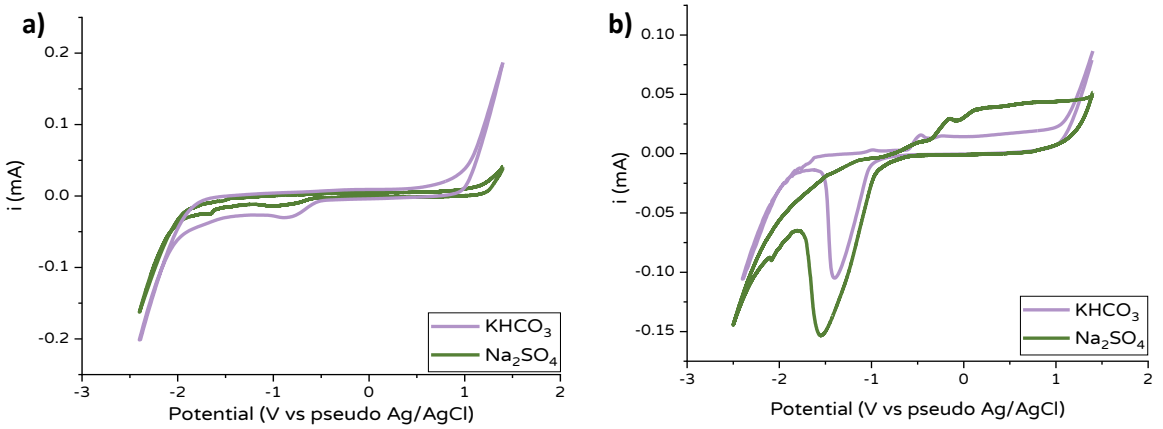

Figure 7.17: CVs for large potential window in two different electrolytes: 0.1 M $KHCO_3$ (purple) and 0.1 M Na_2SO_4 (green) using a) C/G_{40}-SPEs and b) C/G/Bi_{40}-SPEs. c) zoom of the oxidation peaks at C/G/Bi-SPE. Scan rate 100 mV/s

7.3.1.2.1 Electroactive area and quantity of Bi

The electroactive area for C/G/Bi_{40}-SPEs was calculated using the oxygen adsorption method and the mass transfer method, while only the mass transfer method was used for the calculation of ECSA of C/G_{40}-SPEs. The description of the two methods is presented in Section 7.2.1.2.1. In particular, the mass transfer method Equation (1.7) was used and FcMeOH was used as a probe. The diffusion coefficient was equal to 7.6 x10^{-6} cm^2/s, as is found in the literature[413–415]. The results for the electrochemical areas obtained using the two different methods and the roughness factors are shown in Table 7.12.

Table 7.12: Charge, geometrical and real areas, roughness factor and quantity of Bi for C/G/Bi_{40}-SPEs calculated via the reduction of monolayer method

method	electrode	Q_{exp} [µC]	A_{geo} [cm^2]	A_{real} [cm^2]	r_f	moles of Bi per area [nmoles/ cm^2]
oxygen adsorption	C/G/Bi_{40}-SPEs	216 ± 24	0.07	1.2 ± 0.1	16 ± 2	2.5 ± 0.3
mass transfer	C/G/Bi_{40}-SPEs	-	0.07	0.44 ± 0.04	6.3 ± 0.6	-
	C/G_{40}-SPEs	-	0.07	0.49 ± 0.05	6.9 ± 0.7	-

As observed for the first ink formulation, the area of the SPEs calculated using the mass transport method is lower than that obtained using the oxygen adsorption method. Specifically, the area for the oxygen adsorption method is x2.7 times larger than the area of the SPEs printed using the first ink. This would be reasonable if the value obtained with the oxygen adsorption method is inflated by the reduction of multilayers of oxide, as more Bi microspheres are present. However, it seems that the area calculated for C/G/Bi_{40}-SPEs via mass transfer method is underestimated, as it is comparable with the one obtained for C/G_{40}-SPEs. Considering that the quantity of Bi microspheres is higher than in the first ink, this seems unlikely. In comparison with the first ink SPEs, the charge, the A_{real} and the moles of Bi per area of the second ink SPEs are around x2.6 times higher. This was expected, as the content of Bi was four times higher. Interestingly, even if the content of Bi in the ink was four times higher, this was not representative of the surface content, suggesting that, also in the case of C/G/Bi-SPEs, it is likely that less 10% of Bi was exposed.

7.3.1.2.2 Electron transfer: Ferrocene methanol

The electron transfer properties of the SPEs were investigated via scan rate dependent studies using 1 mM FcMeOH as a probe in both Na_2SO_4 and $KHCO_3$ solutions. As for the first ink formulation, the peaks for the oxidation and reduction of the redox couple are well defined for the two types of SPEs in both solutions (see Figure 7.18a, c, e and g). The i_p vs the $v^{1/2}$ is linear, suggesting diffusion control processes at the surface of the electrodes (see Figure 7.18b, d, f and h). The E^0, obtained at 50 mV/s, is equal to 0.017 ± 0.002 and 0.0122 ± 0.0006 V for C/G_{40}-SPEs and C/G/Bi_{40}-SPEs, respectively, in Na_2SO_4, while, in $KHCO_3$, it is equal to 0.048 ± 0.003 and 0.044 ± 0.003 V. The E^0 values are very similar in the same solutions, as was observed for the first ink formulation. The ΔE_p values are comparable for C/G_{40}-SPEs and C/G/Bi_{40}-SPEs in Na_2SO_4, while in $KHCO_3$ the values are 20 mV higher than for C/G_{40}-SPEs at 10 mV/s (see Table 7.13). This suggests similar kinetics for the two types of SPEs in Na_2SO_4, while slightly higher kinetics were observed for C/G_{40}-SPEs than C/G/Bi_{40}-SPEs. This is in contrast with what was observed for the first ink formulation. However, a

difference of 20 mV (calculated at 10 mV/s when the iR drop effects should be minimal) could be due to a potential difference between the WE and the RE and not to a real difference in the electrochemical behaviour of the electrodes.

In comparison with the first ink formulation, the peak-to-peak separation is slightly lower for all the SPEs tested, suggesting a possible higher electron transfer processes with the second ink formulation SPEs. To obtain a quantitative measure of the electron transfer ability of the SPEs, k^0 was calculated using the Nicholson method (see Equation (7.1) and Figure 7.9), while the diffusion coefficient for FcMeOH was calculated using Equation (1.7). The values of the diffusion coefficient and k^0 for C/G_{40}-SPEs and C/G/Bi_{40}-SPEs in both Na_2SO_4 and $KHCO_3$ are shown in Table 7.14.

Table 7.13: Standard potential and ΔEp for Ferrocene methanol at C/G_{40}-SPEs and C/G/Bi_{40}-SPEs at three different scan rates (10, 100 and 500 mV/s) in both 0.1 M Na_2SO_4 and 0.1 M $KHCO_3$

electrolyte	electrode	E^0 at 50 mV/s	Scan rate	ΔE_p [V]
0.1 M Na_2SO_4	C/G_{40}-SPEs	0.017 ± 0.002	10	0.077 ± 0.002
			100	0.110 ± 0.006
			500	0.171 ± 0.009
	C/G/Bi_{40}-SPEs	0.0122 ± 0.0006	10	0.079 ± 0.001
			100	0.118 ± 0.008
			500	0.18 ± 0.02
0.1 M $KHCO_3$	C/G_{40}-SPEs	0.048 ± 0.003	10	0.079 ± 0.002
			100	0.121 ± 0
			500	0.201 ± 0.001
	C/G/Bi_{40}-SPEs	0.044 ± 0.003	10	0.096 ± 0.003
			100	0.132 ± 0.003
			500	0.219 ± 0.007

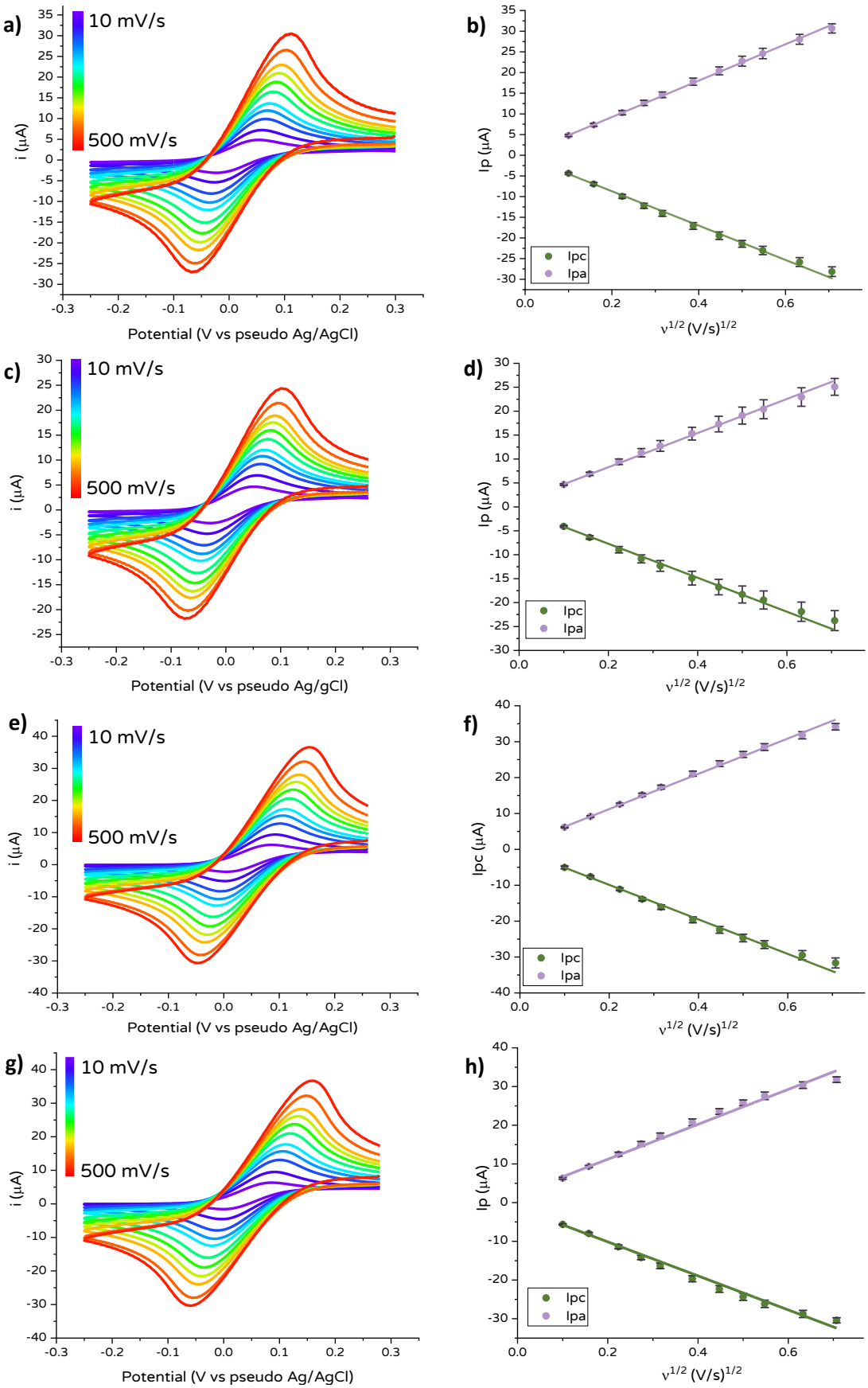

Figure 7.18: Scan rate study in the presence of 1 mM ferrocene methanol on a) C/G_{40}-SPE; and c) C/G/Bi_{40}-SPEs in 0.1 M Na_2SO_4; scan rate study on e) C/G_{40}-SPE; and g) C/G/Bi_{40}-SPEs in 0.1 M $KHCO_3$; plot of ip anodic (purple) and cathodic (green) as a function of the square root of the scan rate at b) C/G_{40}-SPE at d) C/G/Bi_{40}-SPE in 0.1 M Na_2SO_4; plot of ip vs square root of the scan rate on f) C/G_{40}-SPE and h) C/G/Bi_{40}-SPE in 0.1 M $KHCO_3$. The CVs were not corrected for iR drop

The diffusion coefficient values obtained for the two types of SPEs in both the solutions are comparable. They are slightly larger than those obtained for the first ink formulation in Na_2SO4, but smaller than in $KHCO_3$. These values are x1.6 times higher than the literature values[413–415]. All the k^0 values obtained within this work for these SPEs are comparable. In addition, they are quite similar to the k^0 values obtained with the SPEs containing the first ink, suggesting that the electron transfer ability of the SPEs obtained with the two different inks is similar for the out-of-sphere probe: FcMeOH. This is reasonable considering that the components and the nature of the ink did not significantly change, and different electron transfer ability is expected when the nature of the electrode structure is and the conductive characteristic are significantly altered[418]. Considering that Bi metal can easily oxidise in air, this would mean that some oxide was likely formed on the surface of the microspheres, (see Figure 7.13) and that for the SPE surfaces that are affected by oxide other probes, like $Fe^{2+/3+}$, $Eu^{+2/+3}$ or $V^{2+/3+}$, are suggested[203], further investigation using one of different redox probes could be an avenue for future work.

Table 7.14: diffusion coefficient and the heterogenous rate constant for Ferrocene methanol at C/G_{40}-SPEs and C/G/Bi_{40}-SPEs in both 0.1 M Na_2SO_4 and 0.1 M $KHCO_3$

electrolyte	electrode	D [cm^2/s]	k^0 [cm/s]
0.1 M Na_2SO_4	C/G_{40}-SPEs	1.3 (± 0.3) $x10^{-5}$	7.6 (± 0.1) $x10^{-3}$
	C/G/Bi_{40}-SPEs	1.1 (± 0.2) $x10^{-5}$	6.0 (± 0.2) $x10^{-3}$
0.1 M $KHCO_3$	C/G_{40}-SPEs	1.23 (± 0.09) $x10^{-5}$	6.3 (± 0.5) $x10^{-3}$
	C/G/Bi_{40}-SPEs	1.30 (± 0.05) $x10^{-5}$	4.1 (± 0.4) $x10^{-3}$

7.3.1.2.3 Capacitance

The capacitance of the two types of SPEs was calculated in two solutions: one containing 0.1 M Na_2SO_4 and the other containing 0.1 M $KHCO_3$. The scan rate studies for C/G_{40}-SPEs and C/G/Bi_{40}-SPEs in Na_2SO_4 are shown in Figure 7.19a and c, respectively, while the cathodic charging currents as a function of the scan rate are shown in Figure 7.19b and d. For the experiments in $KHCO_3$, the scan rate studies are presented in Figure 7.20a and c, while the cathodic charging currents versus the scan rate plots are shown in Figure 7.20b and d. The scan rate range for the charging currents was set between 10 and 300 mV/s.

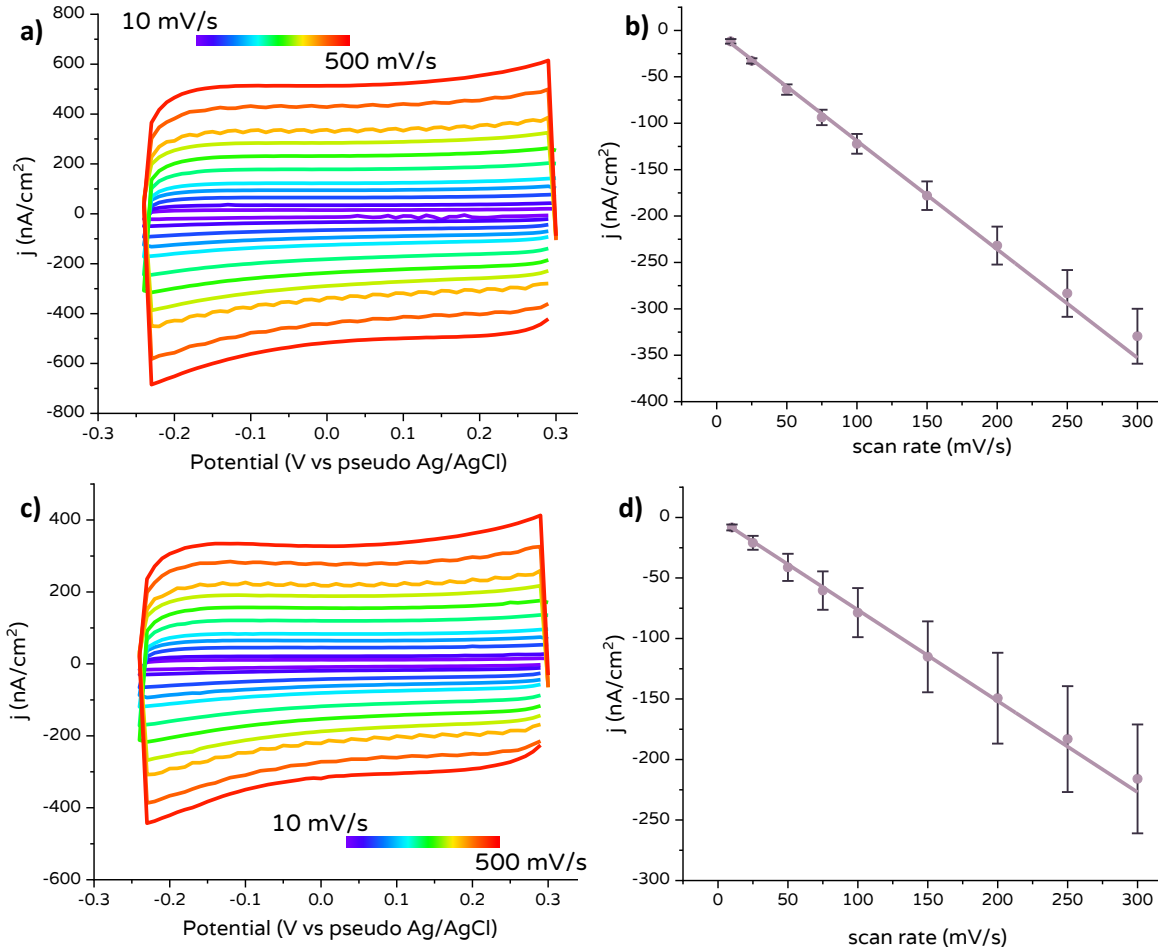

Figure 7.19: Scan rate studies in 0.1 M Na_2SO_4 for a) C/G_{40}-SPEs and c) C/G/Bi_{40}-SPEs; cathodic charging currents as a function of the scan rate for b) C/G_{40}-SPEs and d) C/G/Bi_{40}-SPEs

In Na_2SO_4, the currents for C/G_{40}-SPEs are x1.5 times higher than for C/G/Bi_{40}-SPEs. Considering the fact that the area of C/G_{40}-SPEs used for normalising the current values is slightly higher than for C/G/Bi_{40}-SPEs (see Table 7.12), this could be the reason behind the higher background currents. Similarly, in $KHCO_3$, the currents obtained at C/G_{40}-SPEs are x1.4 times higher. The capacitance values are shown in Table 7.15.

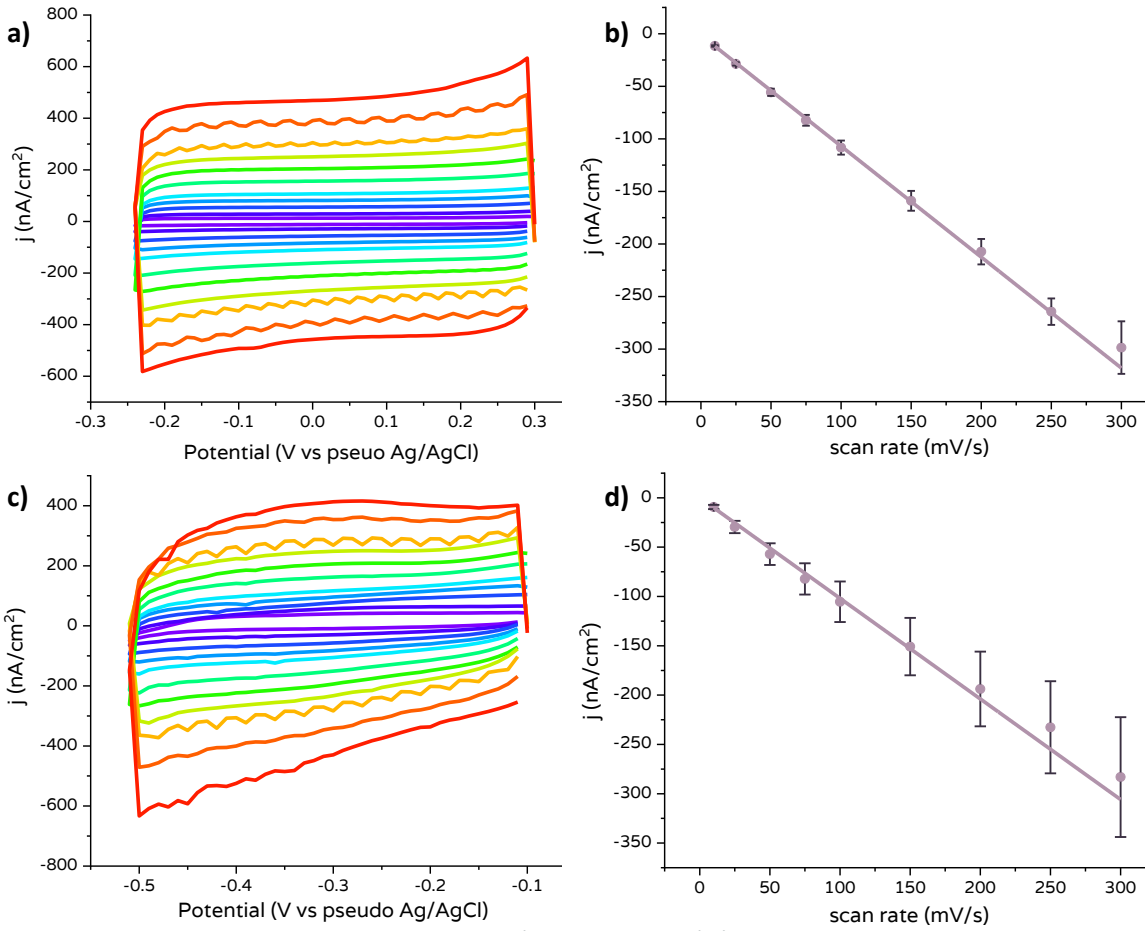

Figure 7.20: Scan rate studies in 0.1 M $KHCO_3$ for a) C/G_{40}-SPEs and c) C/G/Bi_{40}-SPEs; cathodic charging currents as a function of the scan rate for b) C/G_{40}-SPEs and d) C/G/Bi_{40}-SPEs

The capacitance of C/G_{40}-SPEs in the two solutions are comparable, as they were for C/G/Bi_{40}-SPEs. In contrast with the values obtained for the first ink, a decrease in the capacitance of the SPEs containing Bi microspheres is observed, suggesting that the Bi decreases the capacitance of the SPEs. This may indicate that the quantity of Bi in these SPEs is high enough to influence the capacitive behaviour of the SPEs, while it was not for the SPEs obtained printing the first ink.

Table 7.15: Capacitance values for C/G_{40}-SPEs and C/G/Bi_{40}-SPEs obtained in Na_2SO_4 and $KHCO_3$ 0.1 M. Scan rate range: 10 - 300 mV/s

electrode	Electrolyte	Capacitance $\left[\frac{\mu F}{cm^2}\right]$
C/G_{40}-SPEs	Na_2SO_4	1.13 ± 0.03
	$KHCO_3$	1.05 ± 0.01
C/G/Bi_{40}-SPEs	Na_2SO_4	0.75 ± 0.02
	$KHCO_3$	0.98 ± 0.04

7.3.2 Bi SPEs for CO_2 reduction

The catalytic activity of the C/G/Bi_{40}-SPEs was preliminarily tested via cyclic voltammetry under N_2 and successively under CO_2 atmospheres. The CVs acquired in Na_2SO_4 and $KHCO_3$ are shown in

Figure 7.21a and b, respectively. In both N_2-saturated solutions, a small peak between -1.0 and -1.25 V is present in the first cycle (light green curves). This peak disappears in the second cycle (dark green curves), suggesting that the peak is due to the reduction of Bi oxide. Considering that the current associated with the peak is significantly smaller than for C/G/Bi-SPEs (more than one order of magnitude) and that the amount of Bi is higher in C/G/Bi_{40}-SPEs than in C/G/Bi-SPEs, it is possible that the composition of the second ink slowed down the formation of the native oxide on the Bi microspheres. In both CO_2-saturated solutions, a large peak is observed in the first cycle, but not in the second cycle. This peak may be due to the reduction of the Bi oxide as proposed for the N_2-saturated CVs, however, considering the size of the peaks in N_2 and the shape of the peaks under CO_2 (see CVs for Bi M_C/G-SPEs in Figure 7.15), it is possible that the peak it is the result of two processes: the reduction of Bi oxide and also the reduction of CO_2. If this was the case, the same observed for Bi M_C/G-SPEs (see Section 7.2.2) is valid for C/G/Bi_{40}-SPEs: the CO_2RR is occurring in the first cycle, but not in the second. This could be the result of the SPEs being poisoned after the first cycle (see discussion in Section 7.2.2). However, to understand if the peak is due to the reduction of Bi oxide or CO_2, additional analyses need to be performed. Surface composition analyses before and after the cyclic voltammetry experiments, or in-situ experiments should be performed to gain further insight on the behaviour of the SPEs.

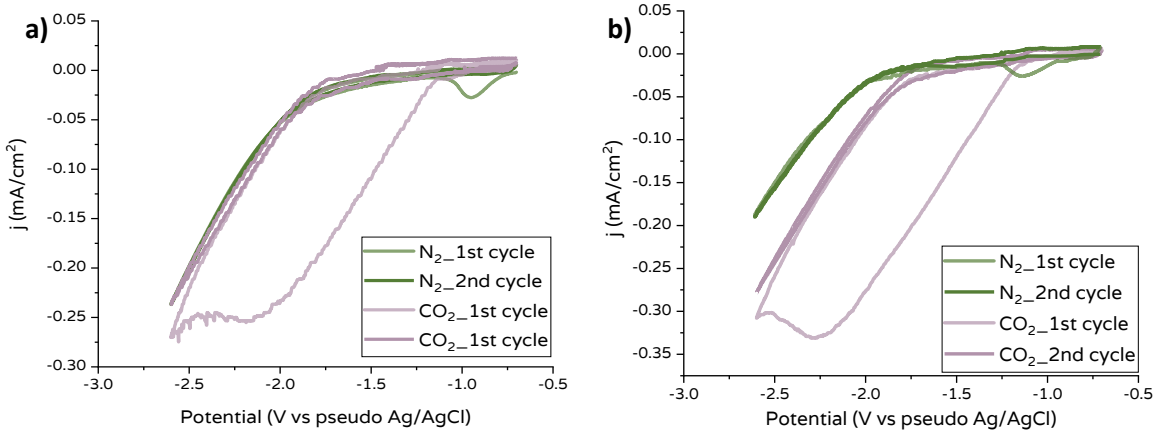

Figure 7.21: CVs at C/G/Bi_{40}-SPEs in a) 0.1 M Na_2SO_4 and b) 0.1 M $KHCO_3$ under N_2 (green) and CO_2 (purple). The curves in light colour (both green and purple) represent the first cycle. Scan rate = 100 mV/s

The catalytic activities of C/G/Bi_{40}-SPEs and C/G_{40}-SPEs were then compared in both Na_2SO_4 and $KHCO_3$ (see Figure 7.22a and b, respectively). As expected, in both Na_2SO_4 and $KHCO_3$ solutions, C/G_{40}-SPEs do not show a significant catalytic activity toward CO_2RR. Specifically, in $KHCO_3$, the current and the onset potential are the same under N_2 and CO_2, while in Na_2SO_4, only a slight increase in current and a slightly more positive onset potential was observed (see green curves in Figure 7.22a). When C/G/Bi_{40}-SPEs were used, no difference between the curve under N_2 (dashed purple curve) and under CO_2 (solid purple curve) is observed in Na_2SO_4, suggesting that the reaction

happening at the C/G/Bi_{40}-SPEs is the HER and the electrodes are not catalytic toward CO_2 reduction. A small shift in the onset potential between the dashed purple curve (N_2-saturated solutions) and the solid purple curve (CO_2-saturated solutions) is observed in $KHCO_3$. This may suggest that C/G/Bi_{40}-SPEs are, to some extent, catalytic toward CO_2 in $KHCO_3$. However, it is necessary to perform electrolysis experiments to qualitatively prove their catalytic activity.

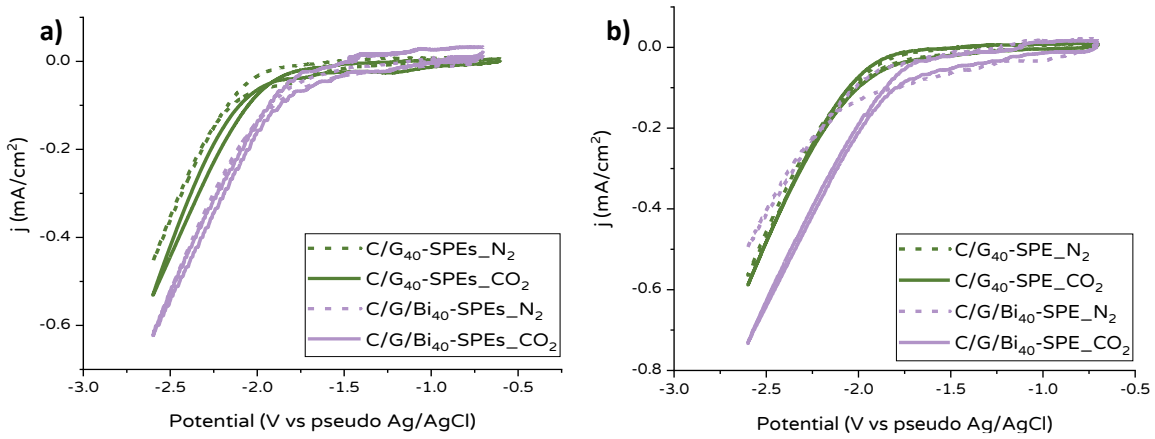

Figure 7.22: CVs at C/G_{40}-SPEs (green) and C/G/Bi_{40}-SPEs (purple) under N_2 (dashed line) and CO_2 (solid) in a) in 0.1 M Na_2SO_4 and b) 0.1 M $KHCO_3$. Scan rate= 100 mV/s. The second cycle is shown

7.4 Conclusion

In conclusion, SPEs electrodes were produced to try and increase the stability of the Bi catalysts (see Section 1.7, **objective 2**). Several inks were production using carbon/graphite and Bi microspheres as conductive fillers. The concentrations of Bi were 10% and 40% w/w of the ink. By using these inks, a total of seven different types of SPEs were printed: two pure carbonaceous SPEs (C/G-SPEs and C/G_{40}-SPEs), two mixed carbonaceous/bismuth SPEs (C/G/Bi-SPEs and C/G/Bi_{40}-SPEs), two two-layer SPEs (Bi M_C/G-SPEs and Bi M_C/G_{40}-SPEs) and a pure Bi metal SPE (Bi M-SPEs). The SPEs were electrochemical and physically characterised

The mixed carbon/Bi SPEs and the pure carbon SPEs, produced with the 1st ink formulation, were tested via cyclic voltammetry to investigate their possible catalytic activity toward the CO_2RR. A slightly higher catalytic performance was observed for C/G/Bi-SPEs than for C/G-SPEs. Additional experiments were performed with the two-layer Bi M_C/G-SPEs, that showed a well-defined peak in the presence of CO_2, that could be attributed to the reduction of CO_2. Unfortunately, the peak was observed only in the first cycle and not in the following ones, suggesting a possible poisoning of the electrode with the products or the intermediated of the reaction. This was unexpected, as, in contrast with carbon electrodes, Bi electrodes are known to be catalytically active for the

reduction of CO_2[100–104,106]. However, electrolysis experiments would need to be performed to quantitatively evaluate the catalytic activity of the C/G/Bi-SPEs toward CO_2RR.

Finally, C/G/Bi_{40}-SPEs were tested for CO_2RR, but no significant difference was observed in comparison with the SPEs produced with the 1st ink formulation. It would therefore be necessary to perform electrolysis experiments to obtain quantitative information about the two types of Bi-SPEs and to validate the proposed poisoning hypothesis (experiments not performed in this work). From these preliminary results, the **objective 2** was fulfilled only partially: a reproducible and cheap method for producing Bi catalyst was used; the SPEs presented high physical stability (the electrodes were not damaged during the experiments), however the stability of the electrodes toward the CO_2RR needs to be further investigated as possible poisoning of the surface was observed. It is important to highlight that this type of electrode has never been used for the CO_2RR, making this work the first example of Bi SPEs produced and investigated for the reduction of CO_2.

Chapter 8 : Conclusions and Future Works

8.1 Conclusions

In this work, three types of electrodes were produced and characterised for the electrochemical reduction of CO_2. The characteristics of these electrodes were compared, and their catalytic activity toward the CO_2 reduction reaction (CO_2RR) compared. A systematic study of the effects of (a) the surface modification of the electrodes and (b) use of co-catalysts was carried out (main objective 1, see Chapter 1, Section 1.7). In addition, attempts on increase the stability of the Bi catalysts were performed (main objective 2).

As far as **objective 1.a** is concerned:

- two types of electrode were produced: bulk Bi (Chapter 3), and Bi modified, electrodes (Chapter 4);
- different types of Bi modified electrodes were produced by changing, as the deposition parameters, the concentration of the Bi precursor in the deposition bath, the addition of a capping agent into the deposition solution and by performing multistep depositions. This led to the formation of Bi crystallites with different morphologies (dendrites, polygons, and spheres), areas and therefore with different number or type of active sites (Chapter 4);

For **objective 1.b** (Chapter 5):

- in the presence of imidazolium based ILs, higher currents and lower onset potentials were observed via CV. Au and Ag were the most active electrodes in the presence of ILs. Bi modified electrodes showed better suitability when used in aqueous systems compared to Ag, as less noise was recorded in the CVs (high production of H_2 was suggested to be reason behind the noise during the experiments)
- Two carboxylic acid functionalised ILs were synthesised and preliminarily tested in CO_2-saturated solutions. Experiments under pH control showed an increase in the current, probably due to the reduction of CO_2, at the pH values below the pK_a of the compounds with only one of the two in house built ILs.

In respect to **objective 2** (Chapter 7):

- Eight screen printed electrodes (SPEs) were printed by using two different ink formulations. Pure carbon SPEs (graphite and carbon black) and mixed carbon/Bi SPEs were preliminarily tested for CO_2 reduction. The electrodes seem particularly physically stable but possible poisoning of the surface (possible due to products irreversible adsorbed) occurs after CV experiments

Finally, the Bi electrodes were tested for the CO_2RR (Chapter 6) and it was observed that:

- Bi modified electrodes were more catalytically active than bulk Bi electrodes, suggesting that the presence of the micro crystallites changed the number and the type of the active sites (objective 1.a)
- Both bulk Bi and Bi modified electrodes presented low total FE, suggesting the presence of an additional process during catalysis (probably the reduction of Bi_2O_3). However, bulk Bi presented maximum FE_{TOT}= 49%, while the Bi modified electrodes presented maximum FE_{TOT}= 68%. From this results it was possible to confirm that Bi modified are more stable than bulk Bi (objective 2).
- The presence of ILs did not increase the catalytic activity of the systems, as, when using Bi modified electrodes, comparable FE and currents were observed (objective 1.b)
- The in house produced IL did not show proton donor abilities (objective 1.b)

8.2 Future work

Based on the results obtained within this work, several aspects can be investigated further. The future work can be divided in three main areas of study/investigation: surface composition analyses; engineering of the catalytic surfaces and of the system; and mechanistic investigations.

1. **<u>Surface composition analyses.</u>**

   This would be applied for both bulk Bi and Bi modified electrodes and includes the investigation of the crystallographic composition (for example, using X-Ray Diffraction, XRD) and the chemical state composition (for example, using X-ray Photoelectron spectroscopy, XPS, or Raman spectroscopy). In particular, for the bulk Bi electrodes the analyses should be performed before and after potential cycling in different electrolytes, as a variation on the colour of the surface was observed. After cycling in $KHCO_3$ the surface became black, while in Na_2SO_4, a shiny yellow colour was observed. This is particularly important, as similar colours were observed after catalysis experiments, meaning that the Bi surface is indeed changing during the experiments and therefore different properties of the electrocatalysts are expected. Different composition of the surface will influence the catalytic response of the electrodes. Of particular interest is the adsorption of CO_2, its intermediates and the products of the reduction reaction. Similarly, analyses can be performed for the Bi modified electrodes. XPS studies were already performed before catalysis experiments for three types of Bi modified electrodes and the presence of the native oxide was confirmed. For this reason, the samples prepared for these

analyses need to be protected from the external environment (by storing in them in inert atmosphere, for instance), or performed immediately after the control potential electrolysis (CPE) experiments. Of particular interest, would be the *in-situ* composition analyses, as it would allow a deep understanding of the differences on the surface during electrolysis experiments. In addition, based on the literature finding, the best crystal facets of the bismuth crystallites for CO_2RR seems to be the 0 1 2, the 1 1 0 and the 1 0 4. Information on the crystal structure of the electrocatalysts might give additional information on the low catalytic activity of the bismuth electrodes produced within this work.

Investigation of the ability of CO_2 to be adsorbed on the Bi surface before and after (CPE) can be performed using Brunauer–Emmett–Teller (BET) analyses. Possible differences in the adsorption abilities of the surface before and after application of the negative potential can offer an insight on the stability of the electrocatalyst. In addition, as BET analyses can be performed using several molecules, with CO being one of those, it would be particularly interesting to obtain information on the adsorption of CO on the Bi surface. This would address two aspects: one, the higher formation of CO than formate on Bi cylinders (Chapter 5) and two, the possible passivation of the Bi surfaces by this product. Poisoning of the surface by CO has been observed for other electrodes[43,337].

2. <u>Engineering of the catalytic surfaces and of the system</u>

During the electrodeposition procedure and after catalysis experiments, low adhesion of the Bi microcrystals was observed. Even if electrodeposition of Bi has been extensively performed in carbonaceous substrates, it has been demonstrated that the employment of carbon substrates containing a high quantity of oxygen-carbon functionality resulted in a more uniform and robust film[150]. For this reason, treatment of glassy carbon electrodes (GCEs) with compounds (like chlorosulfonic acid) that can add these types of functionalities may improve the characteristics of the Bi films and its stability during catalysis.

Additional deposition studies can be performed by shortening the length of the electrodeposition steps. In this way, higher control of the rate of the nucleation and more compact films can be achieved. Further investigation of the effect of the overpotential on the characteristics of the final deposit could be also led to the refining of the electrodeposition technique. The investigation can be optimised by significantly decreasing the number of experiments performed. This can be achieved by using statistical methods such ANOVA that allows the investigation of the influence of a specific parameter (like the concentration of the precursor, the deposition potential and time) over the others.

Two-layer Bi-SPEs can be produced by printing the Bi M ink on only the working area. This would allow a low enough resistance for the electrodes to be tested. Further investigation can be performed for the CO_2RR with these types of electrodes as they represent a facile and low-cost alternative to the Bi electrode produced via electrodeposition.

Finally, of particular interest would be the scale up the reactor to build a CO_2 electrolyser using gas diffusion electrodes. This would allow the investigation of the ability of the system to reduce CO_2 in a larger scale, without the limitations given by the use of an aqueous-fed electrolyser (CO_2 is dissolved in water and a H-cell is used a reactor), such as the low concentration of CO_2 in the system and the mass diffusion issues. Using a carefully engineered reactor could significantly increase the rates of reduction of CO_2. However, it is important to highlight that even a excellently engineered reactor will not show a significant improvement in the catalytic performance if the characteristic of the electrode (such as his crystallographic and/or chemical composition) are not selective for CO_2RR.

3. Mechanistic investigations

Based on the composition analyses, the possible intermediates for the reaction and their absorption on the surface of the electrodes can be investigated using modelling techniques such as DFT analyses. Furthermore, studies on the rate-determining step and the kinetic order of CO_2RR by using current transients from catalysis and Tafel analyses can be obtained. In addition, considering the poor description of the solid-state diffusion for the oxidation of Bi_2O_3 and its reduction given by the Laviron method (Chapter 3) different modelling solutions should be attempted for the calculation of k^0.

Further investigation on the ability of the ionic liquid [1-CP-3-MIM]BF_4 to behave as an intramolecular proton donor would be interesting, using *in-situ* techniques, like infrared spectroscopy (specifically surface-enhanced infrared adsorption spectroscopy, SEIRAS) or Raman spectroscopy.

Summarising, bismuth is a promising material for the production of electrocatalysts for CO_2 reduction because of its low cost, low toxicity and its ability to supress the hydrogen evolution reaction. Green materials are essential for the production of the next generation of catalysts, and even more so for environmental applications. However, more investigation needs to be done to systematically engineering active and selective Bi electrodes. For this reason, in this work, efforts were made to try and investigate the outcome of Bi electrocatalysts with different

properties, especially in relation with the area of the surface of the electrodes. In the context of CO_2 reduction and, in particular, on the catalytic activity of Bi films, the results obtained within this work differ from those present in the literature as, generally, in laboratory scale, FEs approaching 100% are obtained with micro- and nanostructures in aqueous solutions. It is therefore clear that the electrode pre-treatment methods or longer electrolysis times need to be performed in order to obtain higher faradaic efficiencies and to enable the study of the kinetics of the reaction.

References

(1) Alvarez-Guerra, M.; Albo, J.; Alvarez-Guerra, E.; Irabien, A. Ionic Liquids in the Electrochemical Valorisation of CO $_2$. *Energy Env. Sci* **2015**, *8* (9), 2574–2599. https://doi.org/10.1039/C5EE01486G.

(2) Karl, T. R.; Trenberth, K. E. Modern Global Climate Change. *Science* **2003**, *302* (5651), 1719–1723. https://doi.org/10.1126/science.1090228.

(3) Zhong, W.; Haigh, J. D. The Greenhouse Effect and Carbon Dioxide. *Weather* **2013**, *68* (4), 100–105. https://doi.org/10.1002/wea.2072.

(4) Berger, A.; Tricot, C. The Greenhouse Effect. 27.

(5) Murugananthan, M.; Kaneco, S.; Katsumata, H.; Suzuki, T.; Kumaravel, M. Electrocatalytic Reduction of CO2 in Methanol Medium. In *Green Carbon Dioxide*; John Wiley & Sons, Ltd, 2014; pp 191–214. https://doi.org/10.1002/9781118831922.ch7.

(6) GMS: Carbon and Climate Briefing - November 12, 2015 https://svs.gsfc.nasa.gov/12044 (accessed 2019 -05 -27).

(7) Aresta, M.; Dibenedetto, A. Utilisation of CO2 as a Chemical Feedstock: Opportunities and Challenges. *Dalton Trans.* **2007**, No. 28, 2975–2992. https://doi.org/10.1039/B700658F.

(8) Canadell, J. G.; Le Quéré, C.; Raupach, M. R.; Field, C. B.; Buitenhuis, E. T.; Ciais, P.; Conway, T. J.; Gillett, N. P.; Houghton, R. A.; Marland, G. Contributions to Accelerating Atmospheric CO_2 Growth from Economic Activity, Carbon Intensity, and Efficiency of Natural Sinks. *Proc. Natl. Acad. Sci.* **2007**, *104* (47), 18866. https://doi.org/10.1073/pnas.0702737104.

(9) Change, N. G. C. Carbon Dioxide Concentration | NASA Global Climate Change https://climate.nasa.gov/vital-signs/carbon-dioxide (accessed 2019 -05 -27).

(10) User, S. CO2 Acceleration https://www.co2.earth/co2-acceleration (accessed 2019 -05 -27).

(11) Hughes, L. Biological Consequences of Global Warming: Is the Signal Already Apparent? *Trends Ecol. Evol.* **2000**, *15* (2), 56–61. https://doi.org/10.1016/S0169-5347(99)01764-4.

(12) Meehl, G. A.; Washington, W. M.; Collins, W. D.; Arblaster, J. M.; Hu, A.; Buja, L. E.; Strand, W. G.; Teng, H. How Much More Global Warming and Sea Level Rise? *Science* **2005**, *307* (5716), 1769–1772. https://doi.org/10.1126/science.1106663.

(13) Doney, S. C.; Fabry, V. J.; Feely, R. A.; Kleypas, J. A. Ocean Acidification: The Other CO2 Problem. *Annu. Rev. Mar. Sci.* **2009**, *1* (1), 169–192. https://doi.org/10.1146/annurev.marine.010908.163834.

(14) Masson-Delmotte; Zhai, V. P.; Pörtner, H.-O.; Roberts, D.; Skea, J.; Shukla, P. R.; Pirani, A.; Moufouma-Okia, W.; Péan, C.; Pidcock, R.; Connors, S.; Matthews, J. B. R.; Chen, Y.; Zhou, X.; Gomis, M. I.; Lonnoy, E.; Maycock; Tignor, M.; Waterfield, T. *IPCC, 2018: Summary for Policymakers*; Global Warming of 1.5°C. An IPCC Special Report on the impacts of global warming of 1.5°C above pre-industrial levels and related global greenhouse gas emission pathways, in the context of strengthening the global response to the threat of climate change, sustainable development, and efforts to eradicate poverty; World Meteorological Organization: Geneva, Switzerland; p 32.

(15) Masson-Delmotte, V.; Zhai, P.; Pörtner, H. O.; Roberts, D.; Skea, J.; Shukla, P. R.; Pirani, A.; Moufouma-Okia, W.; Péan, C.; Pidcock, R.; Connors, S.; Matthews, J. B. R.; Chen, Y.; Zhou, X.; Gomis, M. I.; Lonnoy, E.; Maycock, T.; Tignor, M.; Waterfield, T. *IPCC, 2018: Global Warming of 1.5°C. An IPCC Special Report on the Impacts of Global Warming of 1.5°C above Pre-Industrial Levels and Related Global Greenhouse Gas Emission Pathways, in the Context of Strengthening the Global Response to the Threat of Climate Change, Sustainable Development, and Efforts to Eradicate Poverty*; 2018.

(16) Strefler, J.; Bauer, N.; Kriegler, E.; Popp, A.; Giannousakis, A.; Edenhofer, O. Between Scylla and Charybdis: Delayed Mitigation Narrows the Passage between Large-Scale CDR

and High Costs. *Environ. Res. Lett.* **2018**, *13* (4), 044015. https://doi.org/10.1088/1748-9326/aab2ba.

(17) Figueroa, J. D.; Fout, T.; Plasynski, S.; McIlvried, H.; Srivastava, R. D. Advances in CO2 Capture Technology—The U.S. Department of Energy's Carbon Sequestration Program. *Int. J. Greenh. Gas Control* **2008**, *2* (1), 9–20. https://doi.org/10.1016/S1750-5836(07)00094-1.

(18) Yu, C.-H.; Huang, C.-H.; Tan, C.-S. A Review of CO2 Capture by Absorption and Adsorption. *Aerosol Air Qual. Res.* **2012**, *12* (5), 745–769. https://doi.org/10.4209/aaqr.2012.05.0132.

(19) Rochelle, G. T. Amine Scrubbing for CO2 Capture. *Science* **2009**, *325* (5948), 1652–1654. https://doi.org/10.1126/science.1176731.

(20) Luis, P. Use of Monoethanolamine (MEA) for CO2 Capture in a Global Scenario: Consequences and Alternatives. *Desalination* **2016**, *380*, 93–99. https://doi.org/10.1016/j.desal.2015.08.004.

(21) Brennecke, J. F.; Gurkan, B. E. Ionic Liquids for CO2 Capture and Emission Reduction. *J. Phys. Chem. Lett.* **2010**, *1* (24), 3459–3464. https://doi.org/10.1021/jz1014828.

(22) Koytsoumpa, E. I.; Bergins, C.; Kakaras, E. The CO2 Economy: Review of CO2 Capture and Reuse Technologies. *J. Supercrit. Fluids* **2018**, *132*, 3–16. https://doi.org/10.1016/j.supflu.2017.07.029.

(23) Blanchard, L. A.; Hancu, D.; Beckman, E. J.; Brennecke, J. F. Green Processing Using Ionic Liquids and CO 2. *Nature* **1999**, *399* (6731), 28. https://doi.org/10.1038/19887.

(24) Zhao, S.-F.; Horne, M.; Bond, A. M.; Zhang, J. Is the Imidazolium Cation a Unique Promoter for Electrocatalytic Reduction of Carbon Dioxide? *J. Phys. Chem. C* **2016**, *120* (42), 23989–24001. https://doi.org/10.1021/acs.jpcc.6b08182.

(25) Lau, G. P. S.; Schreier, M.; Vasilyev, D.; Scopelliti, R.; Grätzel, M.; Dyson, P. J. New Insights Into the Role of Imidazolium-Based Promoters for the Electroreduction of CO2 on a Silver Electrode. *J. Am. Chem. Soc.* **2016**, *138* (25), 7820–7823. https://doi.org/10.1021/jacs.6b03366.

(26) Faggion, D. J.; Gonçalves, W. D. G.; Dupont, J. CO2 Electroreduction in Ionic Liquids. *Front. Chem.* **2019**, *7*. https://doi.org/10.3389/fchem.2019.00102.

(27) Rafiee, A.; Rajab Khalilpour, K.; Milani, D.; Panahi, M. Trends in CO2 Conversion and Utilization: A Review from Process Systems Perspective. *J. Environ. Chem. Eng.* **2018**, *6* (5), 5771–5794. https://doi.org/10.1016/j.jece.2018.08.065.

(28) Muradov, N. Industrial Utilization of CO2: A Win–Win Solution. In *Liberating Energy from Carbon: Introduction to Decarbonization*; Muradov, N., Ed.; Lecture Notes in Energy; Springer New York: New York, NY, 2014; pp 325–383. https://doi.org/10.1007/978-1-4939-0545-4_9.

(29) KRASE, N. W.; GADDY, V. L. Synthesis of Urea from Ammonia and Carbon Dioxide. *J. Ind. Eng. Chem.* **1922**, *14* (7), 611–615. https://doi.org/10.1021/ie50151a009.

(30) Garcia-Herrero, I.; Cuéllar-Franca, R. M.; Enríquez-Gutiérrez, V. M.; Alvarez-Guerra, M.; Irabien, A.; Azapagic, A. Environmental Assessment of Dimethyl Carbonate Production: Comparison of a Novel Electrosynthesis Route Utilizing CO2 with a Commercial Oxidative Carbonylation Process. *ACS Sustain. Chem. Eng.* **2016**, *4* (4), 2088–2097. https://doi.org/10.1021/acssuschemeng.5b01515.

(31) Olah, G. A.; Goeppert, A.; Prakash, G. K. S. Chemical Recycling of Carbon Dioxide to Methanol and Dimethyl Ether: From Greenhouse Gas to Renewable, Environmentally Carbon Neutral Fuels and Synthetic Hydrocarbons. *J. Org. Chem.* **2009**, *74* (2), 487–498. https://doi.org/10.1021/jo801260f.

(32) Langanke, J.; Wolf, A.; Hofmann, J.; Böhm, K.; Subhani, M. A.; Müller, T. E.; Leitner, W.; Gürtler, C. Carbon Dioxide (CO2) as Sustainable Feedstock for Polyurethane Production. *Green Chem.* **2014**, *16* (4), 1865–1870. https://doi.org/10.1039/C3GC41788C.

(33) Zhan, Z.; Kobsiriphat, W.; Wilson, J. R.; Pillai, M.; Kim, I.; Barnett, S. A. Syngas Production By Coelectrolysis of CO2/H2O: The Basis for a Renewable Energy Cycle. *Energy Fuels* **2009**, *23* (6), 3089–3096. https://doi.org/10.1021/ef900111f.

(34) Li, W.; Wang, H.; Shi, Y.; Cai, N. Performance and Methane Production Characteristics of H2O–CO2 Co-Electrolysis in Solid Oxide Electrolysis Cells. *Int. J. Hydrog. Energy* **2013**, *38* (25), 11104–11109. https://doi.org/10.1016/j.ijhydene.2013.01.008.

(35) James, O. O.; Mesubi, A. M.; Ako, T. C.; Maity, S. Increasing Carbon Utilization in Fischer–Tropsch Synthesis Using H2-Deficient or CO2-Rich Syngas Feeds. *Fuel Process. Technol.* **2010**, *91* (2), 136–144. https://doi.org/10.1016/j.fuproc.2009.09.017.

(36) SciencesRoundtable, N. R. C. (US) C. *Carbon Dioxide as a Feedstock*; National Academies Press (US), 2001.

(37) Lu, Q.; Jiao, F. Electrochemical CO2 Reduction: Electrocatalyst, Reaction Mechanism, and Process Engineering. *Nano Energy* **2016**, *29*, 439–456. https://doi.org/10.1016/j.nanoen.2016.04.009.

(38) Mikkelsen, M.; Jørgensen, M.; Krebs, F. C. The Teraton Challenge. A Review of Fixation and Transformation of Carbon Dioxide. *Energy Environ. Sci.* **2010**, *3* (1), 43–81. https://doi.org/10.1039/B912904A.

(39) Roy, S.; Cherevotan, A.; Peter, S. C. Thermochemical CO2 Hydrogenation to Single Carbon Products: Scientific and Technological Challenges. *ACS Energy Lett.* **2018**, *3* (8), 1938–1966. https://doi.org/10.1021/acsenergylett.8b00740.

(40) Appel, A. M.; Bercaw, J. E.; Bocarsly, A. B.; Dobbek, H.; DuBois, D. L.; Dupuis, M.; Ferry, J. G.; Fujita, E.; Hille, R.; Kenis, P. J. A.; Kerfeld, C. A.; Morris, R. H.; Peden, C. H. F.; Portis, A. R.; Ragsdale, S. W.; Rauchfuss, T. B.; Reek, J. N. H.; Seefeldt, L. C.; Thauer, R. K.; Waldrop, G. L. Frontiers, Opportunities, and Challenges in Biochemical and Chemical Catalysis of CO2 Fixation. *Chem. Rev.* **2013**, *113* (8), 6621–6658. https://doi.org/10.1021/cr300463y.

(41) Whipple, D. T.; Kenis, P. J. A. Prospects of CO2 Utilization via Direct Heterogeneous Electrochemical Reduction. *J. Phys. Chem. Lett.* **2010**, *1* (24), 3451–3458. https://doi.org/10.1021/jz1012627.

(42) Kumar, B.; Llorente, M.; Froehlich, J.; Dang, T.; Sathrum, A.; Kubiak, C. P. Photochemical and Photoelectrochemical Reduction of CO2. *Annu. Rev. Phys. Chem.* **2012**, *63* (1), 541–569. https://doi.org/10.1146/annurev-physchem-032511-143759.

(43) Hori, Y. Electrochemical CO2 Reduction on Metal Electrodes. In *Modern Aspects of Electrochemistry*; Vayenas, C. G., White, R. E., Gamboa-Aldeco, M. E., Eds.; Modern Aspects of Electrochemistry; Springer New York: New York, NY, 2008; pp 89–189. https://doi.org/10.1007/978-0-387-49489-0_3.

(44) Schneider, J.; Jia, H.; T. Muckerman, J.; Fujita, E. Thermodynamics and Kinetics of CO2 , CO , and H+ Binding to the Metal Centre of CO2 Reduction Catalysts. *Chem. Soc. Rev.* **2012**, *41* (6), 2036–2051. https://doi.org/10.1039/C1CS15278E.

(45) Bard, A. J.; Faulkner. *Electrochemical Methods: Fundamentals and Applications*, 2nd ed.; John Wiley & Sons: Hoboken, NJ, 2001; p .

(46) Kotrel, S.; Bräuninger, S. Industrial Electrocatalysis. In *Handbook of Heterogeneous Catalysis*; American Cancer Society, 2008; pp 1936–1958. https://doi.org/10.1002/9783527610044.hetcat0103.

(47) Inamuddin; Boddula, R.; Asiri, A. M. *Methods for Electrocatalysis: Advanced Materials and Allied Applications*; Springer Nature, 2020.

(48) Pollok, D.; R. Waldvogel, S. Electro-Organic Synthesis – a 21 St Century Technique. *Chem. Sci.* **2020**, *11* (46), 12386–12400. https://doi.org/10.1039/D0SC01848A.

(49) Karthik, P. E.; Alessandri, I.; Sengeni, A. Review—A Review on Electrodes Used in Electroorganic Synthesis and the Significance of Coupled Electrocatalytic Reactions. *J. Electrochem. Soc.* **2020**, *167* (12), 125503. https://doi.org/10.1149/1945-7111/abb0f2.

(50) Ibl, N.; Vogt, H. Inorganic Electrosynthesis. In *Comprehensive Treatise of Electrochemistry: Electrochemical Processing*; Bockris, J. O., Conway, B. E., Yeager, E., White, R. E., Eds.; Comprehensive Treatise of Electrochemistry; Springer US: Boston, MA, 1981; pp 167–250. https://doi.org/10.1007/978-1-4684-3785-0_3.
(51) Hämäläinen, J.; Ritala, M.; Leskelä, M. Atomic Layer Deposition of Noble Metals and Their Oxides. *Chem. Mater.* **2014**, *26* (1), 786–801. https://doi.org/10.1021/cm402221y.
(52) Yuan, N.; Jiang, Q.; Li, J.; Tang, J. A Review on Non-Noble Metal Based Electrocatalysis for the Oxygen Evolution Reaction. *Arab. J. Chem.* **2020**, *13* (2), 4294–4309. https://doi.org/10.1016/j.arabjc.2019.08.006.
(53) Yan, Y.; Yu Xia, B.; Zhao, B.; Wang, X. A Review on Noble-Metal-Free Bifunctional Heterogeneous Catalysts for Overall Electrochemical Water Splitting. *J. Mater. Chem. A* **2016**, *4* (45), 17587–17603. https://doi.org/10.1039/C6TA08075H.
(54) Mistry, H.; Varela, A. S.; Kühl, S.; Strasser, P.; Cuenya, B. R. Nanostructured Electrocatalysts with Tunable Activity and Selectivity. *Nat. Rev. Mater.* **2016**, *1* (4), 1–14. https://doi.org/10.1038/natrevmats.2016.9.
(55) Burke, L. D.; Murphy, M. M. The Electrocatalytic Behavior of Cobalt (and Iron) Electrodes at Low Potential in Base. *J. Electrochem. Soc.* **1991**, *138* (1), 88. https://doi.org/10.1149/1.2085584.
(56) Cossar, E.; Oyarce Barnett, A.; Seland, F.; Baranova, E. A. The Performance of Nickel and Nickel-Iron Catalysts Evaluated As Anodes in Anion Exchange Membrane Water Electrolysis. *Catalysts* **2019**, *9* (10), 814. https://doi.org/10.3390/catal9100814.
(57) Zhao, J.; Xue, S.; Barber, J.; Zhou, Y.; Meng, J.; Ke, X. An Overview of Cu-Based Heterogeneous Electrocatalysts for CO2 Reduction. *J. Mater. Chem. A* **2020**, *8* (9), 4700–4734. https://doi.org/10.1039/C9TA11778D.
(58) Alonso-Vante, N.; Feng, Y.; Yang, H. Novel Non-Precious Metal Electrocatalysts for Oxygen Electrode Reactions. *Catalysts* **2019**, *9* (9), 731. https://doi.org/10.3390/catal9090731.
(59) Pauliukaitė, R.; Hočevar, S. B.; Ogorevc, B.; Wang, J. Characterization and Applications of a Bismuth Bulk Electrode. *Electroanalysis* **2004**, *16* (9), 719–723. https://doi.org/10.1002/elan.200302783.
(60) Napporn, T.; Holade, Y. *Metal Oxide-Based Nanostructured Electrocatalysts for Fuel Cells, Electrolyzers, and Metal-Air Batteries*; Elsevier, 2021.
(61) Rennie, R. R.; Law, J. L. Bismuth. In *A Dictionary of Chemistry*; Rennie, R., Law, J., Eds.; Oxford University Press, 2016.
(62) Smith, J. D. 1 - THE ELEMENTS. In *The Chemistry of Arsenic, Antimony and Bismuth*; Smith, J. D., Ed.; Pergamon Texts in Inorganic Chemistry; Pergamon, 1973; pp 547–558. https://doi.org/10.1016/B978-0-08-018778-5.50006-4.
(63) Chapter 1 - Introduction. In *Organobismuth Chemistry*; Suzuki, H., Matano, Y., Eds.; Elsevier Science: Amsterdam, 2001; pp 1–20. https://doi.org/10.1016/B978-044420528-5/50003-3.
(64) Rajamani, A. R.; Ragula, U. B. R.; Kothurkar, N.; Rangarajan, M. Nano- and Micro-Hexagons of Bismuth on Polycrystalline Copper: Electrodeposition and Heavy Metal Sensing. *CrystEngComm* **2014**, *16* (10), 2032–2038. https://doi.org/10.1039/C3CE41686K.
(65) Verni, G. A.; Long, B.; Gity, F.; Lanius, M.; Schüffelgen, P.; Mussler, G.; Grützmacher, D.; Greer, J.; D. Holmes, J. Oxide Removal and Stabilization of Bismuth Thin Films through Chemically Bound Thiol Layers. *RSC Adv.* **2018**, *8* (58), 33368–33373. https://doi.org/10.1039/C8RA06840B.
(66) Švancara, I.; Prior, C.; Hočevar, S. B.; Wang, J. A Decade with Bismuth-Based Electrodes in Electroanalysis. *Electroanalysis* **2010**, *22* (13), 1405–1420. https://doi.org/10.1002/elan.200970017.
(67) DiPalma, J. R. Bismuth Toxicity, Often Mild, Can Result in Severe Poisonings. *Emerg. Med. News* **2001**, *23* (3), 16.

(68) Miller, N. C.; Bernechea, M. Research Update: Bismuth Based Materials for Photovoltaics. *APL Mater.* **2018**, *6* (8), 084503. https://doi.org/10.1063/1.5026541.
(69) Wang, J.; Lu, J.; Hocevar, S. B.; Farias, P. A. M.; Ogorevc, B. Bismuth-Coated Carbon Electrodes for Anodic Stripping Voltammetry. *Anal. Chem.* **2000**, *72* (14), 3218–3222. https://doi.org/10.1021/ac000108x.
(70) Barón-Jaimez, J. A.; Marulanda-Arévalo, J. L.; Barba-Ortega, J. J. Electrodes Friendly with the Environment for Detect Heavy Metal. *DYNA* **2014**, *81* (187), 122–128. https://doi.org/10.15446/dyna.v81n186.40758.
(71) Wang, J. Stripping Analysis at Bismuth Electrodes: A Review. *Electroanalysis* **2005**, *17* (15–16), 1341–1346. https://doi.org/10.1002/elan.200403270.
(72) Alberich, A.; Serrano, N.; Díaz-Cruz, J. M.; Ariño, C.; Esteban, M. Substitution of Mercury Electrodes by Bismuth-Coated Screen-Printed Electrodes in the Determination of Quinine in Tonic Water. *J. Chem. Educ.* **2013**, *90* (12), 1681–1684. https://doi.org/10.1021/ed400288a.
(73) Sosa, V.; Serrano, N.; Ariño, C.; Díaz-Cruz, J. M.; Esteban, M. Voltammetric Determination of Pb(II) and Cd(II) Ions in Well Water Using a Sputtered Bismuth Screen-Printed Electrode. *Electroanalysis* **2014**, *26* (10), 2168–2172. https://doi.org/10.1002/elan.201400319.
(74) Ghazali, N. N.; Mohamad Nor, N.; Abdul Razak, K.; Lockman, Z.; Hattori, T. Hydrothermal Synthesis of Bismuth Nanosheets for Modified APTES-Functionalized Screen-Printed Carbon Electrode in Lead and Cadmium Detection. *J. Nanoparticle Res.* **2020**, *22* (7), 211. https://doi.org/10.1007/s11051-020-04946-z.
(75) Domańska, K.; Tyszczuk-Rotko, K. Integrated Three-Electrode Screen-Printed Sensor Modified with Bismuth Film for Voltammetric Determination of Thallium(I) at the Ultratrace Level. *Anal. Chim. Acta* **2018**, *1036*, 16–25. https://doi.org/10.1016/j.aca.2018.06.078.
(76) Rojas-Romo, C.; Aliaga, M. E.; Arancibia, V. Determination of Molybdenum(VI) via Adsorptive Stripping Voltammetry Using an Ex–situ Bismuth Screen–printed Carbon Electrode. *Microchem. J.* **2020**, *154*, 104589. https://doi.org/10.1016/j.microc.2019.104589.
(77) Korolczuk, M.; Rutyna, I.; Tyszczuk, K. Adsorptive Stripping Voltammetry of Nickel at an In Situ Plated Bismuth Film Electrode. *Electroanalysis* **2010**, *22* (13), 1494–1498. https://doi.org/10.1002/elan.200970011.
(78) Dal Borgo, S.; Sopha, H.; Smarzewska, S.; Hočevar, S. B.; Švancara, I.; Metelka, R. Macroporous Bismuth Film Screen-Printed Carbon Electrode for Simultaneous Determination of Ni(II) and Co(II). *Electroanalysis* **2015**, *27* (1), 209–216. https://doi.org/10.1002/elan.201400422.
(79) Khairy, M.; Kadara, R. O.; Kampouris, D. K.; Banks, C. E. Disposable Bismuth Oxide Screen Printed Electrodes for the Sensing of Zinc in Seawater. *Electroanalysis* **2010**, *22* (13), 1455–1459. https://doi.org/10.1002/elan.200900519.
(80) Bi, Z.; Chapman, C. S.; Salaün, P.; Berg, C. M. G. van den. Determination of Lead and Cadmium in Sea- and Freshwater by Anodic Stripping Voltammetry with a Vibrating Bismuth Electrode. *Electroanalysis* **2010**, *22* (24), 2897–2907. https://doi.org/10.1002/elan.201000429.
(81) Kadara, R. O.; Tothill, I. E. Development of Disposable Bulk-Modified Screen-Printed Electrode Based on Bismuth Oxide for Stripping Chronopotentiometric Analysis of Lead (II) and Cadmium (II) in Soil and Water Samples. *Anal. Chim. Acta* **2008**, *623* (1), 76–81. https://doi.org/10.1016/j.aca.2008.06.010.
(82) Jothimuthu, P.; Wilson, R. A.; Herren, J.; Pei, X.; Kang, W.; Daniels, R.; Wong, H.; Beyette, F.; Heineman, W. R.; Papautsky, I. Zinc Detection in Serum by Anodic Stripping

Voltammetry on Microfabricated Bismuth Electrodes. *Electroanalysis* **2013**, *25* (2), 401–407. https://doi.org/10.1002/elan.201200530.

(83) Injang, U.; Noyrod, P.; Siangproh, W.; Dungchai, W.; Motomizu, S.; Chailapakul, O. Determination of Trace Heavy Metals in Herbs by Sequential Injection Analysis-Anodic Stripping Voltammetry Using Screen-Printed Carbon Nanotubes Electrodes. *Anal. Chim. Acta* **2010**, *668* (1), 54–60. https://doi.org/10.1016/j.aca.2010.01.018.

(84) Mandil, A.; Amine, A. Screen-Printed Electrodes Modified by Bismuth Film for the Determination of Released Lead in Moroccan Ceramics. *Anal. Lett.* **2009**, *42* (9), 1245–1257. https://doi.org/10.1080/00032710902901772.

(85) Xu, H.; Zeng, L.; Huang, D.; Xian, Y.; Jin, L. A Nafion-Coated Bismuth Film Electrode for the Determination of Heavy Metals in Vegetable Using Differential Pulse Anodic Stripping Voltammetry: An Alternative to Mercury-Based Electrodes. *Food Chem.* **2008**, *109* (4), 834–839. https://doi.org/10.1016/j.foodchem.2007.12.065.

(86) Riman, D.; Avgeropoulos, A.; Hrbac, J.; Prodromidis, M. I. Sparked-Bismuth Oxide Screen-Printed Electrodes for the Determination of Riboflavin in the Sub-Nanomolar Range in Non-Deoxygenated Solutions. *Electrochimica Acta* **2015**, *165*, 410–415. https://doi.org/10.1016/j.electacta.2015.03.056.

(87) Lezi, N.; Economou, A. Voltammetric Determination of Neonicotinoid Pesticides at Disposable Screen-Printed Sensors Featuring a Sputtered Bismuth Electrode. *Electroanalysis* **2015**, *27* (10), 2313–2321. https://doi.org/10.1002/elan.201500127.

(88) Merkoçi, A.; Anik, U.; Çevik, S.; Çubukçu, M.; Guix, M. Bismuth Film Combined with Screen-Printed Electrode as Biosensing Platform for Phenol Detection. *Electroanalysis* **2010**, *22* (13), 1429–1436. https://doi.org/10.1002/elan.200970002.

(89) Lezi, N.; Economou, A.; Barek, J.; Prodromidis, M. Screen-Printed Disposable Sensors Modified with Bismuth Precursors for Rapid Voltammetric Determination of 3 Ecotoxic Nitrophenols. *Electroanalysis* **2014**, *26* (4), 766–775. https://doi.org/10.1002/elan.201400001.

(90) María-Hormigos, R.; Gismera, M. J.; Sevilla, M. T.; Rumbero, Á.; Procopio, J. R. Rapid and Easy Detection of Deoxynivalenol on a Bismuth Oxide Screen-Printed Electrode. *Electroanalysis* **2017**, *29* (1), 60–66. https://doi.org/10.1002/elan.201600484.

(91) Narumoto, N.; Okamoto, N.; Saito, T. Surface Structure Control and Charge/Discharge Characteristics of Bismuth Anode Materials by Electrodeposition for Magnesium-Ion Batteries. *J. Mater. Sci. Mater. Electron.* **2021**. https://doi.org/10.1007/s10854-021-05656-5.

(92) Shao, Y.; Gu, M.; Li, X.; Nie, Z.; Zuo, P.; Li, G.; Liu, T.; Xiao, J.; Cheng, Y.; Wang, C.; Zhang, J.-G.; Liu, J. Highly Reversible Mg Insertion in Nanostructured Bi for Mg Ion Batteries. *Nano Lett.* **2014**, *14* (1), 255–260. https://doi.org/10.1021/nl403874y.

(93) Benmayza, A.; Ramanathan, M.; Singh, N.; Mizuno, F.; Prakash, J. Electrochemical and Thermal Studies of Bismuth Electrodes for Magnesium-Ion Cells. *J. Electrochem. Soc.* **2015**, *162* (8), A1630. https://doi.org/10.1149/2.0841508jes.

(94) Zheng, F.-L.; Li, G.-R.; Ou, Y.-N.; Wang, Z.-L.; Su, C.-Y.; Tong, Y.-X. Synthesis of Hierarchical Rippled Bi2O3 Nanobelts for Supercapacitor Applications. *Chem. Commun.* **2010**, *46* (27), 5021–5023. https://doi.org/10.1039/C002126A.

(95) Qu, D.; Wang, L.; Zheng, D.; Xiao, L.; Deng, B.; Qu, D. An Asymmetric Supercapacitor with Highly Dispersed Nano-Bi2O3 and Active Carbon Electrodes. *J. Power Sources* **2014**, *269*, 129–135. https://doi.org/10.1016/j.jpowsour.2014.06.084.

(96) Qiu, Y.; Fan, H.; Chang, X.; Dang, H.; Luo, Q.; Cheng, Z. Novel Ultrathin Bi2O3 Nanowires for Supercapacitor Electrode Materials with High Performance. *Appl. Surf. Sci.* **2018**, *434*, 16–20. https://doi.org/10.1016/j.apsusc.2017.10.171.

(97) Yang, S.; Qian, L.; Ping, Y.; Zhang, H.; Li, J.; Xiong, B.; Fang, P.; He, C. Electrochemical Performance of Bi2O3 Supercapacitors Improved by Surface Vacancy Defects. *Ceram. Int.* **2021**, *47* (6), 8290–8299. https://doi.org/10.1016/j.ceramint.2020.11.190.

(98) Qin, T.; Wang, D.; Zhang, X.; Wang, Y.; Drewett, N. E.; Zhang, W.; Dong, T.; Li, T.; Wang, Z.; Deng, T.; Pan, Z.; Yue, N.; Yang, R.; Huang, K.; Feng, S.; Huang, R.; Zheng, W. Unlocking the Optimal Aqueous δ-Bi2O3 Anode via Unifying Octahedrally Liberated Bi-Atoms and Spilled Nano-Bi Exsolution. *Energy Storage Mater.* **2021**, *36*, 376–386. https://doi.org/10.1016/j.ensm.2021.01.013.

(99) Zhang, X.; Hou, X.; Zhang, Q.; Cai, Y.; Liu, Y.; Qiao, J. Polyethylene Glycol Induced Reconstructing Bi Nanoparticle Size for Stabilized CO2 Electroreduction to Formate. *J. Catal.* **2018**, *365*, 63–70. https://doi.org/10.1016/j.jcat.2018.06.019.

(100) Zhang, W.; Hu, Y.; Ma, L.; Zhu, G.; Zhao, P.; Xue, X.; Chen, R.; Yang, S.; Ma, J.; Liu, J.; Jin, Z. Liquid-Phase Exfoliated Ultrathin Bi Nanosheets: Uncovering the Origins of Enhanced Electrocatalytic CO2 Reduction on Two-Dimensional Metal Nanostructure. *Nano Energy* **2018**, *53*, 808–816. https://doi.org/10.1016/j.nanoen.2018.09.053.

(101) Koh, J. H.; Won, D. H.; Eom, T.; Kim, N.-K.; Jung, K. D.; Kim, H.; Hwang, Y. J.; Min, B. K. Facile CO2 Electro-Reduction to Formate via Oxygen Bidentate Intermediate Stabilized by High-Index Planes of Bi Dendrite Catalyst. *ACS Catal.* **2017**, *7* (8), 5071–5077. https://doi.org/10.1021/acscatal.7b00707.

(102) Kim, S.; Dong, W. J.; Gim, S.; Sohn, W.; Park, J. Y.; Yoo, C. J.; Jang, H. W.; Lee, J.-L. Shape-Controlled Bismuth Nanoflakes as Highly Selective Catalysts for Electrochemical Carbon Dioxide Reduction to Formate. *Nano Energy* **2017**, *39*, 44–52. https://doi.org/10.1016/j.nanoen.2017.05.065.

(103) Pander, J. E.; Baruch, M. F.; Bocarsly, A. B. Probing the Mechanism of Aqueous CO2 Reduction on Post-Transition-Metal Electrodes Using ATR-IR Spectroelectrochemistry. *ACS Catal.* **2016**, *6* (11), 7824–7833. https://doi.org/10.1021/acscatal.6b01879.

(104) Hara, K.; Kudo, A.; Sakata, T. Electrochemical Reduction of Carbon Dioxide under High Pressure on Various Electrodes in an Aqueous Electrolyte. *J. Electroanal. Chem.* **1995**, *391* (1), 141–147. https://doi.org/10.1016/0022-0728(95)03935-A.

(105) Yang, F.; Elnabawy, A. O.; Schimmenti, R.; Song, P.; Wang, J.; Peng, Z.; Yao, S.; Deng, R.; Song, S.; Lin, Y.; Mavrikakis, M.; Xu, W. Bismuthene for Highly Efficient Carbon Dioxide Electroreduction Reaction. *Nat. Commun.* **2020**, *11* (1), 1088. https://doi.org/10.1038/s41467-020-14914-9.

(106) Dutta, A.; Zelocualtecatl Montiel, I.; Kiran, K.; Rieder, A.; Grozovski, V.; Gut, L.; Broekmann, P. A Tandem (Bi2O3 → Bimet) Catalyst for Highly Efficient Ec-CO2 Conversion into Formate: Operando Raman Spectroscopic Evidence for a Reaction Pathway Change. *ACS Catal.* **2021**, 4988–5003. https://doi.org/10.1021/acscatal.0c05317.

(107) Yu, M.; Feng, X. Thin-Film Electrode-Based Supercapacitors. *Joule* **2019**, *3* (2), 338–360. https://doi.org/10.1016/j.joule.2018.12.012.

(108) Moral-Vico, J.; Casañ-Pastor, N.; Camón, A.; Pobes, C.; Jáudenes, R. M.; Strichovanec, P.; Fàbrega, L. Microstructure and Electrical Transport in Electrodeposited Bi Films. *J. Electroanal. Chem.* **2019**, *832*, 40–47. https://doi.org/10.1016/j.jelechem.2018.10.041.

(109) Hsu, J.-H.; Sun, Y.-S.; Wang, H.-X.; Kuo, P. C.; Hsieh, T.-H.; Liang, C.-T. Substrate Dependence of Large Ordinary Magnetoresistance in Sputtered Bi Films. *J. Magn. Magn. Mater.* **2004**, *272–276*, 1769–1771. https://doi.org/10.1016/j.jmmm.2003.12.743.

(110) Baron, J.; Silva-Bermudez, P.; Rodil, S. E. Sputtered Bismuth Thin Films as Trace Metal Electrochemical Sensors. *MRS Online Proc. Libr.* **2012**, *1477* (1), 40–51. https://doi.org/10.1557/opl.2012.1722.

(111) Yan, D. (闫代康); Divan, R.; Gades, L. M.; Kenesei, P.; Madden, T. J.; Miceli, A.; Park, J.-S.; Patel, U. M.; Quaranta, O.; Sharma, H.; Bennett, D. A.; Doriese, W. B.; Fowler, J. W.; Gard, J. D.; Hays-Wehle, J. P.; Morgan, K. M.; Schmidt, D. R.; Swetz, D. S.; Ullom, J. N.

Eliminating the Non-Gaussian Spectral Response of X-Ray Absorbers for Transition-Edge Sensors. *Appl. Phys. Lett.* **2017**, *111* (19), 192602. https://doi.org/10.1063/1.5001198.
(112) Du, X.; Hebard, A. F. Large Magnetoresistance of Bismuth/Gold Films Thermally Deposited onto Glass Substrates. *Appl. Phys. Lett.* **2003**, *82* (14), 2293–2295. https://doi.org/10.1063/1.1566461.
(113) Agapescu, C.; Cojocaru, A.; Cotarta, A.; Visan, T. Electrodeposition of Bismuth, Tellurium, and Bismuth Telluride Thin Films from Choline Chloride–Oxalic Acid Ionic Liquid. *J. Appl. Electrochem.* **2013**, *43* (3), 309–321. https://doi.org/10.1007/s10800-012-0487-0.
(114) Jiang, S.; Huang, Y.-H.; Luo, F.; Du, N.; Yan, C.-H. Synthesis of Bismuth with Various Morphologies by Electrodeposition. *Inorg. Chem. Commun.* **2003**, *6* (6), 781–785. https://doi.org/10.1016/S1387-7003(03)00104-7.
(115) Yang, M.; Hu, Z. Electrodeposition of Bismuth onto Glassy Carbon Electrodes from Nitrate Solutions. *J. Electroanal. Chem.* **2005**, *583* (1), 46–55. https://doi.org/10.1016/j.jelechem.2005.04.019.
(116) Basile, F.; Benito, P.; Fornasari, G.; Monti, M.; Scavetta, E.; Tonelli, D.; Vaccari, A. A Novel Electrochemical Route for the Catalytic Coating of Metallic Supports. In *Studies in Surface Science and Catalysis*; Gaigneaux, E. M., Devillers, M., Hermans, S., Jacobs, P. A., Martens, J. A., Ruiz, P., Eds.; Scientific Bases for the Preparation of Heterogeneous Catalysts; Elsevier, 2010; Vol. 175, pp 51–58. https://doi.org/10.1016/S0167-2991(10)75007-2.
(117) Gamburg, Y. D.; Zangari, G. Introduction to Electrodeposition: Basic Terms and Fundamental Concepts. In *Theory and Practice of Metal Electrodeposition*; Gamburg, Y. D., Zangari, G., Eds.; Springer: New York, NY, 2011; pp 1–25. https://doi.org/10.1007/978-1-4419-9669-5_1.
(118) Overview. In *Fundamentals of Electrochemical Deposition*; John Wiley & Sons, Ltd, 2006; pp 1–6. https://doi.org/10.1002/0470009403.ch1.
(119) Yang, M. Fern-Shaped Bismuth Dendrites Electrodeposited at Hydrogen Evolution Potentials. *J. Mater. Chem.* **2011**, *21* (9), 3119–3124. https://doi.org/10.1039/C0JM03213A.
(120) Xiao, Z.-L.; Han, C. Y.; Kwok, W.-K.; Wang, H.-H.; Welp, U.; Wang, J.; Crabtree, G. W. Tuning the Architecture of Mesostructures by Electrodeposition. *J. Am. Chem. Soc.* **2004**, *126* (8), 2316–2317. https://doi.org/10.1021/ja0315154.
(121) Zhu, D.; Lei, W. N.; Qu, N. S.; Xu, H. Y. Nanocrystaline Electroforming Process. *CIRP Ann.* **2002**, *51* (1), 173–176. https://doi.org/10.1016/S0007-8506(07)61493-0.
(122) Tatiparti, S. S. V.; Ebrahimi, F. Potentiostatic versus Galvanostatic Electrodeposition of Nanocrystalline Al–Mg Alloy Powders. *J. Solid State Electrochem.* **2012**, *16* (3), 1255–1262. https://doi.org/10.1007/s10008-011-1522-5.
(123) Eskhult, J.; Nyholm, L. Pulsed Galvanostatic and Potentiostatic Electrodeposition of Cu and Cu2O Nanolayers from Alkaline Cu(II)-Citrate Solutions. *J. Electrochem. Soc.* **2007**, *155* (2), D115. https://doi.org/10.1149/1.2806793.
(124) Vázquez, M. *Magnetic Nano- and Microwires: Design, Synthesis, Properties and Applications*; Woodhead Publishing, 2015.
(125) Kumar, S.; Pande, S.; Verma, P. Factor Effecting Electro-Deposition Process. *undefined* **2015**.
(126) Ritzdorf, T. Monitoring and Control. In *Modern Electroplating*; John Wiley & Sons, Ltd, 2010; pp 527–554. https://doi.org/10.1002/9780470602638.ch25.
(127) Ebrahimi, F.; Ahmed, Z. The Effect of Current Density on Properties of Electrodeposited Nanocrystalline Nickel. *J. Appl. Electrochem.* **2003**, *33* (8), 733–739. https://doi.org/10.1023/A:1025049802635.
(128) Abdel-Karim, R. Electrochemical Synthesis of Nanocomposites. *Electrodepos. Compos. Mater.* **2016**. https://doi.org/10.5772/62189.

(129) Moravej, M.; Amira, S.; Prima, F.; Rahem, A.; Fiset, M.; Mantovani, D. Effect of Electrodeposition Current Density on the Microstructure and the Degradation of Electroformed Iron for Degradable Stents. *Mater. Sci. Eng. B* **2011**, *176* (20), 1812–1822. https://doi.org/10.1016/j.mseb.2011.02.031.

(130) Sharma, A.; Bhattacharya, S.; Das, S.; Das, K. A Study on the Effect of Pulse Electrodeposition Parameters on the Morphology of Pure Tin Coatings. *Metall. Mater. Trans. A* **2014**, *45* (10), 4610–4622. https://doi.org/10.1007/s11661-014-2389-8.

(131) Nikolić, N. D.; Popov, K. I.; Pavlović, Lj. J.; Pavlović, M. G. Morphologies of Copper Deposits Obtained by the Electrodeposition at High Overpotentials. *Surf. Coat. Technol.* **2006**, *201* (3), 560–566. https://doi.org/10.1016/j.surfcoat.2005.12.004.

(132) Das, A.; V. Sangaranarayanan, M. Shape-Controlled Synthesis of Three-Dimensional Triangular Bismuth Microstructures and Sensing of H 2 O 2. *CrystEngComm* **2016**, *18* (7), 1147–1155. https://doi.org/10.1039/C5CE02326B.

(133) Sadale, S. B.; Patil, P. S. Nucleation and Growth of Bismuth Thin Films onto Fluorine-Doped Tin Oxide-Coated Conducting Glass Substrates from Nitrate Solutions. *Solid State Ion.* **2004**, *167* (3), 273–283. https://doi.org/10.1016/j.ssi.2004.01.017.

(134) Prados, A.; Ranchal, R. Electrodeposition of Bi Thin Films on N-GaAs(111)B. II. Correlation between the Nucleation Process and the Structural and Electrical Properties. *J. Phys. Chem. C* **2018**, *122* (16), 8886–8893. https://doi.org/10.1021/acs.jpcc.7b12263.

(135) Youbi, B.; Lghazi, Y.; El Bachiri, A.; Ait Himi, M.; Elibrizy, O.; Bimaghra, I. Investigation of Nucleation and Growth Mechanism of Bismuth Electrodeposited on ITO Substrate in Nitric Acid Medium. *Mater. Today Proc.* **2020**, *22*, 6–11. https://doi.org/10.1016/j.matpr.2019.08.055.

(136) de Torresi, S. I. C.; Carlos, I. A. Optical Characterization of Bismuth Reversible Electrodeposition. *J. Electroanal. Chem.* **1996**, *414* (1), 11–16. https://doi.org/10.1016/0022-0728(96)04638-4.

(137) Tishkevich, D.; Grabchikov, S.; Zubar, T.; Vasin, D.; Trukhanov, S.; Vorobjova, A.; Yakimchuk, D.; Kozlovskiy, A.; Zdorovets, M.; Giniyatova, S.; Shimanovich, D.; Lyakhov, D.; Michels, D.; Dong, M.; Gudkova, S.; Trukhanov, A. Early-Stage Growth Mechanism and Synthesis Conditions-Dependent Morphology of Nanocrystalline Bi Films Electrodeposited from Perchlorate Electrolyte. *Nanomaterials* **2020**, *10* (6). https://doi.org/10.3390/nano10061245.

(138) Bilican, D.; Fornell, J.; Sort, J.; Pellicer, E. Electrochemical Synthesis of Bismuth Particles: Tuning Particle Shape through Substrate Type within a Narrow Potential Window. *Mater. Basel Switz.* **2017**, *10* (1). https://doi.org/10.3390/ma10010043.

(139) Petrović, M. M.; Najdanović, S. M.; Kostić, M. M.; Vučić, M. D. R.; Velinov, N. D.; Bojić, D. V.; Bojić, A. L. Effect of Electrochemical Parameters and Working Electrode Material on the Characteristics of Bismuth (III) Oxide Obtained by Electrodeposition and Thermal Oxidation (Extended Abstract). *J. Serbian Chem. Soc.* **2019**, *84* (5), 483–488. https://doi.org/10.2298/JSC190130014P.

(140) Hsieh, L.-Y.; Fong, J.-D.; Hsieh, Y.-Y.; Wang, S.-P.; Sun, I.-W. Electrodeposition of Bismuth in a Choline Chloride/Ethylene Glycol Deep Eutectic Solvent under Ambient Atmosphere. *J. Electrochem. Soc.* **2018**, *165* (9), D331. https://doi.org/10.1149/2.0411809jes.

(141) Park, J. Y.; Kim, S.; Hong, D. M.; Lim, J. W.; Yoo, C. J.; Dong, W. J.; Lee, J.-L. The Effect of Pulse Electrodeposition of Bismuth on Electrochemical Reduction of Carbon Dioxide to Formate. *Electron. Mater. Lett.* **2019**, *15* (4), 454–461. https://doi.org/10.1007/s13391-019-00145-8.

(142) Prados, A.; Ranchal, R. Electrodeposition of Bi Thin Films on N-GaAs(111)B. I. Correlation between the Overpotential and the Nucleation Process. *J. Phys. Chem. C* **2018**, *122* (16), 8874–8885. https://doi.org/10.1021/acs.jpcc.8b01838.

(143) Palomar-Pardavé, M.; Miranda-Hernández, M.; González, I.; Batina, N. Detailed Characterization of Potentiostatic Current Transients with 2D-2D and 2D-3D Nucleation Transitions. *Surf. Sci.* **1998**, *399* (1), 80–95. https://doi.org/10.1016/S0039-6028(97)00813-3.
(144) Armstrong, R. D.; Fleischmann, M.; Thirsk, H. R. The Anodic Bbhaviour of Mercury in Hydroxide Ion Solutions. *J. Electroanal. Chem. 1959* **1966**, *11* (3), 208–223. https://doi.org/10.1016/0022-0728(66)80083-9.
(145) Scharifker, B.; Hills, G. Theoretical and Experimental Studies of Multiple Nucleation. *Electrochimica Acta* **1983**, *28* (7), 879–889. https://doi.org/10.1016/0013-4686(83)85163-9.
(146) O'Brien, B.; Plaza, M.; Zhu, L. Y.; Perez, L.; Chien, C. L.; Searson, P. C. Magnetotransport Properties of Electrodeposited Bismuth Films. *J. Phys. Chem. C* **2008**, *112* (31), 12018–12023. https://doi.org/10.1021/jp802802j.
(147) Mandati, S.; Sarada, B. V.; Dey, S. R.; V.Joshi, S. Pulsed Electrochemical Deposition of CuInSe2 and Cu(In,Ga)Se2 Semiconductor Thin Films. *Semicond. - Growth Charact.* **2017**. https://doi.org/10.5772/intechopen.71857.
(148) Rabiee, H.; Ge, L.; Zhang, X.; Hu, S.; Li, M.; Smart, S.; Zhu, Z.; Yuan, Z. Shape-Tuned Electrodeposition of Bismuth-Based Nanosheets on Flow-through Hollow Fiber Gas Diffusion Electrode for High-Efficiency CO2 Reduction to Formate. *Appl. Catal. B Environ.* **2021**, *286*, 119945. https://doi.org/10.1016/j.apcatb.2021.119945.
(149) Vladislavić, N.; Brinić, S.; Grubač, Z.; Buzuk, M. Study of Bi Film Formation on Different Carbon Based Electrodes for Possible Applicability in Electroanalytical Determination of Cysteine. *Int J Electrochem Sci* **2014**, *9*, 13.
(150) Jiang, H. R.; Zeng, Y. K.; Wu, M. C.; Shyy, W.; Zhao, T. S. A Uniformly Distributed Bismuth Nanoparticle-Modified Carbon Cloth Electrode for Vanadium Redox Flow Batteries. *Appl. Energy* **2019**, *240*, 226–235. https://doi.org/10.1016/j.apenergy.2019.02.051.
(151) Abdallah, R.; Derghane, A.; Lou, Y.-Y.; Merdrignac-Conanec, O.; Floner, D.; Geneste, F. New Porous Bismuth Electrode Material with High Surface Area. *J. Electroanal. Chem.* **2019**, *839*, 32–38. https://doi.org/10.1016/j.jelechem.2019.03.023.
(152) Karar, Y.; Boudinar, S.; Kadri, A.; Leprêtre, J.-C.; Benbrahim, N.; Chaînet, E. Ammonium Chloride Effects on Bismuth Electrodeposition in a Choline Chloride-Urea Deep Eutectic Solvent. *Electrochimica Acta* **2021**, *367*, 137481. https://doi.org/10.1016/j.electacta.2020.137481.
(153) Zhong, H.; Qiu, Y.; Zhang, T.; Li, X.; Zhang, H.; Chen, X. Bismuth Nanodendrites as a High Performance Electrocatalyst for Selective Conversion of CO 2 to Formate. *J. Mater. Chem. A* **2016**, *4* (36), 13746–13753. https://doi.org/10.1039/C6TA06202D.
(154) Lv, W.; Zhou, J.; Bei, J.; Zhang, R.; Wang, L.; Xu, Q.; Wang, W. Electrodeposition of Nano-Sized Bismuth on Copper Foil as Electrocatalyst for Reduction of CO2 to Formate. *Appl. Surf. Sci.* **2017**, *393*, 191–196. https://doi.org/10.1016/j.apsusc.2016.10.017.
(155) Nunes, L. M. S.; Faria, R. C. The Influence of the Electrodeposition Conditions on the Electroanalytical Performance of the Bismuth Film Electrode for Lead Determination. *Electroanalysis* **2008**, *20* (20), 2259–2263. https://doi.org/10.1002/elan.200804293.
(156) Giurlani, W.; Cavallini, M.; Picca, R. A.; Cioffi, N.; Passaponti, M.; Fontanesi, C.; Lavacchi, A.; Innocenti, M. Underpotential-Assisted Electrodeposition of Highly Crystalline and Smooth Thin Film of Bismuth. *ChemElectroChem* **2020**, *7* (1), 299–305. https://doi.org/10.1002/celc.201901678.
(157) Sandnes, E.; Williams, M. E.; Bertocci, U.; Vaudin, M. D.; Stafford, G. R. Electrodeposition of Bismuth from Nitric Acid Electrolyte. *Electrochimica Acta* **2007**, *52* (21), 6221–6228. https://doi.org/10.1016/j.electacta.2007.04.002.

(158) Bertin, E.; Garbarino, S.; Roy, C.; Kazemi, S.; Guay, D. Selective Electroreduction of CO2 to Formate on Bi and Oxide-Derived Bi Films. *J. CO2 Util.* **2017**, *19*, 276–283. https://doi.org/10.1016/j.jcou.2017.04.006.
(159) Li, L.; Zhang, Y.; Li, G.; Zhang, L. A Route to Fabricate Single Crystalline Bismuth Nanowire Arrays with Different Diameters. *Chem. Phys. Lett.* **2003**, *378* (3), 244–249. https://doi.org/10.1016/S0009-2614(03)01264-8.
(160) Reim, N.; Littig, A.; Behn, D.; Mews, A. Controlled Electrodeposition of Bismuth Nanocatalysts for the Solution–Liquid–Solid Synthesis of CdSe Nanowires on Transparent Conductive Substrates. *J. Am. Chem. Soc.* **2013**, *135* (49), 18520–18527. https://doi.org/10.1021/ja408265s.
(161) Sarno, M. Chapter 22 - Nanotechnology in Energy Storage: The Supercapacitors. In *Studies in Surface Science and Catalysis*; Basile, A., Centi, G., Falco, M. D., Iaquaniello, G., Eds.; Catalysis, Green Chemistry and Sustainable Energy; Elsevier, 2020; Vol. 179, pp 431–458. https://doi.org/10.1016/B978-0-444-64337-7.00022-7.
(162) Michaelson, H. B. The Work Function of the Elements and Its Periodicity. *J. Appl. Phys.* **1977**, *48* (11), 4729–4733. https://doi.org/10.1063/1.323539.
(163) Gamburg, Y. D.; Zangari, G. Technologies for the Electrodeposition of Metals and Alloys: Electrolytes and Processes. In *Theory and Practice of Metal Electrodeposition*; Gamburg, Y. D., Zangari, G., Eds.; Springer: New York, NY, 2011; pp 265–316. https://doi.org/10.1007/978-1-4419-9669-5_13.
(164) Hsu, P.-C.; Seol, S.-K.; Lo, T.-N.; Liu, C.-J.; Wang, C.-L.; Lin, C.-S.; Hwu, Y.; Chen, C. H.; Chang, L.-W.; Je, J. H.; Margaritondo, G. Hydrogen Bubbles and the Growth Morphology of Ramified Zinc by Electrodeposition. *J. Electrochem. Soc.* **2008**, *155* (5), D400. https://doi.org/10.1149/1.2894189.
(165) Narasimman, P.; Pushpavanama, M.; Periasamyb, V. M. Effect of Surfactants on the Electrodeposition of Ni-SiC Composites. **2012**. https://doi.org/10.4152/PEA.201201001.
(166) Valkova, T.; Krastev, I. Electrodeposition of Bismuth from Alkaline Thiocyanate-Tartrate Electrolytes Investigated by Cyclic Voltammetry. *Trans. IMF* **2017**.
(167) Atifi, A.; Boyce, D. W.; DiMeglio, J. L.; Rosenthal, J. Directing the Outcome of CO2 Reduction at Bismuth Cathodes Using Varied Ionic Liquid Promoters. *ACS Catal.* **2018**, *8* (4), 2857–2863. https://doi.org/10.1021/acscatal.7b03433.
(168) Zhang, Z.; Chi, M.; Veith, G. M.; Zhang, P.; Lutterman, D. A.; Rosenthal, J.; Overbury, S. H.; Dai, S.; Zhu, H. Rational Design of Bi Nanoparticles for Efficient Electrochemical CO2 Reduction: The Elucidation of Size and Surface Condition Effects. *ACS Catal.* **2016**, *6* (9), 6255–6264. https://doi.org/10.1021/acscatal.6b01297.
(169) DiMeglio, J. L.; Rosenthal, J. Selective Conversion of CO2 to CO with High Efficiency Using an Inexpensive Bismuth-Based Electrocatalyst. *J. Am. Chem. Soc.* **2013**, *135* (24), 8798–8801. https://doi.org/10.1021/ja4033549.
(170) Tishkevich, D. I.; Grabchikov, S. S.; Tsybulskaya, L. S.; Shendyukov, V. S.; Perevoznikov, S. S.; Trukhanov, S. V.; Trukhanova, E. L.; Trukhanov, A. V.; Vinnik, D. A. Electrochemical Deposition Regimes and Critical Influence of Organic Additives on the Structure of Bi Films. *J. Alloys Compd.* **2018**, *735*, 1943–1948. https://doi.org/10.1016/j.jallcom.2017.11.329.
(171) Lim, B.; Xia, Y. Metal Nanocrystals with Highly Branched Morphologies. *Angew. Chem. Int. Ed.* **2011**, *50* (1), 76–85. https://doi.org/10.1002/anie.201002024.
(172) Elgrishi, N.; Rountree, K. J.; McCarthy, B. D.; Rountree, E. S.; Eisenhart, T. T.; Dempsey, J. L. A Practical Beginner's Guide to Cyclic Voltammetry. *J. Chem. Educ.* **2018**, *95* (2), 197–206. https://doi.org/10.1021/acs.jchemed.7b00361.
(173) Hayyan, M.; Mjalli, F. S.; Hashim, M. A.; AlNashef, I. M.; Mei, T. X. Investigating the Electrochemical Windows of Ionic Liquids. *J. Ind. Eng. Chem.* **2013**, *19* (1), 106–112. https://doi.org/10.1016/j.jiec.2012.07.011.

(174) Tomiyasu, H.; Shikata, H.; Takao, K.; Asanuma, N.; Taruta, S.; Park, Y.-Y. An Aqueous Electrolyte of the Widest Potential Window and Its Superior Capability for Capacitors. *Sci. Rep.* **2017**, *7* (1), 45048. https://doi.org/10.1038/srep45048.
(175) Zoski, C. G. *Handbook of Electrochemistry*; Elsevier, 2006.
(176) Grubač, Z.; Metikoš-Huković, M. Nucleation and Growth of Anodic Oxide Films on Bismuth. *Electrochimica Acta* **1998**, *43* (21), 3175–3181. https://doi.org/10.1016/S0013-4686(98)00005-X.
(177) Williams, D. E.; Wright, G. A. Nucleation and Growth of Anodic Oxide Films on Bismuth—I. Cyclic Voltammetry. *Electrochimica Acta* **1976**, *21* (11), 1009–1019. https://doi.org/10.1016/0013-4686(76)85079-7.
(178) Williams, D. E. Mechanism of the Cathodic Reduction of a Bismuth Oxide Anodic Film. *Electrochimica Acta* **1976**, *21* (11), 1097–1098. https://doi.org/10.1016/0013-4686(76)85092-X.
(179) Metikoš-Huković, M. The Photoelectrochemical Properties of Anodic Bi2O3 Films. *Electrochimica Acta* **1981**, *26* (8), 989–1000. https://doi.org/10.1016/0013-4686(81)85067-0.
(180) Lezi, N.; Kokkinos, C.; Economou, A.; Prodromidis, M. I. Voltammetric Determination of Trace Tl(I) at Disposable Screen-Printed Electrodes Modified with Bismuth Precursor Compounds. *Sens. Actuators B Chem.* **2013**, *182*, 718–724. https://doi.org/10.1016/j.snb.2013.02.110.
(181) Rennie, R. R.; Law, J. L. Group 15 Elements. In *A Dictionary of Chemistry*; Rennie, R., Law, J., Eds.; Oxford University Press, 2016.
(182) Lovreček, B.; Metikoš-Hukovič, M. Mechanism of Anodic Oxide Growth on Bismuth. *J. Electroanal. Chem. Interfacial Electrochem.* **1980**, *106*, 127–136. https://doi.org/10.1016/S0022-0728(80)80162-8.
(183) Grubač, Z.; Metikoš-Huković, M. Kinetics and Mechanism of Electrocrystallization of Bismuth in Oxide Matrix. *Electrochimica Acta* **1999**, *44* (25), 4559–4571. https://doi.org/10.1016/S0013-4686(99)00174-7.
(184) Lou, Y.-Y.; Hapiot, P.; Floner, D.; Fourcade, F.; Amrane, A.; Geneste, F. Efficient Dechlorination of α-Halocarbonyl and α-Haloallyl Pollutants by Electroreduction on Bismuth. *Environ. Sci. Technol.* **2020**, *54* (1), 559–567. https://doi.org/10.1021/acs.est.9b05732.
(185) Pérez, M. A.; López Teijelo, M. Cathodic Behavior of Bismuth. I. Ellipsometric Study of the Electroreduction of Thin Bi2O3 Films. *J. Electroanal. Chem.* **2005**, *583* (2), 212–220. https://doi.org/10.1016/j.jelechem.2005.06.005.
(186) Li, W. S.; Long, X. M.; Yan, J. H.; Nan, J. M.; Chen, H. Y.; Wu, Y. M. Electrochemical Behaviour of Bismuth in Sulfuric Acid Solution. *J. Power Sources* **2006**, *158* (2), 1096–1101. https://doi.org/10.1016/j.jpowsour.2006.01.093.
(187) Hurlen, T.; Gulbrandsen, E. Growth of Anodic Films on Valve Metals. *Electrochimica Acta* **1994**, *39* (14), 2169–2172. https://doi.org/10.1016/S0013-4686(94)85069-0.
(188) Modestov, A. D.; Davydov, A. D. Oxidizing Valve Metals: Effect of Electronic Properties of the Oxide Films. *Russ. J. Electrochem.* **2000**, *36* (10), 1137–1143. https://doi.org/10.1007/BF02757535.
(189) Habazaki, H.; Uozumi, M.; Konno, H.; Shimizu, K.; Skeldon, P.; Thompson, G. E. Crystallization of Anodic Titania on Titanium and Its Alloys. *Corros. Sci.* **2003**, *45* (9), 2063–2073. https://doi.org/10.1016/S0010-938X(03)00040-4.
(190) Leach, J. S. L.; Pearson, B. R. Crystallization in Anodic Oxide Films. *Corros. Sci.* **1988**, *28* (1), 43–56. https://doi.org/10.1016/0010-938X(88)90005-4.
(191) Chen, Y.-P.; Lai, C.-C.; Tsai, W.-S. Full-Color Based on Bismuth Core-Shell Nanoparticles in One-Step Fabrication. *Opt. Express* **2020**, *28* (17), 24511–24525. https://doi.org/10.1364/OE.398903.

(192) Pérez, M. A.; Linarez Pérez, O. E.; López Teijelo, M. Cathodic Behavior of Bismuth. II. Electrochemical and Ellipsometric Study of the Hydrogen Insertion into Bulk Bismuth. *J. Electroanal. Chem.* **2006**, *596* (2), 149–156. https://doi.org/10.1016/j.jelechem.2006.07.029.
(193) Gervasi, C. A.; Biaggio, S. R.; Vilche, J. R.; Arvia, A. J. A Kinetic Study of the Electroreduction of Anodically Formed Cobalt Oxide Layers. *Electrochimica Acta* **1991**, *36* (14), 2147–2152. https://doi.org/10.1016/0013-4686(91)85223-T.
(194) Romann, T.; Lust, E. Electrochemical Properties of Porous Bismuth Electrodes. *Electrochimica Acta* **2010**, *55* (20), 5746–5752. https://doi.org/10.1016/j.electacta.2010.05.012.
(195) Ammar, I. A.; Khalil, M. W. Anodic Oxidation of Bismuth in H2SO4 Solutions. *Electrochimica Acta* **1971**, *16* (9), 1379–1394. https://doi.org/10.1016/0013-4686(71)80011-7.
(196) Doña Rodríguez, J. M.; Herrera Melián, J. A.; Pérez Peña, J. Determination of the Real Surface Area of Pt Electrodes by Hydrogen Adsorption Using Cyclic Voltammetry. *J. Chem. Educ.* **2000**, *77* (9), 1195. https://doi.org/10.1021/ed077p1195.
(197) Trasatti, S.; Parsons, R. Interphases in Systems of Conducting Phases (Recommendations 1985). *Pure Appl. Chem.* **1986**, *58* (3), 437–454. https://doi.org/10.1351/pac198658030437.
(198) Trasatti, S.; Petrii, O. A. Real Surface Area Measurements in Electrochemistry. *Pure Appl. Chem.* **1991**, *63* (5), 711–734. https://doi.org/10.1351/pac199163050711.
(199) Gutz, I. G. R. An Accurate Mercury Electrode Drop-Time Measuring Instrument Based on a Piezoelectric Transducer. *J. Electroanal. Chem. Interfacial Electrochem.* **1984**, *179* (1), 99–106. https://doi.org/10.1016/S0022-0728(84)80279-X.
(200) Hoogvliet, J. C.; Dijksma, M.; Kamp, B.; van Bennekom, W. P. Electrochemical Pretreatment of Polycrystalline Gold Electrodes To Produce a Reproducible Surface Roughness for Self-Assembly: A Study in Phosphate Buffer PH 7.4. *Anal. Chem.* **2000**, *72* (9), 2016–2021. https://doi.org/10.1021/ac991215y.
(201) Bonroy, K.; Friedt, J.-M.; Frederix, F.; Laureyn, W.; Langerock, S.; Campitelli, A.; Sára, M.; Borghs, G.; Goddeeris, B.; Declerck, P. Realization and Characterization of Porous Gold for Increased Protein Coverage on Acoustic Sensors. *Anal. Chem.* **2004**, *76* (15), 4299–4306. https://doi.org/10.1021/ac049893u.
(202) Daiyan, R.; Lu, X.; Ng, Y. H.; Amal, R. Highly Selective Conversion of CO2 to CO Achieved by a Three-Dimensional Porous Silver Electrocatalyst. *ChemistrySelect 2* (3), 879–884. https://doi.org/10.1002/slct.201601980.
(203) García-Miranda Ferrari, A.; Foster, C. W.; Kelly, P. J.; Brownson, D. A. C.; Banks, C. E. Determination of the Electrochemical Area of Screen-Printed Electrochemical Sensing Platforms. *Biosensors* **2018**, *8* (2), 53. https://doi.org/10.3390/bios8020053.
(204) Mistry, K. K.; Deepthy, T. S.; Chau, C. R.; Saha, H. Electrochemical Characterization of Some Commercial Screen-Printed Electrodes in Different Redox Substrates. **2015**. https://doi.org/10.18520/CS/V109/I8/1427-1436.
(205) Jarzabek, G.; Borkowska, Z. On the Real Surface Area of Smooth Solid Electrodes. *Electrochimica Acta* **1997**, *42* (19), 2915–2918. https://doi.org/10.1016/S0013-4686(97)00112-6.
(206) Gira, M. J.; Tkacz, K. P.; Hampton, J. R. Physical and Electrochemical Area Determination of Electrodeposited Ni, Co, and NiCo Thin Films. *Nano Converg.* **2016**, *3*. https://doi.org/10.1186/s40580-016-0063-0.
(207) Thommes, M.; Kaneko, K.; Neimark, A. V.; Olivier, J. P.; Rodriguez-Reinoso, F.; Rouquerol, J.; Sing, K. S. W. Physisorption of Gases, with Special Reference to the Evaluation of Surface Area and Pore Size Distribution (IUPAC Technical Report). *Pure Appl. Chem.* **2015**, *87* (9–10), 1051–1069. https://doi.org/10.1515/pac-2014-1117.

(208) Stojek, Z. The Electrical Double Layer and Its Structure. In *Electroanalytical Methods: Guide to Experiments and Applications*; Scholz, F., Ed.; Springer: Berlin, Heidelberg, 2002; pp 3–8. https://doi.org/10.1007/978-3-662-04757-6_1.
(209) Soam, A.; Kumar, R.; C, M.; Singh, M.; Thatoi, D.; Dusane, R. O. Development of Paper-Based Flexible Supercapacitor: Bismuth Ferrite/Graphene Nanocomposite as an Active Electrode Material. *J. Alloys Compd.* **2020**, *813*, 152145. https://doi.org/10.1016/j.jallcom.2019.152145.
(210) Parsons, R. The Electrical Double Layer: Recent Experimental and Theoretical Developments. *Chem. Rev.* **1990**, *90* (5), 813–826. https://doi.org/10.1021/cr00103a008.
(211) Ge, Y.; Xie, X.; Roscher, J.; Holze, R.; Qu, Q. How to Measure and Report the Capacity of Electrochemical Double Layers, Supercapacitors, and Their Electrode Materials. *J. Solid State Electrochem.* **2020**, *24* (11), 3215–3230. https://doi.org/10.1007/s10008-020-04804-x.
(212) Helseth, L. E. Comparison of Methods for Finding the Capacitance of a Supercapacitor. *J. Energy Storage* **2021**, *35*, 102304. https://doi.org/10.1016/j.est.2021.102304.
(213) Shiraishi, S. Chapter 10 - Electrochemical Performance. In *Materials Science and Engineering of Carbon*; Inagaki, M., Kang, F., Eds.; Butterworth-Heinemann, 2016; pp 205–226. https://doi.org/10.1016/B978-0-12-805256-3.00010-6.
(214) McCrory, C. C. L.; Jung, S.; Peters, J. C.; Jaramillo, T. F. Benchmarking Heterogeneous Electrocatalysts for the Oxygen Evolution Reaction. *J. Am. Chem. Soc.* **2013**, *135* (45), 16977–16987. https://doi.org/10.1021/ja407115p.
(215) Huang, J.; Guo, X.; Huang, X.; Wang, L. Metal (Sn, Bi, Pb, Cd) in-Situ Anchored on Mesoporous Hollow Kapok-Tubes for Outstanding Electrocatalytic CO2 Reduction to Formate. *Electrochimica Acta* **2019**, *325*, 134923. https://doi.org/10.1016/j.electacta.2019.134923.
(216) Teng, Y.; Teng, F. Investigation on Surface Metal Vacancy Electrochemistry. *Electrochimica Acta* **2017**, *244*, 1–7. https://doi.org/10.1016/j.electacta.2017.05.107.
(217) Sarma, B.; Jurovitzki, A. L.; Smith, Y. R.; Mohanty, S. K.; Misra, M. Redox-Induced Enhancement in Interfacial Capacitance of the Titania Nanotube/Bismuth Oxide Composite Electrode. *ACS Appl. Mater. Interfaces* **2013**, *5* (5), 1688–1697. https://doi.org/10.1021/am302738r.
(218) Li, L.; Zhang, X.; Zhang, Z.; Zhang, M.; Cong, L.; Pan, Y.; Lin, S. A Bismuth Oxide Nanosheet-Coated Electrospun Carbon Nanofiber Film: A Free-Standing Negative Electrode for Flexible Asymmetric Supercapacitors. *J. Mater. Chem. A* **2016**, *4* (42), 16635–16644. https://doi.org/10.1039/C6TA06755G.
(219) Ciszewski, M.; Mianowski, A.; Szatkowski, P.; Nawrat, G.; Adamek, J. Reduced Graphene Oxide–Bismuth Oxide Composite as Electrode Material for Supercapacitors. *Ionics* **2015**, *21* (2), 557–563. https://doi.org/10.1007/s11581-014-1182-4.
(220) Huang, X.; Zhang, W.; Tan, Y.; Wu, J.; Gao, Y.; Tang, B. Facile Synthesis of Rod-like Bi2O3 Nanoparticles as an Electrode Material for Pseudocapacitors. *Ceram. Int.* **2016**, *42* (1, Part B), 2099–2105. https://doi.org/10.1016/j.ceramint.2015.09.157.
(221) Walcarius, A. Template-Directed Porous Electrodes in Electroanalysis. *Anal. Bioanal. Chem.* **2010**, *396* (1), 261–272. https://doi.org/10.1007/s00216-009-3069-1.
(222) Kas, R.; Yang, K.; Bohra, D.; Kortlever, R.; Burdyny, T.; Smith, W. A. Electrochemical CO2 Reduction on Nanostructured Metal Electrodes: Fact or Defect? *Chem. Sci.* **2020**, *11* (7), 1738–1749. https://doi.org/10.1039/C9SC05375A.
(223) Li, C. W.; Ciston, J.; Kanan, M. W. Electroreduction of Carbon Monoxide to Liquid Fuel on Oxide-Derived Nanocrystalline Copper. *Nature* **2014**, *508* (7497), 504–507. https://doi.org/10.1038/nature13249.

(224) Li, C. W.; Kanan, M. W. CO2 Reduction at Low Overpotential on Cu Electrodes Resulting from the Reduction of Thick Cu2O Films. *J. Am. Chem. Soc.* **2012**, *134* (17), 7231–7234. https://doi.org/10.1021/ja3010978.
(225) Hsieh, Y.-C.; Senanayake, S. D.; Zhang, Y.; Xu, W.; Polyansky, D. E. Effect of Chloride Anions on the Synthesis and Enhanced Catalytic Activity of Silver Nanocoral Electrodes for CO2 Electroreduction. *ACS Catal.* **2015**, *5* (9), 5349–5356. https://doi.org/10.1021/acscatal.5b01235.
(226) Zhang, B. A.; Ozel, T.; Elias, J. S.; Costentin, C.; Nocera, D. G. Interplay of Homogeneous Reactions, Mass Transport, and Kinetics in Determining Selectivity of the Reduction of CO2 on Gold Electrodes. *ACS Cent. Sci.* **2019**, *5* (6), 1097–1105. https://doi.org/10.1021/acscentsci.9b00302.
(227) Appl Max. Ammonia, 3. Production Plants. *Ullmanns Encycl. Ind. Chem.* **2011**. https://doi.org/10.1002/14356007.o02_o12.
(228) Zhang, S.; Kang, P.; Meyer, T. J. Nanostructured Tin Catalysts for Selective Electrochemical Reduction of Carbon Dioxide to Formate. *J. Am. Chem. Soc.* **2014**, *136* (5), 1734–1737. https://doi.org/10.1021/ja4113885.
(229) Zhang, S.; Kang, P.; Ubnoske, S.; Brennaman, M. K.; Song, N.; House, R. L.; Glass, J. T.; Meyer, T. J. Polyethylenimine-Enhanced Electrocatalytic Reduction of CO2 to Formate at Nitrogen-Doped Carbon Nanomaterials. *J. Am. Chem. Soc.* **2014**, *136* (22), 7845–7848. https://doi.org/10.1021/ja5031529.
(230) Medina-Ramos, J.; Pupillo, R. C.; Keane, T. P.; DiMeglio, J. L.; Rosenthal, J. Efficient Conversion of CO2 to CO Using Tin and Other Inexpensive and Easily Prepared Post-Transition Metal Catalysts. *J. Am. Chem. Soc.* **2015**, *137* (15), 5021–5027. https://doi.org/10.1021/ja5121088.
(231) Rosen, B. A.; Salehi-Khojin, A.; Thorson, M. R.; Zhu, W.; Whipple, D. T.; Kenis, P. J. A.; Masel, R. I. Ionic Liquid-Mediated Selective Conversion of CO_2 to CO at Low Overpotentials. *Science* **2011**, *334* (6056), 643–644. https://doi.org/10.1126/science.1209786.
(232) Frese, K. W. Electrochemical Reduction of CO 2 at Intentionally Oxidized Copper Electrodes. *J. Electrochem. Soc.* **1991**, *138* (11), 3338–3344. https://doi.org/10.1149/1.2085411.
(233) Seshadri, G.; Lin, C.; Bocarsly, A. B. A New Homogeneous Electrocatalyst for the Reduction of Carbon Dioxide to Methanol at Low Overpotential. *J. Electroanal. Chem.* **1994**, *372* (1), 145–150. https://doi.org/10.1016/0022-0728(94)03300-5.
(234) Amatore, C.; Saveant, J. M. Mechanism and Kinetic Characteristics of the Electrochemical Reduction of Carbon Dioxide in Media of Low Proton Availability. *J. Am. Chem. Soc.* **1981**, *103* (17), 5021–5023. https://doi.org/10.1021/ja00407a008.
(235) Lee, J.; Tak, Y. Electrocatalytic Activity of Cu Electrode in Electroreduction of CO2. *Electrochimica Acta* **2001**, *46* (19), 3015–3022. https://doi.org/10.1016/S0013-4686(01)00527-8.
(236) Hori, Y.; Takahashi, R.; Yoshinami, Y.; Murata, A. Electrochemical Reduction of CO at a Copper Electrode. *J. Phys. Chem. B* **1997**, *101* (36), 7075–7081. https://doi.org/10.1021/jp970284i.
(237) Hori, Y.; Kikuchi, K.; Murata, A.; Suzuki, S. PRODUCTION OF METHANE AND ETHYLENE IN ELECTROCHEMICAL REDUCTION OF CARBON DIOXIDE AT COPPER ELECTRODE IN AQUEOUS HYDROGENCARBONATE SOLUTION. *Chem. Lett.* **1986**, *15* (6), 897–898. https://doi.org/10.1246/cl.1986.897.
(238) Hori, Y. Electrochemical CO<Subscript>2</Subscript> Reduction on Metal Electrodes. In *Modern Aspects of Electrochemistry*; Modern Aspects of Electrochemistry; Springer, New York, NY, 2008; pp 89–189. https://doi.org/10.1007/978-0-387-49489-0_3.

(239) Gattrell, M.; Gupta, N.; Co, A. A Review of the Aqueous Electrochemical Reduction of CO2 to Hydrocarbons at Copper. *J. Electroanal. Chem.* **2006**, *594* (1), 1–19. https://doi.org/10.1016/j.jelechem.2006.05.013.

(240) Zhang, H.; Ma, Y.; Quan, F.; Huang, J.; Jia, F.; Zhang, L. Selective Electro-Reduction of CO2 to Formate on Nanostructured Bi from Reduction of BiOCl Nanosheets. *Electrochem. Commun.* **2014**, *46*, 63–66. https://doi.org/10.1016/j.elecom.2014.06.013.

(241) Kumawat, A. S.; Sarkar, A. Comparative Study of Carbon Supported Pb, Bi and Sn Catalysts for Electroreduction of Carbon Dioxide in Alkaline Medium. *J. Electrochem. Soc.* **2017**, *164* (14), H1112–H1120. https://doi.org/10.1149/2.0991714jes.

(242) Jiang, H.; Wang, L.; Li, Y.; Gao, B.; Guo, Y.; Yan, C.; Zhuo, M.; Wang, H.; Zhao, S. High-Selectivity Electrochemical CO2 Reduction to Formate at Low Overpotential over Bi Catalyst with Hexagonal Sheet Structure. *Appl. Surf. Sci.* **2021**, *541*, 148577. https://doi.org/10.1016/j.apsusc.2020.148577.

(243) Miao, C.-C.; Yuan, G.-Q. Morphology-Controlled Bi2O3 Nanoparticles as Catalysts for Selective Electrochemical Reduction of CO2 to Formate. *ChemElectroChem* **2018**, *5* (23), 3741–3747. https://doi.org/10.1002/celc.201801036.

(244) Lee, C. W.; Hong, J. S.; Yang, K. D.; Jin, K.; Lee, J. H.; Ahn, H.-Y.; Seo, H.; Sung, N.-E.; Nam, K. T. Selective Electrochemical Production of Formate from Carbon Dioxide with Bismuth-Based Catalysts in an Aqueous Electrolyte. *ACS Catal.* **2018**, *8* (2), 931–937. https://doi.org/10.1021/acscatal.7b03242.

(245) Medina-Ramos, J.; DiMeglio, J. L.; Rosenthal, J. Efficient Reduction of CO2 to CO with High Current Density Using in Situ or Ex Situ Prepared Bi-Based Materials. *J. Am. Chem. Soc.* **2014**, *136* (23), 8361–8367. https://doi.org/10.1021/ja501923g.

(246) Ma, C.; Li, J.; Peng, J.; Bai, Y.; Zhang, G.; Xiao, W.; Lai, G. Effect of Carboxyl-Functionalized Imidazolium Salts on the Rhodium-Catalyzed Hydrosilylation of Alkene. *J. Organomet. Chem.* **2013**, *727*, 28–36. https://doi.org/10.1016/j.jorganchem.2012.12.016.

(247) Yi, F. P.; Sun, H. Y.; Pan, X. H.; Xu, Y.; Li, J. Z. Synthesis of Fischer Indole Derivatives Using Carboxyl-Functionalized Ionic Liquid as an Efficient and Recyclable Catalyst. *Chin. Chem. Lett.* **2009**, *20* (3), 275–278. https://doi.org/10.1016/j.cclet.2008.11.010.

(248) Fei, Z.; Zhao, D.; Geldbach, T. J.; Scopelliti, R.; Dyson, P. J. Brønsted Acidic Ionic Liquids and Their Zwitterions: Synthesis, Characterization and PKa Determination. *Chem. – Eur. J.* **2004**, *10* (19), 4886–4893. https://doi.org/10.1002/chem.200400145.

(249) Laviron, E. General Expression of the Linear Potential Sweep Voltammogram in the Case of Diffusionless Electrochemical Systems. *J. Electroanal. Chem. Interfacial Electrochem.* **1979**, *101* (1), 19–28. https://doi.org/10.1016/S0022-0728(79)80075-3.

(250) Material Science and Catalysis Design. In *The Development of Catalysis*; John Wiley & Sons, Ltd, 2017; pp 205–242. https://doi.org/10.1002/9781119181286.ch6.

(251) Fu, Y.; Ehrenburg, M. R.; Broekmann, P.; Rudnev, A. V. Surface Structure Sensitivity of CO2 Electroreduction on Low-Index Gold Single Crystal Electrodes in Ionic Liquids. *ChemElectroChem* **2018**, *5* (5), 748–752. https://doi.org/10.1002/celc.201701209.

(252) Ahn, S. T.; Abu-Baker, I.; Palmore, G. T. R. Electroreduction of CO2 on Polycrystalline Copper: Effect of Temperature on Product Selectivity. *Catal. Today* **2017**, *288*, 24–29. https://doi.org/10.1016/j.cattod.2016.09.028.

(253) Feng, Q.; Liu, S.; Wang, X.; Jin, G. Nanoporous Copper Incorporated Platinum Composites for Electrocatalytic Reduction of CO2 in Ionic Liquid BMIMBF4. *Appl. Surf. Sci.* **2012**, *258* (12), 5005–5009. https://doi.org/10.1016/j.apsusc.2012.01.030.

(254) Ariño, C.; Serrano, N.; Díaz-Cruz, J. M.; Esteban, M. Voltammetric Determination of Metal Ions beyond Mercury Electrodes. A Review. *Anal. Chim. Acta* **2017**, *990*, 11–53. https://doi.org/10.1016/j.aca.2017.07.069.

(255) Pendyala, P.; Bobji, M. S.; Madras, G. Evolution of Surface Roughness During Electropolishing. *Tribol. Lett.* **2014**, *55* (1), 93–101. https://doi.org/10.1007/s11249-014-0336-x.
(256) Kecskeméthy, A.; Flores, F. G.; Carrera, E.; Elias, D. A. *Interdisciplinary Applications of Kinematics: Proceedings of the Third International Conference (IAK)*; Springer, 2019.
(257) Mitchell, D. S. *Conservation of Architectural Ironwork*; Taylor & Francis, 2016.
(258) Zuzuarregui, A.; Arana, S.; Pérez-Lorenzo, E.; Sánchez-Gómez, S.; Martínez de Tejada, G.; Mujika, M. Novel Fully-Integrated Biosensor for Endotoxin Detection via Polymyxin B Immobilization onto Gold Electrodes. *J. Sens. Sens. Syst.* **2013**, *2* (2), 157–164. https://doi.org/10.5194/jsss-2-157-2013.
(259) Singman, C. N. Atomic Volume and Allotropy of the Elements. *J. Chem. Educ.* **1984**, *61* (2), 137. https://doi.org/10.1021/ed061p137.
(260) Brett, C. M. A.; Brett, A. M. O. *Electrochemistry: Principles, Methods, and Applications*; Oxford University Press, 1993.
(261) Bruckenstein, Stanley.; Sharkey, J. W.; Yip, J. Y. Effect of Polishing with Different Size Abrasives on the Current Response at a Rotating Disk Electrode. *Anal. Chem.* **1985**, *57* (1), 368–371. https://doi.org/10.1021/ac00279a085.
(262) Samsonov, G. V. Mechanical Properties of the Elements. In *Handbook of the Physicochemical Properties of the Elements*; Samsonov, G. V., Ed.; Springer US: Boston, MA, 1968; pp 387–446. https://doi.org/10.1007/978-1-4684-6066-7_7.
(263) Nucleation and Growth Models. In *Fundamentals of Electrochemical Deposition*; John Wiley & Sons, Ltd, 2006; pp 113–138. https://doi.org/10.1002/0470009403.ch7.
(264) Pajkossy, T. Atypical Electric Behavior of the Double Layer. Experimental Case Studies: Rh(111) in Aqueous HCl Solutions, and Au(111) in an Ionic Liquid, BMIPF6. *Pure Appl. Chem.* **2010**, *83* (2), 259–268. https://doi.org/10.1351/PAC-CON-10-06-10.
(265) Connor, P.; Schuch, J.; Kaiser, B.; Jaegermann, W. The Determination of Electrochemical Active Surface Area and Specific Capacity Revisited for the System MnOx as an Oxygen Evolution Catalyst. *Z. Für Phys. Chem.* **2020**, *234* (5), 979–994. https://doi.org/10.1515/zpch-2019-1514.
(266) Benck, J. D.; Chen, Z.; Kuritzky, L. Y.; Forman, A. J.; Jaramillo, T. F. Amorphous Molybdenum Sulfide Catalysts for Electrochemical Hydrogen Production: Insights into the Origin of Their Catalytic Activity. *ACS Catal.* **2012**, *2* (9), 1916–1923. https://doi.org/10.1021/cs300451q.
(267) Zhang, Y.; Li, F.; Zhang, X.; Williams, T.; Easton, C. D.; Bond, A. M.; Zhang, J. Electrochemical Reduction of CO2 on Defect-Rich Bi Derived from Bi2S3 with Enhanced Formate Selectivity. *J. Mater. Chem. A* **2018**, *6* (11), 4714–4720. https://doi.org/10.1039/C8TA00023A.
(268) Imbeaux, J. C.; Savéant, J. M. Linear Sweep Voltammetry. Effect of Uncompensated Cell Resistance and Double Layer Charging on Polarization Curves. *J. Electroanal. Chem. Interfacial Electrochem.* **1970**, *28* (2), 325–338. https://doi.org/10.1016/S0022-0728(70)80127-9.
(269) Zhang, X.; Lei, T.; Liu, Y.; Qiao, J. Enhancing CO2 Electrolysis to Formate on Facilely Synthesized Bi Catalysts at Low Overpotential. *Appl. Catal. B Environ.* **2017**, *218*, 46–50. https://doi.org/10.1016/j.apcatb.2017.06.032.
(270) Bei, J.; Zhang, R.; Chen, Z.; Lv, W.; Wang, W. Efficient Reduction of CO2 to Formate Using in Situ Prepared Nano-Sized Bi Electrocatalyst. *Int. J. Electrochem. Sci.* **2017**, *12* (3), 2365–2375. https://doi.org/10.20964/2017.03.72.
(271) Nolan, M. Adsorption of CO2 on Heterostructures of Bi2O3 Nanocluster-Modified TiO2 and the Role of Reduction in Promoting CO2 Activation. *ACS Omega* **2018**, *3* (10), 13117–13128. https://doi.org/10.1021/acsomega.8b01957.

(272) Dunwell, M.; Lu, Q.; Heyes, J. M.; Rosen, J.; Chen, J. G.; Yan, Y.; Jiao, F.; Xu, B. The Central Role of Bicarbonate in the Electrochemical Reduction of Carbon Dioxide on Gold. *J. Am. Chem. Soc.* **2017**, *139* (10), 3774–3783. https://doi.org/10.1021/jacs.6b13287.
(273) Nicholson, R. S. Theory and Application of Cyclic Voltammetry for Measurement of Electrode Reaction Kinetics. *Anal. Chem.* **1965**, *37* (11), 1351–1355. https://doi.org/10.1021/ac60230a016.
(274) Klingler, R. J.; Kochi, J. K. Electron-Transfer Kinetics from Cyclic Voltammetry. Quantitative Description of Electrochemical Reversibility. *J. Phys. Chem.* **1981**, *85* (12), 1731–1741. https://doi.org/10.1021/j150612a028.
(275) Cook, S. K.; Horrocks, B. R. Heterogeneous Electron-Transfer Rates for the Reduction of Viologen Derivatives at Platinum and Bismuth Electrodes in Acetonitrile. *Chemelectrochem* **2017**, *4* (2), 320–331. https://doi.org/10.1002/celc.201600536.
(276) Shakil Hussain, S. M.; Kamal, M. S.; Hossain, M. K. Recent Developments in Nanostructured Palladium and Other Metal Catalysts for Organic Transformation. *J. Nanomater.* **2019**, *2019*, e1562130. https://doi.org/10.1155/2019/1562130.
(277) Yang, Z.; Oropeza, F. E.; Zhang, K. H. L. P-Block Metal-Based (Sn, In, Bi, Pb) Electrocatalysts for Selective Reduction of CO2 to Formate. *APL Mater.* **2020**, *8* (6), 060901. https://doi.org/10.1063/5.0004194.
(278) Yang, H.; Han, N.; Deng, J.; Wu, J.; Wang, Y.; Hu, Y.; Ding, P.; Li, Y.; Li, Y.; Lu, J. Selective CO2 Reduction on 2D Mesoporous Bi Nanosheets. *Adv. Energy Mater.* **2018**, *8* (35), 1801536. https://doi.org/10.1002/aenm.201801536.
(279) Zhang, X.; Sun, X.; Guo, S.-X.; Bond, A. M.; Zhang, J. Formation of Lattice-Dislocated Bismuth Nanowires on Copper Foam for Enhanced Electrocatalytic CO2 Reduction at Low Overpotential. *Energy Environ. Sci.* **2019**, *12* (4), 1334–1340. https://doi.org/10.1039/C9EE00018F.
(280) Han, N.; Wang, Y.; Yang, H.; Deng, J.; Wu, J.; Li, Y.; Li, Y. Ultrathin Bismuth Nanosheets from in Situ Topotactic Transformation for Selective Electrocatalytic CO 2 Reduction to Formate. *Nat. Commun.* **2018**, *9* (1), 1320. https://doi.org/10.1038/s41467-018-03712-z.
(281) Gao, T.; Wen, X.; Xie, T.; Han, N.; Sun, K.; Han, L.; Wang, H.; Zhang, Y.; Kuang, Y.; Sun, X. Morphology Effects of Bismuth Catalysts on Electroreduction of Carbon Dioxide into Formate. *Electrochimica Acta* **2019**, *305*, 388–393. https://doi.org/10.1016/j.electacta.2019.03.066.
(282) Choi, W.; Kim, M.; Kim, B.; Park, Y.; Han, D. S.; Hoffmann, M. R.; Park, H. Electrocatalytic Arsenite Oxidation in Bicarbonate Solutions Combined with CO2 Reduction to Formate. *Appl. Catal. B Environ.* **2020**, *265*, 118607. https://doi.org/10.1016/j.apcatb.2020.118607.
(283) Díaz-Sainz, G.; Alvarez-Guerra, M.; Ávila-Bolívar, B.; Solla-Gullón, J.; Montiel, V.; Irabien, A. Improving Trade-Offs in the Figures of Merit of Gas-Phase Single-Pass Continuous CO2 Electrocatalytic Reduction to Formate. *Chem. Eng. J.* **2021**, *405*, 126965. https://doi.org/10.1016/j.cej.2020.126965.
(284) Sun, J.; Zheng, W.; Lyu, S.; He, F.; Yang, B.; Li, Z.; Lei, L.; Hou, Y. Bi/Bi2O3 Nanoparticles Supported on N-Doped Reduced Graphene Oxide for Highly Efficient CO2 Electroreduction to Formate. *Chin. Chem. Lett.* **2020**, *31* (6), 1415–1421. https://doi.org/10.1016/j.cclet.2020.04.031.
(285) Yang, X.; Chen, Y.; Qin, L.; Wu, X.; Wu, Y.; Yan, T.; Geng, Z.; Zeng, J. Boost Selectivity of HCOO− Using Anchored Bi Single Atoms towards CO2 Reduction. *ChemSusChem n/a* (n/a). https://doi.org/10.1002/cssc.202001609.
(286) Singh, M. R.; Clark, E. L.; Bell, A. T. Effects of Electrolyte, Catalyst, and Membrane Composition and Operating Conditions on the Performance of Solar-Driven Electrochemical Reduction of Carbon Dioxide. *Phys. Chem. Chem. Phys.* **2015**, *17* (29), 18924–18936. https://doi.org/10.1039/C5CP03283K.

(287) König, M.; Vaes, J.; Klemm, E.; Pant, D. Solvents and Supporting Electrolytes in the Electrocatalytic Reduction of CO2. *iScience* **2019**, *19*, 135–160. https://doi.org/10.1016/j.isci.2019.07.014.
(288) Sa, Y. J.; Lee, C. W.; Lee, S. Y.; Na, J.; Lee, U.; Hwang, Y. J. Catalyst–Electrolyte Interface Chemistry for Electrochemical CO2 Reduction. *Chem. Soc. Rev.* **2020**, *49* (18), 6632–6665. https://doi.org/10.1039/D0CS00030B.
(289) Goyal, A.; Marcandalli, G.; Mints, V. A.; Koper, M. T. M. Competition between CO2 Reduction and Hydrogen Evolution on a Gold Electrode under Well-Defined Mass Transport Conditions. *J. Am. Chem. Soc.* **2020**, *142* (9), 4154–4161. https://doi.org/10.1021/jacs.9b10061.
(290) Raciti, D.; Mao, M.; Wang, C. Mass Transport Modelling for the Electroreduction of CO2 on Cu Nanowires. *Nanotechnology* **2017**, *29* (4), 044001. https://doi.org/10.1088/1361-6528/aa9bd7.
(291) Lim, C. F. C.; Harrington, D. A.; Marshall, A. T. Effects of Mass Transfer on the Electrocatalytic CO2 Reduction on Cu. *Electrochimica Acta* **2017**, *238*, 56–63. https://doi.org/10.1016/j.electacta.2017.04.017.
(292) Recent Advances in the Catalyst Design and Mass Transport Control for the Electrochemical Reduction of Carbon Dioxide to Formate - ProQuest https://search.proquest.com/openview/8577d7c1c70b66a71022823f8b2bb5d9/1?pq-origsite=gscholar&cbl=2032420 (accessed 2020 -11 -17).
(293) Electrochemical Methods: Fundamentals and Applications, 2nd Edition | Wiley https://www.wiley.com/en-us/Electrochemical+Methods%3A+Fundamentals+and+Applications%2C+2nd+Edition-p-9780471043720 (accessed 2021 -01 -11).
(294) Zhang, D.; Deutschmann, O.; Seidel, Y. E.; Behm, R. J. Interaction of Mass Transport and Reaction Kinetics during Electrocatalytic CO Oxidation in a Thin-Layer Flow Cell. *J. Phys. Chem. C* **2011**, *115* (2), 468–478. https://doi.org/10.1021/jp106967s.
(295) Gong, S.; Han, Q.; Wang, X.; Zhu, J. Controlled Synthesis of Bismuth-Containing Compounds (α-, β- and δ-Bi2O3, Bi5O7NO3 and Bi6O6(OH)2(NO3)4·2H2O) and Their Photocatalytic Performance. *CrystEngComm* **2015**, *17* (47), 9185–9192. https://doi.org/10.1039/C5CE01787D.
(296) Kudo, A.; Omori, K.; Kato, H. A Novel Aqueous Process for Preparation of Crystal Form-Controlled and Highly Crystalline BiVO4 Powder from Layered Vanadates at Room Temperature and Its Photocatalytic and Photophysical Properties. *J. Am. Chem. Soc.* **1999**, *121* (49), 11459–11467. https://doi.org/10.1021/ja992541y.
(297) Halaoui, L. I.; Sharifian, H.; Bard, A. J. Reduction of Nitric Acid to Hydroxylamine at Glassy Carbon Surfaces Modified by the Reduction of P-Phenylenediamine and p-Aminophenol in 1.0 M Nitric Acid: A Scanning Electrochemical Microscopy Study. *J. Electrochem. Soc.* **2001**, *148* (9), E386. https://doi.org/10.1149/1.1389343.
(298) Grujicic, D.; Pesic, B. Electrodeposition of Copper: The Nucleation Mechanisms. *Electrochimica Acta* **2002**, *47* (18), 2901–2912. https://doi.org/10.1016/S0013-4686(02)00161-5.
(299) Back, S.; Yeom, M. S.; Jung, Y. Understanding the Effects of Au Morphology on CO2 Electrocatalysis. *J. Phys. Chem. C* **2018**, *122* (8), 4274–4280. https://doi.org/10.1021/acs.jpcc.7b10439.
(300) Pander, J. E.; Lum, J. W. J.; Yeo, B. S. The Importance of Morphology on the Activity of Lead Cathodes for the Reduction of Carbon Dioxide to Formate. *J. Mater. Chem. A* **2019**, *7* (8), 4093–4101. https://doi.org/10.1039/C8TA10752A.
(301) Tang, W.; A. Peterson, A.; Sofia Varela, A.; P. Jovanov, Z.; Bech, L.; J. Durand, W.; Dahl, S.; K. Nørskov, J.; Chorkendorff, I. The Importance of Surface Morphology in Controlling the

Selectivity of Polycrystalline Copper for CO2 Electroreduction. *Phys. Chem. Chem. Phys.* **2012**, *14* (1), 76–81. https://doi.org/10.1039/C1CP22700A.
(302) Dutta, A.; Rahaman, M.; Luedi, N. C.; Mohos, M.; Broekmann, P. Morphology Matters: Tuning the Product Distribution of CO2 Electroreduction on Oxide-Derived Cu Foam Catalysts. *ACS Catal.* **2016**, *6* (6), 3804–3814. https://doi.org/10.1021/acscatal.6b00770.
(303) Pan, F.; Yang, Y. Designing CO2 Reduction Electrode Materials by Morphology and Interface Engineering. *Energy Environ. Sci.* **2020**, *13* (8), 2275–2309. https://doi.org/10.1039/D0EE00900H.
(304) Liu, Z.; Zheng, M.; Hilty, R. D.; West, A. C. Effect of Morphology and Hydrogen Evolution on Porosity of Electroplated Cobalt Hard Gold. *J. Electrochem. Soc.* **2010**, *157* (7), D411. https://doi.org/10.1149/1.3430076.
(305) Castaing, R. Electron Probe Microanalysis. In *Advances in Electronics and Electron Physics*; Marton, L., Marton, C., Eds.; Academic Press, 1960; Vol. 13, pp 317–386. https://doi.org/10.1016/S0065-2539(08)60212-7.
(306) Afsin, B.; Roberts, M. W. Formation of an Oxy-Chloride Overlayer at a Bi(0001) Surface. *Spectrosc. Lett.* **1994**, *27* (1), 139–146. https://doi.org/10.1080/00387019408002513.
(307) Ismail, F. M.; Hanafi, Z. M. Some Physico-Chemical Properties of Bismuth Chalcogenides. X-Ray Photoelectron and Diffuse Reflectance Spectra. *Z Phys Chem Leipz.* **1986**, *267* (4).
(308) Baer, D. R.; Artyushkova, K.; Brundle, C. R.; Castle, J. E.; Engelhard, M. H.; Gaskell, K. J.; Grant, J. T.; Haasch, R. T.; Linford, M. R.; Powell, C. J.; Shard, A. G.; Sherwood, P. M. A.; Smentkowski, V. S. Practical Guides for X-Ray Photoelectron Spectroscopy (XPS): First Steps in Planning, Conducting and Reporting XPS Measurements. *J. Vac. Sci. Technol. Vac. Surf. Films Off. J. Am. Vac. Soc.* **2019**, *37*. https://doi.org/10.1116/1.5065501.
(309) Dupin, J.-C.; Gonbeau, D.; Vinatier, P.; Levasseur, A. Systematic XPS Studies of Metal Oxides, Hydroxides and Peroxides. *Phys. Chem. Chem. Phys.* **2000**, *2* (6), 1319–1324. https://doi.org/10.1039/A908800H.
(310) Qiu, Y.; Du, J.; Dai, C.; Dong, W.; Tao, C. Bismuth Nano-Flowers as a Highly Selective Catalyst for Electrochemical Reduction of CO2 to Formate. *J. Electrochem. Soc.* **2018**, *165* (10), H594–H600. https://doi.org/10.1149/2.0231810jes.
(311) Steele, J. A.; Lewis, R. A. In Situ Micro-Raman Studies of Laser-Induced Bismuth Oxidation Reveals Metastability of β-Bi_2O_3 Microislands. *Opt. Mater. Express* **2014**, *4* (10), 2133–2142. https://doi.org/10.1364/OME.4.002133.
(312) Ismail, M. Y. A.; Malherbe, J. B.; Odutemowo, O. S.; Njoroge, E. G.; Hlatshwayo, T. T.; Mlambo, M.; Wendler, E. Investigating the Effect of Heat Treatment on the Diffusion Behaviour of Xenon Implanted in Glassy Carbon. *Vacuum* **2018**, *149*, 74–78. https://doi.org/10.1016/j.vacuum.2017.12.021.
(313) Upare, D. P.; Yoon, S.; Lee, C. W. Nano-Structured Porous Carbon Materials for Catalysis and Energy Storage. *Korean J. Chem. Eng.* **2011**, *28* (3), 731–743. https://doi.org/10.1007/s11814-010-0460-8.
(314) Chandrasekar, M. S.; Pushpavanam, M. Pulse and Pulse Reverse Plating—Conceptual, Advantages and Applications. *Electrochimica Acta* **2008**, *53* (8), 3313–3322. https://doi.org/10.1016/j.electacta.2007.11.054.
(315) Zhu, G.; Pan, C.; Guo, W.; Chen, C.-Y.; Zhou, Y.; Yu, R.; Wang, Z. L. Triboelectric-Generator-Driven Pulse Electrodeposition for Micropatterning. *Nano Lett.* **2012**, *12* (9), 4960–4965. https://doi.org/10.1021/nl302560k.
(316) Structure and Properties of Deposits. In *Fundamentals of Electrochemical Deposition*; John Wiley & Sons, Ltd, 2006; pp 273–288. https://doi.org/10.1002/0470009403.ch16.
(317) Imaz, N.; García-Lecína, E.; Díez, J. A. Corrosion Properties of Double Layer Nickel Coatings Obtained by Pulse Plating Techniques. *Trans. IMF* **2010**, *88* (5), 256–261. https://doi.org/10.1179/002029610X12791981507767.

(318) Richoux, V.; Diliberto, S.; Boulanger, C.; Lecuire, J. M. Pulsed Electrodeposition of Bismuth Telluride Films: Influence of Pulse Parameters over Nucleation and Morphology. *Electrochimica Acta* **2007**, *52* (9), 3053–3060. https://doi.org/10.1016/j.electacta.2006.09.042.
(319) Hara, K.; Kudo, A.; Sakata, T. Electrochemical CO2 Reduction on a Glassy Carbon Electrode under High Pressure. *J. Electroanal. Chem.* **1997**, *421* (1), 1–4. https://doi.org/10.1016/S0022-0728(96)01028-5.
(320) Yukhin, Yu. M.; Mishchenko, K. V.; Daminov, A. S. Bismuth Preoxidation for Preparing Solutions of Salts. *Theor. Found. Chem. Eng.* **2017**, *51* (4), 495–502. https://doi.org/10.1134/S0040579517040303.
(321) O'Hara, M. J.; Krzysko, A. J.; Niver, C. M.; Morrison, S. S.; Owsley, S. L.; Hamlin, D. K.; Dorman, E. F.; Scott Wilbur, D. An Automated Flow System Incorporating In-Line Acid Dissolution of Bismuth Metal from a Cyclotron Irradiated Target Assembly for Use in the Isolation of Astatine-211. *Appl. Radiat. Isot.* **2017**, *122*, 202–210. https://doi.org/10.1016/j.apradiso.2017.02.001.
(322) Yang, T.-H.; Shi, Y.; Janssen, A.; Xia, Y. Surface Capping Agents and Their Roles in Shape-Controlled Synthesis of Colloidal Metal Nanocrystals. *Angew. Chem. Int. Ed.* **2020**, *59* (36), 15378–15401. https://doi.org/10.1002/anie.201911135.
(323) Ko, W.-Y.; Chen, W.-H.; Cheng, C.-Y.; Lin, K.-J. Architectural Growth of Cu Nanoparticles Through Electrodeposition. *Nanoscale Res. Lett.* **2009**, *4* (12), 1481–1485. https://doi.org/10.1007/s11671-009-9424-5.
(324) Sobha Jayakrishnan, D. 5 - Electrodeposition: The Versatile Technique for Nanomaterials. In *Corrosion Protection and Control Using Nanomaterials*; Saji, V. S., Cook, R., Eds.; Woodhead Publishing Series in Metals and Surface Engineering; Woodhead Publishing, 2012; pp 86–125. https://doi.org/10.1533/9780857095800.1.86.
(325) Niu, Z.; Li, Y. Removal and Utilization of Capping Agents in Nanocatalysis. *Chem. Mater.* **2014**, *26* (1), 72–83. https://doi.org/10.1021/cm4022479.
(326) Kwon, Y.; Kim, M. G.; Kim, Y.; Lee, Y.; Cho, J. Effect of Capping Agents in Tin Nanoparticles on Electrochemical Cycling. *Electrochem. Solid-State Lett.* **2006**, *9* (1), A34–A38. https://doi.org/10.1149/1.2138447.
(327) Barman, S. R.; Nain, A.; Jain, S.; Punjabi, N.; Mukherji, S.; Satija, J. Dendrimer as a Multifunctional Capping Agent for Metal Nanoparticles for Use in Bioimaging, Drug Delivery and Sensor Applications. *J. Mater. Chem. B* **2018**, *6* (16), 2368–2384. https://doi.org/10.1039/C7TB03344C.
(328) Radi, A.; Pradhan, D.; Sohn, Y.; Leung, K. T. Nanoscale Shape and Size Control of Cubic, Cuboctahedral, and Octahedral Cu−Cu2O Core−Shell Nanoparticles on Si(100) by One-Step, Templateless, Capping-Agent-Free Electrodeposition. *ACS Nano* **2010**, *4* (3), 1553–1560. https://doi.org/10.1021/nn100023h.
(329) Nucleation and Growth of Bismuth Thin Films onto Fluorine-Doped Tin Oxide-Coated Conducting Glass Substrates from Nitrate Solutions. *Solid State Ion.* **2004**, *167* (3–4), 273–283. https://doi.org/10.1016/j.ssi.2004.01.017.
(330) Sandnes, E.; Williams, M. E.; Bertocci, U.; Vaudin, M. D.; Stafford, G. R. Electrodeposition of Bismuth from Nitric Acid Electrolyte. *Electrochimica Acta* **2007**, *52* (21), 6221–6228. https://doi.org/10.1016/j.electacta.2007.04.002.
(331) Sun, S.; Li, H.; Xu, Z. J. Impact of Surface Area in Evaluation of Catalyst Activity. *Joule* **2018**, *2* (6), 1024–1027. https://doi.org/10.1016/j.joule.2018.05.003.
(332) Clark, E. L.; Resasco, J.; Landers, A.; Lin, J.; Chung, L.-T.; Walton, A.; Hahn, C.; Jaramillo, T. F.; Bell, A. T. Standards and Protocols for Data Acquisition and Reporting for Studies of the Electrochemical Reduction of Carbon Dioxide. *ACS Catal.* **2018**, *8* (7), 6560–6570. https://doi.org/10.1021/acscatal.8b01340.

(333) Sun, Z.; Ma, T.; Tao, H.; Fan, Q.; Han, B. Fundamentals and Challenges of Electrochemical CO2 Reduction Using Two-Dimensional Materials. *Chem* **2017**, *3* (4), 560–587. https://doi.org/10.1016/j.chempr.2017.09.009.
(334) Fukami, K.; Nakanishi, S.; Yamasaki, H.; Tada, T.; Sonoda, K.; Kamikawa, N.; Tsuji, N.; Sakaguchi, H.; Nakato, Y. General Mechanism for the Synchronization of Electrochemical Oscillations and Self-Organized Dendrite Electrodeposition of Metals with Ordered 2D and 3D Microstructures. *J. Phys. Chem. C* **2007**, *111* (3), 1150–1160. https://doi.org/10.1021/jp063462t.
(335) Cai, Y. Q.; Lu, F.; Peng, Y. Q.; Song, G. H. Preparation and Characterization of Amino or Carboxyl-Functionalized Ionic Liquids. *Chin. Chem. Lett.* **2007**, *18* (1), 21–23. https://doi.org/10.1016/j.cclet.2006.11.018.
(336) D. Neto, B. A.; Spencer, J. The Impressive Chemistry, Applications and Features of Ionic Liquids: Properties, Catalysis & Catalysts and Trends. *J. Braz. Chem. Soc.* **2012**, *23* (6), 987–1007. https://doi.org/10.1590/S0103-50532012000600002.
(337) Chen, T.-Y.; Shi, J.; Shen, F.-X.; Zhen, J.-Z.; Li, Y.-F.; Shi, F.; Yang, B.; Jia, Y.-J.; Dai, Y.-N.; Hu, Y.-Q. Selection of Low-Cost Ionic Liquid Electrocatalyst for CO2 Reduction in Propylene Carbonate/Tetrabutylammonium Perchlorate. *ChemElectroChem* **2018**, *5* (16), 2295–2300. https://doi.org/10.1002/celc.201800545.
(338) Tamura, J.; Ono, A.; Sugano, Y.; Huang, C.; Nishizawa, H.; Mikoshiba, S. Electrochemical Reduction of CO 2 to Ethylene Glycol on Imidazolium Ion-Terminated Self-Assembly Monolayer-Modified Au Electrodes in an Aqueous Solution. *Phys. Chem. Chem. Phys.* **2015**, *17* (39), 26072–26078. https://doi.org/10.1039/C5CP03028E.
(339) Iijima, G.; Kitagawa, T.; Katayama, A.; Inomata, T.; Yamaguchi, H.; Suzuki, K.; Hirata, K.; Hijikata, Y.; Ito, M.; Masuda, H. CO2 Reduction Promoted by Imidazole Supported on a Phosphonium-Type Ionic-Liquid-Modified Au Electrode at a Low Overpotential. *ACS Catal.* **2018**, *8* (3), 1990–2000. https://doi.org/10.1021/acscatal.7b03274.
(340) Tanner, E. E. L.; Batchelor-McAuley, C.; Compton, R. G. Carbon Dioxide Reduction in Room-Temperature Ionic Liquids: The Effect of the Choice of Electrode Material, Cation, and Anion. *J. Phys. Chem. C* **2016**, *120* (46), 26442–26447. https://doi.org/10.1021/acs.jpcc.6b10564.
(341) Williams, D. B. G.; Lawton, M. Drying of Organic Solvents: Quantitative Evaluation of the Efficiency of Several Desiccants. *J. Org. Chem.* **2010**, *75* (24), 8351–8354. https://doi.org/10.1021/jo101589h.
(342) Sun, L.; Ramesha, G. K.; Kamat, P. V.; Brennecke, J. F. Switching the Reaction Course of Electrochemical CO2 Reduction with Ionic Liquids. *Langmuir* **2014**, *30* (21), 6302–6308. https://doi.org/10.1021/la5009076.
(343) Xiao, L.; Johnson, K. E. Electrochemistry of 1-Butyl-3-Methyl-1H-Imidazolium Tetrafluoroborate Ionic Liquid. *J. Electrochem. Soc.* **2003**, *150* (6), E307–E311. https://doi.org/10.1149/1.1568740.
(344) Ranjan, R.; Olson, J.; Singh, P.; Lorance, E. D.; Buttry, D. A.; Gould, I. R. Reversible Electrochemical Trapping of Carbon Dioxide Using 4,4'-Bipyridine That Does Not Require Thermal Activation. *J. Phys. Chem. Lett.* **2015**, *6* (24), 4943–4946. https://doi.org/10.1021/acs.jpclett.5b02220.
(345) Tomita, Y.; Hori, Y. Electrochemical Reduction of Carbon Dioxide at a Platinum Electrode in Acetonitrile-Water Mixtures. In *Studies in Surface Science and Catalysis*; Inui, T., Anpo, M., Izui, K., Yanagida, S., Yamaguchi, T., Eds.; Advances in Chemical Conversions for Mitigating Carbon Dioxide; Elsevier, 1998; Vol. 114, pp 581–584. https://doi.org/10.1016/S0167-2991(98)80826-4.
(346) Zhao, S.-F.; Wu, L.-X.; Wang, H.; Lu, J.-X.; Bond, A. M.; Zhang, J. A Unique Proton Coupled Electron Transfer Pathway for Electrochemical Reduction of Acetophenone in the Ionic

Liquid [BMIM][BF4] under a Carbon Dioxide Atmosphere. *Green Chem.* **2011**, *13* (12), 3461–3468. https://doi.org/10.1039/C1GC15929A.
(347) de Robillard, G.; Devillers, C. H.; Kunz, D.; Cattey, H.; Digard, E.; Andrieu, J. Electrosynthesis of Imidazolium Carboxylates. *Org. Lett.* **2013**, *15* (17), 4410–4413. https://doi.org/10.1021/ol401949f.
(348) Bourrez, M.; Molton, F.; Chardon-Noblat, S.; Deronzier, A. [Mn(Bipyridyl)(CO)3Br]: An Abundant Metal Carbonyl Complex as Efficient Electrocatalyst for CO2 Reduction. *Angew. Chem. Int. Ed.* **2011**, *50* (42), 9903–9906. https://doi.org/10.1002/anie.201103616.
(349) Rosen, B. A.; Zhu, W.; Kaul, G.; Salehi-Khojin, A.; Masel, R. I. Water Enhancement of CO2 Conversion on Silver in 1-Ethyl-3-Methylimidazolium Tetrafluoroborate. *J. Electrochem. Soc.* **2013**, *160* (2), H138–H141. https://doi.org/10.1149/2.004303jes.
(350) Cuadrado-Prado, S.; Domínguez-Pérez, M.; Rilo, E.; García-Garabal, S.; Segade, L.; Franjo, C.; Cabeza, O. Experimental Measurement of the Hygroscopic Grade on Eight Imidazolium Based Ionic Liquids. *Fluid Phase Equilibria* **2009**, *278* (1), 36–40. https://doi.org/10.1016/j.fluid.2008.12.008.
(351) Perry, D. A.; Cordova, J. S.; Schiefer, E. M.; Chen, T.-Y.; Razer, T. M.; Biris, A. S. Evidence for Charge Transfer and Impact of Solvent Polar Properties on Aminobenzonitrile Adsorption on Silver Nanostructures. *J. Phys. Chem. C* **2012**, *116* (7), 4584–4593. https://doi.org/10.1021/jp208489w.
(352) Jin, X.; Zhang, L.; Wu, N.; Zhang, J.; Hu, Y.; Wang, Z.; Zhuang, L. Imidazolium Ions with an Alcohol Substituent for Enhanced Electrocatalytic Reduction of CO2. *ChemSusChem* **2017**. https://doi.org/10.1002/cssc.201701673.
(353) Costentin, C.; Drouet, S.; Robert, M.; Savéant, J.-M. A Local Proton Source Enhances CO2 Electroreduction to CO by a Molecular Fe Catalyst. *Science* **2012**, *338* (6103), 90–94. https://doi.org/10.1126/science.1224581.
(354) Agarwal, J.; Shaw, T. W.; Schaefer, H. F.; Bocarsly, A. B. Design of a Catalytic Active Site for Electrochemical CO2 Reduction with Mn(I)-Tricarbonyl Species. *Inorg. Chem.* **2015**, *54* (11), 5285–5294. https://doi.org/10.1021/acs.inorgchem.5b00233.
(355) Neri, G.; Aldous, I. M.; Walsh, J. J.; Hardwick, L. J.; Cowan, A. J. A Highly Active Nickel Electrocatalyst Shows Excellent Selectivity for CO2 Reduction in Acidic Media. *Chem. Sci.* **2016**, *7* (2), 1521–1526. https://doi.org/10.1039/C5SC03225C.
(356) Chambers, R. D.; Clark, H. C.; Reeves, L. W.; Willis, C. J. The Fluorine Magnetic Resonance in the Ions [Bf4]− and [Bf3cf3]−. *Can. J. Chem.* **1961**, *39* (1), 258–259. https://doi.org/10.1139/v61-029.
(357) Vasdev, R. A. S.; Findlay, J. A.; Garden, A. L.; Crowley, J. D. Redox Active [Pd2L4]4+ Cages Constructed from Rotationally Flexible 1,1′-Disubstituted Ferrocene Ligands. *Chem Commun* **2019**, *55* (52), 7506–7509. https://doi.org/10.1039/C9CC03321A.
(358) Lesimple, A.; Mamer, O.; Miao, W.; Chan, T. H. Electrospray Mass Spectral Fragmentation Study of N,N′-Disubstituted Imidazolium Ionic Liquids. *J. Am. Soc. Mass Spectrom.* **2006**, *17* (1), 85–95. https://doi.org/10.1016/j.jasms.2005.09.002.
(359) Nousiainen, M.; Tolstogouzov, A.; Holopainen, S.; Jänis, J.; Sillanpää, M. Study of Imidazolium And Pyrrolidinium Ionic Liquids By Ion Mobility Spectrometry And Electrospray Ionization Mass Spectrometry. *Rapid Commun. Mass Spectrom.* **2011**, *25* (17), 2565–2569. https://doi.org/10.1002/rcm.5143.
(360) Ramezani, S.; Jahani, R.; Mashhadizadeh, M. H.; Shahbazi, S.; Jalilian, S. A Novel Ionic Liquid/Polyoxomolybdate Based Sensor for Ultra-High Sensitive Monitoring of Al(III): Optimization by Taguchi Statistical Design. *J. Electroanal. Chem.* **2018**, *814*, 7–19. https://doi.org/10.1016/j.jelechem.2018.02.041.
(361) Louise Mojet, B.; Dalgaard Ebbesen, S.; Lefferts, L. Light at the Interface: The Potential of Attenuated Total Reflection Infrared Spectroscopy for Understanding Heterogeneous

Catalysis in Water. *Chem. Soc. Rev.* **2010**, *39* (12), 4643–4655. https://doi.org/10.1039/C0CS00014K.
(362) McIntosh, I. M.; Nichols, A. R. L.; Tani, K.; Llewellin, E. W. Accounting for the Species-Dependence of the 3500 Cm−1 H2Ot Infrared Molar Absorptivity Coefficient: Implications for Hydrated Volcanic Glasses. *Am. Mineral.* **2017**, *102* (8), 1677–1689. https://doi.org/10.2138/am-2017-5952CCBY.
(363) Reche, I.; Gallardo, I.; Guirado, G. Electrochemical Studies of CO2 in Imidazolium Ionic Liquids Using Silver as a Working Electrode: A Suitable Approach for Determining Diffusion Coefficients, Solubility Values, and Electrocatalytic Effects. *RSC Adv.* **2014**, *4* (110), 65176–65183. https://doi.org/10.1039/C4RA11297K.
(364) Shi, J.; Shi, F.; Song, N.; Liu, J.-X.; Yang, X.-K.; Jia, Y.-J.; Xiao, Z.-W.; Du, P. A Novel Electrolysis Cell for CO2 Reduction to CO in Ionic Liquid/Organic Solvent Electrolyte. *J. Power Sources* **2014**, *259*, 50–53. https://doi.org/10.1016/j.jpowsour.2014.02.072.
(365) Zhou, F.; Liu, S.; Yang, B.; Wang, P.; Alshammari, A. S.; Deng, Y. Highly Selective Electrocatalytic Reduction of Carbon Dioxide to Carbon Monoxide on Silver Electrode with Aqueous Ionic Liquids. *Electrochem. Commun.* **2014**, *46*, 103–106. https://doi.org/10.1016/j.elecom.2014.06.023.
(366) Monteiro, M. C. O.; Koper, M. T. M. Measuring Local PH in Electrochemistry. *Curr. Opin. Electrochem.* **2021**, *25*, 100649. https://doi.org/10.1016/j.coelec.2020.100649.
(367) Bruice, P. Y. *Organic Chemistry By Bruice - International Edition*; Pearson, 2013.
(368) Krężel, A.; Bal, W. A Formula for Correlating PKa Values Determined in D2O and H2O. *J. Inorg. Biochem.* **2004**, *98* (1), 161–166. https://doi.org/10.1016/j.jinorgbio.2003.10.001.
(369) Oomens, J.; Steill, J. D. Free Carboxylate Stretching Modes. *J. Phys. Chem. A* **2008**, *112* (15), 3281–3283. https://doi.org/10.1021/jp801806e.
(370) Roeges, N. P. G. *Guide to the Complete Interpretation of Infrared Spectra of Organic Structures*; Wiley, 1994.
(371) MSDS - 151882 https://www.sigmaaldrich.com/MSDS/MSDS/DisplayMSDSPage.do?country=IE&language=en&productNumber=151882&brand=ALDRICH&PageToGoToURL=https%3A%2F%2Fwww.sigmaaldrich.com%2Fcatalog%2Fproduct%2Faldrich%2F151882%3Flang%3Den (accessed 2019 -06 -22).
(372) Kim, D.; Resasco, J.; Yu, Y.; Asiri, A. M.; Yang, P. Synergistic Geometric and Electronic Effects for Electrochemical Reduction of Carbon Dioxide Using Gold–Copper Bimetallic Nanoparticles. *Nat. Commun.* **2014**, *5* (1), 4948. https://doi.org/10.1038/ncomms5948.
(373) Gonçalves, M. R.; Gomes, A.; Condeço, J.; Fernandes, R.; Pardal, T.; Sequeira, C. A. C.; Branco, J. B. Selective Electrochemical Conversion of CO2 to C2 Hydrocarbons. *Energy Convers. Manag.* **2010**, *51* (1), 30–32. https://doi.org/10.1016/j.enconman.2009.08.002.
(374) Qiao, J.; Jiang, P.; Liu, J.; Zhang, J. Formation of Cu Nanostructured Electrode Surfaces by an Annealing–Electroreduction Procedure to Achieve High-Efficiency CO2 Electroreduction. *Electrochem. Commun.* **2014**, *38*, 8–11. https://doi.org/10.1016/j.elecom.2013.10.023.
(375) Robert, M.; Daasbjerg, K.; Constentin, C. *Carbon Dioxide Electrochemistry*; Royal Society of Chemistry, 2020.
(376) Lee, C. W.; Cho, N. H.; Im, S. W.; Jee, M. S.; Hwang, Y. J.; Min, B. K.; Nam, K. T. New Challenges of Electrokinetic Studies in Investigating the Reaction Mechanism of Electrochemical CO2 Reduction. *J. Mater. Chem. A* **2018**, *6* (29), 14043–14057. https://doi.org/10.1039/C8TA03480J.
(377) Sandford, C.; Edwards, M. A.; Klunder, K. J.; Hickey, D. P.; Li, M.; Barman, K.; Sigman, M. S.; White, H. S.; Minteer, S. D. A Synthetic Chemist's Guide to Electroanalytical Tools for Studying Reaction Mechanisms. *Chem. Sci.* **2019**, *10* (26), 6404–6422. https://doi.org/10.1039/C9SC01545K.

(378) Maiti, A. Theoretical Screening of Ionic Liquid Solvents for Carbon Capture. *ChemSusChem* **2009**, *2* (7), 628–631. https://doi.org/10.1002/cssc.200900086.
(379) Kinetic Analysis on the Role of Bicarbonate in Carbon Dioxide Electroreduction at Immobilized Cobalt Phthalocyanine | ACS Catalysis https://pubs.acs.org/doi/10.1021/acscatal.9b05272 (accessed 2021 -03 -17).
(380) Wuttig, A.; Yoon, Y.; Ryu, J.; Surendranath, Y. Bicarbonate Is Not a General Acid in Au-Catalyzed CO2 Electroreduction. *J. Am. Chem. Soc.* **2017**, *139* (47), 17109–17113. https://doi.org/10.1021/jacs.7b08345.
(381) Garg, S.; Li, M.; Rufford, T. E.; Ge, L.; Rudolph, V.; Knibbe, R.; Konarova, M.; Wang, G. G. X. Catalyst–Electrolyte Interactions in Aqueous Reline Solutions for Highly Selective Electrochemical CO2 Reduction. *ChemSusChem* **2020**, *13* (2), 304–311. https://doi.org/10.1002/cssc.201902433.
(382) Palm, U.; Damaskin, B.; Salve, M.; Tenno, T. Specific Adsorption of Cations and Hydrogen Overvoltage on Bismuth. *J. Electroanal. Chem. Interfacial Electrochem.* **1977**, *84* (2), 333–338. https://doi.org/10.1016/S0022-0728(77)80383-5.
(383) Yoon, S. H.; Piao, G.; Park, H.; Elbashir, N. O.; Han, D. S. Theoretical Insight into Effect of Cation–Anion Pairs on CO2 Reduction on Bismuth Electrocatalysts. *Appl. Surf. Sci.* **2020**, *532*, 147459. https://doi.org/10.1016/j.apsusc.2020.147459.
(384) Piao, G.; Yoon, S. H.; Han, D. S.; Park, H. Ion-Enhanced Conversion of CO2 into Formate on Porous Dendritic Bismuth Electrodes with High Efficiency and Durability. *ChemSusChem* **2020**, *13* (4), 698–706. https://doi.org/10.1002/cssc.201902581.
(385) Vivier, V.; Régis, A.; Sagon, G.; Nedelec, J.-Y.; Yu, L. T.; Cachet-Vivier, C. Cyclic Voltammetry Study of Bismuth Oxide Bi2O3 Powder by Means of a Cavity Microelectrode Coupled with Raman Microspectrometry. *Electrochimica Acta* **2001**, *46* (6), 907–914. https://doi.org/10.1016/S0013-4686(00)00677-0.
(386) Ammeloot, F.; Millet, B.; Fiaud, C.; Robbiola, L.; Sutter, E. Characterization of Naturally Grown Oxide Layers on Copper with and without Benzotriazole by Electrochemical and Photoelectrochemical Measurements. In *METAL 95: International conference on metals conservation*; MacLeod, I., Pennec, S., Robbiola, L., Eds.; James and James Science Publisher, London: Semur-en-Auxois, France, 1995; pp 109–117.
(387) Deng, P.; Wang, H.; Qi, R.; Zhu, J.; Chen, S.; Yang, F.; Zhou, L.; Qi, K.; Liu, H.; Xia, B. Y. Bismuth Oxides with Enhanced Bismuth–Oxygen Structure for Efficient Electrochemical Reduction of Carbon Dioxide to Formate. *ACS Catal.* **2020**, *10* (1), 743–750. https://doi.org/10.1021/acscatal.9b04043.
(388) Front Matter. In *Cooperative Catalysis*; John Wiley & Sons, Ltd, 2015; p I–XXI. https://doi.org/10.1002/9783527681020.fmatter.
(389) Tang, J.; Shen, Y.; Radosz, M.; Sun, W. Isothermal Carbon Dioxide Sorption in Poly(Ionic Liquid)s. *Ind. Eng. Chem. Res.* **2009**, *48* (20), 9113–9118. https://doi.org/10.1021/ie900292p.
(390) Blanchard, L. A.; Gu, Z.; Brennecke, J. F. High-Pressure Phase Behavior of Ionic Liquid/CO2 Systems. *J. Phys. Chem. B* **2001**, *105* (12), 2437–2444. https://doi.org/10.1021/jp003309d.
(391) Cadena, C.; Anthony, J. L.; Shah, J. K.; Morrow, T. I.; Brennecke, J. F.; Maginn, E. J. Why Is CO2 So Soluble in Imidazolium-Based Ionic Liquids? *J. Am. Chem. Soc.* **2004**, *126* (16), 5300–5308. https://doi.org/10.1021/ja039615x.
(392) Husson-Borg, P.; Majer, V.; Costa Gomes, M. F. Solubilities of Oxygen and Carbon Dioxide in Butyl Methyl Imidazolium Tetrafluoroborate as a Function of Temperature and at Pressures Close to Atmospheric Pressure. *J. Chem. Eng. Data* **2003**, *48* (3), 480–485. https://doi.org/10.1021/je0256277.

(393) Pérez-Salado Kamps, Á.; Tuma, D.; Xia, J.; Maurer, G. Solubility of CO2 in the Ionic Liquid [Bmim][PF6]. *J. Chem. Eng. Data* **2003**, *48* (3), 746–749. https://doi.org/10.1021/je034023f.
(394) Anthony, J. L.; Maginn, E. J.; Brennecke, J. F. Solubilities and Thermodynamic Properties of Gases in the Ionic Liquid 1-n-Butyl-3-Methylimidazolium Hexafluorophosphate. *J. Phys. Chem. B* **2002**, *106* (29), 7315–7320. https://doi.org/10.1021/jp020631a.
(395) Kauffman, D. R.; Alfonso, D.; Matranga, C.; Qian, H.; Jin, R. Experimental and Computational Investigation of Au25 Clusters and CO2: A Unique Interaction and Enhanced Electrocatalytic Activity. *J. Am. Chem. Soc.* **2012**, *134* (24), 10237–10243. https://doi.org/10.1021/ja303259q.
(396) Maniam, K. K.; Chetty, R. Electrochemical Synthesis of Palladium Dendrites on Carbon Support and Their Enhanced Electrocatalytic Activity towards Formic Acid Oxidation. *J. Appl. Electrochem.* **2015**, *45* (9), 953–962. https://doi.org/10.1007/s10800-015-0860-x.
(397) Imura, Y.; Kataoka, H.; Saito, H.; Minakawa, M.; Morita-Imura, C.; Kawai, T. Morphological Stability and Catalytic Performance of Supported and Unsupported Dendritic Gold Nanowire Catalysts. *ChemistrySelect* **2019**, *4* (34), 9908–9914. https://doi.org/10.1002/slct.201902594.
(398) Bishop, G. W.; Ahiadu, B. K.; Smith, J. L.; Patterson, J. D. Use of Redox Probes for Characterization of Layer-by-Layer Gold Nanoparticle-Modified Screen-Printed Carbon Electrodes. *J. Electrochem. Soc.* **2016**, *164* (2), B23. https://doi.org/10.1149/2.0431702jes.
(399) Renedo, O. D.; Alonso-Lomillo, M. A.; Martínez, M. J. A. Recent Developments in the Field of Screen-Printed Electrodes and Their Related Applications. *Talanta* **2007**, *73* (2), 202–219. https://doi.org/10.1016/j.talanta.2007.03.050.
(400) Kruusma, J.; Banks, C. E.; Compton, R. G. Mercury-Free Sono-Electroanalytical Detection of Lead in Human Blood by Use of Bismuth-Film-Modified Boron-Doped Diamond Electrodes. *Anal. Bioanal. Chem.* **2004**, *379* (4), 700–706. https://doi.org/10.1007/s00216-004-2639-5.
(401) Liu, X.; Yao, Y.; Ying, Y.; Ping, J. Recent Advances in Nanomaterial-Enabled Screen-Printed Electrochemical Sensors for Heavy Metal Detection. *TrAC Trends Anal. Chem.* **2019**, *115*, 187–202. https://doi.org/10.1016/j.trac.2019.03.021.
(402) Solná, R.; Sapelnikova, S.; Skládal, P.; Winther-Nielsen, M.; Carlsson, C.; Emnéus, J.; Ruzgas, T. Multienzyme Electrochemical Array Sensor for Determination of Phenols and Pesticides. *Talanta* **2005**, *65* (2), 349–357. https://doi.org/10.1016/j.talanta.2004.07.005.
(403) Díaz-González, M.; González-García, M. B.; Costa-García, A. Detection of Pneumolysin in Human Urine Using an Immunosensor on Screen-Printed Carbon Electrodes. *Sens. Actuators B Chem.* **2006**, *113* (2), 1005–1011. https://doi.org/10.1016/j.snb.2005.04.019.
(404) Rao, V. K.; Rai, G. P.; Agarwal, G. S.; Suresh, S. Amperometric Immunosensor for Detection of Antibodies of Salmonella Typhi in Patient Serum. *Anal. Chim. Acta* **2005**, *531* (2), 173–177. https://doi.org/10.1016/j.aca.2004.10.015.
(405) Forster, R. J.; Cumba, L. R. 29 - Optimizing Glucose Sensing for Diabetes Monitoring. In *Bioelectronics and Medical Devices*; Pal, K., Kraatz, H.-B., Khasnobish, A., Bag, S., Banerjee, I., Kuruganti, U., Eds.; Woodhead Publishing Series in Electronic and Optical Materials; Woodhead Publishing, 2019; pp 765–778. https://doi.org/10.1016/B978-0-08-102420-1.00036-4.
(406) Ping, J.; Wang, Y.; Fan, K.; Wu, J.; Ying, Y. Direct Electrochemical Reduction of Graphene Oxide on Ionic Liquid Doped Screen-Printed Electrode and Its Electrochemical Biosensing Application. *Biosens. Bioelectron.* **2011**, *28* (1), 204–209. https://doi.org/10.1016/j.bios.2011.07.018.
(407) Serrano, N.; Alberich, A.; Díaz-Cruz, J. M.; Ariño, C.; Esteban, M. Coating Methods, Modifiers and Applications of Bismuth Screen-Printed Electrodes. *TrAC Trends Anal. Chem.* **2013**, *46*, 15–29. https://doi.org/10.1016/j.trac.2013.01.012.

(408) Kadara, R. O.; Jenkinson, N.; Banks, C. E. Characterisation of Commercially Available Electrochemical Sensing Platforms. *Sens. Actuators B Chem.* **2009**, *138* (2), 556–562. https://doi.org/10.1016/j.snb.2009.01.044.
(409) Niu, P.; Fernández-Sánchez, C.; Gich, M.; Navarro-Hernández, C.; Fanjul-Bolado, P.; Roig, A. Screen-Printed Electrodes Made of a Bismuth Nanoparticle Porous Carbon Nanocomposite Applied to the Determination of Heavy Metal Ions. *Microchim. Acta* **2016**, *183* (2), 617–623. https://doi.org/10.1007/s00604-015-1684-4.
(410) Osborne, M. D.; Seddon, B. J.; Dryfe, R. A. W.; Lagger, G.; Loyall, U.; Schäfer, H.; Girault, H. H. Excimer Laser-Induced Electrochemical Activity in Carbon Ink Films. *J. Electroanal. Chem.* **1996**, *417* (1), 5–15. https://doi.org/10.1016/S0022-0728(96)04781-X.
(411) Martín-Yerga, D.; González-García, M. B.; Costa-García, A. Use of Nanohybrid Materials as Electrochemical Transducers for Mercury Sensors. *Sens. Actuators B Chem.* **2012**, *165* (1), 143–150. https://doi.org/10.1016/j.snb.2012.02.031.
(412) Zittel, H. E.; Miller, F. J. A Glassy-Carbon Electrode for Voltammetry. *Anal. Chem.* **1965**, *37* (2), 200–203. https://doi.org/10.1021/ac60221a006.
(413) Longinotti, M. P.; Corti, H. R. Diffusion of Ferrocene Methanol in Super-Cooled Aqueous Solutions Using Cylindrical Microelectrodes. *Electrochem. Commun.* **2007**, *9* (7), 1444–1450. https://doi.org/10.1016/j.elecom.2007.02.003.
(414) Sun, P.; Mirkin, M. V. Kinetics of Electron-Transfer Reactions at Nanoelectrodes. *Anal. Chem.* **2006**, *78* (18), 6526–6534. https://doi.org/10.1021/ac060924q.
(415) O'Mullane, A. P.; Zhang, J.; Brajter-Toth, A.; Bond, A. M. Higher Harmonic Large-Amplitude Fourier Transformed Alternating Current Voltammetry: Analytical Attributes Derived from Studies of the Oxidation of Ferrocenemethanol and Uric Acid at a Glassy Carbon Electrode. *Anal. Chem.* **2008**, *80* (12), 4614–4626. https://doi.org/10.1021/ac0715221.
(416) Laschi, S.; Palchetti, I.; Marrazza, G.; Mascini, M. Development of Disposable Low Density Screen-Printed Electrode Arrays for Simultaneous Electrochemical Measurements of the Hybridisation Reaction. *J. Electroanal. Chem.* **2006**, *593* (1), 211–218. https://doi.org/10.1016/j.jelechem.2006.04.015.
(417) Cumba, L. R.; Camisasca, A.; Giordani, S.; Forster, R. J. Electrochemical Properties of Screen-Printed Carbon Nano-Onion Electrodes. *Molecules* **2020**, *25* (17), 3884. https://doi.org/10.3390/molecules25173884.
(418) Choudry, N. A.; Kampouris, D. K.; Kadara, R. O.; Banks, C. E. Disposable Highly Ordered Pyrolytic Graphite-like Electrodes: Tailoring the Electrochemical Reactivity of Screen Printed Electrodes. *Electrochem. Commun.* **2010**, *12* (1), 6–9. https://doi.org/10.1016/j.elecom.2009.10.021.
(419) Montiel, M. A.; Iniesta, J.; Gross, A. J.; Marken, F. Dual-Plate Gold-Gold Microtrench Electrodes for Generator-Collector Voltammetry without Supporting Electrolyte. *Electrochimica Acta* **2017**, *224*, 487–495. https://doi.org/10.1016/j.electacta.2016.11.103.
(420) P. Randviir, E.; C. Brownson, D. A.; P. Metters, J.; O. Kadara, R.; E. Banks, C. The Fabrication, Characterisation and Electrochemical Investigation of Screen-Printed Graphene Electrodes. *Phys. Chem. Chem. Phys.* **2014**, *16* (10), 4598–4611. https://doi.org/10.1039/C3CP55435J.
(421) Fletcher, S. Screen-Printed Carbon Electrodes. In *Electrochemistry of Carbon Electrodes*; John Wiley & Sons, Ltd, 2015; pp 425–444. https://doi.org/10.1002/9783527697489.ch12.

Appendix A

Chapter 3

3.3.4 Scan rate studies

3.3.4.1 $KHCO_3$

The graphs plotted for the N_2-saturated solutions are presented in Figure A.3.1. The CVs curves for the Bi electrodes in $KHCO_3$ (see Figure A.3.1a) presented one peak in the anodic region compared to two peaks in Na_2SO_4. In addition, the current after the anodic peak is constant, suggesting the insignificant Bi_2O_3 dissolution and successive crystallisation on the surface of the Bi^{3+} species. This can be due to the higher pH of $KHCO_3$ (pH=8.84) in comparison with Na_2SO_4 (pH= 6.06). The plot of i_p versus the square root of the scan rate presented a linear trend (Figure A.3.1b), suggesting that the reduction and the oxidation of bismuth occurs under diffusion, as observed in Na_2SO_4 solutions. This means that the electrolyte does not influence the mechanism of the processes. This was expected, as the reduction and oxidation reactions are under solid-state diffusion[176,185]. In particular, the species diffusing are the Bi^{3+} ions, during the oxidation and the electrons through the metal oxide layer, for the reduction.

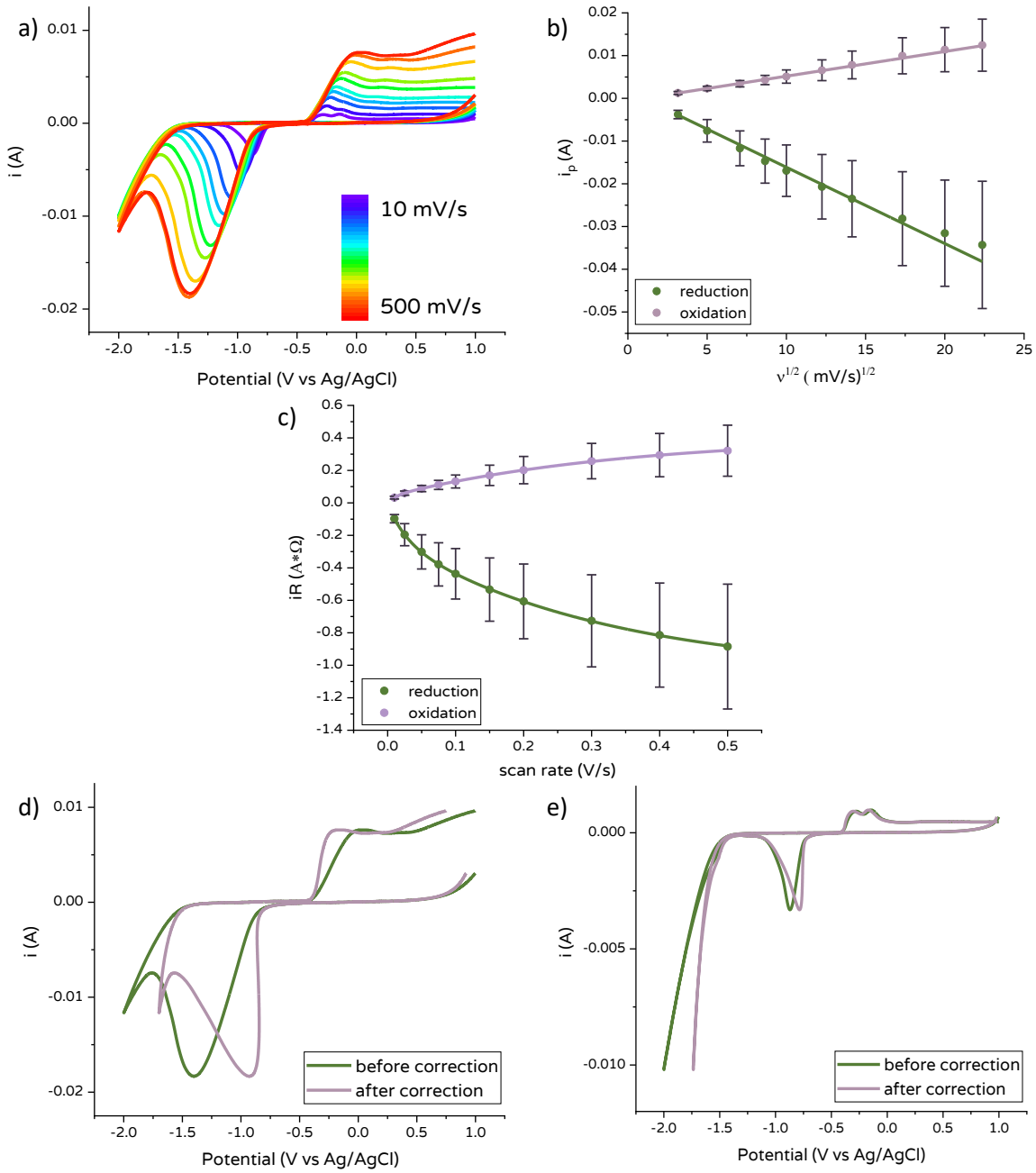

Figure A.3.1: a) scan rate study for the formation and reduction of Bi oxide in 0.1 M $KHCO_3$ under N_2; b) i_p for both cathodic and anodic processes vs square root of scan rate obtained from the scan rate study showed in a; c) iR drop vs scan rate for both reduction (green) and oxidation (purple) calculated at i_p. For fitting equation see equation A.1; CVs for the reduction an oxidation of Bi in 0.1 M $KHCO_3$ under N_2 atmosphere as recorded (green line) and after mathematical correction for iR drop acquired at d) 500 mV/s and e) 10 mV/s

The CEf was calculated for the CVs obtained at 10 mV/s and 500 mV/s. As can be seen in Table A.3.1, the CEf for 10 mV/s is higher than one, as observed in Na_2SO_4 solutions, suggesting the presence of an additional process during the cathodic scan. In contrast, the CEf at 500 mV/s is smaller than one, meaning that higher charge was passed during the anodic scan. This can be due to the presence of an additional process during the anodic scan or the slower kinetics of the reduction reaction. It has been demonstrated before that a small amount of HCO_3^- can be reduced to formate if enough negative potential is applied[99] and the oxidation of formate on Pt electrodes

modified with Bi.[272,273] It is therefore possible that the formate is oxidised back to CO_2 during the anodic scan. However, the possibility of slower kinetics of the reduction reaction seems more likely.

Table A.3.1: current efficiencies, cathodic and anodic charges calculated integrating the area under the cathodic and anodic peaks for CVs performed with Bi cylinder electrodes at 10 and 500 mV/s. Electrolyte: N_2-saturated $KHCO_3$

Scan rate [mV/s]	Q_A [mC]	Q_C [mC]	CEf
10	47.2	55.1	1.2
500	15.5	11.7	0.75

The iR drop was calculated for all the scan rate values applied during the scan rate study and its variation as a function of the scan rate is shown in Figure A.3.1c. As observed for Na_2SO_4 solutions, the iR drop increased exponentially when the scan rate is increased (see Equation A.1, for the fitting equation). The resistance of the system (see Table A.3.2) is quite similar to the one observed in Na_2SO_4, suggesting that the nature of the electrolyte does not influence it.

Table A.3.2: Resistance of the interface electrode solution for Bi cylinders in 0.1 M $KHCO_3$

gas	Resistance [Ω][a]
N_2	25.8
CO_2	24.4

[a] calculated at open circuit potential (OPC)

The influence of the iR drop on the peak to peak separation at different scan rates can be seen in Figure A.3.1d and f, in which the CVs before and after mathematical iR drop correction are shown. As expected, a higher peak to peak separation is present at 500 mV/s than at 10 mV/s. The values of ΔE_p before and after iR drop correction at all the scan rates are shown in Table A.3.3. The iR corrected values for the experiments in $KHCO_3$ are smaller than Na_2SO_4 for scan rates higher than 50 mV/s. However, it is important to highlight that the experimental error at high scan rates for the corrected values in Na_2SO_4 is quite high, therefore a quantitative comparison cannot be performed.

Table A.3.3: ΔE_p for the oxidation and reduction of Bismuth calculated at different scan rate values before and after mathematical correction of the CVs. The experiments were performed in 0.1 M $KHCO_3$ first under N_2 and then under CO_2

scan rate [mV/s]	ΔE_p before correction [V]		ΔE_p after correction [V]	
	N_2	CO_2	N_2	CO_2
10	0.55 ± 0.03	0.75 ± 0.03	0.41 ± 0.07	0.59 ± 0.02
25	0.67 ± 0.04	0.9 ± 0.1	0.4 ± 0.1	0.62 ± 0.05
50	0.78 ± 0.05	1.14 ± 0.09	0.4 ± 0.2	0.68 ± 0.08
75	0.86 ± 0.06	1.3 ± 0.1	0.4 ± 0.2	0.70 ± 0.09
100	0.92 ± 0.06	1.3 ± 0.1	0.3 ± 0.2	0.7 ± 0.1
150	1.03 ± 0.07	1.5 ± 0.1	0.3 ± 0.3	0.7 ± 0.1
200	1.12 ± 0.06	1.54 ± 0.09	0.3 ± 0.3	0.7 ± 0.1
300	1.27 ± 0.03	1.69 ± 0.07	0.3 ± 0.4	0.8 ± 0.2
400	1.37 ± 0.03	1.80 ± 0.04	0.2 ± 0.5	0.8 ± 0.2
500	1.43 ± 0.03	1.84 ± 0.08	0.2 ± 0.5	0.8 ± 0.3

The same set of experiments were performed in CO_2-saturated $KHCO_3$ solutions and the results are shown in Figure A.3.2 (see scheme in Figure 3.11).

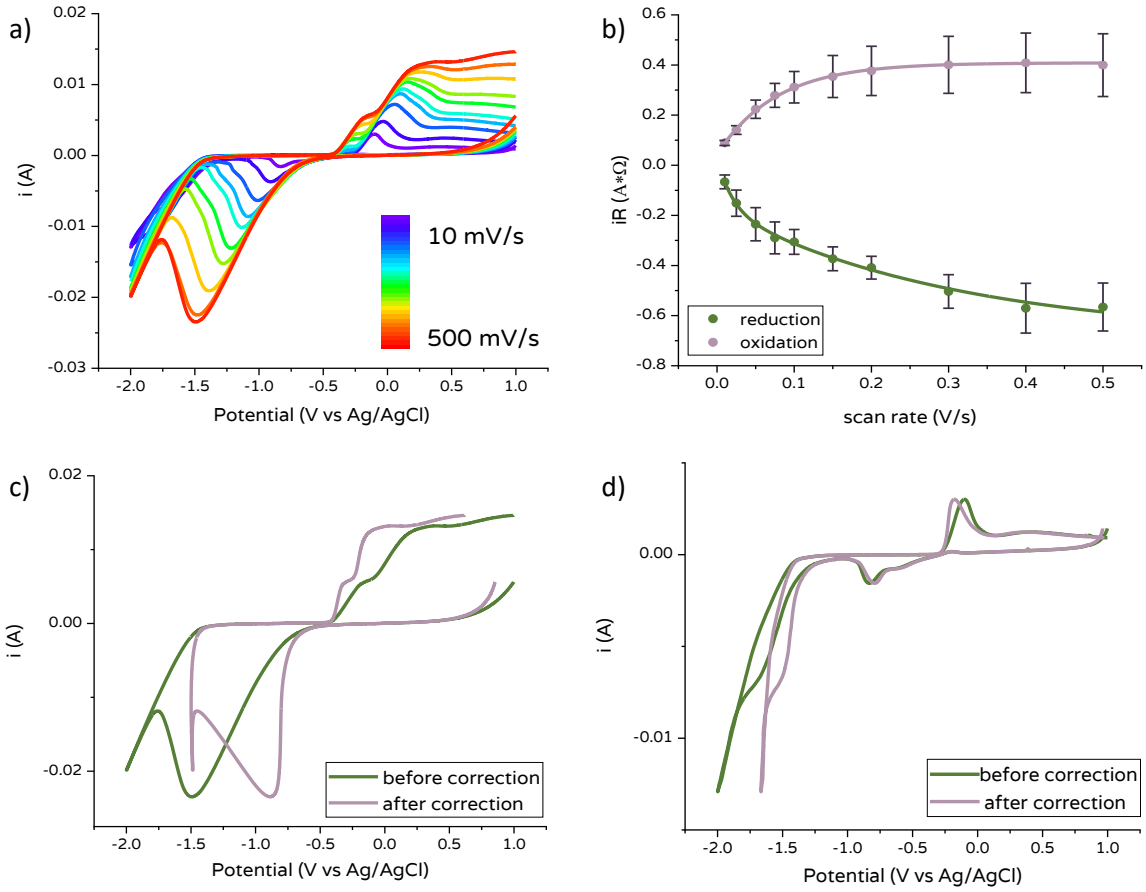

Figure A.3.2: a) scan rate study for the formation and reduction of Bi oxide in 0.1 M $KHCO_3$ under CO_2; b) iR drop vs scan rate for both reduction (green) and oxidation (purple) calculated at i_p. For fitting equation see equation A.1; CVs for the reduction an oxidation of Bi in 0.1 M $KHCO_3$ under CO_2 atmosphere as recorded (green line) and after mathematical correction for iR drop acquired at c) 500 mV/s and d) 10 mV/s

Figure A.3.2a shows that the anodic section of the CVs presented two peaks for scan rates higher than 25 mV/s. The presence of two peaks in the anodic sweep was also observed in Na_2SO_4 under CO_2, but not under N_2, suggesting that the feature may be connected with the presence of CO_2 in solution. At low scan rates, the cathodic peak presented a small second peak that is not completely resolved (see Figure A.3.2d), as observed in CO_2-saturated Na_2SO_4 solutions. Therefore, this peak cannot be attributed to the formation of Bi-sulphate species, suggesting that the process happening during the cathodic sweep is distinct. The formation of sub-carbonate species ($(BiO)_2CO_3$) at OCP has recently been demonstrated by Dutta et al.[106] using in operando Raman spectroscopy on Bi_2O_3 foam electrodes immersed in 0.5 M $KHCO_3$. However, the authors observed sub-carbonate species in both Ar and CO_2-saturated solutions, suggesting that if these species were present on the surface of the Bi cylinders and that the unresolved peak was due to the reduction of these species, the second peak will be also observed in CVs acquired in N_2-saturated solutions. The change in the

surface composition after the scan rate study was clear with visual observation of the electrode (see Figure A.3.3). This reinforces the need for surface composition measurements *in-situ* and *ex-situ* for the Bi cylinders.

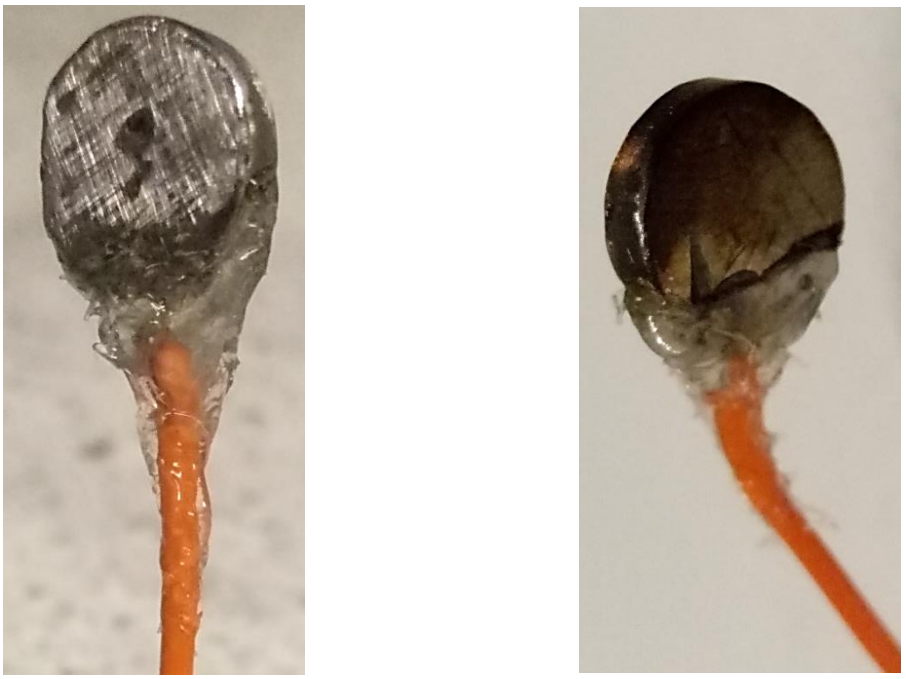

Figure A.3.3: Bi cylinder electrodes before (left) and after (right) scan rate study experiments in N_2-satured $KHCO_3$ solution. The change in colour of the right electrode suggests a change in the composition of the surface after the experiments

The CEf were calculated for the CVs obtained at 10 and 500 mV/s (see Table A.3.4). In contrast to the CEfs obtained for the other three systems, at 10 mV/s, the CEf was smaller than one (0.28), with Q_A being 3.5x times higher than Q_C. This can be due to an additional process during the anodic scan or the impossibility of reducing the Bi oxide during the cathodic scan. Considering that no additional peaks were observed in the anodic scan, it is improbable that another process occurs during the anodic sweep. It is also improbable that the area of the Bi film increased enough during the cathodic scan to justify such a significant increase in the charge value, considering that, if this was the case, an increase should be observed in the N_2-saturated solutions. It is therefore more probable that the reduction kinetics were slowed down by the presence of CO_2. Similar results were obtained at 500 mV/s, with a Q_A 1.5x times higher than Q_C.

Table A.3.4: current efficiencies, cathodic and anodic charges calculated integrating the area under the cathodic and anodic peaks for CVs performed with Bi cylinder electrodes at 10 and 500 mV/s. Electrolyte: CO_2-saturated $KHCO_3$

Scan rate [mV/s]	Q_A [mC]	Q_C [mC]	CEf
10	112.3	31.7	0.28
500	25.0	16.5	0.66

The iR drop increased significantly with increasing scan rate as was seen with the three other systems (see Figure A.3.2b). On the other hand, the current peak as a function of the scan rate differs from the other systems (see Figure A.3.4a). In particular, the anodic current did not follow a linear trend, especially at high scan rates. The fit for the cathodic branch presented an R^2 value of 0.977, that increased to 0.986 when the last point (i_p for scan rate equal to 500 mV/s) was removed from the series (see Figure A.3.4b). However, no difference in the value of R^2 was observed when the last point was removed from the anodic data set (R^2 = 0.921). To exclude the possibility of a change in the main controlling process for the oxidation of Bi, the i_p values were plotted as a function of the scan rate (Figure A.3.4c). Neither the cathodic nor the anodic data set exhibits a linear trend, suggesting that the mechanism of oxidation/reduction of Bi is not controlled by adsorption. A R^2 equal to 0.983 was obtained when the anodic currents values were plotted for scan rates not higher than 150 mV/s.

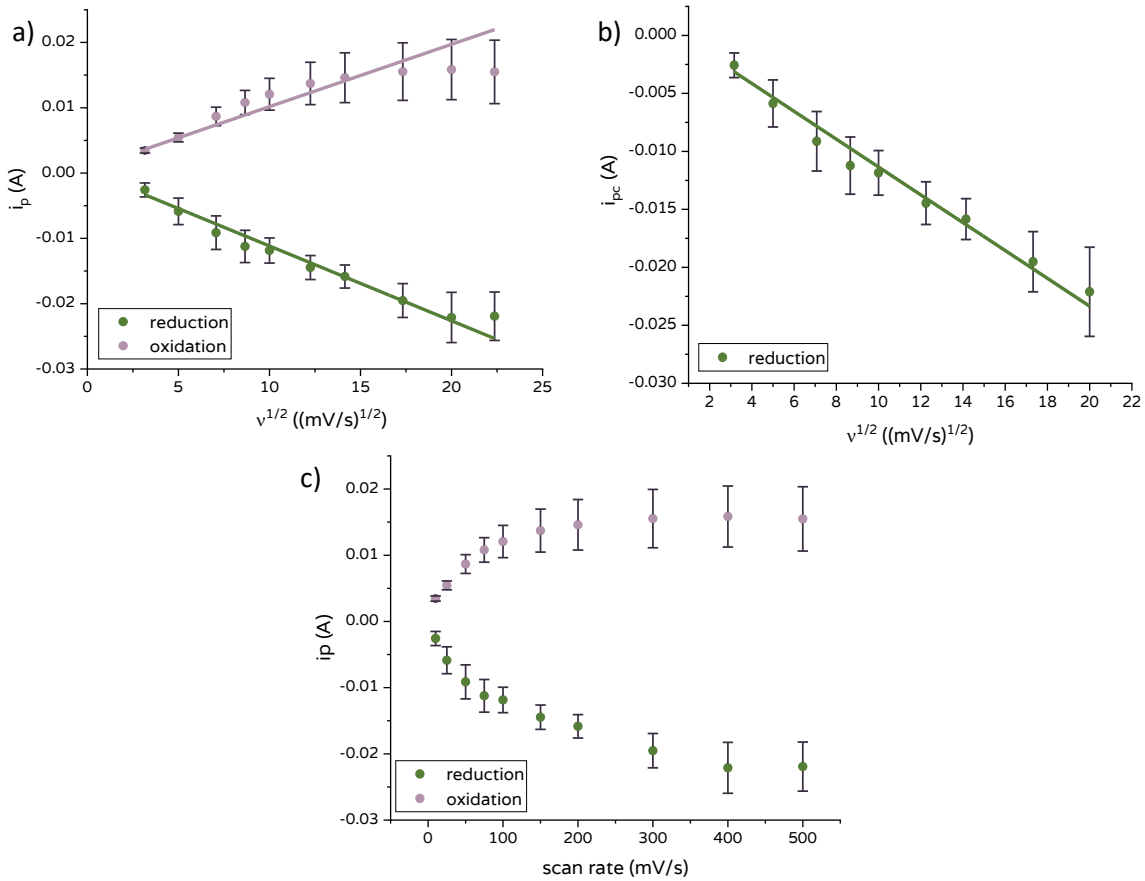

Figure A.3.4: a) i_p for both cathodic and anodic processes vs square root of scan rate obtained with Bi cylinder electrodes from the scan rate study; b) cathodic branch obtained at scan rate values between 10 and 400 mV/s; c) plot of the i_p vs scan rate

The fitting for Figure 3.13c, 3.15c, A.3.1c and A.3.2b was described by the Equation (A.1)

$$y = y_0 + A1\left(1 - e^{-\frac{x}{t_1}}\right) + A2\left(1 - e^{-\frac{x}{t_2}}\right) \quad \text{(A.3)}$$

3.3.5 Heterogeneous electron transfer rate constant

3.3.5.1 Na_2SO_4 solutions

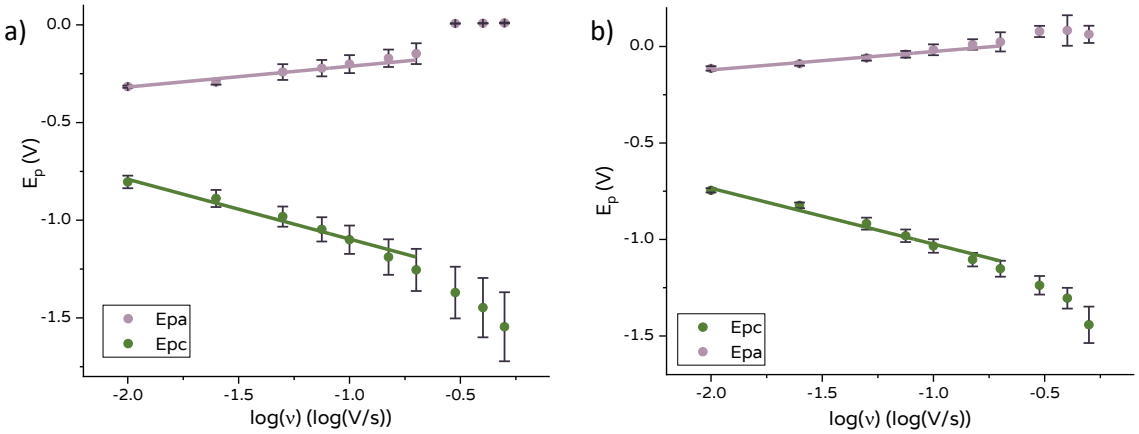

Figure A.3.5: Peak potential as a function of the logarithm of the scan rate for the oxidation (purple) and reduction (green) of Bi in 0.1 M Na_2SO_4 saturated with a) N_2 b) CO_2. Linear fit was calculated for scan rate range between 10 and 200 mV/s. The E_p used was not corrected for the iR drop potential

The E_p values were not corrected for the iR drop because of the high experimental error obtained in Na_2SO_4 solutions after mathematical correction (see Section 3.3.4.1). However, it is important to highlight that effects of the ohmic drop are very similar to those due to the low kinetics of a reaction[277]. In Figure A.3.5a, the values of E_p for the cathodic (green) and anodic (purple) processes are shown as a function of the logarithm of the scan rate for the N_2-saturated Na_2SO_4 solution. The linear fit for the entire data set presented an R^2 value of 0.82 and 0.95 for the anodic and cathodic branches, respectively. If the linear fit was calculated for scan rates between 10 and 200 mV/s, the R^2 increased to 0.93 and 0.97 for the anodic and cathodic branches, respectively. Considering the fact that the E_p used here are the not corrected for the iR drop, the deviation from the linearity of the last points clearly seen in the graph may be due to the high iR drop at large scan rates. The two branches are well separated and do not share any points, confirming complete irreversibility of the process[278]. In the presence of CO_2 (Figure A.3.5b) a similar trend was observed: by using the entire data set for the linear fit, R^2 values equal to 0.93 and 0.97 were obtained for the anodic and cathodic branches, respectively. However, when the scan rate range was limited between 10 and 200 mV/s, R^2 increased to 0.95 for the anodic process and to 0.97 for the cathodic. The result of α and k^0 are shown in Table A.3.5. The transfer coefficient was calculated using a number of electrons equal to three, as it is the number of electrons exchanged for one atom of Bi (see Reaction r1.8 in Chapter 1). The value of α for the reduction process in N_2- and CO_2-saturated solutions are comparable (see Table A.3.5), meaning that the energy barrier is similar for the reduction process in the presence or absence of CO_2 (α was equal to 0.051 and 0.062). On the other hand, α is higher for the oxidation

in N_2- than in CO_2-saturated solutions, suggesting that the presence of CO_2 increases the energy barrier for the oxidation of the Bi metal. The rate constants for the oxidation are five and six orders of magnitude higher than the reduction for the systems saturated in N_2 and CO_2, respectively (see Table A.3.5). This suggests that the reduction process is a slower process than the oxidation and even slower in CO_2-saturated solutions. The heterogeneous electron transfer rate constants for the anodic process, k^0_a, and for the cathodic process, k^0_c, are slightly higher for CO_2-saturated solutions than for N_2-saturated solutions. Specifically, k^0_a and k^0_c are x1.5 times and x1.2 times higher, respectively, in CO_2-saturated solutions. This suggests that both the oxidation of Bi and the reduction of Bi oxide are faster in the presence of CO_2. This is in not in agreement with the ΔE_p values, which suggested slightly faster kinetics in N_2-saturated solutions than in CO_2-saturated solutions. This difference can be due to the inability of the Laviron method to adequately describe the kinetics of the system.

Table A.3.5: values of the electron transfer coefficient and heterogeneous electron transfer rate constant; the value of the slope form the linear fitting of the graph Ep vs the log(scan rate) are shown for both oxidation and reduction in the 0.1 M Na_2SO_4 N_2 and CO_2 saturated solution

gas	process	slope	α	k^0 [s^{-1}][a]
N_2	oxidation	0.158 ± 0.005	0.875 ± 0.004	0.73 ± 0.02
	reduction	-0.38 ± 0.01	0.051 ± 0.001	3.2 (± 0.1) x10^{-6}
CO_2	oxidation	0.11 ± 0.02	0.81 ± 0.03	1.1 ± 0.2
	reduction	-0.32 ± 0.02	0.062 ± 0.004	3.7 (± 0.2) x10^{-6}

[a]calculated for v = 50 mV

3.3.5.2 $KHCO_3$ solutions

When the experiments were performed in $KHCO_3$ solutions, The α values for the oxidation presented slightly higher values in the presence of CO_2, while the α values for the reduction are comparable regardless of the gas used for saturating the solution (see Table A.3.6). In addition, similar values of α were obtained for the reduction process in both $KHCO_3$ and Na_2SO_4, suggesting that the energy barrier for the reduction of Bi oxide is not significantly influenced by the nature of the electrolyte. For the anodic process, a slight difference was observed in the values of α when the two different electrolyte solutions were compared.

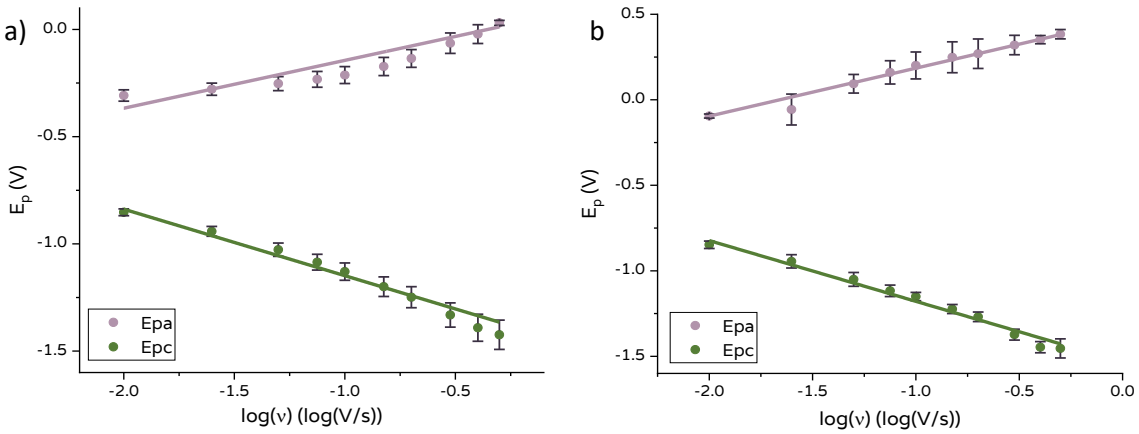

Figure A.3.6: Peak potential as a function of the logarithm of the scan rate for the oxidation (purple) and reduction (green) of Bi in 0.1 M $KHCO_3$ saturated with a) N_2 b) CO_2. The E_p used was not corrected for the iR drop potential.

However, the difference is negligible, as in both cases α > 0.8. In general, α values deviate significantly from the typical assumed value of 0.5. However, values between 0.3 and 0.7 are usually observed[98]. Within this work, the values obtained do not lay between the expected range, suggesting that the Laviron method might not adequately describe the system. The k^0 values are five orders of magnitude higher for the oxidation process than for the reduction process.

Table A.3.6: values of the electron transfer coefficient and heterogeneous electron transfer rate constant; the value of the slope form the linear fitting of the graph Ep vs the log(scan rate) are shown for both oxidation and reduction in the 0.1 M $KHCO_3$ N_2 and CO_2 saturated solution

gas	process	slope	α	k^0 [s^{-1}][a]
N_2	oxidation	0.13 ± 0.01	0.84 ± 0.01	0.92 ± 0.08
	reduction	-0.31 ± 0.02	0.063 ± 0.004	3.8 (±0.2) x10^{-6}
CO_2	oxidation	0.31 ± 0.04	0.936 ± 0.008	0.38 ± 0.05
	reduction	-0.33 ± 0.01	0.060 ± 0.003	3.6 (±0.2) x10^{-6}